Growth, Structure, and Desalination of Refreezing Cracks in Sea Ice

Christian Petrich

a thesis submitted for the degree of

Doctor of Philosophy

at the University of Otago, Dunedin,

New Zealand.

13 December, 2004

Abstract

The aim of this study is to characterise the structure of refrozen cracks, and to deduce the details of their formation. Surveys and experiments are conducted on straight–sided, linear, refrozen cracks of width 80 mm to 340 mm in land–fast first–year sea ice in McMurdo Sound, Antarctica. Refreezing of cracks is simulated analytically, and with a numerical fluid dynamics model of brine movement in the porous sea ice and in the ocean. Systematic arch–shaped patterns of inclusions, upstream–growing crystals, and two–dimensional variations in salinity are identified in completely and partially refrozen, natural cracks, and in artificial cracks.

Using a two–dimensional thermistor array, a relationship between the development of the sea ice structure and the temperature records is found, which identifies the transition from the porous, skeletal layer to consolidated ice in artificial cracks. A two–dimensional analytical model is developed that predicts the measured thickness of consolidated ice in refreezing cracks for this study and for the studies of others. From a heat balance within the refreezing cracks, it is concluded that some of the experiments were conducted in the presence of a negative ocean heat flux. A two–dimensional thermistor array beneath the ice–water interface of a refreezing crack provides evidence for sporadic, cold temperature, advective events at night.

A two–dimensional, numerical fluid dynamics model based on the finite volume method is developed to simulate desalination and fluid flow in refreezing cracks. This requires a permeability–porosity relationship for sea ice, which is deduced from data of other groups, combined with the numerical model. To make comparisons among data sets, an analytical approximation is derived for the relationship between connected pore space and total

pore space of a random porous medium, based on a Monte Carlo model that is adapted to the crystal structure of sea ice. The permeability–porosity relationship derived in this study is in good agreement with permeability functions published recently.

The refreezing of cracks simulated with the numerical fluid dynamics model is consistent with experiments and with the analytical model. In addition, the numerical model simulates the high porosity, arch–shaped freezing front and inclusion structure. Supercooling of the liquid is found to cause excessive heat loss in the simulation. Since a large oceanic heat flux was not observed in the experimental heat balance of refreezing slots, it is suggested that this indicates platelet ice formation or frazil ice formation at the vertical crack interface in Antarctic experiments.

In memory of

Edward and Elke Petrich

Acknowledgements

Thanks a million to Pat Langhorne for supervising my project, for always having time for me and my obscure ideas, and for even working to my schedule. And thanks for fantastic cooking. Thanks to my co–supervisor Zhifa Sun for taking the time to get me going on volume integration, and for encouraging me to do it properly. Thanks to Greg Leonard and Craig Purdie for their cooperation with the numerical simulations. Thanks to my office mates Greg Leonard, Craig Purdie, and Nicole Albrecht for making the office and everything else fun, and for a steady stream of feedback on my project. Thanks to Alice Langhorne for proofreading parts of the appendix. Thanks to Marty Gribble for expressing his hope for my survival of my Ph.D. time in his acknowledgements. I guess I know what he means. And I pass on my hope to Craig: don't panic, mate.

Thanks to the governance of the Physics Department for all the support throughout the years: to Brenda Tustin, Trish Knox, and Joanna Baxter Fielding, to Helen Wreford and Sandy Wilson. They actually managed to make the start of my day delightful. Thanks to Gerry Carrington for lending me his office heater.

Thanks to Neil Thomson, Dave Hardisty, and Myles Thayer for their substantial contribution to the practical aspects of the design, and to the production of the thermistor probes. Thanks to Peter Stroud for designing and building the Antarctic–proof gear; and thanks to Barbara Buchanan and to Dale Watts for their fabulous support in all of this. Thanks to Nicola van Leeuwen for adjusting her project schedule to Antarctic field seasons. Thanks to the late Colin Wells for his enthusiasm to introduce me to the CR10X, and thanks for the wind vane. Thanks to Brent Russell, Terry Cole, Peter Simpson and Peter McCabe for somehow managing to keep the network alive. Thanks to Craig Rodger for recommending to save data in the good ol' ASCII format: that was definitely a good one.

Thanks to Hajo Eicken for giving me encouragement from the world outside every once in a while. Also thanks for providing me with INTERICE data. Thanks to Dave Cole for always being a great source of thoughts and anecdotes. Thanks to Joe Trodahl, to Christian Haas, and to Larry Taylor for their comments on sea ice and cracks. Thanks to Daniel Pringle for trying

to pick me up from a flight that I missed, and to him and to jet–lagged Amy Heaton for the nice chat on sea ice percolation that followed my eventual arrival.

Thanks to Antarctica New Zealand for logistical support in every aspect of the field programme; thanks to Paul Woodgate for an unheard–of support of field parties.

Thanks to Tim Haskell for running the world–famous and most amazing Antarctic sea ice camp ever. And thanks for getting his hands dirty for me on the ice. Thanks to Simon Gibson for excitingly straight slots cut through 2 m of sea ice, and to Dave Cochrane for the chain–saw arts on my ice samples. Thanks to Jonathan Leich for handling all sorts of machinery when Dave and Simon weren't around.

Thanks to Jeff "The Chef" Reid for preparing extra large cream doughnuts for me at Scott Base. Thanks to Dave Cole for sharing interest in what I was doing during my first season on ice. Thanks to Dave Cole, John Dempsey, Saul Shapiro, and Jeff Morley for providing me with lunch at 5 pm and for stopping by at our camp to share their spirit with us.

Thanks to whoever is in charge of supplying field parties with "Bumper Bars" that are at least two years past their best–before date. They became my best friends on the ice. Thanks to Jean–Louis Tison for banana flambe at Cape Evans. Thanks to Lisa Holliday for the trip to the ice caves, and for her concern for my safety on the way back. Thanks to Max Quinn for waking me up for a meal of hot mince in dough with sauce served by the New Zealand Airforce towards the end of a flight in a Hercules bringing us home from McMurdo Sound after I've slept on top of a pile of cargo boxes for five hours. Thanks to the 2001 crew of flight KCH 003 for serving this delicious, hot meal in the first place.

Thanks to everyone who contributed to make my life more sociable and to give me a break from my studies. Thanks in particular to everyone who put me up during my time as a Ph.D. student. They are, roughly in order of appearance: Ilse Petrich and Peter Hahn in Lübeck, Germany; Wiebke Drenckhan and Jürn Schmelzer in Christchurch, New Zealand; Robert Scurr in Christchurch, New Zealand; Pam, Steve, Andrew and Daniel Cook in Raleigh, NC, USA; Koichi, Aiko and Satoshi Naniwae in

Tsukuba Science City and in Ritto, Japan; Glyn and Dafydd Richards in Auckland, New Zealand; Hilde and Manni Strawe in Pönitz, Germany; Inge Sievers in Bad Schwartau, Germany; Valeska Foltin in Hamburg and in Marburg/Lahn, Germany; Sebastian Grübel in Phnom Penh, Cambodia and in Berlin, Germany; Ronald Hattwig and Petra Goldschmidt in Travemünde, Germany; Jane, Uwe, Luca, and my goddaughter Lily Dahl in Berlin, Germany; Martin Lenz in Frankfurt/M, Germany; Erica Robertson in Adukrom E/R, Ghana; Kristin Cannon in Baotou, China; Quick in Ulaanbaatar, Mongolia; Liudmila and Andrew Pyalling and family in Akademgorodok/Novosibirsk, Russian Federation; Alexey, Natalia and Olga Pyalling in Chernogolovka, Russian Federation; Hauke Juranek in Rostock, Germany; Hans–Friedrich Foltin in Marburg/Lahn, Germany; Hermann, Renate, Sarah and Jan Hilmer in Braunlage, Germany; and Ms. Heintz in Hannover, Germany. Thanks also to everyone who's storing my stuff "only for one year" for six years now: Ilse Petrich and Peter Hahn; Franziska and Andreas Klemm; Hilde and Manfred Stawe; and Inge Sievers.

The research was funded by the Foundation of Research, Science & Technology, New Zealand. Field work was supported by Antarctica New Zealand. I was financially supported during my Ph.D. programme by a University of Otago postgraduate scholarship, the Beverly Fund, the Emerging Research Theme "Antarctic science and marine environments of the Southern Ocean", and the Division of Science, all of them at the University of Otago; the field event K131; student travel support provided by IAHR; student travel support provided by the Atlantic Canada Opportunities Agency; and travel support provided by the Trans–Antarctic Association. Thanks.

Contents

List of Tables

List of Figures

Nomenclature

Symbol	Description
a	Length (m); Coefficient; Matrix coefficient
a_0	Length
b	Length; Coefficient
c	Specific heat capacity ($\mathrm{J\,kg^{-1}\,K^{-1}}$);
	Cloud cover fraction
d	Length; Julian day; Transport coefficient
d_0	Dimensionless length
du	Matrix coefficient
dv	Matrix coefficient
e	Vapour pressure (Pa); Error
f	Porosity; Source term; Frequency (Hz)
g	Acceleration due to gravity ($\mathrm{m\,s^{-2}}$)
h	Length (m); Volumetric enthalpy ($\mathrm{J\,m^{-3}}$)
$\mathfrak{h}$	Heat transfer coefficient ($\mathrm{W\,m^{-2}\,K^{-1}}$)
i	Complex number ($i^2 = -1$)
i_0	Coefficient
$\mathbf{j}$	Flux
k	Thermal conductivity ($\mathrm{W\,m^{-1}\,K^{-1}}$)
k_{eff}	Distribution coefficient
l	Length (m); Amount of ozone (cm(NTP))
m	Slope of the liquidus ($\mathrm{K\,m^3\,kg^{-1}}$ or $\mathrm{K\,psu^{-1}}$);
	Mass (kg); Transport coefficient
n	Unit distance normal to a surface
p	Pressure (Pa)
r	Length (m); Length ratio;
	Relaxation factor; Residual
s	Length (m)
s_P	Source term
t	Time (s)
u	Velocity ($\mathrm{m\,s^{-1}}$)
$\mathfrak{u}$	Function
v	Velocity ($\mathrm{m\,s^{-1}}$); Volume
w	Horizontal length (m); Precipitable water (cm)

Symbol	Description
x	Length or coordinate (m)
y	Length or coordinate (m)
z	Length or coordinate (m); Dimensionless coordinate
A	Area (m^2); Matrix of transport coefficients; Coefficient
$\mathcal{A}$	Coefficient
B	Coefficient
C	Solute concentration ($kg\,m^{-3}$); Capacitance (F); Coefficient
C_s	Sensible heat transfer coefficient
D	Solute diffusivity ($m^2\,s^{-1}$); Spectral irradiance ($W\,m^{-2}\,\mu m^{-1}$)
$\mathcal{D}$	Coefficient
DC	Dissipation constant ($W\,K^{-1}$)
E	Electric field ($N\,C^{-1}$)
F	Flux ($W\,m^{-2}$); Force (N)
G	Spectral irradiance ($W\,m^{-2}\,\mu m^{-1}$)
H	Length (m); Enthalpy (J)
I	Spectral irradiance ($W\,m^{-2}\,\mu m^{-1}$); Operator
$I^{(2)}$	Identity tensor
L	Latent heat of fusion ($J\,kg^{-1}$); Linear size
M	Mass (kg)
MB	Mass imbalance
N	Number of samples
P	Power (W)
R	Flow resistance (m^{-2}); Resistance (Ω)
$\mathcal{R}$	Constant ($m^2\,s^{-1}$)
RH	Relative humidity
S	Salinity (psu)
T	Temperature (K or °C)
$\mathcal{T}$	Coefficient
V	Volume (m^3); Electric potential (V)
α	Albedo; Coefficient
β	Coefficient
γ	Coefficient; Free parameter; Phase factor
δ	Coefficient; Declination
ϵ	Temperature difference (°C); Emissivity
θ	Temperature difference (K); Zenith angle

Symbol	Description
κ	Thermal diffusivity ($\mathrm{m^2\,s^{-1}}$);
	Extinction coefficient ($\mathrm{m^{-1}}$); Coefficient
λ	Wavelength (m)
μ	Viscosity ($\mathrm{kg\,m^{-1}\,s^{-1}}$); Mean value
ν	Coefficient
ρ	Density ($\mathrm{kg\,m^{-3}}$); Albedo
σ	Standard deviation;
	Stefan–Boltzmann constant ($\mathrm{J\,K^{-4}\,m^{-2}\,s^{-1}}$)
$\sigma^{(2)}$	Stress tensor ($\mathrm{kg\,m^{-1}\,s^{-2}}$)
τ	Dimensionless time; Transmission coefficient
ϕ	Angle; Latitude
ω	Frequency ($\mathrm{s^{-1}}$); Hour angle; Coefficient
Γ	Diffusion coefficient ($\mathrm{m^2\,s^{-1}}$)
Π	Permeability ($\mathrm{m^2}$)
Φ	Flux; Intrinsic property
Ψ	Intrinsic property

Chapter 1

Introduction

1.1 Overview

The objective of this study is to investigate the refreezing process, desalination, and refrozen structure of straight–sided cracks in land–fast first–year sea ice. A crack is defined as a fracture of fast ice, consolidated ice or a single floe which may have been followed by separation ranging from a few centimetres to 1 m (*WMO*, 1970).

Refreezing cracks affect the heat exchange between ocean and atmosphere. They affect ocean currents due to the rejection of dense, saline brine. Knowledge of properties of refrozen cracks is needed for the safety of operations on sea ice (*Kingery and Coble*, 1963), as they may be of different thickness and strength to the surrounding host ice (*Langhorne and Haskell*, 2004). Refrozen cracks are the starting points for break–up of sea ice in summer. Compared to the surrounding ice, they may be thinner, absorb more solar radiation as they may have a lower albedo, have a higher salinity, have increased capabilities to drain meltwater, and collect meltwater from the surrounding ice sheet, further reducing their albedo (*Perovich et al.*, 2001; *Eicken et al.*, 2002). Once partially melted, they are pathways for meltwater with the potential for bottom ice formation in summer (*Eicken et al.*, 2002). Cracks, like any other inhomogeneity in ice sheets, are a source of scatter of ocean waves, potentially affecting the mechanical break–up of ice sheets (*Barrett and Squire*, 1996; *Langhorne et al.*, 1998; *Williams and Squire*, 2002). Sea ice can be used as a model for the formation of hexagonal alloys. The analogy of the growth process of sea ice and alloys from either a horizontal or a vertical interface has previously been exploited (*Wettlaufer et al.*, 1997; *Bergman et al.*, 2003). The growth process and the structure of sea ice in refrozen cracks are similar to alloy casts (*Kurz and Fisher*, 1998). Refreezing cracks, due to their bidirectional growth, are suitable systems to test theories of ice growth developed for unidirectional

growth of sea ice sheets.

This project comprises observations of structure and salinity of refrozen cracks (Chapter 2); of measurements and an analytical model of the freezing front movement during crack refreezing experiments, a heat balance estimate for the experiments, and an analysis of brine rejection during refreezing (Chapter 3); and of fluid dynamics simulations of refreezing and solute distribution in refrozen cracks (Chapter 6). For the analysis of refrozen cracks, concepts of unidirectional formation of sea ice sheets will be applied to the bidirectional refreezing. However, some of the concepts will have to be developed first. The definition of the freezing front of sea ice from temperature measurements is discussed (Chapter 3); a numerical, fluid dynamics model for sea ice is developed (Chapter 4); and desalination of sea ice sheets is revisited, the permeability of growing sea ice is determined as a function of porosity, and a relationship between connected and total pore space is estimated (Chapter 5).

While fluid dynamics simulations of unidirectional sea ice sheet formation have recently been reported (*Oertling and Watts*, 2004), the underlying model has some shortcomings that make it appear unsuitable for the simulation of refreezing cracks (Section 1.5). Further, a permeability parameterisation has recently been reported (*Eicken et al.*, 2004) that is of a suitable form for the modelling of fluid flow in sea ice with the model of Chapter 4. However, this parameterisation was not available at the time it was needed, which is the reason for the development of such a parametrisation in Chapter 5. A comparison between the developed parameterisation and the reported parameterisation of *Eicken et al.* is nonetheless included in Chapter 5.

This thesis is structured as follows. First, an introduction is given to ice, sea ice (Section 1.2), and some fundamental mechanisms of fluid flow though sea ice and of sea ice desalination (Section 1.3). The relevant literature is reviewed on cracks (Section 1.4) and on two–dimensional numerical modelling of fluid flow through sea ice (Section 1.5). Then, the observed crystal and inclusion structure of natural, refrozen cracks (Section 2.2.1) and crack refreezing experiments (Section 2.2.2) in land–fast first–year sea ice in McMurdo Sound are presented. Vertical salinity profiles of natural cracks and experiments are given in Section 2.2.4. Each refreezing experiment contains one of two two–dimensional thermistor arrays designed to track either the freezing progress (probe 1, Section 3.2), or water temperature variations in the water column during freezing (probe 2, Section 3.3). After the definition of the freezing front (Section 3.2.3), freezing front movement in refreezing cracks is modelled and compared to present measurements and measurements of other groups (Section 3.2.4). The transient heat balance is calculated for experiments with probe 1 in Section 3.2.5. The transient behaviour of brine release detected with probe 2 is investigated in Section 3.3.3. Water

temperature signals, detected with both probe 1 and probe 2, and their relationship to solar radiation are discussed in Section 3.4.

The underlying assumptions and the governing equations of the fluid dynamics model are presented in Section 4.2, and numerical methods are introduced (Section 4.3). A treatment of the numerical freezing front is developed in Section 4.4, which is specific to the case of solidification of a binary liquid at its freezing point. The governing equations of the fluid dynamics model demand a parameterisation of sea ice permeability. The permeability is derived from sea ice desalination measurements of *Cox and Weeks* (1975). The stable solute distribution of a sea ice sheet is parameterised (Section 5.2), and, following that, the permeability–porosity parameterisation is derived (Section 5.3) and compared to measurements of both *Freitag* (1999) and *Eicken et al.* (2004) (Section 5.4). To compare the permeability parameterisation with measurements of *Freitag*, a relationship between effective and total porosity of sea ice is estimated numerically with a Monte Carlo percolation model, and an analytical approximation is given (Section 5.4.3). After the validation of the fluid dynamics model for unidirectional sea ice formation (Section 6.3), refreezing of cracks is simulated with this model as introduced in Chapter 4, and with two different modifications (Section 6.4). The results clarify characteristics of refrozen cracks shown in Chapter 2, and lend further credibility to analytical freezing front model of Chapter 3. The major findings of this thesis are summarised, and future research is suggested in Chapter 7.

1.2 The formation of ice in nature

This brief overview delineates sea ice from other forms of ice. It is obviously incomplete and does not attempt to do justice to the many interesting aspects of each topic.

Extraterrestrial formation Very small ice crystals (nano–crystals) occur naturally in interstellar dust (*Allamandola et al.*, 1999), amorphous ice is found on comets ("dirty snowballs" (*Whipple*, 1976)), and crystalline ice appears on planets and moons (*Zimmer et al.*, 2000; *Vondrak and Crider*, 2003).

Formation in the atmosphere On Earth, ice is a constituent of polar stratospheric clouds and of cirrus clouds, and ice is fundamentally involved in charge transfer during thunderstorm development (*Baker*, 1999; *Wettlaufer*, 1999; *Zondlo et al.*, 2000; *Dash and Wettlaufer*, 2003). It is further observed, for example, as atmospheric ice crystals (*Baker*, 1999; *Walden et al.*, 2003), on airplane wings (*Ashenden and Marwitz*, 1997; *Petrenko and Whitworth*, 1999; *Lynch and Khodadoust*, 2001), and as freezing

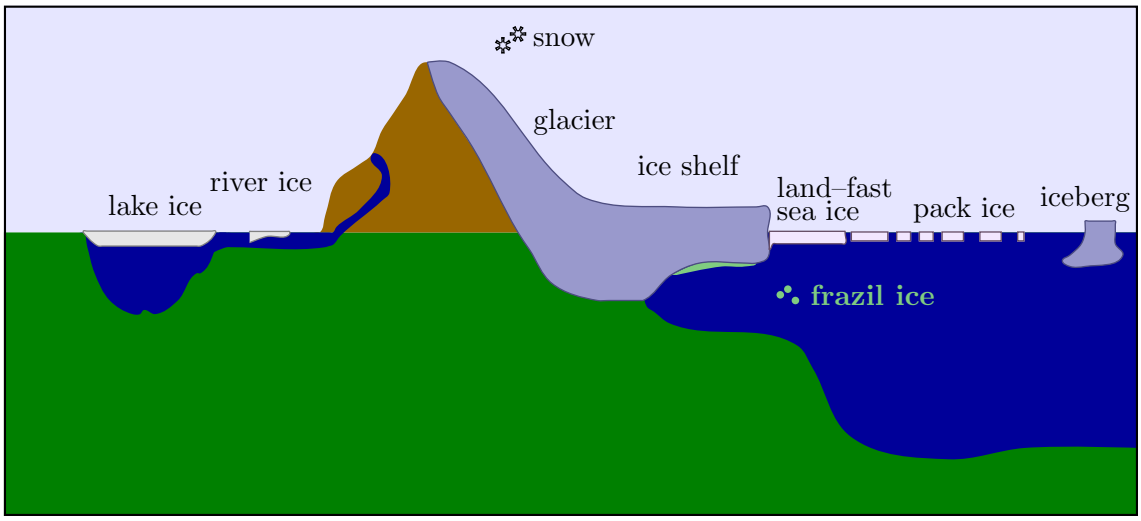

Figure 1.1: Examples of naturally occurring ice with relation to sea ice. The sketch is not to scale.

precipitation on the ground (*Cortinas et al.*, 2004). At medium to high latitudes, ice is commonly found as snow and hail (*List and Schemena*, 1971). In particular, snow that accumulates over a very long period of time may form glaciers and ice caps (*Sharp et al.*, 1994; *Fitzharris et al.*, 1999) (Figure 1.1). Ice shelves form where glacial ice flows onto the sea to produce a rather flat slap of floating ice (*Thomas*, 1979). Icebergs calve from glaciers or ice shelves (*Frezzotti*, 1997).

Subsurface formation Moist soil may freeze in a very dynamic process producing frost heave (*Williams*, 1999; *Wettlaufer*, 1999), or it may be frozen year round, which is called permafrost (*Romanovskii et al.*, 2004). Gas hydrates are solid crystalline inclusion compounds consisting of a hydrogen–bonded water network which encage small gas molecules, for example methane (*Koh*, 2002). They can form in low temperature, elevated pressure environments in the presence of a flux of gas; conditions that can be met for example at the bottom of deep lakes, oceans or in permafrost (*Max and Lowrie*, 1996; *Kuz'min et al.*, 2001).

Formation from the liquid River ice (Figure 1.1) attracts engineering attention since it can jam as a result of the accumulation of either surface ice rubble or frazil ice slush. There is then a possibility of creating an ice run and a sudden release of large amounts of water (*Prowse and Beltaos*, 2002; *Shen and Liu*, 2003). Lake ice is closely related to sea ice, although the different salt content of seawater and lakewater results in significant structural differences (*Weeks and Wettlaufer*, 1996). Frazil ice, or platelet ice, are ice crystals that may form in the water body in the presence of

freshwater and/or saltwater below its freezing temperature (i.e. in supercooled water) (*Dieckmann et al.*, 1986; *Drucker et al.*, 2003). Such conditions can be met under ice shelves and in their vicinity, probably due to a convective process that involves dissolution of ice (*Woods*, 1992) at the base of the ice shelf (*Jenkins and Doake*, 1991; *Souchez et al.*, 1991). Further, in the vicinity of ice shelves at certain times of the year, ice platelets grow attached to the seafloor in shallow waters, where it is called anchor ice[1] (*Dayton et al.*, 1969), to manmade structures in the water (*Dayton et al.*, 1969; *Hunt et al.*, 2003; *Leonard et al.*, unpublished 2004), and to sea ice (*Dayton et al.*, 1969; *Jeffries et al.*, 1993; *Leonard et al.*, unpublished 2004). In the latter two cases, it is usually called platelet ice. Frazil ice that deposits at the underside of ice shelves is called marine ice. It is of very low salinity compared with sea ice, and it can reach thicknesses of over 100 m (*Oerter et al.*, 1992; *Moore et al.*, 1994; *Eicken et al.*, 1994; *Fricker et al.*, 2001; *Tison et al.*, 2001). Frazil ice crystals are further formed at the ocean–atmosphere interface if temperatures are low and the sea is sufficiently rough to incur turbulent mixing (*Weeks and Ackley*, 1986; *Ushio and Wakatsuchi*, 1993).

Sea ice Ice that forms from seawater is called sea ice (*WMO*, 1970). It consists, to a varying degree, of an amalgamation of columnar (congelation) ice, i.e. ice that grows due to a heat flux to the atmosphere; of frazil ice crystals; of platelet ice crystals; and of frozen snow and meltwater (*Weeks and Ackley*, 1986; *Gow and Tucker*, 1990; *Eicken*, 1992; *Jeffries et al.*, 1993; *Doble et al.*, 2003; *Eicken*, 2003). The formation process, and therefore structure and thickness, are somewhat different for ice that grows under relatively calm conditions, for example attached to glaciers or land (land–fast sea ice), and ice that grows under rougher conditions, for example away from the shore (pack ice). Specifically, frazil accumulation and rafting or ridging have been observed to have a larger contribution to sea ice thickness than congelation ice formation in the Weddell Sea (*Lange and Eicken*, 1991), in the outer pack ice in the Ross Sea (*Jeffries and Adolphs*, 1997), and in the Sea of Okhotsk (*Toyota et al.*, 2004). Alternatively, columnar ice dominates in the inner pack ice in the Ross Sea (*Jeffries and Adolphs*, 1997), the land–fast sea ice in McMurdo Sound (*Jeffries et al.*, 1993; *Jones and Hill*, 2001), and in the Eurasian sector of the Arctic (*Eicken et al.*, 1995b). The mechanisms of rafting

[1]Anchor ice is also observed in rivers, lakes, and in Arctic coastal polynyas even though no ice shelf is present in these cases (*Benson*, 1955; *Nürnberg et al.*, 1994; *Kempema et al.*, 2001): it has been suggested that the necessary supercooled water forms by cooling of the river or lake bed due to radiative heat loss at night (*Benson*, 1955). The term anchor ice is used to describe either flocks of frazil ice crystals or growing ice platelets located at the ground (*Kempema et al.*, 1993). Platelets growing on the underside of sea ice have been observed in the Arctic, where sea ice melting mechanisms have been suggested to produce the supercooled water necessary for their formation (*Eicken*, 1994; *Jeffries et al.*, 1995).

and ridging have been compared in a study in the Bellinghausen and Amundsen Seas (*Worby et al.*, 1996), where it was found that sea ice thickens by rafting in the early stages of growth (thinner than 0.3 m), and by ridging (*Tin and Jeffries*, 2003) once the ice is thicker than 0.6 m.

Sea ice is not a single phase material. It contains inclusions of liquid brine that carry up to 1 % of the mass of the ice sheet in the form of dissolved salts, and it may contain sand (*Nürnberg et al.*, 1994; *Eicken et al.*, 1997), bacteria (*Lizotte*, 2003; *Junge et al.*, 2004), algae (*Fritsen et al.*, 1994; *Thomas and Dieckmann*, 2002; *Arrigo*, 2003), foraminifer (*Dieckmann et al.*, 1991) and other small animals (*Schnack-Schiel*, 2003), and pollutants such as organochlorines, radionuclides, and heavy metals (*Pfirman et al.*, 1995). Here we are concerned with land–fast sea ice, with structural components of columnar, frazil, and platelet ice. Further, brine inclusions and algae will be considered.

1.3 The formation of saline ice

Planet Earth has a mass of about 6.0×10^{24} kg (*Blewitt and Clarke*, 2003), 1.4×10^{21} kg of which is due to water (*Harrison*, 1999). Despite its pervasiveness, the structure of liquid water is still evasive, and theories still do not reproduce all experimental observations (*Zubavicus and Grunze*, 2004). Probably the most commonly known anomaly of water is that its density decreases as the temperature drops below 4 °C (*Mishima and Stanley*, 1998; *Tanaka*, 2000). An explanation of this observation has been offered by *Röntgen* (1892), who does not, however, claim ownership of the idea. According to the picture by *Röntgen*, water is a microscopic mixture of two different types of water "molecules", one of which is similar in properties to ice (e.g. in density). Upon change of temperature, the "molecules" undergo a continuous transition in stoichiometry. Water molecules consist of two hydrogen atoms (or isotopes thereof) bonded to one oxygen atom (*Lock*, 1990). Modern theories in the spirit of *Röntgen* therefore employ changing short range order of water molecules to explain the density anomaly of water (*Vedamuthu et al.*, 1994). The density anomaly is of profound significance to life in frozen lakes as it causes them to freeze in stable temperature stratification from the top downwards.

Effect of solute on liquid density and freezing point Ions in water shift the temperature of maximum density towards lower temperatures, so that it eventually falls below the freezing point (Figure 1.2; *Weeks and Wettlaufer*, 1996). However, the freezing point also depresses upon the addition of ions (*UNESCO*, 1983). The latter observation, i.e. that the freezing point depression is proportional to the concentration of the dissolved particles (Raoult's law, *Landau and Lifshitz* (1959); *Fletcher* (1993)),

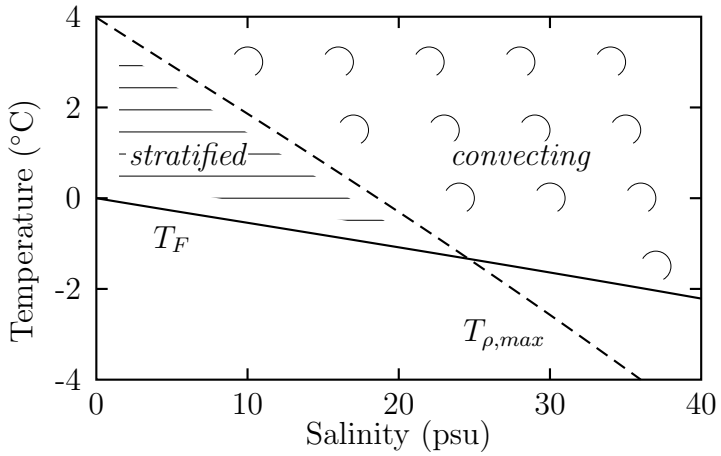

Figure 1.2: Freezing point, T_F, (solid line) and temperature of maximum density, $T_{\rho,max}$, (broken line) of seawater as a function of salinity. Water cooled from above is either stratified or convecting, depending on temperature and salinity.

can be quantified using intriguing analogies involving pistons, cylinders, and semipermeable membranes (*van't Hoff*, 1887). *van't Hoff* shows how the osmotic pressure of dissolved ions shifts the equilibrium between solid and liquid to lower temperatures. Raoult's law, however, is only approximately valid. Strong electrolytes (salts such as NaCl) that completely decompose into ions in solution exhibit a significant electrostatic attraction onto each other, even at low concentrations. This effect has been quantified by *Debye and Hückel* (1923). Figure 1.2 shows that a concentration exists (25 psu for seawater; water in McMurdo Sound is approximately 34 psu) beyond which the temperature of maximum density is below the freezing point (*Josberger and Martin*, 1981; *UNESCO*, 1981b, 1983; *Brewster and Gebhart*, 1994; *Weeks and Wettlaufer*, 1996). Surface cooling of saltwater of solute concentration above this threshold results in the densest water being located at the surface. This leads to convective mixing until the entire water body reaches the freezing point (*Gow and Tucker*, 1990).

Solute exclusion from the ice crystal lattice and entrapment in sea ice The crystal structure of ice that forms from water under atmospheric conditions is termed Ih (*Lobban et al.*, 1998), where the roman 1 is the number of the crystal structure and the letter "h" indicates that the structure is hexagonal (*Glen and Perutz*, 1954). Figure 1.3 illustrates the hexagonal crystal structure. Oxygen atoms, separated 2.76 from each other, are arranged in tetrahedral configuration, maintaining two covalent bonds and two hydrogen bonds per atom to protons (*Lock*, 1990). Since few ions are incorporated into the ice crystal itself (*Buchanan*, 1887a, b; *Whitman*, 1926; *Harrison and Tiller*, 1963; *Moore et al.*, 1994; *Cullen and Baker*, 2001; *Iliescu et al.*, 2002; *Baker et al.*, 2003), these are rejected into the liquid adjacent to the ice crystal during growth.

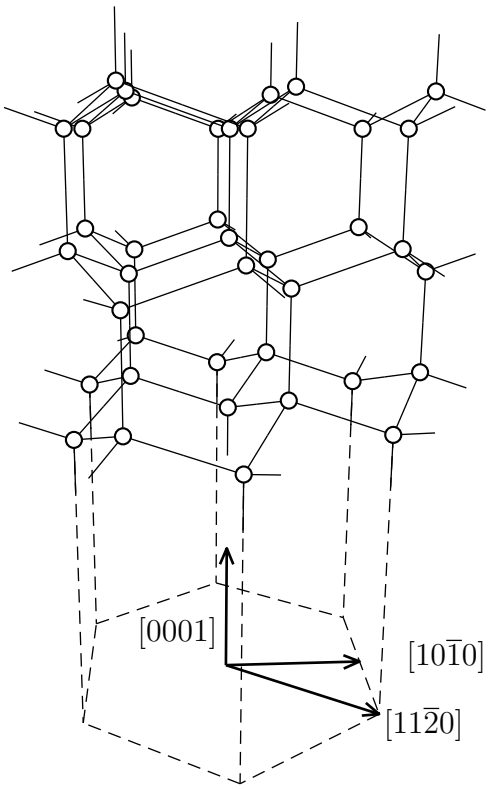

Figure 1.3: Hexagonal lattice structure of ice Ih. The circles indicate the positions of oxygen atoms. The c–axis is the [0001] direction.

In laboratory experiments on saltwater ice and sea ice formation in closed containers, one notices for example that the solute concentration of the liquid increases as freezing progresses (*Wettlaufer et al.*, 1997; *Eicken et al.*, 1998). However, this increase in solute concentration is not necessarily observed in the very early stages of ice growth (a few millimetres to centimetres) (*Farhadieh and Tankin*, 1972; *Wakatsuchi*, 1983; *Wettlaufer et al.*, 1997), indicating that ions, although not incorporated in the crystal lattice itself, are somehow trapped in the ice matrix. However, driven by an unstable hydrostatic pressure gradient due to cold, solute–enriched, dense brine at the top of the ice sheet (*Untersteiner*, 1961; *Cox and Weeks*, 1975; *Wettlaufer et al.*, 1997), most of the solute leaves the ice matrix at distinct locations in the form of plumes (*Lake and Lewis*, 1970; *Wakatsuchi and Ono*, 1983; *Nagashima and Furukawa*, 2003; *Dikarev et al.*, 2004). The onset of brine drainage from the porous matrix is marked by a decrease in the velocity of the advancing freezing interface, while ice continues to be formed inside the ice matrix (*Tait and Jaupart*, 1992; *Wettlaufer et al.*, 1997). The draining brine melts ice as it passes through the warmer bottom layer of the ice sheet, sometimes forming brine drainage channels (*Bennington*, 1967; *Eide and Martin*, 1975; *Niedrauer and Martin*, 1979; *Wakatsuchi and Saito*, 1985; *Wakatsuchi and Kawamura*,

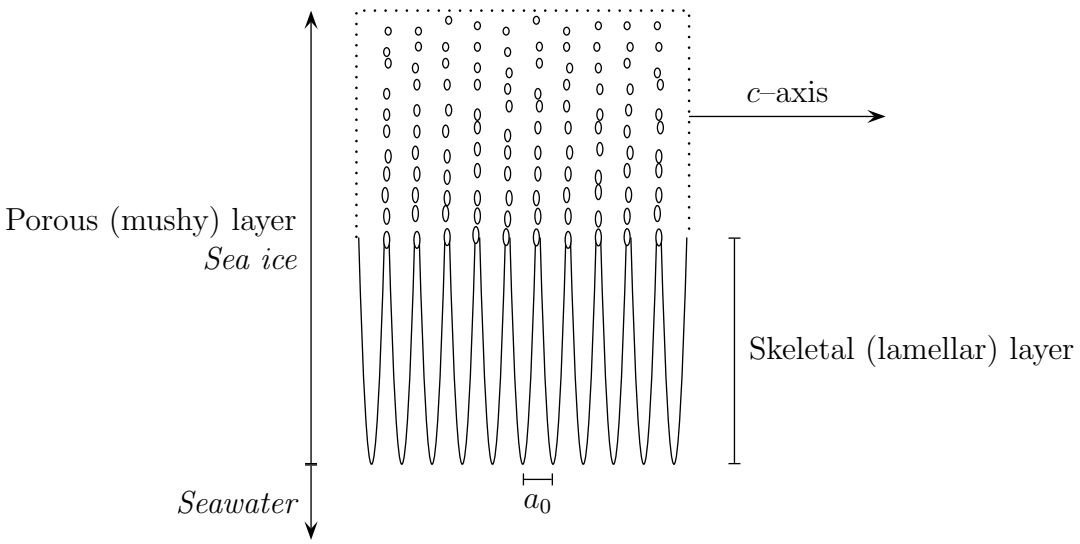

Figure 1.4: Schematic view of a vertical section through a sea ice grain at the ice–water interface. The spacing of lamellae is a_0.

1987; *Weissenberger et al.*, 1992; *Cole and Shapiro*, 1998; *Freitag*, 1999; *Cottier et al.*, 1999). Macroscopic and microscopic observations of ice grown from saltwater further show that solute–enriched brine pockets and layers persist in the ice matrix between ice crystal lamellae (Figure 1.4) and at crystal grain boundaries (*Wright and Priestley*, 1922; *Anderson and Weeks*, 1958; *Perovich and Gow*, 1996; *Cole and Shapiro*, 1998; *Eicken et al.*, 2000; *Cole*, 2001; *Cullen and Baker*, 2001; *Light et al.*, 2003; *Cole et al.*, 2004).

Origin of the lamellar structure Sea ice, growing under calm conditions, has a lamellar structure because a planar sea ice interface is not usually morphologically stable (*Weeks and Gow*, 1978; *Weeks and Wettlaufer*, 1996). Since solute is rejected at the ice–water interface, a solute enriched boundary layer develops at the microscopic ice–water interface. As the freezing point is depressed in this interfacial layer, the interfacial temperature reduces accordingly to maintain thermodynamic equilibrium[2] at the growing interface. However, the thermal diffusivity of water is orders of magnitude larger than the solutal diffusivity, leading to an increase in water temperature with distance from the interface that is more gradual than the increase of the freezing point. Thermodynamic equilibrium at the microscopic ice–water interface is therefore immediately adjacent to a region of supercooled water. This interaction between solute

[2]The temperature at the interface of a growing crystal is actually below the equilibrium freezing point (kinetic supercooling) to overcome the activation energy for molecules to leave the liquid phase and become part of the solid (*Worster*, 1997; *Jeffery and Austin*, 1997). This effect is most pronounced for growth in *c*–axis direction (*Koo et al.*, 1992). Dendrite tip curvature depresses the freezing point further (*Worster*, 1997).

distribution and temperature is termed *constitutional supercooling* (*Tiller et al.*, 1953). Ice that protrudes into the supercooled layer has a growth advantage, which ultimately leads to the breakdown of a planar interface and the formation of ice lamellae or dendrites.

Columnar structure The separation of the ice lamellae (lamellae are also termed platelets[3] or dendrites) shown in Figure 1.4 is of the order of $a_0 \approx 0.5\,\text{mm}$ in sea ice (Figure 5.12), and the lamellar layer, or skeletal layer, that is essentially of zero strength (*Anderson and Weeks*, 1958) has a thickness of approximately 30 mm (20 to 50 mm) (*Weeks and Anderson*, 1958; *Cox and Weeks*, 1975). Since ice crystals are hexagonal, they increase in size much faster in the basal plane (the (0001) plane) than perpendicular to it (along the [0001] direction that is also called the *c*–axis) (*Gosink and Osterkamp*, 1983; *Tirmizi and Gill*, 1987; *Jenkins and Bombosch*, 1995; *Weeks and Wettlaufer*, 1996; *Smedsrud and Jenkins*, 2004). The existence of a preferred growth direction, in addition to mutual physical interference of crystals that grow at an angle to the vertical (geometric selection), causes the crystals in sea ice to have *c*–axes that lie predominantly in the horizontal plane (*Weeks and Ackley*, 1986). In the presence of an under–ice current, the *c*–axes are further found to align preferably parallel to the current direction (*Weeks and Gow*, 1978, 1980; *Langhorne*, 1983; *Weeks and Ackley*, 1986; *Langhorne and Robinson*, 1986). However, it has also been suggested that the vertical alignment of the basal planes of *horizontally* growing saltwater ice is due to current, i.e. in this case the *c*–axes are aligned perpendicular to the current flow (*Bergman et al.*, 2002). Independently of how the crystals are aligned with the flow, they are often found to tilt upstream (*Langhorne*, 1983; *Langhorne and Robinson*, 1986; *Bergman et al.*, 2002; *Petrich et al.*, 2003), an observation that has also been made for freshwater ice growing from supercooled water (*Miksch*, 1969). The upstream tilt is thought to be caused by a redistribution of heat or solute at the interface (*Flemings et al.*, 1956; *Miksch*, 1969).

Sea ice and alloys The composition of seawater is dominated by dissolved NaCl (*Richardson*, 1976), so that NaCl–solution is sometimes used as a seawater substitute in laboratory experiments (*Lofgren and Weeks*, 1969; *Cox and Weeks*, 1975; *Eide and Martin*, 1975; *Niedrauer and Martin*, 1979; *Perovich and Grenfell*, 1981; *Langhorne and Robinson*, 1986; *Bond and Langhorne*, 1997; *Wettlaufer et al.*, 1997; *Tison and*

[3]Unfortunately, the expression "platelet" is used to describe thin ice crystals in three different situations: ice crystals free floating in the water; randomly oriented single ice crystals growing attached to sea ice, to the seabed, or to structures; and parallel lamellae of an ice crystal separated by brine inclusions.

Verbeke, 2001; *Bergman et al.*, 2002). The structure and formation of NaCl–ice is further an analogue for other binary systems, e.g. aqueous NH_4Cl–solution (*Copley et al.*, 1970) and alloys (*Hurle*, 1963; *Weeks and Wettlaufer*, 1996; *Bergman et al.*, 2002), mutually increasing relevant experimental and theoretical studies between the fields. With respect to the aforementioned topics, there have been experiments in aqueous NH_4Cl–solution on convection (*Bennon and Incropera*, 1989; *Tait and Jaupart*, 1992; *McCay et al.*, 1993; *Worster and Kerr*, 1994), and drainage channel development (*Copley et al.*, 1970; *Tait and Jaupart*, 1992; *Chen*, 1995). Upstream crystal growth has been observed in alloys (*Flemings et al.*, 1956; *Flemings*, 1974; *Murakami et al.*, 1983, 1984), as have mechanisms of frazil formation and accumulation (called equiaxed growth) during metal and alloy casting (*Beckermann and Viskanta*, 1993; *Kurz and Fisher*, 1998). Observations and numerical simulations reveal inclusion features in alloys and NH_4Cl–solution (with brine channels called chimneys, and brine pockets called freckles in alloys), that are similar to sea ice (*Felicelli et al.*, 1991; *Tait and Jaupart*, 1992; *Bergman et al.*, 1997; *Schulze and Worster*, 1999).

1.4 Cracks in sea ice

Although the initiation of the natural cracks in the present study has not been observed, they are probably of similar origin to those described by *Taylor* (1922). *Taylor* discriminates between two types of shear cracks in McMurdo Sound. Cracks of the most visible type are "due primarily to the tension in the sea ice existing between two islands, or an island and cape, as it is moved up and down and north and south by the tides and dominant winds." The edges of these cracks were found in many places to be "pressed together so strongly that the edges upturned, forming a wall of ice 6 feet high." "Shear cracks were popular places with the seals and were largely used by them as exits from the sea. Even in the middle of winter with temperatures of $-40\,°F$ or $-50\,°F$ [i.e. $-40\,°C$ or $-46\,°C$] one could always see open water in the shear cracks, the constant motion preventing the formation of new ice in spite of the cold." One of the cracks described by *Taylor* is a pressure ridge, 2.3 miles west of Cape Evans that we also observed in 2002. It seems that this pressure ridge, and a pressure ridge between Inaccessible Island and Tent Island that is mentioned by *Taylor*, appear on the "Ross Island and McMurdo Sound, Antarctica, Satellite Image Map" of the U.S. Geological Survey (USGS) that was recorded in 1986. This suggests that sea ice stresses, at least in that part of McMurdo Sound, have not changed significantly over the past 90 years. The second type of shear crack described by *Taylor* (1922) is "due to a tearing action" from glacial pressure. These cracks do not pile up and "are therefore very hard to

identify when sledging over sea ice newly covered with snow." Instead, "the seaward sea ice (in each 'tension' crack) is pushed away from the landward ice, and so the crack tends to widen with age. This is just the converse of the more usual shear crack, where the walls of ice grow higher with age." Structure and refreezing process of cracks of the type that do not pile up, are investigated in this thesis. The experimental investigations are limited for logistical reasons to cracks in land–fast sea ice that are 90 mm to 340 mm wide.

The strength of refrozen cracks at the described scale in sea ice and in lake ice has been traditionally studied for their importance in engineering (*Kingery and Coble*, 1963; *Metge*, 1976; *Christensen*, 1986; *Timco*, 1987; *Langhorne and Haskell*, 2004). However, few reports are concerned with the structure and fabric of refrozen cracks. Reports on the crystal structure of straight–sided, refrozen cracks in lake and sea ice indicate that crystals grow with their *c*–axes horizontal and parallel to the crack (*Weeks and Lee*, 1958; *Taylor and Lyons*, 1959), which has been attributed to bidirectional heat loss to atmosphere and host ice (*Weeks and Ackley*, 1986). The two–dimensional heat flow has also been used to explain the characteristic arch–shaped crack ice–water freezing interface (cf. Figure 3.11) (*Metge*, 1976; *Weeks and Ackley*, 1986; *Divett*, 2000). There is a small number of detailed experimental and theoretical studies directly relevant to the present study. *Metge* (1976) investigates the structure of refrozen cracks in lake ice. He finds that ice crystals generally seem to grow perpendicular to the arch–shaped freezing interface. He further investigates the refreezing of cracks in freshwater ice in a series of laboratory experiments. Using one thermistor string, he was able to monitor the progression of the freezing interface at the thinnest section of the arch. His experiments were summarised in dimensionless form in a scatter plot that allows the refreezing progress in cracks to be estimated, if the dimensions and surface temperature of the ice are known. *Divett* (2000) carries out a number of laboratory experiments to determine heat and salt transport during the refreezing of cracks in NaCl–ice. He finds that the salinity is highest at the centre of slot, and that the arch–shaped freezing interface is symmetrical, as is the vertical crystal structure. The vertical section of a refrozen crack shows upward–tilting crystals. Although mentioned, this observation is not discussed. Measuring freezing progress with a two–dimensional array of thermistors, he notes that the measured vertical component of growth velocity is higher than the horizontal component. He concludes that the heat flux is higher to the atmosphere than to the host ice. *Haskell and Langhorne* (unpublished 2000) and *Langhorne and Haskell* (2004), in a study primarily concerned with the flexural strength of refrozen cracks in McMurdo Sound, determine the freezing front advance both thermally with the help of a thermistor string and by excavation and direct

observation. They give an empirical relationship between depth of refreezing and time for all of their experiments (*Langhorne and Haskell*, 2004). They further give examples of a vertical salinity profile having the highest salinity at the centre of the crack, and of upward–tilting crystals (*Haskell and Langhorne*, unpublished 2000).

1.5 Two–dimensional modelling of fluid flow through sea ice

Two–dimensional fluid dynamics models to simulate fluid flow in sea ice and in the underlying liquid have apparently only been used by *Medjani* (1996), and by *Oertling and Watts* (2004) who use the model of *Medjani*. *Medjani* (1996), based on the governing equations of *Bennon and Incropera* (1987), models the two–dimensional sea ice formation with the finite volume approach. The model assumes that the densities of solid and liquid are equal. He demonstrates the feasibility of simulating the formation of brine channels and necking. However, he publishes neither coefficients of the permeability parameterisation employed, nor salinity profiles. Later, *Oertling and Watts* (2004) apply the model of *Medjani* to the case of unidirectional formation of a thin sea ice sheet. *Oertling and Watts* simulate ice sheet growth from a liquid at its freezing temperature, assuming local thermodynamic equilibrium everywhere. No explicit provisions are made to ensure the formation of a defined freezing front (cf. Section 4.4). Fluid flow in the porous medium is treated by increasing the fluid viscosity with decreasing porosity, f, down to a porosity of $f = 0.5$, which is equivalent to simulating the flow of a suspension. A Darcy friction term, following the Carman–Kozeny formulation for permeability (cf. Chapter 5), is incorporated into the governing equations for $f < 0.5$. As justification for treating flow though the porous sea ice matrix as the flow of a suspension, it is stated that the results of the simulations appeared more realistic than using a treatment after Carman and Kozeny alone (*Medjani*, 1996). In order to prevent numerical instability, each simulation begins with an assumed ice thickness of 3 mm, or three grid cells, which are assigned intermediate values of liquid fraction between 0 and 1, and temperature between surface temperature and temperature of the bulk liquid. Ice sheet thicknesses up to 70 mm are reported, and development of ice thickness with time is compared to laboratory experiments, albeit performed at different surface temperatures. *Oertling and Watts* find convection penetrating the entire mushy layer but, unlike the observations in laboratory experiments of *Wettlaufer et al.* (1997), there is no delay in the onset of convection. They illustrate the desalination of an ice sheet growing from a constant temperature boundary of $-10\,^{\circ}\mathrm{C}$ over 15 hours. The ice sheet

obtains a thickness of 67 mm. Throughout the growth process, the domain is clearly divided into a region of initial saltwater salinity, 35 psu, and a region of salinity around 10 to 18 psu. The transition zone between these domains has a thickness of less than 2 mm, which is small compared to typical values of 30 mm in laboratory experiments (*Weeks and Anderson*, 1958; *Cox and Weeks*, 1975). Qualitative streamlines are shown that illustrate that the convection pattern in the mush is relatively time–invariant, with distinct regions of downflow. The salinity throughout the ice sheet reduces with time. No regions of increased salinity coincident with downwelling brine develop within the ice sheet, contrary to observations of *Cottier et al.* (1999) in laboratory experiments.

The model of *Medjani* (1996), as applied by *Oertling and Watts* (2004), appears to simulate ice formation at a reasonable speed and at a reasonable rate of desalination. However, solute distribution throughout the ice sheet is not reproduced as expected. We intend to simulate the development of the inclusion and salinity profiles of sea ice that has grown with heat flow in two–dimensions. The limitations of the model of *Medjani* (1996) and *Oertling and Watts* (2004) mean that it is not a promising foundation for this investigation. The finite volume method used for the numerical simulation is introduced in Chapter 4, together with the resulting governing equations and numerical methods. The derivation of the governing equations and their discretised forms are given in Appendix D and Appendix E.2, respectively. In this work we rely only on the permeability to describe fluid flow through sea ice. Moreover, the density difference between ice and water is accounted for.

Chapter 2

Structure of refrozen cracks observed in Antarctica

This chapter presents the structure and salinity of natural refrozen cracks and slot experiments in McMurdo Sound, Antarctica, in the spring of 2001 and 2002. Natural cracks are labelled *crack*, while artificial cracks are labelled *slot*. The cracks in this investigation are linear, parallel–sides and have connection with seawater beneath the host sea ice sheet.

2.1 Approach

Experiments and observations were made in McMurdo Sound, Ross Sea, East Antarctica, within 15 km of Ross Island. Two visits to the area were made for this project as part of Antarctica New Zealand science event *K131*, the first from mid October 2001 to mid November 2001, and the second throughout September 2002. A field camp (*Camp Haskell*) was maintained at the site of experiment *slot 1* at Cape Evans in 2001, while a makeshift shelter and a dive hut for an oceanographic project (*Leonard et al.*, unpublished 2002) were located at the site of *slot 10* to *13* in Erebus Bay (Figure 2.1). Sea ice extended beyond Cape Bird (latitude 77°10′S) in both seasons. Figure 2.1 shows the location of refreezing experiments (*slot*) and excavated, natural, refrozen cracks (*crack*) in the 2001 and 2002 seasons. Single digit numbers refer to 2001, while double digit numbers refer to 2002.

The land–fast, first–year sea ice was initially snow covered in both seasons, with the bare sea ice surface becoming exposed by sublimation at the end of October 2001. The cracks investigated were selected to be narrow enough to be excavated, and wide enough

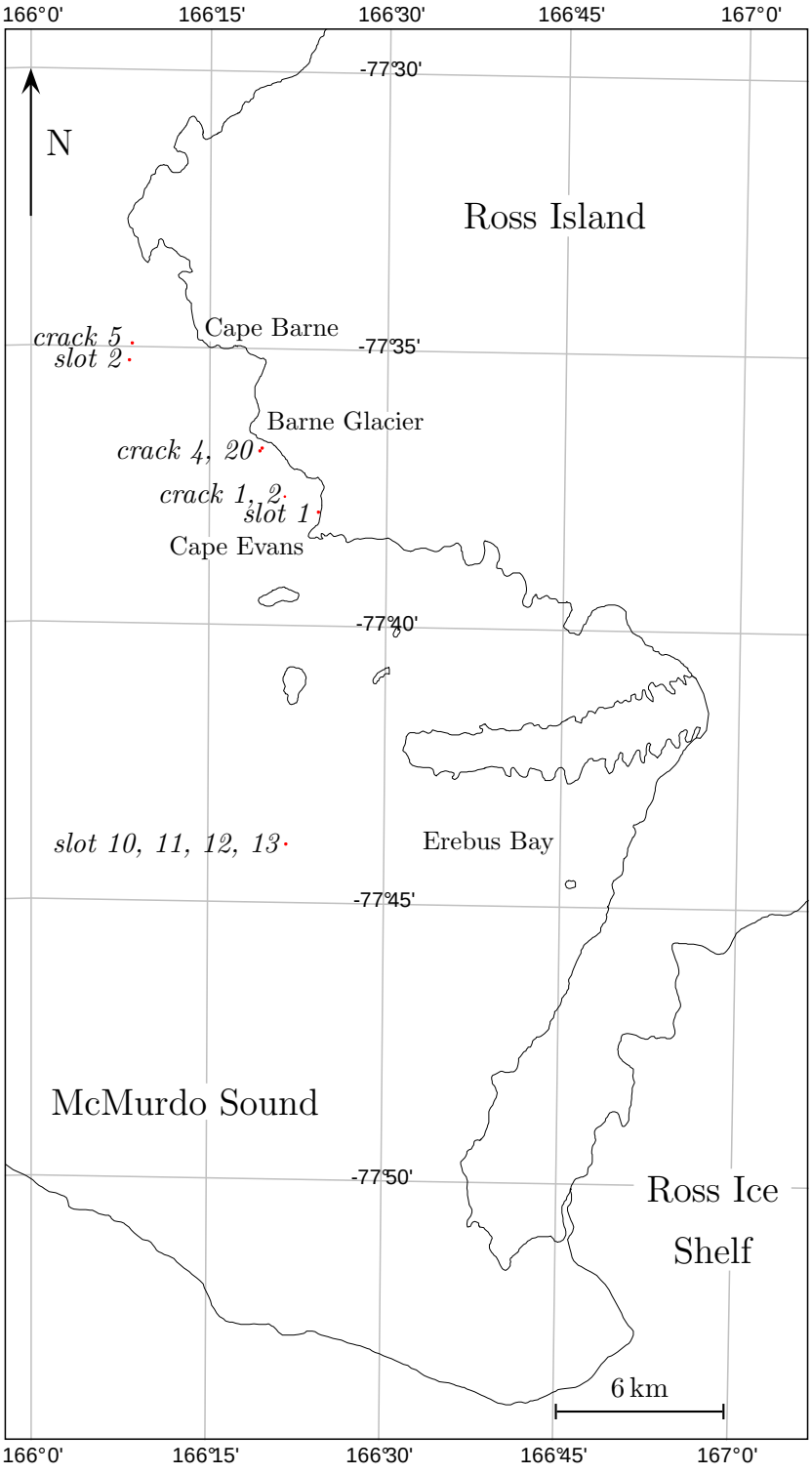

Figure 2.1: Sites of *slot* experiments and *crack* excavations in McMurdo Sound in October and November 2001, and in September 2002. Single digit numbers refer to 2001 sites, two digits numbers indicate 2002 sites. Map generated with *PanMap* provided by the *PANGAEA* network.

Table 2.1: Summary of sites discussed in this chapter. The refrozen thickness is the distance from the ice–air interface of the crack to the ice–water interface at the centre of the crack. Locations are illustrated on the map Figure 2.1.

	date of excavation	width (mm)	freeboard (mm)	refrozen thickness (mm)	host ice thickness (mm)	location
slot 1	20 Oct 2001	230	195	410	2200	Cape Evans
slot 2	5 Nov 2001	320	130	370	1300	Cape Barne
slot 10	9 Sept 2002	180	230	≈ 1000	2200	Erebus Bay
crack 1	18 Oct 2001	270	100	2040	2150	Cape Evans
crack 2	29 Oct 2001	80	105		2150	Cape Evans
crack 4	9 Nov 2001	260	25			Barne Glacier
crack 5	1 Nov 2001	275	85	1250	1380	Cape Barne
crack 20	5 Sept 2002	135	115			Barne Glacier

to be analysed. The width of the cracks is between 80 mm and 320 mm (Table 2.1), and the freeboard at the sites of excavation is in the range 20 mm to 120 mm.

Samples of refrozen cracks and slot experiments were cut from the ice sheet with a ditch digger (*Haskell et al.*, 1996) and crane (only *slot 1*, *slot 2*, *crack 1*), or with a chain saw with a long blade. Samples of *slot 1* and *crack 1* were stored in horizontal position immediately after excavation in order to minimise cross contamination of samples by brine drainage. Extensive brine drainage prevented a salinity analysis in the case of *slot 2*. All other samples were already frozen to an extent that brine movement was not apparent at the time of excavation.

Samples for thick section analysis were first sliced with a chain saw and in some instances with a band saw, placed on black cardboard, and photographed. This allows the identification of the location of inclusions. Thin sections were prepared from thick section samples by freezing them on a glass plate and shaving them with a microtome to the desired thickness. Thin sections observed under cross polarised light are used to identify individual ice crystals.

We will continue with the description of observations after taking a brief look at the nature of thin sections, and the process of salinity measurements.

2.1.1 Thin sections, background

Individual crystal grains in sea ice can be made visible to the naked eye by shaving a sample of sea ice to a thickness typically below 2 mm with a microtome and placing it between cross polarised filters. Sea ice is birefringent (*Petrenko and Whitworth*, 1999), i.e. light propagates at a different speed with its **E**–vector (electric field vector) parallel to the *c*–axis than perpendicular to it. Linearly polarised light that enters an ice crystal

at an angle to the c–axis decomposes into an ordinary ray its **E**–field parallel to the c–axis and an extraordinary ray with its **E**–field perpendicular to the c–axis. Owing to the difference in speed both rays recombine with different phases, resulting in linearly polarised light with a plane of polarisation that is generally rotated with respect to the plane of polarisation of the incident light. Illuminated with white light and placed between cross polarised filters, ice crystals appear coloured since the refractive index, and thus the speed of light, is wavelength dependent, which leads to a wavelength dependent rotation of the plane of polarisation. Since light propagating exactly parallel to the c–axis does not split into ordinary and extraordinary components, the plane of polarisation does not rotate, and the crystals appear black.

2.1.2 Salinity measurements

In order to perform sea ice salinity measurements, the samples were sliced into blocks, kept in screw cap pottles and left to melt at room temperature (i.e. at 14 to 22 °C). Conductivity and temperature of the melt were determined with a Wayne–Kerr cell and digital thermometer, respectively, and measurements were converted to salinity by comparison with a KCl reference solution following the definition of the practical salinity scale (*UNESCO*, 1981a). The salinity of a brine, S, is defined through the conductivity of a solution, and it is expressed in *practical salinity units* (psu), which is a dimensionless quantity[1]. Salinity is calculated in the fluid dynamics model (Chapter 4) as the mass of dissolved NaCl, m_{NaCl}, per mass of solution,

$$S = \frac{m_{\mathrm{NaCl}}}{m_{\mathrm{NaCl}} + m_{\mathrm{H_2O}}}, \tag{2.1}$$

where $m_{\mathrm{H_2O}}$ is the mass of water of the solution. Equation (2.1) is equivalent to

$$S = \frac{C}{C + \rho_w}, \tag{2.2}$$

where C is the solute concentration of the brine in $\mathrm{kg\,m^{-3}}$, and ρ_w is the density of water.

[1]Traditionally, the salinity has been determined as the chlorinity by titration (*UNESCO*, 1981a). A less orthodox approach is the use of fibre optics to excite surface–plasmons (*Esteban et al.*, 1999).

2.2 Observations

We begin with the description of structural observations on thick and thin sections for refrozen cracks (Section 2.2.1), followed by the structure of refrozen slots (Section 2.2.2). We then take a short excursion to examine thermal cracks, observed particularly in 2002 (Section 2.2.3). Finally, the salinity profiles of cracks and slots are compared (Section 2.2.4). Some of the observations from 2001 have been presented previously (*Petrich et al.*, 2003). All depths are given with respect to the ice–air interface of the crack or slot.

General locations and dimensions of the investigated cracks and slots in McMurdo Sound are summarised in Table 2.1. The locations are further illustrated in Figure 2.1.

2.2.1 Natural refrozen cracks

The aim was to investigate cracks without obvious signs of deformation during or after the refreezing process. However, cracks that underwent deformation were observed. The absence of a snow layer during the investigations in November 2001 allowed us to obtain a general overview of crack surface morphology. Some of the cracks in McMurdo Sound showed signs of deformation at the surface in the form of an uneven surface, resembling a field of rubble. Such a morphology could be due to shear or compression during the refreezing process. Other cracks appeared to have blowing snow frozen to them. The anchor point of the snow, the location of firmest attachment to the ice of the refrozen crack, was typically along the centre axis of the cracks. This could be due to a reopening of the crack in the course of the freezing process owing to extension or shear stresses. Deformations at the crack surface were mostly observed in refrozen cracks over 500 mm wide and with small freeboard, around 10 mm.

crack 1 and *crack 2*

The natural refrozen cracks *crack 1* and *crack 2* are in fact two sections of the same crack, a few metres separated from each other. A typical feature of the observed cracks is that they occasionally branch and re–unite. While sample *crack 1* was taken at a location that was unaffected by branching, *crack 2* is a sample from a narrower branch.

Freeboard varied along *crack 1*, where heights between 70 mm and 110 mm were measured. Further, freeboard on the East side (closer to Ross Island) was between 0 mm and 25 mm larger than freeboard on the West side. These differences could be due to different snow cover loads at the time of freezing. To illustrate this, the correlation between freeboard and snow cover during the 2002 season is shown in Table 2.2. There

Table 2.2: Anecdotal correlation between snow cover thickness and freeboard at the Erebus Bay site.

	slot 10	*slot 11*	*slot 12*	*slot 13*
date	2 Sept 02	9 Sept 02	16 Sept 02	17 Sept 02
freeboard (mm)	230	230	190	170
snow cover	little/none	little/none	moderate	substantial

appeared to be a clear negative correlation between the subjectively perceived snow coverage of the ice and the freeboard height. However, Table 2.2 shows a temporal variation, while the freeboard variations along *crack 1* are a spatial variation.

Vertical thick and thin sections of *crack 1* are shown in Figure 2.2. The thick section allows us to identify three regions. The first region is the interior of the refrozen crack from the ice–air interface in the crack to the depth of 900 mm as indicated. Seven vertical bands of inclusions are visible, the two outermost separating crack from host ice. The two most dominant bands appear to trisect the crack. The latter bands bend towards the sides of the cracks in the upper 60 mm. The second region is the host ice sheet to the left and to the right of the crack, again down to 900 mm depth. Horizontal banding is visible in the host ice down to approximately 300 mm. Third, the ice below 900 mm, where inclusions follow lines of $(35 \pm 5)^\circ$ from the horizontal and are arch shaped near the centre. Diagonal bands of inclusions inclined approximately $(40 \pm 10)^\circ$ from the horizontal (measured from figure 6(b) of *Cole et al.* (2002), showing a 40 mm excerpt of a diagonal band) have also been observed in the Chukchi Sea, Alaska (*Cole et al.*, 2002). Brine channels inclined 30° to 60° have been observed in laboratory studies in the presence of slightly non–vertical (up to 13° inclined) temperature gradients (*Niedrauer and Martin*, 1979). The centre of this bottom region is free of inclusions visible to the naked eye.

The two vertical thin sections shown indicate upward–tilting crystals at the centre, and granular crystals at the side of the crack.

Vertical thick and thin sections of *crack 2* are shown in Figure 2.3. Three vertical bands of inclusions are visible, two at the sides of the crack, and one in the centre. In comparison to *crack 1*, *crack 2* does not appear to be vertically sectioned at all. Its width is approximately one third of the width of *crack 1*.

The vertical thin sections show small crystals that increase in size with depth. The black spots in the lower thin section are areas of missing ice that was too porous to stick to the glass plate during microtoming.

Three horizontal thin sections of *crack 2* are shown in Figure 2.4. The thin sections are shown with the host ice to the left (West in McMurdo Sound) and to the right. The

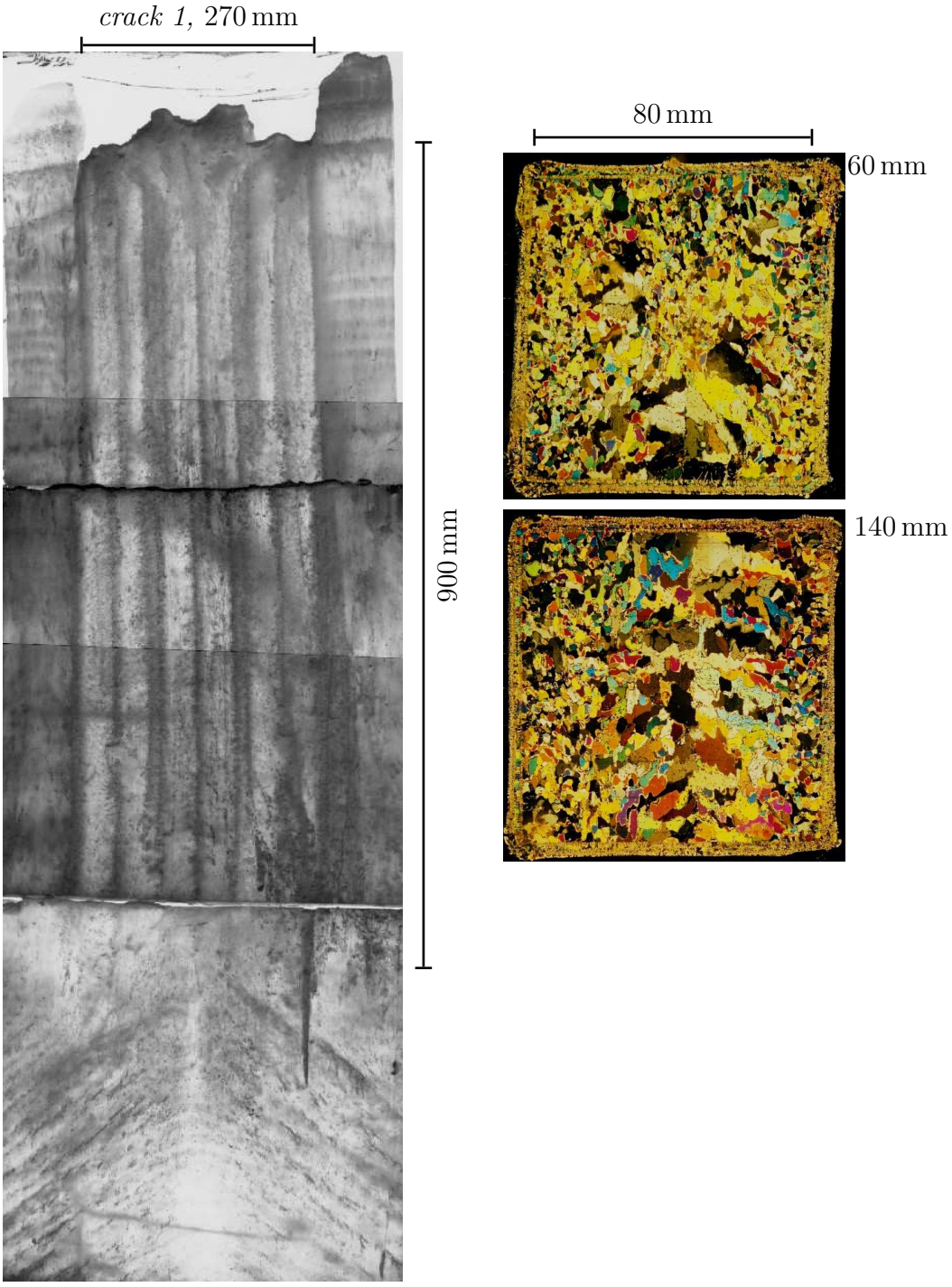

Figure 2.2: Natural refrozen crack, *crack 1.* For clarity, the image of the thick section is inverted, i.e. brine and air inclusions appear dark. The vertical thin sections are cut from the centre of the crack downwards from heights below crack surface of 60 mm and 140 mm, respectively.

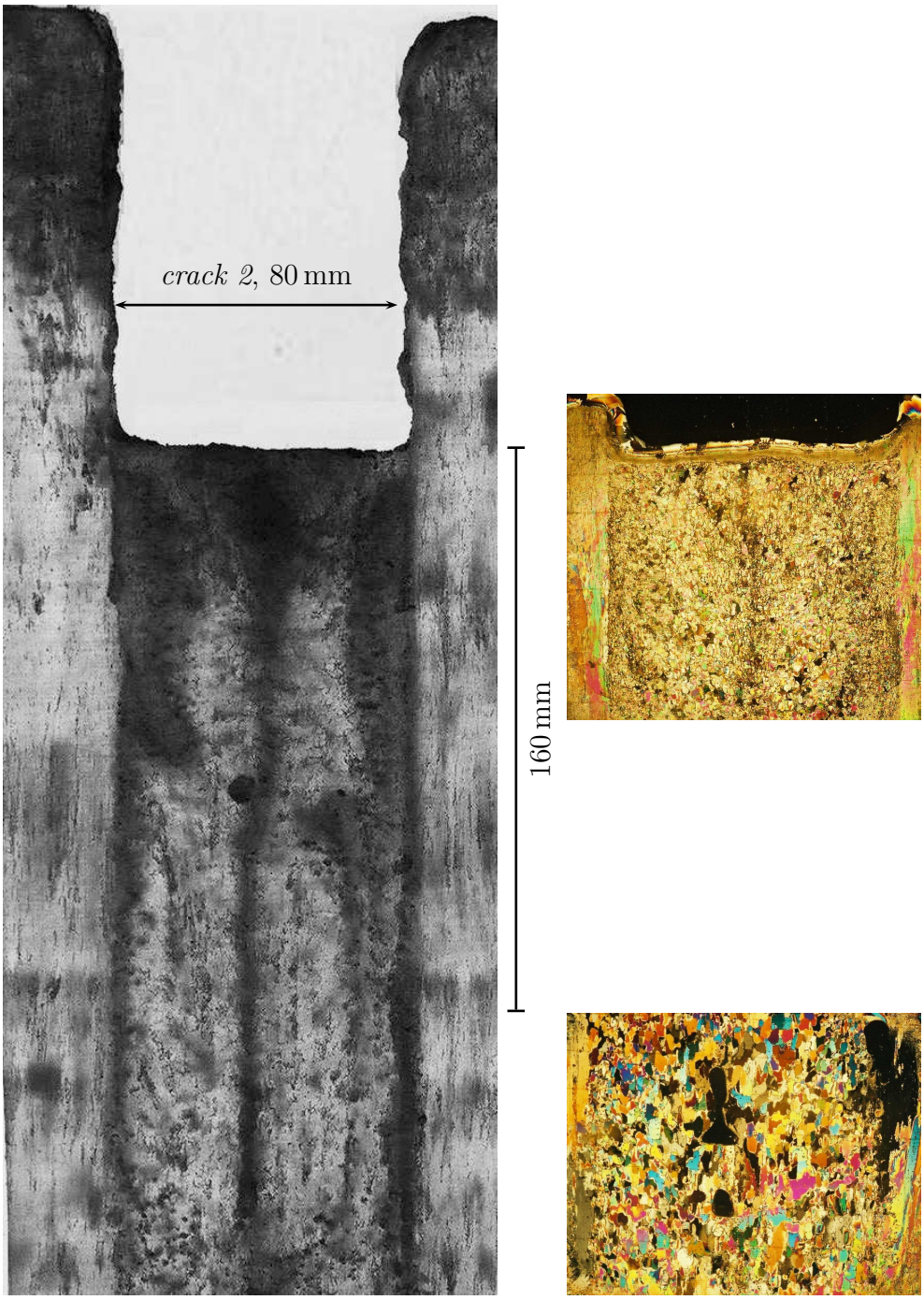

Figure 2.3: Vertical thick and thin sections of *crack 2*. The larger black spots in the bottom thin section are areas of missing ice. The thin sections are to scale with the thick sections and vertically aligned.

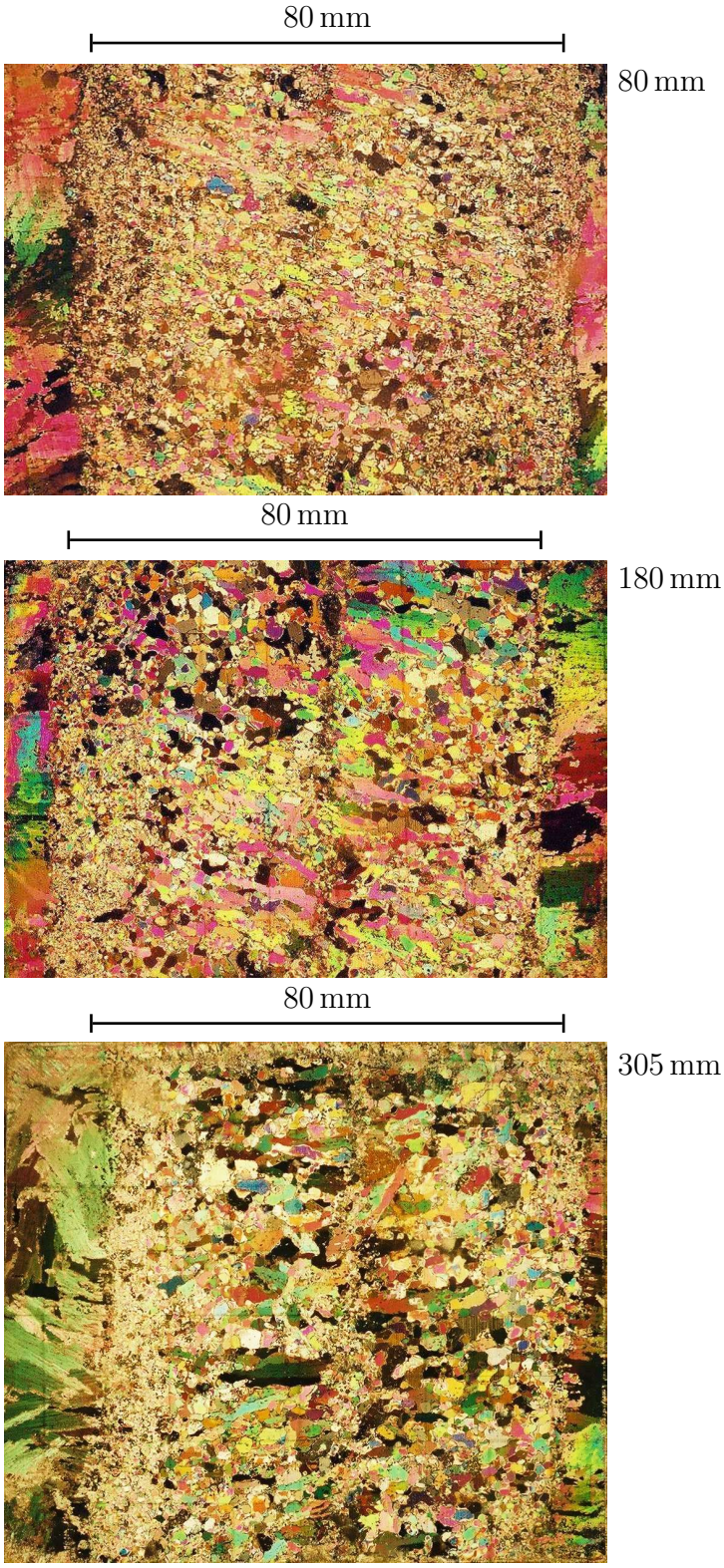

Figure 2.4: Horizontal thin sections of *crack 2* at 80 mm, 180 mm, and 305 mm below the crack surface, respectively. Note that the long axes of the crystals in the upper two thin sections tend not to be perpendicular to the long axis of the crack.

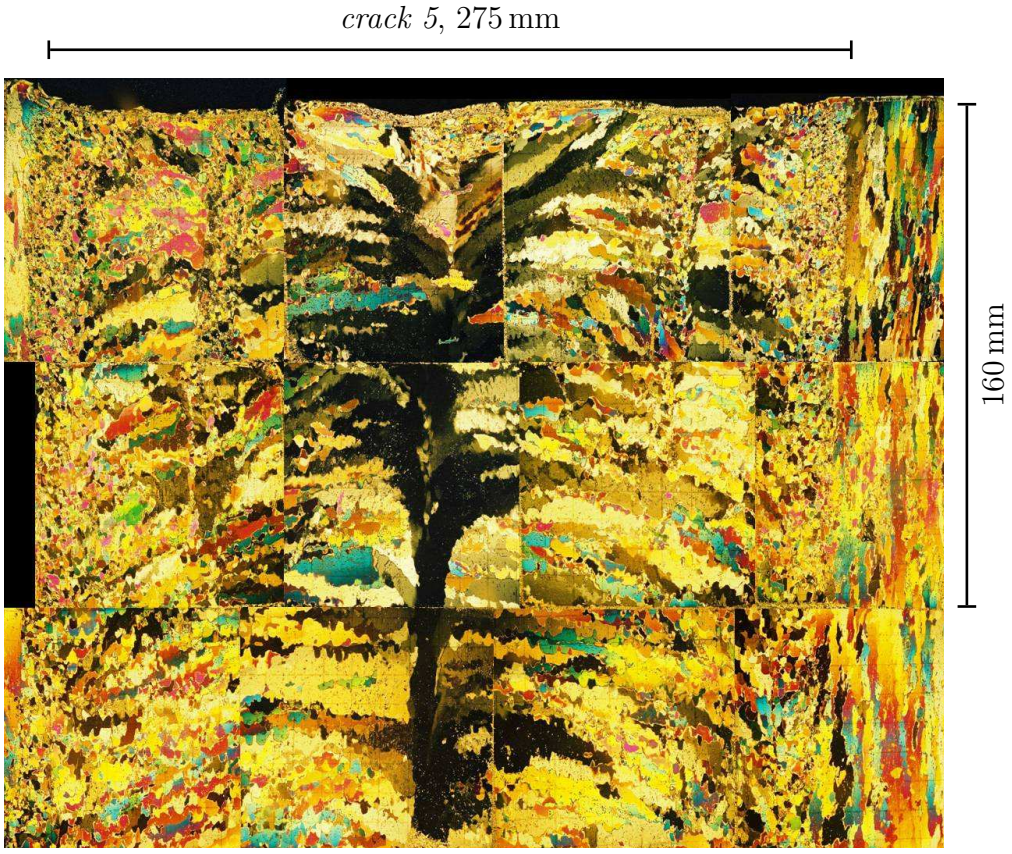

Figure 2.5: Vertical thin section of refrozen crack, *crack 5*. The crystal structure of the crack differs distinctly from the columnar structure of the host ice sheet. Granular crystals have formed at the side of the crack, with upward–tilting crystals closer to the centre. The centre itself is marked by vertically elongated crystals with their c–axes perpendicular to the plane of the page. These *c*–axes are thus aligned along the axis of the crack as described by *Weeks and Ackley* (1986). The host ice above the crack surface is not shown.

signature of columnar ice can be seen in the host ice at both sides of all thin sections. The size of the crystals in the crack increases with depth. Porous bands are visible along the centre of the thin sections and at the sides of the crack. The thin sections taken at 80 mm and 180 mm below the crack surface seem to show elongated crystals within a matrix of small crystals. The long axes of these crystals seem to be tilted at approximately 15° with respect to the direction perpendicular to the long axis of the crack.

crack 4 and *crack 5*

Figure 2.5 shows the vertical thin section of *crack 5*. The crystal structure of the crack is distinctly different from the columnar structure of the host ice sheet that can be seen

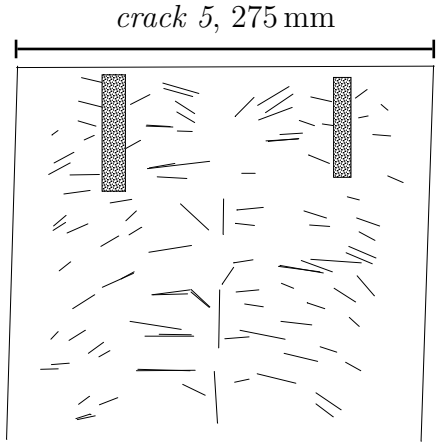

Figure 2.6: Sketch of the long axes of some of the crystals in *crack 5*. Also marked are the two vertical bands of granular ice near the ice–air interface. The sketch is based on the thin section in Figure 2.5.

to the left and to the right of the crack. Granular crystals have formed at the side of the crack, with upward–tilting crystals[2] closer to the centre. Crystals grow downwards into the centre from the ice–air interface. The centre of the crack is marked by vertically elongated crystals (that remain black under rotation of the thin section) with their c–axes perpendicular to the plane of the page. There are two vertical bands of granular ice visible in the top 80 mm close to either side of the crack. Figure 2.6 traces the long axes of some of the crystals. The two short bands of granular ice at the ice–air interface are marked. The trajectories of the crystals seem to follow a fountain–like path: up in the centre and down at the sides.

The thin section allows us to estimate the growth direction of the crystals, which is the direction of the long axis of the crystals, but we note that this direction is not necessarily equal to the preferred growth directions of the crystal dendrites, i.e. the $\langle 11\bar{2}0 \rangle$ directions (*Glen and Perutz*, 1954; *Miksch*, 1969). This point has been illustrated for the case of solidifying alloys (*Murakami et al.*, 1983, 1984). *Murakami et al.* (1983) investigate the effect of flow on crystal growth and dendrite direction during solidification of a cubic alloy (Al–Cu). They begin the experiment by solidifying a stagnant alloy from a water–cooled interface, causing both crystal growth direction and dendrite growth direction ([100]) to be parallel to the heat flow, i.e. normal to the chill surface. When these prepared crystals are then exposed to forced convection, the upstream deflection angle of the crystal growth direction, i.e. the direction of the crystal boundaries, is larger than the deflection angle of the dendrite growth direction. This case is analogous to the experiments of *Miksch* (1969) on ice crystals growing from

[2]The convention in this thesis is that crystals tilting "upwards" or "downwards" are followed in the direction growth, i.e. towards the centre of the crack.

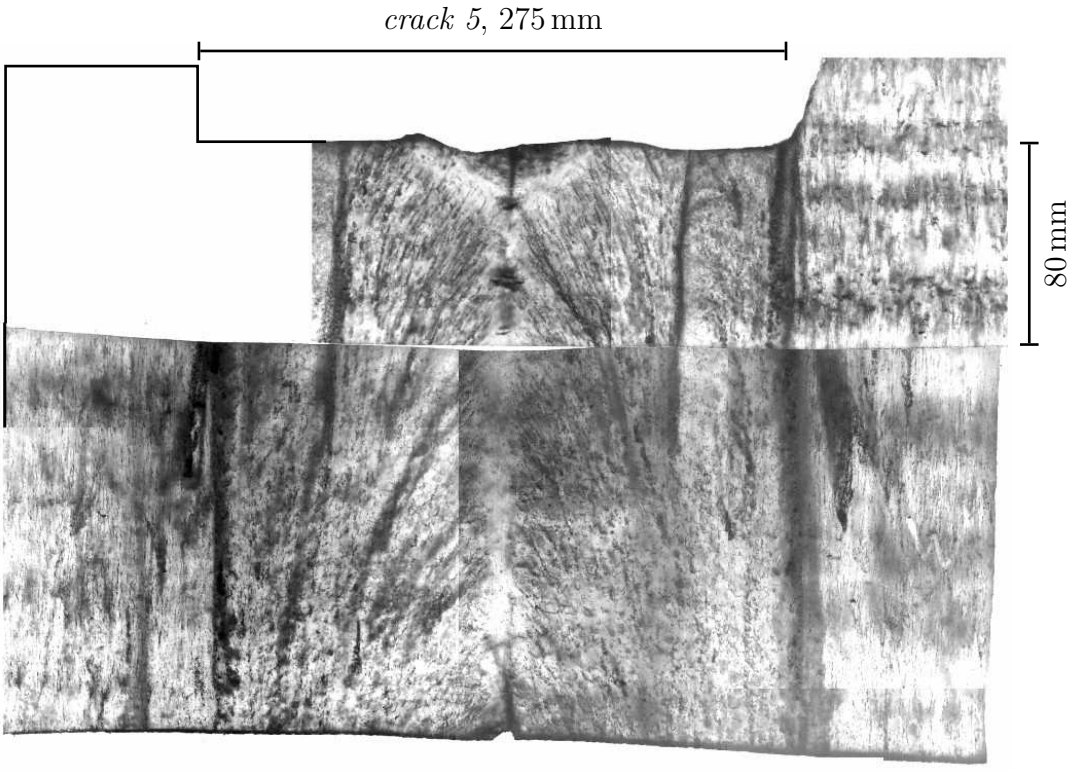

Figure 2.7: Vertical thick section of *crack 5*.

supercooled freshwater. If, however, solidification takes place in the presence of forced convection right from the start of the experiment, the upstream deflection angles of crystals and dendrites are nearly the same (*Murakami et al.*, 1984).

Figure 2.7 shows the vertical thick section of *crack 5*. Two vertical bands of inclusions can be seen at the sides of the crack. Two more vertical bands of inclusions from the ice–air surface down to 110 mm are 40 to 60 mm inward from the sides of the crack. These inclusions could indicate that this crack underwent a fracture event after having refrozen to 110 mm. Between these two bands the inclusions follow arch–shaped patterns. The centre of the crack, coincident with the vertically elongated crystals in Figures 2.5 and 2.6, is almost devoid of inclusions. A "V"–shaped region of clear ice is further visible close to the ice–air surface.

Figure 2.8 shows horizontal thin sections across the width of *crack 5*. The thin section at 70 mm depth shows host ice comprised of small crystal grains, adjacent to crystals elongated perpendicular to the crack axis, a fine grained band corresponding to the short vertical inclusion bands, and again crystals elongated perpendicular to the crack axis. The centre of the crack can be identified by the discontinuity of the crystal pattern.

The thin sections at 240 mm depth show columnar host ice, followed by a granular

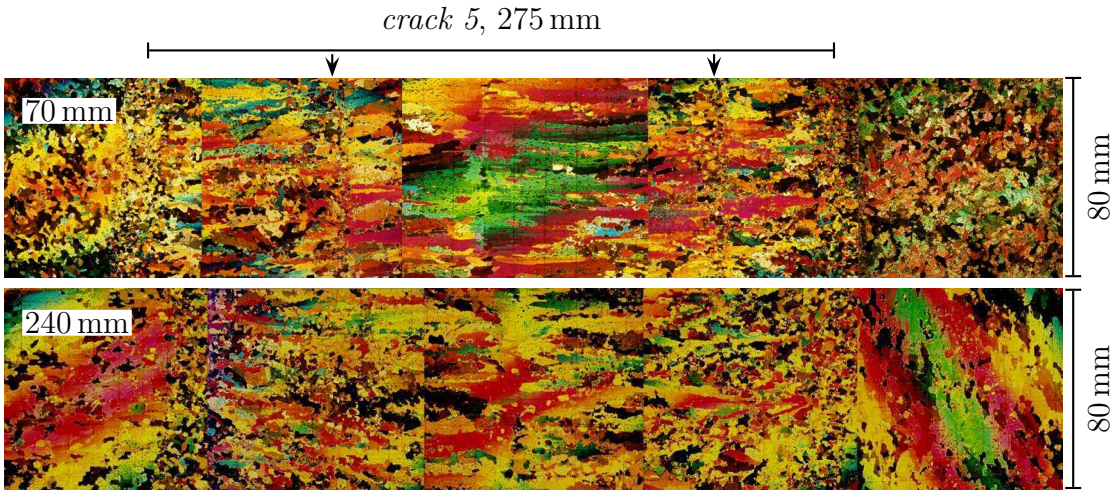

Figure 2.8: Horizontal thin sections of refrozen crack, *crack 5*, 70 mm and 240 mm below the crack's surface. The arrows point at granular bands.

band at the host ice–crack transition, and crystals elongated perpendicular to the crack axis.

Figure 2.9 shows the vertical thin section of *crack 4*. Similar to *crack 5*, crystals close to the side seem to be elongated, pointing upwards into the centre, while crystals close to the centre and at the centre point downwards.

Figure 2.10 shows the vertical thick section of *crack 4*. The host ice to the left and to the right of the crack shows banding features. Inclusions in the crack are generally aligned as arches. Vertical lines of inclusions exist at the crack–host ice transition, and in the upper 70 mm of the crack. One trace of inclusions is seen to run from near the side of the crack to the centre over the course of 250 mm. The centre is relatively devoid of inclusions apart from the upper 100 mm, and below 250 mm.

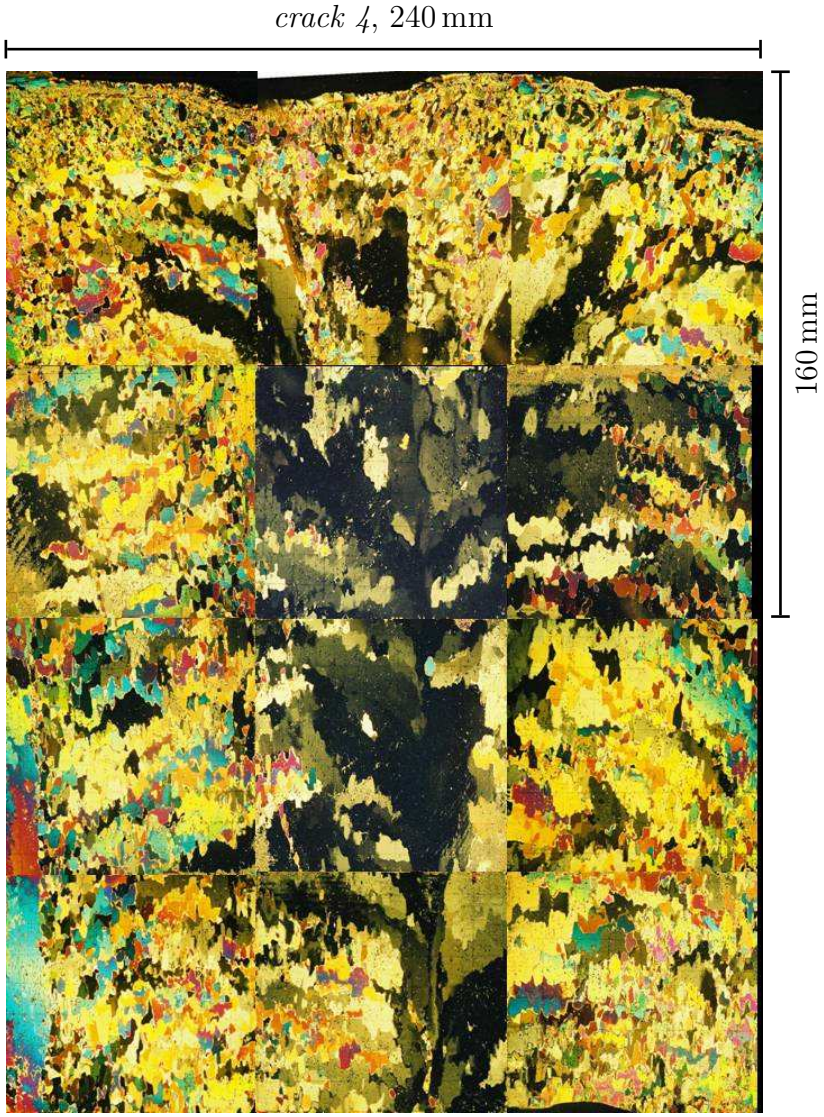

Figure 2.9: Vertical thin section of refrozen crack, *crack 4*. The crack is 240 mm wide. Essentially no crystal structure of the host ice is shown.

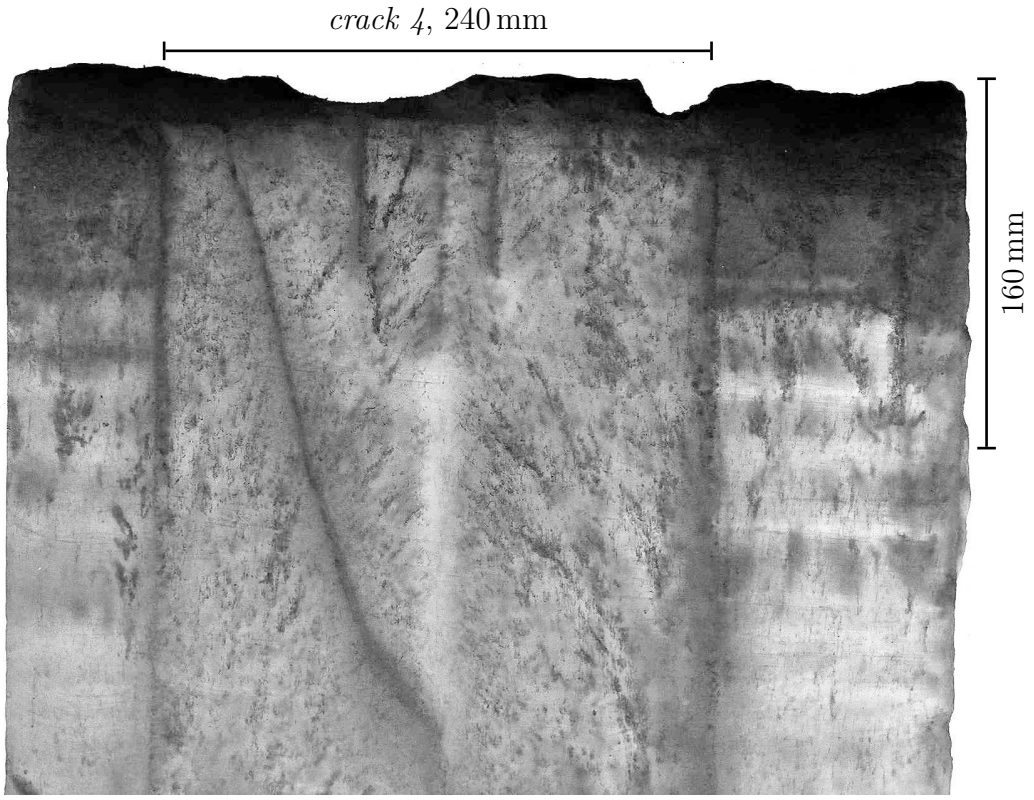

Figure 2.10: Vertical thick section of refrozen crack, *crack 4*. The host ice on either side of the refrozen crack shows banding beneath the top 100 mm of granular ice.

crack 20

Figure 2.11 shows the vertical thin section of *crack 20*. Clearly visible, and distinct from the crack ice, is the columnar structure of the host ice sheet. The refrozen crack consists of 20 to 30 mm of granular ice at both sides, followed by elongated crystals. The elongated crystals consistently point upwards into the centre below 180 mm. No crystals point vertically downwards at the centre of the crack as in the cases of *crack 4* and *crack 5*.

Figure 2.12 shows the vertical thick section of *crack 20*. The host ice on either side of the crack again shows banding features close to the ice–air interface. Further, there are brine channels visible from 120 to 260 mm and from 300 to 380 mm in the host ice sheet on the left hand side. Vertical bands of inclusions are visible at both transitions from host ice to crack ice. These bands are much narrower than the 20 to 30 mm of granular ice seen in the thin section. A third vertical band of inclusions marks the centre of the crack. While the inclusions in the crack outside the vertical bands seem to follow mostly vertical patterns, the traces are arch–shaped in the centre 40 mm of the crack.

Figure 2.13 shows a thin section with the plane of the thin section parallel to the sides of the crack. This thin section is 5 mm off the centre of the crack, at depth 140 to 220 mm as indicated by the sketch. There is a tendency of the crystals to be vertically elongated. The crystals at this depth can be seen to point upwards into the crack in Figure 2.11.

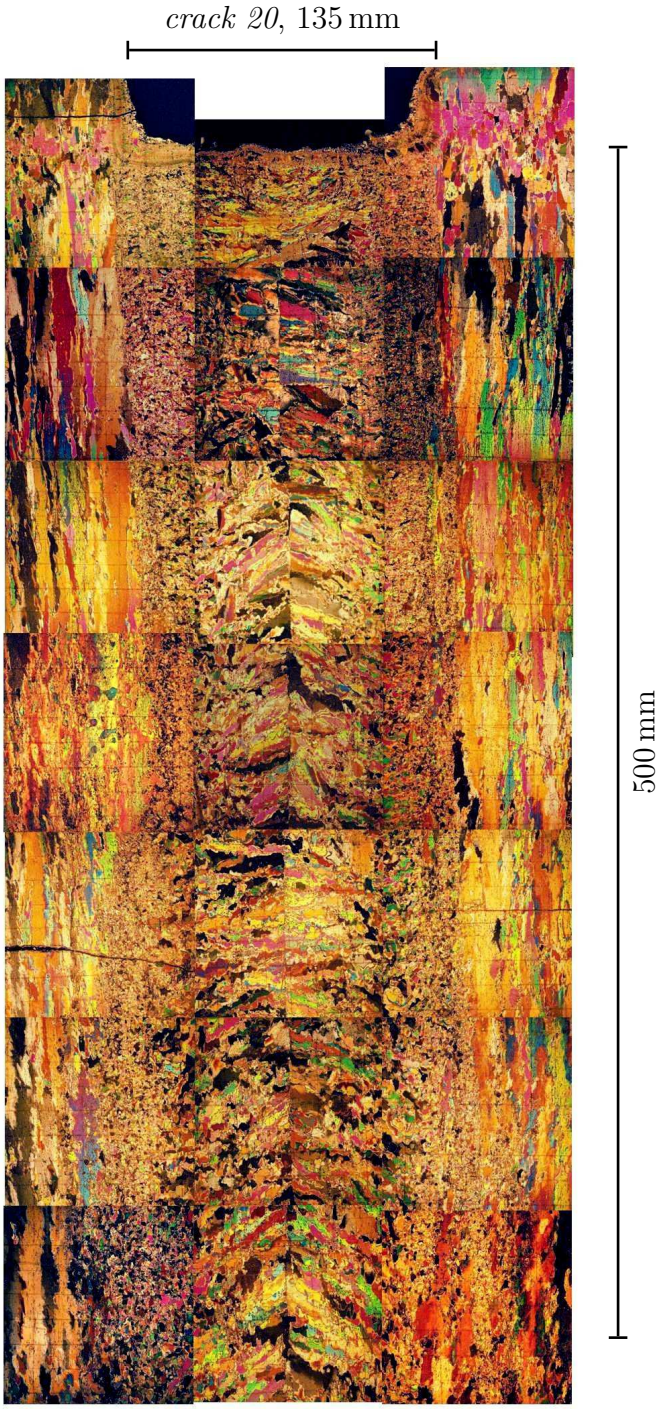

Figure 2.11: Vertical thin section of refrozen crack, *crack 20*. The crystal structure of the crack differs distinctly from the columnar structure of the host ice sheet. Granular crystals have formed at the side of the crack, adjacent to upward–tilting crystals closer to the centre. At the centre, upward–tilting crystals meet from both sides.

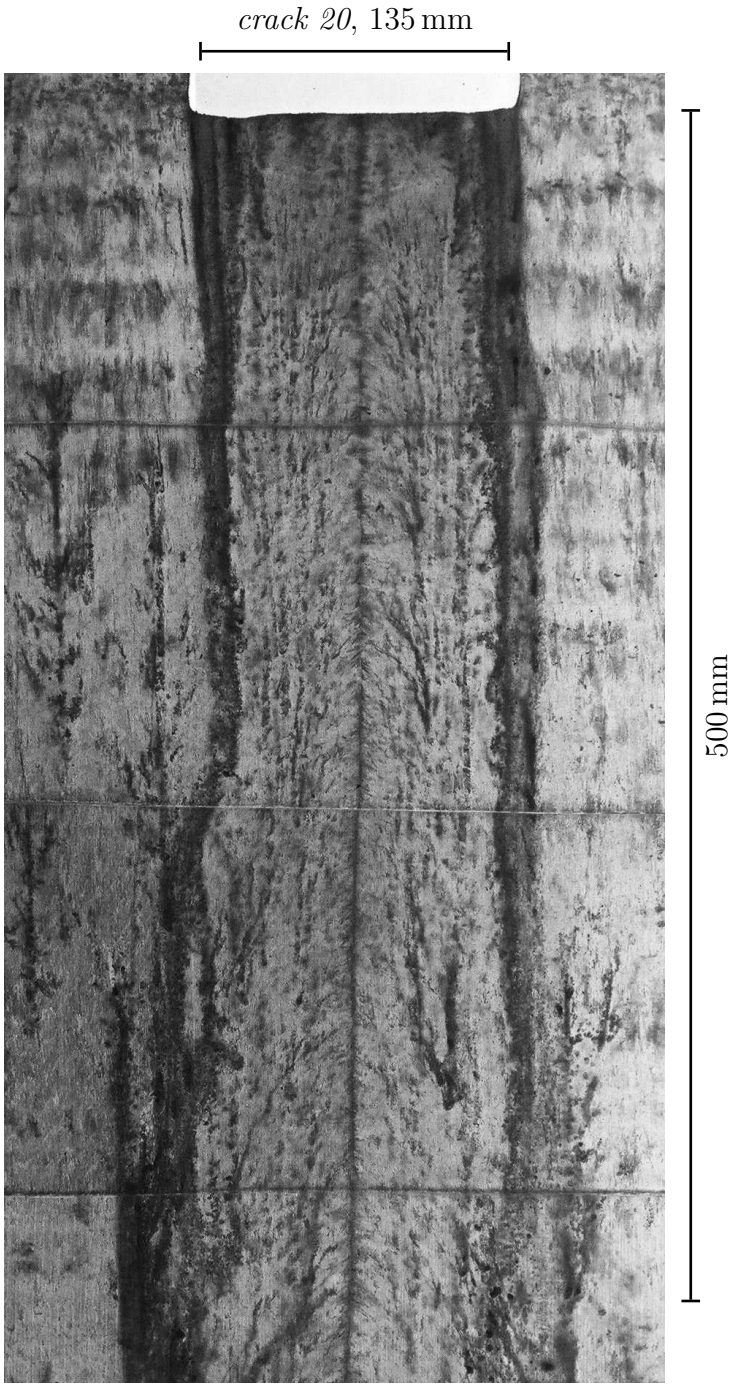

Figure 2.12: Vertical thick section of refrozen crack, *crack 20*.

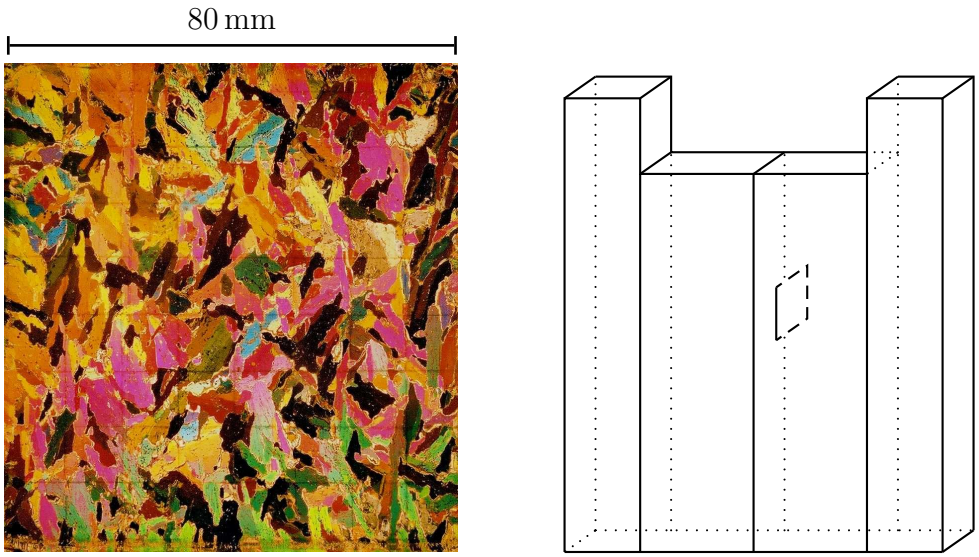

Figure 2.13: Vertical thin section of *crack 20* with the plane of the thin section along the long axis of the crack. The position of this thin section is 5 mm from the centre of the crack, at depth $140 - 220$ mm. This position is indicated in the sketch of a vertical section of the crack.

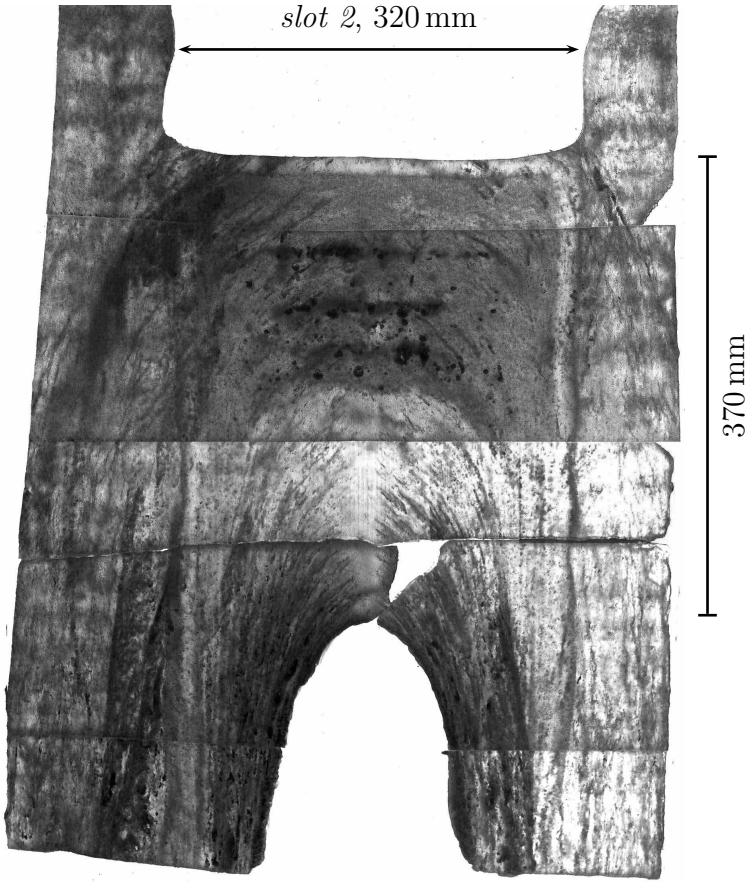

Figure 2.14: Composite vertical thick section of *slot 2*.

2.2.2 Refreezing experiments

During the excavation of *slot 1*, platelets, approximately 20 mm long, were observed growing into the slot (not shown). These platelets were aligned approximately vertically.

Figure 2.14 shows the vertical thick section of *slot 2*. The slot was not completely frozen, and the arch–shaped freezing interface is visible. Inclusions are aligned as arches, and the centre of the slot is devoid of inclusions below 185 mm. The ice above 185 mm is more opaque than observed in thick sections of other cracks and slots. Three thin, horizontal inclusion features are present in that region. These features have a similar origin to a large air inclusion found in *slot 1*, due to the presence of aquatic fauna (Section 2.2.4).

Figure 2.15 compares thick and thin sections of an 80 mm high vertical section of *slot 2*. The thin section shows the usual granular ice at the slot–host ice interface, adjacent to crystals that are aligned horizontally. Crystals point in vertical direction closer to the centre of the slot. A relationship between the alignment of the inclusions

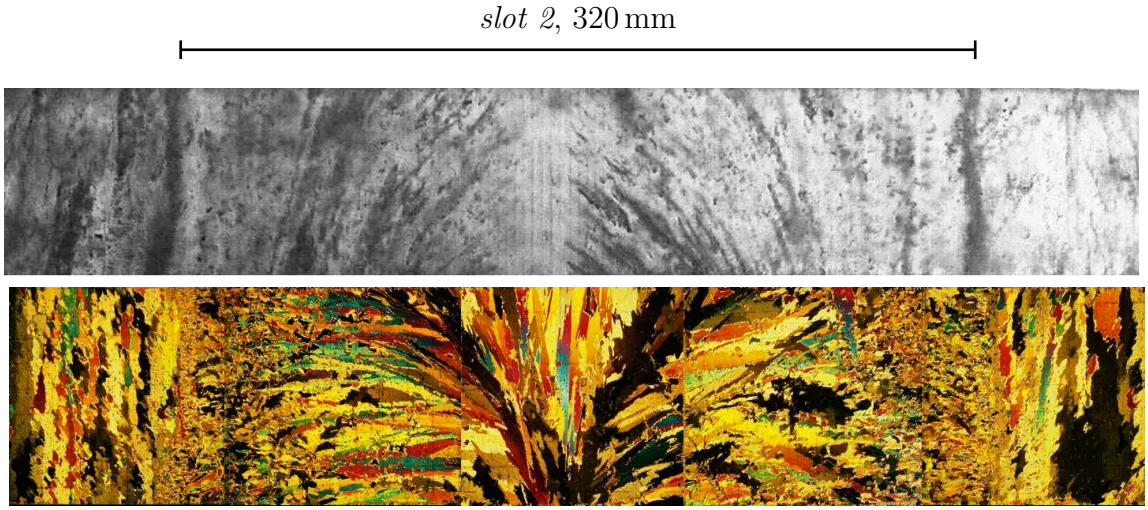

Figure 2.15: Vertical thick section and thin section of *slot 2* 230 mm below the surface of the slot. Height of the thin sections is 80 mm.

and the axes of crystal elongation is not obvious.

Figure 2.16 compares vertical thick and thin section of *slot 10*. The thick section shows a clear demarkation between slot ice and host ice. Inclusions in the slot are aligned as arches. However, the centre above 190 mm is devoid of inclusions, and the devoid area becomes wider as the ice–air interface is approached ("V"–shape). A vertical band of inclusions exists at the centre below 190 mm.

The thin section shows the centre 80 mm of the refrozen slot. Crystals grow vertically downwards at the ice–air interface, but the fraction of crack width they occupy decreases with depth. Crystals that appear to originate at the sides point upwards into the centre. Upward–elongated crystals meet at the centre towards the bottom of the sample. The transition from vertically aligned crystals to upward pointing crystals at the centre of the slot takes place between 180 and 220 mm.

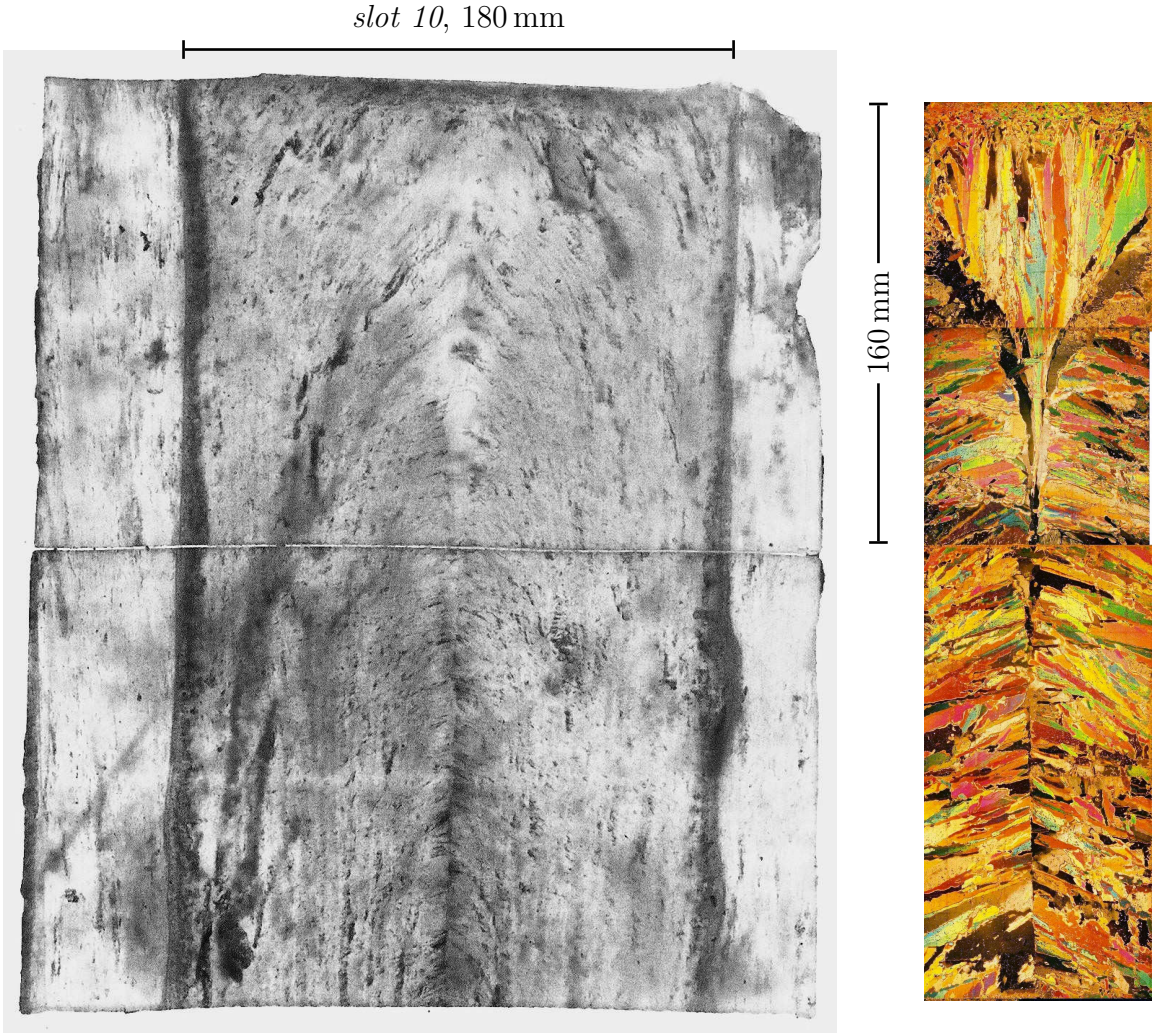

Figure 2.16: Vertical thick and thin section of the top 320 mm of *slot 10*. Thick section (left) is inverted, i.e. brine pockets and air inclusions appear dark, transparent ice appears bright. The transition from host ice to slot is marked by vertical inclusions. The vertical thin section (right) shows the centre 80 mm of the vertical thick section.

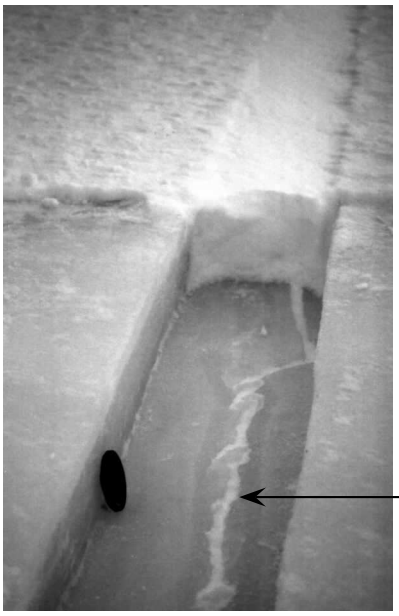

Figure 2.17: Example of a natural, refrozen crack in September, 2002. Snow has been partially removed from the crack. The crack contains a snow–filled thermal crack. A 61 mm outer diameter lens cap is placed upright in the crack for scale.

2.2.3 Thermal cracks

A further eleven different refrozen cracks of width suitable for excavation (100 to 400 mm) were identified in the 2002 season. All of them were snow covered and harboured a secondary crack that was probably not connected to the ocean. The presence of the secondary cracks rendered the cracks unsuitable for excavation and analysis. The secondary cracks were 10 to 40 mm wide at the top, narrowing with depth. Some of the cracks were filled with moist slush. An example is shown in Figure 2.17.

These secondary cracks resembled thermal tension cracks that were also observed in 2001. Some of the thermal cracks were already present at the beginning of the season in 2001, a few of which followed refrozen spreading cracks (similar to Figure 2.17) part of the time. However, many thermal tension cracks appeared over the course of a few days in the early evening hours at the end of October 2001, i.e. in cold nights during a period of general air temperature increase and snow cover removal due to sublimation. The formation of thermal cracks of this length scale has been described for example by *Kingery and Coble* (1963) and analysed by *Evans and Untersteiner* (1971). *Gold* (1963) finds in laboratory experiments on freshwater ice that the thermal stress necessary to induce cracking is equivalent to an abrupt surface temperature reduction of 6 °C. *Cole* (2001) gives evidence for the ability of thermal cracks of several hundred metres length to follow the direction of the basal planes of aligned crystals. On small scales cracks

are found to undergo local deviations into brine drainage structures, even if they follow a generally straight path (*Cole*, 2001).

We may speculate that the secondary cracks observed in 2002 are due to temperature fluctuations earlier in the growth season. For example, the Scott Base temperature record for 2002 indicates a temperature change from around −32 °C down to −52 °C, then rising to −11 °C to return to −30 °C during the course of two weeks in June (data courtesy of the National Institute of Water and Atmospheric Research (NIWA), New Zealand). The tendency of these secondary cracks to follow the centre of the cracks may be due to the general presence of brine inclusions at the centre of the cracks (as we have seen) that reduce tensile strength of sea ice (*Weeks and Ackley*, 1986). However, one crack was found that split into two cracks at some point to reunite a few metres further on. The thermal tension crack followed only one branch, allowing for the excavation of a sample of the intact branch (*crack 20*).

2.2.4 Salinity profiles

Figure 2.18 shows three vertical salinity profiles. Note that all profiles have different length scales but share the same colour scale. Salinity data are listed in Appendix A.1.

Figure 2.18(a) shows the salinity profile of *crack 1*. The samples at the sides of the figure show the salinity of the host ice, and the transitions from crack ice to host ice are marked by the broken lines. The salinity appears to be continuous at the crack–host ice interface. The average salinity across the crack reduces with increasing depth down to 900 mm, which is where the inclusion structure changes (Figure 2.2). The salinity is highest at the crack–host ice interface close to the ice–air interface, while the salinity is highest in the centre of the crack below 200 to 300 mm. Below 900 mm, however, the centre of crack is of lower salinity than the sides. The latter observation corresponds to the observed absence of inclusions at the centre of the crack below 900 mm. The vertical bands of inclusions observed in the thick section of *crack 1*, however, are not reflected in the salinity profile at this spatial resolution. The salinity profile is approximately symmetrical about a line down the centre of the crack.

Figure 2.18(b) shows the salinity profile of *crack 20*. The samples at the sides of the figure show the salinity of the host ice. The width of *crack 20* is half of the width of *crack 1*. Again, the salinity profile appears to be continuous at the transition from crack to host ice, decreasing with increasing distance from the ice–air interface. The salinity is highest at the crack–host ice interface in the upper 200 to 300 mm, while a salinity maximum is found in the centre below 100 mm. The average salinity of *crack 20* is larger than the salinity of *crack 1* at the ice–air interface. Again, the salinity profile is approximately symmetrical.

Figure 2.18(c) shows the salinity profile of *slot 10*, which has a width intermediate between the widths of *crack 20* and *crack 1*. In this case, the salinity of the slot appears to be systematically higher than the salinity of the host ice. While the salinity decreases with depth in the upper 250 mm, it increases below this level. The salinity is highest at the crack–host ice interface in the upper 200 to 300 mm, and a distinct salinity minimum is present at the centre above 150 mm. A salinity maximum exists at the centre of the slot below 250 mm, reaching values between 15 and 18 psu at the bottom of the sample. As before, the salinity profile is symmetrical.

Figure 2.19 shows two more vertical salinity profiles. Again, all profiles have different length scales but share a colour scale with Figure 2.18. Host ice salinity is not measured in these two salinity profiles.

Figure 2.19(a) shows the salinity profile of *slot 1*. The salinity decreases with depth.

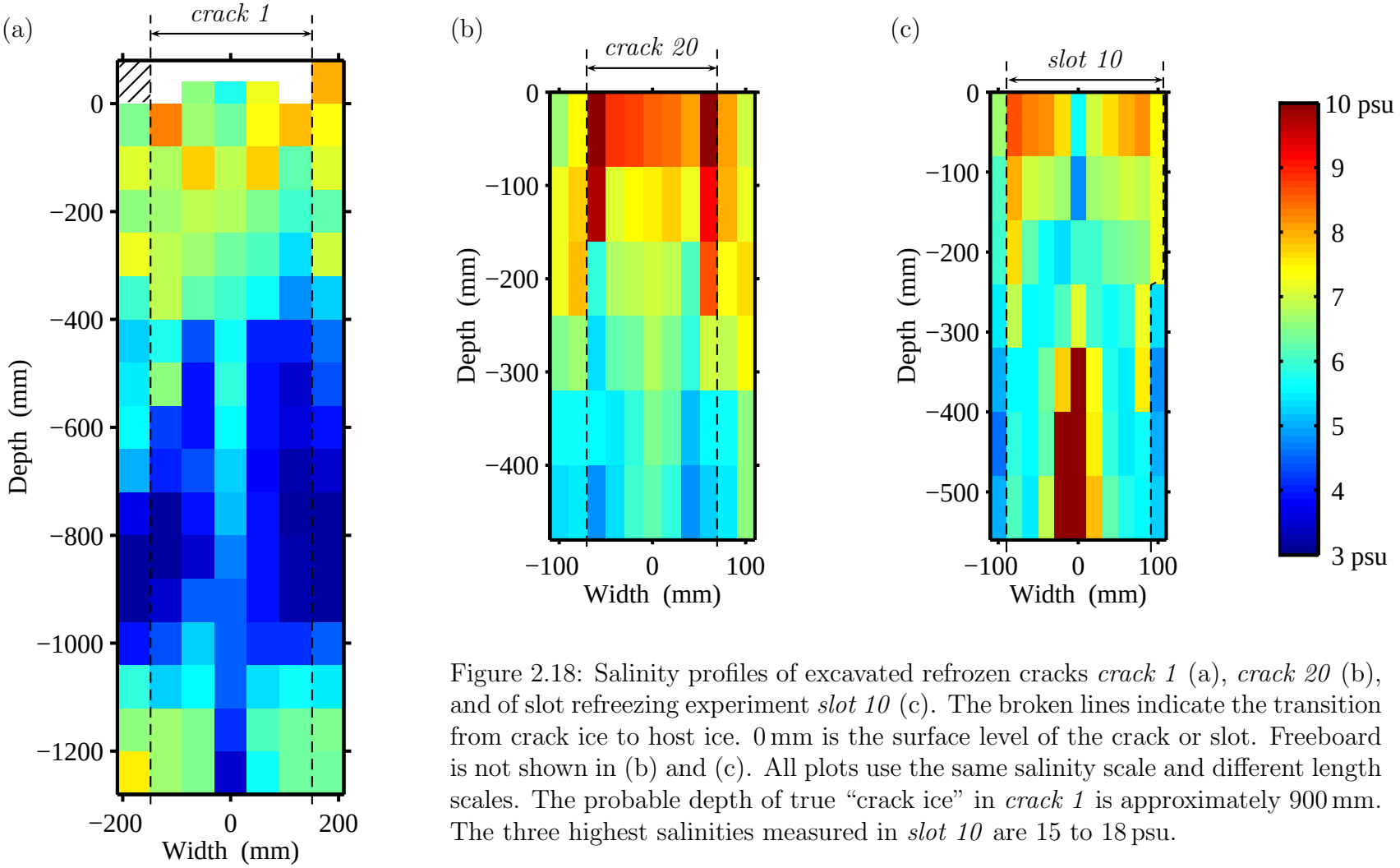

Figure 2.18: Salinity profiles of excavated refrozen cracks *crack 1* (a), *crack 20* (b), and of slot refreezing experiment *slot 10* (c). The broken lines indicate the transition from crack ice to host ice. 0 mm is the surface level of the crack or slot. Freeboard is not shown in (b) and (c). All plots use the same salinity scale and different length scales. The probable depth of true "crack ice" in *crack 1* is approximately 900 mm. The three highest salinities measured in *slot 10* are 15 to 18 psu.

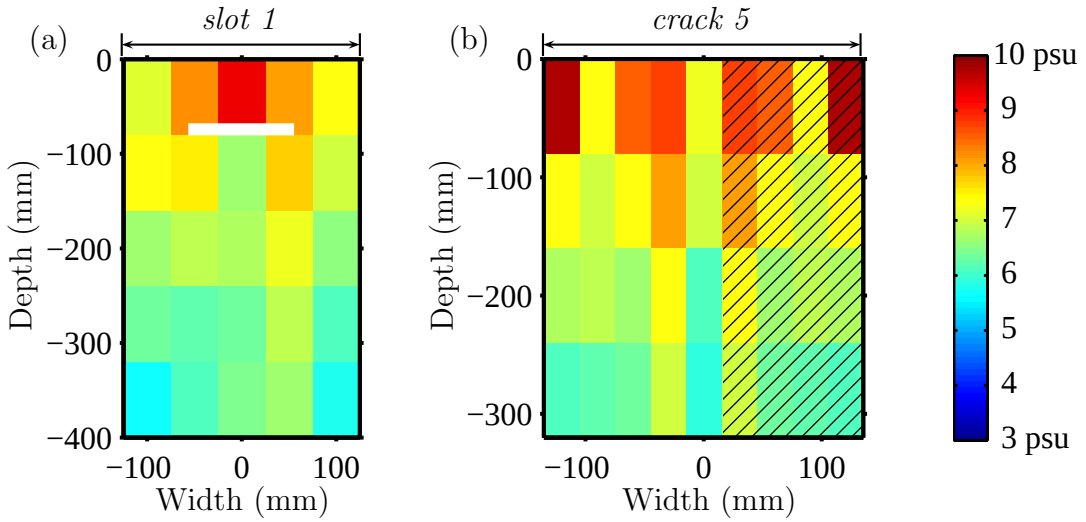

Figure 2.19: Salinity profile of (a) experiment *slot 1* and (b) excavated refrozen crack, *crack 5*. The white spot in (a) indicates the location of an air inclusion 70 mm below the surface, 120 mm wide and 10 mm high. The hatched part in (b) is mirrored, not measured. The largest salinity measured in *crack 5* is 9.7 psu. The salinity scales are the same as in Figure 2.18. Note the different scales of (a) and (b).

However in this case, the horizontal salinity distribution could have been affected by an air inclusion 70 mm below the ice–air surface. This air inclusion was located at the centre of the slot and is 10 mm high and 120 mm wide. It was presumably caused by a seal. Weddell seals were observed blowing bubbles into cracks in sea ice in McMurdo Sound in order to flush out fish (*Davis et al.*, 1999). In fact, a fish (possibly a bald rockcod, *Pagothenia borchgrevinki*) was observed lingering in the slot at the beginning of this refreezing experiment.

Figure 2.19(b) shows the salinity profile of *crack 5*. In this case, the salinity of a little more than half of the crack was measured, and the hatched area in Figure 2.19(b) is a mirror image. The salinity of the crack decreases with depth. It is always lowest at the centre, consistent with absence of inclusions there (Figure 2.7). Another local salinity minimum exists closer to the side of the crack.

2.3 Summary and conclusion

General structure of refrozen cracks An approximate picture of refrozen cracks and slots emerges. First, the crystal structure of refrozen cracks and artificial slots is similar. Granular crystals tend to form at the sides of crack, while elongated crystals grow in the interior. This structure is equivalent to the general structure of alloy casts (*Kurz and Fisher*, 1998). There, the development of the columnar zone is expected to be a result of geometric selection. While granular crystals at the side could

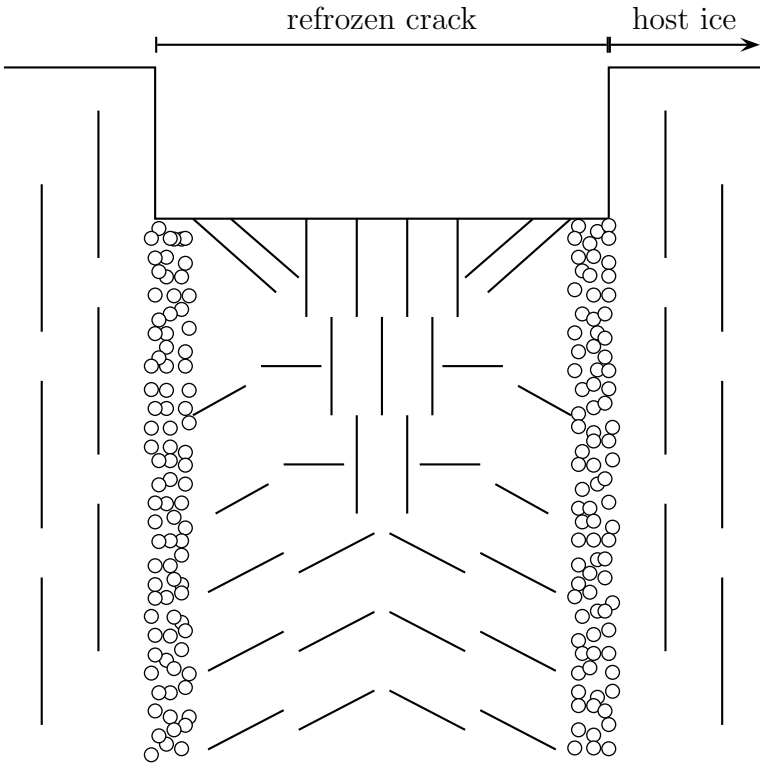

Figure 2.20: Vertical section of the structure of a generic refrozen crack, marked by elongated crystals. Granular crystals exist at the transition from host ice to crack ice. The region of vertically growing crystals is generally devoid of inclusions. A vertical band of inclusions exists at the centre of the crack, where upwards growing crystals meet.

have formed due to supercooled water generated by rejected brine (Jean–Louis Tison, personal communications; *Kurz and Fisher*, 1998), they could alternatively be due to frazil ice sometimes observed in the water column in McMurdo Sound (for example, at the beginning of *slot 1*, *10*, and *12*), or they could be an amalgamation of crystals swept into the crack at the time of crack formation (and possibly during a storm). Crystals tilt upwards into the crack at the sides (Figure 2.20), which would be expected if they grew in the presence of a downward current at the sides (*Flemings*, 1974). Upward–tilting crystals in thin sections of refrozen cracks grown in McMurdo Sound (*Haskell and Langhorne*, unpublished 2000) and in the laboratory (*Divett*, 2000) have previously been presented. Since solute rejected at the freezing interface increases the density of the liquid, such a convective current is to be expected. Crystals were found to grow vertically downwards close to the ice–air interface at the centre of wide cracks (*crack 5*, *slot 10*). The width of this region of downward–growing crystals decreases with increasing depth (*crack 5*, *slot 10*), until eventually upward–tilting crystals meet, growing into the crack from both sides (*slot 10*). A vertical band of inclusions forms

where upward–tilting crystals meet at the centre of the crack (*crack 2*, *crack 20*, *slot 10*), while virtually no inclusions are present where crystal growth is vertically downward (*crack 4*, *crack 5*, *slot 10*).

In wider, naturally refrozen cracks, additional vertical bands of inclusions were found to be present either throughout the vertical extent of the crack, or only close to the surface (*crack 1*, *crack 4*, *crack 5*). It has previously been suggested that such bands may be signs of multiple fracture events of partially refrozen cracks (*Petrich et al.*, 2003). Alternatively, they may be due to minor deformation during the refreezing process (possibly also inducing dynamic recrystallisation). Inclusions often align as arches which is, at least qualitatively, the shape of the freezing front and presumably the path of fluid motion along the freezing front (Chapter 6).

Close to the ice–air surface, the salinity tends to be lowest at the centre (*crack 1*, *crack 20*, *slot 10*), which can be understood by considering one–dimensional ice growth: it is generally observed that ice is of higher salinity if it grows faster (Section 5.2). Since heat is being removed to both ice–air interface and ice–host ice interface close to the surface at the sides, this could result in elevated entrainment of brine at the sides relative to the centre. Another reason for low salinity at the centre could be that seawater enters this part of the newly forming ice. Since seawater is of lower salinity than the brine inside the sea ice, this flow would tend to reduce the salinity locally. Solute enriched brine can easily escape sideways if the crystals grow with their c–axes parallel to the crack (*crack 4*, *crack 5*). Low salinity corresponds to low porosity, which explains the centre devoid of inclusions (*crack 4*, *crack 5*, *slot 10*). Far from the ice–air interface, the relatively high salinity at the centre could be related to disruption of brine drainage by crystal platelets at the centre of the crack as the freezing front arch narrows, or because there may be a shorter time for brine drainage due to a thinner skeletal layer near the centre compared to ice that grows closer to the sides (Sections 3.2.3 and 6.4.5). A high salinity at the centre manifests itself in a high porosity (*crack 1*, *slot 10*).

Crystal tilt Figure 2.21 demonstrates that spatially varying crystal tilt could be due to spatially varying influences on crystal growth. Two contributions to the net growth direction are superimposed in this simplified picture, one is due to the direction of heat flux or a preferred growth direction (e.g. $\langle 11\bar{2}0 \rangle$), and the other one is due to solute redistribution at the crystal tips that results in a growth advantage in upstream direction. Assuming both contributions are of equal magnitude, Figure 2.21(a) demonstrates the case of perpendicular contributions. One contribution is normal to the interface, which is approximately the direction of heat flux, while the other one is

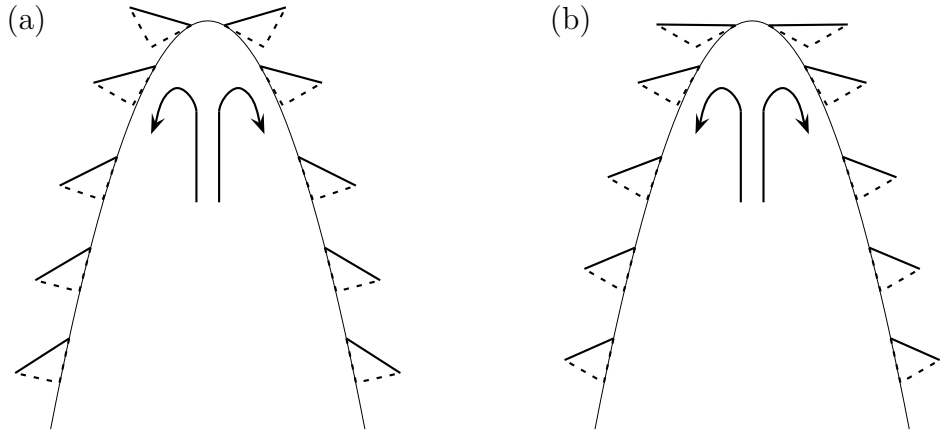

Figure 2.21: Crystal alignment at a parabolic freezing interface. Superposition of two contributions (broken lines), resulting in a net crystal growth direction (solid lines). (a) The contribution parallel to the interface is equal to that normal to the interface curvature; (b) contributions parallel and perpendicular are not equal. The arrows sketch the general path of fluid motion.

parallel to the interface, reflecting the growth advantage in upstream direction. Figure 2.21(b) demonstrates the case for non–perpendicular contributions. Both figures show that crystals could be expected to grow horizontally or downwards close to the centre of the crack, while growing upwards further away, which is particularly clear in *crack 5*. However, the likelihood of the development of downward–pointing crystals is largest in the earlier stages of growth, when the radius of curvature of the interface at the centre of the crack is largest. Thus, for wider cracks close to the ice–air interface, there is a transition from the upward–tilting crystals that grow from the sides to the crystals that grow downwards at the centre of the crack. The impression, as in Figure 2.6, is of a fountain–shaped crystal structure. The crystal structure of narrower cracks (*crack 20*, Figure 2.11) and of wide cracks farther away from the ice–air interface (*slot 10*, Figure 2.16) is dominated by growth from the sides. The details of the crystal structure depend on the preferred crystal growth direction and magnitude in the absence of currents, on the constitution of the liquid, and on the shape of the freezing interface. This topic is open to further investigation.

Chapter 3

Thermal measurements of refreezing cracks in Antarctica

3.1 Approach

Data of refreezing experiments with probes 1 and 2 are discussed in this chapter. Probe 1 is a two–dimensional thermistor array used to record the refreezing progress and temperature in the ice of the refreezing slots. The design of this probe is introduced in Section 3.2.1, and an overview of the experiments is given in Section 3.2.2. In Section 3.2.3, a relationship between the temperature signal and the location of the freezing front is established, which is used in Section 3.2.4 to compare measurements with a model of ice growth developed in the same section. The freezing front definition is further used in Section 3.2.5 to estimate the heat balance during slot refreezing.

Probe 2 is a two–dimensional thermistor array used to record seawater temperature variations in refreezing slots. The physical and electrical design of this probe are introduced in Section 3.3.1, and an overview of the acquired water temperature data is given in Section 3.3.2. In Section 3.3.3, the variation of temperature signal with time of day and with illuminance are discussed.

Diurnal water temperature variations were detected in refreezing experiments with both probes, and Section 3.4 establishes that these variations are due to direct solar radiative heating of the thermistor beads in the water. First, the water temperatures are compared in Section 3.4.1. The illuminance measurements made as part of experiments with probe 2 are correlated with water temperature measurements in Section 3.4.2. A heat transfer model is used in Section 3.4.3 to discern the effects of solar shortwave radiation absorbed by the water and by the thermistor beads, and the findings are discussed in Section 3.4.4. Section 3.5 summarises the key results of this chapter.

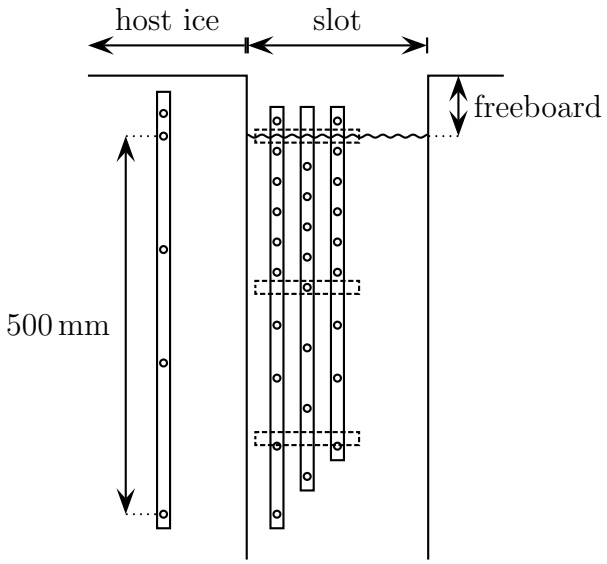

Figure 3.1: Thermistor probe 1 with thermistor strings arranged as in experiments *slot 1* and *slot 2*. Of the four strings of thermistors three are frozen into the slot, while one is frozen into the host ice sheet. The horizontal position of the strings varies between experiments. The vertical positions of the 32 thermistors on the strings are drawn to scale.

3.2 Ice temperature – Probe 1

3.2.1 Design of probe 1

Thermistor probe 1 is designed to track the freezing process in the slot, and to measure the temperature in the host ice and in the air above the ice–air interface of the slot. A sketch of the probe is shown in Figure 3.1. Four individual strings of thermistors are constructed with 5 to 10 thermistors on each string. The support for each string is a plastic conduit filled with potting compound. From this the thermistors protrude 25 mm, held in place by 4 mm outer diameter plastic tubing[1]. The thermistor beads are covered with an electrically insulating coating of nail varnish but are otherwise directly exposed to the environment. One thermistor string is used to measure the temperature profile of the host ice, while three strings are used to monitor the refreezing process of the slot. The three strings in the water are held in place with respect to each other by three horizontal aluminium bars. The strings can slide along the bars, which allows them to be adjusted according to the width of the slot. Two of the thermistors on these strings measure the temperature 20 mm above the slot surface, i.e. air temperature or temperature in a snow cover.

[1] A thermistor string design with protruding thermistors has also been used by *Frey et al.* (2001) to measure ice temperatures.

The thermistor string arrangement in experiments *slot 1* and *slot 2* is as shown in Figure 3.1 with the shortest string in the centre of the slot, and the longest string at the side of the slot. The configuration is reversed in *slot 10* with the longest string in the centre and the shortest one at the side of the slot. Only the two longest strings have been placed in the very narrow slot of *slot 12*.

The thermistors are connected to a 32 : 1 multiplexer. Resistances are converted to voltages with a resistor bridge followed by an amplifier circuit. The voltages are logged by a *Campbell Scientific CR10X* data logger once every 5 or 10 minutes. The system is powered by *Sonnenschein* lead acid batteries. The resistance–voltage converter is designed to be insensitive to air temperature fluctuations in the range −10 to −40 °C, which was accomplished by Dave Hardisty, Electronics Workshop, Physics Department, University of Otago, by choosing components with small temperature coefficients, and appropriate circuit design and layout.

3.2.2 Overview of experiments with probe 1

Description of experiments

Probe 1 has been used for slot refreezing experiments in McMurdo Sound in October and early November 2001 (experiments *slot 1* and *slot 2*) and in September 2002 (experiments *slot 10* and *slot 12*). Experiments always followed the same pattern. After a site on first–year ice had been selected, a slot of more than 2 m length and of specified width[2] was cut in the ice with a ditch digger modified for use on sea ice (*Haskell et al.*, 1996). Initially, the bottom section of the ice sheet was left intact to allow the cutting of slots that were wider than the chain (120 mm), and to keep the amount of saltwater spill on the ice to a minimum. This procedure took about an hour. Eventually the ditch digger was used to cut open the bottom of the slot to its full length. Manual intervention was occasionally required on particularly thick sea ice to remove bridges of ice at the bottom of the sheet that the ditch digger was not able to reach. Once the slot was flooded and a clear path for water was obtained, shovels and kitchen sieves were used to clear the slot of ice debris and frazil until only a clear water column remained in the slot. At the same time, a hole was drilled through the top portion of the sea ice sheet at the side of the slot to deploy a thermistor string to monitor the host ice temperature. This hole was filled up with sea ice chipping and

[2]The ratio between length and width of the slot has been chosen to be typically 10, limiting the lateral heat flux along the axis of the slot to 10 % of the lateral heat flux perpendicular to the slot. Further, vertical heat flux is significant in the examined upper 500 mm of the refreezing slot. Hence, slot refreezing can be considered to be a two–dimensional process at a position half way along the length of the slot.

Table 3.1: Summary of experiments with probe 1.

	slot 1	*slot 2*	*slot 10*	*slot 12*
Location	Cape Evans	Cape Barne	Erebus Bay	Erebus Bay
Slot width (m)	0.23	0.32	0.18	0.12
Ice thickness (m)	2.20	1.39	2.15	2.20
Slot orientation	N–S	N–S	E–W	N–S
Thermistors point	N	N	E	N
Strings in water+ice	3+1	3+1	3+1	2+2
Start date	14 Oct, 01	27 Oct, 01	2 Sept, 02	16 Sept, 02
Start time (local)	22:20	15:30	15:55	15:50
Sampling period (s)	600	600	300	300
Average T_{air} (°C)	−17.5	−13.5	−25	−14.0
Excavation	20 Oct, 01	5 Nov, 01	9 Sept, 02	21 Sept, 02
Excavation time (local)	10:20	12:10	15:35	08:30
Final snow cover (mm)	20	30	200+	200+

either sea water or tap water to freeze the thermistor string in place. Two strings were deployed in the host ice in the case of *slot 12*. The three (two for *slot 12*) remaining thermistor strings were placed in position midway along the long axis of the cleared slot and were attached to a stand. Temperature logging started at once. The time between flooding of the slot and the beginning of the experiment was about one to two hours.

At the beginning of experiments *slot 1*, *10* and *12* tiny crystals of unknown nature floated up to the surface which quickly became covered by a thin, opaque ice sheet.

Data were downloaded and batteries were exchanged on irregular visits to the site during the experiments. The refreezing progress was monitored by preliminary evaluation of data, and by coring through the slot at some distance from the probe. Snow fall was not cleared.

The probe was excavated with the ditch digger and crane (in 2001) or a chain saw with a long blade (in 2002) after the last thermistor froze in, with the exception of *slot 2* which was terminated before the probe was frozen in completely. Samples for salinity profiles and/or structural investigations were taken from *slot 1*, *slot 2*, and *slot 10* at the time of excavation. During the excavation of *slot 10* both thermistors measuring the air temperature in the slot were damaged. The air temperature was therefore measured close to the data logger box during *slot 12*. The bottom of the host ice sheet and the freezing front of the slot in *slot 1* were tinted green, while the bottom of the ice and the freezing front of *slot 2* were brown with algae.

Some characteristics of probe 1 experiments are summarised in Table 3.1. The position of the thermistor strings within the slots is documented in Table B.1 on page 239.

Temperature records

In order to convert resistance measurements of the thermistors to temperature values, the Steinhart–Hart equation (*Steinhart and Hart* (1968) and Appendix B.4) was applied. A temperature offset (in the range $(-0.15 \pm 0.15)\,°C$) was added for each individual thermistor measuring water temperature so that the temperature reading at the beginning of each experiment was $-1.9\,°C$ (one–point calibration). The assumption of a fixed temperature offset between thermistors has previously been used (*Lewis*, 1967; *Trodahl et al.*, 2000). The exceptions to the application of a temperature shift before data processing are detailed on page 104 where the water temperature between experiments are compared. Corrections for solar radiative heating of the probes are not applied as the effect is small (Appendix B.3).

The temperature–time series of all experiments are shown in Figure 3.2 and 3.3. Solar time (*Iqbal*, 1983; *Müller*, 1995) is plotted on the x–axes with time 0 set to true midnight (the time the sun is lowest) after the beginning of the experiment. Several temperature spikes in the record of *slot 1* in Figure 3.2(a) can be seen to propagate through the ice. The record of *slot 2* in Figure 3.2(b) shows a pronounced diurnal temperature signal. The record of *slot 10* in Figure 3.3(a) clearly reveals snow fall around hour 12, when the thermistors measuring the air temperature in the slot were covered in snow. For analysis purposes, a data logger deployed at Scott Base was used to estimate the air temperature following that event (Appendix B.2, Figure B.1). Experiment *slot 12* shown in Figure 3.3(b) became covered in snow between hours 16 and 36. However, that event is not clearly visible in Figure 3.3(b) since the air temperature was measured 500 mm above the sea ice surface. However, the high frequency component of some thermistors in the slot seems to disappear around hour 18.

Vertical temperature profile

A few vertical temperature profiles at the centre of the refreezing slots are shown in Figures 3.4 and 3.5. Profiles are plotted at times shortly before a thermistor freezes in. The temperature profiles of *slot 1* in Figure 3.4(a) are approximately linear with a slight curvature towards the bottom of the refreezing slot. The profiles of *slot 2* are generally not linear due to a strong diurnal temperature signal, which is apparent in Figure 3.4(b) in the profile at 46 h. The water temperature is comparatively constant during the experiments *slot 1* and *slot 2*. Profiles of *slot 10* and *slot 12* in Figures 3.5(a) and (b), respectively, show curvature that is due to the presence of snow cover at the upper slot surface. Due to the small thermal conductivity of snow, heat removal during

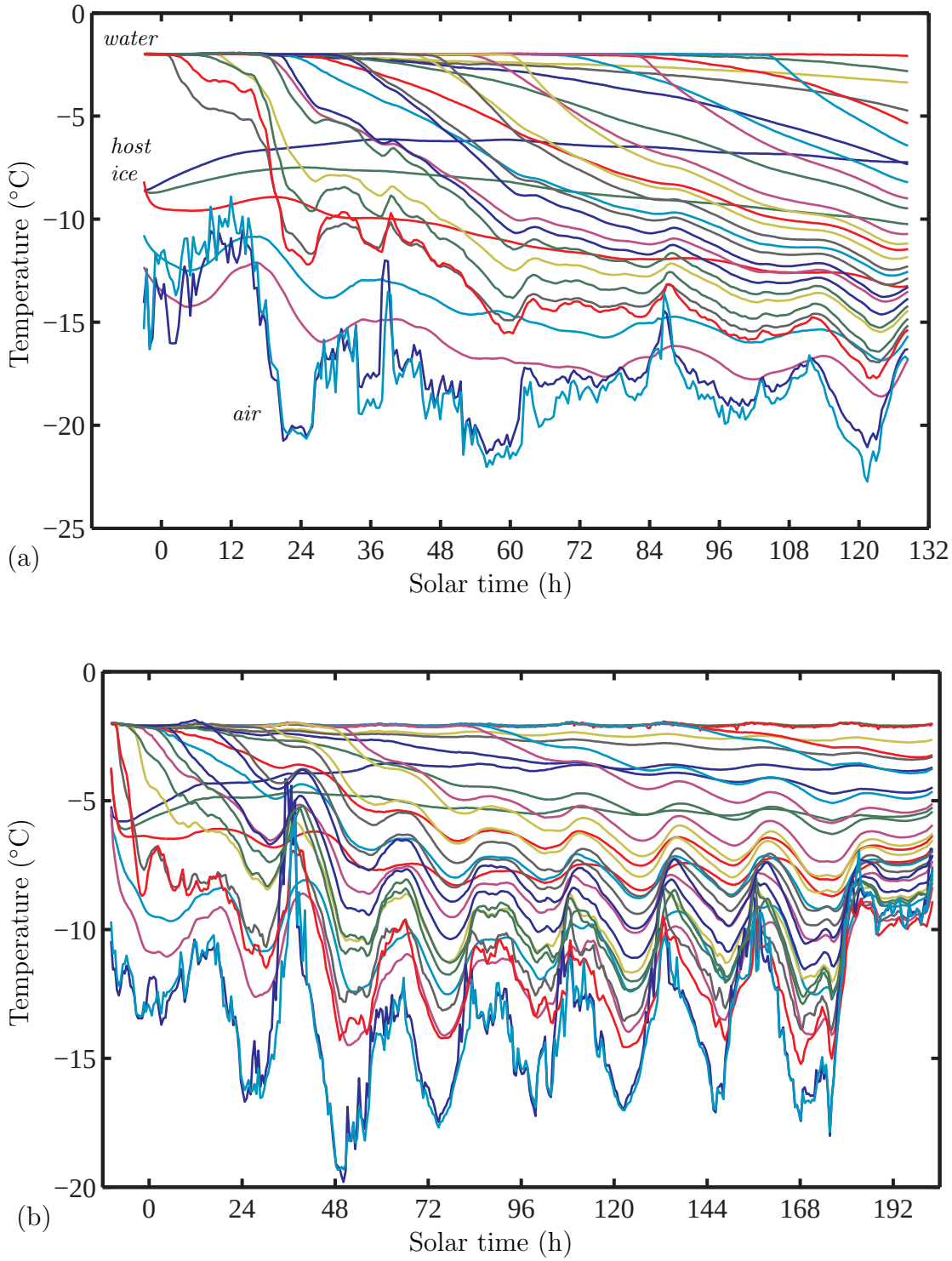

Figure 3.2: Temperature time series of thermistors in (a) *slot 1* and (b) *slot 2*. The thermistors in the slot start at −1.9 °C, the two thermistors in the air generally measure the lowest temperatures, and the five thermistors in the host ice sheet start at intermediate temperatures. See Figure 3.6 for a close–up look at thermistors in the water.

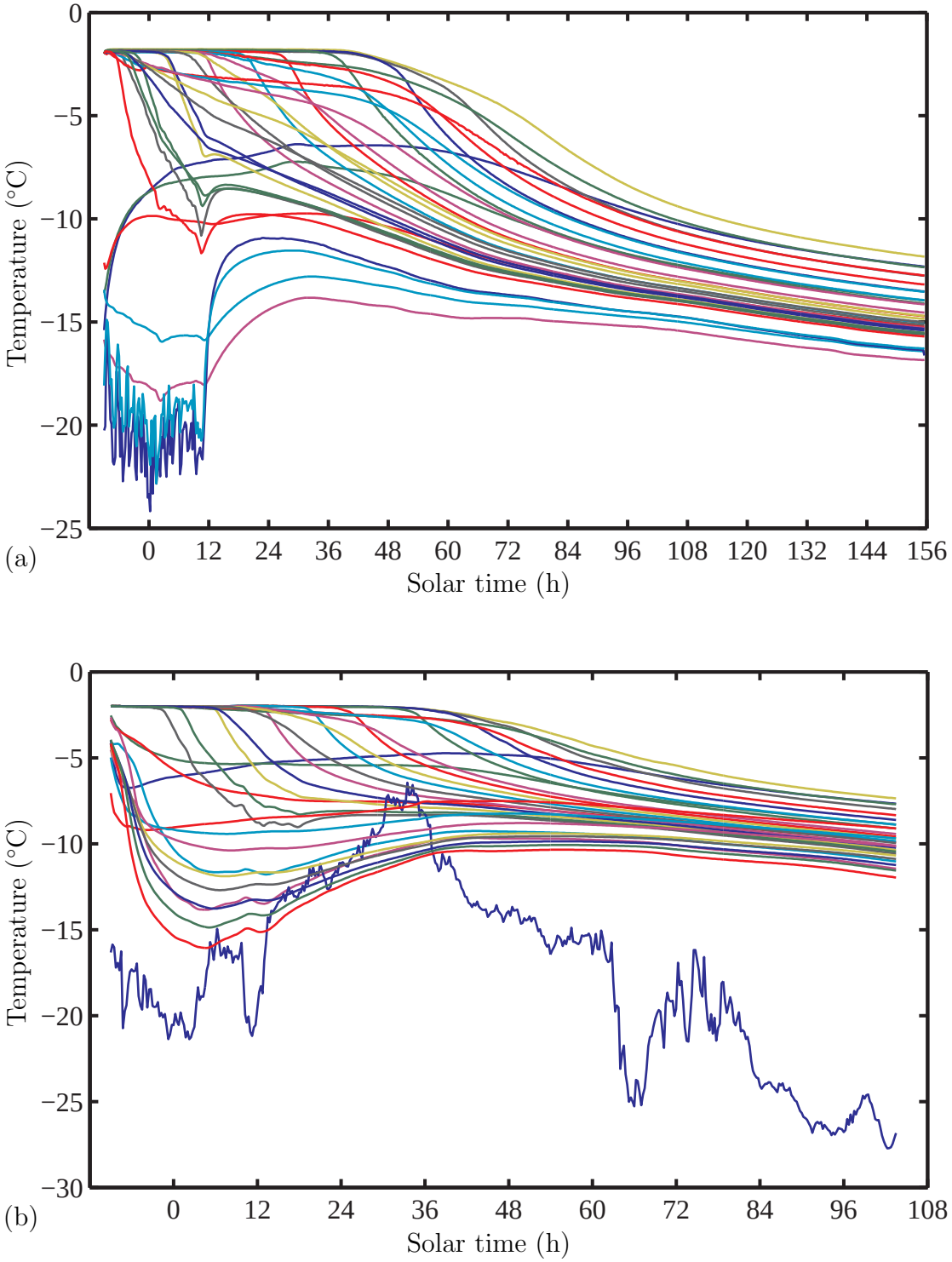

Figure 3.3: Temperature time series of thermistors in (a) *slot 10* and (b) *slot 12*. The air thermistor in *slot 12* is positioned 500 mm above the sea ice surface. The thermistors in the slot start at −1.9 °C, the two thermistors in the air (one thermistor in *slot 12*) show high–frequency temperature variations (except when they are snow covered at hour 12 in *slot 10*), and the thermistors in the host ice sheet start at temperatures below −1.9 °C.

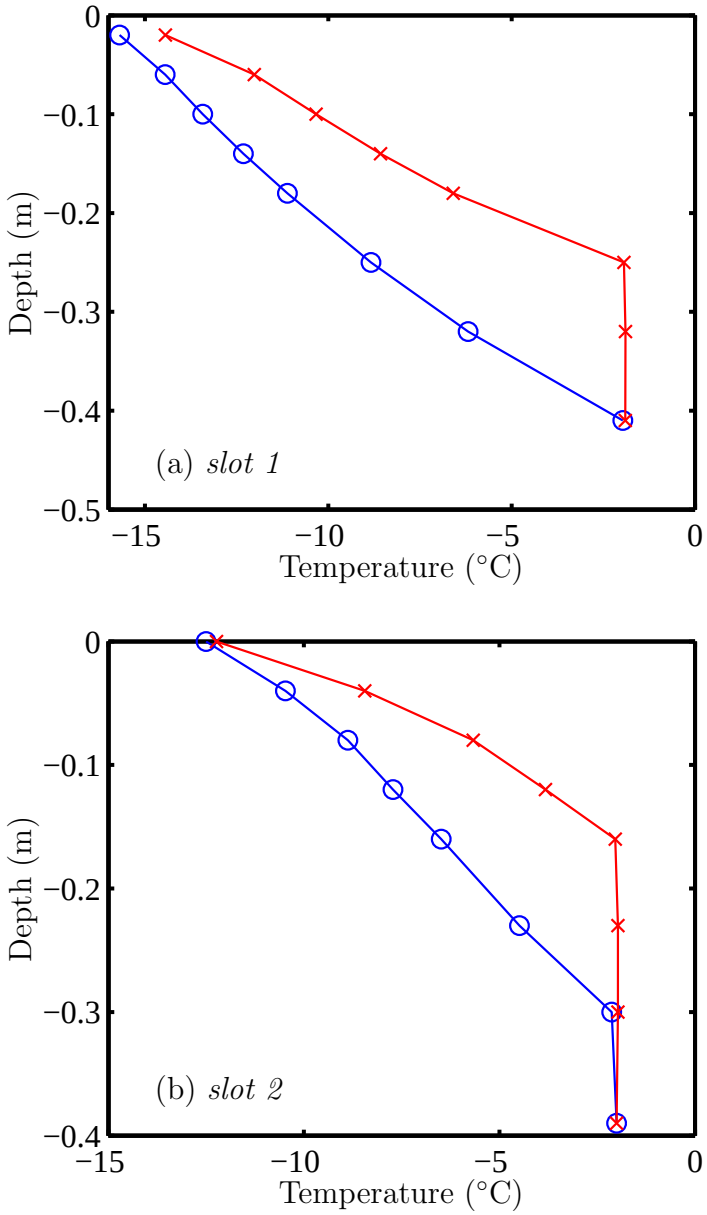

Figure 3.4: Temperature profile at the centre of (a) *slot 1* at 80.3 h (crosses) and 127 h (circles), and (b) *slot 2* at 46 h (crosses) and 142.7 h (circles). The temperature profiles of *slot 2* are particularly subject to diurnal variations.

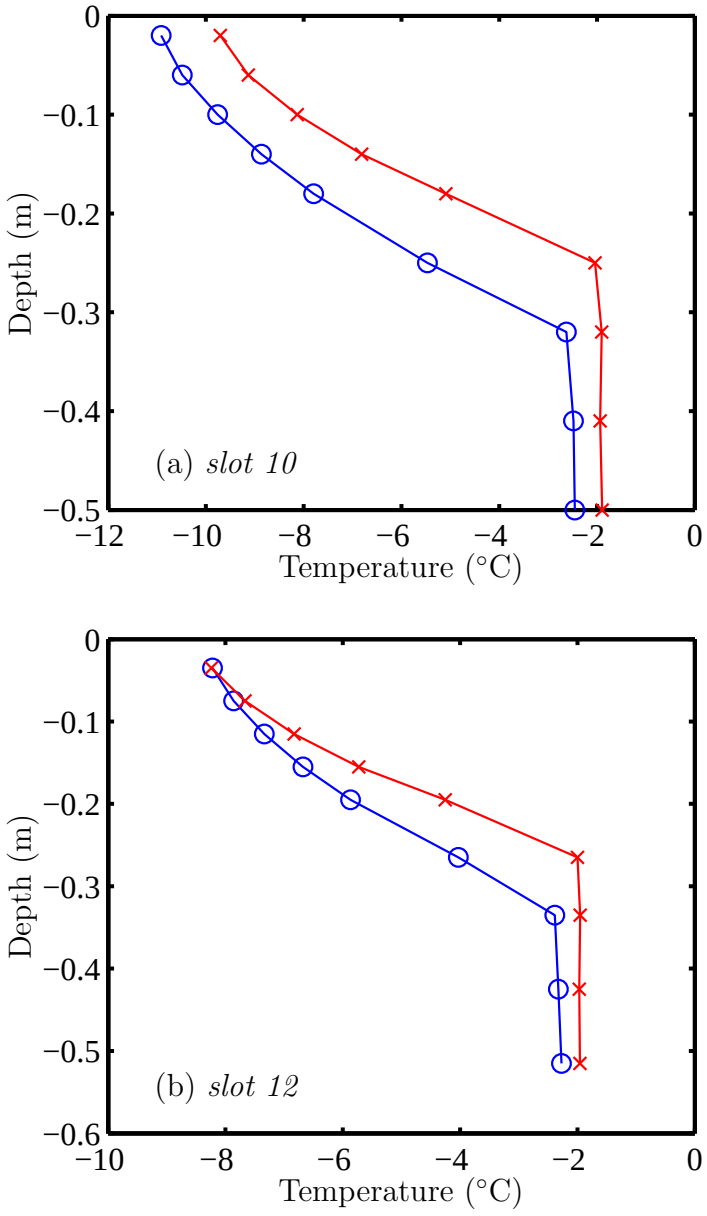

Figure 3.5: Temperature profile at the centre of (a) *slot 10* at 34.3 h (crosses) and 47.6 h (circles), and (b) *slot 12* 30.1 h (crosses) and 39.2 h (circles). Note that slots are snow covered at the shown times.

these times is largely to the sides of the slots. Also visible is a temperature reduction in the thermistors in the water at later times, which is probably an indication of the presence of unconsolidated ice as discussed in Section 3.2.3.

3.2.3 Sea ice freezing front

The location of the freezing "front" of sea ice is ill–defined due to the lamellar growth of sea ice. On a microscopic scale, its location can be defined as the interface between crystalline ice platelets and brine. However, in this thesis a macroscopic approach to sea ice is of interest and this is largely transparent to the details of the microscopic structure (an account of the meaning of "macroscopic" is given in Chapter 4). One possible definition of the location of the macroscopic freezing front is the position one would find from conventional ice thickness measurements by drilling. This definition uses sea ice strength as the defining element. However, this definition is ambiguous as growing sea ice consists of a weak skeletal layer at the bottom of an ice sheet and sea ice of strength above that layer (*Anderson and Weeks*, 1958; *Assur and Weeks*, 1964; *Weeks and Lofgren*, 1967; *Cox and Weeks*, 1975; *Nakawo and Sinha*, 1981; *Gow et al.*, 1990). Depending on the constitution of the skeletal layer, ice thickness measurements are somewhat dependent on the strength of the person taking the measurement.

We need to define the freezing front of sea ice from thermistor temperature measurements. Ideally, the thermally–defined position would coincide with the position found by drilling. It should, in addition, discriminate between the thermal, chemical, and mass transport environment of a liquid ocean, and that of a porous sea ice sheet. Little attention seems to have been paid to the relationship between temperature and sea ice properties at the interface, and since this topic is beyond the focus of this project, we have to adopt an empirical approach to the macroscopic freezing front. We follow the spirit of Ockham's Razor and choose the simplest model that fits the observations.

Threshold temperature approach Probably the simplest approach to the thermal definition of the sea ice freezing front has been used by *Wettlaufer et al.* (2000) to determine the one–dimensional freezing of a lead. *Wettlaufer et al.* define the instant in time that the freezing front passes a thermistor as that instant when the measured temperature falls below the ocean temperature (assumed to be at the freezing temperature) by an amount ϵ. *Wettlaufer et al.* (2000) choose ϵ to be as small as possible, but large enough to leave the determination of freezing unaffected by temperature fluctuations in the ocean. Their value for ϵ is always smaller than 0.25 °C. However, temperature fluctuations due to movement of brine in the skeletal layer have been detected in

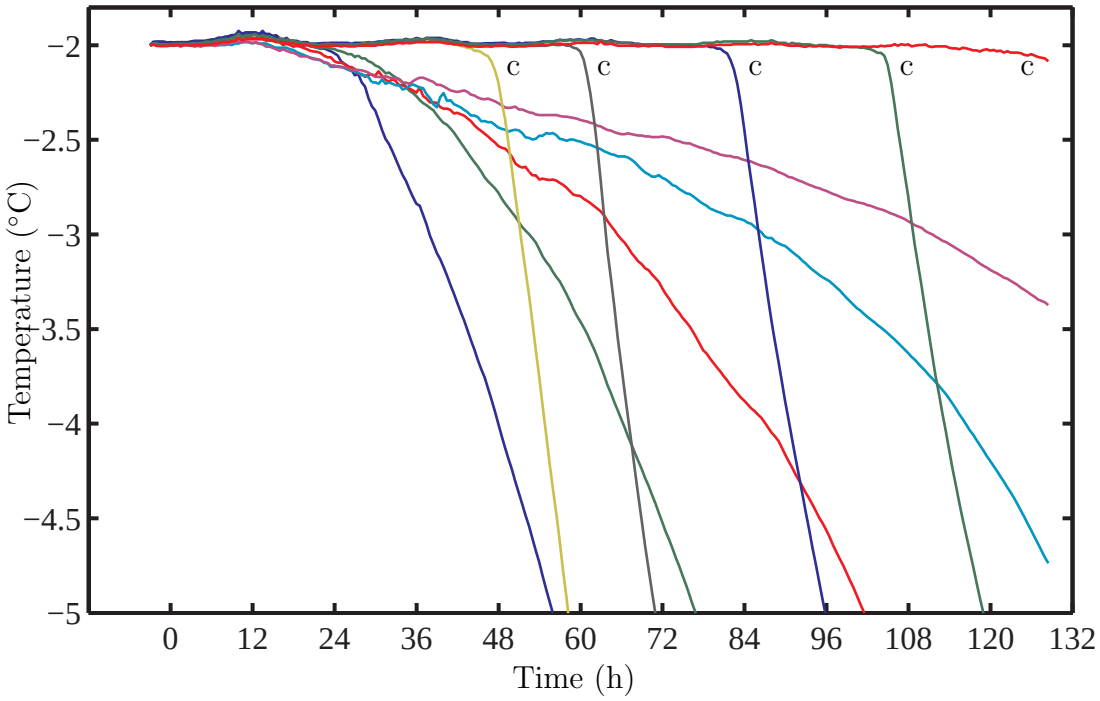

Figure 3.6: Freezing of thermistors of the centre string compared to the side string in *slot 1*. For clarity, only the bottommost five thermistors of each string are shown. The graphs of thermistors of the centre string are tagged "c".

laboratory experiments with values as large as $\epsilon \approx 0.5\,^{\circ}\mathrm{C}$ (*Haas*, 1999). The method is probably defensible if the thermodynamic conditions at the freezing front are constant over the course of the experiment, while the most appropriate choice of ϵ is open to debate. A relationship exists between sea ice structure, in the form of porosity, and sea ice temperature. If the ice salinity S_{ice} is known at the instant of measurement, and if local thermodynamic equilibrium is assumed, a measured temperature T corresponds to an average porosity f of the sea ice of approximately

$$f = m\frac{S_{ice}}{T}, \tag{3.1}$$

where m is the slope of the liquidus.

Although there seems to be nothing wrong with the threshold temperature approach, in the case of refreezing cracks and slots we are dealing with a system that does not allow us to assume that the freezing interface is of similar physical, chemical and thermal constitution at all thermistors at all times. This point is illustrated with a selection of freezing curves from experiment *slot 1* in Figure 3.6. Two observations are immediately apparent. First, thermistors at the centre of the crack freeze into the sea ice in a similar way to thermistors in one–dimensional ice growth (*Lake and Lewis*, 1970; *Haas*, 1999): that is, the measured temperature is initially constant at

the ocean temperature, then decreases rapidly as the freezing front passes. The rapid temperature decrease leads to a certain insensitivity of freezing time determinations to ϵ. Consequently, freezing front velocity measurements are virtually insensitive to the choice of ϵ (Appendix B.5). Second, when applying the threshold temperature method to determine the freezing time of thermistors in the presence of lateral freezing, the choice of ϵ has a major influence on the freezing time.

Although we did not correlate measured temperature with structural or compositional information during the experiments, we can use the computational fluid dynamics (CFD) model introduced in Chapters 4, 5, and 6 to investigate those correlations, although we cannot discriminate between cause and effect. Figure 3.7 shows examples of the calculated freezing process in the centre of a slot, and towards the side of a slot.

We see that the temperature curve in Figure 3.7(a) resembles the measured freezing curves obtained at the centre of the slot shown in Figure 3.6 and in Figure 3.3, while the temperature curve in Figure 3.7(b) resembles the measured freezing curves obtained closer to the side of the slot. We see that in both cases the temperature decreases immediately as solid is formed (i.e. as the porosity f decreases). We also see that in both cases the temperature drops dramatically once the porosity is low. However, while the transition from initial ice formation to stable salinity takes about 30 h at the centre of the slot, the same process takes more than 80 h closer to the side of the slot.

Figure 3.7 suggests that we have to decide how to define the freezing front. If we need the location of the platelet tips, we can apply the threshold temperature approach. We can use the same definition if we want to calculate the movement of the freezing front at the centre of the slot due to simple heat conduction considerations. Those considerations would typically use fixed values for latent heat, porosity, salinity, and so on, that are indeed achieved shortly after freezing, as seen in Figure 3.7(a). However, we need a different definition if we want to apply simple heat transfer considerations throughout the slot. In this case, the time between our definition of freezing and the attainment of fixed properties is probably too large, leading to excessive errors. Since we are going to attempt to model refreezing throughout the slot with a simple heat transfer model, we need an algorithm that defines the time at which sea ice properties have stabilised, i.e. when porosity f is low.

Comparative rate of temperature change approach It is apparent in Figure 3.7 that porosity and sea ice salinity have reached a value close to their final value when the rate of temperature change is largest (around hour 100 in Figures 3.7(a) and (b)). Mathematically, the rate of temperature change is largest at the time when the second

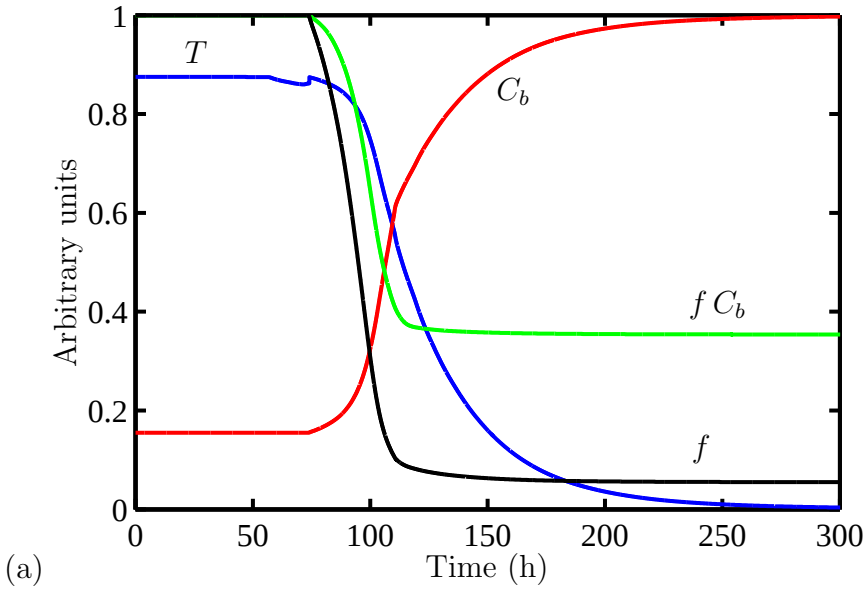

(a)

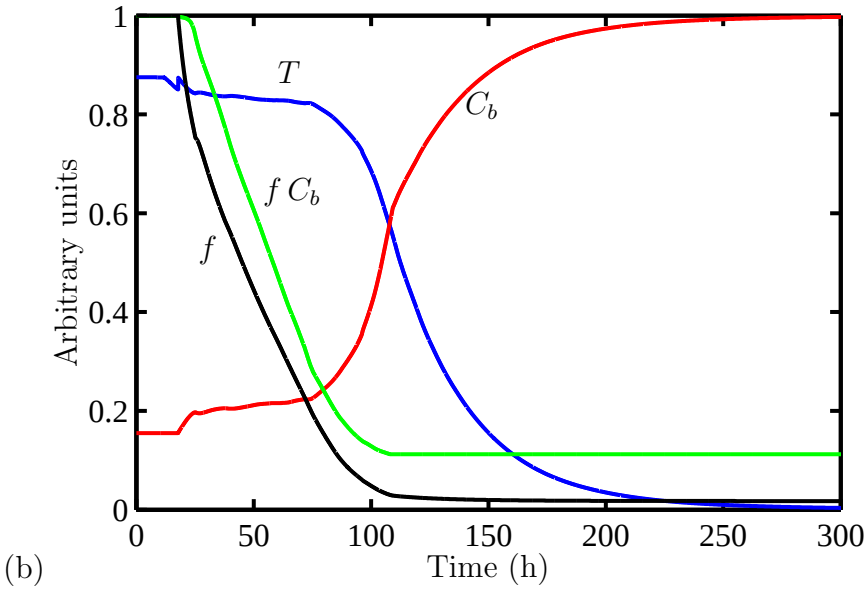

(b)

Figure 3.7: Calculations from the CFD model to illustrate possible relationships between measured temperature T, brine solute concentration C_b, porosity f, and ice salinity $f\,C_b$ (a) at the centre of a refrozen slot, and (b) half way between centre and side of a refrozen slot. Slot dimensions are similar to *slot 10*. Both plots correspond to locations approximately 500 mm below the slot surface.

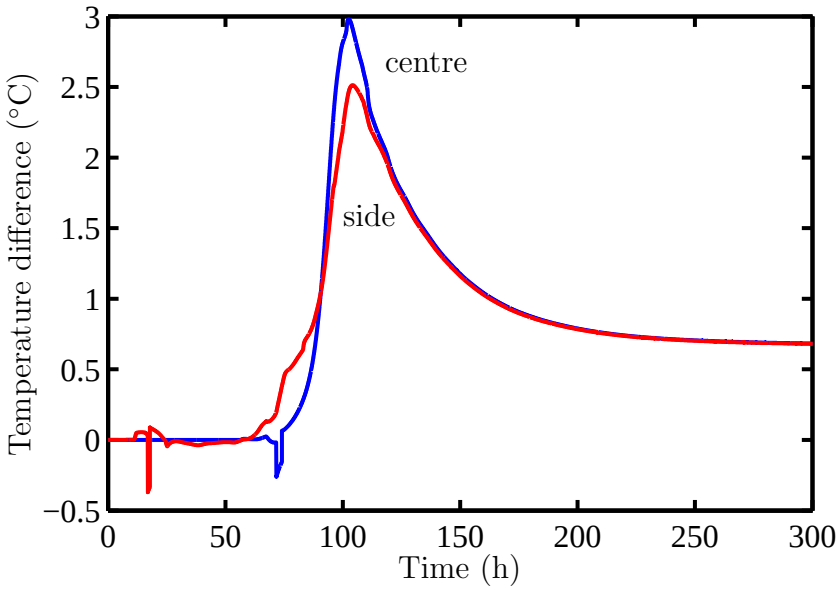

Figure 3.8: Temperature difference between two computational cells at the centre and towards the side of the slot shown in Figure 3.7. The vertical cell size is 62.5 mm.

derivative of temperature with respect to time vanishes. However, the numerical determination of the second derivative of experimental data suffers from noise and is therefore best to be avoided. Fortunately, there is no need to determine this time exactly, as it indicates only approximately when sea ice properties have stabilised. The algorithm to estimate the time of stabilisation suggested here is as follows:

> plot the temperature difference between a thermistor that is about to freeze into the ice, and the thermistor immediately above it that is already in the ice, as a function of time. The time of stabilisation is defined as the time of maximum temperature difference.

This algorithm finds a time of significant rate of temperature change of a thermistor by comparing its rate of temperature change with the rate of temperature change of a thermistor in the ice in its vicinity. This works, provided the temperature curves exhibit a change in curvature with time, and provided temperature fluctuations (e.g. diurnal) are small. The latter prerequisite is not always fulfilled in *slot 2*.

The times of stabilisation determined for the examples in Figure 3.7 are 103.6 h and 104.7 h, respectively, as shown in Figure 3.8. Figure 3.9 shows temperature difference curves of *slot 1* and *slot 10* to illustrate the noise level that has to be dealt with by the algorithm in real data.

A time sensitivity test on the choice of reference thermistor has been performed for experiments *slot 1*, *slot 10*, and *slot 12*. Instead of using the thermistor immediately

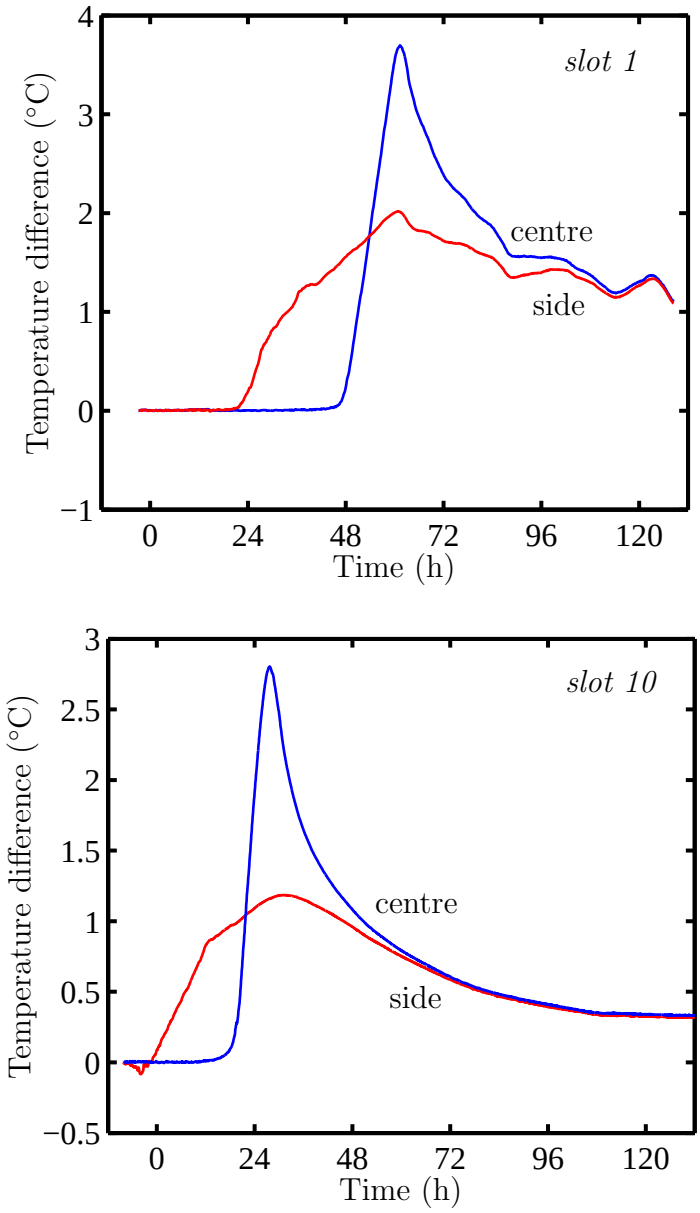

Figure 3.9: Temperature difference between two thermistors (40 mm vertical spacing) on the side string and centre string in *slot 1* and *slot 10*. The thermistors tested for freezing are 180 mm below the slot ice–air interface. Note that *slot 10* becomes snow covered starting at hour 12.

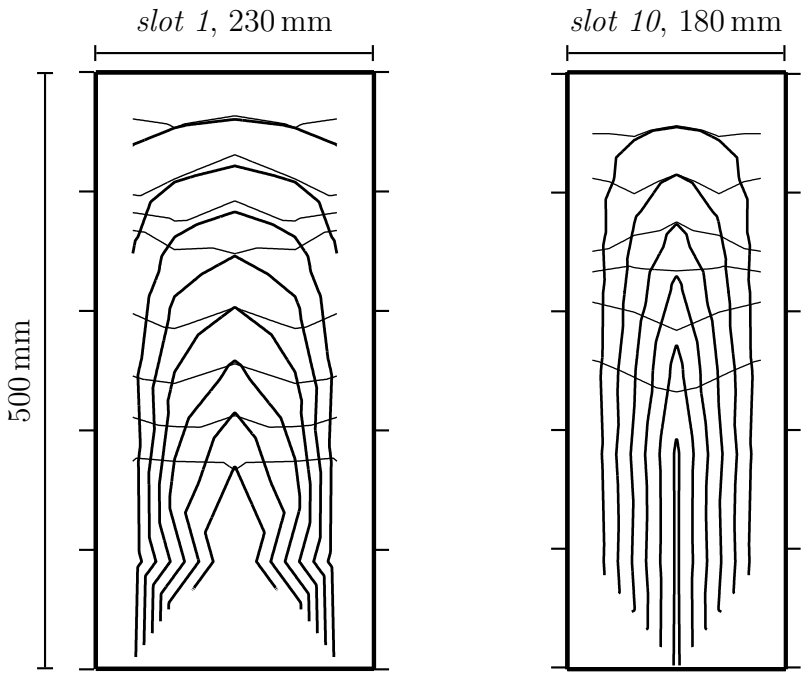

Figure 3.10: Freezing front of *slot 1* and *slot 10* defined by $\epsilon = 0.2\,^{\circ}\mathrm{C}$ (thick lines) and by the comparative rate of temperature change approach (thin lines), respectively. The contour lines follow the position of the freezing front at different times. The separation of contour lines is $5 \times 10^4\,\mathrm{s}$ and $3 \times 10^4\,\mathrm{s}$ for *slot 1* and *slot 10*, respectively.

above the thermistor of interest on the same thermistor string as the reference, the reference thermistor has been taken from the neighbouring thermistor string. The time of stabilisation deviated by less than $\pm 3\,\%$ in $77\,\%$ of all cases. Half of the remaining $23\,\%$ of thermistors came from *slot 1*, which is subject to atmospheric temperature fluctuations.

The freezing front of *slot 1* and *slot 10* is shown in Figure 3.10. The freezing times are derived from the temperature threshold approach with $\epsilon = 0.2\,^{\circ}\mathrm{C}$ and from the comparative rate of temperature change approach, and these are linearly interpolated throughout the area spanned by the probe. The separation of contour lines for *slot 1* is almost twice as large as it is for *slot 10*. The temperature threshold approach reveals an arch–shaped interface (i.e. interface shape of the platelet tips) that becomes narrower with time, while the consolidated front from the comparative rate of temperature change approach moves downwards almost horizontally. The freezing times at the centre of *slot 1* from both approaches are almost the same throughout the experiment, consistent with the one–dimensional character of the temperature curves shown in Figure 3.6. However, in *slot 10*, the freezing front defined by the ice platelets rushes ahead of the consolidated freezing front below a depth of approximately 200 mm, indicating a change in growth mode at the centre. Note that the location of this transition

is similar to the location of the transition from a low salinity centre, that is free from inclusions and marked by downward–growing crystals, to a high salinity centre, with inclusions and upward–tilting crystals (Figures 2.16 and 2.18(c)).

Other reports on freezing front advance We have argued above that the difference between the freezing front of the dendrite tips and the consolidated front is barely discernable from the temperature record of one–dimensional sea ice growth. However, an experimental investigation shows that this distinction has to be made if the skeletal ice layer is of similar thickness to the ice sheet, while basic thermodynamic considerations are used to describe sea ice formation (*Farhadieh and Tankin*, 1972). *Farhadieh and Tankin* (1972) compared measured freezing front advance with simple heat transfer considerations. They were able to measure the progress of both the skeletal, dendritic interface and a "spongy" (presumably consolidated) layer while they controlled the rate of heat removal during ice growth. *Farhadieh and Tankin* investigated the very early stages of sea ice formation in an interferometric and shadowgraph study (*Settles*, 2001). Interferometry, which is sensitive to perturbations in the water, provides a means to measure the temperature profile close to the sea ice interface, while shadowgraphs allow plumes in the water to be resolved and provide a limited view into the ice. The growth cell was about 65 mm high and wide, and, depending on the experiment, between 6 mm and 12 mm deep. Saltwater had an initial concentration of $S = 26$ psu and a temperature of $+7\,^{\circ}\mathrm{C}$ when cooling of the surface began at a constant heat flux. The heat flux, provided by the thermoelectric cooling device in various experiments, was in the range 20 to $50 \times 10^3\,\mathrm{W\,m^{-2}}$, resulting in a freezing front velocity of the order of $10\,\mathrm{m\,day^{-1}}$. *Farhadieh and Tankin* found that freezing began when the surface temperature of the top plate was about $-6\,^{\circ}\mathrm{C}$, at which time the maximum measured supercooling of the water was about $-3\,^{\circ}\mathrm{C}$. Once freezing began, the ice front advanced very rapidly to approximately the $0\,^{\circ}\mathrm{C}$ isotherm, well beyond the isotherm of the freezing temperature of the saltwater. The front retreated after about 10 s and then advanced again. The analysis of shadowgraphs further revealed that two regions in the ice could be discerned, a dendritic region close to the water interface, and a "spongy" opaque region. The dendritic zone retained brine excluded from the ice until it drained in the form of distinct plumes. Brine expulsion started after about 80 s at which time the ice had reached a thickness of about 10 to 30 mm. *Farhadieh and Tankin* (1972) predicted the advance of the freezing front by assuming that all the heat removed is used for the formation of ice and to reduce the temperature. They found reasonable agreement between prediction and the growth of the spongy region (determined from shadowgraphs). The front of the dendritic zone (determined from

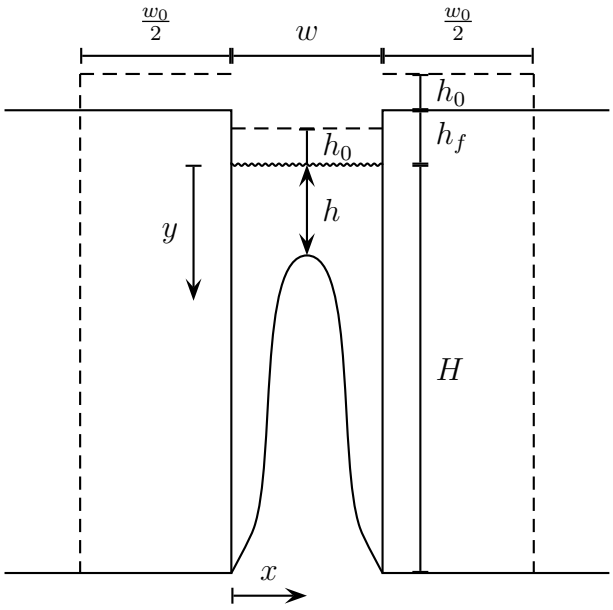

Figure 3.11: Freezing front of a refreezing crack framed by the host ice sheet, and definition of lengths used in the model. The distances h, h_f, and H are measured with respect to the slot ice–air interface. The slots investigated have a larger aspect ratio H/w than sketched. All lengths are positive by convention. Broken lines, h_0, and w_0 are defined in the text.

interferometry), however, was systematically ahead of the predictions.

3.2.4 Freezing front movement

The freezing front of a refreezing slot is arch–shaped (Section 2.2; *Metge*, 1976; *Divett*, 2000; *Petrich et al.*, 2003; *Langhorne and Haskell*, 2004). *Metge* and *Langhorne and Haskell* characterise the refreezing progress of cracks and slots by a single parameter, the refreezing height h which is the distance between the top of the arch and the ice–air interface as illustrated in Figure 3.11. We will do the same as h is the most readily accessible parameter, and possibly the most important parameter with respect to flexural strength (*Metge*, 1976; *Langhorne and Haskell*, 2004).

The aim of this section is to develop a simple analytical model to predict freezing progress at the centre of the slot. The model should be based on physical principles to allow us to gain some insight into the process for future use (e.g. in Chapter 6). It seems prudent to begin by testing the applicability of the 1–dimensional Stefan problem (*Stefan*, 1891; *Carslaw and Jaeger*, 1986) to the growth of slots. We postulate here that refreezing is initially governed by heat transfer to the ice–air interface, while at a later stage in the freezing, heat transfer to the sides becomes dominant, provided the slot is narrow enough. Once the freezing interface has almost reached the ice–water interface of the host ice sheet, the contribution of heat transfer to the sides becomes negligible

and slot refreezing resembles ordinary one–dimensional ice sheet growth. This general process has already been suggested by *Metge* (1976), although *Metge* stops short of developing a quantitative model.

We base the following development on the assumptions that

- the constraints of the Stefan problem apply (i.e. heat capacity negligible, constant temperature boundary condition, water at the freezing point, linear temperature gradient in the ice);
- heat is transported vertically to the ice–air interface and laterally to the sides, independently of each other;
- the Stefan problem can be applied to a freezing interface with a temperature gradient; and
- the host ice sheet does not grow during the refreezing process.

In particular, we will not explicitly account for radiative heat exchange between ice and atmosphere and effects due to snow coverage.

First, we will establish the method for combining heat flow to the top with heat flow to the sides. Following that, we will introduce boundary conditions that allow the Stefan problem to be applied to refreezing slots.

Heat transfer in two directions In the Stefan problem, the solid–liquid interface of a one–dimensionally cooled liquid progresses with time t according to (*Carslaw and Jaeger*, 1986)

$$s^2 = t\frac{2k\,\Delta T}{\rho L}, \tag{3.2}$$

where s is the distance of the freezing front from the cooling interface, ΔT is the temperature difference between the liquid at the freezing point and the cooling interface, $k = 2\,\mathrm{W\,m^{-1}\,K^{-1}}$ is the thermal conductivity, ρ is the density of the solid, and L the latent heat of fusion of sea ice. The latent heat depends on sea ice salinity and temperature, while the density of sea ice depends on salinity, temperature, and air volume. We follow *Cox and Weeks* (1988) and use $\rho = 920\,\mathrm{kg\,m^{-3}}$ and $L = 293 \times 10^3\,\mathrm{J\,kg^{-1}}$ that is relevant to ice–water mixtures (Appendix H.1). Rewriting (3.2) we have

$$\frac{1}{t} = \frac{2}{\rho L}\underbrace{\frac{k\,\Delta T}{s^2}}. \tag{3.3}$$

The last factor in (3.3) is proportional to a rate of change of energy. Since the system of a freezing slot is two–dimensional, heat flow to the ice–air interface is proportional to $k\Delta T_t/h'^2$ (the reason for priming h will become clear, soon. For now assume $h' = h$),

and to the side it is proportional to $k\Delta T_s/x^2$, where ΔT_t and ΔT_s are the temperature differences between the liquid at its freezing point and the air temperature and host ice temperature, respectively, and x is the distance from the closer side. ΔT_s is a function that we assume is linear in height y with

$$\Delta T_s = \Delta T_s^0 \left(1 - \frac{y}{H}\right), \tag{3.4}$$

where H is the thickness of the ice below water level (draft), and ΔT_s^0 is the temperature difference for $y = 0$. In the special case of $x = w'/2$ ($w' = w$ for now), i.e. at the centre of the slot, (3.3) becomes

$$\frac{1}{t} = \frac{2}{\rho L}\left[\frac{k\,\Delta T_t}{h'^2} + \frac{k\,\Delta T_s}{(w'/2)^2}\right], \tag{3.5}$$

and

$$\frac{1}{t} = \frac{2k\,\Delta T_t}{\rho L\,h'^2} + \frac{2k\,\Delta T_s}{\rho L\,(w'/2)^2}. \tag{3.6}$$

Defining

$$t'_t = h'^2\,\frac{\rho L}{2k\,\Delta T_t}, \quad \text{and} \tag{3.7}$$

$$t'_s = \left(\frac{w'}{2}\right)^2 \frac{\rho L}{2k\,\Delta T_s}, \tag{3.8}$$

the perpendicular vertical and lateral heat fluxes add in such a way that using the freezing times t_t ($t_t = t'_t$ for now) derived from the vertical heat flux and t_s ($t_s = t'_s$ for now) from the lateral heat flux, the actual freezing time t can be calculated from

$$\frac{1}{t} = \frac{1}{t_t} + \frac{1}{t_s}. \tag{3.9}$$

Freezing front in a refreezing slot Although we could use (3.6) to predict the position of the freezing front, the results will not be entirely satisfactory. While (3.6) assumes freezing from a surface at constant temperature, this situation is clearly not approximated in the case of refreezing cracks and slots: at the upper ice surface, heat transfer between ice and atmosphere takes place and while the air temperature may be constant, the ice surface temperature usually is not. This observation has been made previously (*Anderson*, 1961). As for the interface at the sides, while a time–independent temperature profile through the host ice may exist far away from the slot, the isotherms deviate significantly from the horizontal close to the host ice–slot interface. The degree of deviation is time dependent, depending on the progress of

slot refreezing. To remedy the situation at the top surface we consider the equation for heat flux F_s between the surface at its real temperature T_r and air temperature T_a following Newton's law of heat transfer (*Beek et al.*, 1999)

$$F_s = \mathfrak{h}\,(T_a - T_r), \tag{3.10}$$

where $\mathfrak{h}$ is the heat transfer coefficient between air and ice surface. The heat transfer coefficient is often expressed as (*Parkinson and Washington*, 1979; *Cox and Weeks*, 1988; *Perovich and Richter-Menge*, 2000)

$$\mathfrak{h} = \rho_a c_p C_s\, u, \tag{3.11}$$

where $\rho_a = 1.3\,\mathrm{kg\,m^{-3}}$ is the density of air, $c_p = 1006\,\mathrm{J\,kg^{-1}\,K^{-1}}$ is the specific heat capacity of air, C_s is the sensible heat aerodynamic bulk transfer coefficient (*Andreas*, 1987), and u is the wind speed. Hence, equation (3.10) can be written

$$F_s = \rho_a c_p C_s\, u(T_a - T_r). \tag{3.12}$$

Unfortunately, as neither u nor C_s are known for the slot experiments, we set $u\,C_s = 0.012\,\mathrm{m\,s^{-1}}$, a value that has been chosen by calibrating this model with the refreezing time series[3]. However, we will calculate the heat transfer coefficient based on this model in Section "Initial refreezing process" on page 71. Considering that Newton's law (3.12) can also be expressed as a heat conduction equation (Fourier's law (*Beek et al.*, 1999))

$$F_s = F_c = k\frac{T_a - T_r}{h_0}, \tag{3.13}$$

where k is the thermal conductivity[4], and h_0 the distance between two surfaces of temperature difference $T_a - T_r$, we notice that we can emulate the effect of ice–air heat transfer expressed by (3.12) by simulating heat conduction through a buffer layer of thickness h_0. This buffer layer argument is equivalent to thermal resistances in series (*Baehr and Stephan*, 1998). We will therefore substitute the height h' in (3.7) by $h + h_0$,

$$h' = h + h_0, \tag{3.14}$$

[3]This corresponds, for example, to $C_s = 0.00214$ as used by *Perovich and Richter-Menge* (2000), and $u = 5.6\,\mathrm{m\,s^{-1}}$, which is similar to $u = 5\,\mathrm{m\,s^{-1}}$ assumed by *Cox and Weeks* (1988).

[4]In order to apply the Stefan problem we will have to use k that is appropriate to the ice that grows in the slot.

where we obtain the value of h_0 from equating (3.12) with (3.13),

$$h_0 = \frac{k}{\rho_a c_p C_s \, u}. \tag{3.15}$$

For example, with the values given above we find $h_0 = 0.127\,\mathrm{m}$. This boundary layer thickness h_0 incurs an offset in time of freezing. We demand that the freezing front be at $h = 0$ at time $t_t = 0$. But if $h = 0$ then $h' = h_0$ from (3.14) and we use this height to define the time offset t_{t0} from (3.7), such that

$$t_{t0} = h_0^2 \, \frac{\rho L}{2k \, \Delta T_t}, \tag{3.16}$$

and

$$t_t = t'_t - t_{t0}. \tag{3.17}$$

Therefore from (3.7), (3.16), and (3.17)

$$\begin{aligned} t_t &= (h + h_0)^2 \, \frac{\rho L}{2k \, \Delta T_t} - h_0^2 \, \frac{\rho L}{2k \, \Delta T_t}, \\ &= \left[(h + h_0)^2 - h_0^2 \right] \, \frac{\rho L}{2k \, \Delta T_t}, \\ &= \tilde{h}^2 \, \frac{\rho L}{2k \, \Delta T_t}, \end{aligned} \tag{3.18}$$

where

$$\tilde{h}^2 = h \, (h + 2h_0) \, . \tag{3.19}$$

Considering the constant temperature boundary at the sides of the slot, we argue that they are not located at the slot–host ice boundary, but further inside the host ice. The thermal slot width w' is therefore wider than the actual slot width w by a width w_0. We expect the width w_0 to depend linearly on the height H of the ice sheet according to

$$w_0 = \gamma \, H. \tag{3.20}$$

The ratio γ is a truly free parameter in this model. We use $\gamma = 0.5$. Following the same argument for time offset correction as above, we find that

$$t_s = \left(\frac{\tilde{w}}{2} \right)^2 \, \frac{\rho L}{2k \, \Delta T_s}, \tag{3.21}$$

where

$$\tilde{w}^2 = w \, (w + 2w_0) \, . \tag{3.22}$$

The only task left for us is to find ΔT_s^0. Since we have already assumed that the temperature profile is linear at the distance of $w_0/2$ away from the slot–host ice interface, the temperature difference at $y = 0$ can be simply expressed as

$$\Delta T_s^0 = \Delta T_t \frac{H}{H + h_f + h_0}, \tag{3.23}$$

where h_f is the freeboard, and where we have again applied the buffer layer h_0 at the top surface and assumed that the imaginary surface h_0 above the true host ice surface is at the air temperature T_a. For a free floating ice sheet without snow cover[5], we find from hydrostatic equilibrium that

$$\frac{\rho_{sw}}{\bar{\rho}_i} H = H + h_f, \tag{3.24}$$

where ρ_{sw} is the seawater density and $\bar{\rho}_i$ is the average sea ice density (see for example *Timco and Frederking* (1996) on the issue of sea ice density). We define the reciprocal ice thickness ratio r_f for convenience,

$$r_f = 1 + \frac{h_f}{H}, \tag{3.25}$$

and note that for a free floating ice sheet $r_f = \rho_{sw}/\bar{\rho}_i \approx 1.1$ is the density ratio, independent of thickness H. Combining (3.23), (3.24), and (3.25) we obtain

$$\Delta T_s^0 = \Delta T_t \frac{1}{r_f + \frac{h_0}{H}}. \tag{3.26}$$

The temperature difference ΔT_t is the difference between air temperature T_a and water temperature $T_w = -2\,^\circ\mathrm{C}$,

$$\Delta T_t = T_w - T_a. \tag{3.27}$$

We are now ready to combine the above equations[6] to obtain an explicit expression of freezing time t as a function of height h. Starting from (3.9) and substituting (3.18) and (3.21) we find

$$\frac{1}{t} = \frac{1}{\tilde{h}^2} \frac{2k\,\Delta T_t}{\rho L} \left[1 + 4 \frac{\tilde{h}^2}{\tilde{w}^2} \frac{\Delta T_s}{\Delta T_t} \right], \tag{3.28}$$

where we apply (3.4) and (3.26) next. The result is shown in Appendix B.6.

[5]Although we shall continue to assume a free floating ice sheet, Table 2.2 shows that snow cover can reduce freeboard by at least 30 % even in land–fast sea ice.

[6]Note that equation (3.2) is the foundation of the model, equations (3.9), (3.19), and (3.22) are the pillars, and equations (3.15), (3.20), and (3.26) are the ornaments.

Unfortunately, since the equations contain a length h_0 that is independent of any physical dimension of the refreezing slot, we are only able to formulate a meaningful scaling relationship for vanishing h_0. Generally, however, defining the dimensionless time

$$\tau = t\frac{2k\,\Delta T_t}{\rho L\,H^2} \tag{3.29}$$

and the dimensionless lengths

$$\left.\begin{aligned} z &= \frac{h}{H}, \quad z_0 = \frac{h_0}{H} = \frac{k}{H\,\rho_a c_p C_s\,u}, \quad \tilde{z}^2 = z(z+2\,z_0), \\ d &= \frac{w}{H}, \quad d_0 = \frac{w_0}{H} = \gamma, \qquad\qquad\quad \tilde{d}^2 = d(d+2\,d_0), \end{aligned}\right\} \tag{3.30}$$

and for notational convenience

$$\delta = \frac{4}{r_f + z_0}, \tag{3.31}$$

we find

$$\tau = \frac{\tilde{z}^2}{1+\delta\,\dfrac{\tilde{z}^2}{\tilde{d}^2}\,(1-z)}. \tag{3.32}$$

For a multitude of laboratory experiments of different ice thickness H, *Metge* plots[7] the dimensionless refrozen thickness z as a function of dimensionless time, τ, for different dimensionless widths, d. His graphs do not necessarily collapse onto a single curve, and the shape of the graphs is difficult to predict from d, which can be understood from the complexity of the denominator in (3.32). Owing to the complexity of (3.32), we will plot predicted freezing time τ_p from (3.32) as a function of measured freezing time τ_m for refreezing experiments from this study and from the literature; that is the two 1999 direct refreezing experiments of *Langhorne and Haskell* (2004), and two experiments of *Metge* (1976) that do not experience excessive (though still significant) host ice growth during the course of the experiment (Table 3.2). Since the experiments of *Metge* were performed in freshwater ice, for those cases we use $L = 334 \times 10^3\,\mathrm{J\,kg^{-1}}$ and $T_w = 0\,^\circ\mathrm{C}$. We further deduce from his data that $u\,C_s = 0.02$ in his experiments (Appendix B.6).

Figure 3.12 shows the result. The experiments of this study cover the relatively early stages of refreezing, followed by the experiments of *Langhorne and Haskell*, and experiments of *Metge*. The model predictions are good over two to three orders of magnitude in dimensionless time, for sea ice and freshwater ice, for experiments in McMurdo Sound and in the laboratory, and for different groups.

[7] *Metge* forms dimensionless lengths with respect to $H + h_f$, which is proportional to H in a free floating ice sheet according to (3.24).

Table 3.2: Parameters of the slot refreezing experiments considered in this section. Air temperature T_a is the average over the length of the experiment until the last thermistor has frozen into the ice; or for the experiments of *Langhorne and Haskell* (LH) from *Pat Langhorne* (personal communication). Ice depth below freeboard H is estimated for LH from data given in *Langhorne and Haskell* (2004), calculated for the experiments of this study assuming a free floating ice sheet, and set to the initial ice depth for experiments of *Metge* (M).

	slot 1	*slot 2*	*slot 10*	*slot 12*	LH7d	LH12d	M4a	M4b
w (m)	0.23	0.32	0.18	0.12	0.07	0.12	0.036	0.018
H (m)	2.0	1.2	2.0	2.0	1.77	1.77	0.185	0.185
T_a (°C)	−17.5	−13.5	−25	−14.0	−15	−15	−14	−14
z_0	0.05	0.08	0.05	0.05	0.06	0.06	1.5	1.5
d	0.12	0.27	0.09	0.06	0.04	0.07	0.21	0.11

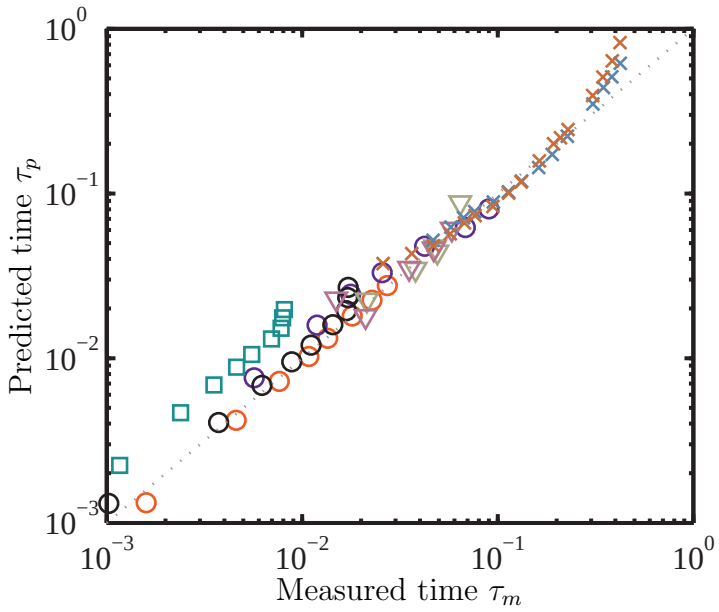

Figure 3.12: Dimensionless freezing time τ_p predicted from (3.32) compared with measured freezing time τ_m for experiments of this study (circles; *slot 12* squares), *Langhorne and Haskell* (triangles), and *Metge* (crosses).

Freezing times of most experiments are predicted well. The most notable exception is *slot 12*, where freezing occurs systematically earlier than predicted ($\tau_m \approx 0.52\,\tau_p$). We suppose that this is due to ice accumulation by frazil or by a negative heat flux from the ocean (Appendix B.9). Considering the snow cover at later times during the freezing of *slot 10* that should have affected heat exchange with the atmosphere, it is rather surprising that the prediction of freezing front movement fits well for this experiment. Again, frazil ice accumulation or a negative heat flux from the ocean could explain this observation.

Refreezing is faster than predicted towards the end of the experiments of *Metge*.

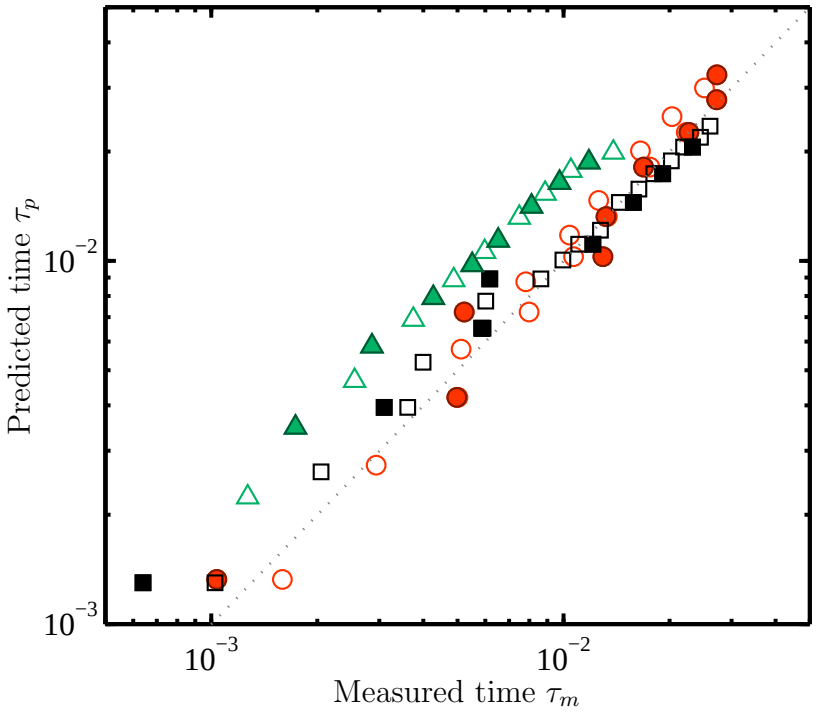

Figure 3.13: Dimensionless freezing time τ_p predicted from (3.32) compared with measured freezing time τ_m determined from the comparative rate of temperature change approach for experiments *slot 1* (circles); *slot 10* (squares); *slot 12* (triangles). Data points from the respective thermistor strings at the side are plotted filled.

This is possibly due to the fact that the ice sheet increases in thickness by 5 to 10 % during the course of the experiment, which facilitates freezing in the slot. The predictions are illustrated in real time and space coordinates in Appendix B.6.

We have assumed the same value for the latent heat of fusion, L, for all sea ice experiments. This value is taken from *Cox and Weeks* (1988), who (presumably) have chosen it empirically. However, Chapter 6 shows that a quantitative comparison of sea ice growth simulated with the numerical model with growth calculated from the Stefan problem requires us to account for the heat capacity of sea ice in the Stefan problem. This can be accomplished by folding the heat capacity into the latent heat of fusion (Appendix H.1). Following this approach to the latent heat in the analytical model does not change the conclusions of this chapter. For reference, Appendix B.7 presents results of the analytical model based on this more sophisticated approach. The calculations show that the conclusions drawn from the model are independent of the exact choice of L and that the value of γ may possibly decrease with increasing ice thickness, H, by approximately 20 % per order of magnitude in H.

Two–dimensional considerations As we have seen in the examples of Figures 3.8, 3.9, and 3.10, the time of stabilisation of sea ice properties as determined from the comparative rate of temperature change approach appears to be independent of the horizontal position within the slot. We can therefore use (3.32) to predict the time of stabilisation of sea ice properties throughout the slots. Figure 3.13 shows that consolidation times of *slot 1* and *slot 10* are again fairly well predicted, while predicted consolidation times of *slot 12* are consistently slow. If the comparative rate of temperature change approach is valid then this gives an indication of why the salinity of refreezing cracks is low towards the side of the cracks: there, the time between the initial formation of ice and the formation of an almost impenetrable structure is longest, facilitating brine drainage.

Initial refreezing process

The heat transfer coefficient $\mathfrak{h}$ used for the *slot* experiments has not been derived, but was obtained from a manual fitting exercise. We shall now estimate this coefficient for each of the experiments. The effect of this coefficient can be expected to be most apparent in the early stages of refreezing.

In order to describe the initial refreezing process of slots where typically $h < w$, we non–dimensionalise the model equations with respect to the slot width w. It follows that

$$\tau = t\frac{2k\,\Delta T_t}{\rho L\,w^2} \tag{3.33}$$

and the dimensionless lengths are

$$\left.\begin{aligned} z &= \frac{h}{w}, & z_0 &= \frac{h_0}{w} = \frac{k}{w\,\rho_a c_p C_s\,u}, & \tilde{z}^2 &= z(z+2\,z_0), \\ d &= \frac{w}{w} = 1, & d_0 &= \frac{w_0}{w} = \gamma\frac{H}{w} = \frac{\gamma}{a}, & \tilde{d}^2 &= d(d+2\,d_0), \end{aligned}\right\} \tag{3.34}$$

where the aspect ratio a is defined

$$a = \frac{w}{H}. \tag{3.35}$$

Further, for notational convenience, we again set

$$\delta = \frac{4}{r_f + z_0\,a}, \tag{3.36}$$

and therefore

$$\tau = \frac{\tilde{z}^2}{1 + \delta\,\dfrac{\tilde{z}^2}{\tilde{d}^2}\,(1 - z\,a)}. \tag{3.37}$$

Table 3.3: Air–ice heat transfer coefficient $\mathfrak{h}$ inside the slots determined from (3.42), assuming the absence of an ocean heat flux.

	slot 1	*slot 2*	*slot 10*	*slot 12*
w (m)	0.23	0.32	0.18	0.12
initial T_a (°C)	−14.4	−11.9	−20.8	−18.4
v ($10^{-7}\,\mathrm{m\,s^{-1}}$)	7.4	7.4	14	16
$\mathfrak{h}$ ($\mathrm{W\,m^{-2}\,K^{-1}}$)	12	15	17	21

In the initial stages of refreezing, i.e. $z < 1$, of a narrow slot with $a \ll 1$, (3.37) reduces to

$$\tau \approx \frac{\tilde{z}^2}{1 + 4a\,\tilde{z}^2}, \tag{3.38}$$

where it is further assumed that $\gamma = 0.5$ and $r_f = 1$. If further $z < z_0$ then

$$\tau \approx 2z\,z_0, \tag{3.39}$$

and the freezing front advances linearly with time. The initial freezing front velocity v is therefore

$$v = \frac{dh}{dt} = \frac{h}{t}, \tag{3.40}$$

applying (3.39) with (3.33) and (3.34) it follows that

$$v = \frac{k\,\Delta T_t}{\rho L\,h_0}, \tag{3.41}$$

that simplifies with (3.11), (3.15) and (3.27) to

$$v = \frac{\mathfrak{h}\,(T_w - T_a)}{\rho L}. \tag{3.42}$$

Note that (3.42) combines the heat transfer coefficient between air and the *ice* surface, $\mathfrak{h}$, with the temperature difference between air and *water*, i.e. (3.42) assumes zero ice thickness h.

Table 3.3 lists the heat transfer coefficients determined from the initial growth velocity v in the slot experiments (Figure B.4 in Appendix B.5) and the average air temperature T_a determined from the start of the experiment until the thermistors used to measure the velocity freeze into the ice. It is further assumed that $T_w = -1.9\,°\mathrm{C}$, $\rho = 920\,\mathrm{kg\,m^{-3}}$, and $L = 293 \times 10^3\,\mathrm{J\,kg^{-1}}$ (*Cox and Weeks*, 1988). The apparent values of $\mathfrak{h}$ will be affected by a non–zero ocean heat flux, and they generally depend

on wind velocity and surface roughness (*Andreas*, 1987). Further, it follows from $h_0 = 0.127\,\mathrm{m}$ used in the previous model predictions and (3.11), that $\mathfrak{h} = 16\,\mathrm{W\,m^{-2}\,K^{-1}}$, which is consistent with the values calculated for $\mathfrak{h}$ in Table 3.3. For reference, $\mathfrak{h} = 20\,\mathrm{W\,m^{-2}\,K^{-1}}$ is obtained from the assumption of *Cox and Weeks* (1988) of $u = 5\,\mathrm{m\,s^{-1}}$ and $C_s = 0.003$, and the same number is given by *Leppäranta* (1993) as a typical value. All the values for $\mathfrak{h}$ shown are reasonable in the sense that they are in the range 10 to $100\,\mathrm{W\,m^{-2}\,K^{-1}}$ that is generally expected for heat transfer between a solid and a flowing gas (*Beek et al.*, 1999).

Summary An analytical model in the form an explicit algebraic equation has been developed to predict the position of the freezing front of a refreezing slot as a function of time. The model is based on the Stefan problem extended to two dimensions. Appropriate boundary conditions have been formulated by expanding the physical size of the slot to a thermally effective size. Ice thickness, slot width, and air temperature are accounted for explicitly. It has been found that, in the framework of this model, the refreezing process of slots cannot be considered scale invariant in the early stages of refreezing or in thin ice. A model that includes a suitable treatment of ice surface temperature in place of air temperature, however, could possibly be scale invariant. The model gives reasonable predictions of the crack refreezing process measured by three different groups, which is surprising in view of the simplistic treatment of heat transfer.

3.2.5 Heat Balance

Next, we will use the temperature data of probe 1 to estimate the heat flux out of the slot during refreezing. We will compare this heat flux with the enthalpy necessary to form ice in the slot as observed, and with incident shortwave radiation. In doing so we will be able to assess if other fluxes contribute to ice formation, for example frazil ice suspected to be present in Section 3.2.3.

However, we will first review estimates of the thermal conductivity of sea ice, and introduce methods of estimating heat flux out of the slot, the rate of change of enthalpy in the slot, and shortwave radiative input into the slot. Finally, the results for the refreezing experiments will be discussed.

Sea ice thermal conductivity

One of the parameters used for heat conduction modelling is the thermal conductivity, k, of sea ice. While the thermal conductivity of pure ice is a function of temperature,

the thermal conductivity of sea ice is expected to further depend on the brine content and physical arrangement of brine inclusions (*Yen*, 1981).

We take a pragmatic view of k by browsing through the sea ice literature to find a generally accepted treatment of the thermal conductivity k. We can classify the approaches into four groups:

- k is calculated from sea ice temperature and salinity after *Untersteiner* (1961): e.g. *Yen* (1981), *Crocker and Wadhams* (1989), *Wettlaufer* (1991), *Eicken* (1992), *Eicken et al.* (1995a), *Bitz and Lipscomb* (1999), *Eisen and Kottmeier* (2000), *Lytle et al.* (2000), *Perovich and Richter-Menge* (2000), *Skyllingstad and Denbo* (2001), *Doble et al.* (2003);
- k is calculated as volume weighted average of constant k_{ice} and constant k_{brine}: e.g. *Cox and Weeks* (1988), *Zeebe et al.* (1996), *Medjani* (1996) and *Oertling and Watts* (2004), *Wettlaufer et al.* (2000);
- k or thermal diffusivity, κ, of sea ice is constant: e.g. *Eicken* (1998), *Toyota* (1998), *McGuinness et al.* (2001), *Feltham et al.* (2002), *Persson et al.* (2002), *Perovich et al.* (2003);
- k is measured: e.g. *Stefan* (1891), *Lewis* (1967), *Trodahl et al.* (2001).

Of this selection the most popular description follows *Untersteiner* (1961),

$$k = k_0 + \beta \frac{S_{ice}}{T_{ice}}, \tag{3.43}$$

where most authors use $k_0 = 2.03\,\mathrm{W\,m^{-1}\,K^{-1}}$, $\beta = 0.117\,\mathrm{W\,m^{-1}\,psu^{-1}}$, and where S_{ice} and T_{ice} are sea ice salinity and temperature (in °C), respectively. Often, S_{ice} is estimated and constant. In numerical simulations where the brine volume fraction f is known explicitly the following treatment may be used

$$k = k_{ice}(1 - f) + k_{brine} f, \tag{3.44}$$

where k_{ice} and k_{brine} are thermal conductivity of pure ice and brine, respectively, and k_{ice} and k_{brine} are constant over temperature. Assuming thermodynamic equilibrium, (3.43) and (3.44) are identical. The assumption of a constant thermal conductivity is frequently justified by the observation that (3.43) leads to negligible changes in k over the range of temperatures considered. If a constant thermal conductivity is assumed, it is usually chosen to be $k = 2.0\,\mathrm{W\,m^{-1}\,K^{-1}}$.

Thermistor probe measurements by *Trodahl et al.* (2001) indicate that $1.2 \leq k \leq 2.4\,\mathrm{W\,m^{-1}\,K^{-1}}$ (plus error bars), while those of *Lewis* (1967) are in the range $1.8 \leq k \leq 2.6\,\mathrm{W\,m^{-1}\,K^{-1}}$, clearly increasing with decreasing temperature. The estimate

of *Stefan* (1891), based on observations of sea ice growth velocities in the Arctic, is $k = 1.8\,\mathrm{W\,m^{-1}\,K^{-1}}$. Interestingly, many of the measurements result in values for the thermal conductivity that are larger than the value assumed for pure ice by most authors and therefore cannot be reached by applying (3.43) or (3.44).

When we consider heat transfer though sea ice in this section, we will follow (3.44) to calculate the thermal conductivity k.

Heat balance estimate

We will attempt to estimate the heat balance of the quasi two–dimensional system of a refreezing slot from 25 thermistor temperature measurements inside the slot. Therefore, we will compare the change of enthalpy in the slot, the rate of heat transfer into or out of the slot, and the heat input due to solar radiation. In order to compare the relative magnitudes between the refreezing experiments we express the rates of change of energy as fluxes with respect to the area of the ice–air interface of the experiment. This choice of reference area is arbitrary, but it may facilitate the assessment of significance the heat fluxes studied. Since the heat fluxes to the host ice are ultimately lost to the atmosphere, a heat flux to the host ice expressed with respect to the horizontal area of the crack is a measure for the atmospheric heat flux incurred by a refreezing crack. Lateral heat fluxes have previously been referenced to both horizontal and vertical areas (*Eicken et al.*, 2002).

The domain considered is the area spanned by the thermistor strings, mirrored about the centre of the slot (Figure 3.14), i.e. it is narrower than the slot.

The heat balance equation considered in this section is

$$F_{SW}^{abs} + F_c + F_h = 0, \tag{3.45}$$

where F_{SW}^{abs} is the flux of shortwave radiation that is absorbed in the domain, F_c is the conductive flux of heat into the domain, and F_h the flux required to change the enthalpy of the domain. Surface fluxes, such as longwave radiative fluxes (Appendix C.3), do not have to be considered explicitly, as their effect on the heat balance is accounted for in the conductive heat flux, F_c.

Shortwave radiation The shortwave radiation absorbed in the slot ice is estimated as follows: the incoming shortwave radiative flux $F_{SW}\downarrow$ is attenuated by cloud cover to a value $F_{SW}\downarrow\ (1 - 0.33c)$ (*Jacobs* (1978) and Appendix C.2). Due to the surface reflectivity, expressed through the wavelength–averaged albedo α, only the fraction $1-\alpha$ of this flux enters the ice (*Perovich and Richter-Menge*, 2000). Of this fraction, a

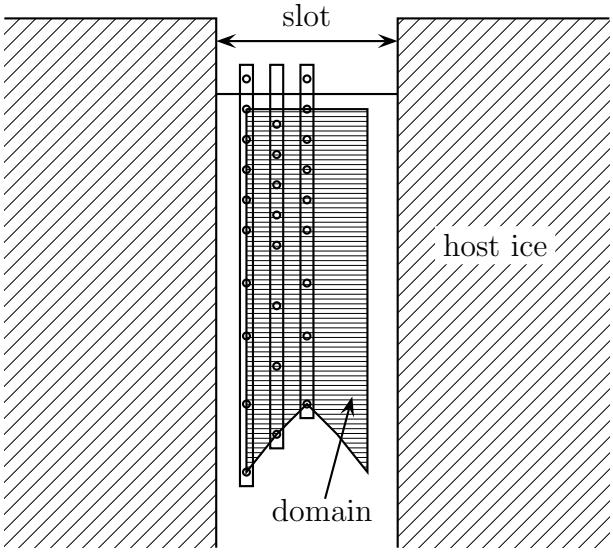

Figure 3.14: Domain (horizontally hatched) for heat balance calculations. The domain is symmetrical around the centre of the slot, and thermistors cover only one half of it.

fraction $1-i_0$ is absorbed in the topmost $h_0 = 100\,\mathrm{mm}$, while the absorption below this level follows Beer's law to depth h with extinction coefficient κ_i (*Grenfell and Maykut*, 1977). The absorbed flux is therefore

$$F_{SW}^{abs} = F_{SW}\downarrow\,(1-0.33c)(1-\alpha)\left[(1-i_0)+i_0\left\{1-\exp\left(-\kappa_i\left[h-h_0\right]\right)\right\}\right],$$

or simply

$$F_{SW}^{abs} = F_{SW}\downarrow\,(1-0.33c)(1-\alpha)\left[(1-i_0\exp\left(-\kappa_i\left[h-h_0\right]\right)\right]. \tag{3.46}$$

We assume a surface albedo of $\alpha = 0.5$ (*Perovich and Richter-Menge*, 2000), extinction coefficient $\kappa_i = 1.5\,\mathrm{m}^{-1}$ (*Grenfell and Maykut*, 1977), and a typical depth $h = 0.3\,\mathrm{m}$ which is slightly more than half the height of the probe. A value of $i_0 = 0.63$ has been given for overcast conditions, while $i_0 = 0.43$ under clear skies (*Grenfell and Maykut*, 1977). With the assumption of $c = 0.63$ (*Zeebe et al.*, 1996) in *slot 1* and *slot 2*, we take $i_0 = 0.56$ for those experiments, and $i_0 = 0.63$ for *slot 10* and *slot 12*. The result is an overestimate of the shortwave radiative flux since no account is taken of shadowing due to the freeboard. The parameters and the result are summarised in Table 3.4. The incoming shortwave radiation $F_{SW}\downarrow$ is predicted from the radiation model of *Iqbal* (1983) and *Brine and Iqbal* (1983) in Appendix C.1.

Table 3.4: Parameters used for the shortwave radiative flux estimate. The uncertainties given for F_{SW}^{abs} are calculated by varying α by ± 0.1 and h by $\pm 0.1\,\mathrm{m}$.

	slot 10	*slot 12*	*slot 1*	*slot 2*
$F_{SW}\downarrow$ ($\mathrm{W\,m^{-2}}$)	7.5	39.0	149	221
c	1.0	1.0	0.63	0.63
α	0.5	0.5	0.5	0.5
i_0	0.63	0.63	0.56	0.56
h (m)	0.3	0.3	0.3	0.3
F_{SW}^{abs} ($\mathrm{W\,m^{-2}}$)	1.4 ± 0.6	7 ± 1.2	35 ± 11	52 ± 16

Heat conduction In order to calculate the heat flux, F_c, conducted into the domain at a given instant in time t, the temperature field of the domain, the thermistor freezing times t_F derived from the comparative rate of temperature change approach with $\epsilon = 0.2\,^{\circ}\mathrm{C}$, and the consolidation times t_s derived from the comparative rate of temperature change approach, are determined from linear interpolation[8], i.e. triangulation, of the thermistor temperature and freezing time data, respectively[9]. The result of the interpolation for *slot 1* and *slot 10* is shown in Figure 3.10. After this has been done, the surface integral

$$F_c = -\frac{1}{A_d} \oint_A \mathbf{\Phi}_c \cdot \mathrm{d}\mathbf{A} \tag{3.47}$$

is computed, where A_d is the top (ice–air) surface area of the domain, A is the bounding surface of the domain, and $\mathbf{\Phi}_c$ is the conductive heat flux,

$$\mathbf{\Phi}_c = -k \nabla T. \tag{3.48}$$

The thermal conductivity k is estimated from the time of freezing t_F determined from the temperature threshold approach, and from the consolidation time t_s, according to

$$f = 1 - \frac{t - t_F}{t_s - t_F} \quad \text{for} \quad t_F < t < t_s, \tag{3.49}$$

$$k = k_i + f\,(k_w - k_i), \tag{3.50}$$

where f is the estimated porosity of ice (set to $f = 1$ for $t < t_F$ and limited to $f \geq 0.06$), and $k_i = 2.1\,\mathrm{W\,m^{-1}\,K^{-1}}$ and $k_w = 0.56\,\mathrm{W\,m^{-1}\,K^{-1}}$ are the thermal conductivity of pure ice and water, respectively. Equation (3.49) assumes a linear decrease of porosity with time (cf. Figure 3.7). The interpolated domain boundary itself is horizontal at the

[8]The *MatLAB* `griddata` function is used to perform the interpolation.

[9]Deviating from this scheme, the consolidation times of thermistors in *slot 2* are defined to be equal to the freezing times t_F at the centre of the slot to avoid artefacts in t_s from the diurnal temperature variations. However, figures for *slot 2* derived from the standard approach are shown in Appendix B.8.

top surface, vertical at the sides and, due to the thermistor arrangement, inclined at the bottom. The top surface is also inclined in the case of *slot 12* since only the two longest thermistor strings were used. The heat flux is calculated every 5 samples for *slot 1* and *slot 2* (with sampling period $\Delta t = 600\,\mathrm{s}$), and every 5 samples for *slot 10* and *slot 12* (with sampling period $\Delta t = 300\,\mathrm{s}$) from the time the top three (two in *slot 12*) thermistors are frozen into the ice (determined from t_F).

Enthalpy The rate of change of enthalpy is calculated from the volumetric enthalpy density, h,

$$h = -(1-f)\rho_i L + (1-f)\rho_i c_i T + f\rho_w c_w T, \tag{3.51}$$

where $\rho_i = 920\,\mathrm{kg\,m^{-3}}$ and $\rho_w = 1000\,\mathrm{kg\,m^{-3}}$ are densities of ice and water, respectively, $c_i = 2100\,\mathrm{J\,kg^{-1}\,K^{-1}}$ and $c_w = 4200\,\mathrm{J\,kg^{-1}\,K^{-1}}$ are the specific heat capacities of ice and water, respectively, and $L = 334 \times 10^3\,\mathrm{J\,kg^{-1}}$ is the latent heat of fusion of ice at $T = 0\,^\circ\mathrm{C}$. The effect of solute on the heat capacity of brine is small (*Ono*, 1966) and therefore neglected. The temperature field is obtained as in the case of conducted heat. The porosity field is estimated from the temperature field assuming thermodynamic equilibrium,

$$f = m\frac{S_{ice}}{T}, \tag{3.52}$$

where the bulk salinity of ice S_{ice} is estimated from

$$S_{ice} = S_{ice}^0 + (S_{ice}^{stable} - S_{ice}^0)\frac{t - t_F}{t_s - t_F} \quad \text{for} \quad t_F < t < t_s. \tag{3.53}$$

The initial salinity is assumed to be $S_{ice}^0 = 35\,\mathrm{psu}$, and the stable salinity is assumed to be $S_{ice}^{stable} = 7\,\mathrm{psu}$. The slope of the liquidus is $m = -0.056\,\mathrm{K\,psu^{-1}}$. The porosity f is further set to $f = 1.0$ wherever $t < t_F$, i.e. in the absence of ice. The value of f within the domain that is used for the enthalpy estimate (3.52) is more dynamic with fluctuating temperature than the value of f at the boundary of the domain used for heat conduction (3.49), where it is merely used to avoid a gross overestimate of heat conduction. The rate of change of enthalpy is calculated nominally at the same instances in time as those at which heat conduction is calculated. Assuming instant thermodynamic equilibrium (as in the Stefan problem) this ensures that the flux calculated from enthalpy change is actually equal to the flux from heat conduction, provided no systematic errors and no other sources are present. The flux through the ice–air interface of the domain A_d due to enthalpy change, F_h, is

$$F_h = -\frac{1}{A_d}\int_V \frac{dh}{dt}\,dV, \tag{3.54}$$

where V is the volume of the domain. The time derivative of h is estimated from the change of h over 5 sampling periods.

Uncertainties

The uncertainty in thermal conductivity contributes to the error in heat flux. The thermal conductivity assumes values between $0.6\,\mathrm{W\,m^{-1}\,K^{-1}}$ (water) and $2.1\,\mathrm{W\,m^{-1}\,K^{-1}}$ (ice) particularly at the host ice interface. While the uncertainty in k in the consolidated ice is probably $< 10\,\%$, the uncertainty in the unconsolidated ice will be around $50\,\%$. However, the temperature of ice in the unconsolidated ice is close to the water temperature, resulting in small heat fluxes and small errors. Uncertainties in thermistor spacing of 2 mm contribute another $< 10\,\%$. Errors due to offsets in temperature measurements are zero at water temperature by definition and negligible at lower temperatures since the thermistors obey the same temperature response (cf. *Trodahl et al.*, 2000). Solar radiative heating should incur approximately equal offsets in all thermistors in close proximity, leaving the derived temperature gradient unaffected. The uncertainty in heat flux estimates is therefore $20\,\%$, plus errors through linear interpolation.

The uncertainty in ice density due to air inclusions is $5\,\%$, errors in temperature measurements are $10\,\%$ due to solar heating of thermistor beads, while temperature offset errors will be $5\,\%$ (i.e. $\pm 0.1\,^{\circ}\mathrm{C}$) at seawater temperature, and less at lower temperatures. Errors in the salinity of the ice are ± 3 psu or $50\,\%$ in consolidated ice. Owing to the large latent heat of fusion of ice, the uncertainties in temperature measurement contribute $< 1\,\%$ to the uncertainty in the enthalpy, while salinity uncertainties, proportional to porosity at constant temperature, at a porosity around $f = 0.1$ amount to an uncertainty of $6\,\%$ from (H.6). The uncertainty in enthalpy estimates is therefore $10\,\%$, plus errors through linear interpolation.

Results

The time series of the heat fluxes are shown in Figures 3.15 and 3.16. The sign of the conductive fluxes is reversed to facilitate the comparison of magnitudes. Figure 3.15(a) shows that the heat conducted from the *slot 1*, F_c, is almost always larger than the heat released by ice formation and temperature reduction, F_h, which is to be expected considering solar radiative heating of the ice (but note that the discrepancy is within measurement uncertainty). Occasional spikes in the fluxes are well correlated to temperature spikes recorded in the original data (Figure 3.2(a)). Heat conduction to the sides is initially minimal since the domain does not extend to the sides of the

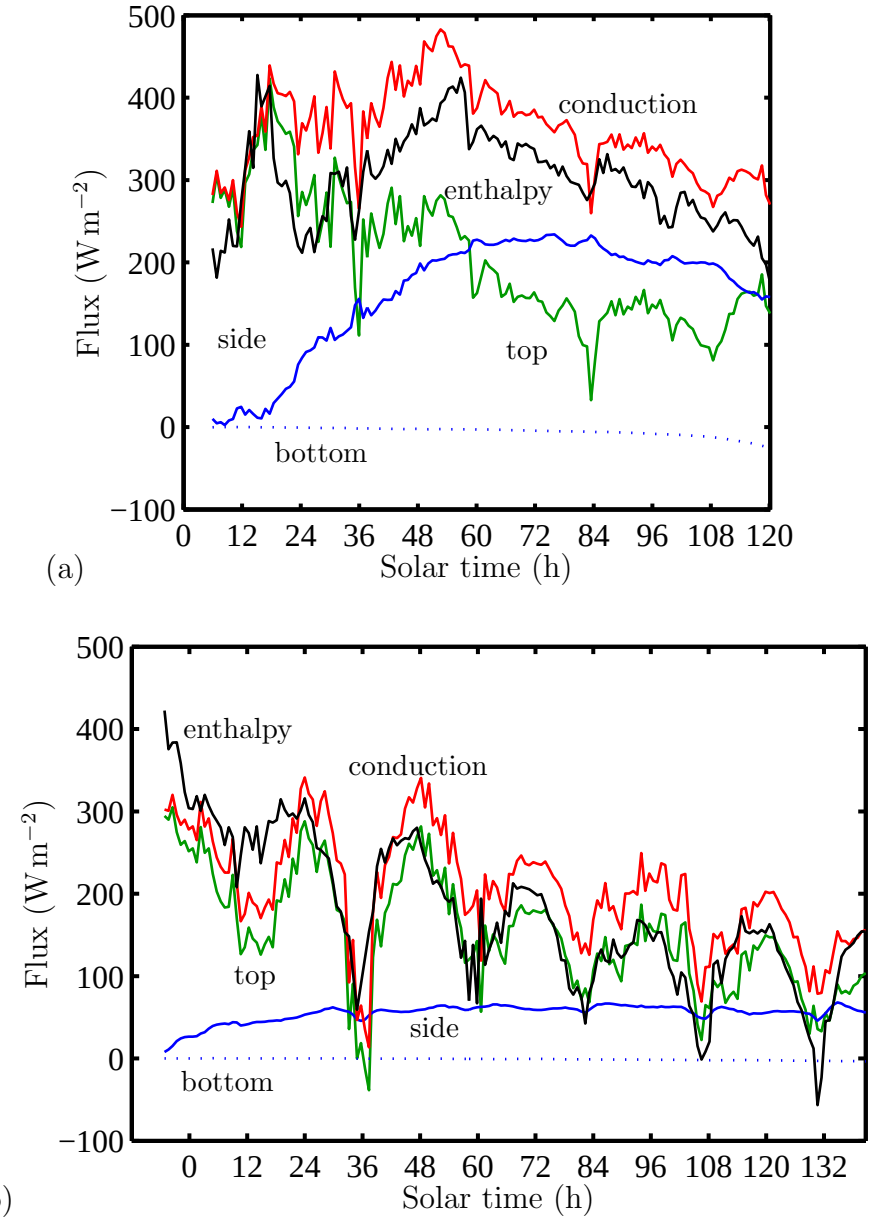

Figure 3.15: Heat flux contributions in (a) *slot 1* and (b) *slot 2*. Vertical flux components through top and bottom (dotted), the horizontal flux through the sides, the sum of these three conductive fluxes $-F_c$, and the rate of change of enthalpy expressed as a flux F_h are shown. Reference area for the fluxes is the surface area of the measured domain. Note the different scales.

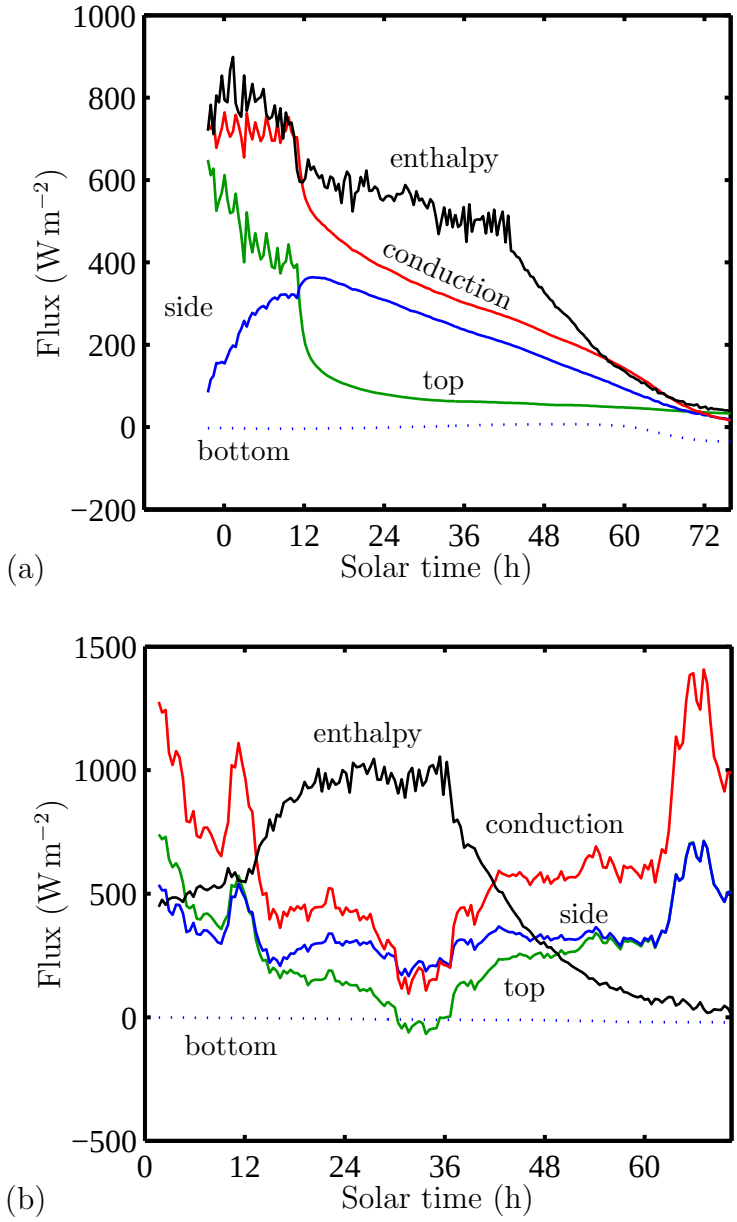

Figure 3.16: Heat flux contributions in (a) *slot 10* and (b) *slot 12*. Vertical flux components through top and bottom (dotted), the horizontal flux through the sides, the sum of these three conductive fluxes $-F_c$, and the rate of change of enthalpy expressed as a flux F_h are shown. Reference area for the fluxes is the surface area of the measured domain. Note the different scales.

slot, and water, at homogeneous temperature, is initially present at the side of the domains. The time series for *slot 2* in Figure 3.15(b) clearly demonstrates a diurnal pattern. Since conduction through the sides is almost constant with time, variations in the conductive flux, F_c, are due to varying conduction through the ice–air interface. The diurnal amplitude is correlated to the air temperature variations seen in Figure 3.2(b) on page 50. As in *slot 1*, heat conduction outweighs the heat released by ice formation and temperature reduction, possibly indicating solar heating (but note that the discrepancy is within measurement uncertainty). Also visible at hours 36, 48, 72 and 120 is a phase difference between $-F_c$ and F_h showing that F_h leads $-F_c$. The phase difference is more obvious in Figure 3.17(b). If heat exchange between ice and environment was by conduction of sensible heat, only, then F_c would be in phase with $-F_h$. If, however, heat exchange was by solar radiative heating of the ice, only, then $-F_h$ would be in phase with the solar radiative heat input, while F_c would be lagging radiative input by 90° (cf. *Trodahl et al.*, 2000). The phase relationship is more complicated when heat conduction, depth dependent absorption of radiation, and the finite thickness of the ice sheet are taken into account. However, we observe that the rate of change of enthalpy, F_h, leads heat conduction, F_c, which is a consequence of the immediate effect of shortwave radiation, F_{sw}^{abs}, on the change in stored energy, while F_c reacts to the amount of energy stored (note that radiative heating is strongest closer to the surface).

Figure 3.16(a) shows that ice formation and ice temperature reduction (expressed by F_h) is larger in *slot 10* than heat conduction, which could be due to a negative heat flux from the ocean (Appendix B.9). Also clearly visible is the onset of snow coverage at hour 12, when heat conduction to top and side decrease considerably. Fluctuations in F_h reduce when the last thermistor freezes into the ice at hour 43. The enthalpy estimate of *slot 12* in Figure 3.16(b) shows an increase around hour 18, which is presumably when snowfall starts (Figure 3.3(b)), and decreases around hour 36 as the last thermistor freezes in. *Dayton et al.* (1969) observe in McMurdo Sound that both anchor ice growth and frazil ice formation set in simultaneously, and that the onset is rather sudden (a few hours).

The sum of heat conducted from the domain, F_c (usually negative), and change of enthalpy in the domain, F_h (usually positive), is shown in Figures 3.17 and 3.18. As shown in Figure 3.17, conducted heat outweighs heat released by ice formation by about $50\,\mathrm{W\,m^{-2}}$ in the later stages of *slot 1* and *slot 2*, which is the same order of magnitude as estimated for the absorbed solar shortwave radiation in Table 3.4. Thus there is satisfactory energy balance without accounting for heat flux from the ocean. However, for *slot 10* and *slot 12* a heat flux from the ocean must be postulated

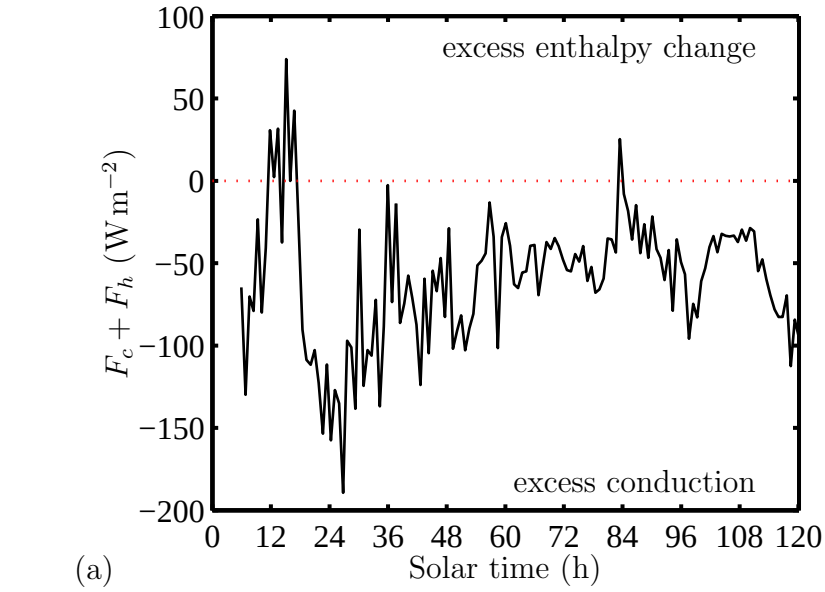

(a)

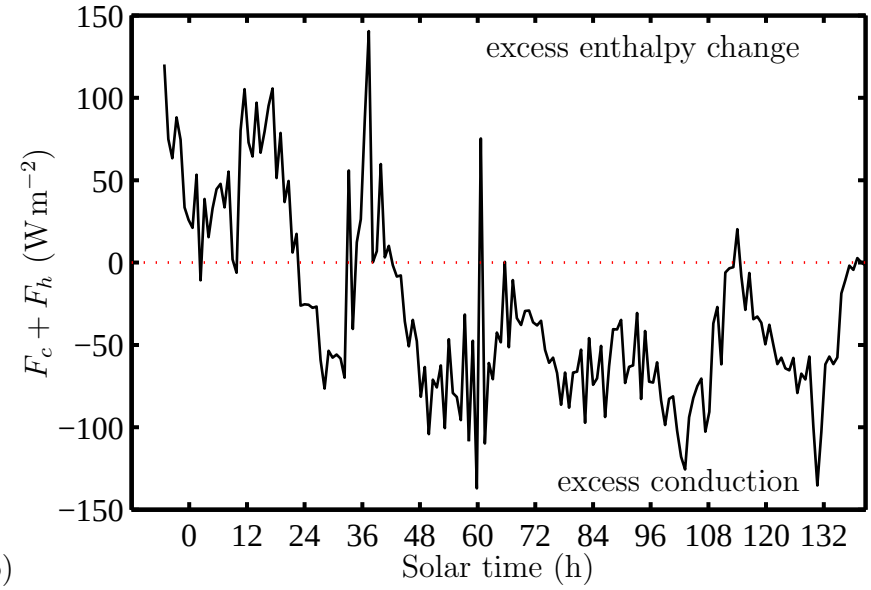

(b)

Figure 3.17: Difference between conducted heat flux F_c (negative) and heat flux used in ice formation F_h (positive) in (a) *slot 1* and (b) *slot 2*.

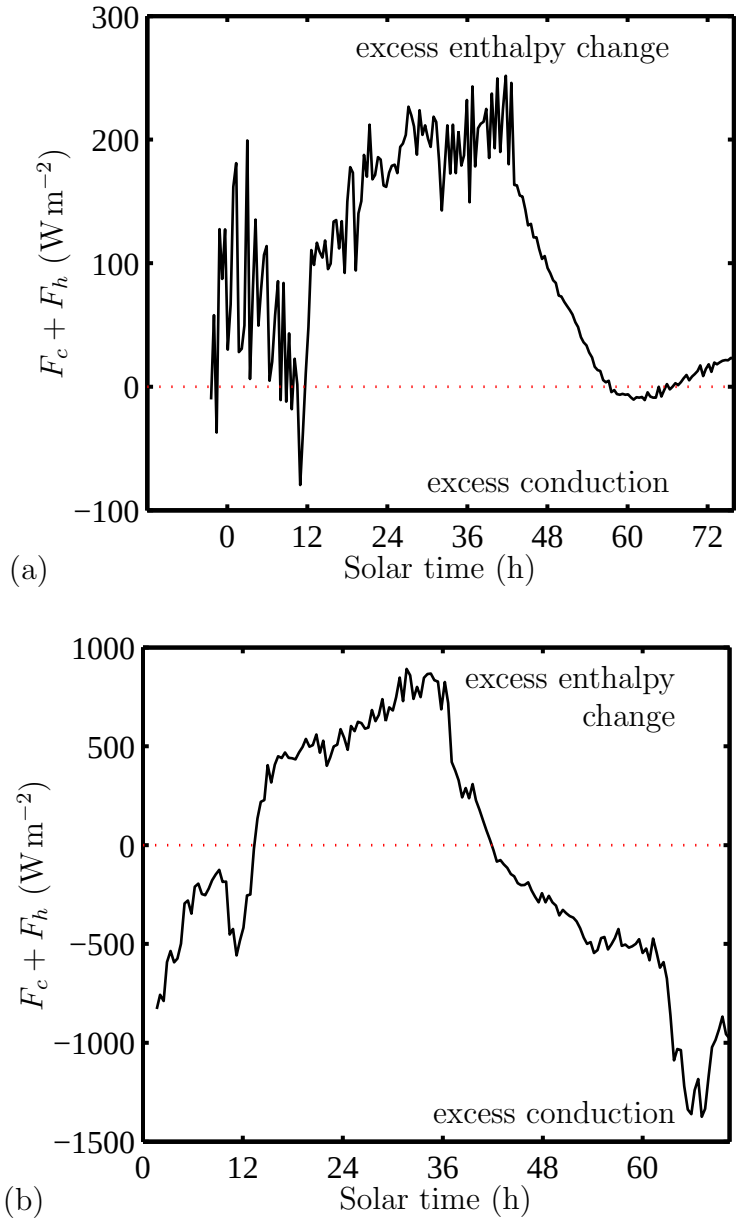

Figure 3.18: Difference between conducted heat flux F_c (negative) and heat flux used in ice formation F_h (positive) in (a) *slot 10* and (b) *slot 12*.

to explain Figure 3.18 (Appendix B.9). The effects of shortwave radiation and or a changing albedo are too small to account for the difference.

Care should be taken in the interpretation of above figures, however. Heat conduction estimates for *slot 12* are based on only two thermistor strings in the slot, which leads to an underestimate of heat conduction to the side if horizontal heat conduction is not uniform horizontally. The situation is potentially similar in *slot 2*, where the distance between the outermost thermistor strings is greatest (both in absolute figures and relative to the width of the slot, see Table B.1). It should finally be pointed out that a lot of data processing has been performed to obtain heat flux and enthalpy estimates, rendering the result sensitive to the choice of parameters. For example, the slope of F_h (i.e. dF_h/dt) in Figure 3.16(a) from hour 12 to 48 is sensitive to the choice of the initial salinity assumed at t_F, which has been set to 35 psu. If 25 psu was used, instead, the slope obtained would be approximately equal to that of F_c (i.e. dF_c/dt).

Summary

The heat budget of refreezing slots has been investigated. It has been found that shortwave radiative flux into the slot, heat conduction out of the slot and change in enthalpy in the slot are in balance within uncertainty limits in experiments *slot 1* and *slot 2*. Experiments *slot 10* and *slot 12* seemed to have experienced an additional flux from the ocean that contributed to the energy balance. The observation of an additional growth–enhancing flux in *slot 10* and *slot 12* is consistent with the conclusions reached by comparison with the freezing front model of Section 3.2.4.

3.3 Water temperature measurements in refreezing slots – Probe 2

3.3.1 Design of probe 2

Physical layout

The primary design goal for the thermistor probe was to detect temperature fluctuations in the water column in order to estimate convective heat and mass transport without disruption to the flow. The flow can be disturbed either by placing obstacles in the flow path, or by inducing thermal convection as a result of dissipated heat. Neither source can be avoided, but attempts are made to minimise their effect. In order to minimise flow disruption due to obstacles the thermistors protrude into the water. This

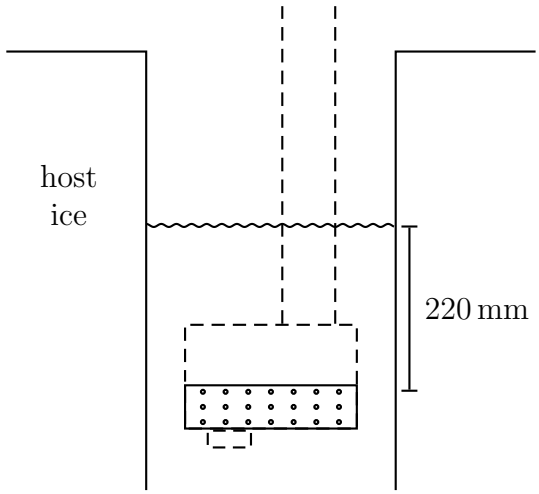

Figure 3.19: Vertical sketch of probe 2 in *slot 11* (to scale). The probe is 30 mm deeper in the water during *slot 13*.

also helps to minimise the thermal mass associated with them. Thermal effects could largely be eliminated by physically separating electronics from the thermistors.

A secondary goal was to assess the correlation between solar radiation and measured temperatures. For this, a CdS light dependent resistor[10] (LDR), *NORP 12*, was added to the probe. Measurements pertaining to LDRs are discussed in Section 3.4.2 and Appendix B.11.

The thermistor probe (Figures 3.19 and 3.20) consists of a rectangular array of 21 thermistors, 7 thermistors per row spaced 30 mm apart, and three thermistors per column spaced 20 mm apart. Each thermistor protrudes 30 mm from a $230 \times 60\,\mathrm{mm}^2$ block of conduit filled with potting compound to provide stability and electrical insulation. The thermistors are supported by 4 mm outer diameter plastic tubes. The black thermistor beads are insulated by a thin coating of nail varnish but otherwise exposed to the environment. An upward facing light dependant resistor is encased at about the center of the conduit block. The block is held 350 mm in front of an air–filled, sealed box containing the oscillator and resistance–voltage signal conditioner circuits that are described in the next section. Water is free to flow between the box and block, with the exception of the area occupied by the 40 mm wide thermistor cable conduit. A 1 m vertical fibreglass support bar is connected to the circuit box. At its top end perches a box that contains a voltage transformer and a bayonet mount signal cable connector. During the experiment the probe is held in place by a horizontal support bar attached

[10]The spectral response of the *NORP 12* light dependent resistor (Appendix C.4) is in the same range as the photobic (daylight) spectral response of the human eye. Such a device gives a good indication (power law relationship between resistance (Ohm) and illuminance (lux)) of brightness perceived by a human being, but it provides a poor measure for total radiative flux.

Figure 3.20: Probe 2 in action. Experiment *slot 11*, width of the slot is 330 mm, true North is to the right as indicated.

to the vertical support bar.

A 3 m long cable connects the probe with the data logger, *Campbell Scientific CR10X*. The data logger is placed in a wooden box that is insulated with 50 mm styrofoam on each side. The same box houses two 12 V *OPTIMA* Deep Cycle lead acid batteries ("Yellow Top") for power supply. A second upward facing LDR is attached to the box.

Illuminance measurements

The LDR, *NORP 12*, has a power law response to illuminance (*RS Components*, 1997). The resistance of the LDRs is measured with a half bridge containing a 1 kΩ fixed resistor (the same resistance as the LDR at 200 lx). This way illuminance from 1 lx to 1×10^4 lx can be resolved. However data below 10 lx are affected by integral linearity errors of the Analogue Digital Converter (ADC) of the *CR10X*. The power law

resistance–illuminance conversion equation is applied using typical values from the data sheet. No calibration has been performed on the LDRs[11].

Design of the signal conditioning circuit

The design of the signal conditioning circuit is based on several requirements that provide a challenge through their cumulative appearance. High temperature resolution was the primary goal, as we expected that water temperature variations due to brine plumes could be below 1 mK (*Lake and Lewis*, 1970). Similarly low temperature fluctuations have been measured in a different context several metres under refreezing leads (*McPhee*, 1992; *McPhee and Stanton*, 1996; *Morison and McPhee*, 1998). We expected that features of 1 mK magnitude should be identifiable if the sampling resolution is 0.2 mK above noise. This temperature resolution had to be mapped to the resolution of the analog digital converter (ADC) of the *CR10X*. Previous experiments with the *CR10X* have shown that 0.6 mV can be resolved with negligible noise. Although the demands on temperature resolution were high, measurement of absolute temperature was not required.

Every electrical current dissipates heat. This is a particular consideration for electrical currents that are used to measure temperature with thermistors. *BetaTHERM* states[12] that their thermistors have a self–heating coefficient of 7 to 8 $\mathrm{mW\,K^{-1}}$ in a well–stirred oil bath at 25 °C. Our experiments neither take place at 25 °C in a well stirred oil bath, nor are the thermistors exposed to the fluid on all sides. We estimate that as little as 1 μW power dissipation in a thermistor is sufficient to raise the thermistor's temperature by 1 mK. To ensure that we measure temperature fluctuations that are not self–induced, we demand a maximum power dissipation of 0.1 μW for each thermistor, the equivalent of about 0.1 mK self heating. Using larger power and later correcting for self heating, as has been done by *Clow et al.* (1996) in ice sheets, is not an option if we want to avoid thermal disturbances.

The entire experiment had to be battery powered, with a single 12 V supply providing power for the *Campbell Scientific* data logger *CR10X*, the external data storage module, and the signal conditioning circuit. The *CR10X* needs 13 mA during processing without analogue measurements and without accessing the data storage module (*Campbell Scientific*, *CR10X* manual). To keep the necessary frequency of the battery replacement low, the desired order of magnitude for current drain of the conditioning

[11] On the sunny, clear blue sky day of 9 September, 2002 the maximum direct (i.e. not diffuse) solar radiation measured at Scott Base was $55\,\mathrm{W\,m^{-2}}$, while the maximum illuminance was 8000 lx in air as measured with an upwards facing LDR in experiment *slot 11*. For reference it may be mentioned that 0.1 lx is typical for moonlight.

[12] `http://www.betatherm.com/`

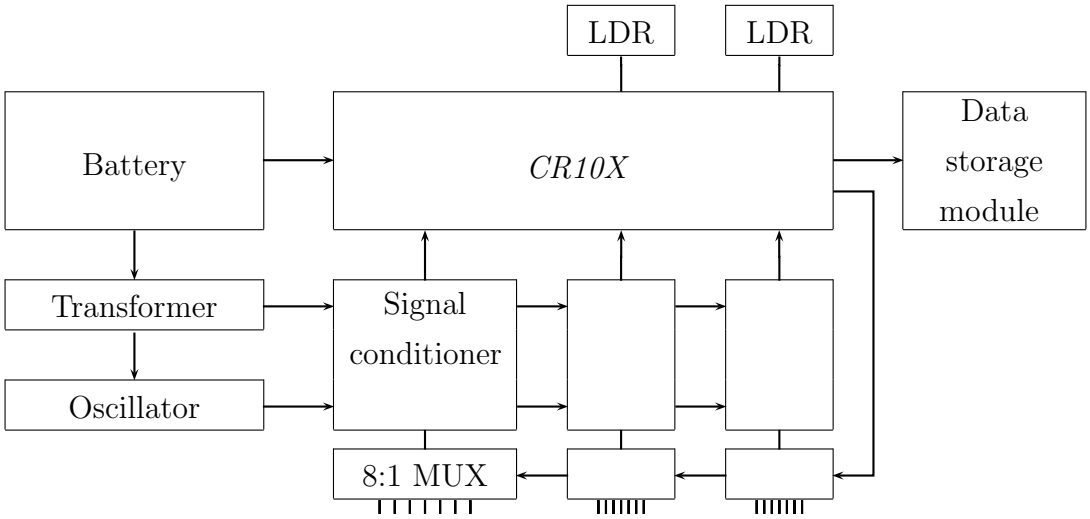

Figure 3.21: Schematic of the components of the data acquisition unit of the 2002 water temperature probe. Three identical signal conditioner and multiplexer (MUX) units are used. The oscillator and three signal conditioners with multiplexers are mounted on the same circuit board.

circuit was therefore $10 - 100\,\mathrm{mA}$. In addition, an essential feature of the circuit design was that the circuit could be maintained at a constant temperature when placed in the water column.

I owe the design of the circuit to Dr. Neil Thomson and Dave Hardisty of the Physics Department at Otago University. All that was left for me to do in this respect was to specify an operating frequency, and the values of the resistor and the capacitor of a low pass filter. The schematic of the data acquisition unit is shown in Figure 3.21. The battery used to power the *CR10X* datalogger that stores measurements at set intervals in a portable data storage module, also powers a transformer that generates the voltages necessary for the signal conditioning units and the oscillator. Three single–channel signal conditioners operate simultaneously. Each of them is connected to a multiplexer that connects resistor bridges either to one of seven thermistors, or to a reference resistor. The multiplexers are controlled by the *CR10X*. Transformer, oscillator and the three signal conditioners together draw a current of 12 mA from the battery.

The resistance–voltage mapping of the signal conditioners is based on an alternating current (AC) circuit. Direct current (DC) measurements are out of the question since offset errors and Johnson noise (thermal noise) of the electrical components exceed the signal (*Dave Hardisty*, personal communication). The signal of a Wien bridge oscillator with output level controlled by a precision voltage reference is coupled to the signal conditioner through an inductor `L1`. Figure 3.22 shows a simplified version of the circuit diagram of the signal conditioner. A Wheatstone bridge converts the resistance of a

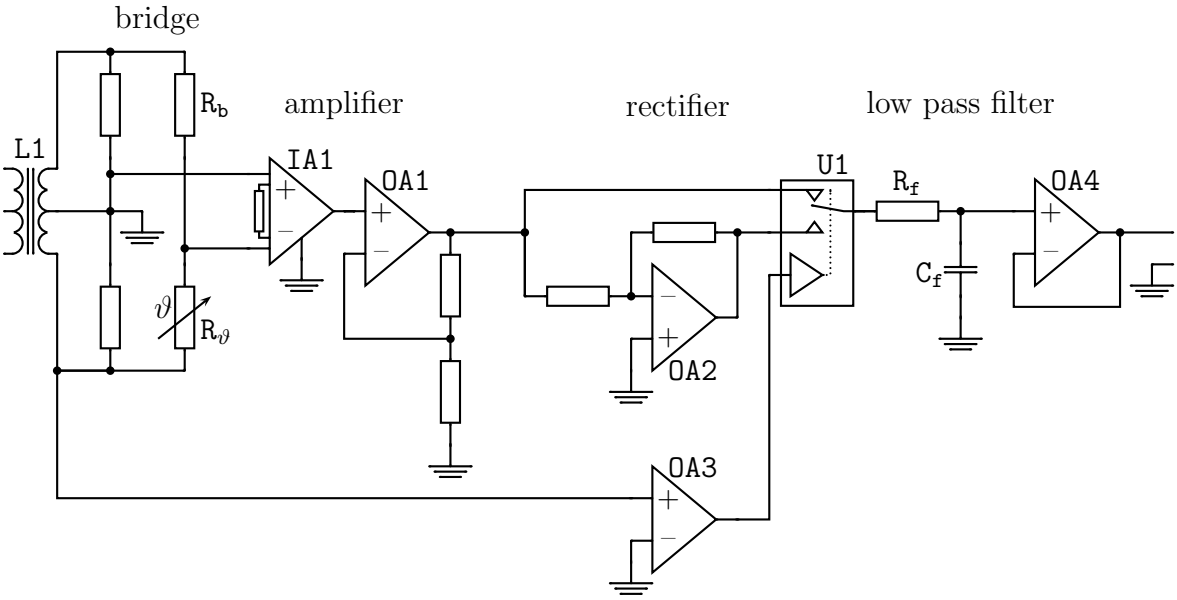

Figure 3.22: Simplified circuit diagram of the resistance–voltage converter of the water temperature probe 2. This circuit is implemented three times in the probe. The negative input of IA1 is multiplexed either to one of seven half bridges R_b/R_ϑ or to a reference half bridge. The bridge is driven through L1 by a Wien bridge oscillator.

thermistor R_ϑ into a voltage. The resistor R_b was chosen in the laboratory to balance the resistance of the thermistor at the expected water temperature. The small AC signal is amplified by instrumentation amplifier IA1, *Texas Instruments INA 128* with gain set to 500, followed by operation amplifier OA1. Provision was made to reduce the gain of the latter after the unit has been sealed, should readings be unexpectedly out of range. OA2 inverts the amplified AC signal. The analog switch U1 switches between signal and inverted signal to rectify the signal. The switch is controlled by comparator OA3 that provides a square wave signal synchronised with the AC signal. The key feature of this method of rectification is that DC offset errors of IA1 and OA1 are removed. The rectified signal is filtered with an RC low pass filter R_f and C_f to provide a DC signal. OA4 buffers this signal before it is digitised by the *CR10X* with 13 bit resolution.

The multiplexer is connected between the negative input of IA1 and the half bridge of R_b and R_ϑ. Every thermistor therefore has an individually matched balance resistor R_b. R_ϑ is replaced by a fixed resistor in the reference channel.

The cut–off frequency of the low pass filter had to be set low enough to keep AC ripples below the resolution of the *CR10X*, and high enough to allow for short settling times after channel switching. This is readily achieved at high oscillator frequencies f. However, the oscillator frequency has to be as low as possible to avoid adverse effects of

Table 3.5: Summary of experiments with probe 2.

	slot 11	*slot 13*
Location	Erebus Bay	Erebus Bay
Slot width (m)	0.33	0.33
Ice thickness (m)	2.20	2.20
Slot orientation	E–W	N–S
Thermistors point	E	N
Start date	9 Sept, 02	17 Sept, 02
Start time (local)	17:24	13:47
Sampling period (s)	10	1
Columns logged	7+1	1+0
Average T_{air} (°C)	−33.9	−17.2
Snow cover during convection experiment (mm)	0	200+
Excavation	16 Sept, 02	21 Sept, 02
Final snow cover (mm)	200	200+

stray capacities in thermistor leads and on the circuit board. Based on the assumption that a settling time of 1 s is sufficiently short, we used $f = 10\,\mathrm{kHz}$, $\mathtt{C_f} = 1\,\mu\mathrm{F}$, and $\mathtt{R_f} = 90\,\mathrm{k}\Omega$. This low pass filter is expected to reduce the amplitude of 10 kHz ripples to $\widehat{V}_{10k} \leq 0.15\,\mathrm{mV}$. To connect the thermistors to the circuit board, shielded four core cables were used with two cores removed to reduce capacitance. No evidence of channel cross talk or capacitive effects was found during probe calibration in the laboratory.

3.3.2 Overview of experiments with probe 2

Description of experiments

Probe 2 was used for water temperature measurements in refreezing slots in McMurdo Sound in September 2002 (experiments *slot 11* and *slot 13*) at the same site as experiments *slot 10* and *slot 12*. The experiments followed the same pattern as the experiments of probe 1 described in Section 3.2.2. However no thermistor string was frozen into the host ice sheet. During the preparation of the slot, probe 2 was placed in sea water in a separate hole in order to cool the electronic circuit. Some characteristics of the probe 2 experiments are listed in Table 3.5.

Temperatures were logged during *slot 11* using the following procedure that was triggered every 10 s: the three multiplexers were set to log the reference resistors of the three signal conditioners. A delay of one second was allowed for the low pass capacitors to charge up, followed by five analogue–digital conversions in quick succession on each conditioner. The multiplexers were then advanced to log the first column of thermistors, followed by a 1 s delay and five measurements in quick succession for the thermistors

of each row. The process was repeated for all thermistor columns before the LDR resistances, battery voltage, and air temperature at the data logger box were logged. Data were written to the data storage module every couple of minutes. One of the two batteries was changed at hour 40.

After preliminary evaluation of data of *slot 11* it has been decided that in experiment *slot 13* only the thermistors of the centre column, the LDRs, battery voltage, and air temperature be logged. The sampling period has been reduced to once every 1 s, and the delay for the charge up of the capacitors has been set to 0.8 s. No battery change was performed during this experiment. The ice thickness h inside the slot at the time of excavation was 90 mm, and no thermistors had frozen into the ice.

Temperature records

The time series of *slot 11* in Figure 3.23 are in groups of three, corresponding to the seven columns of thermistors. The upper graph of each group of three corresponds to the thermistor in the upper row, and the lower graph to the thermistor in the lower row. Column 4 is at the centre of the slot, columns 1 and 7 are closest to the sides. Diurnal temperature fluctuations are visible that do not represent water temperature changes as discussed in Section 3.4. Some thermistors show excessive drift that is likely to be due to the thermistors themselves, possibly from penetrating seawater. The thermistors of columns 1 and 7 start to freeze into the ice around hour 35, which also marks the beginning of electronic drift due to unstable temperatures of the electronic circuit. Temperature deflections are generally towards higher temperatures during daylight hours (hours 11 and 34), while they are smaller in amplitude and towards lower temperature in the absence of sunlight. Figure 3.24 shows an enlargement of the temperature data at night. There are periods of increased and decreased activity that are clearly discernable to the eye. Periods of increased activity appear about every one to two hours, sometimes at all columns simultaneously (e.g. hour 17.3), and sometimes not (e.g. hour 19.0). Figure 3.25 shows daylight activity, using the same temperature scale as in Figure 3.24. Figure B.17 in Appendix B.10 shows another section of nighttime data at higher magnification.

The abrupt temperature changes of up to 50 mK apparent in the overview of *slot 13* in Figure 3.26, suggest that there may have been electronic issues between hours 12 and 36 that abruptly offset the temperature reading. Unfortunately, the high sampling rate did not permit us to log the reference channels, so that the origin of the discontinuities cannot be unambiguously identified. They may have been driven by the weather, as there was a rapid rise in air pressure during the experiment (Figure B.2). Air temper-

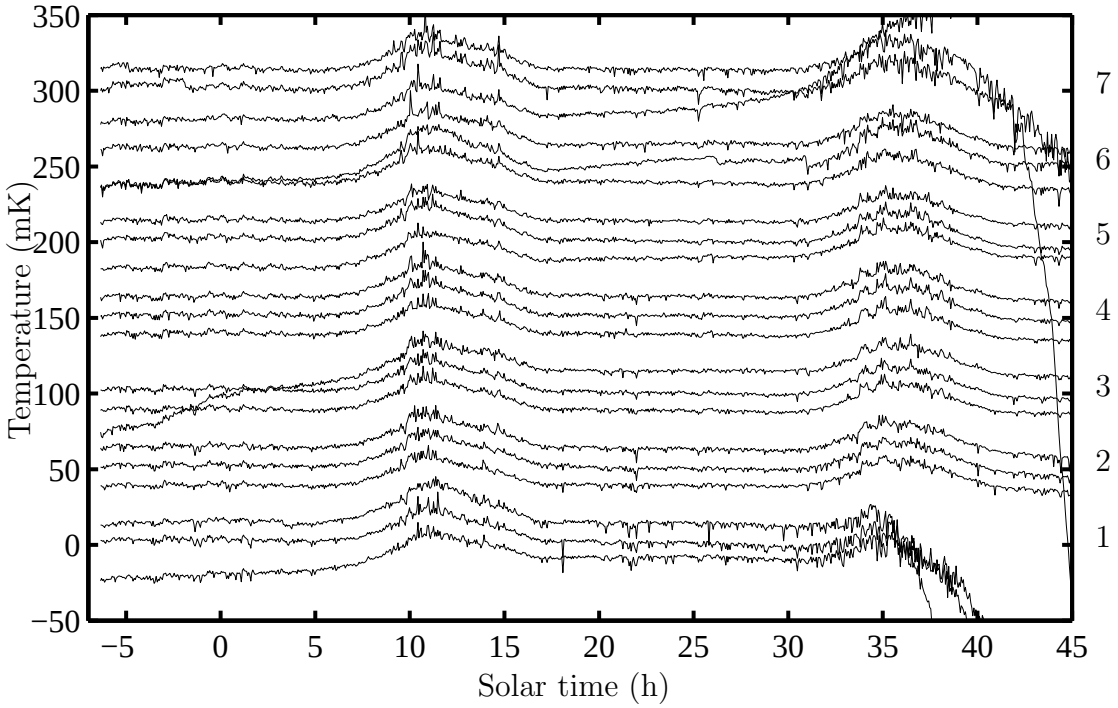

Figure 3.23: Overview of water temperatures beneath an ice skim detected in *slot 11*. Temperatures are offset and only 1 in 20 data points is plotted for clarity. Time series are grouped in columns with the upper thermistor of each column plotted at the top. Column 4 is at the centre of the slot. Some thermistors show excessive drift (1 bottom, 3 top, 5 bottom, 6 centre, 7 bottom). Freezing of the columns at the periphery begins at around 35 h. Diurnal temperature variations are discussed in Section 3.4.

ature reached a maximum at hour 12 and dropped 7 °C to a local minimum at hour 36 (Figure B.1). Note that temperature variations in the water temperature data of *slot 13* are significantly smaller than those of *slot 11*, and temperature deflections larger than 2 mK are very rare in *slot 13*. The sampling rate in *slot 13* is high enough to discern a direction of apparent movement in the water column. Figure 3.27 clearly shows temperature deflections at 49.41 h that seems to propagate downwards. The difference between the time of steepest downwards slope is 7 s from top to middle row, and 6 s from middle to bottom row, giving an average vertical velocity of $3\,\mathrm{mm\,s^{-1}}$. Figure 3.28, on the other hand, shows cold temperature deflection at 63.635 h apparently moving upwards. Since only one column has been logged no information about possible sideward movement is available, and the apparent vertical velocities could be due to horizontal movement of the water.

However, above velocity observations are consistent with laboratory experiments of **?** and *Dikarev et al.* (2004). **?** finds from saltwater ice growth experiments in a tank of height 530 mm vertical brine plume velocities of 2 and $4\,\mathrm{mm\,s^{-1}}$ for ice growth rates of $2 \times 10^{-6}\,\mathrm{m\,s^{-1}}$ and $9 \times 10^{-7}\,\mathrm{m\,s^{-1}}$, respectively. He further observes that, at

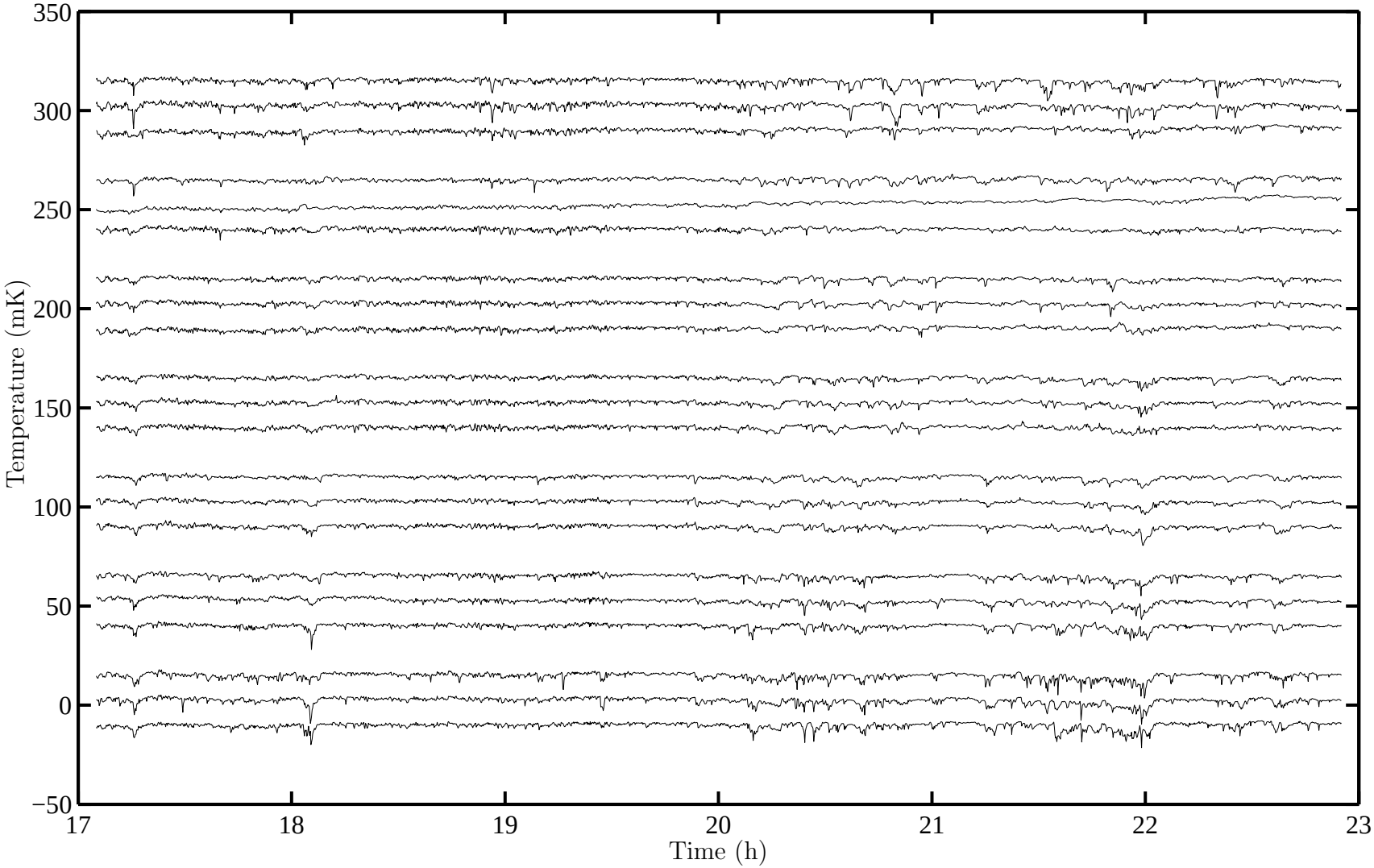

Figure 3.24: Water temperature fluctuations during *slot 11* at night. Time series are offset for clarity and grouped in columns with the upper thermistor at the top. The bottom thermistor in column 7 and the centre thermistor in column 6 are drifting.

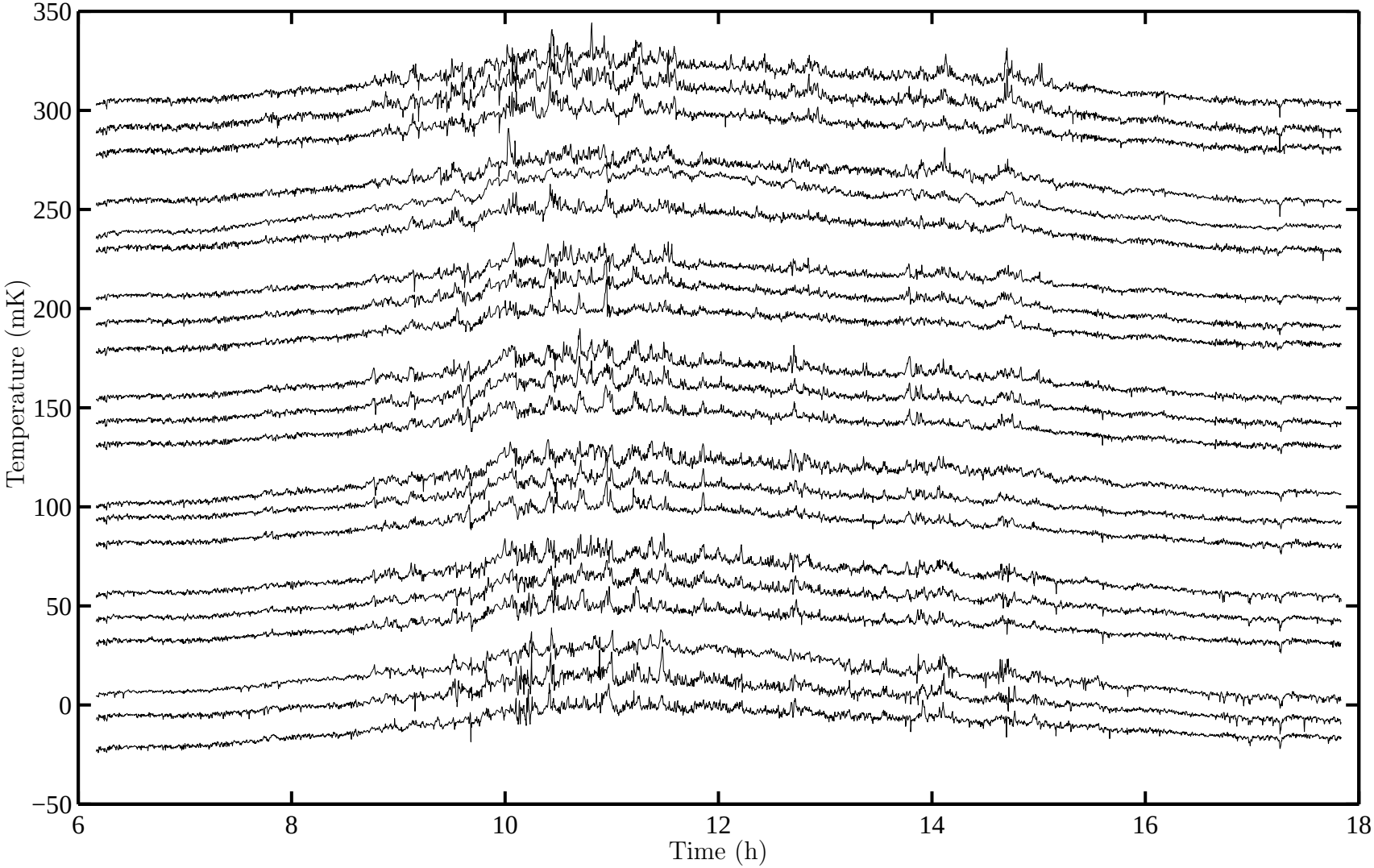

Figure 3.25: Water temperature fluctuations during *slot 11* during the day. Time series are offset for clarity and grouped in columns with the upper thermistor at the top.

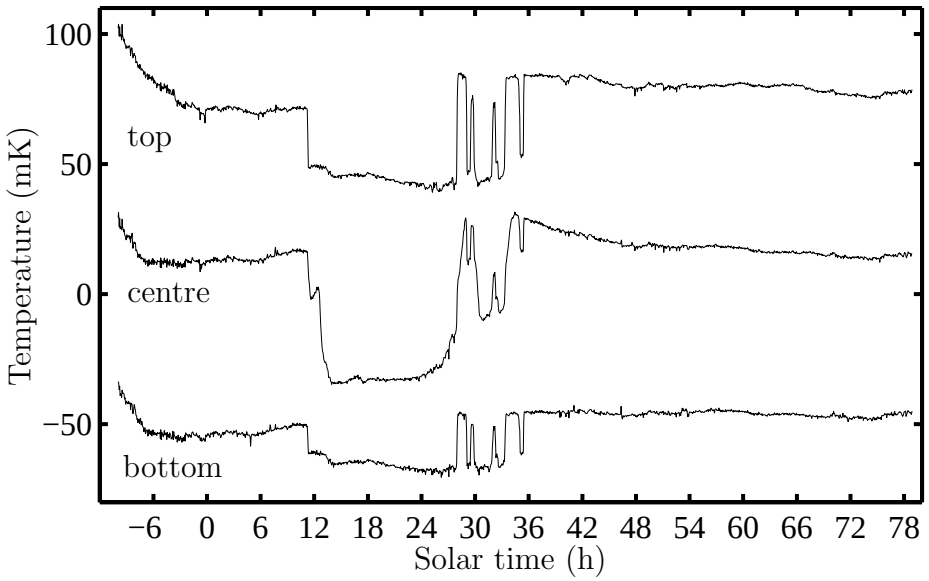

Figure 3.26: Overview of water temperatures during *slot 13*. Time series are offset, and only 1 in 200 data points is plotted for clarity.

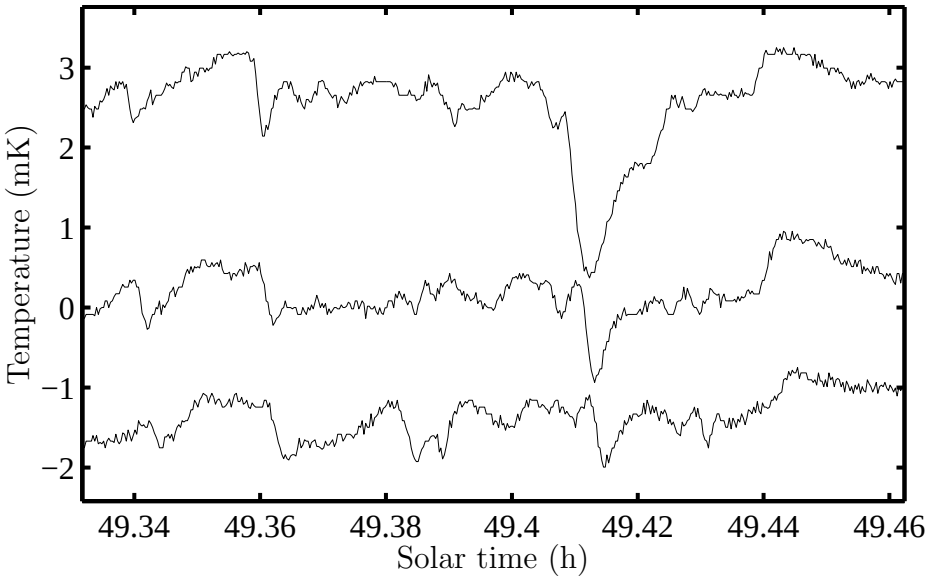

Figure 3.27: Temperature data of *slot 13* showing a time lag of a temperature deflection at 49.41 h between the thermistors in top, centre, and bottom row. The deflection appears to move downwards at $3\,\mathrm{mm\,s^{-1}}$.

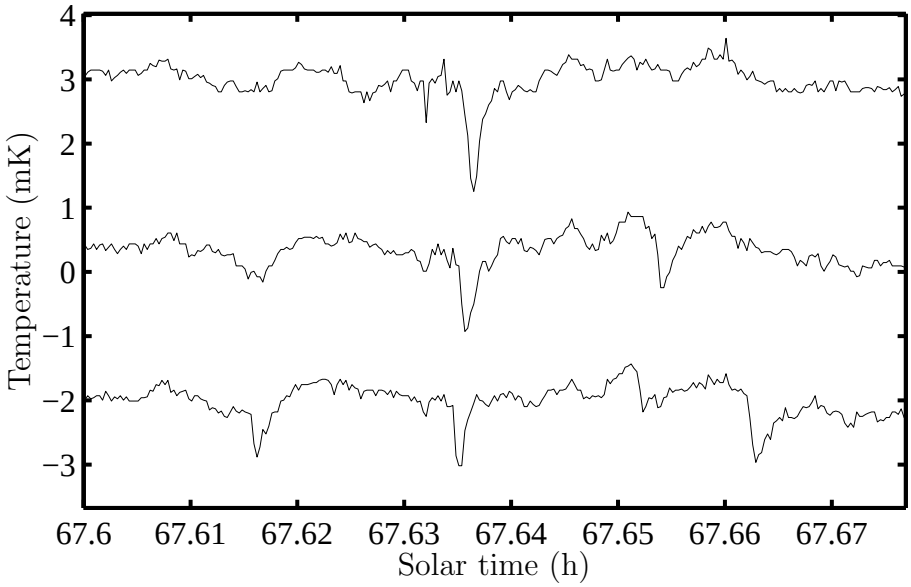

Figure 3.28: Temperature data of *slot 13* showing a time lag of a temperature deflection at 67.635 h between the thermistors in top, centre, and bottom row. The deflection appears to move upwards at $10\,\mathrm{mm\,s^{-1}}$.

high growth rates, some of the descending brine plumes "turn around about half the way of the tank and ascent upwards forming convection cells while diffusing slightly." *Dikarev et al.* (2004) finds from saltwater ice growth experiments in a tank of height 500 mm that brine plumes generally remain intact in the upper 100 to 200 mm below the ice–water interface, but disintegrate between 200 and 300 mm. Once disintegrated, the vertical velocity of the brine vortex rings is between 1 and $5\,\mathrm{mm\,s^{-1}}$. The rings disappear between 300 and 400 mm below the ice sheet. Hence, the vertical velocity component measured in the present experiments is of the same order of magnitude as the vertical velocity determined in laboratory experiments. Further, brine release from growing ice has been observed to induce both downward moving brine and upward moving brine brine.

The observed temperature deflections in the water are small. Assuming thermodynamic equilibrium, temperature deviations of $\Delta T = 10\,\mathrm{mK}$ would correspond to salinity deviations of $\Delta S = 0.2\,\mathrm{psu}$. However, the salinity of brine plumes emerging from growing sea ice (*Wakatsuchi and Ono*, 1983) should be to the order of 50 to 100 psu (Appendix F.2.2). Such brines would be in thermodynamic equilibrium at $\Delta T = 0.9\,^{\circ}\mathrm{C}$ and $\Delta T = 3.7\,^{\circ}\mathrm{C}$ below the freezing point of the ocean water, respectively, which clearly has not been observed in the present experiments.

We seek to explain the discrepancy between measured temperature deviations and temperature deviation expected from *Wakatsuchi and Ono* (1983) assuming thermo-

dynamic equilibrium. Thermal diffusion and turbulent mixing are unlikely candidates to explain this observation since their influence on the temperature signal should decrease significantly as the ice–water interface approaches the probe. However, detected temperature fluctuations do not exceed $\Delta T = 30\,\mathrm{mK}$ even as thermistors are at the brink of freezing (e.g. Figure B.26). The easiest explanation is therefore that the brine plumes are not in thermodynamic equilibrium when they leave the sea ice matrix. They have, on their way through the ice matrix, taken on a temperature similar to the surrounding ice. Thermodynamic equilibrium of the expelled brines is not necessarily reestablished since solutal diffusivity is approximately two orders of magnitude smaller than thermal diffusivity.

3.3.3 Activity in the water column

Definition of activity

We are now going to quantify the "activity" in water column as a function of space and time. We hypothesise that this "activity" is due to brine plume movement, and we are primarily interested in its dependence on location inside the slot.

The following algorithm is applied to each thermistor record: a window of 10 min length is moved over the time record, the record is detrended and the "activity" is determined at each time. The window length of 10 min is somewhat arbitrary but chosen to be longer that the typical time of a single apparent deflection, and shorter than the length of an "activity" event.

Three definitions of "activity" have been tried. First, the Shapiro–Wilk test for normality has been applied (*Conover*, 1980). It allows us to detect segments of the record that are particularly likely to show a normal distribution of temperatures, which would be an indication of noise rather than a plume. Here, we are interested in sections that are particularly unlikely to be normal distributed. Comparing the results of the Shapiro–Wilk test with the subjective impression of "activity" in Figures 3.23 and 3.26 shows that the test is suitable for the detection of sections that are particularly calm, but not suitable for the discrimination between moderately "active" and very "active" sections, which is our particular interest. The second definition of "activity" is simply the standard deviation, or root mean square, of the detrended window. The change in standard deviation with time is shown in Figure 3.29(a). Large standard deviations in Figure 3.29(a) correspond to the subjective impression of "activity" in Figure 3.24. It is also interesting to see that "activity" is sometimes registered at both sides of the slot simultaneously, with only little "activity" in the centre, e.g. at hour 21.5. Note that the description of "activity" does not attempt to correlate the shape of the temperature

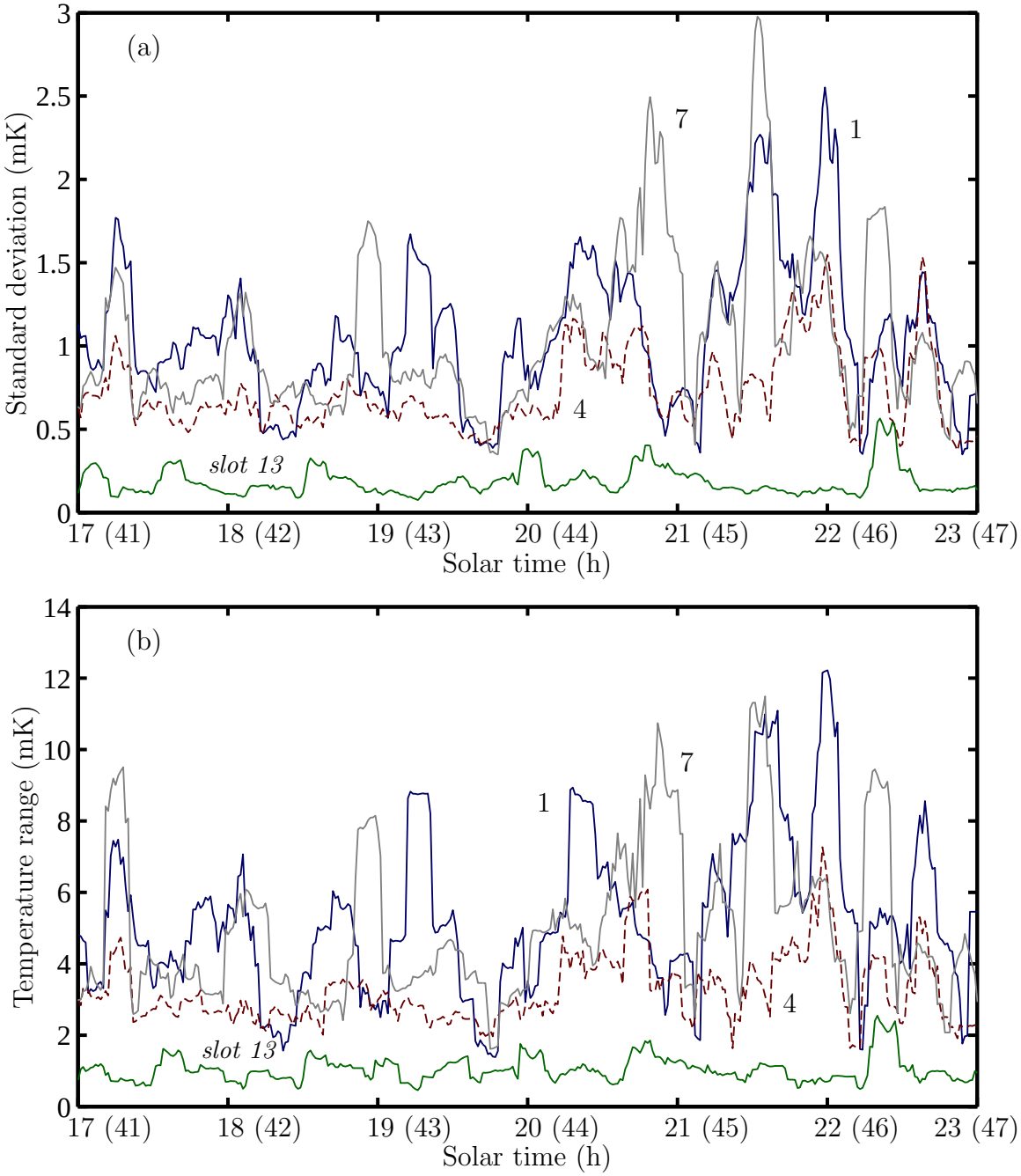

Figure 3.29: (a) Standard deviation and (b) temperature variation calculated for a sliding window of 10 min length for thermistors of the upper row of column 1 (dark), 4 (dashed), and 7 (light) in *slot 11*, and of *slot 13*. Times in brackets refer to *slot 13*.

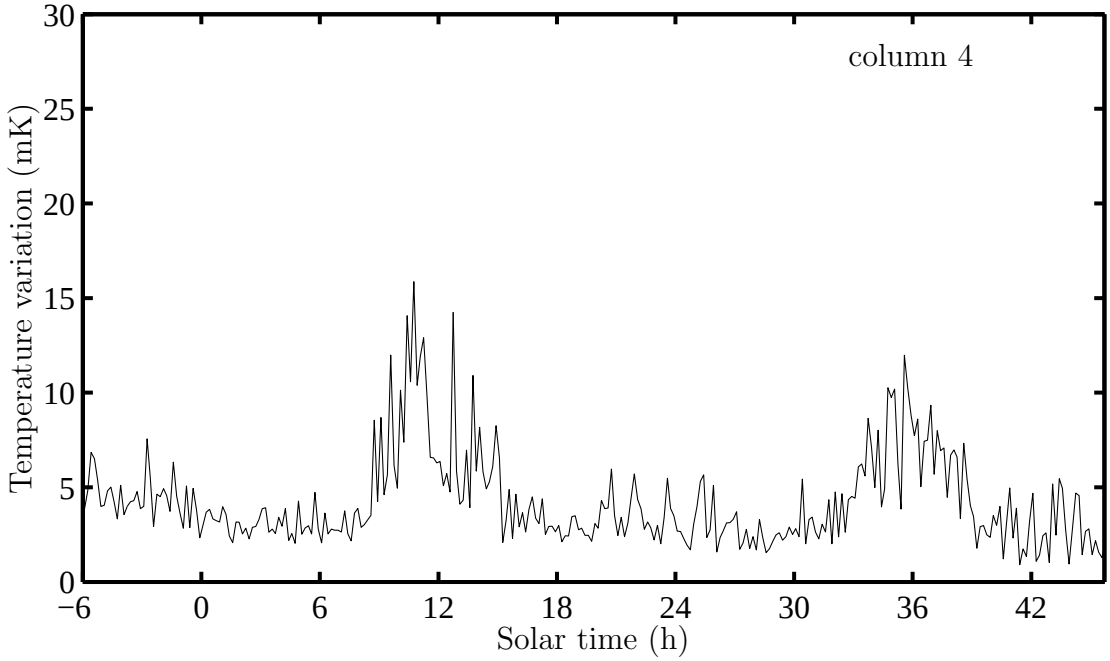

Figure 3.30: Temperature variation in *slot 11* measured by the upper thermistor in centre column, column 4.

deflections between the columns. While the base level of the standard deviation is about 0.6 mK for *slot 11*, it is distinctly lower in *slot 13*, with a level of 0.2 mK, which is consistent with earlier comments. As mentioned earlier, the raw temperature resolution of the system without any form of averaging over multiple measurements is 0.2 mK. The third definition of "activity" is simply the signal variation, i.e. the difference between maximum and minimum temperature, within each window. The result is shown in Figure 3.29(b). It suggests "activity" at about the same times as the standard deviation approach. Similar figures for the range of hours 29 to 35 are shown in Appendix B.10.

With temperature variation as a measure for "activity", Figure 3.30 shows the temperature variation at the upper thermistor in the centre column for the first 48 hours of *slot 11*. As suspected before, the nighttime is calm compared to daytime.

Figures 3.31(a) and (b) show the temperature variation at the upper thermistor at the side columns for the first 48 hours of *slot 11*. Apart from the difference between daytime and nighttime "activity", "activity" is further elevated during the second night, only a few hours before the freezing front of the slot reaches the probe.

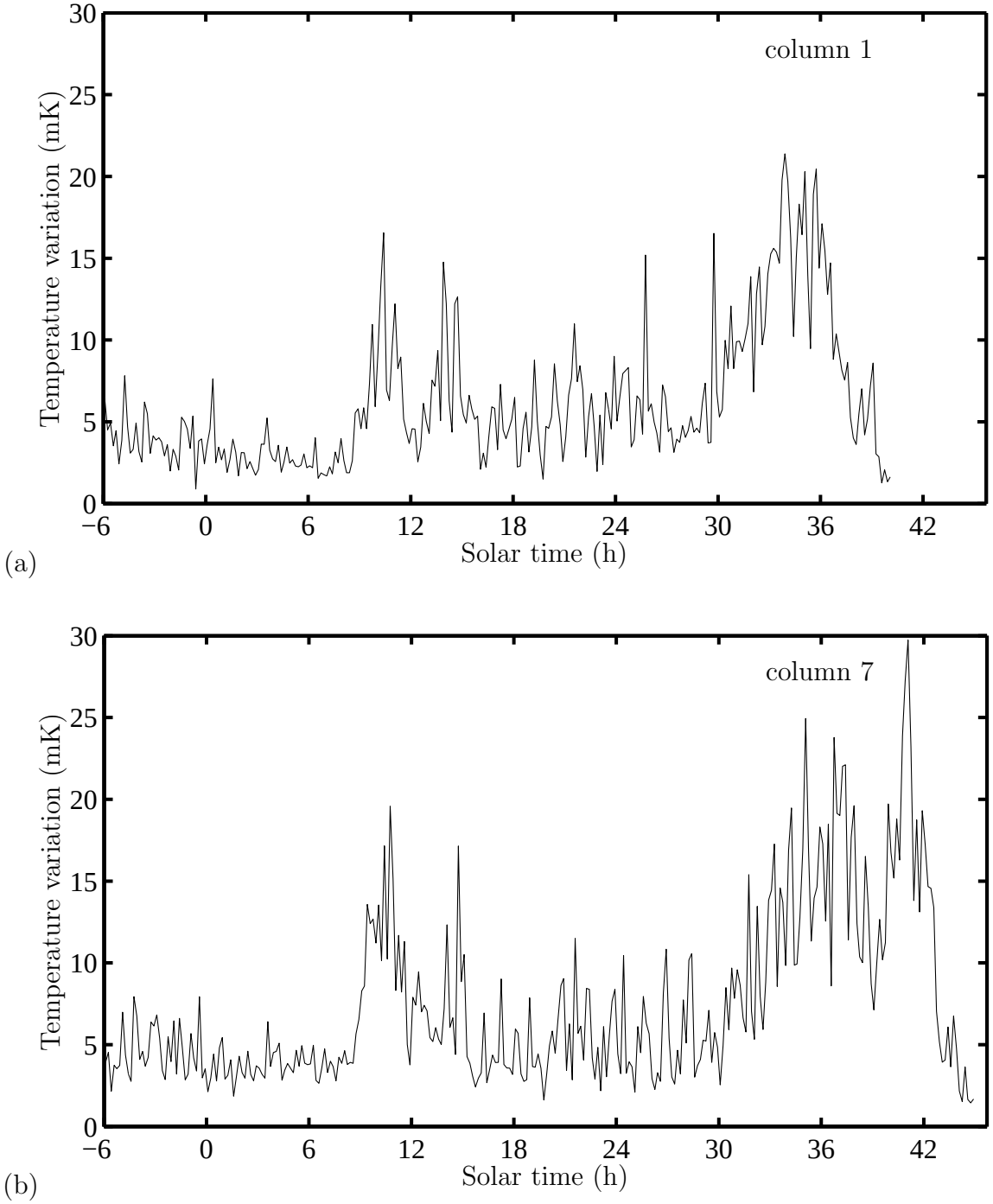

Figure 3.31: Temperature variation in *slot 11* measured by the upper thermistor in columns (a) 1 and (b) 7, respectively.

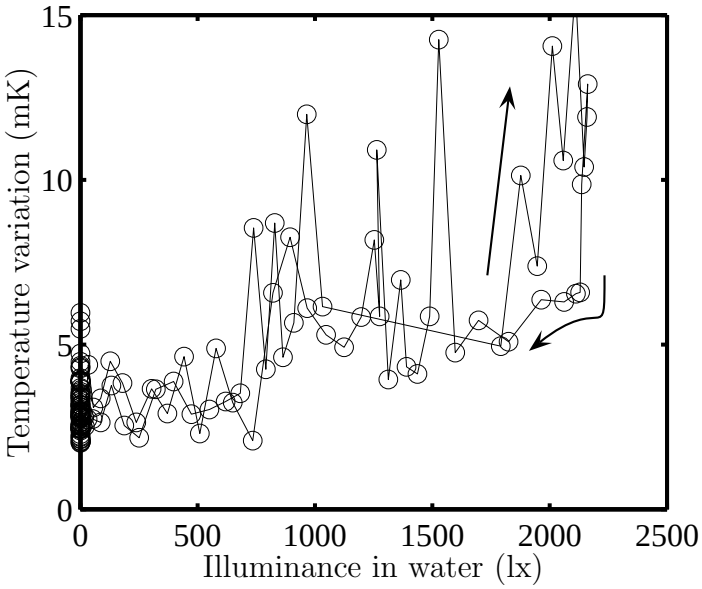

Figure 3.32: Temperature variation (temperature difference per detrended 10 min window) of the upper centre (column 4) thermistor in *slot 11* as a function of illuminance measured close to the thermistors in the water. Data of hours 0 to 24, arrows indicate the path direction.

Illuminance dependent temperature variation

We have seen that "activity" in the water is higher during daylight hours than it is at nighttime. We will next determine the point of onset of increased "activity". Based on the hypothesis that solar radiation is correlated with increased brine release we plot temperature variation as a function of illuminance detected close to the thermistors in the water. Illuminance is a measure for solar radiative flux as discussed in Section 3.4.

Figures 3.32 and B.19 show a scatter plot of temperature variation at the upper centre thermistor in *slot 11* versus illuminance. Temperature variations have been calculated for detrended windows of 10 min. Points are connected to allow an assessment of the presence of a hysteresis loop. It appears as though the signal variation is around 3 mK until illuminance reaches about 700 lx (hour 8.6). From 700 lx onward a trend towards increased variation with increased illuminance is visible. The variation–illuminance relationship in the morning hours seems to be the same as the relationship in the afternoon. 700 lx is reached again at hour 15.3.

Figure 3.33 is a similar plot for the upper thermistor at the side of *slot 11*. The signal is again calm for illuminances below 700 lx, and a marked increase with increasing illuminance is visible beyond 700 lx. Further, temperature variations are larger in the morning hours than in the afternoon. None of the figures shows a significant hysteresis (where the reference is Figure 3.36).

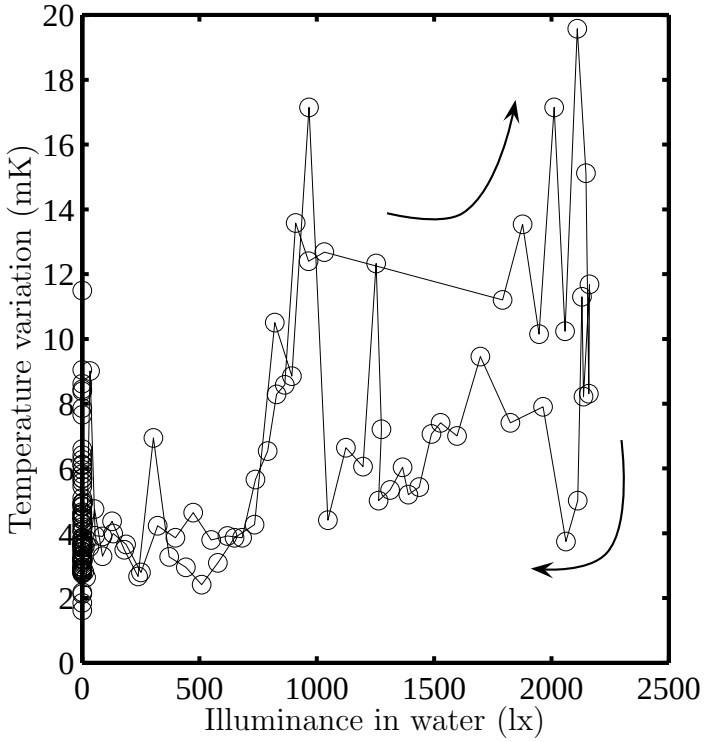

Figure 3.33: Temperature variation (temperature difference per detrended 10 min window) of the upper side (column 1) thermistor in *slot 11* as a function of illuminance measured close to the thermistors in the water. Data of hours 0 to 24, arrows indicate the path direction.

Interpretation An illuminance of 700 lx in the water is equivalent to a shortwave flux of 1 to 2 $\mathrm{W\,m^{-2}}$ arriving at the thermistor probe, as estimated by three different means in Appendix C.5. The radiation absorbed in the ice can be estimated from the predicted diffuse radiation (the experiment is in the shade) at hour 8.6, which is 5 $\mathrm{W\,m^{-2}}$ (Appendix C.1; Table C.4). With a surface albedo of about 0.5 and 1.5 $\mathrm{W\,m^{-2}}$ penetrating the ice, the radiation absorbed in the ice would be 1 $\mathrm{W\,m^{-2}}$. However, the estimates in Appendix C.5 show that the diffuse shortwave flux of the radiation model may be underpredicted by as much as a factor of 2 at this low solar angle. Should that be the case, then the shortwave radiation absorbed in the ice could be as high as 4 $\mathrm{W\,m^{-2}}$.

The absorbed shortwave heat flux is small compared to the heat removed for freezing: the ice growth velocity is to the order of $v = 10^{-6}\,\mathrm{m\,s^{-1}}$, suggesting that 270 $\mathrm{W\,m^{-2}}$ are removed from the ice to the atmosphere, over 50 times the absorbed shortwave flux at hours 8.6 and 15.3. No convincing explanation can be offered for the significant effect of a shortwave flux of seemingly insignificant magnitude.

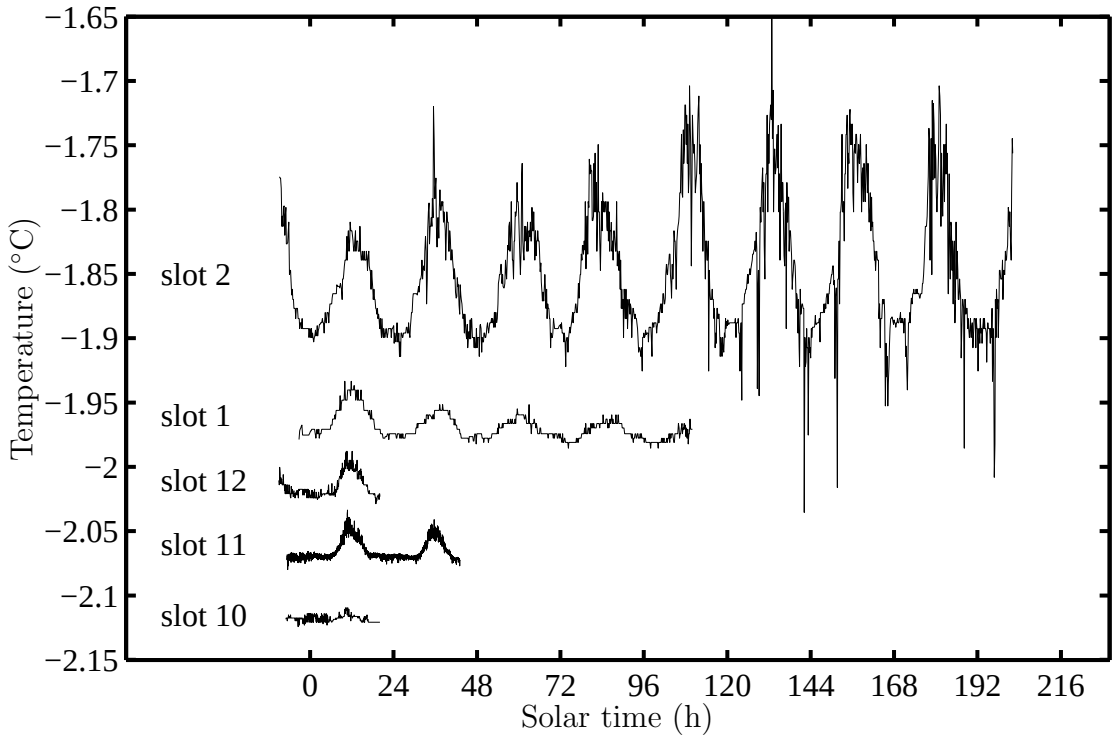

Figure 3.34: Temperature detected by thermistors in the water during the slot refreezing experiments. The sun is due North at hour 12. Temperatures of *slot 10* and *slot 12* coincide with temperatures of *slot 1* and are shifted for clarity. Water temperatures during *slot 2* are 80 mK higher than in *slot 1*.

3.4 Diurnal temperature variations

We will establish the nature of the detected water temperature variations, and the nature of the steady water temperature decrease during the refreezing experiments in this section.

3.4.1 Water temperature comparison between experiments

Absolute water temperatures The water temperature during experiment *slot 2* is significantly larger than than the water temperature during all other experiments. Figure 3.34 compares the water temperature records of the refreezing experiments. The initial nighttime water temperatures of *slot 1*, *slot 10*, and *slot 12* are the same[13]. The nighttime water temperature of *slot 2* is 80 mK higher than the temperature of *slot 1*. Experiment *slot 11* was performed with a different probe, and the nighttime water

[13]Thermistor #24 was used to assess water temperatures for *slot 1* and *slot 2*, while thermistor #6 was used for *slot 10* and *slot 12*. To make data comparable, water temperatures in *slot 10* and *slot 12* have been shifted by the initial temperature offset between thermistors #6 and #24 measured in experiment *slot 1*.

Table 3.6: Dates and characteristics of experiments with observed diurnal water temperature oscillation. Temperature variation is measured in the centre of the slot.

	slot 10	*slot 11*	*slot 12*	*slot 1*	*slot 2*
probe	1	2	1	1	1
start date	2 Sept 02	9 Sept 02	16 Sept 02	14 Oct 01	27 Oct 01
location	Erebus Bay	Erebus Bay	Erebus Bay	Cape Evans	Cape Barne
air temperature (°C)	−20 to −30	−25 to −40	−5 to −25	−10 to −22	−10 to −17
approx. slot orientation	E–W	E–W	N–S	N–S	N–S
slot width (mm)	180	330	120	230	320
depth below surface (mm)	500	220	500	410	410
first temperature variation (mK)	5 ± 3	25 ± 7	26 ± 5	34 ± 7	78 ± 10
temperature drift ($\mathrm{mK\,day^{-1}}$)	?	-3.2 ± 0.5	-2.7 ± 1.0	-1.8 ± 0.5	-0.76 ± 1.0
sampling period (s)	300	10	300	600	600

temperature is likely to be the same as in *slot 10* and *slot 12*. The absolute water temperature of *slot 11* is determined in Appendix B.10. Experiment *slot 2* is the only experiment that took place in the absence of sunset (i.e. after 25 October). The dates of the experiments are summarised in Table 3.6.

Water temperature decrease We note a water temperature decrease with time in all experiments that contain a water temperature record of at least 36 h (Table 3.6). The steady rate of decrease of the lowest recorded water temperature could be related to the rate of heat removal from the water and solute input into the water through brine plumes from the newly forming ice.

Assuming the seawater is at its freezing temperature, we will confirm that the water temperature reduction could be related to an increase in salinity of the water in the slot. We will therefore compare the rate of increase of seawater salinity with the rate at that solute is rejected from the growing sea ice. The observed rate of temperature decrease of $\Delta T/\Delta t = -3\,\mathrm{mK\,day^{-1}}$ is related to the rate of increase of solute concentration in the seawater, $\Delta C_s/\Delta t$, through the phase relationship

$$\frac{\Delta C_s}{\Delta t} = \frac{1}{m}\frac{\Delta T}{\Delta t}, \tag{3.55}$$

where m is the slope of the liquidus. If sea ice grows from a reservoir of concentration $C_0 = 34\,\mathrm{kg\,m^{-3}}$ at a vertical velocity, $v = 1 \times 10^{-6}\,\mathrm{m\,s^{-1}}$, then the mean solute flux into the water is

$$\Phi_s = v\,(C_0 - C_{ice}), \tag{3.56}$$

where $C_{ice} = 7\,\mathrm{kg\,m^{-3}}$ is the solute concentration in the ice. Supposing that the rejected brine were contained in a volume $V = H\,A$, where $H = 2\,\mathrm{m}$ is the height of the slot and A is the horizontal cross section of the slot, then the average rate of increase of solute concentration in the slot, $\Delta C_H/\Delta t$, is from (3.56)

$$\frac{\Delta C_H}{\Delta t} = \frac{v}{H}\,(C_0 - C_{ice}). \tag{3.57}$$

While the measured increase in solute concentration from (3.55) is $6 \times 10^{-7}\,\mathrm{kg\,m^{-3}\,s^{-1}}$, the increase considered theoretically possible from (3.57) is $1 \times 10^{-5}\,\mathrm{kg\,m^{-3}\,s^{-1}}$, i.e. one order of magnitude larger. Therefore, brine rejection and partial retention of solute in the slot could explain the steady temperature decrease observed during the refreezing experiments. This result is consistent with the observed increase in salinity of the seawater close to ice–ocean interface during one–dimensional sea ice sheet growth, which has been attributed to turbulent disintegration of brine plumes (*Dikarev et al.*, 2004).

Diurnal temperature variations Diurnal temperature variations visible in Figure 3.34 appear in all temperature records, with the exception of the electronically and climatically ill fated experiment *slot 13*. The amplitude of these oscillations decreases with time, apart from *slot 2*, where it increases to a maximum of 150 mK at the end of the experiment. This increase could be a signature of algae thriving under conditions of increased solar radiation (*McMinn et al.*, 2000).

The diurnal variations are unlikely to be an electronic artefact as no diurnal signature is visible in the reference channels of *slot 11*, and since neither air pressure nor air temperature are dominated by a 24 h cycle in the September experiments (cf. Figure B.1 during *slot 12*). Further, the electronic circuit of *slot 11* was kept in seawater at a constant temperature. The data logger, *CR10X*, registered temperature excursions in a build–in thermistor during *slot 10*, *slot 11*, and *slot 12* only during times of maintenance (typically 1 °C), and the times of excursions are not correlated to the temperature signal. Diurnal temperature variations of the data logger during experiments *slot 1* and *slot 2* show a phase lag with respect to solar noon of 3 h to 5 h and 0 h to 7 h, respectively, which is not reflected in the water temperature signals. Variations in ocean temperature due to currents are more likely to follow the approximately 25 h tidal cycle in McMurdo Sound. Solar radiative heating of the thermistors is the most likely cause of the 24 h periodicity. We will investigate the measured relationship between solar radiation and apparent water temperature in the next two sections.

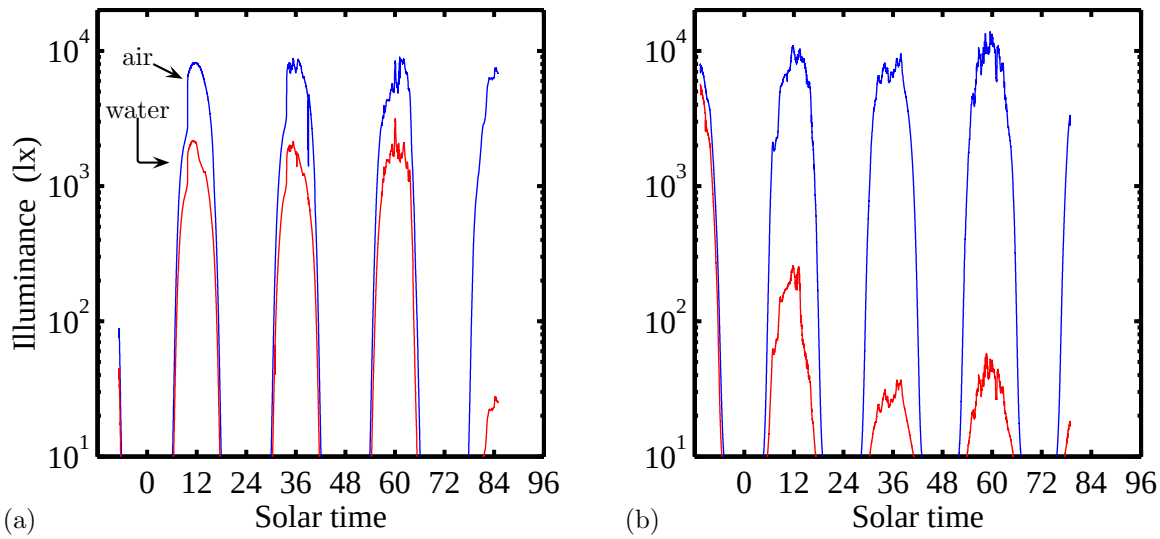

Figure 3.35: Illuminance measured in air and in the water during (a) *slot 11* and (b) *slot 13*. The sky was cloudless the first day of *slot 11*. 200 mm snow accumulated during *slot 11* in the night between the third and fourth day. Experiment *slot 13* experienced initial snow accumulation only hours after the deployment of the probe.

3.4.2 Temperature correlation with solar radiation

Solar radiation at the surface and in the water Figure 3.35 shows illuminance measurements during *slot 11* and *slot 13* on logarithmic scale. The smooth curves of illuminance on the first day of *slot 11*, measured both in air and in water, typify the absence of clouds. The high sampling rates during *slot 11* and *slot 13* of 10 s and 1 s, respectively, allowed us to resolve signal variations on all other days. These features are related to the cloud cover, and they appear on both LDRs without phase shift. Experiment *slot 11* experienced 200 mm snow accumulation during the night between the third and fourth day. This coincides with a decrease in illuminance in the water of more than two orders of magnitude. Experiment *slot 13* experienced initial snow accumulation only hours after the deployment of the probe. A quantification of this event is attempted in Appendix B.11. The asymmetry of the illumination curve that is particularly pronounced on the first day of *slot 11* is due to the morning shadow of Ross Island cast on the experiment. We take from Figure 3.35 that the experiment becomes abruptly exposed to direct sunlight within a period of 3 minutes at 9:50.

The cloud–free first day of *slot 11* allows us to assess the different illuminance signatures of the LDRs under solely diffuse light conditions and during exposure to direct sunlight. Figure 3.36 shows the illuminance measured on the ice surface as a function of illuminance registered in the slot. The hysteresis loop is followed in the counterclockwise sense during the course of the day. Two slopes are apparent. At

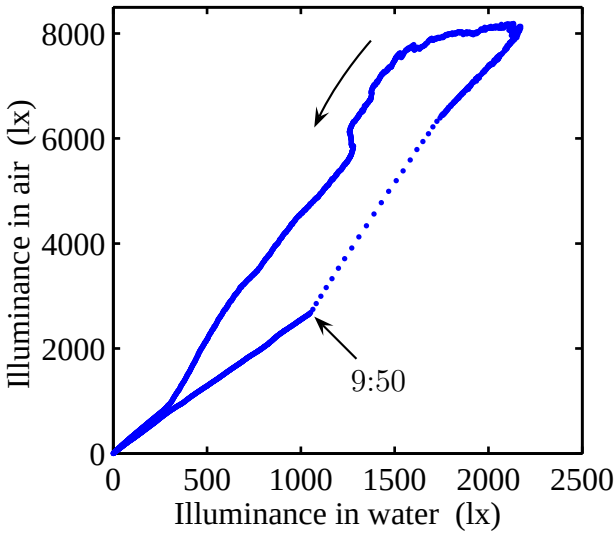

Figure 3.36: Relationship between illuminance measured at the ice surface and illuminance measured at the probe in the water during the first day of *slot 11*. The two slopes reflect the difference between diffuse and global illuminance. The hysteresis loop is due to the asymmetry of the experiment with respect to North. The loop is followed in the counterclockwise sense in the course of the day, the first change in slope appears at 9:50.

low illuminance both LDRs detect diffuse radiation. However, owing to the East–West alignment of the slot and the low solar altitude, the LDR in the water continues to receive diffuse[14] light even when the surface LDR is exposed to direct solar radiation. This leads to a second slope that is begun at 9:50. At 11:45±0:05 maximum solar radiation is registered by the surface LDR[15]. This early time could be a consequence of misalignment of the LDR from the vertical. With the probe facing East shadowing effects occur in the slot that reduce the illuminance of the LDR in the water. This leads to the plateau at the top of the hysteresis loop, where the signal remains for about 50 minutes. For the reminder of the day the slope characteristic of global radiation vs. diffuse radiation is followed. At 16:20 the hysteresis loop closes at the same point that was occupied at 7:45. The last hours of daylight again produce a slope of diffuse–only light. The curves obtained on other days of experiments *slot 11* and *slot 13* can be understood with similar reasoning. We conclude here by stressing the observation that the solar radiation that we measure at the ice surface (note: this is not the crack surface) is generally not simply proportional to the radiation arriving at the thermistors of the probe.

[14]Part of it may be scattered off the side of the slot.
[15]Note that this happens after the LDR in the water registers maximum illuminance at 11:10±0:05.

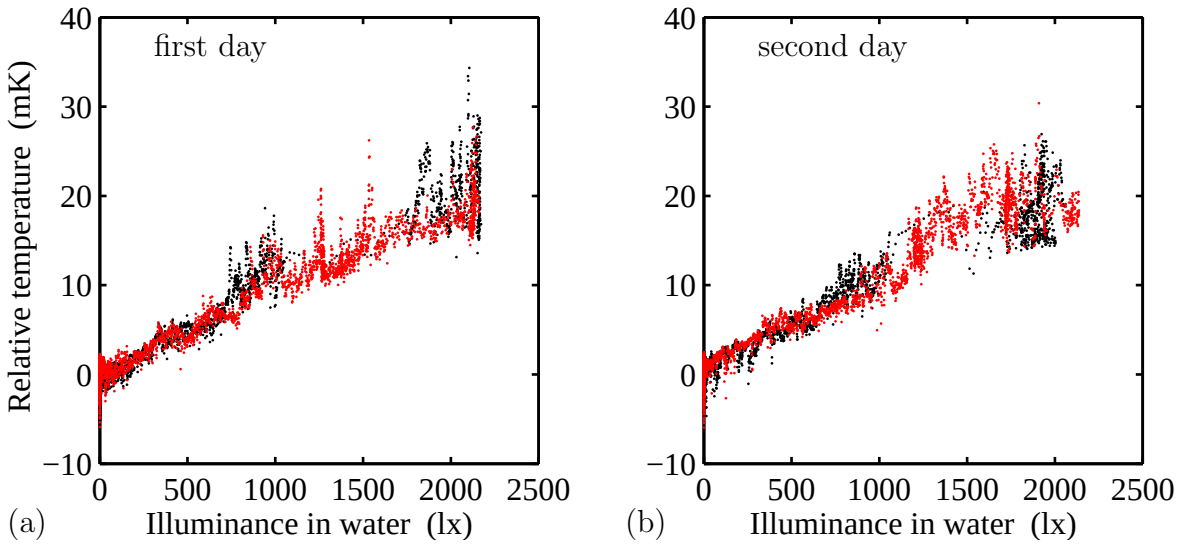

Figure 3.37: Relationship between temperature measured with the upper thermistor in the centre of the slot and illuminance measured at the probe in the water during (a) the first day of *slot 11*, and (b) the second day of *slot 11*. Temperature data are detrended with $+3.2\,\mathrm{mK\,day^{-1}}$. Dark dots indicate measurements in the morning, the other dots indicate measurements in the afternoon. Data of other thermistors look similar.

Correlation between illuminance and temperature We will now compare illuminance in the water with the temperature detected by the thermistors. Figures 3.37(a) and (b) show the illuminance dependence of temperature measured with the upper thermistor at the centre of the probe in *slot 11*. Data have been detrended with $+3.2\,\mathrm{mK\,day^{-1}}$ (cf. Table 3.6). The general picture is the same on both days. Temperature is proportional to illuminance if the illuminance is smaller than about 1700 lx. Further, temperature fluctuations are smaller below 700 to 1000 lx than above. On the first day there is a pronounced hump around 1000 lx. These general observations are valid for all thermistors.

The temperature fluctuations probably go hand in hand with advective activity in the slot, as discussed in Section 3.3.3. The very existence of a slope in Figures 3.37(a) and (b) could have two origins. Radiative heating of the water, and radiative heating of the thermistors. The absence of a hysteresis loop in Figures 3.37(a) and (b) indicates the absence of a phase shift between illuminance and heating. We will develop a simple analytical model in the following subsection to assess if one of the two effects prevails.

3.4.3 Radiative heating modelled

There are three ways for heat to reach the thermistors that can result in diurnal temperature variation: radiative heating of the thermistors, radiative heating of the water

body, and advective heat transport from the ice–water interface to the thermistors. In the next section, we will outline the mathematical framework of a simple linear one–dimensional model to help us assess the relative importance of these contributions.

We will calculate the reduced thermistor temperature, θ_t, that we define as the difference between the absolute thermistor temperature T_t and the temperature of the ice–water interface T_i,

$$\theta_t = T_t - T_i. \tag{3.58}$$

We consider two linear independent contributions to the thermistor temperature θ_t: a temperature contribution due to the surrounding water body θ_w, and a temperature contribution due to radiative heating of the thermistor beads θ_r,

$$\theta_t = \theta_w + \theta_r. \tag{3.59}$$

Although very similar in nature, we treat θ_w and θ_r differently in the following subsections. For the radiative contribution θ_r, the manufacturer of the thermistors gives an equation that we can use. However, it is then up to us to estimate the temperature of the water body θ_w. We will do that with a simple model that balances radiative heating of the water body with a turbulent advective heat flux from the ice–water interface. Eventually, the ratio of θ_w and θ_r will be expressed as a function of phase angle between solar radiation and the temperature oscillation detected at the thermistor. The primary experimental quantity used for the assessment will therefore be the phase angle. For both contributions, θ_w and θ_r, we need an estimate of the amount of radiation that penetrates sea ice. This is where we will begin.

Radiation reaching the ice–water interface

We are concerned with the shortwave radiation reaching the thermistor probe in the slot. Since light travels predominantly vertically through sea ice (*Buckley and Trodahl*, 1987; *Light et al.*, 2004), we consider only radiation incident in the slot. Not all solar radiation that strikes the sea ice surface penetrates down to the ice–water interface (cf. Figure 3.38). Radiation is partly reflected at the ice–air interface of the slot, characterised by the surface albedo α,

$$F_{reflected} = \alpha F_{incident}, \tag{3.60}$$

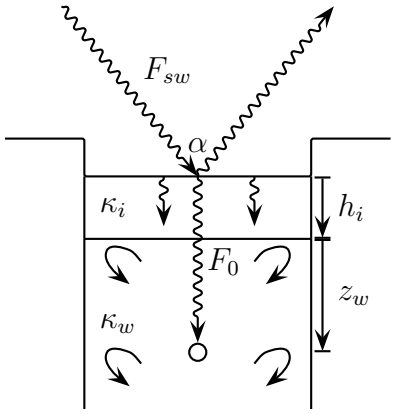

Figure 3.38: Contributions to the heat budget of the system discussed. Incident radiation F_{sw} gets partially reflected at the slot surface of albedo α. Of the remainder, radiation is absorbed in the ice of thickness h_i and extinction coefficient κ_i, leaving a flux F_0 that arrives at the ice–water interface. Of this flux, one fraction radiatively heats the water of extinction coefficient κ_w, while another fraction radiatively heats the thermistor at water depth z_w. Convection in the slot leads to heat exchange between the water body and the interface.

and radiation is absorbed in the sea ice body extending from $z = 0$ to $z = h_i \geq 0$,

$$F_{absorbed} = \int_0^{h_i} -\frac{dF(z)}{dz}\, dz, \tag{3.61}$$

where $F(z)$ is the radiation at any given depth z. We assume that the radiation $F(z)$ follows an exponential extinction law (Beer's law) (*Perovich and Grenfell*, 1981) with extinction coefficient κ_i of the form

$$F(z) = F_{sw}\, e^{-\kappa_i z}. \tag{3.62}$$

The extinction coefficient κ_i is a function of wavelength (*Perovich and Grenfell*, 1981). To account for this, *Zeebe et al.* (1996) and *Perovich and Richter-Menge* (2000) apply a numerical model to model spectral extinction in sea ice and heat transfer into the water at a freezing lead, respectively, while *Trodahl et al.* (2000) assume a single characteristic extinction coefficient in an order of magnitude estimate of the lower limit of solar radiative heating of sea ice. *Grenfell and Maykut* (1977) parameterise the spectral dependence of the extinction coefficient in Arctic sea ice based on the observation that most of the light penetrating sea ice is in the visible range, where the extinction coefficient is relatively independent of wavelength. Radiation beyond 1000 nm is mostly absorbed in the top 100 mm of the sea ice sheet. Owing to the change in solar spectrum with cloud coverage *Grenfell and Maykut* express the amount of radiation penetrating

the topmost 100 mm of ice as

$$F^{100} = i_0\, F_{sw}, \tag{3.63}$$

with coefficient i_0 for blue ice $i_0 = 0.63$ under cloudy skies, and $i_0 = 0.43$ for clear skies. Absorption below $h_{bulk} = 100\,\mathrm{mm}$ is modelled with an exponential function using $\kappa_i = 1.5\,\mathrm{m}^{-1}$. A similar approach has been used by *Maykut and Untersteiner* (1971), which is also applied in the simulations of *Maksym and Jeffries* (2000).

Combining (3.60) to (3.63) we get the relationship between the incident radiation F_{sw} and the radiation at the ice–water interface F_0,

$$\begin{aligned} F_0 &= (1-\alpha)\, F^{100} - (1-\alpha) \int_{h_{bulk}}^{h_i} -\frac{dF(z)}{dz}\, dz, \\ &= (1-\alpha)\, i_0\, F_{sw} \left[1 - \int_0^{h_i - h_{bulk}} -\frac{d \exp(-\kappa_i\, z)}{dz}\, dz \right], \\ &= (1-\alpha)\, i_0\, F_{sw} e^{-\kappa_i\,(h_i - h_{bulk})}. \end{aligned} \tag{3.64}$$

If the incident flux is time varying between zero and $\widehat{F}^0$ with a frequency ω then the flux at the ice–water interface is

$$F_0 = (1-\alpha)\, i_0\, \widehat{F}^0\, e^{-\kappa_i\,(h_i - h_{bulk})}\, \frac{1}{2} \left(1 - e^{i\omega\, t}\right). \tag{3.65}$$

Radiative heating of the thermistor

Upon energy input, the temperature of the thermistor rises. If the thermistor is immersed in a constant temperature bath, the thermistor temperature will eventually settle at an equilibrium temperature that depends on the efficiency of the heat exchange between thermistor and environment. Suppose we know the rate of energy dissipation, we can calculate the increase of thermistor temperature θ_r given the radiative power P from

$$\begin{aligned} \theta_r &= \frac{1}{\mathrm{DC}}\, P, \\ &= \frac{1}{\mathrm{DC}}\, A_t F(z_t, t). \end{aligned} \tag{3.66}$$

Here, DC is a dissipation constant, A_t is the surface area of the thermistor exposed to radiation, and $F(z_t, t)$ is the radiation at the thermistor position z_t at time t. We assume that all radiative energy is converted to thermal energy at the dark thermistor beads, and none is reflected.

The manufacturer gives heat dissipation constants, DC, for the case of a thermistor in still air at 25 °C, $\mathrm{DC} = 1\,\mathrm{mW\,K^{-1}}$, and for the case of a thermistor in a well stirred

oil bath at 25 °C, DC = 8 mW K^{-1}. This gives us an estimate for the dissipation constant in our refreezing slot system. The dissipation constant should be somewhat smaller than in the case of a well stirred oil bath, since plastic tubing is attached to the thermistors at one side.

We suppose a simple harmonic variation of the radiation in the water,

$$F(z,t) = \widehat{F}_0\, e^{-\kappa_w\, z}\, \frac{1}{2}\left(1 - e^{i\omega\, t}\right). \tag{3.67}$$

Here κ_w is the extinction coefficient in water and ω the frequency of the diurnal change in radiation. Radiation is assumed to vary between zero and $\widehat{F}_0$.

Temperature increase θ_r and solar radiation $F(z_t, t)$ are in phase (i.e. DC is a real number) since the thermal time constant of the thermistors is of the order of seconds, which is very fast compared to the period of change of $F(z_t, t)$, which is one day.

Heat exchange with water

For the thermistor temperature contribution θ_w we assume that θ_w is always equal to the water temperature. The water temperature is a result of two balancing mechanisms; radiative heating of the water body, and cooling through advection of water from the ice–water interface. We assume that the rate of advective heat exchange is proportional to the temperature difference between interface and water body. The temperature change can then be expressed through the energy balance

$$\frac{\partial \theta_w}{\partial t}\, c_w\, \rho_w\, A_s\, h_w = A_s \int_0^{h_w} -\frac{dF(z)}{dz}\, dz - A_s\, h_w\, c_w\, \rho_w \gamma\, \theta_w, \tag{3.68}$$

where A_s is the surface area of the water body through that radiation enters, $h_w \geq 0$ is the height of the water mass considered, c_w and ρ_w are respectively the heat capacity and density of water, and γ is the reciprocal of the response time of advective heat exchange. With a radiative field in the water (3.67), solving the integral in (3.68) and defining $\delta \geq 0$ as

$$\delta = \frac{\widehat{F}_0}{c_w\, \rho_w} \frac{1}{h_w} \left(1 - e^{-\kappa_w\, h_w}\right) \tag{3.69}$$

the differential equation (3.68) acquires the form

$$\frac{\partial \theta_w}{\partial t} = -\,\gamma\, \theta_w + \delta \frac{1}{2}\left(1 - e^{i\omega\, t}\right). \tag{3.70}$$

We are interested in the solution of (3.70) for the quasi–stationary case of a temperature field that has already developed and use the ansatz

$$\theta_w = \hat{\theta}\frac{1}{2}\left(1 - e^{i\omega\, t}\right) + \theta_0, \tag{3.71}$$

where θ_w varies between θ_0 and $\hat{\theta} + \theta_0$ during the course of a cycle of ω. Substituting (3.71) into (3.70) we find that

$$\hat{\theta} = \frac{\delta}{i\omega + \gamma} \quad \text{and} \quad \theta_0 = \frac{\delta}{2\,\gamma} - \hat{\theta}. \tag{3.72}$$

The temperature variation $\hat{\theta}$ is obviously a complex number and as such defines a phase angle φ between incident radiation and system response. The phase angle

$$\tan\varphi = \frac{\mathrm{Im}(\hat{\theta})}{\mathrm{Re}(\hat{\theta})} = -\frac{\omega}{\gamma} \tag{3.73}$$

allows us to express the reciprocal response time γ by the readily measurable phase angle φ. The angle φ is negative since the temperature variation $\hat{\theta}$ lags behind the incident radiation F.

We can express the magnitude of $\hat{\theta}$ from (3.72) after substituting γ with (3.73), which gives

$$\left|\hat{\theta}\right| = \frac{\delta}{\omega}\frac{|\tan\varphi|}{\sqrt{1+\tan^2\varphi}} = \frac{\delta}{\omega}\,|\sin\varphi|\,. \tag{3.74}$$

The minimum water temperature θ_0 is similarly found to be

$$\theta_0 = -\frac{\delta\,\tan\varphi}{2\,\omega} = \frac{1}{2}\,\left|\hat{\theta}\right|\,\frac{1}{\cos\varphi}, \tag{3.75}$$

which is always positive since $\varphi \leq 0$. For future reference, we substitute (3.69) in (3.74) and get the range of temperature variation

$$\begin{aligned}\left|\hat{\theta}\right| &= \widehat{F}_0\,\frac{|\sin\varphi|}{\omega\,c_w\,\rho_w}\frac{1}{h_w}\left(1 - e^{-\kappa_w\,h_w}\right),\\ &\approx \widehat{F}_0\,\frac{\kappa_w}{\omega\,c_w\,\rho_w}\;|\sin\varphi|\end{aligned} \tag{3.76}$$

for small values of $\kappa_w\,h_w$.

Summary and Discussion

We have derived expressions for thermistor temperature changes θ_t as a consequence of radiative heating of the thermistor bead θ_r, and due to radiative heating of the water θ_w. Starting with diurnal variations of solar radiation at the ice surface $\widehat{F}^0$ we found that direct radiative heating of the thermistor beads is

$$\theta_r = (1-\alpha)\, e^{-\kappa_i\,(h_i - h_{bulk})}\, i_0\, \widehat{F}^0\, e^{-\kappa_w\, z_t} \frac{1}{\mathrm{DC}}\, A_t, \tag{3.77}$$

or for small $\kappa_w\, z_t$

$$\theta_r = (1-\alpha)\, e^{-\kappa_i\,(h_i - h_{bulk})}\, i_0\, \widehat{F}^0\, \frac{1-\kappa_w\, z_t}{\mathrm{DC}}\, A_t. \tag{3.78}$$

This temperature change is in phase with the incident radiation.

The magnitude of temperature changes due to radiative heating of the water $|\hat{\theta}|$ has been found to be related to the phase angle φ between incident radiation and temperature response. It is

$$\left|\hat{\theta}\right| = (1-\alpha)\, e^{-\kappa_i\,(h_i - h_{bulk})}\, i_0\, \widehat{F}^0\, \frac{\kappa_w}{\omega\, c_w\, \rho_w}\, \left|\sin\varphi\right|. \tag{3.79}$$

Comparing the magnitude of both contributions we find

$$\frac{\theta_r}{\left|\hat{\theta}\right|} = \frac{1-\kappa_w\, z_t}{\kappa_w\, \left|\sin\varphi\right|}\, (\omega\, c_w\, \rho_w)\, \frac{A_t}{\mathrm{DC}}. \tag{3.80}$$

With $\kappa_w \approx 0.1\,\mathrm{m}^{-1}$ in the visible, $z_t = 0.2\,\mathrm{m}$, $\omega = 2\pi \times 1.2 \times 10^{-5}\,\mathrm{s}^{-1}$, $c_w = 4 \times 10^3\,\mathrm{J\,kg^{-1}\,K^{-1}}$, $\rho_w = 1 \times 10^3\,\mathrm{kg\,m^{-3}}$, $A_t = \pi\, 1.44 \times 10^{-6}\,\mathrm{m}^2$, and $\mathrm{DC} = 1 \times 10^{-3}\,\mathrm{W\,K^{-1}}$ we estimate

$$\frac{\theta_r}{\left|\hat{\theta}\right|} \approx 1.4\, \frac{1-\kappa_w\, z_t}{\kappa_w\, \left|\sin\varphi\right|} \quad \approx \frac{14}{\left|\sin\varphi\right|}. \tag{3.81}$$

In experiment *slot 11* we could not detect a phase shift φ, so with an upper bound of $\varphi < 10^\circ$ temperature variations due to radiative heating of the thermistor beads should outweigh temperature variations in the water due to radiative heating by two orders of magnitude. As can be seen from Figure 3.39, the temperature variations due to radiative heating of the thermistor beads should in fact always outweigh temperature variations of the water within the framework of this model.

The ratio of thermistor heating to water heating shifts towards water heating if a configuration is used with a larger dissipation constant DC, if boundary conditions

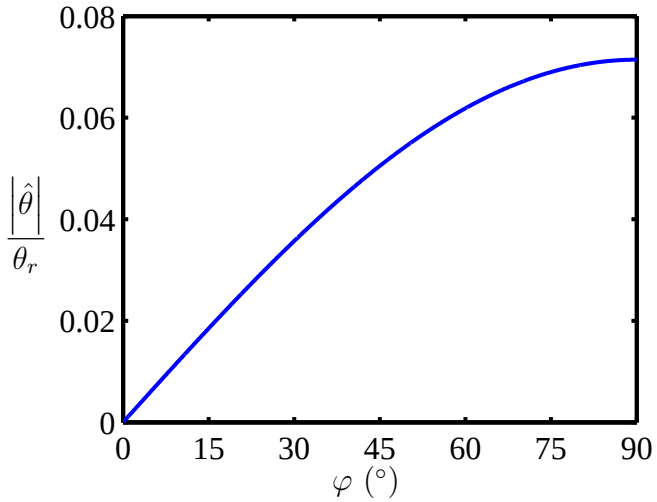

Figure 3.39: Ratio of temperature variation due to heating of the water, $\left|\hat{\theta}\right|$, to direct radiative heating of the thermistor, θ_r, as a function of phase shift, φ, between measured temperature and measured radiation. Plotted is the reciprocal of (3.81).

are such that a phase shift between incident radiation and water temperature occurs, or if the extinction coefficient κ_w is larger. In particular, κ_w is larger by orders of magnitude for light in the infrared. However, since ice, too, absorbs light much better in the infrared, radiative heating of exposed thermistors should always exceed radiative heating of the water close to the ice–water interface in completely ice–covered waters, within the limits of this model.

To estimate from (3.78) the absolute temperature change that could have been brought about by solar radiation in *slot 11*, we assume a diffuse solar radiation of $\widehat{F}^0 = 30\,\mathrm{W\,m^{-2}}$ (this estimate is from the radiation model in Appendix C.1) for the first day of *slot 11*. An ice layer of $h_i = 0.1\,\mathrm{m}$ could have grown during the preceding night, i.e. $h_i = h_{bulk}$. Spectral albedo varies considerably with wavelength (*Perovich et al.*, 2002), and to a lesser extent with ice type and thickness (*Weller*, 1972; *Ebert and Curry*, 1993; *Toyota*, 1998). We assume an average wavelength–integrated albedo of $\alpha = 0.5$ for this young ice (*Perovich and Richter-Menge*, 2000). For a blue sky day, we have $i_0 = 0.43$ from *Grenfell and Maykut*. The expected flux at the ice–water interface would then be $\widehat{F}_0 = 6.5\,\mathrm{W\,m^{-2}}$. With all other coefficients as before we obtain $\theta_r = 28\,\mathrm{mK}$ for the thermistor temperature variation, which is consistent with the total diurnal temperature variation measured in *slot 11* of 25 mK (Table 3.6). Considering that for diffuse radiation due to shadowing a larger fraction of solar radiation is in the visible spectrum than it is the case for direct or global radiation (Appendix C.1), extinction could be overestimated using the parameterisation of *Grenfell and Maykut*.

3.4.4 Discussion

We have seen that we detected a low frequency, diurnal temperature signal in the water column during all refreezing experiments. The amplitude seems to increase with the time of year. In order to assess whether this low frequency variation is an effect of radiative water heating or of radiative thermistor heating we have recorded illuminance data under water at the probe of *slot 11*. This data shows clearly that temperature and illuminance, used as proxy for solar radiation, are in phase.

We have modelled the temperature evolution of the water by balancing radiative heat transfer with an average flux due to advective mixing. Comparing the possible temperature variations based on this model with the possible temperature variations based on radiative heating of the thermistors we were able to exclude radiative heating of the water as source for the observed low frequency temperature variation. In fact, the model led us to expect that radiative heating of exposed thermistor beads is always more effective than radiative heating of the water column close to the ice–water interface in completely ice–covered water.

Periodic brine release can be excluded as a source of the diurnal temperature variations, since the proportionality between illuminance and temperature appears even at low illuminances, before increased brine rejection begins (Section 3.3.3). Further, temperature changes due to brine release have a high frequency fingerprint.

However, brown algae growing at the ice–water interface at the end of the growth season (*Maykut and Grenfell*, 1975; *Arrigo et al.*, 1993; *Günther and Dieckmann*, 1999; *Gerland et al.*, 1999; *McMinn et al.*, 2000) in *slot 2* could very well modulate the water temperature near the interface. *Zeebe et al.* (1996) model the influence of a bottom algal layer on the melting process of sea ice. They estimate for a mid December day in McMurdo Sound a temperature gradient of $25\,\mathrm{K\,m^{-1}}$ at the bottom 40 mm of the ice sheet, will increase the temperature of the ice and brine by up to 1 °C. While we cannot quantify from these figures the temperature of the water close to the interface at the beginning of November, we may yet speculate that algae could modulate the water temperature measurably. On the other hand, if there is enough algae in the water close to the ice–water interface the extinction coefficient of the water could increase, leading to a diurnal signature of radiative heating of the water body. An investigation of the phase between water temperature and solar radiation in the presence of algae could elucidate this issue.

3.5 Summary

We have developed a method to determine the front of consolidated sea ice from the temperature signal of thermistor probes. Discrimination between consolidated sea ice and skeletal sea ice in refreezing cracks shows that the time of desalination of sea ice is longer at the sides of the crack than it is in the centre. The method to determine the consolidated front has proven to be very useful in the comparison with an analytical model of crack refreezing. Further, the analytical model delivers useful predictions of experiments of other groups. The comparison between data and prediction from the analytical model suggest that a significant negative ocean heat flux occurred during *slot 12*. Consistent with this observation, the calculated heat balances suggest that *slot 10* and *slot 12* experienced a negative oceanic heat flux.

High frequency, water temperature fluctuations due to desalination in slots have been found to be sporadic throughout nighttime. They are stronger during daytime. The transition between daytime and nighttime behaviour is sharp and occurs at a low level of shortwave radiation. The fluctuations are largest close to the vertical freezing interface.

A steady temperature decrease in the refreezing slots is detected that can be explained by the cooling and salination of the water column by released brine plumes. The low frequency, diurnal temperature signal of the thermistors in the water could further been assigned to direct heating of the thermistor beads. Further, it is very likely that algal growth at the ice–ocean interface has affected water temperature and temperature signal in *slot 2*.

Chapter 4

Numerical model

4.1 Introduction

This chapter describes the numerical model that we use to address the salinity distribution in refrozen cracks, treating fluid motion in sea ice as flow through a porous medium. The porous medium, or mushy zone, described here is a macroscopic region of a microscopic distribution of solid and liquid phases.

Fluid flow in sea ice has previously been modelled as flow though a porous medium. For example, *Wettlaufer et al.* (1997) use a porous medium approach to model the initial brine drainage process from laboratory grown saltwater ice, *Freitag* (1999) uses porous medium equations to illustrate the flow resistance of an Arctic sea ice sheet, and *Feltham et al.* (2002) base their prediction of the influence of an external flow field on desalination on a porous medium assumption. In the special case of a simple, well defined interface between porous sea ice and liquid ocean, boundary conditions can be formulated that allow us to limit the computational domain to the porous medium. This is very desirable from an analytical point of view as simplified governing equations can be employed, and from a computational point of view as fluid velocities are orders of magnitude smaller in the porous medium than they are in the liquid. Unfortunately, this approach is not straight–forward for the more complicated case of a refreezing crack: the interface is curved and its shape is time–dependent (Chapter 2), and non–trivial fluid motion takes place in the liquid (Chapter 3).

Consequently we address the issue of crack desalination by implementing a complete fluid dynamical simulation of both liquid and porous regions including phase transition, in order to be able to assess what factors actually determine the salinity profile of a refrozen crack. The entire domain, liquid and porous, is modelled with a single set of governing equations.

Writing a computational fluid dynamics (CFD) package is a big project. However, the fundamental principles are not new and are well developed. No similarly standardised method exists, however, for dealing with the phase transition and parameterisation of the porous medium. In particular, no solution for the case of sea ice has been developed[1]. The main contributions of this thesis to the numerical modelling of fluid flow through sea ice are therefore the freezing front tracking discussed in Section 4.4, the phenomenological approach to sea ice permeability parameterisation taken in Chapter 5, and the demonstration of the success and limitations of the model in Chapter 6.

This chapter is mostly descriptive. More comprehensive accounts on the derivation of the volume averaged governing equations can be found in the excellent contribution of *Bear and Bachmat* (1991), and the numerical principles of finite volume fluid dynamics calculation are clearly presented in *Patankar* (1980), *Versteeg and Malalasekera* (1995), *Ferziger and Perić* (2002), and in the thesis of *Norris* (2001). The method of discretisation is presented in Appendix E.1, and the discretised equations are given in Appendix E.2. The idea behind the implemented numerical solver is illustrated well for the case of finite differences by *Briggs et al.* (2000). The extension to finite volumes is shown in Appendix E.4.

4.2 Governing equations

4.2.1 Overview

We describe the movement of brine during sea ice growth as the flow of a Newtonian fluid in a two-dimensional domain that is partly pure liquid, and partly porous ice. The solid matrix of the porous medium is stationary in position, but time variable as governed by the phase change. The governing equations reduce to the Navier-Stokes equations with Boussinesq approximation (*Ferziger and Perić*, 2002; *Zeytounian*, 2003) in the liquid region, while flow in the porous medium is dominated by friction that is expressed through a term after Darcy (*Brinkman*, 1947). Permeability (*Freitag and Eicken*, 2003) is treated as a function of local porosity. The porous medium undergoes phase change, and local thermodynamic equilibrium is assumed.

The governing equations of the finite volume method are volume–averaged formulations of the Navier–Stokes equations for a pure liquid. We chose the integration volume to be large enough that small changes in position cause only small changes in average properties. We use a governing set of equations that is valid if all physical properties of

[1]This has already been noted by *Medjani* (1996).

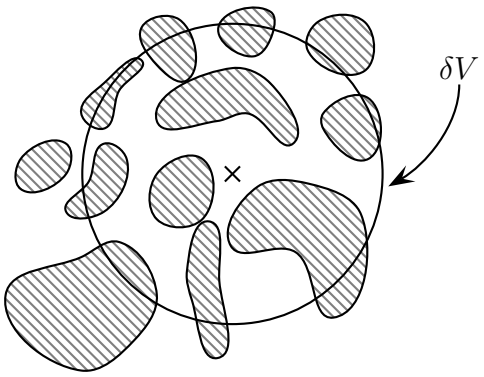

Figure 4.1: Two dimensional section of a volume δV in the porous medium. Hatched regions represent the solid. The liquid region is interconnected.

the pure liquid and of the pure solid are constant in time and independent of position. In the momentum equations we apply the Boussinesq approximation, i.e. the density of the liquid is constant except in the buoyancy term, where it is treated as a function of local temperature and salinity.

Section 4.2.2 illustrates the mathematical concept and methods of volume averaging in a porous medium, and Section 4.2.3 details the governing equations.

4.2.2 Porous medium volume average

Concept and assumptions

When we describe fluid flow, we are interested in the spatial and temporal evolution of state variables, such as momentum, solute mass density, temperature, and pressure. Since the transport equations are known on a microscopic level, we are, in principle, able to solve every flow problem. However, in the presence of two phases, for example solid ice and liquid brine, the microscopic geometry of the interface, or surface, that separates the phases is generally not known. On a macroscopic level, however, quantities can be defined that are measurable, continuous and differentiable. We will describe fluid transport in a porous medium based on this macroscopic continuum approach.

In the following, we will assume that the porous domain consists of two microscopic phases, a stationary solid matrix of ice, and a liquid that completely fills the remaining volume, called the void fraction. The solid is distributed throughout the porous medium such that a representative macroscopic volume δV can be found that contains both, solid and void space, no matter where we place δV in the porous medium. Further, a surface δA can be found that intersects both, solid and void space, no matter where we place it in the porous medium. The size of δV is such that the geometrical characteristics of the microstructure it contains are functions of position and time only,

and do not depend on the size of δV. Similarly, the geometrical characteristics of the area intersected by δA depend on position and time only. In the continuum approach the centre point of volume δV is assigned the volume averaged set of state variables of δV.

Further, the void fraction is interconnected, i.e. a path exists from any point in the void fraction to any other point, see Figure 4.1. This specifically precludes the existence of isolated brine pockets, the consequence of which we discuss in Chapter 6. On the other hand this assumption implies that we do not need to account for fractures during volume expansion. We define the total volumetric porosity (void fraction) that is equal to the effective, interconnected volumetric porosity,

$$f_l = \frac{\delta V_l}{\delta V}, \tag{4.1}$$

where f_l is the volumetric porosity, or liquid volume fraction, δV_l the volume occupied by the liquid, and δV is the macroscopic volume considered. Since solid volume δV_s and liquid volume δV_l fill the volume δV completely, it follows that $\delta V_l + \delta V_s = \delta V$ and particularly the volume fraction of the solid $f_s = 1 - f_l$. Since we will give all expressions in this and in the following chapters in terms of the liquid volume fraction f_l, we drop the index, and it is understood that $f = f_l$.

Mathematical methods

Volume integration of any of the conservation equations follows a simple pattern. Starting with the differential form of a microscopic conservation equation, the volume integral over δV leads to an expression containing averages of time derivatives and gradients. This expression is then transformed into an expression containing time derivatives and gradients of averages. In the course of this process surface integrals appear that are related to fluxes, state variables, and interface velocity[2] at the microscopic solid–liquid boundary (Appendix D.2).

Some surface integrals can be solved assuming, for example, mass conservation, zero velocity, or a specific solute concentration at the interface. Other integrals are found to describe macroscopic phenomena, for example flow resistance. They eventually appear in the macroscopic formulation where they may, without knowledge of their origin, be mistaken as manually introduced source terms. Few integrals are neglected owing to incomplete knowledge of the microscopic system; the effects on fluid motion of tortuosity and local (i.e. within δV) anisotropic solid redistribution (e.g. due to remelting) are two examples. Further, for simplicity, volume integrals are neglected in all transport

[2]The interface moves during phase change due to the density difference between solid and liquid.

equations that deal with the inhomogeneous local distribution[3] of momentum and the respective state variables. For the same reason, all physical constants, such as heat capacity and mass diffusion coefficient, are assumed to be locally constant. Viscosity is even assumed to be globally constant (Appendix D.3).

Having gone through the tedious process of integrating, substituting and neglecting some terms one obtains the desired set of governing equation for *macroscopic*, volume averaged state variables. The set of governing equations is identical to the result obtained by educated guesswork. We shall therefore restrict ourselves to the presentation of the result of the process, with a brief discussion of the most relevant assumptions that were used in the derivation.

The interested reader is referred to Appendix D, and to the papers of *Gray and O'Neill* (1976) and *Ganesan and Poirier* (1990) who exemplify the derivation of mass and momentum conservation equations, or to *Gray* (1975) for the solute transport equation. The classic works of *Slattery* (1967) and *Whitaker* (1977) discuss transport in porous media from an engineering perspective, while a mathematically sound derivation and comprehensive discussion of the conservation equations in porous media is given by *Bear and Bachmat* (1991). While the governing equations in this work treat solid–liquid interactions, similar equations can be derived for liquid–gas systems (*Sun et al.*, 2000).

4.2.3 Governing equations

The result of the volume averaging of the governing equations shall be discussed in this section. All state variables given are understood to be intrinsic volume averaged quantities (Appendix D.1). The intrinsic volume average[4] Ψ of a variable Ψ_l defined in the liquid volume δV_l is defined as

$$\Psi = \frac{1}{\delta V_l} \int_{\delta V_l} \Psi_l \, \mathrm{d}V. \tag{4.2}$$

Examples of the intrinsic volume average are the interdendritic (interstitial) fluid velocity u, temperature of the liquid T, and the brine solute concentration C. The governing equations are derived in Appendix D. Unless otherwise stated, all physical properties of liquid and solid, for example density and heat capacity, are assumed to be constant locally, i.e. within the averaging volume δV. The advantage of the math-

[3] As a consequence, the only volume integrals that remain are the ones that deal with local average quantities.

[4] A more specific average notation is used in Appendix D.

ematical form of the advection terms will become clear during the discretisation for the finite volume scheme in Appendix E.1.

The volume averaged mass conservation equation is

$$\left[1 - \frac{\rho_s}{\rho_l}\right] \frac{\partial f}{\partial t} + \frac{\partial (fu)}{\partial x} + \frac{\partial (fv)}{\partial y} = 0, \tag{4.3}$$

where u and v are the fluid velocity components in the x and y directions, respectively, f is the volume fraction of the liquid, and ρ_l and ρ_s are the constant densities of liquid and solid. (We will later use the y–component to describe vertical movement.) To derive this equation one assumes mass conservation at the freezing interface. Since no terms have been neglected during the averaging process, the mass conservation equation is the only conservation equation that is exact.

The volume averaged momentum conservation equations are

$$\rho_l \left[\frac{\partial (fu)}{\partial t} + \frac{\partial (fu\,u)}{\partial x} + \frac{\partial (fu\,v)}{\partial y}\right] = \mu \left[\frac{\partial^2 (fu)}{\partial x^2} + \frac{\partial^2 (fu)}{\partial y^2}\right] - f\frac{\partial p}{\partial x} + f\rho\, g_x - f\,\frac{\mu}{\Pi_x}\, fu, \tag{4.4}$$

$$\rho_l \left[\frac{\partial (fv)}{\partial t} + \frac{\partial (fv\,u)}{\partial x} + \frac{\partial (fv\,v)}{\partial y}\right] = \mu \left[\frac{\partial^2 (fv)}{\partial x^2} + \frac{\partial^2 (fv)}{\partial y^2}\right] - f\frac{\partial p}{\partial y} + f\rho\, g_y - f\,\frac{\mu}{\Pi_y}\, fv, \tag{4.5}$$

where ρ is the variable density of the liquid in the buoyancy term (*UNESCO*, 1981b), μ is the dynamic viscosity, p the pressure, Π_x and Π_y the permeability[5] of the porous medium, and g_x and g_y the x and y components of the gravitational field. Underlying the momentum equations are two core assumptions: the Boussinesq approximation of constant liquid density apart from the buoyant term, and the assumption of a *globally* constant viscosity μ. With a globally constant viscosity, terms that couple horizontal fluid motion with vertical fluid motion disappear from the stress tensor. The last three terms on the right hand side of (4.4) and (4.5) form the Darcy equation for stationary fluid flow (*Brinkman*, 1947).

The volume integrated form of the energy balance (heat transport) equation is

$$\overline{\rho c}\frac{\partial T}{\partial t} + \rho_l c_l \frac{\partial (fu\,T)}{\partial x} + \rho_l c_l \frac{\partial (fv\,T)}{\partial y} = \frac{\partial}{\partial x}\left[\bar{k}\frac{\partial T}{\partial x}\right] + \frac{\partial}{\partial y}\left[\bar{k}\frac{\partial T}{\partial y}\right] - [T\Delta(\rho c) + L\rho_s]\,\frac{\partial f}{\partial t}, \tag{4.6}$$

[5]The way scalar permeabilities Π_x and Π_y are used in (4.4) and (4.5) supposes that the principal directions of permeability coincide with the x and y directions, i.e. the non–diagonal coefficients of the permeability tensor Π are zero. Higher order anisotropic solid–liquid friction terms are neglected in (4.4) and (4.5).

where T is the temperature of solid and liquid, $L > 0$ is the latent heat of fusion at 0 °C, and the average quantities in the porous medium are defined as

$$\overline{\rho c} = f\rho_l c_l + (1-f)\,\rho_s c_s, \tag{4.7}$$

$$\Delta(\rho c) = \rho_l c_l - \rho_s c_s \tag{4.8}$$

$$\bar{k} = f k_l + (1-f)\,k_s, \tag{4.9}$$

with the specific heat capacities c_l and c_s, and heat conductivities k_l and k_s of liquid and solid, respectively. Underlying (4.6) is the assumption of local thermal equilibrium, i.e. the local temperature of the liquid is the same as the local temperature of the solid. In the derivation of the energy balance equation (4.6) the conservation of enthalpy has been assumed.

The volume averaged solute transport equation is

$$f\frac{\partial C}{\partial t} + \frac{\partial(f u\, C)}{\partial x} + \frac{\partial(f v\, C)}{\partial y} = \frac{\partial}{\partial x}\left[fD\,\frac{\partial C}{\partial x}\right] + \frac{\partial}{\partial y}\left[fD\,\frac{\partial C}{\partial y}\right] - C\frac{\partial f}{\partial t}, \tag{4.10}$$

with the concentration C of solute in the liquid, and the solute diffusion coefficient D. Equation (4.10) implies that the concentration of solute in the solid is zero, and that solute is rejected into the liquid phase during freezing. The solute concentration at the microscopic solid–liquid interface is equal to the average solute concentration in the liquid fraction[6] of δV, while conserving solute mass. The effect of tortuosity on diffusion is neglected.

Finally, an equation is needed that governs phase transition. We suppose local thermodynamic equilibrium, which means that in any volume δV the temperature T is equal to the freezing point T_F of the brine of concentration C,

$$T = T_F(C). \tag{4.11}$$

With consideration given to latent heat release and solute partition at the microscopic interface, (4.11) actually constitutes a condition for the local liquid volume fraction f (Appendix E.3).

We will come back to the issue of freezing in Section 4.4 after we have introduced the grid structure of the numerical model.

[6]The assumption of a microscopic solid–liquid boundary value equal to the intrinsic average in the liquid is used in the derivation of both the solute transport equation (4.10) and the heat transport equation (4.6), while the assumption of a zero momentum microscopic boundary condition is used in the derivation of the momentum equations (4.4) and (4.5). This difference is reflected in the diffusion terms that contain the gradient of the intrinsic quantity, only, in (4.6) and (4.10) (e.g. $f\partial C$ vs. $\partial(fC)$, cf. (D.61)).

4.3 Numerical methods

In order to obtain a numerical solution of the governing equations we need to discretise the geometric domain. We will limit ourselves to the simplest case of a structured rectangular grid, or mesh, for two reasons: first we are dealing with a system that undergoes significant changes of the flow pattern over time, due to the moving freezing front. This makes it difficult to optimise a static grid for an entire simulation, although incorporating an adaptive grid (*Zhang and Moallemi*, 1995; *Zhang et al.*, 1996) would circumvent this problem. The second reason is to keep the computer code efficient and its complexity at a manageable level. Grid and nomenclature are presented in Section 4.3.1.

The next step to a numerical solution is the discretisation of the governing equations. Three methods are commonly used, Finite Difference, Finite Volume, and Finite Element (*Ferziger and Perić*, 2002). We will use the Finite Volume Method (FVM) as it implicitly conserves mass and energy, unlike the Finite Difference Method. It is further intuitive and easy to implement, unlike the Finite Element Method. FVM assigns a set of volume averaged state variables to every elementary volume defined by the grid, and treats the interaction between these averages. The finite volume discretisation methods are introduced in Appendix E.1. Complete discussions may be found in any textbook on the Finite Volume Method, in particular in *Patankar* (1980), or in the Ph.D. thesis of *Norris* (2001).

Finally, the coupling of the governing equations needs to be honoured. We employ a derivative of the widely used SIMPLE algorithm (Section 4.3.2) that was originally developed by *Patankar and Spalding* (1972). Fractional time step algorithms (*Ferziger and Perić*, 2002) designed to avoid iteration between the governing equations provide no computational advantage in our case due to the strong coupling of equations in the presence of a phase transition. This point will be illustrated in Section 4.3.2.

4.3.1 Grid

Simulations are performed in two–dimensional rectangular domains that we split into an array of equidistant rectangular control volumes. This array is called a grid or a mesh. Other common names for the control volume are elementary volume, finite volume, or computational cell.

We will often have to refer to the neighbouring cells of a particular cell, irrespective of its absolute position in the domain. A convenient notation is the compass notation (*Patankar*, 1980; *Norris*, 2001; *Ferziger and Perić*, 2002), where the cell under consideration is referred to as P, and the cells in the immediate neighbourhood are

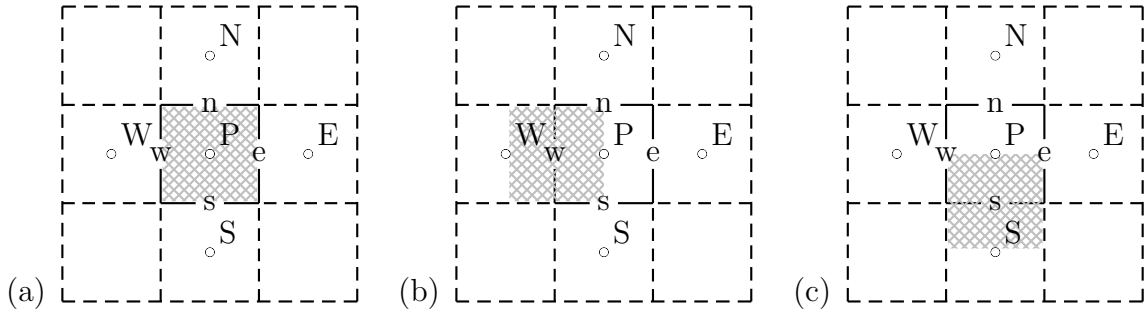

Figure 4.2: Staggered grid. (a) All average values apart from velocity are stored at the centre of the control volume. (b) Horizontal velocity components are staggered horizontally by half of the control volume width. (c) Vertical velocity components are staggered vertically by half of the control volume height.

referred to by their relative direction as N, S, E, and W. This system is illustrated in Figure 4.2(a). The notation is extendable in that the cell to the North–West of P would be NW, and the cell two steps to the East of P would be EE. The boundary between two cells is labelled by small characters, with the boundary between P and S being s, and so on.

We assign volume averaged scalar values Φ to each cell, for example temperature and solute concentration. The average value in P is Φ_P, the average value in E is Φ_E, and the value at the boundary (cell face) between P and E is Φ_e. It is not straight–forward to find appropriate values at the boundaries, and this issue is covered in Appendix E.1.

While all state variables are stored in the grid introduced, velocity components are stored in separate, staggered grids that are staggered by half a cell size (*Patankar*, 1980) (Figures 4.2(b) and (c)). This configuration is of advantage for numerical reasons since velocity components for the transport equations are needed at the cell boundaries (see Appendix E.1), while the pressure *gradient* that is needed for the momentum conservation equation in the velocity cell, is readily obtained from the two neighbouring cells. Above all, the staggered arrangement automatically avoids the numerical artefact of pressure–velocity decoupling (*Ferziger and Perić*, 2002), i.e. cells of alternating high and low pressure.

4.3.2 Pressure–velocity coupling

Appendix E.1 presents the discretisation of the governing equations for all but one quantity, pressure. Since the mass conservation equation merely specifies a constraint on momentum, one can use the mass conservation equation to calculate a pressure

field that enforces mass conservation. The general idea of the SIMPLE[7] algorithm by *Patankar and Spalding* (1972) is to calculate a pressure *correction* field that, when applied to the present best guess of the momentum (velocity) field, yields a mass conserving momentum field. The pressure correction is further used to update the pressure field. The new momentum field generally then does not satisfy momentum conservation anymore, but it is expected that repetitive solution of momentum conservation equation and pressure correction equations leads to a converged, mass and momentum conserving solution.

A pressure correction equation is obtained by expressing the true velocity u_e in terms of the present best guess of the velocity $u_e^\star$ and the gradient of the pressure correction field $d_e\,(p'_E - p'_P)$,

$$u_e = u_e^\star + d_e\,(p'_E - p'_P), \tag{4.12}$$

where d_e is a constant related to the transfer coefficients a of the momentum equation, and p' is the pressure of the pressure correction field. The trick is to estimate d_e well in order to get fast convergence. Substituting (4.12) into the mass conservation equation (4.3) one obtains an equation for p', that resembles a diffusion equation with source term. The source term reflects the present mass imbalance, or mass deficit, at P. The pressure correction field p' is then used to update velocities according to (4.12), and pressure according to

$$p_P = p_P^\star + p'_P. \tag{4.13}$$

Details of the pressure correction process are laid out for example in *Patankar* (1980) and *Versteeg and Malalasekera* (1995). We use the SIMPLEC algorithm in this work that is identical to SIMPLE apart from the way the coefficients d are estimated[8].

In order to obtain coupling between the governing equations they are solved consecutively and multiple times for one time step. Figure 4.3 illustrates the coupling between the governing equations. The vertical arrows indicate interactions present in purely liquid systems, the horizontal arrows indicate additional coupling in the presence of a phase transition. Two points shall be made, here. First, the process of solving the set of governing equations is not trivial, since there are sufficient feedback loops to cause oscillation. Second, interaction is through state variables and the time derivative of the liquid volume fraction f. In order to be able to provide every equation with a current estimate of the time derivative of f we place the solution of the phase transition

[7] Semi–Implicit Method for Pressure–Linked Equations

[8] Further, no under–relaxation of velocity and pressure is applied. Another derivative, SIMPLER (*Patankar*, 1980), did not show any advantage over SIMPLEC but was slower.

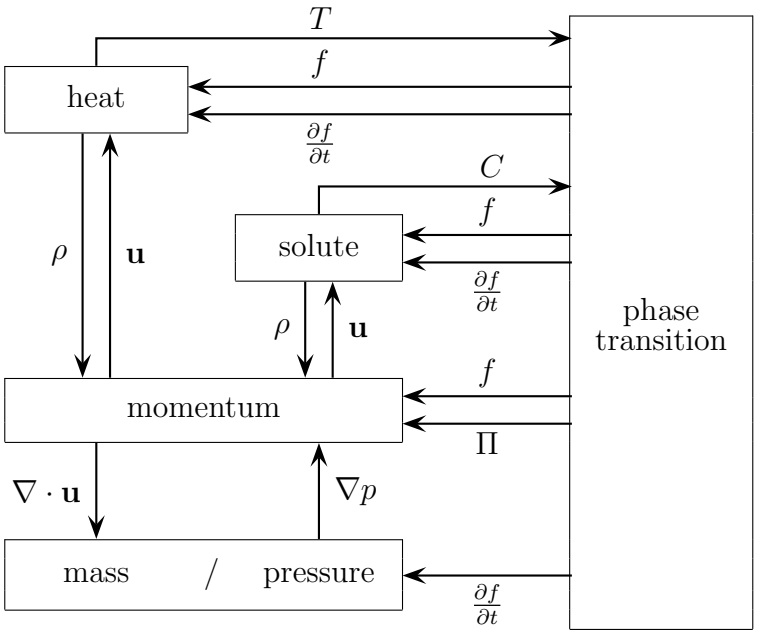

Figure 4.3: Schematic of the feedback mechanism of the coupled governing equations in Section 4.2.3. The six vertical arrows represent feedback paths in an incompressible system with Boussinesq approximation. The nine horizontal arrows show added feedback paths if a solid–liquid phase transition is incorporated. Arrow labels indicate the variable or term that conveys the feedback.

equation at the beginning of the outer loop, or iterative cycle for the time step. The algorithm is as follows:

1. guess the solution of all fields, i.e. $u^\star = u^{n-1}$, $v^\star = v^{n-1}$, $p^\star = p^{n-1}$, $T^\star = T^{n-1}$, $C^\star = C^{n-1}$
2. calculate $f^\star$ from $T^\star$ and $C^\star$ assuming local thermodynamic equilibrium
3. calculate $\partial f/\partial t$ from $f^\star$, f^{n-1} and Δt
4. solve momentum equations $u^\star$ and $v^\star$ based on flow field $u^\star$, $v^\star$, density field calculated from $T^\star$, $C^\star$, pressure $p^\star$ and $f^\star$
5. calculate pressure correction field p' from $u^\star$, $v^\star$, $\partial f/\partial t$
6. adjust $u^\star$, $v^\star$, $p^\star$
7. solve $T^\star$ based on T^{n-1}, $u^\star$, $v^\star$, $f^\star$, $\partial f/\partial t$
8. solve $C^\star$ based on C^{n-1}, $u^\star$, $v^\star$, $f^\star$, $\partial f/\partial t$
9. solution not converged? continue at (2)
10. from $u^\star$ and $v^\star$ adjust mass balance field for future use in the pressure correction equation
11. $u^n = u^\star$, $v^n = v^\star$, $p^n = p^\star$, $T^n = T^\star$, $C^n = C^\star$, $f^n = f^\star$
12. $n = n + 1$, continue at (1)

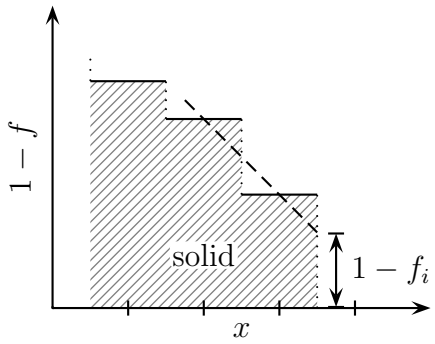

Figure 4.4: One–dimensional example of the solid volume fraction profile close to the interface. Linear extrapolation of the solid volume fraction of two neighbouring cells is used to determine the virtual solid volume fraction $1 - f_i$ at the interface.

4.4 Freezing front tracking

The governing equations derived in previous sections describe our system well, apart from one weakness. The initial condition is usually a water temperature very close to the freezing point so, if heat is removed, the water quickly becomes supercooled. Since local thermodynamic equilibrium is enforced, supercooling is turned immediately into ice formation. The model would therefore predict rapid formation of a small ice fraction throughout the entire domain. Depending on the permeability function imposed this could lead to an artificial flow resistance[9]. In reality on the scale of the finite volume grid, a freezing front can be defined as having pure liquid on one side, and a porous medium on the other side. To simulate the freezing front, we allow ice formation only in volumes that either already contain ice, or have a sufficiently high ice fraction, $1-f_i$, at at least one of their interfaces, where f_i is the liquid volume fraction at the interface.

The solid fraction, $1 - f_i$, at the interface of a cell is calculated from linear extrapolation of the solid fraction of two neighbouring cells (see Figure 4.4). Provided the gradient of f at the freezing front is truly linear, freezing front movement is grid independent. The freezing front velocity will depend on the choice of f_i, since we introduce f_i in order to favour the initial consolidation of the porous medium.

To estimate a reasonable value for f_i we consider the washing depth of a fluid flowing past a dentritic interface. The washing depth is the depth a moving fluid penetrates into the dendritic matrix. *Langhorne and Robinson* (1986) find in laboratory experiments that the washing depth is 0.6 times the dendrite spacing when turbulence at the interface sets in. This is consistent with observations of *Takahashi et al.* (1972)

[9] *Medjani* (1996) and *Oertling and Watts* (2004) increase the viscosity of water for porosities $f > 0.5$, assuming infinite permeability. They apply flow resistance through a finite permeability only for porosities $f < 0.5$.

in solidifying Al–Cu alloys, who find a value of 0.7. *Stewart and Weinberg* (1972) carry out experiments on the solidification of Pb–Sn alloys. Using radioactively tagged lead they find that fluid flowing past the interface penetrates the dendritic interface to the point where the solid volume fraction is $1-f = 0.12$ to 0.22. We adapt this observation as definition of the dendritic interface of sea ice, and demand that the liquid fraction at a cell interface reduces to $f_i = 0.8$ before ice can form.

4.5 Implementation

4.5.1 Code validation

The model accurately finds the critical Rayleigh number for Rayleigh–Bernard convection (*Norris*, 2001); the dependence of the critical Rayleigh number on the fourth power of the aspect ratio in tall cavities (*Catton and Edwards*, 1970); and the evolution and steady state solution of recirculating flow over a backward facing step in a domain with open boundary condition (*Blosch et al.*, 1993). Global solute mass conservation and enthalpy conservation are verified during phase transition under the condition of $\rho_w \neq \rho_i$.

4.5.2 Numerical limitation

An instability occurs during calculations if the permeability range within the domain is too large. The permissable permeability range, or rather, the permissable range of coefficients of the Darcy friction term in the momentum equation, is limited by the numerical resolution of the program. The limit depends on the solid distribution within the mushy zone and on boundary conditions. A minimum permeability of $\Pi = 1 \times 10^{-13}\,\mathrm{m}^2$ or $\Pi = 1 \times 10^{-14}\,\mathrm{m}^2$ has been used in calculations of unidirectional solidification and refreezing cracks, respectively. This proved to be large enough to avoid artefacts. More detail is given in Appendix E.6.

Chapter 5

Permeability–porosity relationship

5.1 Motivation

The unresolved issue in the development of the fluid dynamics model in Chapter 4 is the permeability function of sea ice. This chapter is devoted to the quest for such a function. Several models are developed and applied in this chapter, and experimental data of various groups will be used. A flow chart is provided in Figure 5.1 to help the reader.

It would be most useful for the CFD model if the permeability could be expressed as a function of porosity f, alone. Two related functional dependencies have been given by *Freitag* (1999), based on experiments in the Arctic. They describe vertical sea ice permeability Π_v as functions of effective porosity f_e, which is the pore fraction that actively takes part in fluid transport through sea ice. The fact that *Freitag* gives two permeability functions, one for young first–year sea ice and one for older ice, already indicates that a unique relation between f_e and Π_v may not exist. In fact, *Freitag* shows examples of samples with similar effective porosity, but completely different distributions of the pore sizes that he deems responsible for permeability.

All hope of the existence of a simple permeability–porosity relationship is not lost, however, as our aim is to simulate only a very specific process: the initial freezing process of sea ice. Considering that the salinity distribution in first–year sea ice sheets is predictable (*Weeks and Ackley*, 1986; *Eicken*, 1992), we have reason to expect that the desalinating fluid flow through sea ice responsible for this distribution follows a characteristic pattern (cf. *Niedrauer and Martin* (1979)). This may indicate that the microstructure of sea ice, including the pore structure, is predictable too. So, for the case of newly–forming young sea ice a relationship may exist that links permeability to porosity.

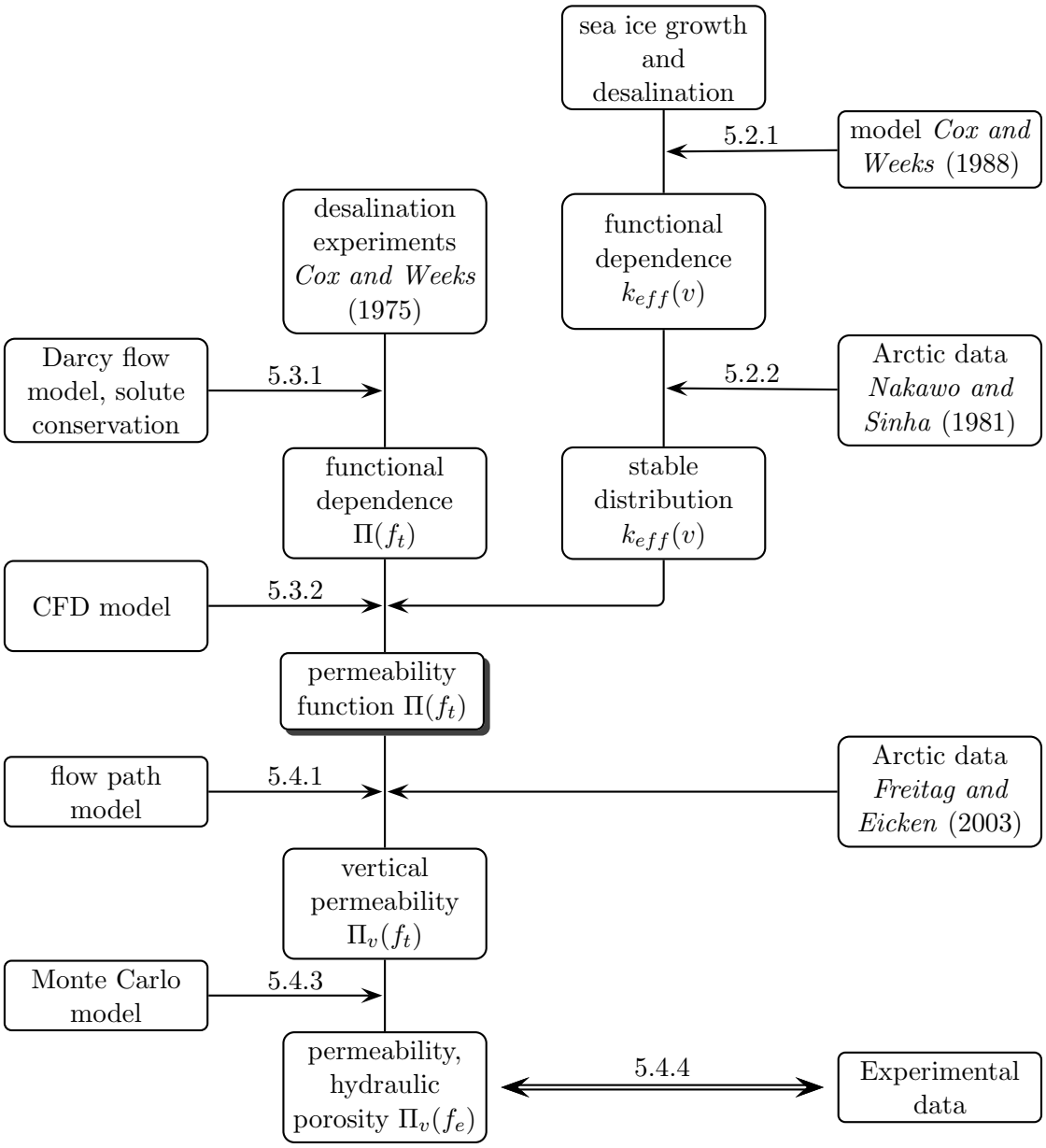

Figure 5.1: Recipe for a permeability function. The horizontal lines indicate where to add the ingredients. We use $\Pi(f_t)$ in subsequent chapters.

In order to find a permeability function for sea ice, *Maksym and Jeffries* (2000) compile permeability data of various groups as a function of total porosity. The collection of points has been fitted to an expression after Kozeny and Carman (*Carman*, 1937). However, the fit is not very convincing due to the large scatter and the comparatively small range covered by data. Further, unsatisfactory results have been repeatedly reported in simulations of sea ice desalination when only a permeability expression after Kozeny and Carman has been employed (*Medjani*, 1996; *Petrich et al.*, 2002; *Oertling and Watts*, 2004). *Eicken et al.* (2004) have presented permeability (presumed vertical component) as a function of total porosity but this was not available when this project began.

In the next sections we find a function that relates sea ice permeability, Π, to total porosity, f. We transform this to an expression that can be compared to the experimental sea ice permeability functions of *Freitag* (1999) and *Eicken et al.* (2004).

5.1.1 The procedure

Fluid flow in the mushy layer is dominated by solid–liquid friction effects that we express in terms of the permeability, Π, of the mush. Following Darcy's law for steady state fluid flow through an isotropic, homogeneous porous medium (*Brinkman*, 1947), volume flux, $f\mathbf{u}$, is proportional to the pressure gradient, ∇p, where the constant of proportionality is the ratio of viscosity, μ, and permeability, Π,

$$-\nabla p = \frac{\mu}{\Pi} f\mathbf{u}. \tag{5.1}$$

The permeability of a medium is a function of its microstructure, e.g. its porosity, f, dendrite size, pore size distribution, and tortuosity. For simplicity in this chapter we will seek an expression for sea ice permeability, Π, as a function of only one parameter, the porosity, f, following the procedure laid out in Figure 5.1 and in *Petrich et al.* (2004). We will also assume that the process of sea ice desalination can be described by an isotropic permeability function, in spite of the observation of *Freitag* (1999) that the vertical permeability of columnar sea ice may exceed the horizontal permeability by one to two orders of magnitude. This assumption should be justified if a characteristic desalination flow path exists for sea ice.

We will use the laboratory measurements of the rate of gravity drainage from *Cox and Weeks* (1975) to estimate an effective volume flux during desalination in young sea ice. This results directly in a relationship between permeability and porosity through Darcy's law (5.1), if we assume that the driving pressure gradient ∇p is constant. We make this assumption and treat the pressure gardient as a free parameter that we

adjust until model calculations of ice sheet growth agree with the expected salinity profile.

In order to determine what salinity profile to expect for a given set of growth conditions we derive a relationship between growth velocity and stable distribution (segregation) coefficient k_{eff}^{stable}, by calculating the expected salinity profile based on the desalination model of *Cox and Weeks* (1988). The stable distribution coefficient,

$$k_{eff}^{stable} = \frac{S_{ice}^{stable}}{S_0}, \tag{5.2}$$

is the ratio of quasi steady–state sea ice salinity, S_{ice}^{stable}, and the salinity of the water the ice originally formed from, S_0. From this model we find a power law relationship between growth rate and stable salinity. We then use that relationship to fit the set of data from experiments in the Arctic of *Nakawo and Sinha* (1981).

Having obtained an expression for the isotropic permeability Π as a function of total porosity, f, we would like to compare it to sea ice permeability functions obtained from measurements of other authors (*Freitag*, 1999; *Eicken et al.*, 2004). The function suggested by *Eicken et al.* describes the vertical permeability component, Π_v, conveniently as a function of total porosity f_t. The functions of *Freitag*, however, describe the vertical component of the permeability, Π_v, as a function of the hydraulically active, connected pore space volume fraction, or effective porosity f_e. Generally, effective porosity and total porosity differ in sea ice. We first seek a transformation between the isotropic permeability and the vertical permeability component assuming a well defined flow path through the sea ice during ice growth. The next step is to find a relationship between total porosity f, that we then label f_t for clarity, and effective porosity f_e. Although this relationship is probably not unambiguous we estimate a relationship that may be suitable in our case, by applying a Monte Carlo percolation model with a domain description adapted to the platelet structure of sea ice. The permeability function that we finally obtain is similar to the functional relationships determined by *Freitag* (1999) (shown in part in *Eicken* (2003)) and *Eicken et al.* (2004) from measurements in the Arctic.

Since the development of an expression for the stable distribution coefficient k_{eff}^{stable} is an excursion from our development of the permeability function we will begin at this point.

5.2 Stable distribution coefficient

Untersteiner (1968) identifies four mechanisms that control the difference in seawater salinity and first–year sea ice salinity. First, the amount of entrapped solute in the sea ice matrix is a function of growth velocity (amongst other variables). An initial distribution coefficient k_{eff} (*Cox and Weeks*, 1975) may be defined as

$$S_{ice} = k_{eff}\, S_0, \tag{5.3}$$

where S_0 is the salinity of the seawater from which the ice grows, and S_{ice} is the salinity of sea ice. The initial segregation is followed by desalination by three mechanisms that take place at the same time.

Gravity drainage arises from unstable stratification of brine in sea ice. If sea ice permeability is large enough, the hydrostatic pressure force may become supercritical and drive brine out of the ice. Gravity drainage is also dominant in brine channel formation.

Brine expulsion is the result of the density difference of ice and water. Brine pockets continue to freeze as the ice temperature decreases. The ice–water density mismatch results in pressure build–up within each pocket that ultimately forces brine to migrate towards the warm end of the sea ice.

Brine pocket migration, driven by concentration gradients inside a pocket in the presence of an external temperature gradient, is too slow to contribute significantly to sea ice sheet desalination. It has been suggested (*Dave Cole*, personal communication), though, that this mechanism may affect inclusion morphology, which could be relevant during the melting season (*Tuckey et al.*, submitted manuscript).

Cox and Weeks (1988) have introduced a numerical model to quantify the sea ice sheet desalination process. They draw heavily on laboratory experiments of *Cox and Weeks* (1975). We will use a simplified version of their model to find a relationship between the stable distribution coefficient and the initial growth velocity. In the following, the governing equations will be introduced and the algorithm that reproduces calculations of *Cox and Weeks* will be presented.

5.2.1 Model after *Cox and Weeks* (1988)

Energy balance

In the model of *Cox and Weeks* (1988) ice sheet growth is driven balancing several heat fluxes (*Maykut and Untersteiner*, 1971). Snow cover is not considered. Since we are interested in the magnitude of heat flux but not in the details of its origin we limit ourselves to one contribution, balancing the conductive heat flux through the ice F_c with the heat flux into the atmosphere F_s (*Cox and Weeks* refer to it as sensible heat flux), i.e.

$$F_s + F_c = 0. \tag{5.4}$$

The conductive heat flux F_c through ice of thickness H, with thermal conductivity of the surface layer k, surface temperature T_0, and temperature T_b at the ice–water interface is

$$F_c = \frac{k}{H} \left(T_b - T_0 \right), \tag{5.5}$$

assuming a linear temperature gradient. The heat flux F_s is expressed as

$$F_s = \rho_a \, c_p \, C_s \, u \, \left(T_a - T_0 \right), \tag{5.6}$$

where $\rho_a = 1.3\,\mathrm{kg\,m^{-3}}$ is the air density, $c_p = 1006\,\mathrm{J\,kg^{-1}\,K^{-1}}$ is the specific heat of air at constant pressure, $C_s = 0.003$ is the sensible heat aerodynamic bulk transfer coefficient, u is the average wind velocity that *Cox and Weeks* (1988) set to $5\,\mathrm{m\,s^{-1}}$, and T_a is the ambient air temperature. Limiting ourselves to the balance of two heat fluxes allows us to find an explicit expression for the conductive heat flux F_c as a function of ambient temperature T_a. Combining (5.4), (5.5), and (5.6) yields

$$F_c = \frac{\rho_a \, c_p \, C_s \, u}{1 + \rho_a \, c_p \, C_s \, u \, (H/k)} \left(T_a - T_b \right). \tag{5.7}$$

Cox and Weeks (1988) use an expression after *Ono* (1975),

$$k = k_i \, (1 - f) + k_b \, f \tag{5.8}$$

to combine thermal conductivity of ice k_i and brine k_b. Our experience is that the salinity predicted by this model differs by only 0.1 to 0.2 psu when a constant $k = 2\,\mathrm{W\,m^{-1}\,K^{-1}}$ is used instead of the more sophisticated treatment of (5.8). The exception to the rule is ice in the top 150 mm of an ice sheet when simulated growth is driven by a surface at constant temperature. In that case, ice salinity may be overestimated by typically 0.5 to 2 psu close to the interface. We will use a constant $k = 2\,\mathrm{W\,m^{-1}\,K^{-1}}$.

Ice growth

Cox and Weeks (1988) use a finite difference scheme to describe ice growth and to calculate changes in ice temperature. In their model runs, 5 mm layers of ice were incrementally added to the bottom of the ice sheet. The time required to grow each layer was then calculated from Stefan's equation

$$\Delta t = \frac{\rho_i \, L \, \Delta H}{F_c}, \tag{5.9}$$

where Δt is the time required to grow the ice layer of thickness $\Delta H = 5\,\mathrm{mm}$, ρ_i is the density of the ice layer, L is the latent heat of fusion, and F_c is the average conductive heat flux. Following *Cox and Weeks* (1988) we use a constant $L = 2.93 \times 10^5\,\mathrm{J\,kg^{-1}}$ for sea ice. We further assume ρ_i is constant. The freezing front velocity v is calculated from

$$v = \frac{\Delta H}{\Delta t}. \tag{5.10}$$

Desalination

Cox and Weeks (1975) have studied the desalination of NaCl ice grown in laboratory with radioactive Na–22 tracer isotopes. This method allowed them to measure sea ice salinity nondestructively. However, it required considerable post–processing of the data. They give equations (*Cox and Weeks*, 1975, 1988) to quantify the three main processes that determine the relationship between water salinity S_0 and ice salinity S_{ice}. They are initial solute segregation, brine expulsion, and brine drainage. Initial solute segregation is expressed through the initial distribution coefficient k_{eff},

$$S_{ice} = S_0 \, k_{eff}, \tag{5.11}$$

where k_{eff} is expressed as a function of freezing front velocity v in $\mathrm{m\,s^{-1}}$ according to

$$k_{eff} = \begin{cases} \dfrac{0.26}{0.26 + 0.74 \times \exp(-724300\,v)} & \\ \qquad\qquad \text{for} \quad v > 3.6 \times 10^{-7}\,\mathrm{m\,s^{-1}}, & \\ 0.8925 + 0.0568\,\ln(100\,v) & \\ \qquad\qquad \text{for} \quad 2.0 \times 10^{-8}\,\mathrm{m\,s^{-1}} \le v \le 3.6 \times 10^{-7}\,\mathrm{m\,s^{-1}}, & \\ 0.12 & \\ \qquad\qquad \text{for} \quad v < 2.0 \times 10^{-8}\,\mathrm{m\,s^{-1}}. & \end{cases} \tag{5.12}$$

The functional dependence at high velocities stems from work of *Burton et al.* (1953)[1], while the assumption of $k_{eff} = 0.12$ at low velocities is consistent with observations in sea ice in the Arctic (*Nakawo and Sinha*, 1981) and Antarctic (*Eicken*, 1998).

Gravity drainage results from brine density inversion in the ice sheet. *Cox and Weeks* (1988) give a linear fit of their earlier data that can be written as

$$\frac{\Delta S_{ice}}{\Delta t} = -3.37 \times 10^{-6}\,\mathrm{psu\,m\,s^{-1}\,K^{-1}}\ (f - 0.050)\ \frac{\Delta T}{\Delta z}, \tag{5.13}$$

where $\Delta T/\Delta z$ is the vertical temperature gradient in the ice. The rate of desalination is set to zero for $f < 0.050$.

Brine expulsion is a direct consequence of volume expansion during freezing. *Cox and Weeks* (1986) derive an expression for the relationship between sea ice salinities S_{ice} at temperatures T_1 and T_2 of the form

$$\frac{S_{ice}(T_2)}{S_{ice}(T_1)} = \frac{S_b(T_2)}{S_b(T_1)}\,\frac{\rho_b(T_2)}{\rho_b(T_1)}\,\frac{f(T_2)}{f(T_1)}, \tag{5.14}$$

where S_b is the brine salinity and ρ_b the corresponding brine density. They express the ratio of liquid volume fractions f during cooling by

$$\frac{f(T_2)}{f(T_1)} = \left(\frac{S_b(T_2)}{S_b(T_1)}\right)^{\left[-\frac{\rho_l}{\rho_i}\right]} \exp\left(\frac{\beta}{\rho_i}\left[S_b(T_1) - S_b(T_2)\right]\right), \tag{5.15}$$

where $\beta = 0.8\,\mathrm{kg\,m^{-3}\,psu^{-1}}$ is the change in brine density with salinity, ρ_l is the density of pure water, and ρ_i is the density of pure ice. With this expression, (5.14) becomes

$$\frac{S_{ice}(T_2)}{S_{ice}(T_1)} = \left(\frac{S_b(T_2)}{S_b(T_1)}\right)^{\left[1-\frac{\rho_l}{\rho_i}\right]} \frac{\rho_b(T_2)}{\rho_b(T_1)} \exp\left(\frac{\beta}{\rho_i}\left[S_b(T_1) - S_b(T_2)\right]\right). \tag{5.16}$$

Thermodynamic equilibrium

The exact form of the freezing point equation is not crucial to the prediction of the salinity profile, and even simple linear relationships for the freezing point $T_F(S_b)$ give sensible results. We use a piece–wise linear fit of the data given in *Cox and Weeks* (1982). For temperatures $T \geq -7.736\,^\circ\mathrm{C}$, i.e. above the eutectic temperature of $Na_2SO_4 \cdot 10H_2O$, we have

$$T_F = -0.06083\,^\circ\mathrm{C\,psu^{-1}}\ \frac{S_{ice}}{f}. \tag{5.17}$$

[1]Their theory seems to work for sea ice even though it is developed for the case of impurities incorporated in a crystal, not for brine concentrated in pockets.

A temperature of $-7.736\,°\mathrm{C}$ that is approximately $0.5\,°\mathrm{C}$ above the true eutectic temperature of $Na_2SO_4 \cdot 10H_2O$, is used to give a continuous expression for $T_F(S_b)$. We further use

$$T_F = 10.981\,°\mathrm{C} - 0.14717\,°\mathrm{C\,psu^{-1}}\,\frac{S_{ice}}{f} \tag{5.18}$$

for temperatures $-7.736\,°\mathrm{C} > T \geq -22.82\,°\mathrm{C}$, i.e. down to the eutectic temperature of $NaCl{\cdot}2H_2O$, and

$$T_F = 249.084°\mathrm{C} - 1.18377\,°\mathrm{C\,psu^{-1}}\,\frac{S_{ice}}{f} \tag{5.19}$$

for $T < -22.82\,°\mathrm{C}$.

Algorithm

The algorithm suggested by *Cox and Weeks* (1988) is forward explicit, which implies that it contains no iteration between the coupled governing equations. As a consequence, the resulting salinity profile depends on the order in which the equations are solved. The algorithm implemented in this study is as follows: sea ice formation is simulated starting with seawater at prescribed salinity $S_b = S_0$, $f = 1$, and temperature $T = T_b$ equal to the freezing temperature. The ambient air temperature T_a is given as a function of time. Each time step begins by calculating the heat flux F_c from (5.7). Time step Δt and growth velocity v are calculated from (5.9) and (5.10), respectively. Next, brine expulsion in the ice that already exists is treated with (5.16), the new liquid volume fraction f is calculated from (5.15), and the temperature profile T in the ice is updated assuming constant F_c and k throughout the ice. All ice layers with $0.05 < f < 1$ are then prone to brine drainage according to (5.13). Following this, initial segregation (5.12) is applied to the newly–formed bottommost layer. Finally, the new brine volumes f are calculated from (5.17) to (5.19) assuming local thermodynamic equilibrium $T = T_F$, and the new brine salinity profile is deduced from

$$S_b = \frac{S_{ice}}{f}. \tag{5.20}$$

Model validation

To confirm that the model is implemented consistently we perform a model calculation with an ambient temperature similar to the one assumed by *Cox and Weeks* (1988). The ambient temperature T_a decreases linearly from $-15\,°\mathrm{C}$ initially to $-32\,°\mathrm{C}$ within 70 days, and then remains constant at $-32\,°\mathrm{C}$. *Cox and Weeks* (1988) do not specify the salinity of the seawater they use in their calculations. We use $S_0 = 34\,\mathrm{psu}$. Figure 5.2

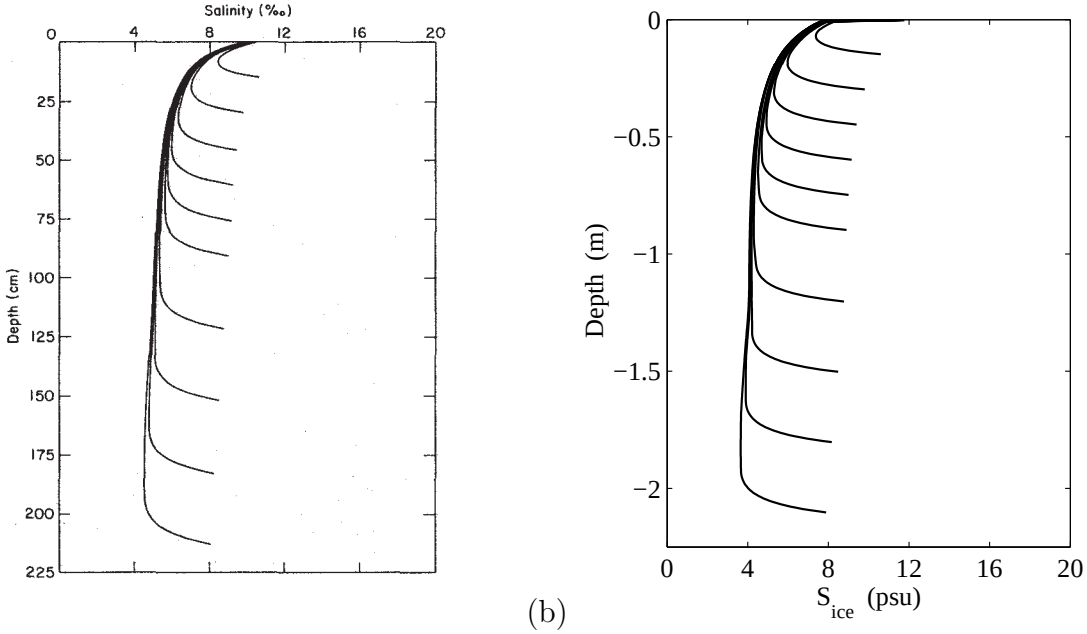

(a) (b)

Figure 5.2: Calculated salinity profiles from (a) figure 5 in *Cox and Weeks* (1988); (b) the model after *Cox and Weeks* (1988) described in this chapter with simplified boundary condition.

juxtaposes salinity profiles for ice sheets at various depths shown in figure 5 in *Cox and Weeks* (1988) and results calculated from the model presented in this section. The results are reassuringly similar. We note, however, that the salinity reported by *Cox and Weeks* is systematically higher, by about 1 psu at the bottom of the ice sheet. This could be due to our neglect of radiative and latent heat fluxes at the surface. For example, adding a constant heat flux of $-30\,\mathrm{W\,m^{-2}}$ (a typical value for the net longwave radiation, see Appendix C.3) shifts the salinity profile by 1 psu towards larger salinities. Of concern to us is the relationship between heat flux (proportional to growth velocity) and desalination. This relationship is only weakly dependent on the choice of the heat flux boundary condition.

5.2.2 Stable salinity distribution coefficient

We will next apply the model developed in Section 5.2.1 to find a relationship between stable distribution coefficient k_{eff}^{stable} and freezing front velocity v. We therefore simulate 2.25 m ice growth with the boundary condition used in the previous section, and with each of the constant temperature boundary conditions of $T_0 = -8\,^\circ\mathrm{C}$, $T_0 = -14\,^\circ\mathrm{C}$, and $T_0 = -20\,^\circ\mathrm{C}$. Figure 5.3 shows the distribution coefficient as a function of growth velocity. The range of growth velocities supported by measurements of *Cox and Weeks* (1975) is $2 \times 10^{-8}\,\mathrm{m\,s^{-1}}$ to $3 \times 10^{-6}\,\mathrm{m\,s^{-1}}$. Data corresponding to the ice layer closest

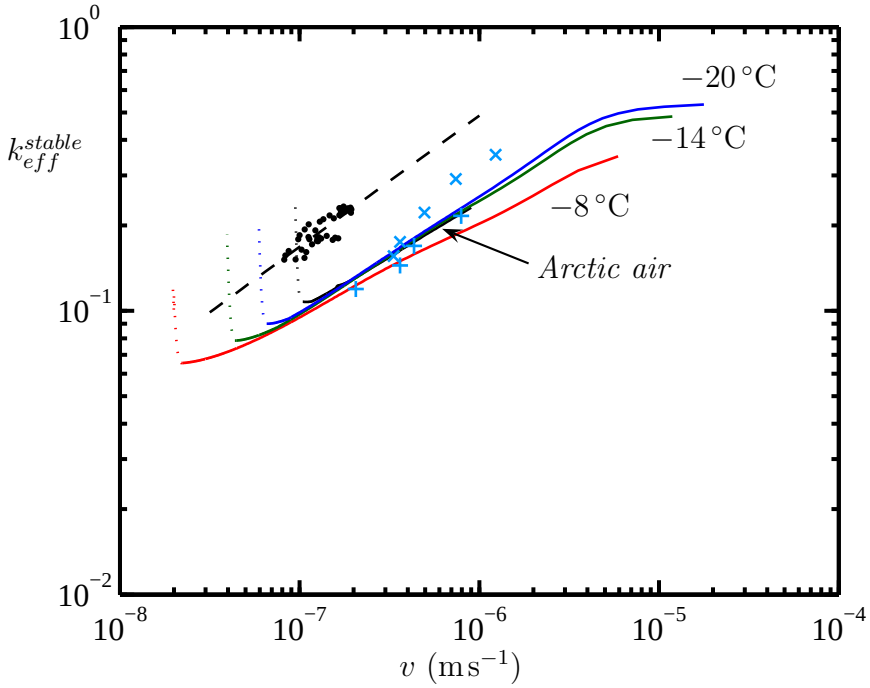

Figure 5.3: Calculated stable distribution coefficient k_{eff}^{stable} of 2.25 m thick ice as a function of growth rate v. Surface boundary conditions are Arctic air, $-20\,°C$, $-14\,°C$, and $-8\,°C$. The bottommost 250 mm of each simulated ice sheet are shown as dotted lines. Measurements in the Arctic (dots) are from Figure 11 in *Nakawo and Sinha* (1981). The broken line is the best fit power law through their data. Also shown are *estimated* stable distribution coefficient data (pluses and crosses) from the laboratory experiment of *Cox and Weeks* (1975) as obtained in Appendix F.1. Data are from growth runs at $-10\,°C$ (pluses) and $-20\,°C$ (crosses).

to the ice–air interface are not shown. The bottom 0.25 m are drawn as dotted lines as brine drainage is not yet complete. The stable distribution coefficient becomes constant with velocity towards larger growth rates, but depends on the air temperature. We see that the relationships calculated with boundary conditions of ambient air temperatures of $-14\,°C$, and $-20\,°C$ collapse onto each other. The distribution coefficients calculated for the high air temperature of $-8\,°C$ are systematically lower, but the functional dependence is similar to the other boundary conditions. The distribution coefficient is a function of ambient air temperature particularly at high growth velocities.

The most interesting regime for us of growth velocities, 1 to $10 \times 10^{-7}\,\mathrm{m\,s^{-1}}$ at air temperatures below $-14\,°C$, suggests a correlation that follows a power law

$$k_{eff}^{stable} = 0.11 \left(\frac{v}{v_0} \right)^{0.41} . \tag{5.21}$$

with $v_0 = 1.35 \times 10^{-7}\,\mathrm{m\,s^{-1}}$ (as in (5.22)).

It is also possible to estimate the stable distribution coefficient directly from experiments of *Cox and Weeks* (1975). This is done in Appendix F.1, and some data points are shown in Figure 5.3 for reference. Reassuringly, the model calculations are consistent with the experiments on which the model is based.

However, Figure 5.3 also shows are the stable distribution coefficient field data of *Nakawo and Sinha* (1981). The salinity data of *Nakawo and Sinha* are larger, by a factor of 2, than the model predictions. Assuming that this discrepancy is systematic, and that a power law is still an appropriate choice for a fit function, we fit data of *Nakawo and Sinha*, which centres around $v_0 = 1.35 \times 10^{-7}\,\mathrm{m\,s^{-1}}$, with

$$k_{eff}^{stable} = 0.19 \times \left(\frac{v}{v_0}\right)^{0.46}. \tag{5.22}$$

We will come back to the difference after examining some more desalination measurements.

Discussion

Cox and Weeks (1975) are not the only authors who have investigated the desalination process of sea ice. Other groups have related desalination to the growth velocity of sea ice in the Arctic (*Nakawo and Sinha*, 1981), in the Arctic, Antarctica and Japan (*Wakatsuchi*, 1983), and in the laboratory (*Tsurikov*, 1965; *Weeks and Lofgren*, 1967; *Wakatsuchi and Ono*, 1983; *Wakatsuchi*, 1983).

Initial distribution coefficient *Tsurikov* suggests an equation for the initial distribution coefficient k_{eff} in sea ice that is based on previous structural investigations of sea ice and that does not contain fit parameters, unlike all other equations for distribution coefficients discussed in this chapter. He gives a parametric equation of the form

$$k_{eff} = 1.006\,\frac{7\sqrt{3.6 \times 10^6\, v}}{7\sqrt{3.6 \times 10^6\, v} + 10.30}, \tag{5.23}$$

with interface velocity v in $\mathrm{m\,s^{-1}}$. The corresponding experimental data are obtained from freezing of saltwater of various salinities and of seawater in a Dewar flask.

The results for stable distribution coefficients k_{eff}^{stable} and initial distribution coefficients k_{eff} obtained by various groups are compared in Figure 5.4.

Of the initial distribution coefficients, laboratory measurements by *Tsurikov* are largest, followed by *Cox and Weeks* and *Weeks and Lofgren*. Owing to the vast amount of data of *Weeks and Lofgren*, only their fit function is shown. That function is further shown only for the range of velocities that fit their measurements well. Data of *Weeks*

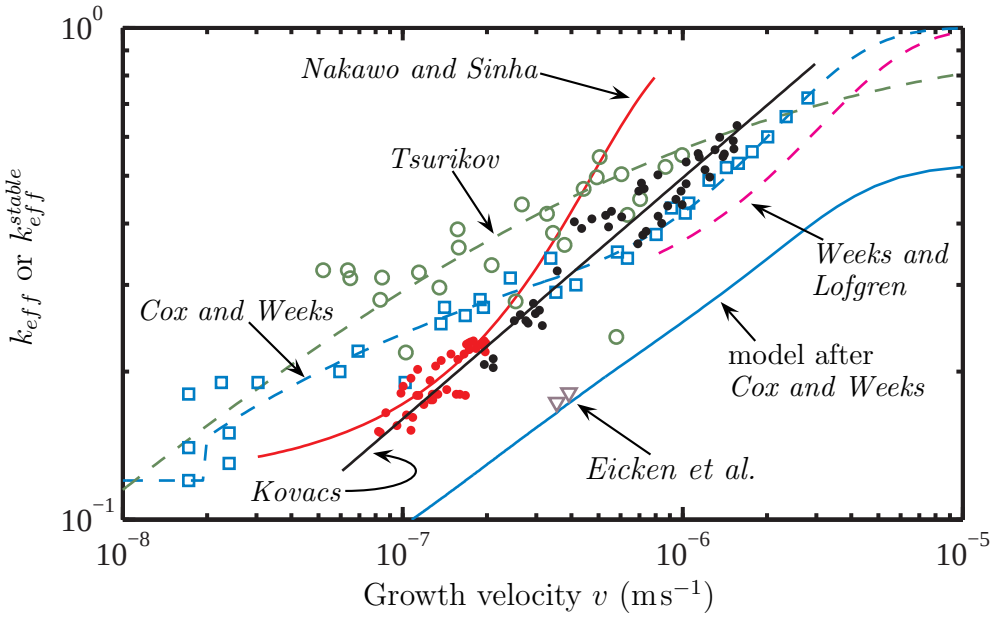

Figure 5.4: Comparison of effective distribution coefficients for initial distribution k_{eff} (broken lines) and stable distribution k_{eff}^{stable} (solid lines). Data points of initial distribution coefficients are laboratory measurements of *Tsurikov* (1965) (circles) and *Cox and Weeks* (1975) (squares). Data points of stable distribution coefficients are laboratory experiments of *Eicken et al.* (1998) (triangles), and field data of *Nakawo and Sinha* (1981) (dots) and field and laboratory data of *Wakatsuchi* (1983) (dark dots).

and Lofgren are lower than data of *Cox and Weeks* probably because of partial brine drainage prior to measurement (*Weeks and Ackley*, 1986). Comparing the best fit functions of *Cox and Weeks* and *Tsurikov* their similarity at velocities below $10^{-7}\,\mathrm{m\,s^{-1}}$ is most noticeable.

Stable distribution coefficient Of stable distribution coefficient data, *Nakawo and Sinha* give an interpolation function that they advise against using beyond the range of their data. *Kovacs* (1996) gives a power law fit function of data of *Nakawo and Sinha* combined with that of *Wakatsuchi* (1983), which is

$$k_{eff}^{stable} = 0.17 \left(\frac{v}{1.182 \times 10^{-7}\,\mathrm{m\,s^{-1}}} \right)^{0.49}, \tag{5.24}$$

where the velocity in the denominator is $1\,\mathrm{cm\,day^{-1}}$ and v is in $\mathrm{m\,s^{-1}}$. It is reassuring that the *Kovacs*' fit suggests the same functional dependence that we have obtained from the model after *Cox and Weeks* (1988). It is further particularly interesting to see that the stable distribution coefficient data of *Wakatsuchi* are larger than the initial distribution coefficient found by *Cox and Weeks* (1975) at velocities above $3 \times$

$10^{-7}\,\mathrm{m\,s^{-1}}$. Data points of *Wakatsuchi* (1983) shown in Figure 5.4 appear to line up on two distinct lines. The line of higher distribution coefficients comprises data points mostly obtained in the Arctic, Japan, and in the laboratory, while the lower line comprises data points from Antarctica and laboratory experiments. Unlike *Nakawo and Sinha* (1981), however, *Wakatsuchi* (1983) calculates the distribution coefficient from the average salinity of an entire ice sheet and relates this to ice thickness divided by time of growth. Data of *Wakatsuchi and Ono* (1983) have to be re–scaled and this is therefore shown in Appendix F.2. The data of the stable distribution coefficient of *Eicken* (1998), provided by *Hajo Eicken* (personal communication), stem from an INTERICE I ice growth experiment in a $30 \times 6 \times 1.2\,\mathrm{m^3}$ basin with $0.16\,\mathrm{m\,s^{-1}}$ water current under the growing sea ice. More details of this experiment are given in *Eicken et al.* (2000) and in Appendix F.3. Further, stable distribution coefficients can be derived[2] from data of *Rahlves* (2003) from laboratory experiments of ice freezing in a tank of $1.9 \times 0.9 \times 0.6\,\mathrm{m^3}$ in the nominal absence of currents. These data are closer to the fit line of *Kovacs* (1996) than to the line derived from the model after *Cox and Weeks* (1988).

The systematic difference in stable distribution coefficient data between *Cox and Weeks* (1975) and *Eicken* (1998) on the one hand, and *Nakawo and Sinha* (1981), *Wakatsuchi* (1983), and probably *Wakatsuchi and Ono* (1983) and others on the other hand could be related to currents in the water, as discussed in Appendix F.4. The cylindrical vessel of *Cox and Weeks* (1975) was small at 140 mm diameter, which could have led to more vigorous convective currents than observed in larger experiments, while the experiment of *Eicken* (1998) deliberately imposed a strong under–ice current.

Summary The power law expression for the stable distribution coefficient k_{eff}^{stable} as a function of growth velocity v is presently our best estimate for sea ice. However, the maximum growth velocity for its application remains undetermined. Errors are therefore potentially large at high growth velocities, and errors are probably large if sea ice forms under low heat fluxes or high surface temperatures. We will continue to use the expression (5.22) for the stable distribution coefficient as it is based on one consistent set of data. Note that choosing to use (5.24) instead of (5.22) would lead to the same permeability–porosity relation.

[2]Experiments Run 1: $v = 1 \times 10^{-7}\,\mathrm{m\,s^{-1}}$, $k_{eff}^{stable} = 0.2$; Run 3: $v = 4.5 \times 10^{-7}\,\mathrm{m\,s^{-1}}$, $k_{eff}^{stable} = 0.35$.

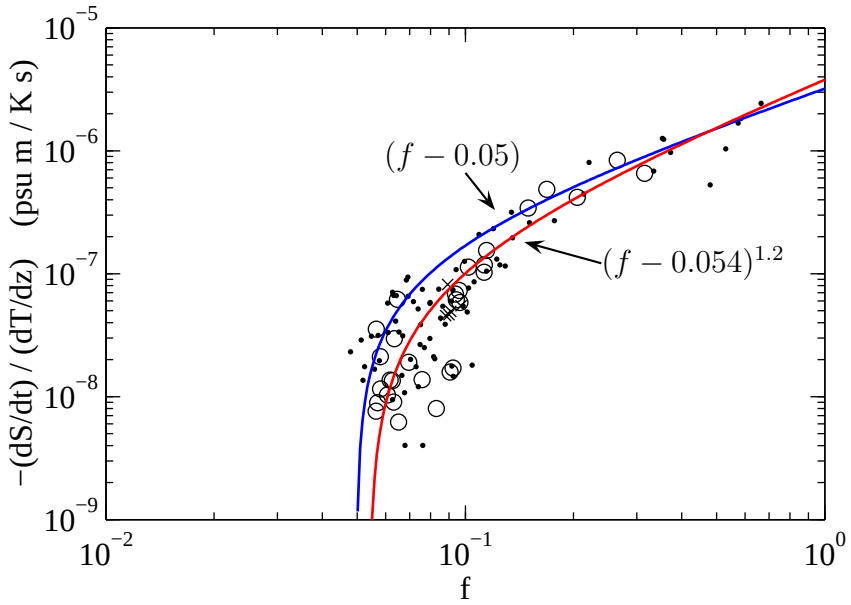

Figure 5.5: Gravity drainage data of *Cox and Weeks* (1975), Figures 30 and 31. Temperature gradients in $\mathrm{K\,m^{-1}}$: (·) 10 to 60; (∘) 60 to 120; (×) 120 to 180. The linear fit function (5.13) of *Cox and Weeks* (1988) with $f_c = 0.050$, and the fitted power law (5.30) with $f_c = 0.054$ and exponent 1.2 are shown.

5.3 Permeability function

5.3.1 Functional dependence

Cox and Weeks (1975) have measured the rate of gravity drainage of laboratory grown sea ice above the skeletal layer. They present data deemed unaffected by brine expulsion, and give a fit function that we can write as

$$\frac{\Delta S_{ice}}{\Delta t} = -A\,(f - f_c)\,\frac{\Delta T}{\Delta z}, \tag{5.25}$$

where $A = 3.37 \times 10^{-6}\,\mathrm{psu\,m\,s^{-1}\,K^{-1}}$ and $f_c = 0.05$ are constants, $f > f_c$, and the temperature gradient is $\Delta T/\Delta y > 0$. Since the quality of that fit is not apparent from the published figures in linear scale, the data points of their figures have been resampled (shown in Figure 5.5), and fitted to a function

$$-\mathfrak{u} = a\,(f - f_c)^{\gamma}\,, \tag{5.26}$$

where $a = A/A_0$ with the constant $A_0 = 1 \times 10^{-6}\,\mathrm{psu\,m\,s^{-1}\,K^{-1}}$, chosen to make (5.26) dimensionless. The value f_c is a critical porosity below which no brine drainage is

Table 5.1: Best fit parameters of (5.28) and (5.29).

	a	f_c	γ	fit function	fixed parameter
(a)	6.6	0.015	1.9	(5.28)	
(b)	1.3	0.043	1	(5.28)	$\gamma \stackrel{\text{def}}{=} 1$
(c)	8.2	0	2.1	(5.28)	$f_c \stackrel{\text{def}}{=} 0$
(d)	4.2	0.054	1.2	(5.29)	
(e)	3.6	0.069	1	(5.29)	$\gamma \stackrel{\text{def}}{=} 1$
(f)	6.0	0	1.8	(5.29)	$f_c \stackrel{\text{def}}{=} 0$

observed, i.e. $\mathfrak{u} = 0$ for $f < f_c$. We have introduced the function $\mathfrak{u} > 0$

$$\mathfrak{u} = \frac{\Delta S_{ice}}{\Delta t} \left[\frac{\Delta T}{\Delta z}\right]^{-1} \frac{1}{A_0} \tag{5.27}$$

for notational convenience. For the purpose of curve fitting, we express (5.26) as

$$\ln(\mathfrak{u}) = \ln(a) + \gamma \ln(f - f_c). \tag{5.28}$$

It is obvious that a least square fit of (5.28) forces f_c to be smaller than the smallest f of the data points. We therefore perform alternate fits of the inverse of (5.28),

$$f = \exp\left(\frac{\ln(\mathfrak{u}) - \ln(a)}{\gamma}\right) + f_c. \tag{5.29}$$

The difference between fitting (5.28) and (5.29) is that a fit of (5.28) assumes that all uncertainty is in $\mathfrak{u}$ while f is known exactly, while a fit of (5.29) assumes that all uncertainty is in f while $\mathfrak{u}$ is known exactly (*Fuller*, 1987).

A selection of best fit parameters for the data set is shown in Table 5.1. The set of parameters (a) and (b) in Table 5.1 are biassed in f_c as (5.28) requires f_c be smaller than the smallest f. Keeping in mind that there is some scatter in the measurement of f, these two parameter sets are probably the least meaningful of all sets shown. Sets (c) and (f) force $f_c = 0$ and would give identical results if there was no scatter in the data. Both fits return an exponent in the range $\gamma = 2 \pm 0.2$. Set (e) suggests that the curve fit (5.13) of *Cox and Weeks* actually presupposed that $f_c = 0.050$ and that $\gamma = 1$, leaving only a as the free parameter. Such an approach would be justified on the grounds of simplicity. Seen in this light, set (d) is very attractive as the fitted parameter f_c has physical meaning that is backed up by direct observation of *Cox and Weeks*. We will therefore assume for the purpose of obtaining a permeability function,

that

$$\frac{\Delta S_{ice}}{\Delta t} = -A\ (f - f_c)^{\gamma}\ \frac{\Delta T}{\Delta z}, \tag{5.30}$$

with[3] $A = 4.2 \times 10^{-6}\,\mathrm{psu\,m\,s^{-1}\,K^{-1}}$, $f_c = 0.054$, and $\gamma = 1.2$. This fit is shown in Figure 5.5.

Now, assuming that within the error of measurement $\Delta S_{ice} = \Delta C_{ice}$, i.e. that the difference in salinity (in psu) is equal to the difference in concentration (in $\mathrm{kg\,m^{-3}}$), and that local thermodynamic equilibrium applies, i.e. $\Delta T = m\Delta C$, where m is the slope of the liquidus, we write (5.30) as

$$\frac{\Delta C_{ice}}{\Delta t} = -m\,A\ (f - f_c)^{\gamma}\ \frac{\Delta C}{\Delta z}. \tag{5.31}$$

If we compare (5.31) to the solute transport equation[4]

$$\frac{\partial fC}{\partial t} + fu\frac{\partial C}{\partial z} = 0, \tag{5.32}$$

with brine concentration C, we obtain an expression for the gravity driven mass flow[5] in sea ice during ice growth,

$$fu = -m\,A\,(f - f_c)^{\gamma}\,. \tag{5.33}$$

After substituting (5.33) into Darcy's law (5.1) for one–dimensional flow we obtain an expression for the permeability Π of the form

$$\Pi = \frac{\mu\,m}{\nabla p}\,A\,(f - f_c)^{\gamma}\,. \tag{5.34}$$

Viscosity, μ, and liquidus slope, m, each vary by a few percent per Kelvin. Since this is an attempt to find a permeability[6] function that depends on f alone, we neglect this

[3]Data displayed by *Cox and Weeks* (1975) in Figures 30 and 31 is binned into three temperature gradient ranges. All fits in Table 5.1 and data shown in Figure 5.5 assume a temperature gradient equal to the corresponding bin average for each individual data point. An uncertainty can be estimated by using bin boundary gradients, instead. The best fit of (5.29) based on average gradient values yields $f_c = 0.0538$, $\gamma = 1.24$ (Table 5.1(d)), while the best fit considering described uncertainty is $f_c = 0.055 \pm 0.005$, $\gamma = 1.25 \pm 0.15$. The error introduced in the resampling process is assumed to produce random scatter.

[4]This is (4.10) with $\partial fu/\partial z = 0$, i.e. we assume mass conservation and the absence of volume expansion for simplicity. The solute diffusion coefficient is small in porous media (*Bear and Bachmat*, 1991), so we have further set $D = 0$.

[5]Strictly speaking, fu in (5.32) is the effective velocity at which *solute* is advected, which is actually smaller than the *fluid* velocity fu in Darcy's law (5.1) that is relevant for flow resistance. The difference is due to solute dispersion and possibly solute adsorption (or a microscopic solute boundary layer) (*Bear and Bachmat*, 1991).

[6]Permeability, unlike hydraulic conductivity, is a function of the porous medium and independent

change with temperature.

The driving pressure gradient ∇p should be only slightly dependent on the thermal environment, apart from the early stages of growth and when growth takes place at high temperatures. If the ice–air interface temperature is cold enough, and an ice sheet is already present, there should be a horizontal layer in the ice of approximately $f = 0.05$ above which fluid exchange is inhibited (cf. assumptions in model of *Cox and Weeks* (1988)). The driving hydrostatic pressure force (*Wettlaufer et al.*, 1997; *Eicken et al.*, 2002) then depends on the difference between densities of brine in the layer where $f = 0.05$ and that of seawater. As density is primarily a function of salinity, ∇p will be relatively constant[7].

We also assume that the desalination flow path is always the same, which allows us to postulate the existence of a characteristic, isotropic permeability function Π to describe the desalination process in sea ice,

$$\Pi \propto (f - f_c)^{\gamma} . \tag{5.35}$$

The obvious first approach to a constant of proportionality is to equate it to the factor in (5.34). We find

$$\frac{\mu\, m}{\nabla p} A = 6 \times 10^{-13}\,\mathrm{m}^2, \tag{5.36}$$

with $A = 4.2 \times 10^{-6}\,\mathrm{psu\,m\,s^{-1}\,K^{-1}}$, $\mu = 1.8 \times 10^{-3}\,\mathrm{kg\,m^{-1}\,s^{-1}}$, $m = -0.054\,^{\circ}\mathrm{C\,psu^{-1}}$, $\nabla p = g\Delta C$ with acceleration due to gravity $g = -9.8\,\mathrm{m\,s^{-2}}$, and brine concentration difference $\Delta C \approx (100 - 34)\,\mathrm{kg\,m^{-3}}$. This permeability is too low, which could either be because the fluid flow rate is significantly higher than the solute flow rate, or because the effective pressure gradient ∇p is actually smaller than the hydrostatic pressure gradient. A higher fluid flow rate is sensible in light of solute dispersion and adsorption in porous media flow (*Bear and Bachmat*, 1991), and a smaller effective driving pressure gradient would be likely considering that not only is brine driven out of the ice but seawater is drawn back into the ice at the same time. We use the computer model from Chapter 4 and the conventional trial–and–error method to find the constant of proportionality of (5.35).

of fluid properties like viscosity μ. In (5.34) μ appears as a property of the fluid that we use to probe the permeability, therefore no dependence of permeability on fluid properties is implied.

[7]For example, let the driving hydrostatic pressure force be $F \propto S_b - S_w$ (*Wettlaufer et al.*, 1997). 5 psu ice at $f = 0.05$ has a brine salinity of around $S_b = 100\,\mathrm{psu}$. If the ice was of 10 psu, instead, brine salinity would be around $S_b = 200\,\mathrm{psu}$. With seawater salinity $S_w = 35\,\mathrm{psu}$ we estimate the ratio of forces as $F_{10}/F_5 = 165/65 = 2.5$.

5.3.2 Constant of proportionality

We will determine a constant of proportionality for the permeability function (5.35). The requirement we impose on that constant is that it should cause the numerical model developed in Chapter 4 to produce ice sheets of horizontally averaged vertical salinity profiles predicted by the distribution function (5.22). The task is reasonably straight–forward with only one parameter to determine[8]. We find by trial–and–error that

$$\Pi = 1.0 \times 10^{-10}\,\mathrm{m}^2\ (f - 0.054)^{1.2} \quad \text{for} \quad 0.054 < f < 1, \tag{5.37}$$

$\Pi \to \infty$ for $f = 1$, and $\Pi = 1 \times 10^{-13}\,\mathrm{m}^2$ for $f \leq 0.054$ produces salinity profiles close to those expected from the stable distribution function fitted through data of *Nakawo and Sinha* (1981) in equation (5.22). Example calculations for ice grown from the upper surface with a constant temperature boundary condition of either $-10\,^\circ\mathrm{C}$ or $-20\,^\circ\mathrm{C}$ in a periodic domain are shown in Figures 5.6(a) and (b) (*Petrich et al.*, 2004). Figure 5.6(a) is a superposition of three scatter plots at $-10\,^\circ\mathrm{C}$ and five scatter plots at $-20\,^\circ\mathrm{C}$ of calculations with various grid and domain sizes. Clearly visible is a certain amount of scatter that resembles natural variability of salinity profiles (*Bennington*, 1967; *Cottier et al.*, 1999). The bottom sections of the profiles where the salinity profile has not yet been stabilised are not shown. Figure 5.6(b) shows two example profiles with particularly little scatter. The domain size is $1.28\,\mathrm{m} \times 1.28\,\mathrm{m}$, and the grid is 16×16. The salinity profiles follow the "typical C–shape" (*Eicken*, 1992). We further observe that desalination first sets in after a characteristic ice sheet depth is reached[9] (*Foster*, 1969; *Wettlaufer et al.*, 1997).

5.3.3 Discussion

Probably the most popular permeability–porosity relationship in the literature is the relationship after Kozeny and Carman (*Carman*, 1937), where

$$\Pi \propto \frac{f^3}{(1-f)^2}. \tag{5.38}$$

[8]To put the straight–forwardness into perspective: 50 computational sea ice sheets were calculated specifically to obtain this one parameter. Over 150 computational ice sheets were calculated before this, which showed that a guess for the permeability function can lead to sensible salinity profiles. It also showed that very different functions can lead to sensible salinity profiles, and this ultimately triggered the quest for a theoretically or experimentally founded description of permeability. Each computational ice sheet growth takes usually 12 to 48 h.

[9]Unlike the simulations of *Medjani* (1996) and *Oertling and Watts* (2004), simulations with the present model are numerically stable without having an initial ice layer present.

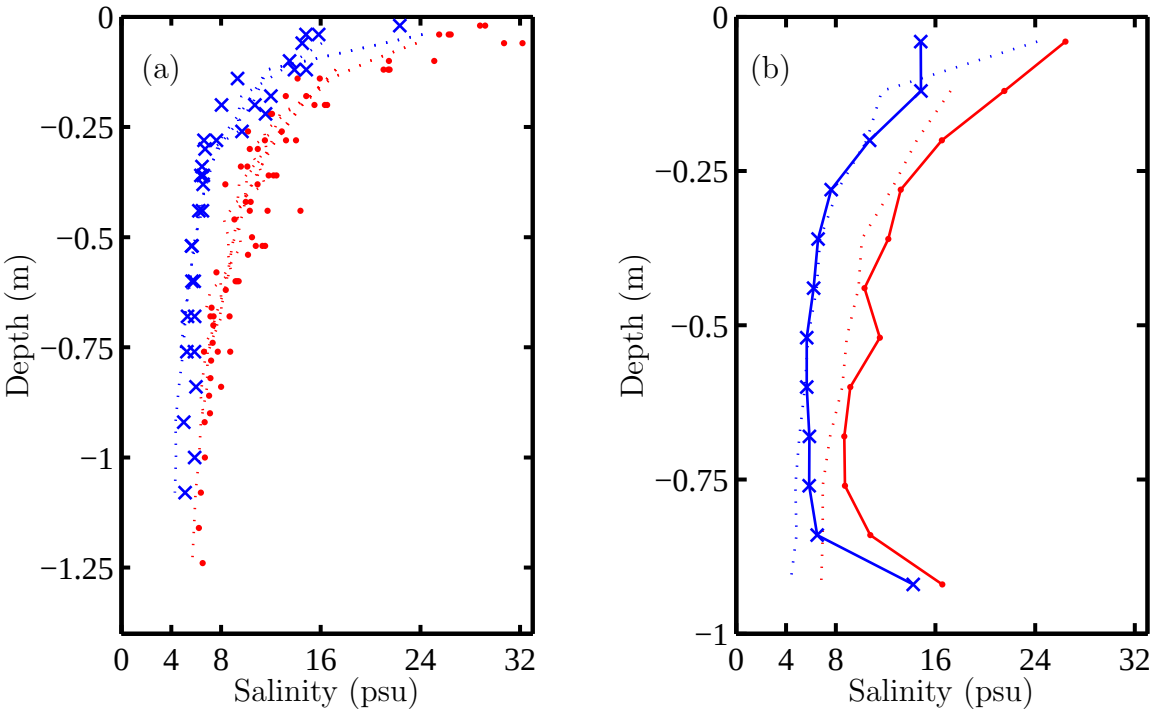

Figure 5.6: Comparison of salinity profiles predicted from (5.22) (dotted lines) and computed (data points and solid lines) with permeability function (5.37) for surface temperatures −10 °C (crosses) and −20 °C (dots). Shown are (a) scatter plots of eight calculations (bottom data not shown), and (b) two complete profiles. Note the different scales.

This relationship is proven to predict permeability well in unconsolidated granular beds such as sand. It does not contain a critical porosity f_c, reduces to a power law with exponent 3 in the limit of small void fractions f, and diverges as the porosity reaches $f = 1$. We have seen earlier (Table 5.1) that we could fit the data of *Cox and Weeks* (1975) with a power law of exponent 2, not 3, if we set $f_c = 0$. Further, the lamellar structure of columnar sea ice is considerably different from the granular structure of sand. In some systems, the predictions of the Kozeny–Carman relationship have been found to deteriorate at low porosities f (*van der Marck*, 1999). This has been demonstrated for example in compressed calcite (*Zhang et al.*, 1994), where experimental observations were found to be consistent with concepts of percolation theory (*Knackstedt and Cox*, 1995; *Knackstedt and Duplessis*, 1996).

The relationship (5.37) is equivalent to the form of the permeability–porosity relationship predicted from percolation theory near the critical porosity[10], f_c. Percola-

[10]Note that by following *Cox and Weeks* (1975) in the choice of fit function for their data we have *chosen* to use a functional form that is used in percolation theory. Note also that the existence of a critical porosity f_c in sea ice has been questioned by *Freitag* (1999). Likewise, *Weissenberger et al.* (1992) show that they centrifuged 70 % of the liquid brine out of Antarctic sea ice samples at a sample

tion theory predicts (*Stauffer and Aharony*, 1992) that porous media exhibit a critical porosity f_c, close to which permeability increases according to the relationship

$$\Pi \propto (f - f_c)^{\gamma} . \tag{5.39}$$

Both, the critical porosity f_c and the critical exponent γ are found to depend primarily on the dimension of the system. In continuum models the critical exponent may further depend on the choice of conductivity of the pores.

Berkowitz and Balberg (1992) perform numerical Monte–Carlo percolation simulations for a continuum of spheres with three different assumptions for the hydraulic conductivity between spheres. In all cases, the critical exponent calculated for two–dimensional systems is $\gamma = 1.2 \pm 0.1$. They find in three dimensional systems that $\gamma = 1.9 \pm 0.1$ or $\gamma = 2.3 \pm 0.1$, depending on the details of the assumed conductivity. These values are in agreement with permeability exponents 1.3 and 1.9 that are accepted for two and three–dimensional discrete lattice percolation models, respectively (*Feng et al.*, 1987). *Feng et al.* (1987) further expect that the permeability exponent near the percolation threshold is 1.3 and 2.4 in two and three–dimensional inverse Swiss–cheese continuum percolation systems (e.g. where connected pores conduct fluid), respectively. *Dardis and McCloskey* (1998) find from lattice Boltzmann simulations of flow in two–dimensional porous media an exponent of 1.31 near the percolation threshold. In permeability measurements on calcite aggregates *Zhang et al.* (1994) find an exponent of 2.2.

The critical exponent of 1.3 for a two–dimensional percolating system agrees within error limits with the exponent of 1.2 ± 0.2 that we have determined from the experimental data of *Cox and Weeks* (1975). However, the exponent derived here is largely based on the permeability–porosity relationship for $f \gg f_c$, which is outside the scope of percolation theory.

5.3.4 Summary

The permeability relationship (5.37) allows the realistic simulation of sea ice sheet desalination during quasi one–dimensional ice sheet growth. This is the primary justification for its use in model calculations in the following chapter. Two of the three parameters are derived from the results of the laboratory experiments of *Cox and Weeks* (1975), which gives (5.37) some experimental support.

temperature of $-15\,^{\circ}\mathrm{C}$, i.e. possibly $f < f_c$ (sea ice salinity is not given). This indicates that the concept of a critical porosity in sea ice is approximate at best.

The primary goal of this chapter is now accomplished, and the next section is devoted to a transformation of (5.37) into a form that can be compared to the permeability functions given by *Freitag* (1999) and *Eicken et al.* (2004).

5.4 Comparison with data from the literature

We shall compare the permeability function (5.37) to experimental permeability–porosity relationships. *Freitag* (1999), *Eicken et al.* (2002) and *Freitag and Eicken* (2003) have performed *in–situ* bail–test measurements of the permeability of sea ice. *Freitag* (1999) fits vertical permeability data with a power law expressed as a function of effective porosity f_e. Possible systematic errors in the determination of permeability and porosity are discussed by *Freitag* (1999) and by *Eicken* (1991), and will be omitted from the following.

Close to the percolation threshold, f_c, only a fraction of the brine inclusions in a sea ice sheet actually participate in fluid motion. Consequently, we face the challenge of trying to compare our permeability which is a function of the total porosity f_t, with a permeability function of *Freitag* that depends on the effective porosity f_e. We will therefore introduce a model in Section 5.4.2 and in Section 5.4.3 and use this to estimate a relationship between f_t and f_e. Further, our permeability function is isotropic, while *Freitag* (1999) and *Eicken et al.* (2004) give relationships for the vertical component. We estimate the vertical component of our isotropic permeability in the following section.

5.4.1 Vertical permeability component

Having found an isotropic permeability for sea ice, Π, that is suitable for CFD modelling, we now estimate the corresponding vertical permeability component, Π_v, that is suitable for comparison with data in the literature. A transformation between characteristic permeability and the vertical permeability component has previously been applied to experimental data (*Freitag*, 1999; *Freitag and Eicken*, 2003; *Eicken et al.*, 2004). However, that transformation is designed for a flow path not applicable to natural desalination of sea ice.

In order to estimate the vertical component of the permeability, we will assume that a typical desalination path exists, and furthermore that the relationship between horizontal $\Pi_{h1,2}$ and vertical Π_v permeability components is well defined (Figure 5.7). *Freitag* (1999) reports that even horizontal sea ice permeability is anisotropic, and reports, for extreme cases, up to almost one order of magnitude difference between the

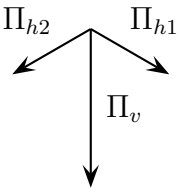

Figure 5.7: Perpendicular components of sea ice permeability Π_{h1} and Π_{h2} horizontally, and Π_v vertically.

two components Π_{h1} and Π_{h2}. However, for simplicity we follow *Freitag and Eicken* (2003) by assuming that the relationship between the three orthogonal permeability components in sea ice can be expressed as

$$\Pi_{h1} = \Pi_{h2} = \frac{1}{\kappa}\Pi_v, \tag{5.40}$$

where κ is the ratio of vertical and horizontal permeability, and the permeability is horizontally isotropic.

Similar to *Freitag and Eicken* (2003), we further neglect variations of the permeability along the desalination flow path other than due to anisotropy. We define the flow resistance R as

$$R \propto \frac{1}{\Pi}. \tag{5.41}$$

The resistance to flow in direction ϕ along an infinitesimal line element ds (Figure 5.8) is

$$R(\phi)\, ds = \left[\left(R_h \cos\phi\right)^2 + \left(R_v \sin\phi\right)^2\right]^{1/2} ds, \tag{5.42}$$

where R_h and R_v are proportional to the reciprocals of the horizontal and vertical permeability, respectively. We then calculate the average flow resistance along flow path l from

$$R_{avg} = \frac{1}{l}\int_l R(\phi(s))\, ds. \tag{5.43}$$

For the simple case of a path of inflowing seawater and outflowing brine that resembles a half circle (i.e. a simplification of the path sketched by *Worster* (1992) and by *Wettlaufer et al.* (1997)) as illustrated in Figure 5.8, R_{avg} is expressed as

$$R_{avg} = \frac{1}{\pi}\int_{\pi/2}^{3\pi/2} \left[\left(R_h \cos\phi\right)^2 + \left(R_v \sin\phi\right)^2\right]^{1/2} d\phi. \tag{5.44}$$

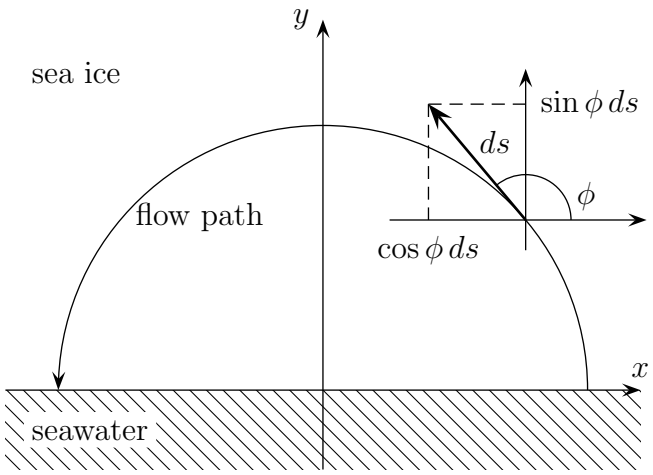

Figure 5.8: Schematic of the simplified typical desalination flow path used to estimate the relationship between isotropic permeability Π and vertical permeability component Π_v.

With $R_h = \kappa\, R_v$ from (5.40) it follows that

$$R_{avg} = R_v \frac{1}{\pi} \int_{\pi/2}^{3\pi/2} \left[1 + (\kappa^2 - 1)\cos^2\phi\right]^{1/2} d\phi. \tag{5.45}$$

Equation (5.45) shows that $R_{avg} = R_v$ for $\kappa = 1$, and that $R_{avg} = 2/\pi R_v$ for $\kappa \to 0$. Further, (5.45) can be approximated with less than 5 % error for $\kappa \geq 3$ by

$$R_{avg} = \frac{2\kappa + 0.5}{\pi}\, R_v \quad \text{for} \quad \kappa \geq 3, \tag{5.46}$$

so that from (5.41),

$$\Pi_v = \frac{2\kappa + 0.5}{\pi}\, \Pi \quad \text{for} \quad \kappa \geq 3. \tag{5.47}$$

From (5.47) we see that the half–circle flow path allows us to estimate the vertical permeability component Π_v directly from the isotropic permeability Π as a function of sea ice anisotropy κ. The permeability derived from (5.47) represents the upper limit on vertical permeability (with lower limit $\Pi_v = \Pi$), if the flow path is narrower than assumed. *Freitag* (1999) finds that the anisotropy κ of sea ice is $\kappa = 10$ to 100, which according to (5.47) leads to a vertical permeability that is higher than the isotropic permeability by a factor 7 to 64. *Freitag and Eicken* (2003) report a typical value of $\kappa = 10$. Our vertical permeability function is then

$$\Pi_v = 7 \times 10^{-10}\,\mathrm{m}^2\,(f_t - 0.054)^{1.2}. \tag{5.48}$$

5.4.2 Brine layer model

We seek a relationship between total porosity f_t and effective porosity f_e using a simple Monte Carlo model. Pockets, representing brine inclusions, are added into a domain, representing sea ice, and the relationship between total porosity and effective porosity is evaluated. This model is described next.

Monte Carlo models are used in percolation theory, which is a branch of probability theory that deals with properties of random media, usually close to a percolation threshold (*Broadbent and Hammersley*, 1957; *Berkowitz and Ewing*, 1998). Concepts of percolation theory have previously been applied to sea ice (*Golden et al.*, 1998; *Golden*, 2003) to explain the origin of the critical porosity (percolation threshold) f_c of sea ice, i.e. the porosity below that sea ice becomes virtually impermeable to fluid flow. *Cox and Weeks* (1975) report that no brine drainage from sea ice was observed for total porosities below $f_c = 0.05$. However, common two and three dimensional systems of randomly distributed conducting circles or spheres exhibit much larger critical porosities, i.e. $f_c \approx 0.6763$ and $f_c \approx 0.2896$ in two and three dimensions, respectively (*Baker et al.*, 2002). The precise value of the critical porosity has been found to depend on pocket shape (*de Bondt et al.*, 1992; *Xia and Thorpe*, 1988; *Garboczi et al.*, 1995; *Baker et al.*, 2002; *Yi and Sastry*, 2004), pocket distribution (*Rintoul*, 2000; *Blower*, 2001; *Consiglio et al.*, 2003; *Gaonac'h et al.*, 2003), and system dimension (*Thomsen*, 2002). For example, a reduction of the three dimensional percolation threshold to a value observed in sea ice is expected in media with randomly oriented ellipsoid pockets, approximately 15 times longer than wide, distributed throughout the domain (*Garboczi et al.*, 1995). *Golden et al.* (1998) choose a different explanation for the low percolation threshold in sea ice, exploiting the size ratio of sea ice platelets and brine pockets to account for this observation. In order to quantify their argument they apply a compressed powder model (*Kusy*, 1977). This compressed power model has been shown to be the limiting case of a simpler and more rigorous approach suggested by *Janzen* (1975) (*Janzen*, 1980). *Janzen* (1975) notes that percolation can sometimes be treated considering only the volume to which the pores have random access. *Blower* (2001) applies this idea to magmatic systems, where he discriminates between the porosity of the melt and the total porosity of a magmatic system that contains crystals.

Analytical considerations

Applying *Janzen* (1975) to columnar sea ice, we discriminate between a brine layer of width b that contains ice and brine pockets, and pure ice platelets of width $a_0 - b$, to which brine inclusions have no random access (Figure 5.9). This picture is not

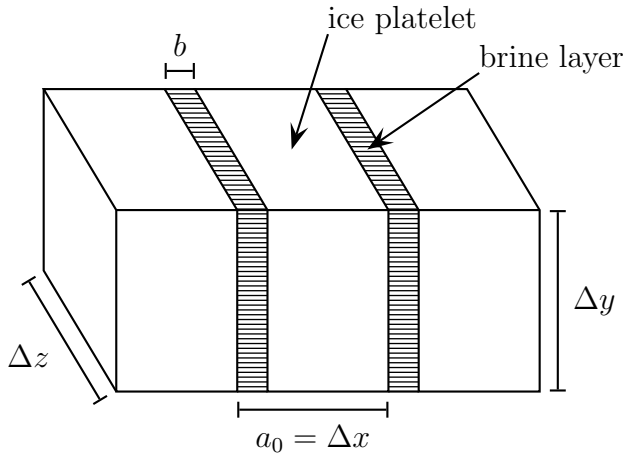

Figure 5.9: Schematic of the periodic stacking of brine layers and ice platelets in sea ice (sandwich model). The brine layer width is b, and the platelet spacing is $a_0 = \Delta x$.

applicable in the limit of high porosity, i.e. when b is variable, for example in the skeletal layer (Figure 1.4). We will account for this latter situation in Section 5.4.3, however.

With the total porosity of the brine layer, f_{bt}, a scaling relationship exists from percolation theory in infinite systems for the effective porosity in the brine layer, f_{be},

$$f_{be} \propto (f_{bt} - f_{bc})^{\beta} \quad \text{for} \quad f_{bt} \gtrsim f_{bc}, \tag{5.49}$$

where f_{bc} is the critical porosity of the brine layer, and β is some ("critical") exponent. Equation (5.49) is defined for f_{bt} larger but similar to f_{bc} (*Stauffer and Aharony*, 1992). The effective brine layer porosity f_{be} is zero for total brine layer porosities below the critical brine layer porosity. It is further known that the exponent $\beta = 5/36 \approx 0.139$ and $\beta \approx 0.41$ in two and three dimensional systems, respectively (*Stauffer and Aharony*, 1992; *Sahimi*, 1993). However, percolation theory does not predict the constant of proportionality.

Assuming that no pockets can be present in the ice platelets, simple relationships exist between brine layer porosity and total porosity from geometric considerations, i.e.

$$f_t = \frac{b}{a_0} f_{bt}, \tag{5.50a}$$

$$f_e = \frac{b}{a_0} f_{be}, \tag{5.50b}$$

$$f_c = \frac{b}{a_0} f_{bc}. \tag{5.50c}$$

Substituting (5.50) into (5.49), the expected relationship between effective porosity

and total porosity of sea ice is

$$f_e \propto \frac{b}{a_0}\left(f_t\frac{a_0}{b} - f_c\frac{a_0}{b}\right)^{\beta}, \tag{5.51}$$

$$f_e \propto \left(\frac{b}{a_0}\right)^{1-\beta}(f_t - f_c)^{\beta}. \tag{5.52}$$

Equation (5.52) suggests that the relationship between effective porosity f_e and total porosity f_t depends on the microstructure of sea ice: equation (5.50c) states that the critical porosity of sea ice, f_c, depends on sea ice microstructure, b/a_0, and on the critical porosity of the brine layer, f_{bc}. The latter could be a function of pore structure.

Since the constant of proportionality in (5.52) is still undetermined, we find a possible relationship between f_t and f_e from a Monte Carlo model, and compare that relationship with (5.52).

Description of the Monte Carlo model

In our model, the sea ice sheet is a cubical domain that is riddled with pockets shaped as rectangular boxes. Rectangular boxes are chosen as the exact calculation of total and effective volumes is possible and even trivial[11]. Pockets are aligned with the sides of the domain. The model is continuous, which means that no grid is used. In the course of the simulation, pockets are sequentially inserted into the domain at random locations[12]. The pockets have a "soft core", i.e. they may overlap. If pockets overlap they form a cluster. After a pocket has been added the total porosity f_t of the domain is calculated, accounting for pocket overlap, and the total volume that is occupied by clusters that connect to both the top boundary and the bottom boundary is determined (y–direction). The latter volume is the effective porosity f_e. The domain is periodic in x and in z–directions in order to reduce finite size effects. The computational algorithm is described in more detail in Appendix G.1.

The Monte Carlo model is validated by determining the critical porosity in both two and three dimensions. As shown in Appendix G.2, the critical porosities for squares in two dimensions and for cubes in three dimensions are determined to be $f_c = 0.667$ and $f_c = 0.277$, respectively. These results are in excellent agreement with the results

[11]The determination of the total volume fraction is trivial also in other cases: the total volume fraction of a large number of randomly oriented, convex, overlapping pockets of random shape can be calculated for an infinite domain from $f_t = 1 - \exp(-nV)$, where n is the number density of pockets and V is the volume of a pocket (*Mack*, 1956; *Gaonac'h et al.*, 1996).

[12]The random number generator used is *Mersenne Twister* (*Matsumoto and Nishimura*, 1998; *Nishimura*, 2000), implemented as `mt19937ar.c`, 26 January, 2002, by Makoto Matsumoto and Takuji Nishimura with 53 bit number generation due to Isaku Wada.

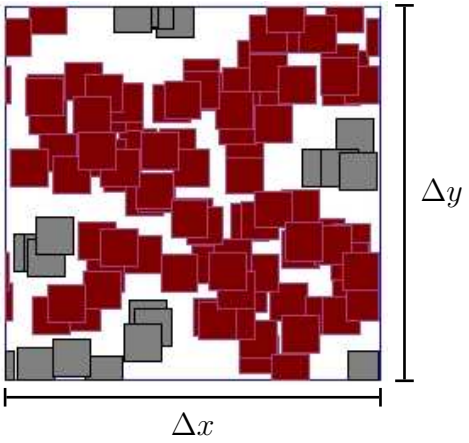

Figure 5.10: Example of a two–dimensional domain of the Monte Carlo model at the percolation threshold. The domain size is 10×10, and the pocket size is 1×1. The dark pockets form a cluster that connects the top with the bottom. They define the effective porosity f_e. All pockets contribute to the total porosity f_t. This particular example shows 112 pockets in 7 clusters at a total porosity of $f_t = 0.65$, $f_e = 0.54$, periodic boundaries are imposed horizontally.

of *Baker et al.* (2002), who use a method more suitable for the determination of the critical porosity (*Leath*, 1976) (Appendix G.2).

For the sake of illustration, Figure 5.10 gives an impression of a small domain in two dimensions. Domain sizes, here 10×10, are given in multiples of the pocket size, which will always be 1×1 and $1 \times 1 \times 1$ in two and three dimensions, respectively. In the example of Figure 5.10 a total number of 112 pockets had to be added in order to reach the critical porosity, which is $f_c = f_t = 0.65$ in this particular case. The effective porosity is $f_e = 0.54$. In finite domains, the critical porosity f_c is only defined as an average critical porosity $\bar{f}_c$ (*Berkowitz and Ewing*, 1998) with a distribution illustrated in Appendix G.2. However, in the following, we use domains large enough to approximate infinite domains.

We exploit the platelet structure of sea ice when simulating a percolating system with a percolation threshold far below that of two and three–dimensional systems. The platelet structure is approximated by a sandwich layer model of alternating brine layers and ice platelets as illustrated in Figure 5.9 and described by *Perovich and Gow* (1996). An attempt is made to add pockets to the domain at random locations. If they fall completely into a brine layer, treatment is as before in a three–dimensional domain. If they partially or completely fall into the domain of a platelet, however, they are added only if they connect to an existing cluster.

The physical significance of this difference is that we allow clusters to come into existence and to grow in brine layers, while, in platelets, clusters are only allowed to grow. The cluster creation is similar to an observation of *Perovich and Gow* (1996). At

first glance they find, upon warming, that brine inclusions seem to appear at random locations. Closer investigation, however, revealed that inclusions already existed at those locations, but that their sizes were below the detection limit. A similar observation has been made by *Eicken et al.* (2000). The insertion of pockets into the brine layers is therefore equivalent to pre–existing brine inclusions reaching the detection limit[13]. On the other hand, the prohibition of pocket insertion in the platelet regions means that the only way for inclusions to interfere with the platelets is by melting or dissolving into them (*Woods*, 1992).

We anticipate that this model will produce a percolation threshold f_c that can be calibrated by adjusting brine layer thickness b and platelet spacing a_0 of the stacking sequence in Figure 5.9 following (5.50c). Further, we expect that the model will yield the desired relationship $f_e = f_t$ for $f_t \to 1$, i.e. in the skeletal layer.

5.4.3 Relationship between effective porosity and total porosity

Simulated relationships

We will discuss the relationships between total porosity and effective porosity determined for two–dimensional and in three–dimensional domains, and in the sandwich domain of Figure 5.9.

Figures 5.11(a) and (b) show the relationship between effective porosity f_e and total porosity f_t for three example calculations: a two–dimensional domain of 2000×2000, a three–dimensional domain of $200 \times 200 \times 200$, and a sandwich domain of $a_0 = \Delta x = 1000$, $b = 195.1$, and $\Delta y = \Delta z = 200$, respectively. The relationship between a_0 and b has been selected to yield a critical porosity of $f_c = 0.054$, which is the critical porosity that we use in the permeability function (5.37).

It is clear from Figure 5.11(a) that a relationship $f_e = f_t$ is approached for $f_t \gg f_c$. Figure 5.11(b) shows the relationship between f_e and $f_t - f_c$. From percolation theory it is expected that

$$f_e = \alpha \left(f_t - f_c\right)^{\beta} \quad \text{for} \quad f_t \gtrsim f_c, \tag{5.53}$$

where $\beta \approx 0.14$ in two dimensions, and $\beta \approx 0.41$ in three dimensions (*Stauffer and Aharony*, 1992; *Sahimi*, 1993), and α is a constant of proportionality (cf. equation (5.52)). The straight portions of the double logarithmic plot of Figure 5.11(b)

[13]We also confirm that there is no apparent difference in the $f_e(f_t)$ relationship generated by models that add pockets to a two–dimensional or three–dimensional domain at random, and by models that continuously expand pockets in size. However, the latter method can be computationally much more expensive.

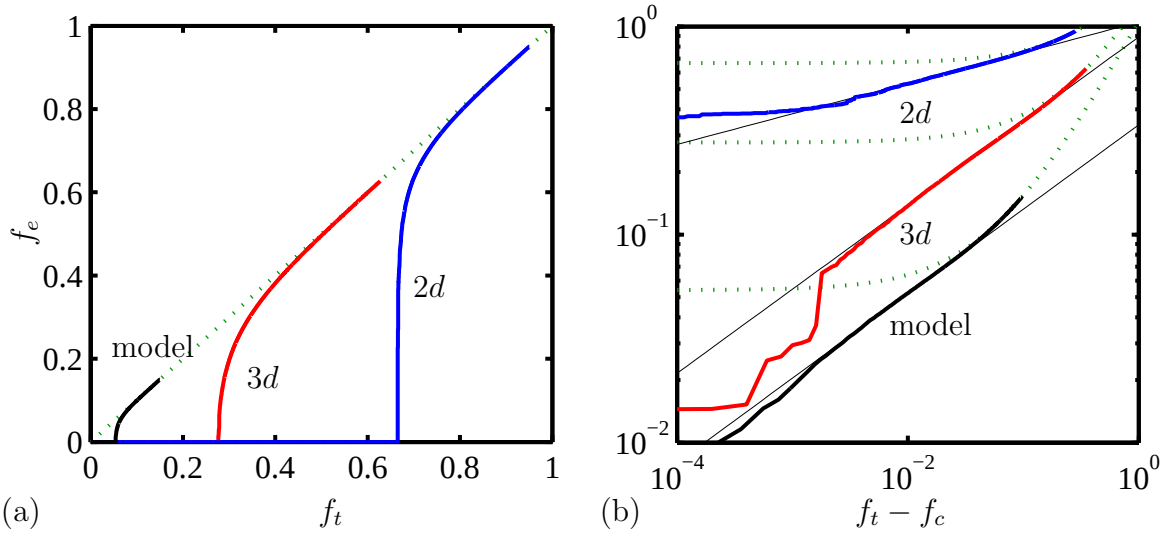

Figure 5.11: Effective porosity f_e as a function of (a) total porosity f_t, and (b) total porosity above critical porosity $f_t - f_c$ for the cases of two–dimensional ($2d$), three-dimensional ($3d$), and sandwich model domains. The dotted lines follow $f_e = f_t$. The critical porosity f_c appropriate for each domain is used in (b). The thin lines in (b) are the best fit power law functions (5.53) with parameters listed in Table 5.2. Note the different scales in (a) and (b).

Table 5.2: Parameters α and β determined from the percolation model in domains 2000×2000 ($2d$, squares), $200 \times 200 \times 200$ ($3d$, cubes), and in the sandwich domain ($a_0 = 1000$, $b = 195.1$, $\Delta y = \Delta z = 200$).

	$2d$	$3d$	sandwich
fit interval $f_t - f_c$	$[2, 6] \times 10^{-2}$	$[1, 10] \times 10^{-2}$	$[3, 30] \times 10^{-3}$
α	1.050	0.890	0.337
β	0.149	0.404	0.406
f_c	0.667	0.277	0.0540

can be approximated by the power law (5.53) with best–fit parameters summarised in Table 5.2. The parameters α and β are determined from averages of three runs each that produced a critical porosity to within ± 0.001 of the expected value for the cases of two and three dimensions. The parameters for α, β, and f_c for the sandwich model are averages of 16 runs. We see that the exponents β are close to the expectations for two and three–dimensional systems, respectively. Since finite size effects may still be present, and since the values of the fit parameters depend slightly on the choice of the interval used for fitting (given in Table 5.2), we accept this discrepancy between the current and the literature values.

With parameters from Table 5.2 for the sandwich model, the relationship between

effective and total porosities is

$$f_e = \begin{cases} 0 & \text{for} \quad f_t \leq 0.054, \\ 0.34\,(f_t - 0.054)^{0.41} & \text{for} \quad 0.054 < f_t \leq 0.09, \\ f_t & \text{for} \quad 0.09 < f_t, \end{cases} \tag{5.54}$$

where $f_t = 0.09$ is the porosity at which the discontinuity in f_e is minimised. (Equation (5.54) has a discontinuity in f_e of 3×10^{-3} at $f_t = 0.09$. The discontinuity can be reduced to 4×10^{-4} by choosing $\alpha = 0.35$ and a transit porosity of 0.091, or to 4×10^{-6} with $\alpha = 0.3516$ and transit porosity 0.0915.)

Using α, β, and $f_{bc} = f_c$ determined for the three–dimensional system, and $b = 195.1$ and $a_0 = 1000$ from the sandwich model it is expected from (5.50c) and (5.52) that

$$f_e = \alpha \left(\frac{b}{a_0}\right)^{1-\beta} \left[f_t - \frac{b}{a_0} f_{bc}\right]^{\beta}, \tag{5.55}$$

$$f_e = 0.336\,(f_t - 0.054)^{0.404}. \tag{5.56}$$

Parameters in (5.54) and (5.56) differ by less than 0.5 % for $f_t \gtrsim 0.054$, which confirms the consistency of analytical and Monte Carlo calculations. Since we neglected dissolution of platelets in the derivation of (5.56), this indicates that the simulated dissolution of ice platelets (i.e. clusters growing into platelets) is slow.

Discussion of model parameters

Parameters a_0 and b We have selected a ratio between brine layer width and platelet spacing of $b/a_0 = 195.1/1000$ that results in a critical porosity of 0.054 for the sandwich model. We will now check whether this ratio is realistic for sea ice.

Anderson and Weeks (1958) analyse the transition from skeletal layer to consolidated ice from horizontal sections through laboratory grown saltwater ice sheets. The brine film is found to decompose into distinct pockets when it reaches a width of $b = 70\,\mu$m. *Anderson and Weeks* infer, from the relationship between the width of the emerging brine pockets, b, and the separation of the pockets, that the splitting event is controlled by surface tension. With a platelet width $a_0 = 460\,\mu$m of the ice investigated, this splitting event happened at a porosity of $f_t \approx 0.15$. *Eicken et al.* (1998) give the mean horizontal pore space area of inclusions at the porosity *Anderson and Weeks* observe brine layer decomposition as $0.096\,\text{mm}^2$ (at $f_t = 0.154$, platelet width a_0 is not given). After estimating the aspect ratio of the inclusions we may transform the pore space area into a brine layer width. *Cole and Shapiro* (1998) measure the

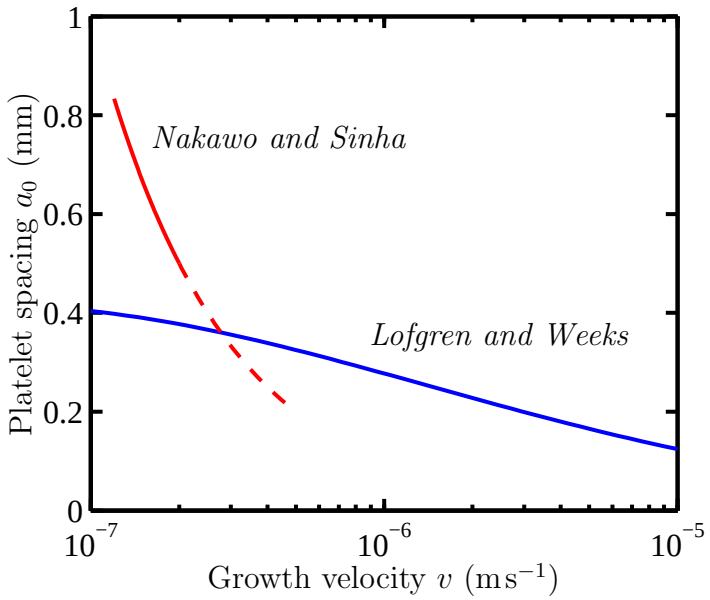

Figure 5.12: Platelet spacing a_0 as a function of sea ice growth velocity v determined by *Lofgren and Weeks* (1969) and *Nakawo and Sinha* (1984), respectively. The broken line is an extrapolation of data.

horizontal aspect ratio of brine inclusions larger than approximately 100 μm in sea ice at different times of the year. Their graphs suggest that the aspect ratio is mostly between 1 and 5, and typically 2 to 4. Later measurements result in an aspect ratio of 2.8 ± 1.3 (*Cole et al.*, 2004). Assuming an elliptical cross section for the pores, the cross sectional pore area can be related to the lengths of major and minor axes of the inclusions[14]. With a pore aspect ratio between 2 and 4, measurements of *Eicken et al.* (1998) therefore suggest a brine layer thickness of about $b = 100 \pm 30\,\mu$m, which is consistent with *Anderson and Weeks* (1958).

Assuming a brine layer width of $b = 70\,\mu$m, we question is whether a platelet spacing of $a_0 = 70\,\mu\mathrm{m} \times 1000/195.1 = 360\,\mu$m is a reasonable value for sea ice. Platelet spacings have been measured in laboratory grown saltwater ice (*Anderson and Weeks*, 1958; *Assur and Weeks*, 1964; *Lofgren and Weeks*, 1969) and in Arctic ice (*Nakawo and Sinha*, 1984). *Lofgren and Weeks* (1969) and *Nakawo and Sinha* (1984) give fitted relationships between the platelet spacing a_0 and the growth velocity v of the ice that are plotted in Figure 5.12. The parametric relationship of *Lofgren and Weeks* is

$$\log_{10}(a_0^{cm} v^{cm}) = -4.069 - 0.093 \left(\log_{10} v^{cm}\right)^2, \tag{5.57}$$

where a_0^{cm} and v^{cm} are the platelet spacing in cm, and the growth velocity in $\mathrm{cm\,s^{-1}}$,

[14]The area of an ellipse is $A = \pi b^2 \gamma$, where b is the minor axis of the ellipse, and $\gamma = a/b$ the aspect ratio with major axis a.

respectively. The relationship found by *Nakawo and Sinha* for all but two data points is

$$a_0 v = 1 \times 10^{-10}\,\mathrm{m^2\,s^{-1}}. \tag{5.58}$$

Both functional descriptions show that a platelet spacing of $a_0 = 360\,\mu\mathrm{m}$ can be expected at a growth velocity $v = 2.8 \times 10^{-7}\,\mathrm{m\,s^{-1}}$, which is a reasonable growth velocity for sea ice.

Note that *Lofgren and Weeks* (1969) find a virtually constant platelet separation, a_0, at small growth velocities, and that *Anderson and Weeks* (1958) define one brine layer width that, combined with the sea ice sandwich model (5.50c) for a three–dimensional system lead to a critical porosity of sea ice of about 0.05, which is what *Cox and Weeks* (1975) observe. The assumed sea ice structure is therefore consistent with those three laboratory studies.

Exponent β The exponent β for the sandwich model coincides with $\beta = 0.41$ expected in three dimensions. This implies that percolation in the brine layers of the sandwich model has a strong three–dimensional character, which again (cf. page 153) cautions against the interpretation of the exponent of 1.2 in the permeability–porosity relationship as suggesting a two-dimensional percolating system. It may further be noted, that in lattice percolation systems, that even two–dimensional systems that are only weakly coupled in three dimensions exhibit three dimensional characteristics in infinite domains (*Thomsen*, 2002).

Approximation of the best fit curve

The model has predicted that we can expect an exponent $\beta = 0.41$ in the relationship between effective and total porosity for $f_t \gtrsim f_c$, and that the relationship between effective and total porosity follows

$$f_e = \begin{cases} \alpha(f_t - f_c)^\beta & \text{for} \quad f_c < f_t \leq f_x, \\ f_t & \text{for} \quad f_x < f_t, \end{cases} \tag{5.59}$$

where (5.59) and the first derivative are continuous at a transfer porosity f_x. Equation (5.59) and the assumptions of continuity will generally not apply exactly, possibly not even in good approximation. However, they apply approximately in the three examples considered in this chapter, and apparently even for anisotropic pockets in infinite domains investigated in Appendix G.4.

We possess enough information to calculate α and f_x directly if f_c and β are given. From the continuity of f_e at f_x it follows that

$$f_x = \alpha(f_x - f_c)^\beta, \tag{5.60}$$

and from the continuity of the first derivative it is at f_x

$$1 = \alpha\beta(f_x - f_c)^{\beta-1}. \tag{5.61}$$

Dividing (5.61) by (5.60) we find

$$f_x = \frac{f_c}{1-\beta}, \tag{5.62}$$

and substituting (5.62) into (5.61) we further see that

$$\alpha = \frac{1}{\beta}\left(f_c\frac{\beta}{1-\beta}\right)^{1-\beta}. \tag{5.63}$$

For a random percolating system in three dimensions ($\beta = 0.41$) with $f_c = 0.054$ we can calculate from (5.62) and (5.63) that $\alpha = 0.3516$ and $f_x = 0.09153$. In the two ($\beta = 0.139$, squares $f_c = 0.667$) and three ($\beta = 0.41$, cubes $f_c = 0.277$) dimensional cases we have $\alpha = 1.056$ and $\alpha = 0.923$, respectively.

Experimental data relating effective porosity to total porosity have been obtained for compressed calcite aggregates (*Zhang et al.*, 1994). Comparing measurements of total and effective porosity, *Zhang et al.* find that $f_e = f_t$ for high porosities, but deviates from equality for $f_t < f_x = 0.07$. They further note that the effective porosity vanishes for total porosities below $f_t \leq f_c = 0.04$. While they do not discuss the relationship between f_c and f_x, we note that their observation is consistent with (5.62) with $\beta = 0.41$.

5.4.4 Comparison

Next, we will compare the permeability function obtained in this chapter with borehole bail test measurements in the Arctic (*Freitag and Eicken*, 2003) of sea ice permeability given by *Freitag* (1999) and by *Eicken et al.* (2004). Studies of other groups exist (see summaries by *Maksym and Jeffries* (2000) and *Freitag and Eicken* (2003)), but we focus on the above studies as they give explicit expressions for permeability–porosity relationships.

Freitag (1999) gives[15] two relationships between the vertical permeability and effective porosity, for young first–year sea ice,

$$\Pi_v = 3 \times 10^{-8}\,\mathrm{m}^2\, f_e^{3.9} \quad \text{for} \quad 0.05 \leq f_e \leq 0.2, \tag{5.64}$$

and for old first–year, multiyear, and ridged sea ice,

$$\Pi_v = 6 \times 10^{-10}\,\mathrm{m}^2\, f_e^{1.6} \quad \text{for} \quad 6 \times 10^{-4} \leq f_e \leq 0.6. \tag{5.65}$$

Data scatter by ± 0.5 orders of magnitude in the case of young first–year sea ice, and by ± 1 order of magnitude in the case of old sea ice.

Eicken et al. (2004) give the following best fit line for the (presumed) vertical permeability as a function of total porosity,

$$\Pi_v = \begin{cases} 4.708 \times 10^{-14}\,\mathrm{m}^2\, \exp(76.90\, f_t) & \text{for} \quad f_t \leq 0.096, \\ 3.738 \times 10^{-11}\,\mathrm{m}^2\, \exp(7.265\, f_t) & \text{for} \quad f_t > 0.096. \end{cases} \tag{5.66}$$

However, no data are shown, nor are the outer limits of the porosity range stated.

The vertical permeability–effective porosity relationships (5.48) (this work, scaled with (5.54)), (5.64) (*Freitag*, young), (5.65) (*Freitag*, old), and (5.66) (*Eicken et al.*, scaled with (5.54)) are compared in Figure 5.13. The vertical permeability predicted from the current work is bounded by the best fit lines of *Freitag* (1999) on the lower side, and by measurements of *Eicken et al.* (2004) on the higher side. The permeability predicted by the functions shown differs markedly in the limit of low effective porosities f_e.

The vertical permeability–total porosity relationships (5.48) (this work), (5.64) (*Freitag*, young, scaled with (5.54)), (5.65) (*Freitag*, old, scaled with (5.54)), and (5.66) (*Eicken et al.*) are compared in Figure 5.14. Also plotted for reference are the data of *Cox and Weeks* (1975) on which the permeability function of this work is based, scaled according to the development in Section 5.4.1. Even when allowing for scatter of data of *Eicken et al.* and young sea ice of *Freitag*, the young sea ice data of *Freitag* (1999) seem to be significantly lower than the measurements of *Eicken et al.* (2004). This difference is unlikely to be a result of the method used to convert between effective porosity and total porosity, since effective and total porosities are essentially the same for $f_t > 0.1$ (which is illustrated by the existence of brine films rather than pockets for $f_t > 0.15$ (*Anderson and Weeks*, 1958)), while measured permeabilities seem to differ

[15]The constants of proportionality of the fit functions given by *Freitag* (1999) have been adjusted to match the graphs shown by *Freitag* (1999).

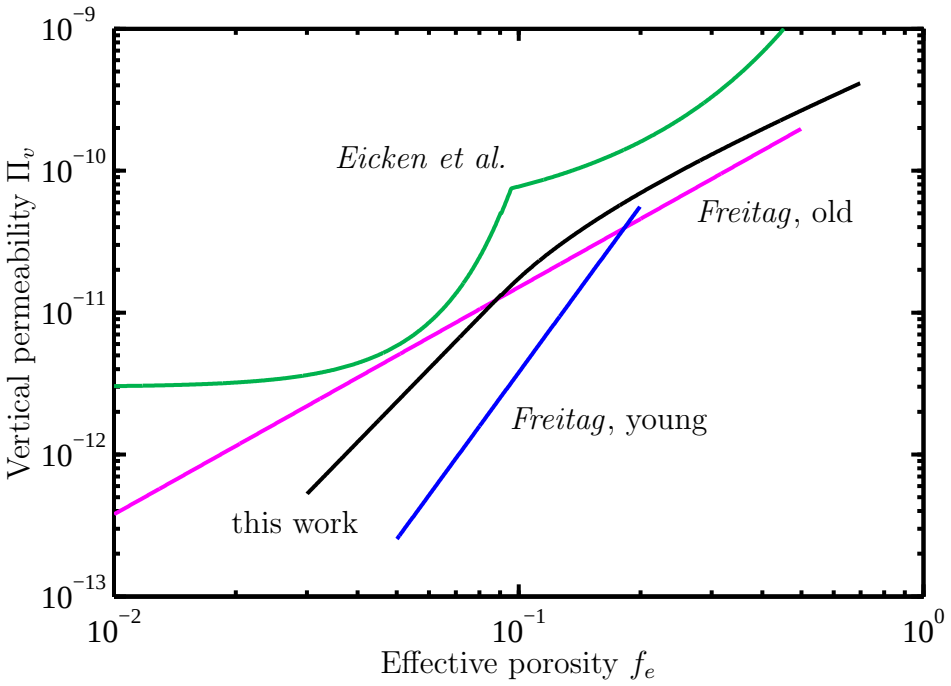

Figure 5.13: Vertical permeability as a function of effective porosity.

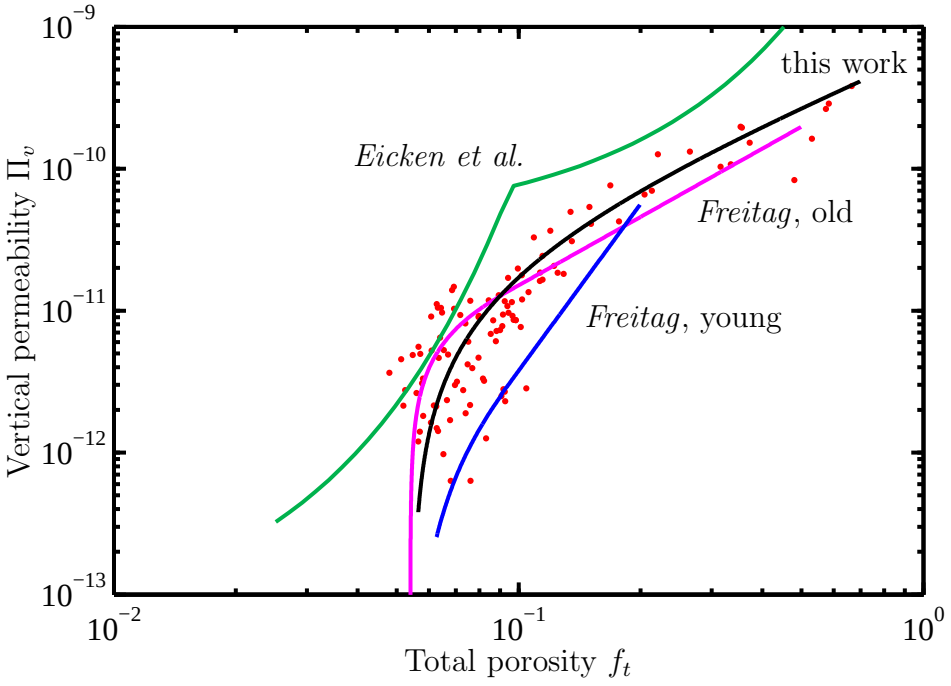

Figure 5.14: Vertical permeability as a function of total porosity. Data points are the scaled data of *Cox and Weeks* (1975).

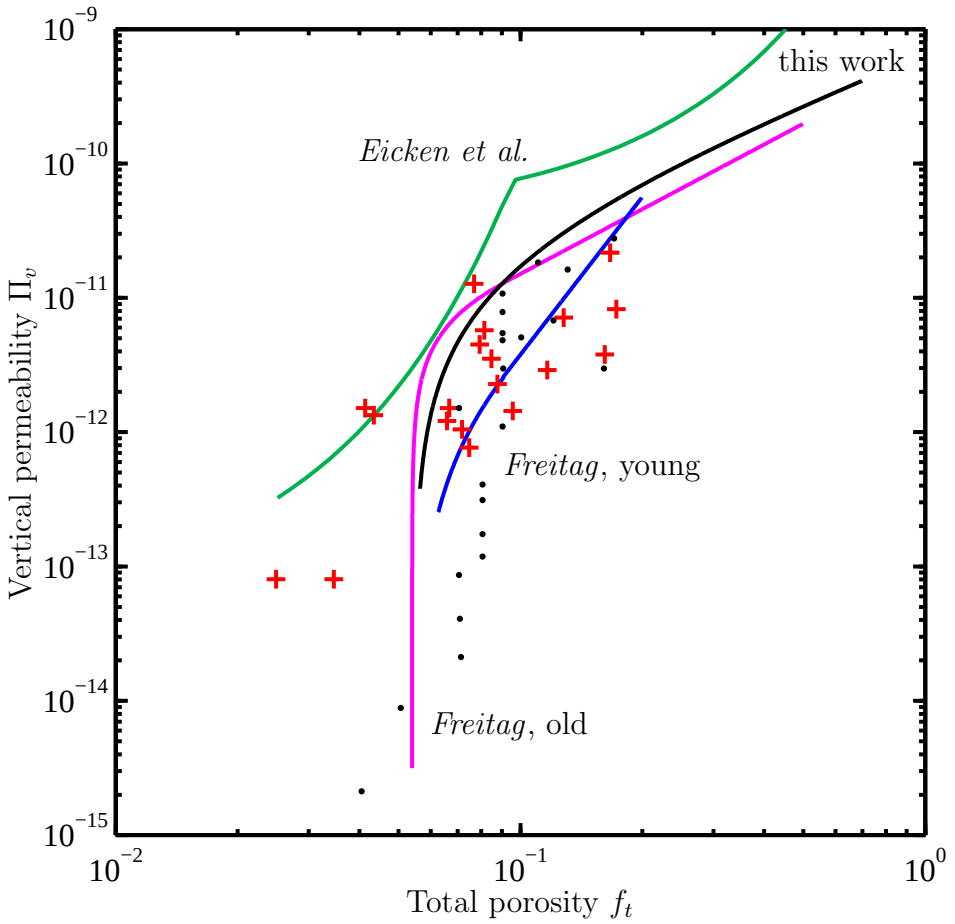

Figure 5.15: Vertical permeability as a function of total porosity. Data based on porosity measurements (pluses) and estimates (dots) are taken from the compilation of *Maksym and Jeffries* (2000).

in that range. The difference between the measurements of *Freitag* (1999) in young first–year sea ice, and the measurements of *Eicken et al.* (2004) may be related to differences in the ice investigated, or to methodological differences. A discussion does not seem to be warranted as the details of the measurements of *Eicken et al.* (2004) are not reported.

Maksym and Jeffries (2000) compile sea ice permeability measurements of three groups. They estimate the porosity of the investigated sea ice in two instances, where porosity measurements were not given. Figure 5.15 compares their compilation of data (data are taken from figure 3 of *Maksym and Jeffries* (2000)) with the the present permeability parameterisation and the parameterisations of *Freitag* (scaled with (5.54)) and *Eicken et al.*. Data given by *Maksym and Jeffries* are in the same range as the four permeability–porosity relationships. However, data scatter too much to derive an unambiguous functional dependence.

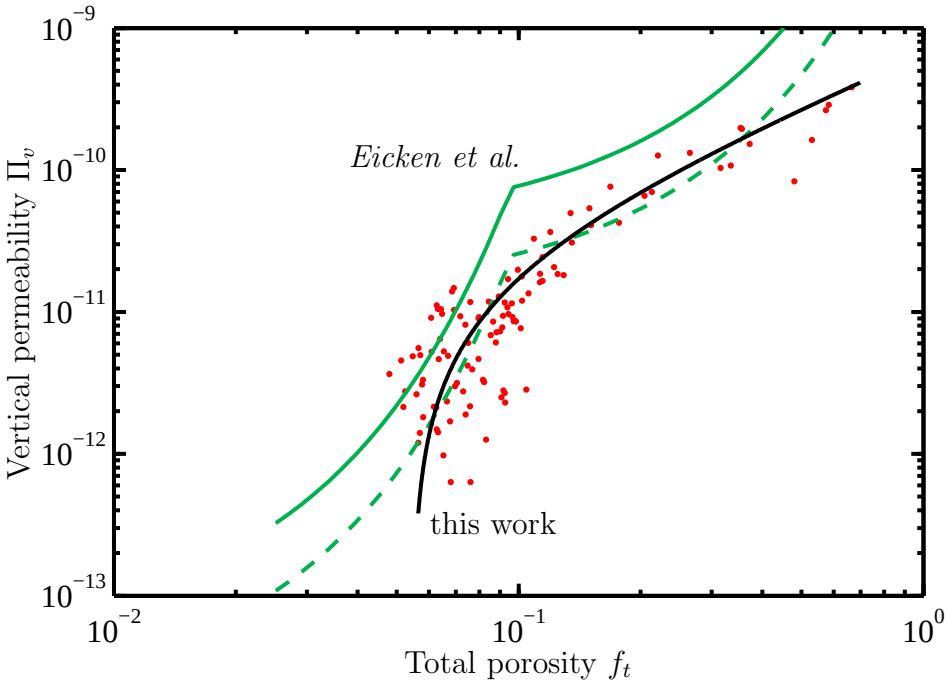

Figure 5.16: Vertical permeability as a function of total porosity. The broken line is the function of *Eicken et al.* (2004) divided by three. Data points are the scaled data of *Cox and Weeks* (1975).

Figure 5.16 illustrates the similarity of the present permeability–porosity relationship (5.48) with the relationship given by *Eicken et al.* (2004) by dividing the latter arbitrarily by three. Both functions fit the *Cox and Weeks* data equally well in the porosity interval $0.06 \leq f_t \leq 0.4$. Again, it would be necessary to know the data (in particular the range of porosities) underlying the function of *Eicken et al.* for a more sophisticated comparison.

5.5 Summary and conclusion

We have found a permeability–porosity $\Pi(f_t)$ relationship from existing experimental data that allows us to calculate at least the one–dimensional salinity profile of sea ice during growth conditions using the fluid dynamics model of Chapter 4. We have compared this relationship with results given by *Freitag* (1999) for the effective porosity f_e and *Eicken et al.* (2004) for total porosity f_t. The agreement is satisfactory.

In addition to the permeability–porosity relationship we have deduced a relationship between stable distribution coefficient k_{eff}^{stable} and sea ice growth velocity v from the model of *Cox and Weeks* (1988). The functional dependence is found to be the same as the empirical fit given by *Kovacs* (1996). However, a systematic discrepancy in

absolute values is apparent. It is thought that the difference is related to systematic differences in the growth conditions of the ice.

We have further estimated a relationship between a sea ice isotropic permeability Π and the vertical component Π_v assuming that desalinating brine flow in young sea ice follows a half–circle.

Lastly, we obtained a relationship between effective porosity f_e and total porosity f_t from a Monte Carlo model supposing a simplified structure of sea ice (columnar; random distribution of equally sized, overlapping pockets; infinite domain size). The result is consistent with predictions from percolation theory, and we find that it can be approximated as a function of critical porosity f_c. We noted that the assumed sea ice structure of this model is consistent with the set of measurements of *Anderson and Weeks* (1958), *Lofgren and Weeks* (1969), and *Cox and Weeks* (1975).

General conclusions that arise from the observations are that scattered permeability data can be fitted to many different functions. It would be nice to have a theoretical foundation for the fit function for the case of sea ice. Such a theory could possibly limit the range of its applicability. Further, a consistent, generally valid picture of structure and properties of laboratory grown or naturally grown sea ice does not seem to exist yet. Clearly, more work is needed.

Chapter 6

Numerical simulations of crack refreezing

6.1 Overview

In this chapter the refreezing of cracks will be simulated with the numerical model of Chapter 4 using the permeability function derived in Chapter 5. The goal is to simulate desalination of refreezing cracks, as this aspect has not been investigated in previous chapters. However, the simulations in this chapter are closely linked to issues discussed previously: to the crystal structure at the sides of the cracks; to the definition of the sea ice freezing interface; to the progress of refreezing at the centre of the crack; to the heat balance of refreezing slots; to the effective and total porosity; and to sea ice permeability. The structure of this chapter is best explained after sketching out one of the results.

We will find in this chapter that crack refreezing and desalination can be simulated with the numerical model. We will also find that the freezing front tracking introduced in Section 4.4 still oversimplifies the freezing process at vertical interfaces. Freezing front tracking was introduced to ensure an abrupt boundary between a porous ice–brine matrix and seawater at its freezing point. This is achieved by requiring sea ice to consolidate to a certain extent (i.e. f to decrease to a prescribed value) before allowing the freezing front to move. However, this requirement causes supercooling of water ahead of the freezing front. Therefore, three approaches to sea ice formation will be followed in this chapter. One approach is to use the model as developed in Chapter 4, with the permeability–porosity relationship of Chapter 5. The second approach is to simulate freezing in the absence of fluid motion in the liquid (i.e. velocity components $u = v = 0$, where porosity $f = 1$), apart from motion that is necessary to obtain

mass conservation. With respect to refreezing cracks, the most significant difference between these is that the former approach leads to a significant advective heat exchange with the ocean, while the latter avoids the oceanic heat flux. The third approach is a compromise based on the results obtained from the first two approaches. It follows the model as outlined in Chapter 4, but disregards freezing front tracking of Section 4.4. This requires the permeability–porosity relationship of Chapter 5 to be modified for very high porosities. Results from this third approach are shown in order to support the conclusions drawn from the first two approaches.

This chapter is structured as follows. First, in Section 6.2 the underlying assumptions specific to the fluid dynamics simulations of this chapter are introduced. Section 6.3 discusses one–dimensional freezing front movement in the absence of convection in the liquid. This is done in order to test the methods of freezing front determination of Section 3.2.3, which will be applied in subsequent sections. The freezing front movement is further compared with the Stefan problem. In Section 6.4, simulations in two dimensions are performed under conditions similar to experiments *slot 1* and *slot 10*, as comprehensive experimental data are available for comparison. Section 6.4.1 introduces the two–dimensional domain used for the simulation of refreezing cracks. Following that, Section 6.4.2 compares the simulated refreezing process in the absence of convection in the liquid with data and the predictions of the analytical model of Section 3.2.4. Section 6.4.3 does the same for simulations in the presence of convection in the liquid and discusses the origin of the difference between the two approaches. Section 6.4.4 shows the freezing front progress without freezing front tracking. Simulated time series of the two–dimensional freezing fronts of refreezing cracks are compared in Section 6.4.5, similar to experimental data in Section 3.2.3. The simulated desalination of cracks is discussed in Section 6.4.6. Section 6.5 summarises the results of this chapter and makes recommendations for future work.

6.2 Basic methods and assumptions

Numerical simulations are performed with the model of Chapter 4, using the constants listed in Table 6.1.

The permeability is described by

$$\Pi = \begin{cases} \infty & \text{for} \quad f = 1, \\ \Pi_0 (f - 0.054)^{1.2} & \text{for} \quad 0.054 \lessapprox f < 1, \\ 10^{-14}\,\mathrm{m}^2 & \text{for} \quad f \lessapprox 0.054, \end{cases} \tag{6.1}$$

Table 6.1: Constants used in fluid dynamics calculations.

	magnitude	unit	comment
k_i	2.12	$\mathrm{W\,m^{-1}\,K^{-1}}$	thermal conductivity of ice
k_w	0.56	$\mathrm{W\,m^{-1}\,K^{-1}}$	thermal conductivity of water
c_i	2100	$\mathrm{J\,kg^{-1}\,K^{-1}}$	specific heat capacity of ice
c_w	4200	$\mathrm{J\,kg^{-1}\,K^{-1}}$	specific heat capacity of water
L	334×10^3	$\mathrm{J\,kg^{-1}}$	latent heat of fusion at 0 °C
ρ_i	920	$\mathrm{kg\,m^{-3}}$	density of pure ice
ρ_w	1000	$\mathrm{kg\,m^{-3}}$	density of water
D	3.6×10^{-10}	$\mathrm{m^2\,s^{-1}}$	solute diffusivity in water
μ	1.79×10^{-3}	$\mathrm{kg\,m^{-1}\,s^{-1}}$	dynamic viscosity of brine
g_y	-9.8	$\mathrm{m\,s^{-2}}$	vertical acceleration due to gravity
f_i	0.8		liquid volume fraction at the interface (Section 4.4)

with $\Pi_0 = 1 \times 10^{-10}\,\mathrm{m^2}$ unless otherwise stated. As discussed in Section 4.5.2, the permeability is never reduced below $\Pi = 1 \times 10^{-14}\,\mathrm{m^2}$ in simulations in this chapter for numerical reasons.

Disconnected brine pockets One further amendment is made to the model that has proven very useful in two–dimensional freezing processes. A non zero permeability never completely inhibits brine movement. As we have seen in Chapter 5, this is not a problem in the case of one–dimensional ice growth, where the pressure gradient is negligibly small compared to the friction in the low porosity regions. However, complete desalination is observed in simulations of two–dimensional growth close to the sides of the slot where large horizontal pressure gradients exist in the presence of large horizontal porosity inhomogeneities. The problem of excess desalination is related to the assumption that the model pore space is interconnected, which is probably not the case for natural sea ice of low porosity (Section 5.4.3). A method of retaining solute, while allowing fluid motion for mass conservation, is therefore employed.

In a rudimentary attempt to retain solute in almost impermeable numerical cells of low porosity, $f \leq f_c = 0.054$, (i.e. to simulate the presence of isolated brine pockets), advection, diffusion, buoyancy, and pressure forces are removed from the momentum equation, and the velocity is set to zero. The only term that remains is the Darcy friction term. This term influences the pressure correction equation (i.e. the mass conservation equation), where it allows fluid motion due to volume expansion[1]. This approach has not been used in the one–dimensional simulations of Chapter 5.

[1]Computationally, all contributions to transport coefficients of the discretised momentum conservation equations are set to zero (with the exception of the Darcy friction term) if either cell face of the staggered velocity cells (faces e and w for the u–component, and faces n and s for the v–component) is located in cells of porosity $f \leq f_c = 0.054$ (cf. Figure 4.2). See Appendix E.2 for details of the implementation.

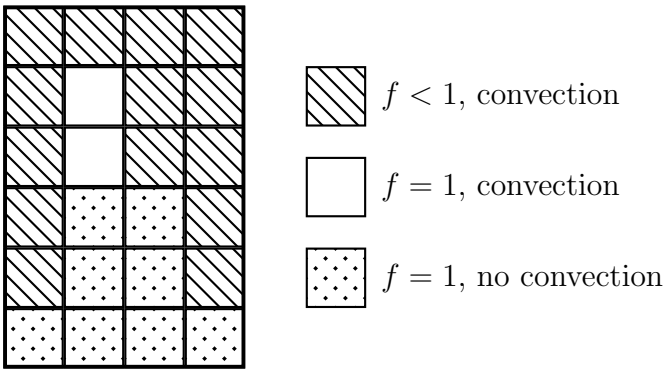

Figure 6.1: Illustration of a 4×6 domain with porous (hatched) and liquid (empty and dotted) cells in a simulation nominally without convection in the liquid. Fluid velocity components, u and v, are set to zero if they lead into liquid cells (dotted) that are adjacent to liquid cells both horizontally and vertically.

Simulations without convection in the liquid

Some simulations in this chapter consider ice growth without the advection of heat and solute carried by cold and possibly supercooled water. However, since volume expansion demands that fluid movement in the domain conserves mass, the following rule is applied: before and after the solution of the momentum conservation equations, velocity components u and v are set to zero at the faces of all cells that are completely liquid and that have at least one liquid neighbour in each of the horizontal and vertical directions (Figure 6.1). Fluid motion is permitted in liquid cells that are surrounded by porous cells as shown in Figure 6.1 as they are treated as part of the porous medium.

Simulations without freezing front tracking

In order to demonstrate the plausibility of conclusions drawn from simulations with and without convection, some simulations in this chapter are performed without freezing front tracking as described in Section 4.4. Without freezing front tracking, any supercooling of the liquid is unconditionally released by the formation of stationary ice. However, since the permeability expression (6.1) yields permeabilities for large liquid fractions that are unrealistically low, the following permeability expression is used,

$$\Pi = \begin{cases} \infty & \text{for} \quad f = 1, \\ 10^{-5}\,\mathrm{m}^2 & \text{for} \quad 0.9 \leq f < 1, \\ 10^{-10}\,\mathrm{m}^2 (f - 0.054)^{1.2} & \text{for} \quad 0.054 \lessapprox f < 0.9, \\ 10^{-14}\,\mathrm{m}^2 & \text{for} \quad f \lessapprox 0.054. \end{cases} \tag{6.2}$$

Both, the value of $\Pi = 1 \times 10^{-5}\,\mathrm{m}^2$ and the threshold porosity $f = 0.9$ are arbitrarily chosen since no data are available for such liquid fractions. With $\Pi = 1 \times 10^{-5}\,\mathrm{m}^2$, close to the freezing interface, the magnitude of the Darcy friction term is equal to one order of magnitude larger than the advection term in the vertical momentum conservation equation. Note that the discontinuity in Π at $f = 0.9$ is neither physical, nor is it numerically desirable.

6.3 One–dimensional freezing

6.3.1 Freezing without convection in the liquid

In this section, we will investigate the effect of the definition of the freezing front in one–dimensional freezing. One–dimensional freezing is simulated with seawater (34 psu) or freshwater initially at its freezing temperature. Heat is lost to a constant temperature interface that is 10 °C below the water temperature. To simplify the comparison with the Stefan problem, advection of seawater (and heat) is inhibited outside the mushy layer. The domain dimensions are 160 mm × 320 mm divided into 16 × 32 cells. The domain is periodic in the horizontal direction.

Three definitions of the freezing front are compared (Figures 6.2 to 6.4): a temperature depression of $\epsilon = 0.5\,°\mathrm{C}$ below the freezing point (triangles); comparative rate of temperature change approach ("ΔT", squares); a porosity of $f = 0.5$ (circles). The former two approaches are discussed in Section 3.2.3. The porosity threshold approach is employed as a reference, independent of temperature. Unfortunately, *Oertling and Watts* (2004) do not mention how they define the sea ice freezing front in their numerical simulations of ice sheet formation. However, judging from the salinity profiles they show, the location of their freezing interface probably corresponds to $f = 0.5 \pm 0.1$.

Temperatures and porosities are evaluated at the centre of the domain. For reference, the advance of the freezing front is treated as a Stefan problem (solid line) (*Carslaw and Jaeger*, 1986). An average porosity of the sea ice of $f = 0.08$, and a mean temperature reduction of the ice of 5 °C are used to find effective latent heats (Appendix H.1; *Yen*, 1981) of $L = 345\,\mathrm{kJ\,kg^{-1}}$ and $L = 324\,\mathrm{kJ\,kg^{-1}}$ for freshwater and seawater, respectively.

Freshwater ice Figure 6.2 shows the result of the simulation for the freshwater case. Defining the freezing front by $f = 0.5$ (circles) or by a constant offset from the freezing point results in equal agreement with the prediction of the Stefan problem. The comparative rate of temperature change approach overpredicts growth in the later

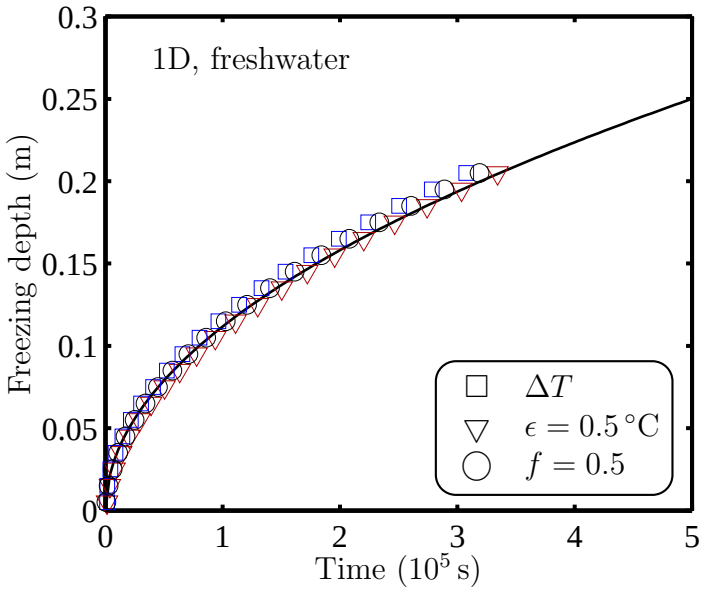

Figure 6.2: Simulated freezing front movement during one–dimensional freezing of freshwater.

stages by one computational cell. The freezing front determined with the constant temperature approach is independent of the exact choice of threshold in the range $0.1\,°C \leq \epsilon \leq 0.6\,°C$, i.e. any ϵ in this range would produce a negligible change.

Sea ice Figure 6.3 shows the result of the simulation for the seawater case with $\Pi_0 = 4 \times 10^{-10}\,m^2$. The definition of the freezing front porosity is again closest to the Stefan problem, slightly underpredicting the thickness. Again, the comparative rate of temperature change approach predicts freezing times that are too high. The temperature threshold approach yields early freezing times due to the supercooling of the water ahead of the freezing front that is not removed by frazil ice formation or by advection.

Figure 6.4 shows the result of the simulation for the seawater case with $\Pi_0 = 1 \times 10^{-10}\,m^2$. Due to the absence of convection in the liquid and the relatively low permeability, a temperature perturbation had to be introduced manually at the freezing front at $t = 7 \times 10^4\,s$ in order to trigger brine release. While the constant temperature threshold approach is again of little use due to supercooling, both the porosity approach and the comparative rate of temperature change approach trace the Stefan problem well, albeit with more scatter than at higher permeability (Figure 6.3).

The salinity profiles of the ice sheets of Figures 6.3 and 6.4 at $t = 4 \times 10^5\,s$ are illustrated in Figure 6.5. Salinity variations are mostly in the range $4\,psu \leq S_{ice} \leq 20\,psu$ in the case of $\Pi_0 = 4 \times 10^{-10}\,m^2$, and drainage features (columns of increased

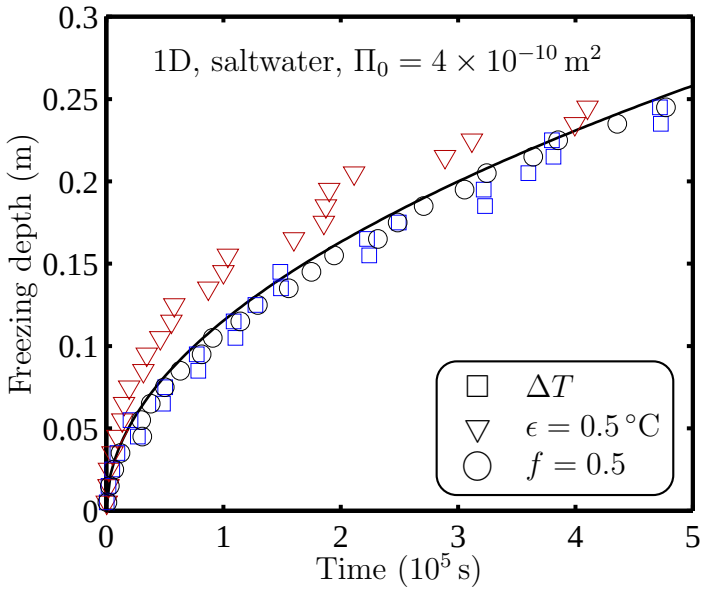

Figure 6.3: Simulated freezing front movement during one–dimensional freezing of seawater, assuming $\Pi_0 = 4 \times 10^{-10}\,\mathrm{m}^2$.

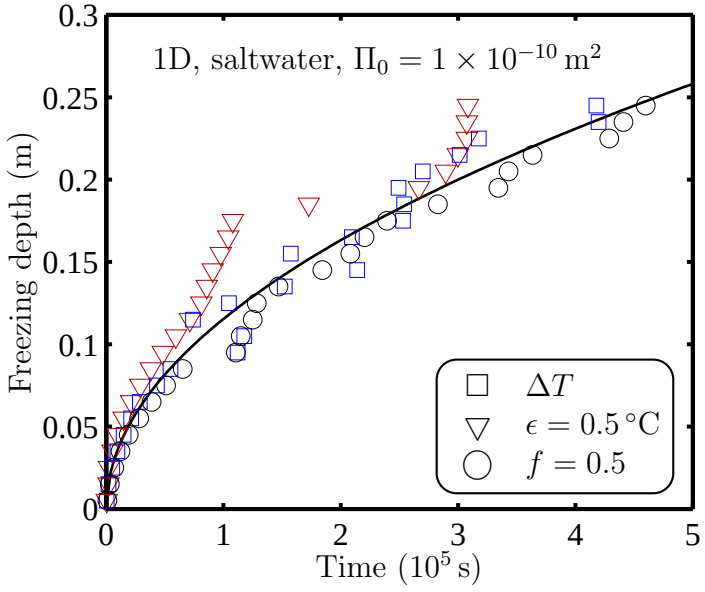

Figure 6.4: Simulated freezing front movement during one–dimensional freezing of seawater, assuming $\Pi_0 = 1 \times 10^{-10}\,\mathrm{m}^2$.

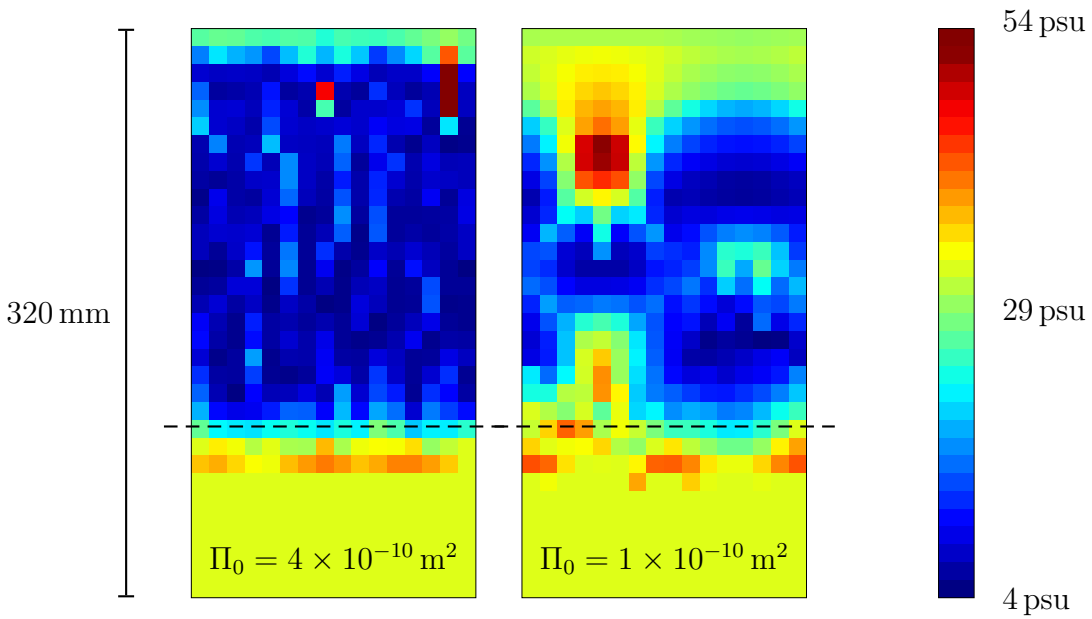

Figure 6.5: Salinity profiles at $t = 4 \times 10^5$ s for $\Pi_0 = 4 \times 10^{-10}\,\mathrm{m}^2$ and $\Pi_0 = 1 \times 10^{-10}\,\mathrm{m}^2$, respectively. The broken line indicates the approximate position of the consolidated front.

salinity) are one cell wide. The range of salinity variations is larger in the case of $\Pi_0 = 1 \times 10^{-10}\,\mathrm{m}^2$, and drainage systems are wider than one cell. A region of increased salinity about 80 mm below the surface bears witness to a zone of draining brine. The cusp of low salinity at the same level marks the region where seawater entered the ice sheet. The average salinity at the vertical centre of the ice sheet is approximately 13 psu, consistent with the expectations of the stable distribution coefficient (5.22).

In summary, we find that the temperature threshold approach is not suitable to determine the location of the freezing front in our numerical simulations due to the presence of supercooled water. However, both the porosity and comparative rate of temperature change approaches may be useful.

6.4 Two–dimensional freezing

6.4.1 Overview

The refreezing of *slot 1* and *slot 10* is simulated next. In this section, the boundary conditions of the domain will be introduced as shown in Figure 6.6. Following that, the freezing front development in simulations in the absence (Section 6.4.2) and presence of convection (Section 6.4.3), and in the absence of freezing front tracking (Section 6.4.4) are analysed. Overviews of the development of the two–dimensional freezing front for

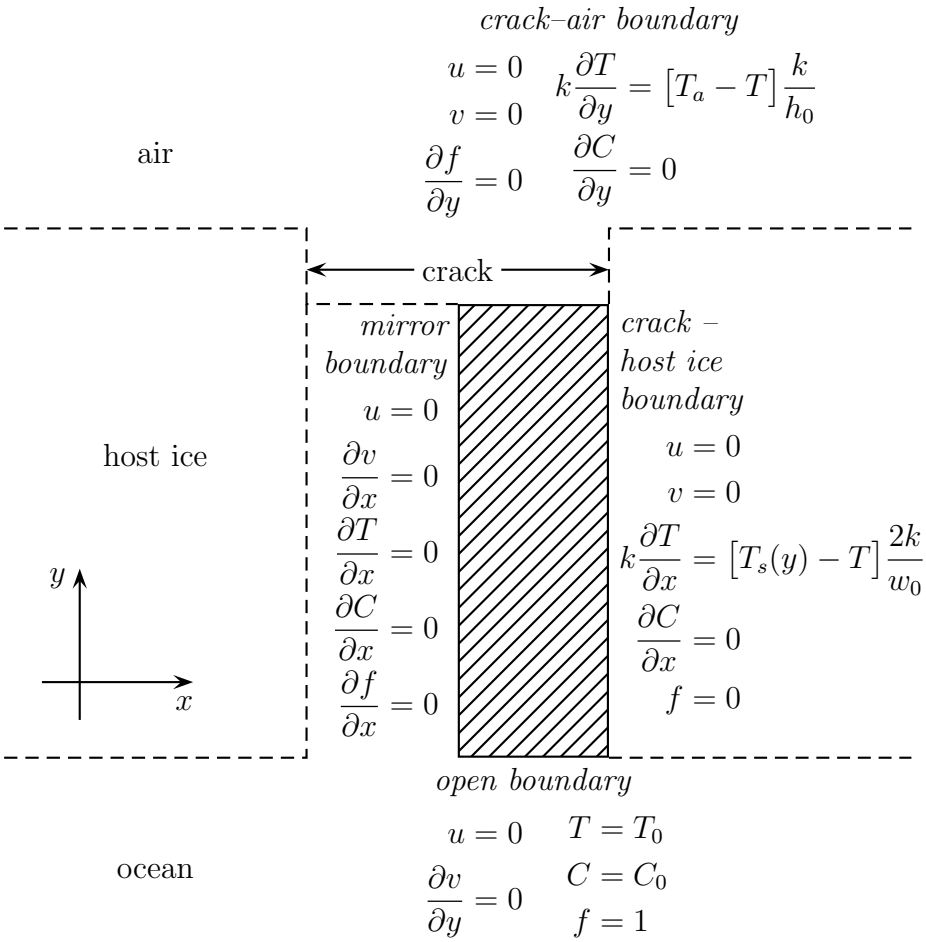

Figure 6.6: Boundary conditions of the two–dimensional domain (hatched). Only one half of the crack is simulated.

these cases are given in Section 6.4.5. Finally, the salinity profiles are discussed in Section 6.4.6, and conclusions are drawn in Section 6.5.

The conditions at the slot–air interface and at the slot–host ice interface are no–slip boundary conditions, with the condition for heat flux at the boundary determined by the analytical model in Section 3.2.4. The air temperature T_a and height h_0, resulting in heat transfer coefficient $\mathfrak{h} = k/h_0$, are spatially constant in each experiment. The reference temperature T_s for heat flux to the host ice follows the linear profile

$$T_s(y) = \left[T_a \frac{1}{1 + \frac{h_f}{H} + \frac{h_0}{H}} - T_0\right]\left(1 - \frac{y}{H}\right) + T_0, \tag{6.3}$$

where T_0 is the initial water temperature, h_f is the freeboard, and H the height of the ice sheet below freeboard. The width w_0 is defined as $w_0 = \gamma H$ with $\gamma = 0.5$. The boundary at the left hand side of the domain acts as a mirror, exploiting the symmetry

Table 6.2: Parameters used for the simulations of refreezing of *slot 1* and *slot 10* in Section 6.4.2.

	slot 1	*slot 10*
Domain size (m × m)	0.23 × 2.0	0.18 × 2.0
Grid size	12 × 64	16 × 32
Convection in the liquid	no	no
T_a (°C)	−17.5	−25
$\mathfrak{h}$ ($\mathrm{W\,m^{-2}\,K^{-1}}$)	16	16

of refrozen cracks found in Chapter 2. The bottom boundary is an open boundary that allows water to leave the domain, and water of prescribed temperature, T_0, and solute concentration, C_0, to be advected into the domain.

6.4.2 Freezing progress without convection in the liquid

The results from the computed refreezing of *slot 1* and *slot 10* in the absence of advection are presented in this section. The absence of advection of the liquid outside the mushy layer is simulated as in the previous section. Reference calculations are performed with the analytical model of Section 3.2.4. Parameters of the domains are summarised in Table 6.2. As mentioned in Section 6.3, an average effective latent heat of fusion of sea ice is calculated for the numerical simulations to allow the comparison with the analytical model. For the analytical model, we use $L = 340\,\mathrm{kJ\,kg^{-1}}$ and $L = 350\,\mathrm{kJ\,kg^{-1}}$ for *slot 1* and *slot 10*, respectively. The vertical position of the numerical freezing interface is determined either from a porosity threshold of $f = 0.5$, or with the comparative rate of temperature change approach (marked "ΔT"), using adjacent cells.

Figure 6.7 shows the progress of the freezing interface in the case of *slot 1*, as determined from the porosity threshold. Also shown for reference are data of *slot 1* evaluated with the comparative rate of temperature change approach (cf. figures in Appendix B.6). The solid lines are the predictions from the analytical model using the latent heat of $L = 293\,\mathrm{kJ\,kg^{-1}}$ and $L = 340\,\mathrm{kJ\,kg^{-1}}$ appropriate to experiment and simulation, respectively. The numerical model systematically underpredicts the position of the freezing interface with respect to the analytical model. However, the discrepancy is never more than 50 mm, which is less than the height of two computational cells.

Figure 6.8 shows the calculated advance of the freezing interface in the case of *slot 1*, as determined from the comparative rate of temperature change approach. Again, the numerical model systematically underpredicts the position of the freezing interface with respect to the analytical model. In this case, the discrepancy is larger, reaching

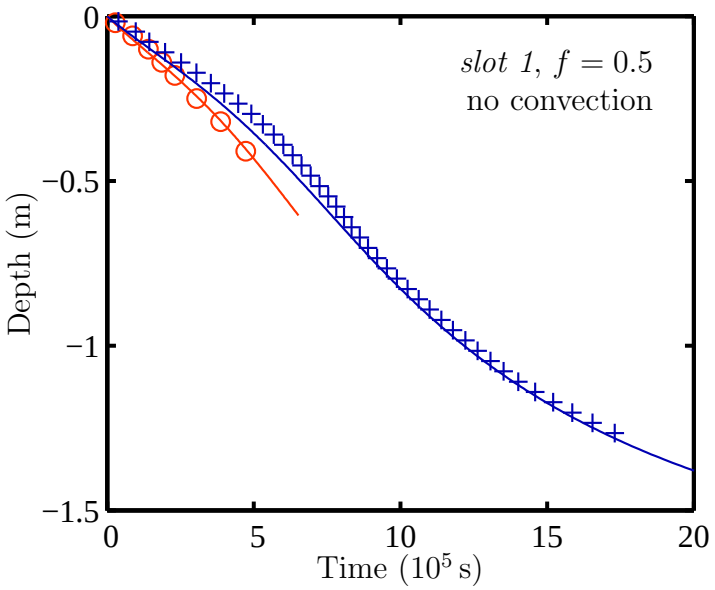

Figure 6.7: Measurements (circles) and simulations (pluses) for *slot 1*. The position of the freezing front at the centre of the slot is defined as $f = 0.5$. The lines are the predictions from the analytical model with the relevant values for latent heat.

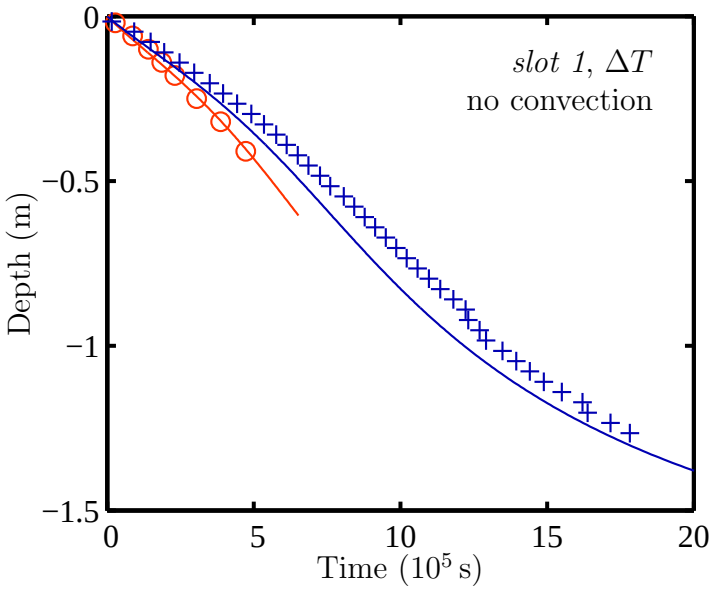

Figure 6.8: Measurements (circles) and simulations (pluses) for *slot 1*. The position of the freezing front at the centre of the slot is determined from the comparative rate of temperature change approach. The lines are the predictions from the analytical model with the relevant values for latent heat.

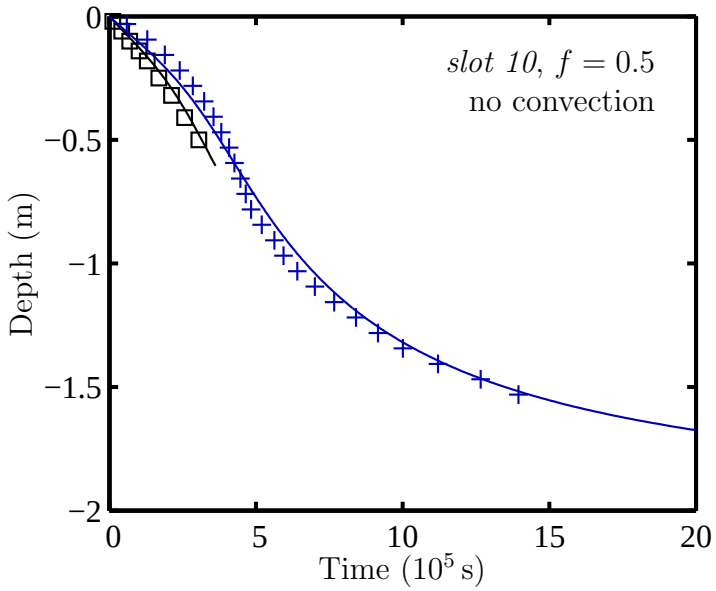

Figure 6.9: Measurements (squares) and simulations (pluses) for *slot 10*. The position of the freezing front at the centre of the slot is defined as $f = 0.5$. The lines are the predictions from the analytical model with the relevant values for latent heat.

up to 120 mm, which is less than four computational cells. The maximum discrepancy reduces if the freezing point is determined by comparing the temperature of cells that are not adjacent to each other[2].

Figure 6.9 tracks the freezing interface in the case of *slot 10*, as determined from the porosity threshold. The numerical model underpredicts growth with respect to the analytical model in the early stages of refreezing, while it overpredicts growth in the later stages. The discrepancy is never larger than 70 mm, which is slightly more than one computational cell. For the comparative rate of temperature change approach (Figure 6.10), the prediction of the numerical model is less than the prediction from the analytical model for $t < 1 \times 10^6$ s. The discrepancy is never more than 80 mm.

The predictions of the position of the freezing front of the numerical model are generally less than those from the analytical model of Section 3.2.4, if an appropriate value for the latent heat of fusion is used. This discrepancy could be partially due to the different treatment of the thermal conductivity, which is set to $k = 2\,\mathrm{W\,m^{-1}\,K^{-1}}$ in the analytical model, but varies between between the values for liquid ($0.6\,\mathrm{W\,m^{-1}\,K^{-1}}$) and ice ($2.1\,\mathrm{W\,m^{-1}\,K^{-1}}$) in the numerical model. However, a more significant difference is that the numerical model removes heat for the formation of unconsolidated (high porosity) ice, which is neglected in the analytical model. Large volumes of this ice form from the sides of the crack. While little of this unconsolidated ice is present in

[2]For example, if three cells are skipped, the maximum discrepancy is 70 mm.

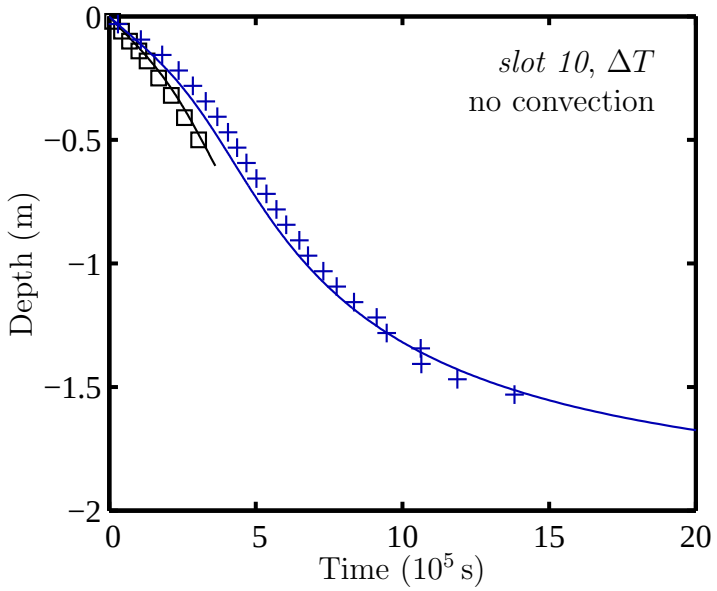

Figure 6.10: Measurements (squares) and simulations (pluses) for *slot 10*. The position of the freezing front at the centre of the slot is determined from the comparative rate of temperature change approach. The lines are the predictions from the analytical model with the respective values for latent heat.

the initial stages and in the final stages of refreezing, it is present in the transitional stage, where the largest discrepancy between the models appears. The consistency between the numerical calculations of this section and the analytical model further confirm that the heat transfer assumptions underlying the analytical model as outlined in Section 3.2.4 are reasonable.

6.4.3 Freezing progress with convection

We now consider the refreezing of *slot 10* in the presence of convection in the water. Simulations are performed for one half of the slot, and data shown in this section is mirrored at the vertical axis. The numerical grid for the calculation of *slot 10* is 6×32, the parameters T_a and $\mathfrak{h}$ are as before.

Figure 6.11 shows the calculated freezing front advance at the centre of the crack, as determined from the comparative rate of temperature change approach (a figure based on the porosity approach looks very similar. With an average temperature of $T = -12.5\,^{\circ}\mathrm{C}$, and an average salinity $S_{ice} = 12.5\,\mathrm{psu}$ in the slot, a characteristic latent heat of fusion is $L = 340\,\mathrm{kJ\,kg^{-1}}$. It can be seen that the growth rate simulated with the numerical model is too low. Running the analytical model with $\gamma = 1.4$ instead of $\gamma = 0.5$ (cf. equation (3.20)) results in a reasonable fit to the numerical simulation. Since γ represents the heat flux to the host ice interface, this fit suggests that the effect

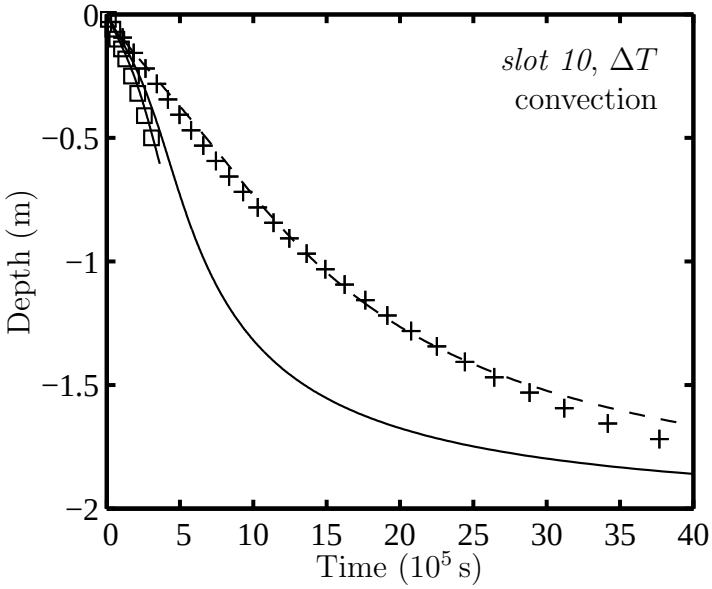

Figure 6.11: Simulated advance of the freezing front at the centre of the crack from the numerical model for *slot 10* (pluses). The solid line is the prediction of the analytical model ($\gamma = 0.5$). The broken line is the analytical prediction with $\gamma = 1.4$. Also shown are experimental data from *slot 10* (squares).

of convection is to reduce the effective heat flux to the host ice. We will next compare various heat fluxes in the numerical simulations to confirm this assessment.

Comparing the conductive heat flux to the top boundary in simulations with and without convection, Figure 6.12 shows that the presence of convection leaves this heat flux largely unaffected. However, the heat fluxes to the sides of the domain differ significantly from each other. While initially the same in both cases, the heat flux without convection reduces more rapidly than it does in the presence of convection.

Figure 6.13 shows a balance of heat fluxes in the simulation with convection. The sum of the advective heat flux and conductive heat flux to the sides happens to have an average value of approximately equal to 0.5/1.4 times the conductive heat flux to the side, which explains the need to use $\gamma = 1.4$ in the analytical model in order to fit model and simulation.

Interpretation The fact that the numerically modelled refreezing of the crack when convection is permitted in the fluid, is incompatible with the experiment has implications for the refreezing process of the crack. If advection of heat were to take place as modelled then the freezing process would be unrealistically slow. The source of incompatibility has been identified to be ice formation at the sides of the crack. Therefore, the model misses at least one feature of ice growth at a *vertical* interface that is important under the present circumstances. There are several possibilities that pre-

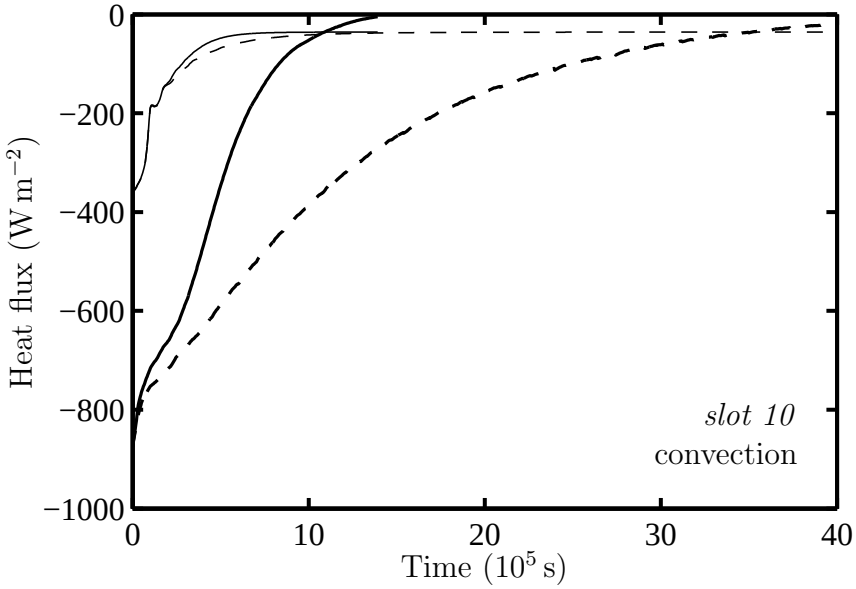

Figure 6.12: Heat flux to the top (thin lines) and to the sides (thick lines) of *slot 10* from the numerical model with convection (broken lines) and without convection (solid lines) convection.

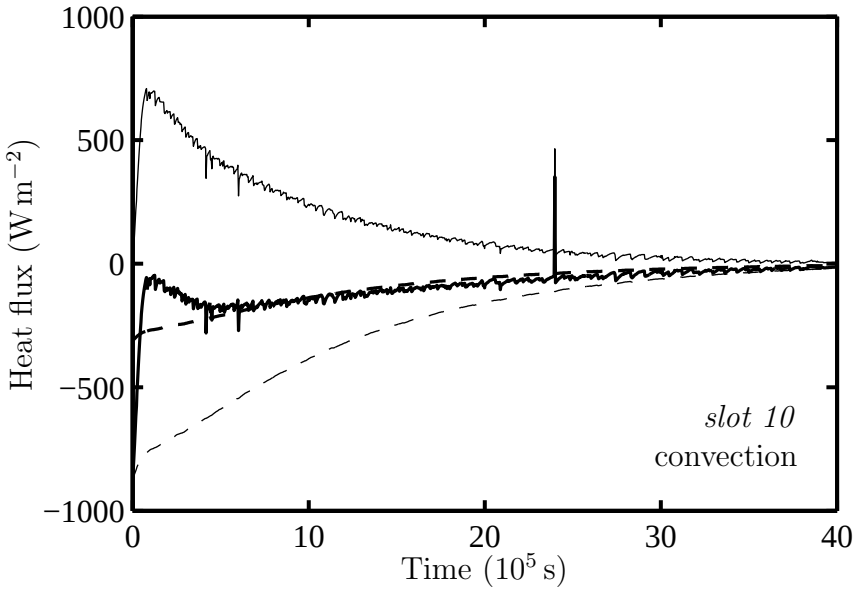

Figure 6.13: Conducted heat flux to the sides (broken, thin) and advected (solid, thin) heat flux in *slot 10*. Also shown are the sum of conducted and advected heat flux (solid, thick), and the conducted heat flux multiplied by 0.5/1.4 (broken, thick).

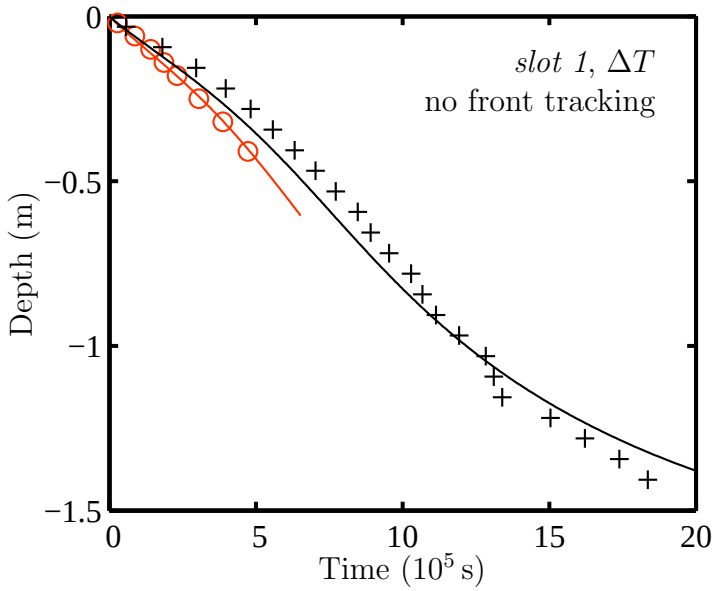

Figure 6.14: Measurements (circles) and simulations (pluses) for *slot 1*. The position of the freezing front at the centre of the slot is determined from the comparative rate of temperature change approach.

vent heat from being advected at the modelled rate. First, the texture of the interface could be constituted in a way that prevents cooled liquid from draining. Second, in the experiment, platelet ice may have grown from the sides into the slot, converting possible constitutional supercooling of the liquid into ice formation. This process has not been modelled. Third, double–diffusion and mixing at the interface could result in frazil ice formation or in the growth of frazil ice crystals that are already present in the seawater. Again, this has not been modelled.

6.4.4 Freezing progress without freezing front tracking

The freezing front progress in simulations of *slot 1* without freezing front tracking is shown next. Unlike the approach followed in Section 6.4.3, this avoids supercooling of the liquid through the formation of ice. The computational domain is mirrored and contains of 8×32 cells. Figure 6.14 shows the freezing front progress at the centre of the crack determined from the comparative rate of gradient approach. The progress follows the prediction of the analytical model to within two cell heights.

Figure 6.15 shows the freezing front progress at the centre of the crack if the freezing front is defined as $f = 0.5$. Clearly, the numerical results deviate markedly from the analytical prediction when horizontal growth becomes significant as described in Section 3.2.4. This deviation is related to the choice of threshold porosity. If the

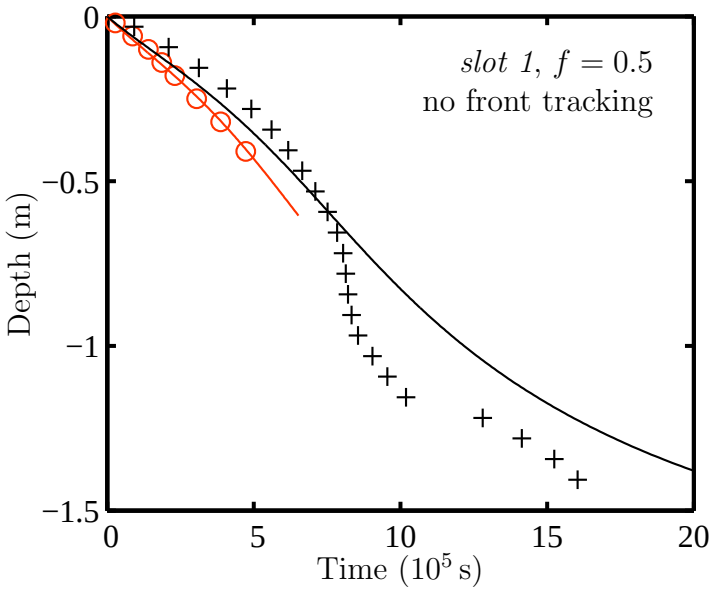

Figure 6.15: Measurements (circles) and simulations (pluses) for *slot 1*. The position of the freezing front at the centre of the slot is defined as $f = 0.5$.

freezing interface is defined as the position of $f = 0.2$, then the match shown in Figure 6.16 is obtained.

The removal of freezing front tracking results in a significant sensitivity of freezing front location to the choice of threshold porosity if the freezing interface is not horizontal. However, the comparative rate of temperature change approach, which does not contain free parameters, seems to be insensitive to the details of the structure of the freezing interface. Growth simulated by the numerical model without freezing front tracking is consistent with the analytical model (that represents measurements), provided care is taken in the definition of the freezing interface. As expected, a sizable heat exchange with the ocean has been avoided in this simulation.

6.4.5 Two–dimensional freezing front

While the analytical model is capable of predicting the time of sea ice consolidation in the crack, it tells us nothing about the shape of the dendritic ice–water interface, desalination, and fluid motion in the porous ice. The time evolution of porosity in the simulations of *slot 10* will now be presented for three cases: freezing without convection in the liquid, with convection, and with convection but without freezing front tracking. Figure 6.17 juxtaposes the evolution of the $f = 0.8$, $f = 0.5$ and $f = 0.2$ contours for the case without convection. The first contour shown is at $t = 1 \times 10^5$ s, the last contour is at $t = 1 \times 10^6$ s, and the separation between the lines is $\Delta t = 1.5 \times 10^5$ s.

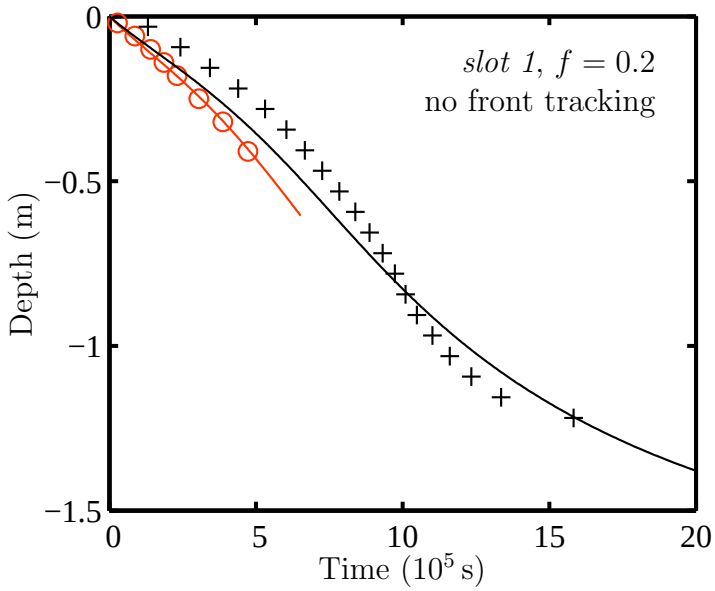

Figure 6.16: Measurements (circles) and simulations (pluses) for *slot 1*. The position of the freezing front at the centre of the slot is defined as $f = 0.2$.

The grid size of the mirrored domain is 8×64. The freezing interface as defined by $f = 0.8$ is arch–shaped, the arch becoming narrower with time, and moving downwards at non–constant speed. The shape of the lines of constant porosity depends on porosity, i.e. the thickness of the skeletal layer, however it may be defined, depends on position. These figures may be compared with the experimental measurements in Figure 3.10.

Figure 6.18 displays the evolution of the $f = 0.8$, $f = 0.5$ and $f = 0.2$ contours for the case with convection. The grid size is 6×32. The lack of ice formation at the sides of the cracks is clearly visible. Refreezing resembles a one–dimensional process.

In Figure 6.19, the evolution of the $f = 0.8$, $f = 0.5$ and $f = 0.2$ contours for the case without freezing front tracking is shown. The grid size is 8×32. The freezing front is arch–shaped as can be seen in the case of $f = 0.8$. There is a remarkably high porosity at the sides of the domain. This phenomenon has also been observed in numerical simulations of *Felicelli* (1991) during fast cooling of alloys. Although the salinity at the side of the crack may naturally be high, the solute concentration may be exaggerated by the presence of an impermeable domain boundary since the flow pattern is disturbed, forcing the flow to be parallel to the boundary.

6.4.6 Salinity profiles

The salinity profiles considered in this section are calculated in a mirrored domain (grid 16×64 without convection; 8×32 without freezing front tracking) first in the absence

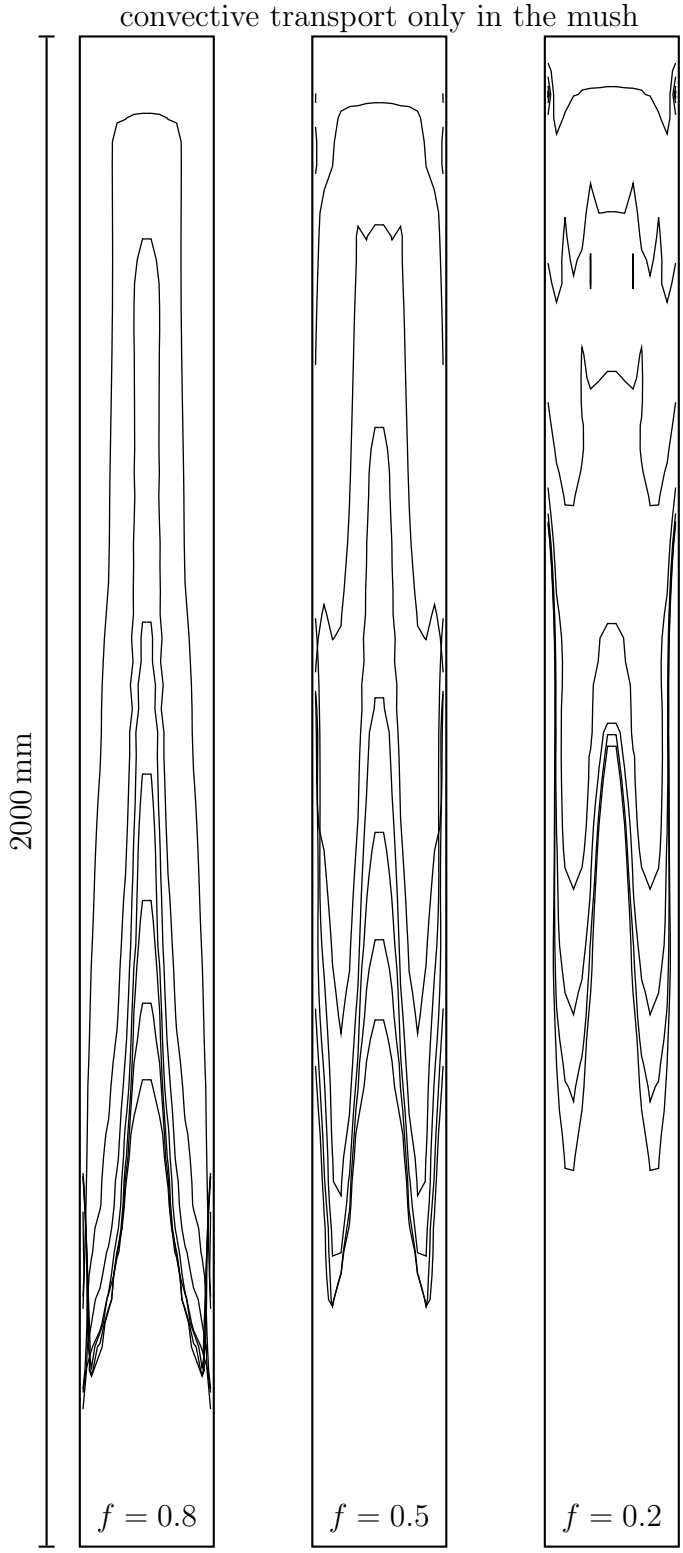

Figure 6.17: Freezing interface of *slot 10* from 1×10^5 s to 10×10^5 s without convection in the liquid, but with convection in the mush. The separation of profiles is 1.5×10^5 s (approximately 42 h). The interface is defined as the position at which the porosity is $f = 0.8$, $f = 0.5$, and $f = 0.2$, respectively.

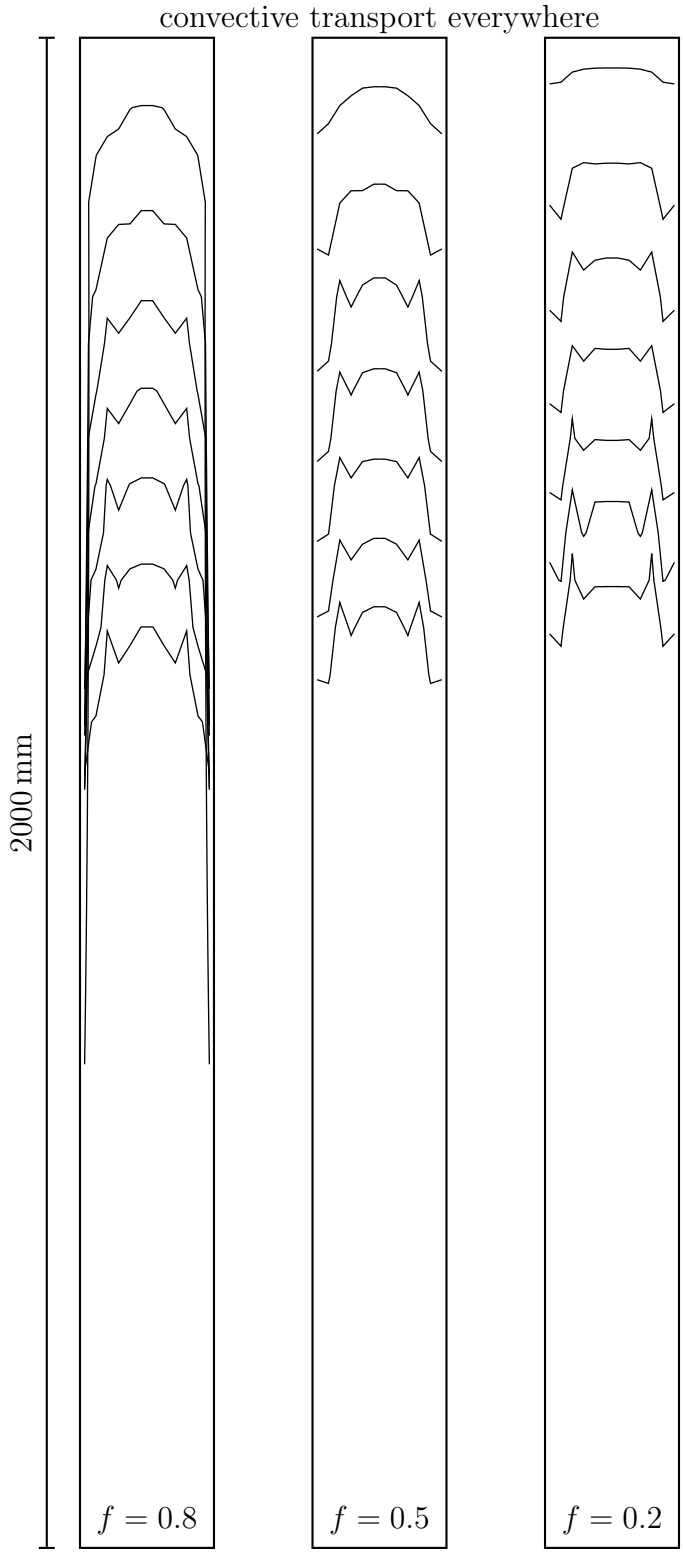

Figure 6.18: Freezing interface of *slot 10* from 1×10^5 s to 10×10^5 s with convection in the liquid. The separation of profiles is 1.5×10^5 s. The interface is defined as the position at which the porosity is $f = 0.8$, $f = 0.5$, and $f = 0.2$, respectively.

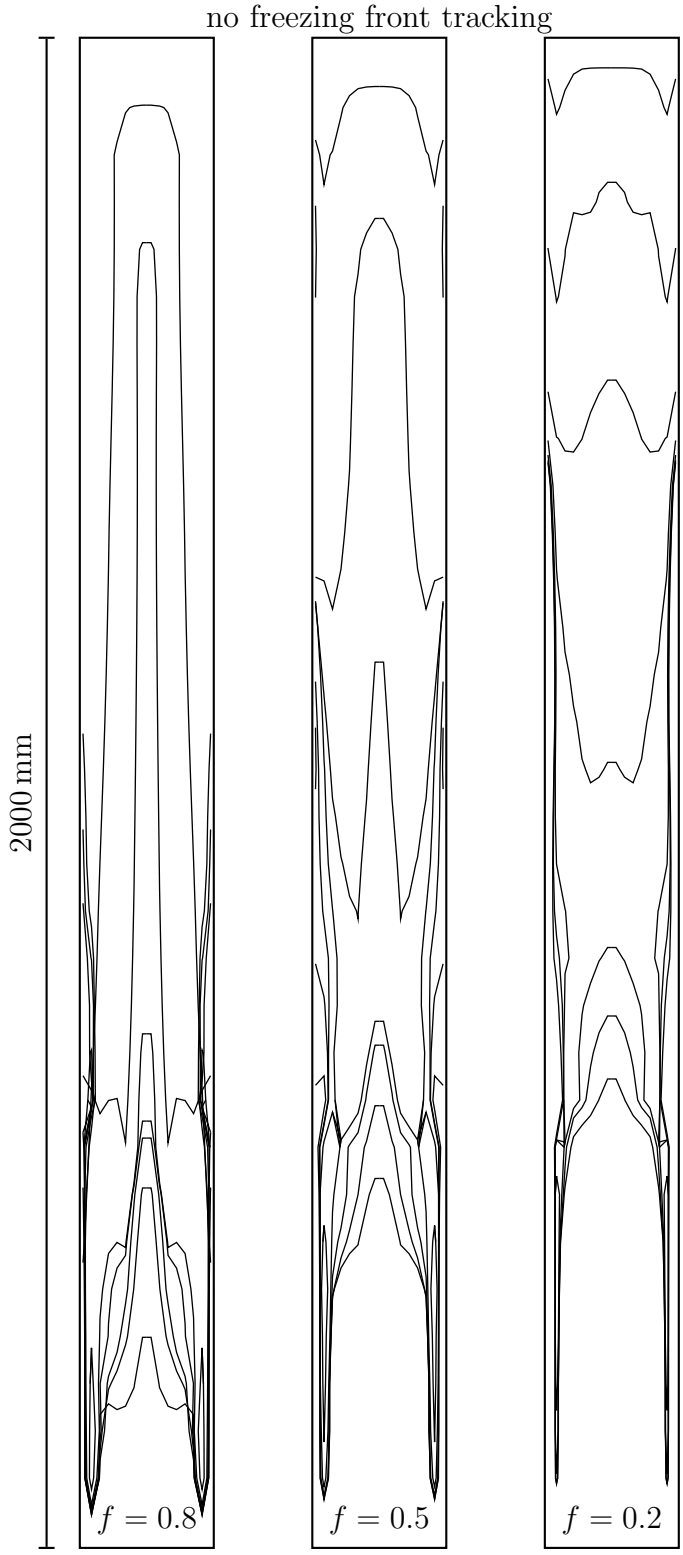

Figure 6.19: Freezing interface of *slot 10* from 1×10^5 s to 10×10^5 s without freezing front tracking. The separation of profiles is 1.5×10^5 s. The interface is defined as the position at which the porosity is $f = 0.8$, $f = 0.5$, and $f = 0.2$, respectively.

of convection in the liquid, and then in the absence of freezing front tracking. These simulations are considered since the simulated growth velocities match the measured growth velocity and ice–water interface profile shapes more closely than simulations with convection.

Simulations in the absence of convection in the liquid Calculations for *slot 1* and *slot 10* are shown in Figure 6.20. Salinity profiles are shown at the respective times when the interface of the skeletal layers at the centre of the crack (defined as $f = 0.8$) is at depth 850 mm. The fronts of the skeletal layers are arch–shaped, and it can be seen that the arch is wider in *slot 1* than it is in *slot 10*.

The simulated salinities in the region closest to the ice–air interface are higher than the measured salinities shown in Figures 2.18(c) and 2.19(a) in Section 2.2.4. The simulated salinity profile is stable (time–independent), showing an average salinity of 13.7 psu and 15.2 psu in the upper 400 mm of *slot 1* and in the upper 560 mm of *slot 10*, respectively. These values are approximately twice as high as the measured salinity averages of 6.9 psu and 7.1 psu in *slot 1* and *slot 10*, respectively (Section 2.2.4, Appendix A.1). The high salinity is partly due to the absence of convection in the liquid in these simulations.

Both profiles show arches of high salinity, equivalent to high porosity. A low salinity region develops at the centre close to the ice–air interface, and this region narrows with depth in the form of a "V". The high–salinity arches emerge from the arms of this "V". Arches of inclusions emerging from a "V"–shaped boundary are also shown in thick sections of *crack 5* (Figure 2.7) and *slot 10* (Figure 2.16). The thick section of *slot 10* further shows a "V"– shaped region of low porosity at the centre.

The centre of the simulated *slot 10* is of low salinity in the upper 200 mm compared to the sides, but increases in salinity around 200 mm so that, at 500 mm, it is of higher salinity than the sides. The reversal from relatively low salinity at the centre to high salinity at the centre is consistent with the salinity profile of *slot 10* (Figure 2.18(c)), which shows a reversal around 200 mm. A reversal can also be seen in the salinity profiles of *crack 1* and *crack 20* (Figures 2.18(a) and (b)), albeit less clearly.

The arches develop in this simulation in the absence of significant convection in the liquid, i.e. their presence in the simulations is due to solute redistribution in the porous sea ice. While they mark the pathways of downflowing brine, the source of the brine is partly the ice adjacent to them. Consistent with this observation, laboratory studies of *Cottier et al.* (1999) in one–dimensionally grown sea ice sheets show a correlation between the presence of brine drainage channels (that are zones of downflowing brine) and high salinity on the centimeter–scale.

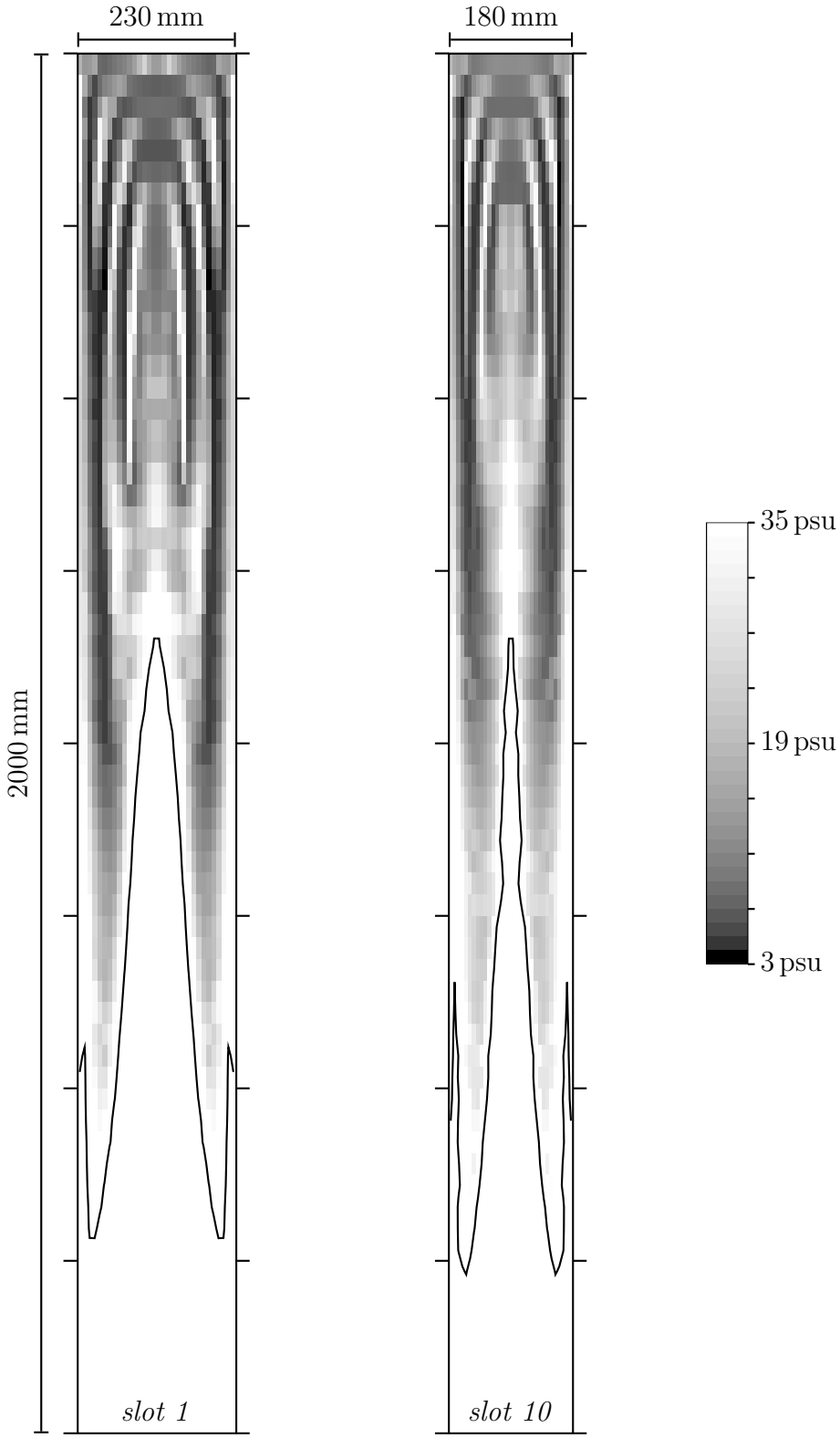

Figure 6.20: Salinity profiles of simulated *slot 1* at $t = 1 \times 10^6$ s, and of *slot 10* at $t = 5.5 \times 10^5$ s. Contour lines trace porosity $f = 0.8$.

Simulations without freezing front tracking The salinity profiles obtained in simulations without freezing front tracking are shown in Figure 6.21 for the same times as the profiles in Figure 6.20. The salinity profiles are similar to the previous calculations. However, the absolute salinity of the ice is lower than previously, presumably because the liquid is now available for advective transport, facilitating desalination and solute removal from the interface. Average salinities of 12.5 psu and 14 psu are measured in the upper 400 mm of *slot 1* and in the upper 560 mm of *slot 10*, respectively. Because excess solute in the liquid is removed into the ocean, the line of porosity $f = 0.8$ is deeper than in the case without convection.

Summary The salinity profiles shown in this section resemble many features seen in thick sections and salinity profiles of refrozen cracks and slots in McMurdo Sound (Chapter 2): arch–shaped inclusion alignment, a low salinity region at the centre close to the ice–air interface, and a high salinity region at the centre at depth. These structures form in the absence of significant convection in the liquid, linking their existence to convection in the porous sea ice. The average salinity of the refrozen cracks is significantly higher than that observed in McMurdo Sound, indicating that the permeability of crack ice could be higher than is assumed from the desalination of one–dimensional ice sheets (Chapter 5).

6.5 Summary and future work

Qualitative features of refreezing progress and desalination of cracks in sea ice has been successfully simulated. The numerical simulations provide insight into the refreezing process of cracks. High porosity, high salinity arches develop as a consequence of solute redistribution in the porous sea ice alone, and convection ahead of the interface does not seem to be a prerequisite. However, it is noteworthy that the present method shows that expected desalination patterns develop independently of convection patterns in the liquid. This is not a trivial result, as it has been suggested that fluid motion in the liquid affects fluid motion in the porous medium (Chapter 5; *Lofgren and Weeks*, 1969; *Worster and Kerr*, 1994; *Chung and Chen*, 2001; *Feltham et al.*, 2002). All simulations that allow convection in the liquid show downwelling water at the sides of the crack. This is consistent with the observation of crystals growing upstream (*Flemings*, 1974). From the numerical simulations it can be concluded that the downwelling water in the experiments is unlikely to be supercooled, implying that either frazil ice or platelet ice forms at the sides of the cracks in the experiments. Further, it is likely that the

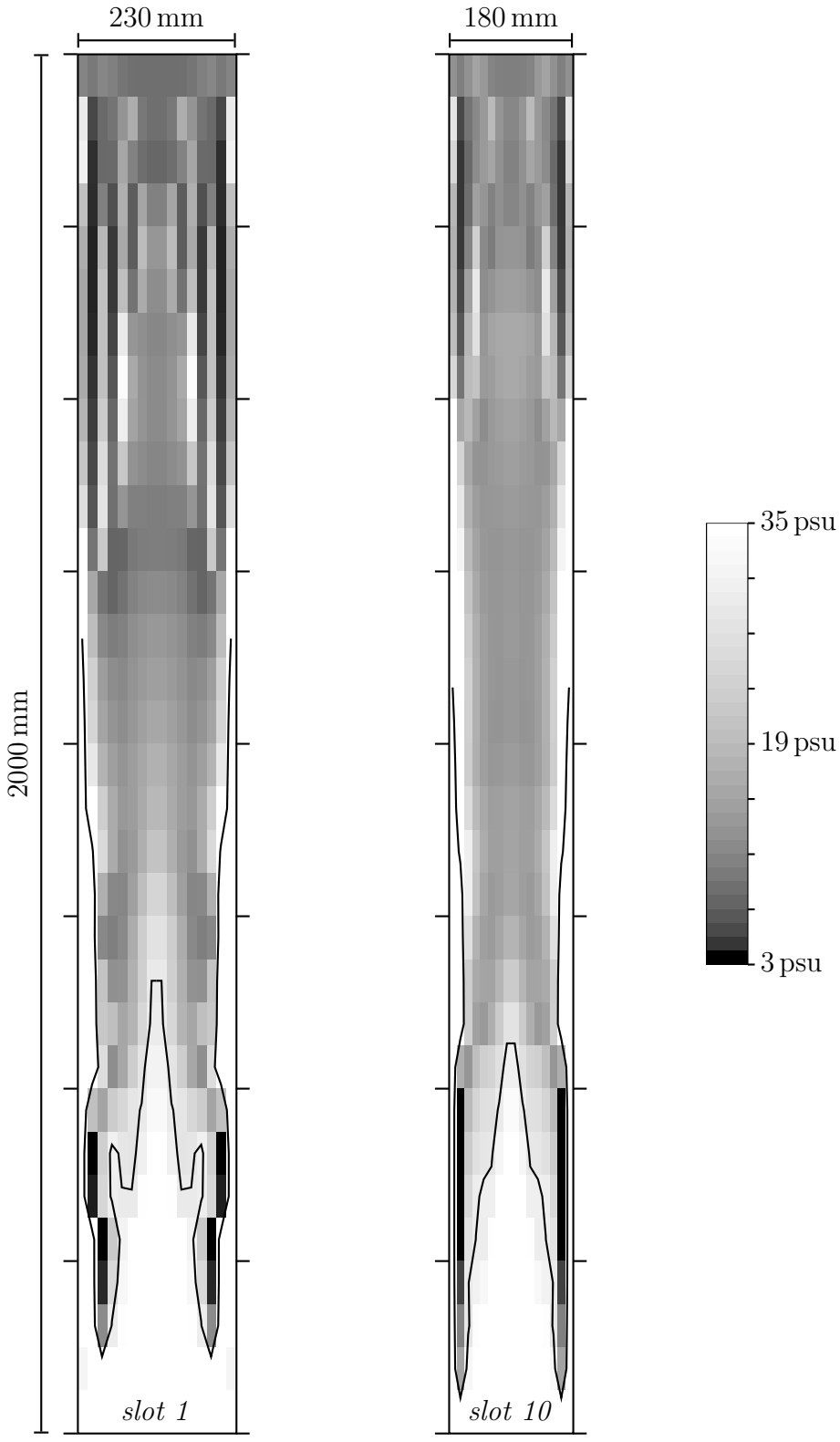

Figure 6.21: Salinity profiles of simulations without freezing front tracking. Salinity profiles of *slot 1* and *slot 10* after $1 \times 10^6\, s$ and 5.5×10^5 s, respectively. The contour line traces porosity $f = 0.8$.

connected pore space of sea ice reduces more rapidly than the total pore space as porosity is decreased. The latter two points shall finally receive closer attention.

Treatment of solute retention at low porosities The strategy followed to avoid complete desalination is a numerical method for finite permeabilities, based only on limited insight into the physical processes in the sea ice. In the future, a consistent treatment of the retention of solute in isolated brine pockets may be applied. As a starting point, the literature on alloy solidification may be consulted, where inclusions are incorporated into the solid (*Poirier et al.*, 1991; *Felicelli et al.*, 1998). Alternatively, a distinction between effective and total porosity could be introduced into the governing equations. A possible relationship between effective and total porosity has been derived in Chapter 5. Ultimately, a solution for the treatment of mass conservation in the presence of volume expansion will have to be found that is satisfactory at small total porosities, i.e. vanishing effective porosities.

Treatment of convection and the freezing front Simulations without convection in the liquid were introduced in order to reduce heat loss that is deemed unrealistically high. However, this could also be achieved by simulating frazil ice formation and advection (*Omstedt*, 1985; *Jenkins and Bombosch*, 1995; *Skyllingstad and Denbo*, 2001; *Khazendar and Jenkins*, 2003) or platelet ice growth at the vertical interface.

Related to the convection issue, the method employed for freezing front tracking is also subject to scrutiny. This was introduced in order to simulate the formation of sea ice that is consolidated to some degree, preventing the formation of ice crystals of arbitrary length ahead of the interface. Removal of freezing front tracking from the governing equations results in ice formation throughout the downwelling part of the domain of the refreezing slot within a few hours. In addition, supercooling is removed and advection of heat is largely eliminated. Depending on the magnitude of the assumed permeability of very low porosity ice, flow may be impeded but still possible. *Medjani* (1996) and *Oertling and Watts* (2004), do not use any form of freezing front tracking. Further, they increase the viscosity of the seawater until $f = 0.5$, before permeability enters the momentum equations through a Darcian flow term. Application of this approach to the case of refreezing slots would lead to increased shear in the "liquid", which, again, would reduce the fluid velocity. This would also lead to ice formation throughout the entire downwelling volume.

In order to treat convection and heat transport at the freezing interface appropriately, a mechanism of release of supercooling needs to be identified and implemented that accommodates the structure of sea ice and fluid motion at the interface. None of

the options discussed is entirely satisfactory. However, in order to show that relaxation of supercooling in the presence of convection has the potential to lead to more realistic simulations, some of the simulations have been performed without freezing front tracking.

Chapter 7

Summary and conclusion

7.1 Summary and conclusion

7.1.1 Refreezing of cracks

The growth, structure, and desalination of straight–sided, fluid–filled, linear refreezing cracks in sea ice have been investigated in the previous chapters. Broadly, three techniques have been used to investigate the cracks: observations of refreezing in experiments on land–fast, first–year sea ice in McMurdo Sound, Antarctica, analytical modelling of heat transfer and growth rate, and numerical, fluid–dynamical simulation of refreezing. The principal unknown in the development of the numerical model was the permeability–porosity relationship, and an expression has been derived in this thesis.

The refreezing of the cracks is essentially a two–dimensional process, characterised by the formation of an arch–shaped interface of skeletal ice. This two–dimensional shape is a consequence of a conductive heat flux into the host ice and into the atmosphere. We may identify three stages of refreezing. Initially, heat removal to the atmosphere dominates the freezing process. Crystallographically, ice formed in the centre of the cracks is similar to congelation ice. The first stage is missing in narrow cracks. The second stage is observed below a depth, where a transition is observed to ice formation dominated by heat transfer to the sides of the crack. During both stages, the liquid region at the centre of the crack becomes narrower with time. Finally, the third stage is reached close to the bottom of the host ice sheet, where heat transfer into the host ice becomes negligible again, and vertical heat transfer dominates.

Owing to a downward movement of brine at its freezing temperature along the arch–shaped interface, ice crystals grow upstream. The upstream tilt manifests itself in a fountain–like crystal structure close to the ice–air interface in wide cracks (i.e. in

ice formed in the first stage), while upward–growing crystals meet at the centre where the liquid region at the centre of the crack is narrow enough (i.e. in the second stage). At the same time, arch–shaped inclusion patterns form due to solute redistribution inside the newly forming ice. These arch–shaped inclusions appear in both numerical simulations and in Antarctic experiments. They arise due to fluid motion in the porous sea ice at the sides of the crack.

In the initial stages of refreezing of wide cracks, close to the ice–air interface, the freezing interface is almost horizontal, and a generally upward–flowing current at the centre of crack causes the formation of a region at the centre of the crack with low salinity. Later, although the skeletal interface is arch–shaped, the consolidated ice continues to develop with an approximately horizontal, downward–moving front. Since the time available for desalination of sea ice is therefore largest close to the host ice interface, a lower salinity develops at the sides compared to the centre of the crack. Further, during the second stage, the rapid formation of skeletal ice at the centre hinders desalination. The modelled salinities in cracks are higher than those observed, implying that the permeability–porosity relationship in refreezing slots is probably different in magnitude and anisotropy to the permeability of sea ice sheets that grow in one dimension in the absence of under–ice currents.

There is evidence that some of the cracks in this study refroze in the presence of an additional negative heat flux from the ocean, possibly in the form of upward–floating ice crystals. In other cracks, where there is no such flux, the energy balance of a refreezing slot is adequately described by conductive heat transfer to host ice and atmosphere, shortwave radiative heat input, and formation of ice in the crack. Although brine is removed into the ocean, this convection does not incur a large positive ocean heat flux since the brine does not supercool.

Brine released into the crack mixes in the crack, slightly increasing salinity and depressing temperature with time. The desalinating activity is influenced by solar shortwave radiation, with increased high–frequency temperature perturbations during the day compared to the night. In addition, desalination at night has a sporadic component.

In this work, light has been shed on the growth and structure of refreezing cracks in sea ice. It has been found that inclusion and crystal structure of a refrozen crack exhibit many features that are absent from ordinary sea ice sheets, which is due to differences in direction of heat transfer and to convection.

7.1.2 Sea ice in general

Some of the results obtained in this work may be useful beyond the scope of refreezing cracks, and a selection are briefly listed in this section.

- An alternative definition of the freezing interface of sea ice has been found that may be applied to thermistor measurements of freezing of sea ice.
- The sporadic nature of brine release in cracks should have a counterpart during the formation of ice sheets.
- The observed coupling of solar radiation and brine release is relevant to sea ice formation in general.
- The numerical fluid dynamics model can simulate sea ice processes in many geometries and under a variety of boundary conditions.
- A relationship between effective and total porosity has been suggested, based on a stochastic model. This model suggests a relationship between the crystal structure of sea ice and a critical porosity.
- Evidence of an influence of under–ice currents on ice sheet salinity has been shown. This dependence may affect sea ice permeability.
- Both the permeability and the development of isolated brine pockets affect the desalination of sea ice.
- A method of obtaining a permeability–porosity relationship from laboratory experiments has been applied successfully.

7.2 Future work

Some questions arose during the investigation of cracks that need further attention.

- The origin of the crystal structure of refrozen cracks could be qualitatively explained by assuming upstream growth of crystals. The angle of tilt of crystals has yet to be quantified.
- A definition of the front of consolidated sea ice from temperature measurements was found that proved useful in the analytical model of crack refreezing, the heat balance estimate, and the fluid dynamics simulations. However, this definition has not been derived rigorously, calling for further investigations into the applicability of this definition and into the experimental definition of the freezing interface in general.
- Some refreezing experiments seem to have experienced a substantial negative ocean heat flux, possibly in the form of upward–floating, small ice crystals. The nature and origin of this heat flux should be investigated.

- The solar radiative shortwave flux necessary to trigger increased brine release was found at a distinct level, which is very low compared to the conductive heat flux. The process responsible for increased brine release needs to be quantified.
- We saw evidence of an ambiguous relationship between sea ice growth velocity and the stable salinity distribution coefficient. Systematic differences between experiments were revealed, and the differences were assigned tentatively to the presence or absence of significant under–ice currents. This topic needs further investigation.
- The Monte Carlo percolation model was used to find a relationship between effective and total porosity. There is indication that the relationship is valid for materials other than sea ice, yet, it has still to be validated for sea ice. In particular, the inclusion size distribution produced by the model, although in qualitative agreement, is quantitatively different from at least one observation in sea ice. This discrepancy merits investigation.
- The derivation of the permeability parameterisation does not explicitly account for the initial segregation of solute from the ice, yet, it is able to produce realistic salinity profiles. The origin of this situation should be examined.
- It was found that the numerical simulation of sea ice would gain credibility from an improved parameterisation of the processes at the dendritic freezing front of sea ice. This parameterisation should lead to the formation of a defined dendritic interface and to the release of supercooling near the interface.
- Although the governing equations of the fluid dynamics model account for most phenomena relevant to the growth of sea ice, no distinction is made between effective and total porosity. A rigorous derivation of a description of fluid flow though sea ice including this distinction would be the logical next step.

References

Allamandola, L. J., M. P. Bernstein, S. A. Sandford, and R. L. Walker (1999), Evolution of interstellar ices, *Space Science Reviews*, *90*, 219–232.

Allison, I., R. E. Brandt, and S. G. Warren (1993), East Antarctic sea–ice – albedo, thickness distribution, and snow cover, *Journal of Geophysical Research*, *98*(C7), 12,417–12,429.

Anderson, D. L. (1961), Growth rate of sea ice, *Journal of Glaciology*, *3*, 1170–1172.

Anderson, D. L., and W. F. Weeks (1958), A theoretical analysis of sea ice strength, *American Geophysical Union, Transactions*, *39*(4), 632–640.

Andreas, E. L. (1987), A theory for the scalar roughness and the scalar transfer coefficients over snow and sea ice, *Boundary Layer Meteorology*, *38*, 159–184.

Andreas, E. L., P. S. Guest, P. O. G. Persson, C. W. Fairall, T. W. Horst, R. E. Moritz, and S. R. Semmer (2002), Near–surface water vapor over polar sea ice is always near ice saturation, *Journal of Geophysical Research*, *107*(C10), 8033, doi: 10.1029/2000JC000411.

Arrigo, K. R. (2003), Primary production in sea ice, in *Sea Ice – An Introduction to its Physics, Biology, Chemsitry and Geology*, edited by D. N. Thomas and G. S. Dieckmann, pp. 143–183, Blackwells Scientific Ltd., London, UK.

Arrigo, K. R., J. N. Kremer, and C. W. Sullivan (1993), A simulated Antarctic fast ice ecosystem, *Journal of Geophysical Research*, *98*(C4), 6929–6946.

Ashenden, R., and J. D. Marwitz (1997), Turboprop aircraft performance response to various environmental conditions, *Journal of Aircraft*, *34*(3), 278–287.

Assur, A., and W. F. Weeks (1964), Growth, structure, and strength of sea ice, *Research Report 135*, Cold Regions Research and Engineering Laboratory, Hanover, NH, USA.

Baehr, H. D., and K. Stephan (1998), *Heat and Mass Transfer*, Springer–Verlag, Berlin, Germany.

Baker, D. R., G. Paul, S. Sreenivasan, and H. E. Stanley (2002), Continuum percolation threshold for interpenetrating squares and cubes, *Physical Review E*, *66*, 046136.

Baker, I., D. Cullen, and D. Iliescu (2003), The microstructural location of impurities in ice, *Canadian Journal of Physics*, *81*(1–2), 1–9.

Baker, M. B. (1999), Ice in the troposphere, in *Proceedings of the NATO Advanced Research Workshop "Ice Physics and the Natural Environment", Maratea, Italy, September 1997, NATO ASI Series, Series I: Global Environmental Change*, vol. 56, edited by J. S. Wettlaufer, J. G. Dash, and N. Untersteiner, pp. 121–142, Springer–Verlag, Berlin, Germany.

Barrett, M. D., and V. A. Squire (1996), Ice–coupled wave propagation across an abrupt change in ice rigidity, density, or thickness, *Journal of Geophysical Research*, *101*(C9), 20,825–20,832.

Batchelor, G. K. (1970), *An Introduction to Fluid Dynamics*, Cambridge University Press, Cambridge, UK, reprint.

Bear, J., and Y. Bachmat (1991), *Introduction to Modeling of Transport Phenomena in Porous Media, Theory and Application of Transport in Porous Media*, vol. 4, Kluwer Academic Publishers, Dordrecht, The Netherlands.

Beckermann, C., and R. Viskanta (1993), Mathematical modeling of transport phenomena during alloy solidification, *Applied Mechanics Reviews*, *46*(1), 1–27.

Beek, W. J., K. M. K. Muttzall, and J. W. van Heuven (1999), *Transport Phenomena*, 2nd ed., John Wiley & Sons, Ltd, New York, NY, USA.

Bennington, K. O. (1967), Desalination features in natural sea ice, *Journal of Glaciology*, *6*(48), 845–857.

Bennon, W. D., and F. P. Incropera (1987), A continuum model for momentum, heat and species transport in binary solid–liquid phase change systems. 1. Model formulation, *International Journal of Heat and Mass Transfer*, *30*(10), 2161–2170.

Bennon, W. D., and F. P. Incropera (1989), An experimental investiagtion of binary solidification in a vertical channel with thermal and solutal mixed convection, *111*, 706–712.

Benson, N. G. (1955), Observations of anchor ice in a Michigan trout stream, *Ecology*, *36*(3), 529–530.

Bergman, M. I., D. R. Fearn, J. Bloxham, and M. C. Shannon (1997), Convection and channel formation in solidifying Pb–Sn alloys, *Metallurgical and Materials Transactions*, *28A*, 859–866.

Bergman, M. I., D. M. Cole, and J. R. Jones (2002), Preferred crystal orientations due to melt convection during directional solidification, *Journal of Geophysical Research*, *107*(B9), 2201, doi:10.1029/2001JB000601.

Bergman, M. I., S. Agrawal, M. Carter, and M. Macleod-Silberstein (2003), Transverse solidification textures in hexagonal close–packed alloys, *Journal of Crystal Growth*, *255*(1–2), 204–211.

Berkowitz, B., and I. Balberg (1992), Percolation approach to the problem of hydraulic conductivity in porous media, *Transport in Porous Media*, *9*(3), 275–286.

Berkowitz, B., and R. P. Ewing (1998), Percolation theory and network modelling applications in soil physics, *Surveys in Geophysics*, *19*, 23–72.

Bitz, C. M., and W. H. Lipscomb (1999), An energy–conserving thermodynamic model of sea ice, *Journal of Geophysical Research*, *104*(C7), 15,669–15,677.

Blewitt, G., and P. Clarke (2003), Inversion of Earth's changing shape to weight sea level in static equilibrium with surface mass redistribution, *Journal of Geophysical Research*, *108*(B6), 2311, doi:10.1029/2002JB002290.

Blosch, E., W. Shyy, and R. Smith (1993), The role of mass conservation in pressure–based algorithms, *Numerical Heat Transfer, Part B*, *24*, 415–429.

Blower, J. D. (2001), Factors controlling permeability–porosity relationships in magma, *Bulletin of Volcanology*, *63*, 497–504.

Bolling, G. F., and W. A. Tiller (1960), Growth from the melt. II. Cellular interface morphology, *Journal of Applied Physics*, *31*(11), 2040–2045.

Bond, P. E., and P. J. Langhorne (1997), Fatigue behavior of canterlever beams of saline ice, *Journal of Cold Regions Engineering*, *11*(2), 99–112.

de Bondt, S., L. Froyen, and A. Deruyttere (1992), Electrical conductivity of composites: A percolation approach, *Journal of Materials Science*, *27*, 1983–1988.

Brewster, R. A., and B. Gebhart (1994), The effects of supercooling and freezing on natural convection in seawater, *International Journal of Heat and Mass Transfer*, *37*(4), 543–552.

Briggs, W. L., V. E. Henson, and S. F. McCormick (2000), *A Multigrid Tutorial*, 2nd ed., SIAM, Philadelphia, PA, USA.

Brine, D. T., and M. Iqbal (1983), Diffuse and global solar spectral irradiance under cloudless skies, *Solar Energy*, *30*, 447–453.

Brinkman, H. C. (1947), A calculation of the viscous force exerted by a flowing fluid on a dense swarm of particles, *Applied Science Research A*, *1*, 27–34.

Broadbent, S. R., and J. M. Hammersley (1957), Percolation processes. I. Crystals and mazes, *Proceedings of the Cambridge Philosophical Society*, *53*(3), 629–641.

van den Broeke, M., C. Reijmer, and R. van de Wal (2004), Surface radiation balance in Antarctica as measured with automatic weather stations, *Journal of Geophysical Research*, *109*, D09103, doi:10.1029/2003JD004394.

Buchanan, J. Y. (1887a), On ice and brines. I., *Nature*, *35*(913), 608–611.

Buchanan, J. Y. (1887b), On ice and brines. II., *Nature*, *36*(914), 9–12.

Buck, A. L. (1981), New equations for computing vapor pressure and enhancement factor, *Journal of Applied Meteorology*, *20*, 1527–1532.

Buckley, R. G., and H. J. Trodahl (1987), Scattering and absorption of visible light by sea ice, *Nature*, *326*(6116), 867–869.

Burton, J. A., R. C. Prim, and W. P. Slichter (1953), The distribution of solute in crystals grown form the melt. Part I. Theoretical, *Journal of Chemical Physics*, *21*(11), 1987–1991.

Carman, P. C. (1937), Fluid flow through granular beds, *Transactions of the Institution of Chemical Engineers*, *15*, 150–166.

Carmona, F., and J. Ravier (2003), To what extent is the structure of a random composite compatible with a percolation model?, *Physica B*, *338*, 247–251.

Carslaw, H. S., and J. C. Jaeger (1986), *Conduction of Heat in Solids*, 2nd ed., Clarendon Press, Oxford, UK.

Catton, I., and D. K. Edwards (1970), Initiation of thermal convection in finite right circular cylinders, *AIChE Journal*, *16*(4), 594–601.

Chen, C. F. (1995), Experimental study of convection in a mushy layer during solidification, *Journal of Fluid Mechanics*, *293*, 81–98.

Christensen, F. T. (1986), Refreezing of cracks formed by bending of floating ice sheets, *Cold Regions Science and Technology*, *12*, 29–37.

Chung, C. A., and F. Chen (2001), Morthological instability in a directionally solidifying binary solution with an imposed shear flow, *Journal of Fluid Mechanics*, *436*, 85–106.

Clow, G. D., R. W. Saltus, and E. D. Waddington (1996), A new high–precision borehole–temperature logging system used at GISP2, Greenland, and Taylor Dome, Antarctica, *Journal of Glaciology*, *42*(142), 576–584.

Cole, D. M. (2001), The microstructure of ice and its influence on mechanical properties, *Engineering Fracture Mechanics*, *68*, 1797–1822.

Cole, D. M., and L. H. Shapiro (1998), Observations of brine drainage networks and microstructure of first–year sea ice, *Journal of Geophysical Research*, *103*(C10), 21,739–21,750.

Cole, D. M., H. Eicken, L. H. Shapiro, and K. Frey (2002), Some observations of high porosity layers and brine drainage features in first–year sea ice, in *Ice in the Environment: Proceedings of the 16th IAHR International Symposium on Ice*, vol. 2, edited by V. Squire and P. Langhorne, pp. 179–186, University of Otago, Dunedin, New Zealand.

Cole, D. M., H. Eicken, K. Frey, and L. H. Shapiro (2004), Observations of banding in first–year Arctic sea ice, *Journal of Geophysical Research*, *109*, C08012, doi:10.1029/2003JC001993.

Conover, W. J. (1980), *Practical Nonparametric Statistics*, 2nd ed., John Wiley & Sons, New York, NY, USA.

Consiglio, R., D. R. Baker, G. Paul, and H. E. Stanley (2003), Continuum percolation thresholds for mixtures of spheres of different sizes, *Physica A*, *319*, 49–55.

Copley, S. M., A. F. Giamei, S. M. Johnson, and M. F. Hornbeck (1970), Origin of freckles in unidirectionally solidified castings, *Metallurgical Transactions*, *1*(8), 2193–2204.

Cortinas, J. V., B. C. Bernstein, C. C. Robbins, and J. W. Strapp (2004), An analysis of freezing rain, freezing drizzle, and ice pellets across the United States and Canada: 1976–90, *Weather and Forecasting*, *19*(2), 377–390.

Cottier, F., H. Eicken, and P. Wadhams (1999), Linkages between salinity and brine channel distribution in young sea ice, *Journal of Geophysical Research*, *104*(C7), 15,859–15,871.

Cox, G. F. N., and W. F. Weeks (1975), Brine drainage and initial salt entrapment in sodium chloride ice, *Research Report 345*, Cold Regions Research and Engineering Laboratory, Hanover, NH, USA.

Cox, G. F. N., and W. F. Weeks (1982), Equations for determining the gas and brine volumes in sea ice samples, *Report 82–30*, Cold Regions Research and Engineering Laboratory, Hanover, NH, USA.

Cox, G. F. N., and W. F. Weeks (1986), Changes in the salinity and porosity of sea–ice samples during shipping and storage, *Journal of Glaciology*, *32*(112), 371–375.

Cox, G. F. N., and W. F. Weeks (1988), Numerical simulations of the profile properties of undeformed first–year sea ice during the growth season, *Journal of Geophysical Research*, *93*(C10), 12,449–12,460.

Crocker, G. B., and P. Wadhams (1989), Modelling Antarctic fast–ice growth, *Journal of Glaciology*, *35*(119), 3–8.

Cullen, D., and I. Baker (2001), Observation of impurities in ice, *Microscopy Research and Technique*, *55*, 198–207.

Dardis, O., and J. McCloskey (1998), Permeability porosity relationship from numerical simulations of fluid flow, *Geophysical Research Letters*, *25*(9), 1471–1474.

Dash, J. G., and J. S. Wettlaufer (2003), The surface physics of ice in thunderstorms, *Canadian Journal of Physics*, *81*(1–2), 201–207.

Davis, R. W., L. A. Fuiman, T. M. Williams, S. O. Collier, W. P. Hagey, S. B. Kanatous, S. Kohin, and M. Horning (1999), Hunting behavior of a marine mammal beneath the Antarctic fast ice, *Science*, *283*(5404), 993–996.

Dayton, P. K., G. A. Robillia, and A. L. DeVries (1969), Anchor ice formation in McMurdo Sound Antarctica and its biologial effects, *Science*, *163*(3864), 273–274.

Debye, P., and E. Hückel (1923), Zur Theorie der Elektrolyte, *Physikalische Zeitschrift*, *9*, 185–206.

Dieckmann, G., G. Rohardt, H. Hellmer, and J. Kipfstuhl (1986), The occurrence of ice platelets at 250 m depth near the Filchner Ice Shelf and its significance for sea ice biology, *Deep–Sea Research Part A*, *33*(2), 141–148.

Dieckmann, G. S., M. Spindler, M. A. Lange, S. F. Ackley, and H. Eicken (1991), Antarctic sea ice: A habitat for the foraminifer *Neogloboquadrina pachyderma*, *Journal of Foraminiferal Research*, *21*(2), 182–189.

Dikarev, S. N., S. G. Poyarkov, and S. I. Chuvil'chikov (2004), Laboratory modeling of small–scale convection under a growing ice cover in winter Arctic leads, *Oceanology*, *44*(1), 62–70.

Divett, T. A. (2000), Refreezing cracks in sea ice, B.Sc. Hons. project report, University of Otago, Physics Department, Dunedin, New Zealand.

Doble, M. J., M. D. Coon, and P. Wadhams (2003), Pancake ice formation in the Weddell Sea, *Journal of Geophysical Research*, *108*(C7), 3209, doi:10.1029/2002JC001373.

Drucker, R., S. Martin, and R. Moritz (2003), Observations of ice thickness and frazil ice in the St. Lawrence Island polynya from satellite imagery, upward looking sonar, and salinity/temperature moorings, *Journal of Geophysical Research*, *108*(C5), 3149, doi:10.1029/2001JC001213.

Ebert, E. E., and J. A. Curry (1993), An intermediate one–dimensional thermodynamic sea–ice model for investigating ice–atmosphere interactions, *Journal of Geophysical Research*, *98*(C6), 10,085–10,109.

Efimova, N. A. (1961), К методике расчета месячных величин эффективного излучения (On methods of calculating monthly values of net longwave radiation), *Метеорология и гидрология (Meteorologiya i Gidrologiya)*, *10*, 28–33, in Russian.

Ehn, J., M. A. Granskog, A. Reinart, and A. Erm (2004), Optical properties of melting landfast sea ice and underlying seawater in Santala Bay, Gulf of Finland, *Journal of Geophysical Research*, *109*, C09003, doi:10.1029/2003JC002042.

Eicken, H. (1991), Quantification of sea–ice properties: Automated image analysis of thin sections and parameterization of chlorophyll and salinity distributions, *Berichte zur Polarforschung*, *82*, in German.

Eicken, H. (1992), Salinity profiles of Antarctic sea ice: Field data and model results, *Journal of Geophysical Research*, *97*(C10), 15,545–15,557.

Eicken, H. (1994), Structure of under–ice melt ponds in the central Arctic and their effect on the sea ice cover, *Limnology and Oceanography*, *39*, 682–694.

Eicken, H. (1998), Deriving modes and rates of ice growth in the Weddell Sea from microstructural, salinity, and stable–isotope data, in *Antarctic Sea Ice: Physical Processes, Interactions and Variablility*, *American Geophysical Society, Antarctic Research Series*, vol. 74, edited by M. O. Jeffries, pp. 89–122.

Eicken, H. (2003), From the microscopic to the macroscopic to the regional scale: Growth, microstructure and properties of sea ice, in *Sea Ice – An Introduction to its Physics, Biology, Chemsitry and Geology*, edited by D. N. Thomas and G. S. Dieckmann, pp. 22–81, Blackwells Scientific Ltd., London, UK.

Eicken, H., H. Oerter, H. Miller, W. Graf, and J. Kipfstuhl (1994), Textural characteristics and impurity content of meteoric and marine ice in the Ronne–Ice–Shelf, Antarctica, *Journal of Glaciology*, *40*(135), 386–398.

Eicken, H., H. Fischer, and P. Lemke (1995a), Effects of the snow cover on Antarctic sea ice and potential modulation of its response to climate change, *Annals of Glaciology*, *21*, 369–376.

Eicken, H., M. Lensu, M. Leppäranta, W. B. Tucker, III, A. J. Gow, and O. Salmela (1995b), Thickness, structure, and properties of level summer multiyear ice in the Eurasian sector of the Arctic Ocean, *Journal of Geophysical Research*, *100*(C11), 22,697–22,710.

Eicken, H., E. Reimnitz, V. Alexandrov, T. Martin, H. Kassens, and T. Viehoff (1997), Sea–ice processes in the Laptev Sea and their importance for sediment export, *Continental Shelf Research*, *17*(2), 205–213.

Eicken, H., J. Weissenberger, I. Bussmann, J. Freitag, W. Schuster, F. Valero Delgado, K.-U. Evers, P. Jochmann, C. Krembs, R. Gradinger, F. Lindemann, F. Cottier, R. Hall, P. Wadhams, M. Reisemann, H. Kousa, J. Ikävalko, G. H. Leonard, H. Shen, S. F. Ackley, and L. H. Smedsrud (1998), Ice–tank studies of physical and biological sea–ice processes, in *Ice in Surface Waters. Proceedings of the 14th International Symposium on Ice*, edited by H. T. Shen, pp. 363–370.

Eicken, H., C. Bock, R. Wittig, H. Miller, and H.-O. Poertner (2000), Magnetic resonance imaging of sea–ice pore fluids: Methods and thermal evolution of pore microstructure, *Cold Regions Science and Technology*, *31*, 207–225.

Eicken, H., H. R. Krouse, D. Kadko, and D. K. Perovich (2002), Tracer studies of pathways and rates of meltwater transport through Arctic summer sea ice, *Journal of Geophysical Research*, *107*(C10), 8046, doi:10.1029/2000JC000583.

Eicken, H., T. C. Grenfell, D. K. Perovich, J. A. Richter-Menge, and K. Frey (2004), Hydraulic controls of summer Arctic pack ice albedo, *Journal of Geophysical Research*, *109*, C08007, doi:10.1029/2003JC001989.

Eide, L. I., and S. Martin (1975), The formation of brine drainage features in young sea ice, *Journal of Glaciology*, *14*(70), 137–154.

Eisen, O., and C. Kottmeier (2000), On the importance of leads in sea ice to the energy balance and ice formation in the Weddell Sea, *Journal of Geophysical Research*, *105*(C6), 14,045–14,060.

Esteban, Ó., M. Cruz-Navarette, A. González–Cano, and E. Bernabeu (1999), Measurement of the degree of salinity of water with a fibre–optic sensor, *Applied Optics*, *38*(25), 5267–5271.

Evans, R. J., and N. Untersteiner (1971), Thermal cracks in floating ice sheets, *Journal of Geophysical Research*, *76*(3), 694–703.

Farhadieh, R., and R. S. Tankin (1972), Interferometric study of freezing of sea water, *Journal of Geophysical Research*, *77*(9), 1647–1657.

Felicelli, S. D. (1991), Simulation of freckles during vertical solidification of binary alloys, Ph.D. thesis, The University of Arizona, Tucson, AZ, USA.

Felicelli, S. D., J. C. Heinrich, and D. R. Poirier (1991), Simulation of freckles during vertical solidification of binary alloys, *Metallurgical Transactions B*, *22B*, 847–859.

Felicelli, S. D., J. C. Heinrich, and D. R. Poirier (1998), Finie element analysis of directional solidification of multicomponent alloys, *International Journal for Numerical Methods in Fluids*, *27*, 207–227.

Feltham, D. L., M. G. Worster, and J. S. Wettlaufer (2002), The influence of ocean flow on newly forming sea ice, *Journal of Geophysical Research*, *107*(C2), 3009.

Feng, S., B. I. Halperin, and P. N. Sen (1987), Transport properties of continuum systems near the percolation threshold, *Physical Review B*, *35*(1), 197–214.

Ferziger, J. H., and M. Perić (2002), *Computational Methods for Fluid Dynamics*, 3rd ed., Springer–Verlag, Berlin, Germany.

Fitzharris, B., W. Lawson, and I. Owens (1999), Research on glaciers and snow in New Zealand, *Progress in Physical Geography*, *23*(4), 469–500.

Flemings, M. C. (1974), *Solidification Processing*, McGraw–Hill, Inc., New York, NY, USA.

Flemings, M. C., C. M. Adams, E. E. Hucke, and H. F. Taylor (1956), Metal solidification in a flowing stream, *Transactions of the American Foundrymen's Society*, *64*, 636–639.

Fletcher, P. (1993), *Chemical Thermodynamics for Earth Scientists*, Longman Scientific & Technical, Harlow, England.

Foster, T. D. (1969), Experiments on haline convection induced by the freezing of sea water, *Journal of Geophysical Research*, *74*(28), 6967–6974.

Freitag, J. (1999), The hydraulic properties of Arctic sea ice – implications for the small scale particle transport, *Berichte zur Polarforschung*, *325*, in German.

Freitag, J., and H. Eicken (2003), Meltwater circulation and permeability of Arctic summer sea ice derived from hydrological field experiments, *Journal of Glaciology*, *49*(166), 349–358.

Frey, K., H. Eicken, D. K. Perovich, T. C. Grenfell, B. Light, L. H. Shapiro, and A. P. Stierle (2001), Heat budget and decay of clean and sediment–laden sea ice off the northern coast of Alaska, in *Proceedings of the Port and Ocean Engineering in the Arctic Conference (POAC)*, vol. 3, pp. 1405–1412.

Frezzotti, M. (1997), Ice front fluctuation, iceberg calving flux and mass balance of Victoria Land glaciers, *Antarctic Science*, *9*(1), 61–73.

Fricker, H. A., S. Popov, I. Allison, and N. Young (2001), Distribution of marine ice beneath the Amery Ice Shelf, *Geophysical Research Letters*, *28*(11), 2241–2244.

Fritsen, C. H., V. I. Lytle, S. F. Ackley, and C. W. Sullivan (1994), Autumn bloom of Antarctic pack–ice algae, *Science*, *266*(5186), 782–784.

Fuller, W. A. (1987), *Measurement Error Models*, John Wiley & Sons, New York, NY, USA.

Ganesan, S., and D. R. Poirier (1990), Conservation of mass and momentum for the flow of interdendritic liquid during solidification, *Metallurgical Transactions B*, *21B*(1), 173–181.

Gaonac'h, H., S. Lovejoy, J. Six, and D. Schertzer (1996), A scaling growth model for bubbles in basaltic lava flows, *Earth and Planetary Science Letters*, *139*, 395–409.

Gaonac'h, H., S. Lovejoy, and D. Schertzer (2003), Percolating magmas and explosive volcanism, *Geophysical Research Letters*, *30*(11), 1559, doi:10.1029/2002GL016022.

Garboczi, E. J., K. A. Snyder, J. F. Douglas, and M. F. Thorpe (1995), Geometrical percolation–threshold of overlapping ellipsoids, *Physical Review E*, *52*(1), 819–828, part B.

Gerland, S., J.-G. Winther, J. B. Ørbæk, and B. V. Ivanov (1999), Physical properties, spectral reflectance and thickness development of first year fast ice in Kongsfjorden, Svalbard, *Polar Research*, *18*(2), 275–282.

Glen, J. W., and M. F. Perutz (1954), The growth and deformation of ice crystals, *Journal of Glaciology*, *2*(16), 397–403.

Gold, L. W. (1963), Crack formation in ice plates by thermal shock, *Canadian Journal of Physics*, *41*, 1712–1728.

Golden, K. M. (2003), Critical behavior of transport in sea ice, *Physica B*, *338*, 274–283.

Golden, K. M., S. F. Ackley, and V. I. Lytle (1998), The percolation phase transition in sea ice, *Science*, *282*(5397), 2238–2241.

Gosink, J. P., and T. E. Osterkamp (1983), Measurements and analyses of velocity profiles and frazil ice–crystal rise velocities during periods of frazil–ice formation in rivers, *Annals of Glaciology*, *4*, 79–84.

Gow, A. J., and W. B. Tucker, III (1990), Sea ice in the polar regions, in *Polar Oceanography*, edited by W. O. Smith, Jr., Part A, Physical Science, pp. 47–122, Academic Press, Inc., San Diego, CA, USA.

Gow, A. J., D. A. Meese, D. K. Perovich, and W. B. Tucker, III (1990), The anatomy of a freezing lead, *Journal of Geophysical Research*, *95*(C10), 18,221–18,232.

Gray, W. G. (1975), A derivation of the equations for multi–phase transport, *Chemical Engineering Science*, *30*, 229–233.

Gray, W. G., and K. O'Neill (1976), On the general equations for flow in porous media and their reduction to Darcy's law, *Water Resources Research*, *12*, 148–154.

Grenfell, T. C., and G. A. Maykut (1977), The optical properties of ice and snow in the Arctic basin, *Journal of Glaciology*, *18*(80), 445–463.

Grenfell, T. C., and D. K. Perovich (1984), Spectral albedos of sea ice and incident solar irradiance in the Southern Beaufort Sea, *Journal of Geophysical Research*, *89*(C3), 3573–3580.

Grenfell, T. C., S. G. Warren, and P. C. Mullen (1994), Reflection of solar radiation by the Antarctic snow surface at ultraviolet, visible, and near–infrared wavelengths, *Journal of Geophysical Research*, *99*(D9), 18,669–18,684.

Grenfell, T. C., D. G. Barber, A. K. Fung, A. J. Gow, K. C. Jezek, E. J. Knapp, S. V. Nghiem, R. G. Onstott, D. K. Perovich, C. S. Roesler, C. T. Swift, and F. Tanis (1998), Evolution of electromagnetic signatures of sea ice from initial formation of the establishment of thick first–year ice, *IEEE Transactions on Geoscience and Remote Sensing*, *36*(5), 1642–1654, part 2.

Günther, S., and G. S. Dieckmann (1999), Seasonal development of algal biomass in snow–covered fast ice and the underlying platelet layer in the Weddell Sea, Antarctica, *Antarctic Science*, *11*(3), 305–315.

Haas, C. (1999), Ice tank investigations of the microstructure of artificial sea ice grown under different boundary conditions during INTERICE II, in *Proceedings of the HYDRALAB Workshop*, edited by K.-U. Evers, J. Grüne, and A. van Os, pp. 107–113, Hannover, Germany.

Haas, C., F. Cottier, L. H. Smedsrud, D. Thomas, U. Buschmann, D. Dethleff, S. Gerland, V. Giannelli, J. Hoelemann, J.-L. Tison, and P. Wadhams (1999), Multidisciplinary ice tank study shedding new light on sea ice growth processes, *EOS, Transactions, American Geophysical Union*, *80*(43), 507–513.

Haines, E. M., R. G. Buckley, and H. J. Trodahl (1997), Determination of the depth dependent scattering coefficient in sea ice, *Journal of Geophysical Research*, *102*(C1), 1141–1151.

Harrison, C. G. A. (1999), Constraints on ocean volume change since the Archean, *Geophysical Research Letters*, *26*(13), 1913–1916.

Harrison, J. D., and W. A. Tiller (1963), Controlled freezing of water, in *Ice and Snow, Properties, Processes, and Applications*, edited by W. D. Kingery, Proceedings of a Conference held at The Massachusetts Institute of Technology, February 12–16, 1962, pp. 215–225, The M.I.T. Press, Cambridge, MA, USA.

Haskell, T. G., and P. J. Langhorne (unpublished 2000), Some properties of refrozen cracks in sea ice, *Poster at the International Symposium on Sea Ice and its Interactions with the Ocean, Atmosphere and Biosphere held in Fairbanks, AK, USA during June 2000.*

Haskell, T. G., W. H. Robinson, and P. J. Langhorne (1996), Preliminary results from fatigue tests on in situ sea ice beams, *Cold Regions Science and Technology*, *24*(2), 167–176.

Hayase, T., J. A. C. Humphrey, and R. Greif (1992), A consistently formulated QUICK scheme for fast and stable convergence using finite–volume iterative calculation procedures, *Journal of Computational Physics*, *98*, 108–118.

van't Hoff, J. H. (1887), Die Rolle des osmotischen Druckes in der Analogie zwischen Lösungen und Gasen, *Zeitschrift für Physikalische Chemie*, *1*, 481–508.

Hunt, B. M., K. Hoefling, and C.-H. C. Cheng (2003), Annual warming episodes in seawater temperatures in McMurdo Sound in releationship to endogenous ice in notothenioid fish, *Antarctic Science*, *15*(3), 333–338.

Hurle, D. T. J. (1963), Mechanisms of growth of metal single crystals from the melt, *Progress in Materials Science*, *10*, 79–147.

Iliescu, D., I. Baker, and D. Cullen (2002), Preliminary microstructural and microchemical observations on pond and river accretion ice, *Cold Regions Science and Technology*, *35*(2), 81–99.

Intrieri, J. M., C. W. Fairall, M. D. Shupe, P. O. G. Persson, E. L. Andreas, P. S. Guest, and R. E. Moritz (2002), An annual cycle of Arctic surface cloud forcing at SHEBA, *Journal of Geophysical Research*, *107*(C10), 8039, doi:10.1029/2000JC000439.

Iqbal, M. (1983), *An Introduction to Solar Radiation*, Academic Press, Toronto, Canada.

Jacobs, J. D. (1978), Radiation climate of Broughton Island, in *Energy Budget Studies in Relation to Fast–Ice Breakup Processes in Davis Strait*, *Occasional Papers*, vol. 26, edited by R. G. Barry and J. D. Jacobs, pp. 105–120, Institute of Arctic and Alpine Research, University of Colorado, Boulder, CO, USA.

Janzen, J. (1975), On the critical conductive filler loading in antistatic composites, *Journal of Applied Physics*, *46*(2), 966–969.

Janzen, J. (1980), Short derivation of the influence of particle size ratio on the conductivity threshold in binary aggregates, *Journal of Applied Physics*, *51*(4), 2279–2280.

Jeffery, C. A., and P. H. Austin (1997), Homogeneous nucleation of superccoled water: Results from a new equation of state, *Journal of Geophysical Research*, *102*(D21), 25,269–25,279.

Jeffries, M. O., and U. Adolphs (1997), Early winter ice and snow thickness distribution, ice structure and development of the western Ross Sea pack ice between the ice edge and the Ross Ice Shelf, *Antarctic Science*, *9*(2), 188–200.

Jeffries, M. O., W. F. Weeks, R. Shaw, and K. Morris (1993), Structural characteristics of congelation and platelet ice and their role in the development of Antarctic land–fast sea–ice, *Journal of Glaciology*, *39*(132), 223–238.

Jeffries, M. O., K. Schwartz, K. Morris, A. D. Veazey, H. R. Krouse, and S. Cushing (1995), Evidence for platelet ice accretion in Arctic sea ice development, *Journal of Geophysical Research*, *100*(C6), 10,905–10,914.

Jenkins, A., and A. Bombosch (1995), Modeling the effects of frazil ice crystals on the dynamics and thermodynamics of ice shelf water plumes, *Journal of Geophysical Research*, *100*(C4), 6967–6981.

Jenkins, A., and C. S. M. Doake (1991), Ice–ocean interaction on Ronne Ice Shelf, Antarctica, *Journal of Geophysical Research*, *96*(C1), 791–813.

Jones, S. J., and B. T. Hill (2001), Structure of sea ice in McMurdo Sound, Antarctica, *Annals of Glaciology*, *33*, 5–12.

Josberger, E. G., and S. Martin (1981), A laboratory and theoretical study of the boundary layer adjacent to a vertical melting ice wall in salt water, *Journal of Fluid Mechanics*, *111*, 439–473.

Junge, K., H. Eicken, and J. W. Deming (2004), Bacterial activity at −2 to −20 °C in Arctic wintertime sea ice, *Applied and Environmental Microbiology*, *70*(1), 550–557, doi:10.1128/AEM.70.1.550-557.2004.

Kempema, E. W., E. Reimnitz, J. R. Clayton, and J. R. Payne (1993), Interactions of frazil and anchor ice with sedimentary particles in a flume, *Cold Regions Science and Technology*, *21*(2), 137–149.

Kempema, E. W., E. Reimnitz, and P. W. Barnes (2001), Anchor–ice formation and ice rafting in southwestern Lake Michigan, USA, *Journal of Sedimentary Research, Part A*, *71*(3), 346–354.

Key, J. R., R. A. Silcox, and R. S. Stone (1996), Evaluation of surface radiative flux parameterizations for use in sea ice models, *Journal of Geophysical Research*, *101*(C2), 3839–3849.

Khazendar, A., and A. Jenkins (2003), A model of marine ice formation within Antarctic ice shelf rifts, *Journal of Geophysical Research*, *108*(C7), 3235, doi: 10.1029/2002JC001673.

Kingery, W. D., and R. L. Coble (1963), Cracks in sea ice and their effect on operations, in *Ice and Snow: Properties, Processes and Applications*, edited by W. D. Kingery, Proceedings of a Conference held at The Massachusetts Institute of Technology, February 12–16, 1962, pp. 322–334, The M.I.T. Press, Cambridge, MA, USA.

Klug, C., K. V. Cashman, and C. R. Bacon (2002), Structure and physical characteristics of pumice from the climatic eruption of Mount Mazama (Crater Lake), Oregon, *Bulletin of Volcanology*, *64*, 486–501.

Knackstedt, M. A., and S. F. Cox (1995), Percolation and the pore geometry of crustal rocks, *Physical Review E*, *51*(6), R5181–R5184.

Knackstedt, M. A., and J. P. Duplessis (1996), Simple permeability model of natural granular media, *Geophysical Research Letters*, *23*(13), 1609–1612.

Koh, C. A. (2002), Towards a fundamental understanding of natural gas hydrates, *Chemical Society Review*, *31*(3), 157–167.

König-Langlo, G., and E. Augstein (1994), Parameterisation of the downward long–wave radiation at the Earth's surface in polar regions, *Meteorologische Zeitschrift*, *3*(6), 343–347.

Koo, K.-K., R. Ananth, and W. N. Gill (1992), Thermal convection, morphological stability and the dendritic grwoth of crystals, *AIChE Journal*, *38*(6), 945–954.

Kovacs, A. (1996), Sea ice: Part I. Bulk salinity versus ice floe thickness, *Report 96–7*, Cold Regions Research and Engineering Laboratory, Hanover, NH, USA.

Kundu, P. K. (1990), *Fluid Mechanics*, Academic Press, San Diego, CA, USA.

Kurz, W., and D. J. Fisher (1998), *Fundamentals of Solidification*, 4th ed., Trans Tech Publications, Ltd., Uetikon–Zürich, Switzerland.

Kusy, R. P. (1977), Influence of particle–size ratio on continuity of aggregates, *Journal of Applied Physics*, *48*(12), 5301–5305.

Kuz'min, M. I., E. B. Karabanov, T. Kawai, D. Williams, V. A. Bychinskii, E. V. Kerber, V. A. Kravchinskii, E. V. Bezrukova, A. A. Prokopenko, V. F. Geletii, G. V. Kalmychkov, A. V. Goreglyad, V. S. Antipin, M. Y. Khomotova, N. M. Soshina, E. V. Ivanov, G. K. Khursevich, L. L. Tkachenko, E. P. Solotchina, N. Ioshida, and A. N. Gvozdkov (2001), Deep drilling on Lake Baikal: Main results, *Геология и геофизика (Geologiya i Geofizika)*, *42*(1–2), 8–34, in Russian.

Lake, R. A., and E. L. Lewis (1970), Salt rejection by sea ice during growth, *Journal of Geophysical Research*, *75*(3), 583–597.

Landau, L. D., and E. M. Lifshitz (1959), *Statistical Physics*, *Course of Theoretical Physics*, vol. 5, 2nd ed., Pergamon Press, London, UK.

Lange, M. A., and H. Eicken (1991), Textural characteristics of sea ice and the major mechanism of ice growth in the Weddell Sea, *Annals of Glaciology*, *15*, 210–215.

Langhorne, P. J. (1983), Laboratory experiments on crystal oriantation in NaCl ice, *Annals of Glaciology*, *4*, 163–169.

Langhorne, P. J., and T. G. Haskell (2004), The flexural strength of partially refrozen cracks in sea ice, in *Proceedings of The Fourteenth International Offshore and Polar Engineering Conference*, pp. 819–824, The International Society of Offshore and Polar Engineers, Toulon, France.

Langhorne, P. J., and W. H. Robinson (1986), Alignment of crystals in sea ice due to fluid motion, *Cold Regions Science and Technology*, *12*, 197–214.

Langhorne, P. J., V. A. Squire, C. Fox, and T. G. Haskell (1998), Break–up of sea ice by ocean waves, *Annals of Glaciology*, *27*, 438–442.

Leath, P. L. (1976), Cluster size and boundary distribution near percolation threshold, *Physical Review B*, *14*(11), 5046–5055.

Leckner, B. (1978), The spectral distribution of solar radiation at the earth's surface – elements of a model, *Solar Energy*, *20*(2), 143–150.

Leonard, G., C. Purdie, M. Williams, T. Haskell, and P. Langhorne (unpublished 2002), Proposed observations of the growth of land–fast sea ice in McMurdo Sound, Antarctica during the winter of 2003, *Poster at the 16th IAHR International Symposium on Ice held in Dunedin, New Zealand, December 2002.*

Leonard, G. H., C. R. Purdie, P. J. Langhorne, T. G. Haskell, M. J. M. Williams, and R. D. Frew (submitted), Observations of platelet ice growth and oceanographic conditions during the winter of 2003 in McMurdo Sound, Antarctica, *submitted manuscript.*

Leonard, G. H., C. R. Purdie, J. G. Leitch, P. J. Langhorne, and T. G. Haskell (unpublished 2004), Observations of platelet ice growth and oceanographic conditions during winter 2003 in McMurdo Sound, Antarctica, *Poster at the AGU/CGU Spring Meeting held in Montreal, Canada, May 2004.*

Leppäranta, M. (1993), A review of analytical models of sea–ice growth, *Atmosphere–Ocean*, *31*(1), 123–138.

Lewis, E. L. (1967), Heat flow through winter ice, in *Physics of Snow and Ice, International Conference on Low Temperature Science, Proceedings*, vol. 1, edited by H. Oura, pp. 611–631, Institute of Low Temperature Science, Hokkaido University, Sapporo, Japan.

Lewis, E. L. (1985), The calibration of CTD sensors, in *Evaluation, Comparison and Calibration of Oceanographic Intruments*, *Advances in Underwater Technology and Offshore Engineering*, vol. 4, pp. 129–146, Graham & Trotman Ltd.

Lewis, E. L., and R. B. Sudar (1972), Measurement of conductivity and temperature in the sea for salinity determination, *Journal of Geophysical Research*, *77*(33), 6611–6617.

Light, B., H. Eicken, G. A. Maykut, and T. C. Grenfell (1998), The effect of included particulates on the spectral albedo of sea ice, *Journal of Geophysical Research*, *103*(C12), 27,739–27,752.

Light, B., G. A. Maykut, and T. C. Grenfell (2003), Effects of temperature on the microstructure of first–year Arctic sea ice, *Journal of Geophysical Research*, *108*(C2), doi:10.1029/2001JC000887.

Light, B., G. A. Maykut, and T. C. Grenfell (2004), A temperature–dependent, structural–optical model of first–year sea ice, *Journal of Geophysical Research*, *109*(C6), C06013.

List, R., and R. S. Schemena (1971), Free–fall behavior of planar snow crystals, conical graupel and small hail, *Journal of the Atmospheric Sciences*, *28*(1), 110.

Lizotte, M. P. (2003), The microbiology of sea ice, in *Sea Ice – An Introduction to its Physics, Biology, Chemsitry and Geology*, edited by D. N. Thomas and G. S. Dieckmann, pp. 184–210, Blackwells Scientific Ltd., London, UK.

Lobban, C., J. L. Finney, and W. F. Kuhs (1998), The structure of a new phase of ice, *Nature*, *391*, 268–270.

Lock, G. S. H. (1990), *The Growth and Decay of Ice*, Studies in Polar Research, Cambridge University Press, Cambridge, UK.

Lofgren, G., and W. F. Weeks (1969), Effect of growth parameters on substructure spacing in NaCl ice crystals, *Journal of Glaciology*, *8*(52), 153–164.

Lowe, P. R. (1977), An approximating polynomial for the computation of saturation vapor–pressure, *Journal of Applied Meteorology*, *16*(1), 100–103.

Lubensky, T. C., and A. J. McKane (1981), Cluster size distribution above the percoaltion threshold, *Journal of Physics A: Mathematical and General*, *14*(5), L157–L161.

Lynch, F. T., and A. Khodadoust (2001), Effects of ice accretions on aircraft aerodynamics, *Progress in Aerospace Sciences*, *37*(8), 669–767.

Lytle, V. I., R. Massom, N. Bindoff, A. Worby, and I. Allison (2000), Wintertime heat flux to the underside of East Antarctic pack ice, *Journal of Geophysical Research*, *105*(C12), 28,759–28,769.

Mack, C. (1956), On clumps formed when convex laminae or bodies are placed at random in two or three dimensions, *Proceedings of the Cambridge Philosophical Society*, *52*, 246–256.

Makshtas, A. P., E. L. Andreas, P. N. Svyashchennikov, and V. F. Timachev (1998), Accounting for clouds in sea ice models, *Report 98–9*, Cold Regions Research and Engineering Laboratory, Hanover, NH, USA.

Maksym, T., and M. O. Jeffries (2000), A one–dimensional percolation model of flooding and snow ice formation on Antarctic sea ice, *Journal of Geophysical Research*, *105*(C11), 26,313–26,331.

Malmgren, F. (1927), On the properties of sea ice, in *The Norwegian Polar Expedition "Maud" 1918–1925*, *Scientific Results*, vol. 1a(5), pp. 1–67.

van der Marck, S. C. (1999), Evidence for a nonzero transport threshold in porous media, *Water Resources Research*, *35*(2), 595–599.

Matsumoto, M., and T. Nishimura (1998), Mersenne Twister: A 623–dimensionally equidistributed uniform pseudorandom number generator, *ACM Transactions on Modeling and Computer Simulation*, *8*(1), 3–30.

Max, M. D., and A. Lowrie (1996), Oceanic methane hydrates: A "frontier" gas resource, *Journal of Petroleum Geology*, *19*(1), 41–56.

Maykut, G. A., and T. C. Grenfell (1975), The spectral distribution of light beneath first–year sea ice in the Arctic Ocean, *Limnology and Oceanography*, *20*(4), 554–563.

Maykut, G. A., and N. Untersteiner (1971), Some results from a time–dependent thermodynamic model of sea ice, *Journal of Geophysical Research*, *76*, 1550–1575.

McCay, M. H., T. D. McCay, and J. A. Hopkins (1993), The nature and influence of convection on the directional dendritic solidification of a metal alloy analog, NH_4Cl, and H_2O, *Metallurgical Transactions B*, *24B*, 669–675.

McGuinness, M. J., K. A. Landman, H. J. Trodahl, and A. E. Pantoja (2001), Solar radiative heating in first–year sea ice, *Annals of Glaciology*, *33*, 261–266.

McMinn, A., C. Ashworth, and K. G. Ryan (2000), In situ net primary productivity of an Antarctic fast ice bottom algal community, *Aquatic Microbial Ecology*, *21*(2), 177–185.

McPhee, M. G. (1992), Turbulent heat flux in the upper ocean under sea ice, *Journal of Geophysical Research*, *97*(C4), 5365–5379.

McPhee, M. G., and T. P. Stanton (1996), Turbulence in the statically unstable oceanic boundary layer under Arctic leads, *Journal of Geophysical Research*, *101*(C3), 6409–6428.

Medjani, K. (1996), Numerical simulation of the formation of brine pockets during the freezing of the NaCl–H_2O compound from above, *International Communications in Heat and Mass Transfer*, *23*(7), 917–928.

Metge, M. (1976), Thermal cracks in lake ice, Ph.D. thesis, Queen's University, Kingston, Ontario, Canada.

Miksch, E. S. (1969), Solidification of ice dendrites in flowing supercooled water, *Transactions of the Metallurgical Society AIME*, *245*, 2069–2072.

Mishima, O., and H. E. Stanley (1998), The relationship between liquid, supercooled and glassy water, *Nature*, *396*, 329–335.

Moore, J. C., A. P. Reid, and J. Kipfstuhl (1994), Microstructure and electrical properties of marine ice and its relationship to meteoric ice and sea ice, *Journal of Geophysical Research*, *99*(C3), 5171–5180.

Morison, J. H., and M. G. McPhee (1998), Lead convection measured with an autonomous underwater vehicle, *Journal of Geophysical Research*, *103*(C2), 3257–3281.

Müller, M. (1995), Equation of time – problem in astronomy, *Acta Physica Polonica A*, *88*, S49–S67, supplement.

Murakami, K., T. Fujiyama, A. Koike, and T. Okamoto (1983), Influence of melt flow on the growth directions of columnar grains and columnar dendrites, *Acta Metallurgica*, *31*(4), 1425–1432.

Murakami, K., H. Aihara, and T. Okamoto (1984), Growth direction of columnar crystals solidified in flowing melt, *Acta Metallurgica*, *32*(6), 933–939.

Nagashima, K., and Y. Furukawa (2003), Effects of gravity on directional growth and melting of ice crystals in solution, *Canadian Journal of Physics*, *81*(1–2), 99–105.

Nakawo, M., and N. K. Sinha (1981), Growth rate and salinity profile of first–year sea ice in the high Arctic, *Journal of Glaciology*, *27*(96), 315–330.

Nakawo, M., and N. K. Sinha (1984), A note on brine layer spacing of first–year sea ice, *Atmosphere–Ocean*, *22*(2), 193–206.

Namiki, A., T. Hatakeyama, A. Toramaru, K. Kurita, and I. Sumita (2003), Bubble size distributions in a convecting layer, *Geophysical Research Letters*, *30*(15), 1784, doi:10.1029/2003GL017156.

Niedrauer, T. M., and S. Martin (1979), An experimental study of brine drainage and convection in young sea ice, *Journal of Geophysical Research*, *84*(C3), 1176–1186.

Nishimura, T. (2000), Tables of 64–bit Mersenne Twisters, *ACM Transactions on Modeling and Computer Simulation*, *10*(4), 348–357.

Norris, S. E. (2001), A parallel Navier–Stokes solver for natural convection and free surface flow, Ph.D. thesis, University of Sydney, Sydney, Australia.

Nürnberg, D., I. Wollenburg, D. Dethleff, H. Eicken, H. Kassens, T. Letzig, E. Reimnitz, and J. Thiede (1994), Sediments in Arctic sea ice: Implications for entrainment, transport and release, *Marine Geology*, *119*(3–4), 185–214.

Oerter, H., J. Kipfstuhl, J. Determann, H. Miller, D. Wagenbach, A. Minikin, and W. Graf (1992), Evidence for basal marine ice in the Filchner–Ronne ice shelf, *Nature*, *358*(6385), 399–401.

Oertling, A. B., and R. G. Watts (2004), Growth of and brine drainage from NaCl–H_2O freezing: A simulation of young sea ice, *Journal of Geophysical Research*, *109*, C04013, doi:10.1029/2001JC001109.

Omstedt, A. (1985), On supercooling and ice formation in turbulent sea–water, *Journal of Glaciology*, *31*(109), 263–271.

Ono, N. (1966), Thermal properties of sea ice. III. On the specific heat of sea ice, *Teion-Kagaku (Low Temperature Science), Series A*, *24*, 249–258, in Japanese with English summary.

Ono, N. (1975), Thermal properties of sea ice IV, *CRREL Draft Translation 467*, Cold Regions Research and Engineering Laboratory, Hanover, NH, USA.

Parkinson, C. L., and W. M. Washington (1979), A large–scale numerical model of sea ice, *Journal of Geophysical Research*, *84*(NC1), 311–337.

Patankar, S. V. (1980), *Numerical Heat Transfer and Fluid Flow*, Hemisphere Publishing Co., New York, NY, USA.

Patankar, S. V., and D. B. Spalding (1972), A calculation procedure for heat, mass and momentum transfer in three–dimensional parabolic flows, *International Journal of Heat and Mass Transfer*, *15*, 1787–1806.

Perovich, D. K., and A. J. Gow (1996), A quantitative description of sea ice inclusions, *Journal of Geophysical Research*, *101*(C8), 18,327–18,343.

Perovich, D. K., and T. C. Grenfell (1981), Laboratory studies of the optical properties of young sea ice, *Journal of Glaciology*, *27*(96), 331–346.

Perovich, D. K., and J. A. Richter-Menge (2000), Ice growth and solar heating in springtime leads, *Journal of Geophysical Research*, *105*(C3), 6541–6548.

Perovich, D. K., J. A. Richter-Menge, and W. B. Tucker, III (2001), Seasonal changes in Arctic sea–ice morphology, *Annals of Glaciology*, *33*, 171–176.

Perovich, D. K., T. C. Grenfell, B. Light, and P. V. Hobbs (2002), Seasonal evolution of the albedo of multiyear Arctic sea ice, *Journal of Geophysical Research*, *107*(C10), 8044, doi:10.1029/200JC000438.

Perovich, D. K., T. C. Grenfell, J. A. Richter-Menge, B. Light, W. B. Tucker, III, and H. Eicken (2003), Thin and thinner: Sea ice mass balance measurements during SHEBA, *Journal of Geophysical Research*, *108*(C3), 8050, doi:10.1029/2001JC001079.

Persson, P. O. G., C. W. Fairall, E. L. Andreas, P. S. Guest, and D. K. Perovich (2002), Measurements near the Atmospheric Surface Flux Group tower at SHEBA: Near–surface conditions an surface energy budget, *Journal of Geophysical Research*, *107*(C10), 8045, doi:10.1029/2000JC000705.

Petrenko, V. F., and R. W. Whitworth (1999), *Physics of Ice*, Oxford University Press, Oxford, UK.

Petrich, C., P. J. Langhorne, and T. G. Haskell (2002), Modelling of refrozen cracks in sea ice, in *Ice in the Environment: Proceedings of the 16th IAHR International Symposium on Ice*, vol. 2, edited by V. Squire and P. Langhorne, pp. 235–242, University of Otago, Dunedin, New Zealand.

Petrich, C., T. G. Haskell, and P. J. Langhorne (2003), Structure of refrozen cracks in first–year sea ice, *Canadian Journal of Physics*, *81*(1–2), 293–299.

Petrich, C., P. J. Langhorne, and Z. Sun (2004), Numerical simulation of sea ice growth and desalination, in *Proceedings of the 17th IAHR International Symposium on Ice*, vol. 3, All–Russian Research Institute of Hydraulic Engineering (VNIIG), St. Petersburg, Russian Federation, in press.

Pfirman, S. L., H. Eicken, D. Bauch, and W. F. Weeks (1995), The potential transport of pollutants by Arctic sea ice, *Science of the Total Environment*, *159*(2–3), 129–146.

Poirier, D. R., P. J. Nandapurkar, and S. Ganesan (1991), The energy and solute conservation equations for dendritic solidification, *Metallurgical Transactions B*, *22B*, 889–900.

Prowse, T. D., and S. Beltaos (2002), Climatic control of river–ice hydrology: A review, *Hydrological Processes*, *16*, 805–822.

Rahlves, M. (2003), Laboratory experiments on banding in saline ice, *Project report*, University of Otago, Physics Department, Dunedin, New Zealand.

Richardson, C. (1976), Phase relationships in sea ice as a function of temperature, *Journal of Glaciology*, *17*(77), 507–519.

Rintoul, M. D. (2000), Precise determination of the void percolation threshold for two distributions of overlapping spheres, *Physical Review E*, *62*(1), 68–72.

Rohatgi, P. K., and C. M. Adams, Jr (1967), Ice–brine dendritic aggregate formed on freezing of aqueous solutions, *Journal of Glaciology*, *6*(47), 663–679.

Romanovskii, N. N., H. W. Hubberten, A. Gavrilov, V. E. Tumskoy, and A. L. Kholodov (2004), Permafrost of the east Siberian Arctic shelf and coastal lowlands, *Quaternary Science Reviews*, *23*(11–13), 1359–1369.

Röntgen, W. C. (1892), Ueber die Constitution des flüssigen Wassers, *Annalen der Physik und Chemie*, *45*, 91–97.

RS Components (1997), Light dependent resistors, *Data Sheet 232-3816*, RS Components, Northants, UK.

Sahimi, M. (1993), Nonlinear transport process in disordered media, *AIChE Journal*, *39*(3), 369–386.

Schlosser, E. (1988), Optical studies of Antarctic sea ice, *Cold Regions Science and Technology*, *15*, 289–293.

Schnack-Schiel, S. B. (2003), The macrobiology of sea ice, in *Sea Ice – An Introduction to its Physics, Biology, Chemsitry and Geology*, edited by D. N. Thomas and G. S. Dieckmann, pp. 211–239, Blackwells Scientific Ltd., London, UK.

Schulze, T. P., and M. G. Worster (1999), Weak convection, liquid inclusions and the formation of chimneys in mushy layers, *Journal of Fluid Mechanics*, *388*, 197–215.

Settles, G. S. (2001), *Schlieren and Shadowgraph Techniques*, Experimental Fluid Mechanics, Springer–Verlag, Berlin, Germany.

Sharp, M., J. Jouzel, B. Hubbard, and W. Lawson (1994), The character, structure and origin of the basal ice layer of a surge–type glacier, *Journal of Glaciology*, *40*(135), 327–340.

Shen, H. T., and L. Liu (2003), Shokotsu River ice jam formation, *Cold Regions Science and Technology*, *37*, 35–49.

Shine, K. P. (1984), Parameterization of the shortwave flux over high albedo surfaces as a function of cloud thickness and surface albedo, *Quarterly Journal of the Royal Meteorological Society*, *110*, 747–764.

Shupe, M. D., and J. M. Intrieri (2004), Cloud radiative forcing of the Arctic surface: The influence of cloud properties, surface albedo, and solar zenith angle, *Journal of Climate*, *17*(3), 616–628.

Skyllingstad, E. D., and D. W. Denbo (2001), Turbulence beneath sea ice and leads: A coupled sea ice/large eddy simulation study, *Journal of Geophysical Research*, *106*(C2), 2477–2497.

Slattery, J. C. (1967), Flow of viscoelastic fluids through porous media, *AIChE Journal*, *13*, 1066–1071.

Slattery, J. C. (1981), *Momentum, Energy, and Mass Transfer in Continua*, 2nd ed., Robert E. Krieger Publishing Co., New York, NY, USA.

Smedsrud, L. H., and A. Jenkins (2004), Frazil ice formation in an ice shelf water plume, *Journal of Geophysical Research*, *109*, C03025, doi:10.1029/2003JC001851.

SooHoo, J. B., A. C. Palmisano, S. T. Kottmeier, M. P. Lizotte, S. L. SooHoo, and C. W. Sullivan (1987), Spectral light absorption and quantum yield of photosynthesis in sea ice microalgae and a bloom of *Phaeocystis pouchetii* from McMurdo Sound, Antarctica, *Marine Ecology Progress Series*, *39*, 175–189.

Souchez, R., M. Meneghel, J.-L. Tison, R. Lorrain, D. Ronveaux, C. Baroni, A. Lozej, I. Tabacco, and J. Jouzel (1991), Ice composition evidence of marine ice transfer along the bottom of a small Antarctic ice shelf, *Geophysical Research Letters*, *18*(5), 849–852.

Stauffer, D. (1986), Percolation and cluster size distribution, in *On Growth and Form*, edited by H. E. Stanley and N. Ostrowsky, pp. 79–100, Martinus Nijhoff Publishers, Dordrecht, The Netherlands.

Stauffer, D., and A. Aharony (1992), *Introduction to Percolation Theory*, 2nd ed., Taylor and Francis, London, UK.

Stefan, J. (1891), Ueber die Theorie der Eisbildung, insbesondere über die Eisbildung im Polarmeere, *Annalen der Physik, 3. Serie*, *42*, 269–286.

Steinhart, J. S., and S. R. Hart (1968), Calibration curves for thermistors, *Deep–Sea Research*, *15*(4), 497–503.

Stewart, M. J., and F. Weinberg (1972), Fluid flow through a solid–liquid dendritic interface, *Metallurgical Transactions*, *3*(1), 333–337.

Sun, Z. F., C. G. Carrington, and P. Bannister (2000), Dynamic modelling of the wood stack in a wood drying kiln, *Transactions of the Institution of Chemical Engineers, Part A*, *78*, 107–117.

Tait, S., and C. Jaupart (1992), Compositional convection in a reactive crystalline mush and melt differentiation, *Journal of Geophysical Research*, *97*(B5), 6735–6756.

Takahashi, T., I. Hagiwara, and K. Ichikawa (1972), Significance of the solidifying zone on ingot solidification, *Transactions of the Iron and Steel Institute of Japan*, *12*(6), 412–421.

Tanaka, H. (2000), Simple physical model of liquid water, *Journal of Chemical Physics*, *112*(2), 799–809.

Taylor, G. (1922), The physiography of the McMurdo Sound and Granite Harbour region, in *British Antarctic (Terra Nova) Expedition 1910–1913*, Harrison and Sons, Ltd., London, UK.

Taylor, L. D., and J. B. Lyons (1959), Ice structure, Angiussaq Lake, northwest Greenland, *Scientific Report 1*, Air Force Cambridge Research Center, Hanscom Field, MA, USA.

Tetens, O. (1930), Über einige meterologische Begriffe, *Zeitschrift für Geophysik*, *6*, 297–309.

Thomas, D. N., and G. S. Dieckmann (2002), Ocean science – Antarctic sea ice – a habitat for extremophiles, *Science*, *295*(5555), 641–644.

Thomas, R. H. (1979), Ice shelfs: A review, *Journal of Glaciology*, *24*(90), 273–286.

Thomsen, C. (2002), Critical exponents and percolation thresholds in two–dimensional systems with a finite interplane coupling, *Physical Review E*, *65*, 065104(R).

Tiller, W. A., K. A. Jackson, J. W. Rutter, and B. Chalmers (1953), The redistribution of solute atoms during the solidification of metals, *Acta Metallurgica*, *1*, 428–437.

Timco, G. W. (1987), Ice structure interaction tests with ice containing flaws, *Journal of Glaciology*, *33*(114), 186–194.

Timco, G. W., and R. M. W. Frederking (1996), A review of sea ice density, *Cold Regions Science and Technology*, *24*(1), 1–6.

Tin, T., and M. O. Jeffries (2003), Morphology of deformed first–year sea ice features in the Southern Ocean, *Cold Regions Science and Technology*, *36*, 141–163.

Tirmizi, S. H., and W. N. Gill (1987), Effect of natural convection on growth velocity and morphology of dendritic ice crystals, *Journal of Crystal Growth*, *85*, 488–502.

Tison, J.-L., and V. Verbeke (2001), Chlorinity/salinity distribution patterns in experimental granular sea ice, *Annals of Glaciology*, *33*, 13–20.

Tison, J.-L., A. Khazendar, and E. Roulin (2001), A two–phase approach to the simulation of the combines isotope/salinity signal of marine ice, *Journal of Geophysical Research*, *106*(C12), 31,387–31,401.

Tobin, D. C., F. A. Best, P. D. Brown, S. A. Clough, R. G. Dedecker, R. G. Ellingson, R. K. Garcia, H. B. Howell, R. O. Knuteson, E. J. Mlawer, H. E. Revercomb, J. F. Short, P. F. W. van Delst, and V. P. Walden (1999), Downwelling spectral radiance observations at the SHEBA ice station: Water vapor continuum measurements from 17 to 26 μm, *Journal of Geophysical Research*, *104*(D2), 2081–2092.

Toyota, T. (1998), A study on growth processes of sea ice in the southern region of the Okhotsk Sea, evaluated from heat budget and sea ice sample analysis, Ph.D. thesis, Hokkaido University, Sapporo, Japan.

Toyota, T., T. Kawamura, K. I. Ohshima, H. Shimoda, and M. Wakatsuchi (2004), Thickness distribution, texture and stratigraphy, and a simple probabilistic model for dynamical thickening of sea ice in the southern Sea of Okhotsk, *Journal of Geophysical Research*, *109*, C06001, doi:10.1029/2003JC002090.

Trodahl, H. J., M. J. McGuinness, P. J. Langhorne, K. Collins, A. E. Pantoja, I. J. Smith, and T. G. Haskell (2000), Heat transport in McMurdo Sound first–year fast ice, *Journal of Geophysical Research*, *105*(C5), 11,347–11,358.

Trodahl, H. J., S. O. F. Wilkinson, M. J. McGuinness, and T. G. Haskell (2001), Thermal conductivity of sea ice; dependence on temperature and depth, *Geophysical Research Letters*, *28*(7), 1279–1282.

Tsurikov, V. L. (1965), Formation of the ionic composition and salinity of sea ice, *Oceanology*, *5*, 59–66.

Tuckey, B. J., P. J. Langhorne, and C. Petrich (submitted manuscript), Convectively–driven migration of brine enclosures in sea ice.

UNESCO (1981a), Tenth report of the joint panel on oceanographic tables and standards, *Technical Papers in Marine Science 36*.

UNESCO (1981b), Background papers and supporting data on the international equation of state of seawater 1980, *Technical Papers in Marine Science 38*.

UNESCO (1983), Algorithms for computation of fundamental properties of seawater, *Technical Papers in Marine Science 44*.

Untersteiner, N. (1961), On the mass and heat budget of Arctic sea ice, *Archiv für Meteorologie, Geophysik und Bioklimatologie, Serie A*, *12*, 151–182.

Untersteiner, N. (1968), Natural desalination and equilibrium salinity profile of perennial sea ice, *Journal of Geophysical Research*, *73*(4), 1251–1257.

Ushio, S., and M. Wakatsuchi (1993), A laboratory study on supercooling and frazil ice production processes in winter coastal polynyas, *Journal of Geophysical Research*, *98*(C11), 20,321–20,328.

Vedamuthu, M., S. Singh, and G. W. Robinson (1994), Properties of liquid water: Origin of the density anomalies, *Journal of Physical Chemistry*, *98*, 2222–2230.

Verbeke, V., J.-L. Tison, H. J. Trodahl, and T. G. Haskell (2002), Banding in McMurdo fast ice, in *Ice in the Environment: Proceedings of the 16th IAHR International Symposium on Ice*, vol. 2, edited by V. Squire and P. Langhorne, pp. 225–234, University of Otago, Dunedin, New Zealand.

Versteeg, H. K., and W. Malalasekera (1995), *An Introduction to Computational Fluid Dynamics*, Prentice Hall, Harlow, England.

Vigroux, E. (1953), Contribution à l'ètude expérimentale de l'absorption de l'ozone, *Annales de Physique*, *8*, 709–762.

Vondrak, R. R., and D. H. Crider (2003), Ice at the lunar poles, *American Scientist*, *91*(4), 322–329.

Wakatsuchi, M. (1983), Brine exclusion process from growing sea ice, *Teion-Kagaku (Low Temperature Science)*, *A33*, 29–65.

Wakatsuchi, M., and T. Kawamura (1987), Formation processes of brine drainage channels in sea ice, *Journal of Geophysical Research*, *92*(C7), 7195–7197.

Wakatsuchi, M., and N. Ono (1983), Measurements of salinity and volume of brine excluded from growing sea ice, *Journal of Geophysical Research*, *88*(C5), 2943–2951.

Wakatsuchi, M., and T. Saito (1985), On brine drainage channels of young sea ice, *Annals of Glaciology*, *6*, 200–202.

Walden, V. P., S. G. Warren, and E. Tuttle (2003), Atmospheric ice crystals over the Antarctic Plateau in winter, *Journal of Applied Meteorology*, *42*(10), 1391–1405.

Warren, S. G. (1984), Optical constants of ice from the ultraviolet to the microwave, *Applied Optics*, *23*(8), 1206–1225.

Weeks, W. F., and S. F. Ackley (1986), The growth, structure, and properties of sea ice, in *The Geophysics of Sea Ice*, *NATO ASI Series, Series B: Physics*, vol. 146, edited by N. Untersteiner, pp. 9–164, Plenum Press, New York, NY, USA.

Weeks, W. F., and D. L. Anderson (1958), An experimental study of strength of young sea ice, *American Geophysical Union, Transactions*, *39*(4), 641–647.

Weeks, W. F., and A. J. Gow (1978), Preferred crystal orientation in the fast ice along the margines of the Arctic Ocean, *Journal of Geophysical Research*, *83*(C10), 5105–5121.

Weeks, W. F., and A. J. Gow (1980), Crystal alignment in the fast ice or Arctic Alaska, *Journal of Geophysical Research*, *85*(C2), 1137–1146.

Weeks, W. F., and O. S. Lee (1958), Observations on the physical properties of sea–ice at Hopedale, Labrador, *Arctic*, *11*, 134–155.

Weeks, W. F., and G. Lofgren (1967), The effective solute distribution coefficient during the freezing of NaCl solutions, in *Physics of Snow and Ice, International Conference on Low Temperature Science, Proceedings*, vol. 1, edited by H. Oura, pp. 579–597, Institute of Low Temperature Science, Hokkaido University, Sapporo, Japan.

Weeks, W. F., and J. S. Wettlaufer (1996), Crystal orientations in floating ice sheets, in *The Johannes Weertman Symposium, Proceedings of the 1996 TMS Annual Meeting in Anaheim, CA, USA*, edited by R. J. Arsenault, D. Cole, T. Gross, G. Kostorz, P. K. Liaw, S. Parameswaran, and H. Sizek, pp. 337–350, The Minerals, Metals & Materials Society.

Weissenberger, J., G. Dieckmann, R. Gradinger, and M. Spindler (1992), Sea ice: A cast technique to examine and analyze brine pockets and channel structure, *Limnology and Oceanography*, *37*(1), 179–183.

Weller, G. (1972), Radiation flux investigation, *AIDJEX Bulletin*, *14*, 28–30.

Wendler, G., and A. P. Worby (2001), The surface energy budget in the Antarctic summer sea–ice pack, *Annals of Glaciology*, *33*, 275–279.

Wettlaufer, J. S. (1991), Heat flux at the ice–ocean interface, *Journal of Geophysical Research*, *96*(C4), 7215–7236.

Wettlaufer, J. S. (1999), Crystal growth, surface phase transitions and thermonuclear pressure, in *Ice Physics in the Natural Environment*, *NATO/ASI Series I*, vol. 56, edited by J. S. Wettlaufer, J. G. Dash, and N. Untersteiner, Springer–Verlag, New York, NY, USA.

Wettlaufer, J. S., M. G. Worster, and H. E. Huppert (1997), Natural convection during solidification of an alloy from above with application to the evolution of sea ice, *Journal of Fluid Mechanics*, *344*, 291–316.

Wettlaufer, J. S., M. G. Worster, and H. E. Huppert (2000), Solidification of leads: Theory, experiment, and field observations, *Journal of Geophysical Research*, *105*(C1), 1123–1134.

Whipple, F. L. (1976), Background of modern comet theory, *Nature*, *263*(5572), 15–19.

Whitaker, S. (1977), *Fundamental Principles of Heat Transfer*, Pergamon Press, New York, NY, USA.

Whitman, W. G. (1926), The elemination of salt from sea–water ice, *American Journal of Science*, *211*, 126–132.

Williams, P. J. (1999), The freezing of soil: Ice in a porous medium and its environmantal significance, in *Proceedings of the NATO Advanced Research Workshop "Ice Physics and the Natural Environment", Maratea, Italy, September 1997*, *NATO ASI Series, Series I: Global Environmental Change*, vol. 56, edited by J. S. Wettlaufer, J. G. Dash, and N. Untersteiner, pp. 219–239, Springer–Verlag, Berlin, Germany.

Williams, T. D., and V. A. Squire (2002), Wave propagation across and oblique crack in an ice sheet, *International Journal of Offshore and Polar Engineering*, *12*(3), 157–162.

WMO (1970), WMO sea-ice nomenclature, terminology, codes and illustrated glossary, *WMO/OMM/BMO 259 TP. 145*, Secretariat of the World Meteorological Organization, Geneva, Switzerland, with amendments by ETSI-I, Buenos-Aires, 2002.

Woods, A. W. (1992), Melting and dissolving, *Journal of Fluid Mechanics*, *239*, 429–448.

Worby, A. P., M. O. Jeffries, W. F. Weeks, K. Morris, and R. Jaña (1996), The thickness distribution of sea ice and snow cover during late winter in the Bellinghausen and Amundsen Seas, Antarctica, *Journal of Geophysical Research*, *101*(C12), 28,441–28,455.

Worster, M. G. (1992), Instabilities of the liquid and mushy regions during solidification of alloys, *Journal of Fluid Mechanics*, *237*, 649–669.

Worster, M. G. (1997), Convection in mushy layers, *Annual Review of Fluid Mechanics*, *29*, 91–122.

Worster, M. G., and R. C. Kerr (1994), The transient–behavior of alloys solidified from below prior to the formation of chimneys, *Journal of Fluid Mechanics*, *269*, 23–44.

Wright, C. S., and R. E. Priestley (1922), Glaciology, in *British (Terra Nova) Antarctic Expedition 1910–1913*, Harrison and Sons, Ltd., London, UK.

Xia, W., and M. F. Thorpe (1988), Percolation properties of random ellipses, *Physical Review A*, *38*(5), 2650–2656.

Yen, Y.-C. (1981), Review of thermal properties of snow, ice, and sea ice, *Report 81–10*, Cold Regions Research and Engineering Laboratory, Hanover, NH, USA.

Yi, Y.-B., and A. M. Sastry (2004), Analytical approximation of the percolation threshold for overlapping ellipsoids of revolution, *Proceedings of the Royal Society of London, Series A*, *460*, 2353–2380.

Yi, Y.-B., C.-W. Wang, and A. M. Sastry (2004), Two–dimensional vs. three–dimensional clustering and percolation in fields of overlapping ellipsoids, *Journal of the Electrochemical Society*, *151*(8), A1292–A1300.

Zeebe, R. E., H. Eicken, D. H. Robinson, D. Wolf-Gladrow, and G. S. Dieckmann (1996), Modeling the heating and melting of sea ice through light absorption by microalgae, *Journal of Geophysical Research*, *101*(C1), 1163–1181.

Zeytounian, R. K. (2003), Joseph Boussinesq and his approximation: A contemporary view, *Comptes Rendus Mecanique*, *331*(8), 575–586.

Zhang, H., and M. K. Moallemi (1995), MAGG – A multizone adaptive grid–generation technique for simulation of moving and free–boundary problems, *Numerical Heat Transfer, Part B*, *27*(3), 255–276.

Zhang, H., V. Prasad, and M. K. Moallemi (1996), Numerical algorithm using multizone adaptive grid generation for multiphase transport processes with moving and free boundaries, *Numerical Heat Transfer, Part B*, *29*(4), 399–421.

Zhang, S., M. S. Paterson, and S. F. Cox (1994), Porosity and permeability evolution during hot isostatic pressing of calcite aggregates, *Journal of Geophysical Research*, *99*(B8), 15,741–15,760.

Zhou, X., and S. Li (2003), Comparison between in situ and MODIS–derived spectral reflectances of snow and sea ice in the Amundsen Sea, Antarctica, *International Journal of Remote Sensing*, *24*(24), 5011–5032.

Zimmer, C., K. K. Khurana, and M. G. Kivelson (2000), Subsurface oceans on Europa and Callisto: Constraints from Galileo magnetometer observations, *147*(2), 329–347.

Zondlo, M. A., P. K. Hudson, A. J. Prenni, and M. A. Tolbert (2000), Chemistry and microphysics of polar stratospheric clouds and cirrus clouds, *Annual Review of Physical Chemistry*, *51*, 473–499.

Zubavicus, Y., and M. Grunze (2004), New insights into the structure of water with ultrafast probes, *Science*, *304*(5673), 974–976.

Appendix A

Data

A.1 Salinity and cores

This section lists the data of the vertical salinity profiles of excavated natural refrozen cracks, slot refreezing experiments, and cores. The corresponding plots are shown in Section 2.2.4. For refrozen slots, sea ice chunks are cut into cubical samples with a band saw and melted. For cracks and slots, samples are always 80 mm high, apart from the top row of *crack 1*, and about 100 mm to 150 mm thick. The width varies with profile, and in the case of *crack 5* even slightly with column. Some of the samples were from the host sea ice sheet. The salinity is determined from the conductivity measured with a Wayne–Kerr conductivity bridge, temperature, and application of equations of *UNESCO* (1981a). Individual salinity measurements are performed in random order.

The data is grouped as follows: first listed are data of crack excavations, then slot experiments, and finally salinity cores. Within each group data is given in chronological order. Finally, banding observations are given. For possible mechanisms for their development see for example *Verbeke et al.* (2002) and *Cole et al.* (2004).

```
name:   crack 1
row height (mm): 80, apart from top row
top row height (mm):
               n/a n/a  40  40  40 n/a  80
column width (mm):
                60  60  60  60  60  60  60
location (c: crack, h: host ice):
                h   c   c   c   c   c   h
salinity (psu):
               --- n/a 6.5 5.7 7.2 n/a 7.9
               6.4 8.3 6.6 6.3 7.3 7.8 7.2
               7.1 6.7 7.8 6.8 7.7 6.2 7.0
               6.5 6.6 6.8 6.8 6.4 5.9 6.2
               7.2 6.8 6.6 6.3 6.1 5.3 6.9
               6.0 6.9 6.2 6.0 5.6 4.8 5.2
               5.2 5.8 4.3 5.6 4.0 4.0 4.5
               5.4 6.5 3.9 5.9 3.9 3.5 4.3
               5.5 4.2 3.9 5.5 3.8 3.5 3.8
               4.9 3.9 4.3 5.2 3.7 3.2 3.4
               3.6 3.0 3.8 5.0 3.8 2.9 2.9
               3.0 3.0 3.4 4.6 3.8 3.2 2.6
               2.9 3.5 4.5 4.4 3.9 3.2 3.0
               3.9 4.3 5.2 4.4 4.1 4.0 4.4
               5.8 5.2 5.5 4.4 5.3 5.6 5.4
               6.5 6.6 6.4 4.0 6.1 6.3 6.3
               7.5 6.6 6.4 3.4 5.6 6.3 6.3
```

Figure A.1: Salinity of *crack 1*, Cape Evans, 2001. For an illustration of the top row see Section 2.2.4.

```
name:   crack 5
row height (mm): 80
column width (mm):
                35  30  30  25  35   25  30  30  35
location (c: crack, h: host ice):
                 c   c   c   c   c    c   c   c   c
salinity (psu):
               9.7 7.3 8.5 8.8 7.2 (8.8 8.5 7.3 9.7)
               7.4 7.0 7.4 8.0 6.9 (8.0 7.4 7.0 7.4)
               6.8 6.9 6.6 7.3 6.1 (7.3 6.6 6.9 6.8)
               6.1 6.3 6.3 7.0 5.9 (7.0 6.3 6.3 6.1)
```

Figure A.2: Salinity of *crack 5*, Cape Barne, 2001. Columns in brackets are mirrored data, not measured.

```
name:   crack 20
row height (mm): 80
column width (mm):
                 20  20   20  20  20  20  20  20   20  20  20
location (c: crack, h: host ice):
                 h   h    c   c   c   c   c   c    c   h   h
salinity (psu):
               6.6 7.4 14.3 8.9 8.7 8.6 8.4 8.1 14.7 8.1 7.0
               7.2 7.8  9.7 7.1 7.4 7.5 7.8 7.2  9.2 7.9 7.2
               7.2 7.9  5.8 6.8 6.9 7.0 6.9 6.1  8.6 7.3 7.6
               6.4 6.7  5.4 6.3 6.3 6.8 6.4 5.9  7.0 6.8 7.4
               5.7 5.7  5.6 5.4 5.9 6.4 6.3 5.2  5.6 5.7 6.6
               5.3 5.5  4.8 5.3 6.0 6.2 5.9 4.8  5.3 5.5 6.5
```

Figure A.3: Salinity of *crack 20*, Barne Glacier, 2002.

```
name:   slot 1
row height (mm): 80
column width (mm):
                 50  50  50  50  50
location (s: slot, h: host ice):
                 s   s   s   s   s
salinity (psu):
               7.1 8.2 9.3 8.1 7.3
               7.3 7.6 6.7 7.7 7.0
               6.7 6.9 6.8 7.2 6.5
               6.3 6.2 6.3 6.9 6.1
               5.7 6.1 6.5 6.6 5.7
```

Figure A.4: Salinity of *slot 1*, Cape Evans, 2001.

```
name:   slot 10
row height (mm): 80
column width (mm):
                 20  20  20  20   20   20  20  20  20  20  20
location (s: slot, h: host ice):
                 h   s   s   s    s    s   s   s   s   s  s/h
salinity (psu):
               6.7 8.7 8.3 8.2  7.6  5.7 7.0 7.7 7.9 8.2 7.4
               6.2 8.0 7.0 6.8  6.7  4.8 6.7 6.8 6.9 6.9 7.2
               6.0 7.7 6.2 5.6  5.3  6.0 6.0 6.3 6.4 6.6 7.3
               5.5 6.9 5.6 5.7  6.1  7.1 6.0 5.7 5.9 7.2 5.3
               5.0 5.6 5.5 6.3  7.7 10.6 7.4 5.8 5.5 7.5 4.8
               4.6 5.9 5.6 6.2 10.3 14.7 7.5 5.9 5.4 5.6 5.0
               5.0 6.2 5.4 6.9 15.8 17.7 7.9 6.2 5.8 5.5 5.3
```

Figure A.5: Salinity of *slot 10*, Erebus Bay, 2002.

```
name:   core 1
date: 15 Oct, 2001, location: Cape Evans
vertical sample size: 100 mm
salinity (psu):
                7.2
                6.7
                6.1
                6.1
                5.4
                5.3
                5.2
                5.4
                5.9
                6.7
                5.3
                4.3
                4.8
                4.4
                4.5
                5.4
                6.1
                5.6
                5.1
                4.6
                4.1
                7.0
```

Figure A.6: Salinity profile *core 1* at Cape Evans, 2001.

Date	Core id (ULB)	Core depth (m)	Temp. (oC)	Salinity (ppt)
5-Nov-01	McM01/5C	0.05	-7.2	9.37
		0.15	-7.6	7.70
		0.25	-7.8	7.82
		0.35	-7.8	6.57
		0.45	-7.5	6.25
		0.55	-7.0	5.35
		0.65	-6.5	5.01
		0.75	-5.8	4.83
		0.85	-5.2	6.68
		0.95	-4.5	3.41
		1.05	-4.0	4.24
		1.15	-3.1	3.39
		1.25	-2.8	4.32
		1.35	-2.2	4.60
		1.40	-2.0	6.82

Figure A.7: Salinity profile at Cape Barne, 2001. Data courtesy of Jean–Louis Tison.

```
name:   core 12
date: 11 Sept, 2002
location: Erebus Bay
air temperature: -37.2 oC
vertical sample size: 100 mm
temperature (oC) / salinity (psu):
           -27.4     missing
           -25.5     8.7
           -24.9     7.5
           -23.6     7.0
           -23.1     6.3
           -22.6     5.7
           -22.7     5.7
           -24.5     5.6
           -19.0     5.7
           -17.7     6.0
           -16.8     6.1
           -18.6     6.0
           -15.1     5.2
           -12.7     5.6
           -11.7     5.1
           -11.5     5.4
           -13.0     5.2
            -8.1     5.3
            -5.9     6.0
            -5.1     6.6
            -3.8     5.5
            -2.8     6.0
```

```
name:   core 13
date: 25 Sept, 2002
location: Cape Evans
vertical sample size: 100 mm
salinity (psu):
                9.5
                7.4
                5.4
                4.8
                5.5
                6.3
                7.1
                7.7
                5.4
                5.6
                5.4
                4.9
                4.7
                4.9
                4.4
                3.9
                5.1
```

Figure A.8: Salinity profile *core 12* at Erebus Bay, 2002. The topmost salinity sample is missing. Data courtesy of Greg Leonard. Salinity profile *core 13* at Cape Evans, 2002.

```
name:   core 10
date: 27 Aug, 2002
location: Array Site, near Erebus Glacier Tongue
length of the top section of the core: 800 mm

     surface   0 mm
     dark
              22
     light
              34
     dark
              63
     light
              71 +- 2 mm
     dark
              99
     light
             113
     dark
             134
     light
             160 +- 4 mm
     dark
             188
     a thin milky strip
             188
     dark
             207
             207 mm
     light
             232
     dark
             263
     light
             283
     dark
             303
     light
             316
     dark
             334
     light
             345 (poor visibility)
     dark
             375 (poor visibility)
     light
             385 (poor visibility)
     dark
```

Figure A.9: Banding observation in *core 10* at Array Site, 2002. Given are the depths of transition from dark to light or from light to dark. Note that the dark bands (few inclusions) have a width of 25 ± 7 mm, while the width of the light bands (more or larger inclusions) seems to follow a sine function disturbed only by the narrow milky strip at 188 mm. The total length of the core is slightly larger than 1.90 m.

Appendix B

Thermistor probes

B.1 Thermistor probe 1 characteristics

The position of the thermistor strings relative to the slot are listed in Table B.1.

B.2 Air temperature in September, 2002

A stand–alone data and temperature logger chip *Dallas Semiconductor DS 1616* has been employed to provide a continuous air temperature record for the time of the experiments in 2002. The *DS 1616* is a one–chip solution that requires only a small battery for operation and a simple interface circuit for RS–232 communication. We found the *DS 1616* to be reliable as long as the operating temperature remains at or above the specified $-40\,^{\circ}\mathrm{C}$. We also confirmed that the *DS 1616* stops operation and loses data if the temperature falls below $-40\,^{\circ}\mathrm{C}$. The record of air temperature measurements close to Scott Base is shown in Figure B.1.

Figure B.2 shows the air pressure record of Scott Base for September 2002. Pressure data are courtesy of the National Institute of Water and Atmospheric Research (NIWA), New Zealand.

Table B.1: Position of the thermistor strings relative to the side of the slot. Negative numbers indicate strings deployed in the host ice sheet.

	slot 1	*slot 2*	*slot 10*	*slot 12*
slot width (mm)	230	320	180	120
long string (mm)	30	15	90	60
middle string (mm)	65	85	55	25
short string (mm)	115	160	20	−240
host ice string (mm)	−160	−120	−50	−120

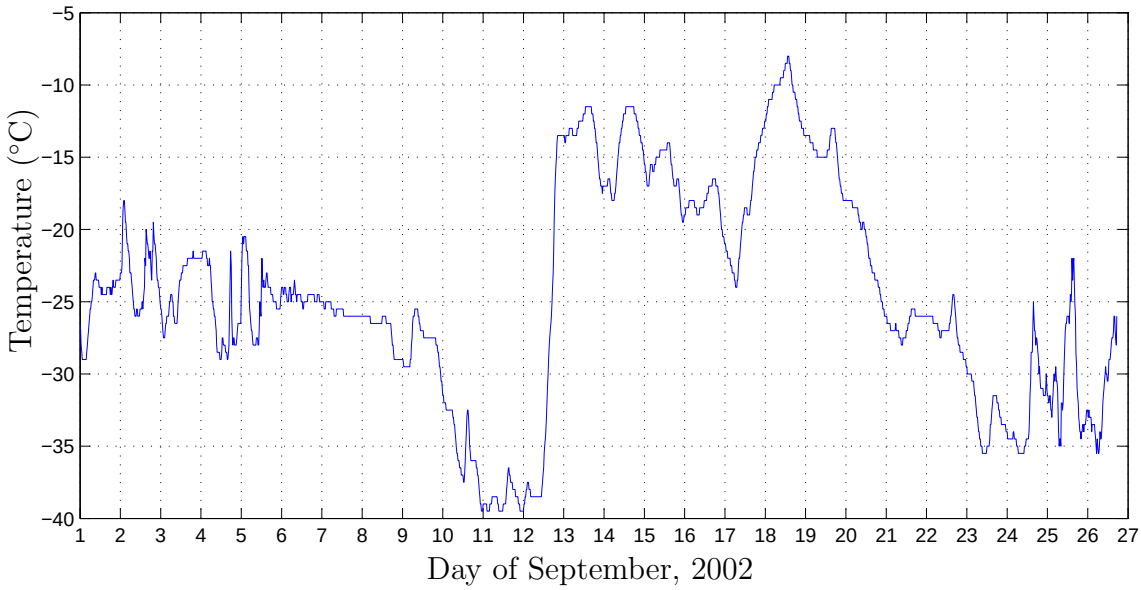

Figure B.1: Air temperature measured with a *DS 1616* data logger outside Scott Base during the period of experiments in September, 2002.

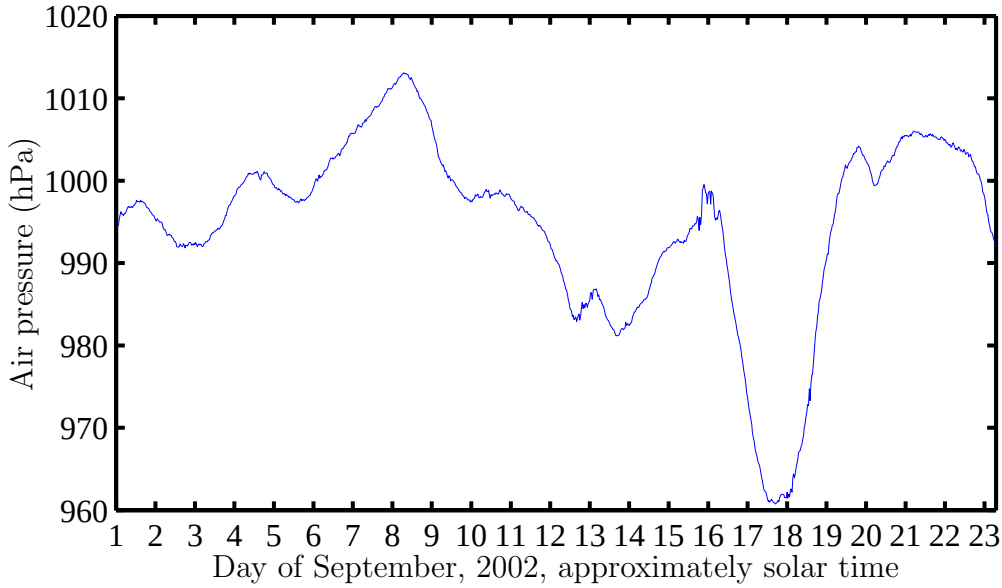

Figure B.2: Air pressure record at Scott Base in September 2002.

B.3 Direct radiative heating of the probe

We will compare the expected temperature increase in the ice due to radiative heating first with the expected temperature increase of the probe due to absorption, and then to the expected temperature increase of a thermistor bead due to absorption.

Ice vs. probe Approximately 100 % of the heat flux F_{sw} reaching the thermistor is absorbed by the thermistor beads; an estimated 4 % by the white probe; and approximately $4\,\mathrm{mm} \times 2\,\mathrm{m}^{-1} = 0.8\,\%$ by 4 mm of ice (the diameter of the probe rods that hold the thermistors in place) of extinction coefficient $\kappa_i = 2\,\mathrm{m}^{-1}$. The thermal conductivity, k, of PVC plastic is less than 10 % of the thermal conductivity of ice, i.e. only approximately 10 % of the absorbed radiation is conducted into the rod. The volumetric heat capacity of PVC is similar to ice, i.e. it is expected that $10\,\% \times 4\,\% = 0.4\,\%$ of the incident flux, F_{sw}, is used for heating the probe. This value is the same order of magnitude as the ice, so it raises no concern.

Ice vs. beads The thermal conductivity of ice is very high, leading to a dissipation constant of $\mathrm{DC} = 30\,\mathrm{mW\,K^{-1}}$ for a thermistor embedded in ice (Appendix B.3.1). However, the thermal conductivity of the PVC rod is only one tenth of the value of ice, which makes it almost appear as a thermal insulator when compared to ice. Since the rod covers almost half a hemisphere of the thermistor, the probe reduces the heat loss from the thermistor to the ice, i.e. it reduces the effective dissipation constant. Assuming that one hemisphere is blocked by the rod, we therefore use $\mathrm{DC} = 15\,\mathrm{mW\,K^{-1}}$ as effective dissipation constant.

The temperature elevation due to direct radiative heating of the thermistor beads embedded in ice is therefore

$$\Delta T = F_{sw} \frac{A}{\mathrm{DC}}, \tag{B.1}$$

$$= 3 \times 10^{-4}\,\mathrm{K\,m^2}\,W^{-1}\,F_{sw}, \tag{B.2}$$

for thermistor beads of cross sectional area $A = \pi\,(1.2\,\mathrm{mm})^2$, and $\mathrm{DC} = 15\,\mathrm{mW\,K^{-1}}$. However, the radiative heating of ice over the length of the bead diameter, $\Delta z = 2a$, is (cf. above)

$$\Delta T = F_{sw}\,\kappa_i \Delta z, \tag{B.3}$$

$$= 5 \times 10^{-3}\,\mathrm{K\,m^2}\,W^{-1}\,F_{sw}, \tag{B.4}$$

which is an order of magnitude larger than the radiative heating of the thermistor beads. We can therefore neglect the shortwave radiative heating of thermistor beads in the sea ice (cf. *Trodahl et al.*, 2000).

B.3.1 Dissipation constant

We will estimate a power dissipation constant, DC, for thermistor beads embedded in sea ice.

Carslaw and Jaeger (1986) give analytical equations for the transient temperature profile for diffusive transport in various situations. For the three–dimensional case of a sphere of radius a of constant surface temperature T_0 in an infinite medium it is (*Carslaw and Jaeger*, page 247)

$$T(r,t) = T_0 \frac{a}{r} \operatorname{erfc}\left(\frac{r-a}{2\sqrt{D\,t}}\right), \tag{B.5}$$

where $T(r,t)$ is the temperature field with $T(r > a, 0) = 0$, $T(r = a, t) = T_0$, r the distance from the origin, and a is the radius of the sphere. The steady state temperature profile ($t \to \infty$) is

$$T(r) = T_0 \frac{a}{r}, \tag{B.6}$$

i.e. the temperature gradient in direction away from the origin is

$$\nabla T = \frac{\partial T}{\partial r} = -T_0 \frac{a}{r^2}. \tag{B.7}$$

With a heat flux, $\mathbf{j}$, in the ice

$$\mathbf{j} = -k \nabla T, \tag{B.8}$$

The power, P, transported through a surface, δA, is

$$P = \int_{\delta A} \mathbf{j} \cdot \mathrm{d}\mathbf{A}. \tag{B.9}$$

For the case of a spherical surface of radius r with heat flux parallel to the surface normal we have

$$P = 4\pi\, r^2 |\mathbf{j}|, \tag{B.10}$$

and therefore the dissipation constant

$$\mathrm{DC} = \frac{P}{\Delta T} = \frac{4\pi\, r^2\, k a T_0}{r^2\, \Delta T}. \tag{B.11}$$

Since the temperature elevation, ΔT, is equal to the bead temperature, T_0, the dissipation constant is independent of temperature, and simply

$$\mathrm{DC} = 4\pi\, k a. \tag{B.12}$$

With $k = 2\,\mathrm{W\,m^{-1}\,K^{-1}}$ for ice and $a = 1.2\,\mathrm{mm}$ for the thermistor beads, the dissipation constant is $\mathrm{DC} = 30\,\mathrm{mW\,K^{-1}}$.

Comparison The steady state dissipation constant depends only on thermal conductivity, k, and size of the sphere, a. According to (B.12) it is $\mathrm{DC} = 2.5\,\mathrm{mW\,K^{-1}}$ and $\mathrm{DC} = 0.4\,\mathrm{mW\,K^{-1}}$ for immobile olive oil ($k = 0.17\,\mathrm{W\,m^{-1}\,K^{-1}}$) and stationary air ($k = 0.025\,\mathrm{W\,m^{-1}\,K^{-1}}$), respectively. The values given by the manufacturer for a well stirred oil bath and free convecting air are $\mathrm{DC} = 7$ to $8\,\mathrm{mW\,K^{-1}}$ and $\mathrm{DC} = 1\,\mathrm{mW\,K^{-1}}$, respectively, i.e. two to three times larger than expected for stationary environments.

This comparison is satisfactory considering the approximations in the derivation of (B.12).

B.4 Steinhart–Hart equation

Steinhart and Hart (1968) give a curve fitting equation for the relationship between thermistor temperature and resistance that outperforms a simple exponential relationship particularly at low temperatures. Following *Lewis* (1985), we use the simplified reduced form with three coefficients. In place of individual thermistor calibration we use average coefficients that are given[1] by the manufacturer *BetaTHERM*. More detailed accounts of thermistor calibration with application to ocean water are given by *Lewis and Sudar* (1972) and *Lewis* (1985). The relationship between absolute temperature T (K) and resistance R (Ω) is

$$\frac{1}{T} = A + B\,\ln(R) + C\,(\ln(R))^3\,, \tag{B.13}$$

where the coefficients A, B, and C of the $3\,\mathrm{k}\Omega$ thermistors used here are

$$\begin{aligned} A &= 1.405027 \times 10^{-3}, \\ B &= 2.369386 \times 10^{-4}, \\ C &= 1.012660 \times 10^{-7}. \end{aligned} \tag{B.14}$$

The coefficients are derived from measurements at $0\,^\circ$C, $25\,^\circ$C, and $70\,^\circ$C, but our own tests in the laboratory suggest that the temperature range down to at least $-30\,^\circ$C is represented sufficiently accurately.

B.5 Significance of temperature threshold

The influence of the choice of temperature threshold T_{thr} used to define the freezing front on the apparent vertical freezing front velocity will be demonstrated. For all four experiments, the freezing front velocity between the topmost two thermistors, and the second and third highest thermistors has been calculated. The calculation has been performed for the thermistor string at the centre of the slot, as well as for the thermistor string that is closest to the side of the slot. Figures B.3 to B.6 show the resulting vertical freezing front velocity v, as a function of chosen temperature threshold, where

$$T_{thr} = T_F - \epsilon, \tag{B.15}$$

with ocean temperature T_F and ϵ the temperature difference between ocean temperature and threshold temperature. Velocity fluctuations in *slot 1* and *slot 2* are largely due to diurnal temperature fluctuations in the ice. Apparently, the choice of ϵ is of less influence on the determined growth velocity if the freezing front is horizontal.

[1] `http://www.betatherm.com/`

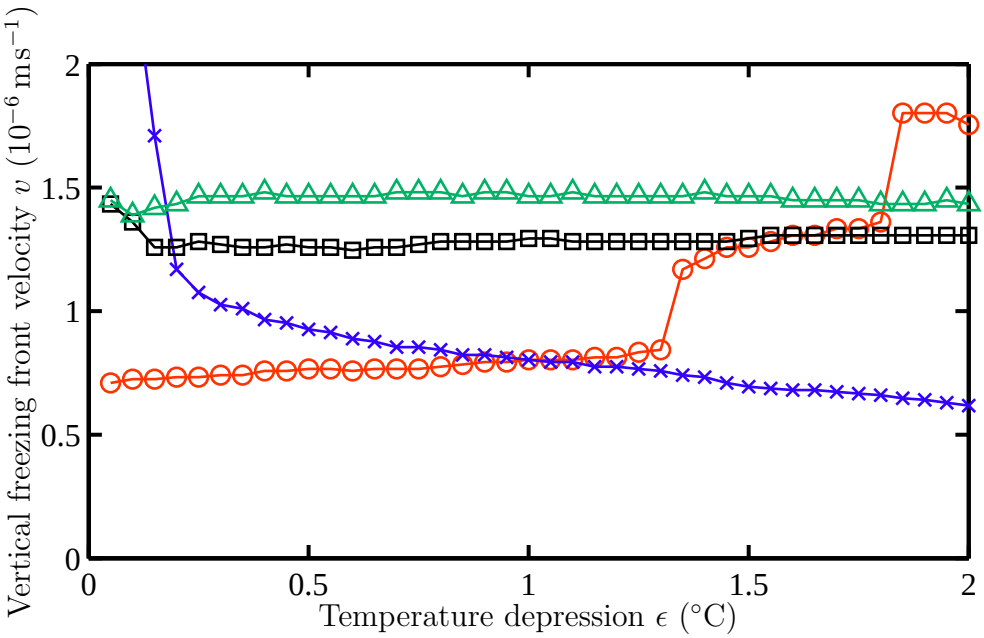

Figure B.3: Vertical freezing front velocity determined from the topmost and second thermistor of the centre string; *slot 1* (circles), *slot 2* (crosses), *slot 10* (squares), *slot 12* (triangles).

An alternative way of interpreting the figures is by recognising that a linear vertical temperature profile will result in a vertical freezing front velocity that is independent of ϵ.

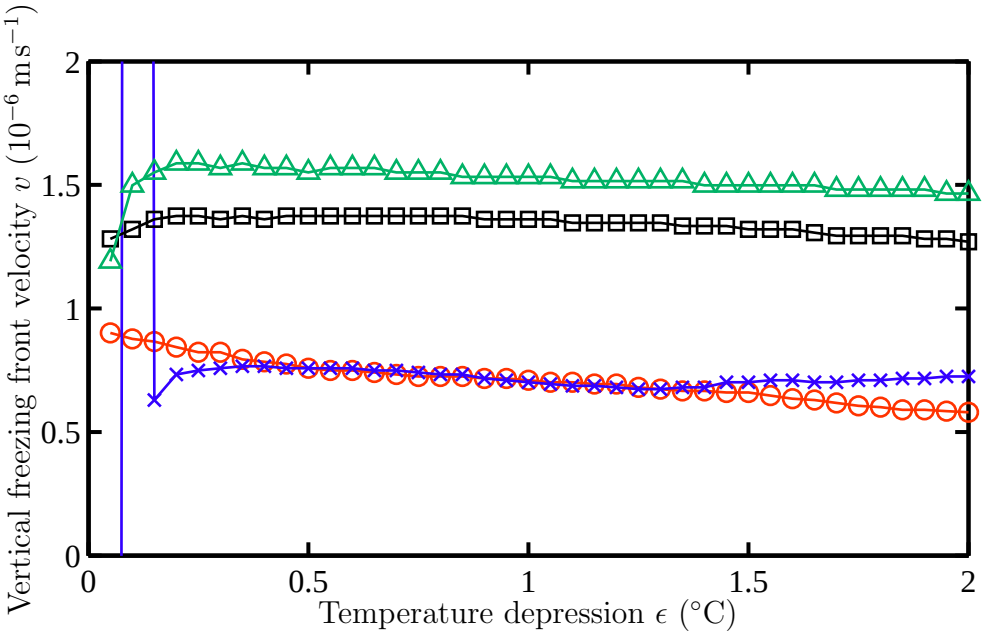

Figure B.4: Vertical freezing front velocity determined from the second and third thermistor of the centre string; *slot 1* (circles), *slot 2* (crosses), *slot 10* (squares), *slot 12* (triangles).

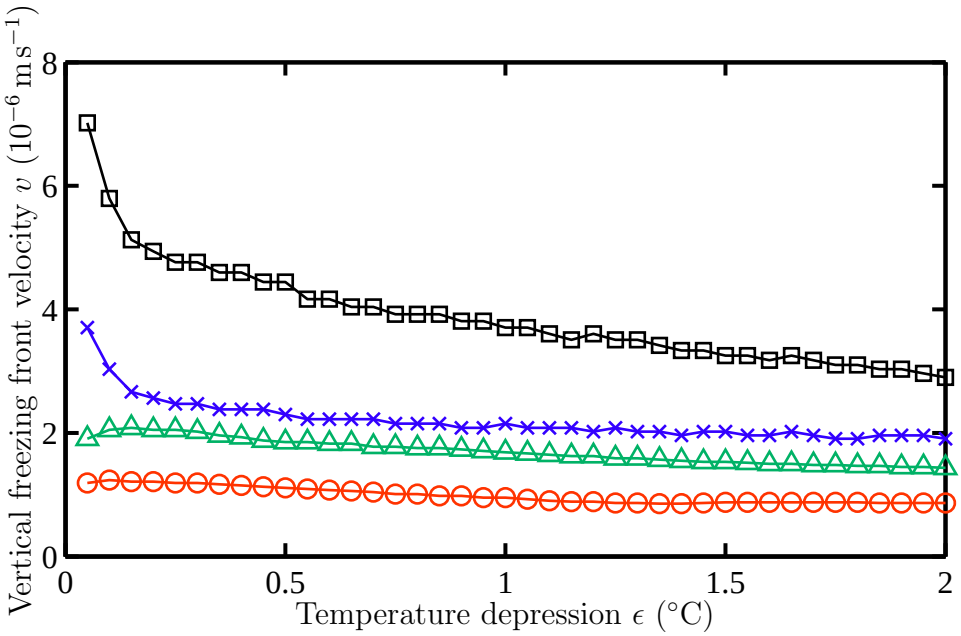

Figure B.5: Vertical freezing front velocity determined from the topmost and second thermistor of the side string; *slot 1* (circles), *slot 2* (crosses), *slot 10* (squares), *slot 12* (triangles).

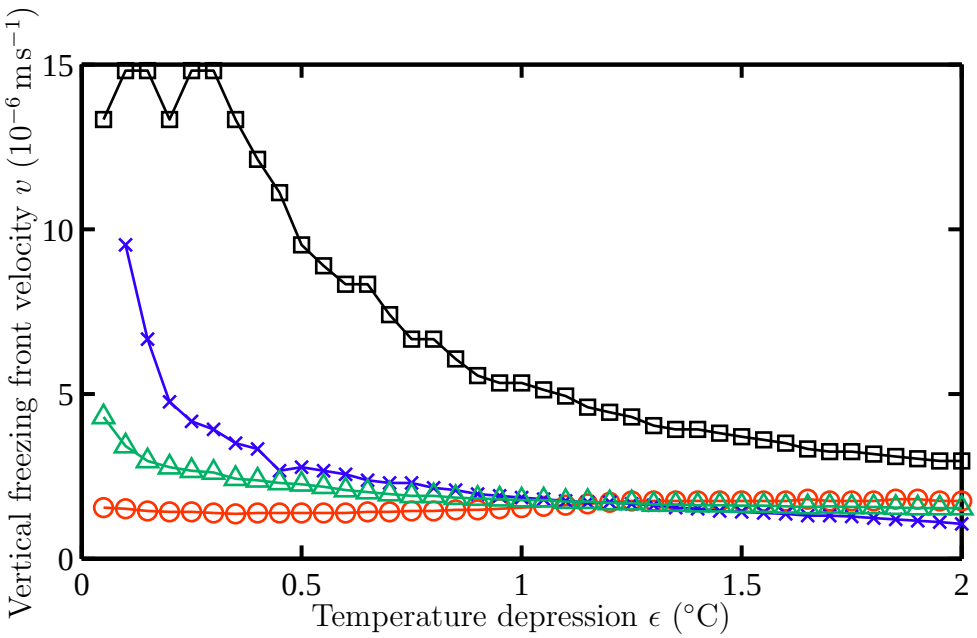

Figure B.6: Vertical freezing front velocity determined from the second and third thermistor of the side string; *slot 1* (circles), *slot 2* (crosses), *slot 10* (squares), *slot 12* (triangles).

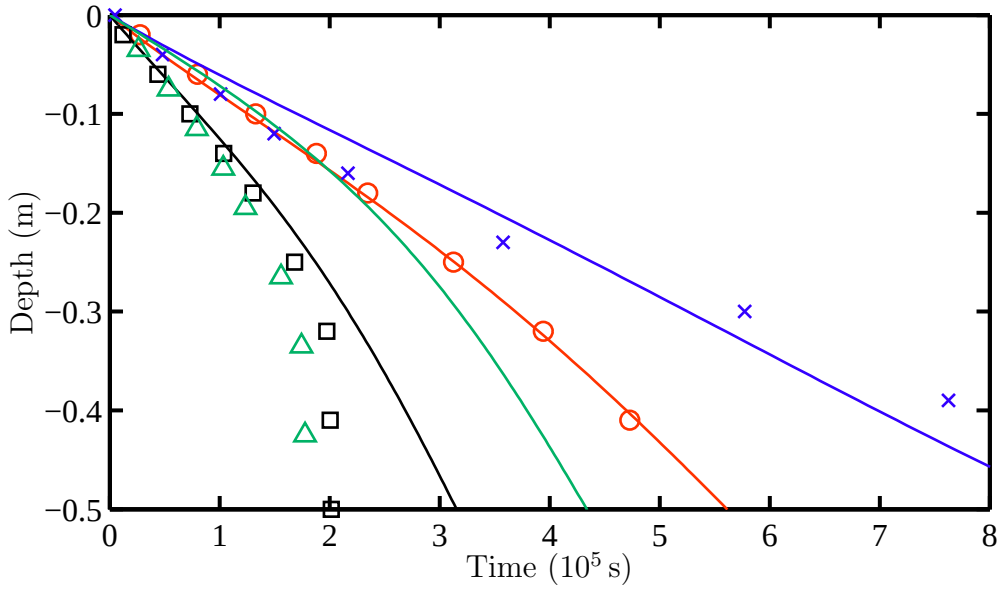

Figure B.7: Prediction and experimental data of *slot 1*, width 0.23 m (circles); *slot 2*, width 0.32 m (crosses); *slot 10*, width 0.18 m (squares); *slot 12*, width 0.12 m (triangles). The prediction for *slot 12* coincides with data points of *slot 2* and *slot 1*. The freezing times are obtained from the temperature threshold approach with $\epsilon = 0.5\,^{\circ}\mathrm{C}$.

B.6 Model predictions illustrated

The predictions of the freezing front model shown in Figure 3.12 of Section 3.2.4 in dimensionless form shall be illustrated here in real time and space coordinates. Written out explicitly, the predicted freezing time t is a function of refreezing height $h \geq 0$ following

$$t = \frac{\rho L}{2k\,(T_w - T_{air})}\,\frac{h^2 + 2\,hh_0}{1 + 4\frac{h^2+2\,hh_0}{w^2+2\,w\,\gamma\,H}\,\frac{1-\frac{h}{H}}{1+\frac{h_f}{H}+\frac{h_0}{H}}}. \tag{B.16}$$

The constants are defined in Section 3.2.4 and Table 3.2. Note that the Figures have different scales.

The predictions for the experiments of this study (Figure B.7) are reasonable apart from the prediction for *slot 12* (predicted freezing front velocity $7 \times 10^{-7}\,\mathrm{m\,s^{-1}}$, measured $1.5 \times 10^{-6}\,\mathrm{m\,s^{-1}}$), which is probably due to a negative heat flux or a positive ice mass flux from the ocean. Also visible is a small underprediction of the freezing front velocity of *slot 10* initially (predicted $1.28 \times 10^{-6}\,\mathrm{m\,s^{-1}}$, measured $1.31 \times 10^{-6}\,\mathrm{m\,s^{-1}}$). The initial parabolic form of the freezing front movement during *slot 2* is not reproduced well. This could be due to an inappropriate choice of $u\,C_s$ for this experiment. The apparently high growth rates of *slot 10* and *slot 12* at later times are not predicted well. This is a result of non–horizontal freezing front on ice formation, which renders the temperature threshold approach to finding the freezing front inappropriate. If we instead use the comparative rate of temperature change approach (page 56) to determine the time at which sea ice of well defined properties has formed, we obtain the result shown in Figure B.8. Note that the predictions have changed slightly since

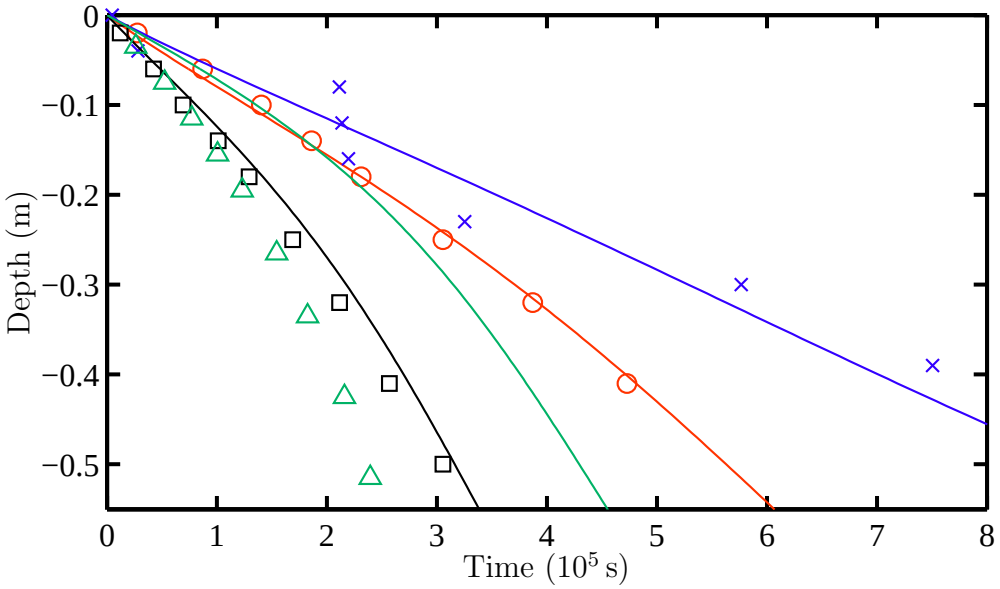

Figure B.8: Prediction and experimental data analysed with the comparative rate of temperature change approach of *slot 1* (circles); *slot 2* (crosses); *slot 10* (squares); *slot 12* (triangles). Note the freezing times of the bottommost thermistors of *slot 10* and *slot 12* compared to Figure B.7.

the total freezing times have changed and the air temperature is an average over the total freezing time.

Langhorne and Haskell (2004) give an empirical best fit line to predict the refreezing progress of their 1998 and 1999 experiments

$$h = A\left(\frac{t}{w}\right) + B\left(\frac{t}{w}\right)^{1/2} + C, \tag{B.17}$$

with refreezing height h and slot width w in m, time t in s, and $A = 1.7 \times 10^{-8}$, $B = 4.1 \times 10^{-4}$, and $C = -0.13$. Their data, the prediction from (B.17), and the prediction from the model in Section 3.2.4 are compared in Figure B.9.

Data of *Metge* (1976) are shown in Figure B.10 using $u\,C_s = 0.02$. The deviation in the later stages of refreezing is likely to be due to the growth of host ice. The ice sheet was not free floating according to *Metge*, and increased in thickness by 10 to 20 mm in the course of refreezing.

Heat transfer coefficient *Metge* (1976) measures wind speed induced by fans over his experiments and gives the wind speed as $u = 2\,\mathrm{m\,s^{-1}}$. However, the height of wind measurement above ground, the surface roughness, and the wind speed affect the appropriate choice of the sensible heat transfer coefficient C_s (*Andreas*, 1987; *Toyota*, 1998). Since *Metge* gives extrapolated measurements for the ice surface temperature T_r we are able to estimate C_s for his experiments, C_s^M. Balancing heat conducted through the ice with the heat flux to the atmosphere (and neglecting all other fluxes

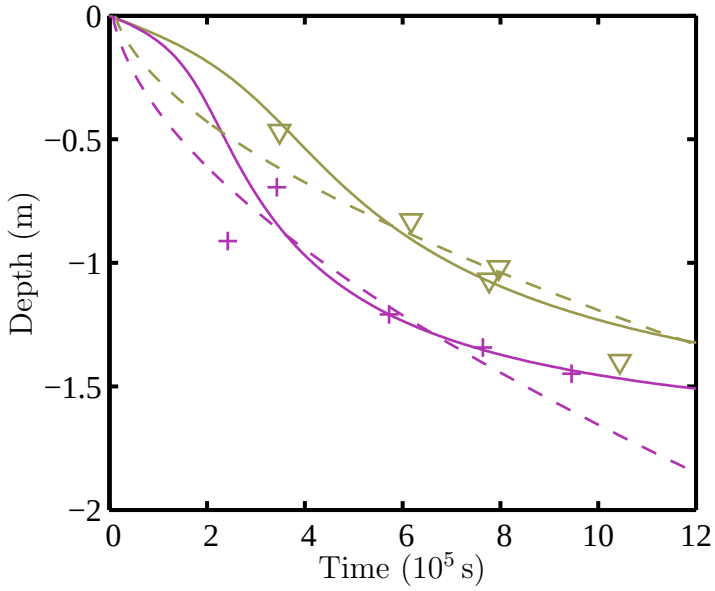

Figure B.9: Prediction (solid line) and experimental data of *Langhorne and Haskell* in McMurdo Sound 1999 (direct measurements). Total ice thickness 1.92 m, slot width 0.07 m (pluses) and 0.12 m (triangles). The dashed line is the prediction from their fit function (B.17).

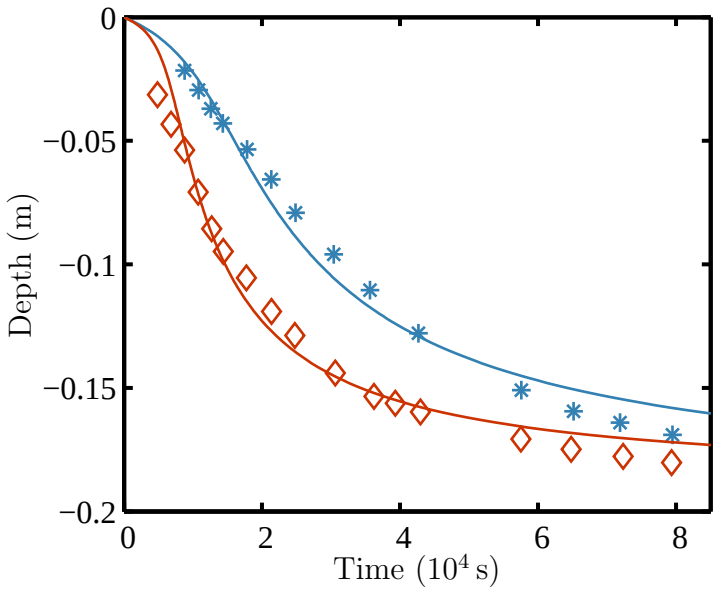

Figure B.10: Prediction and experimental laboratory data of *Metge*, total ice thickness at the start of the experiment and thickness $H = H + h_f = 0.185$ m, slot width 0.018 m (diamonds) and 0.036 m (stars).

as we have done in the development of the model), we obtain

$$k\frac{T_r - T_w}{H + h_f} = \rho_a c_p \, C_s^M u(T_a - T_r), \tag{B.18}$$

or

$$C_s^M = \frac{k}{\rho_a c_p \, u(T_a - T_r)} \, \frac{T_r - T_w}{H + h_f}. \tag{B.19}$$

With $T_a = -14\,°\mathrm{C}$, $T_r = -10\,°\mathrm{C}$ (for $t \geq 18000\,\mathrm{s}$), and $u = 2\,\mathrm{m\,s^{-1}}$ as given by *Metge*, and applying $H + h_f = 0.185$, $\rho_a = 1.3\,\mathrm{kg\,m^{-3}}$, $c_p = 1006\,\mathrm{J\,kg^{-1}\,K^{-1}}$, $k = 2\,\mathrm{W\,m^{-1}\,K^{-1}}$ it follows that $C_s^M = 0.01$. Therefore for *Metge*, we take $u\,C_s^M = 0.02\,\mathrm{m\,s^{-1}}$. This value corresponds to a heat transfer coefficient $\mathfrak{h}$ from equation (3.11) of $\mathfrak{h} = 26\,\mathrm{W\,m^{-2}\,K^{-1}}$.

B.7 Model predictions with alternate latent heat of fusion

In this section the results of the model of Section 3.2.4 (and of Appendix B.6) are shown using a latent heat of fusion, L, that has been determined consistent with Chapter 6. Equation (3.29) indicates that the freezing time, t, is directly proportional to the latent heat of fusion, L. Hence, the model predictions should be adversely affected by a change in L. However, we will see that the free parameter γ may not be a constant.

Equation (H.10) is used to calculate L, with average salinity $S_{ice} = 7\,\mathrm{psu}$ and average temperature $T = (T_a + T_w)/2$. The values for k and ρ are linear averages of values for ice and water, based on a porosity of $f = 0.1$,

$$k = f\,k_{water} + (1 - f)\,k_{ice}, \tag{B.20}$$

$$\rho = f\,\rho_{water} + (1 - f)\,\rho_{ice}. \tag{B.21}$$

Further, $\mathfrak{h}$ has been re-calculated for the Antarctic experiments following (3.42) with the respective values of ρ and L. The parameters used for modelling are listed in Table B.2.

Seawater experiment 5 of *Divett* (2000) (D5) has been added to the comparison. However, both air temperature, T_a, and heat transfer coefficient, $\mathfrak{h}$, are estimates. Due to the presence of a cover over the ice tank (*Divett*, 2000) the heat transfer coefficient, $\mathfrak{h}$, is expected to be small. However, the value of this coefficient has been chosen to give a reasonable fit.

Figures B.11, B.12, and B.13 show the results for $\gamma = 0.37$ and $\gamma = 0.5$.

While the large scale experiments ($H \approx 2\,\mathrm{m}$) are better modelled with $\gamma = 0.37$, the small scale laboratory experiments ($H \approx 0.2\,\mathrm{m}$) are better modelled with $\gamma = 0.5$. This difference could be due to an over-simplified definition of w_0 in (3.20), where a linear dependence on draft, H, has been assumed. Note that the draft differs by an order of magnitude between laboratory experiments and field experiments, suggesting that the value of γ may possibly decrease with increasing draft, H, by approximately 20 % per order of magnitude in H. The growth of *slot 12* is again underpredicted by a factor 2.

Table B.2: Parameters used for model calculations. All calculations for experiments in Antarctica (Aq) assume $\rho = 928\,\mathrm{kgm^{-3}}$, $k = 1.86\,\mathrm{Wm^{-1}K^{-1}}$, both based on $f = 0.1$, and $T_w = -1.9\,^\circ\mathrm{C}$. The simulation of the experiment by *Divett* (2000) uses $T_w = -1.5\,^\circ\mathrm{C}$. Simulations of experiments by *Metge* (1976) use $\rho = 920\,\mathrm{kgm^{-3}}$, $k = 2.0\,\mathrm{Wm^{-1}K^{-1}}$, and $T_w = 0\,^\circ\mathrm{C}$. Values in brackets () are estimates.

Experiment	Location	Date	w (m)	H (m)	$\mathfrak{h}$ ($\mathrm{Wm^{-2}K^{-1}}$)	L ($\mathrm{kJkg^{-1}}$)	T_a (°C)
slot 1	Aq	mid Oct 2001	0.23	2.0	19	340	−17.5
slot 2	Aq	end Oct 2001	0.32	1.2	23	333	−13.5
slot 10	Aq	early Sep 2002	0.18	2.0	24	352	(−25)
slot 12	Aq	mid Sep 2002	0.12	2.0	30	334	−14.2
LH12d	Aq	mid Oct 1999	0.12	1.8	(19)	336	(−15)
LH7d	Aq	mid Oct 1999	0.07	1.8	(19)	336	(−15)
M4a	lab	*Metge* (1976)	0.036	0.185	26	349	−14.0
M4b	lab	*Metge* (1976)	0.018	0.185	26	349	−14.0
D5	lab	*Divett* (2000)	0.025	0.1	(6)	333	(−14)

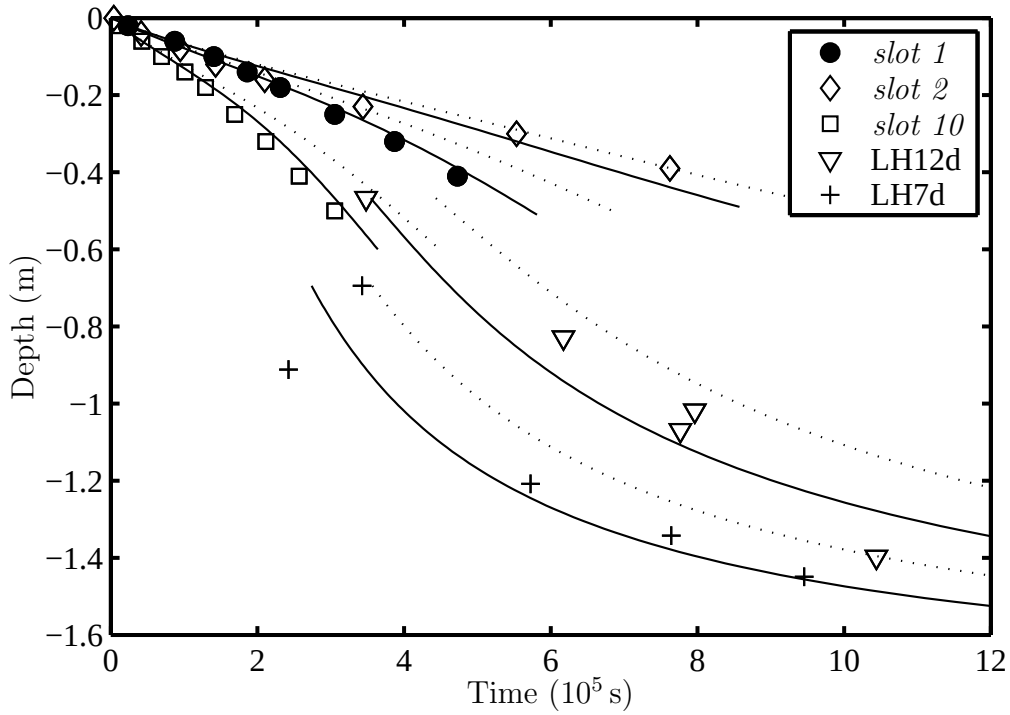

Figure B.11: Model results of field experiments using a variable latent heat of fusion with $\gamma = 0.37$ (solid lines) and $\gamma = 0.5$ (broken lines).

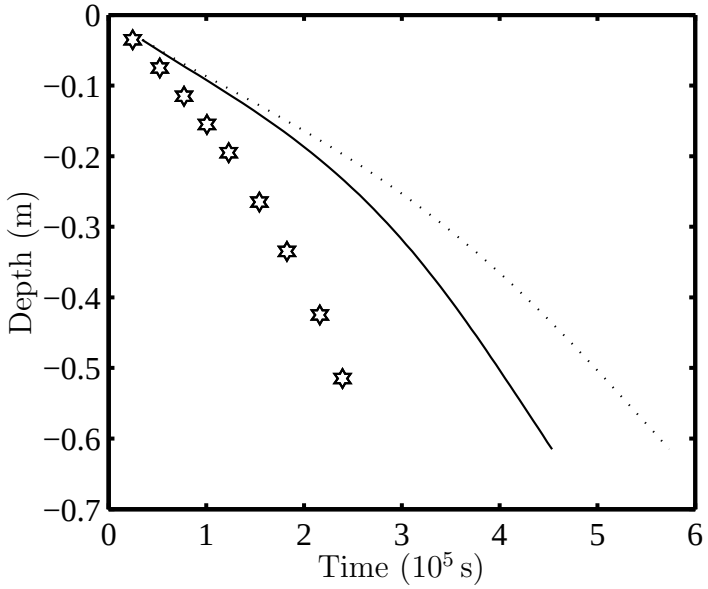

Figure B.12: Model results of experiment *slot 12* using a variable latent heat of fusion with $\gamma = 0.37$ (solid lines) and $\gamma = 0.5$ (broken lines).

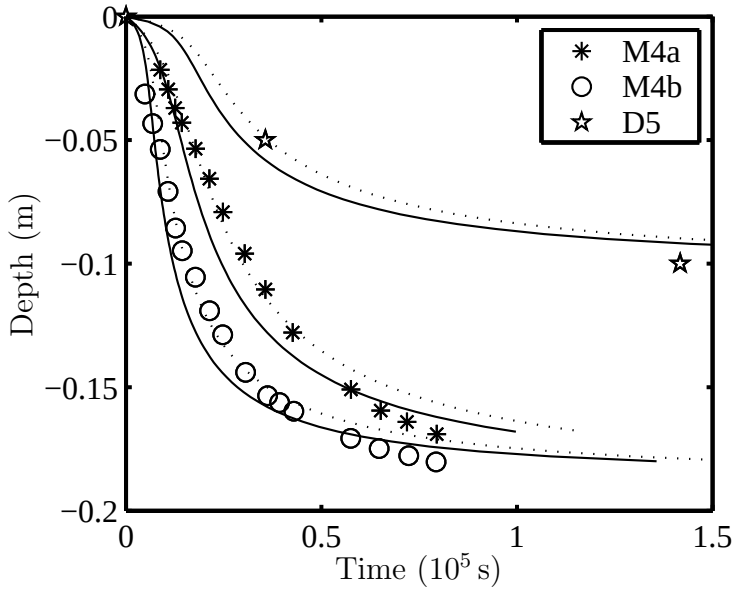

Figure B.13: Model results of laboratory experiments using a variable latent heat of fusion with $\gamma = 0.37$ (solid lines) and $\gamma = 0.5$ (broken lines).

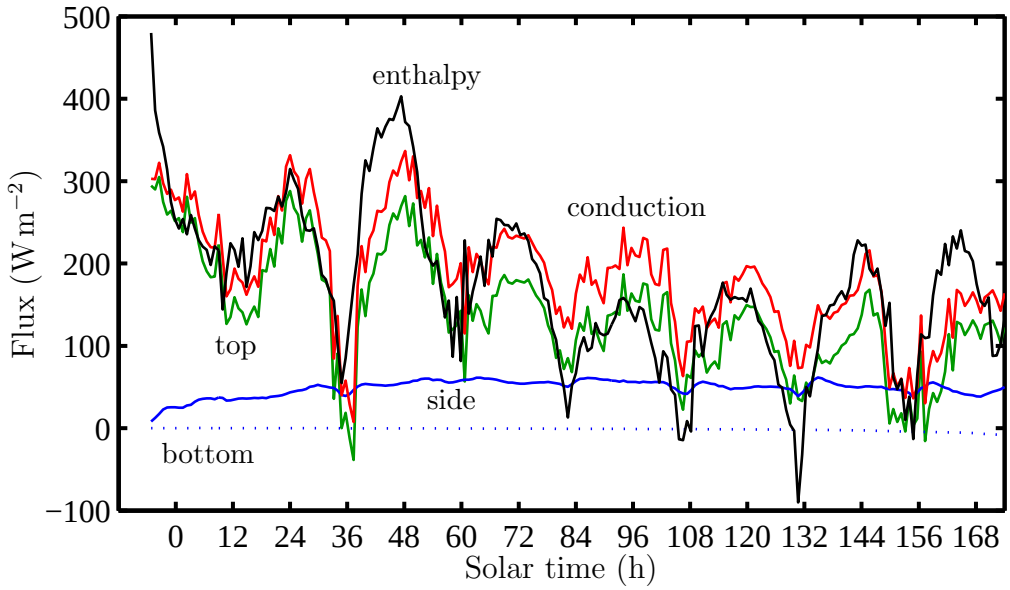

Figure B.14: Heat flux contributions in *slot 2*. Shown are vertical flux components through top and bottom, the horizontal flux through the sides, the sum of these three conductive fluxes F_c, and the rate of change of enthalpy expressed as a flux F_h. Reference area for the fluxes is the surface area of the measured domain.

In conclusion, the model gives reasonable predictions of the crack refreezing process.

B.8 Heat balance II, *slot 2*

In this case freezing times of *slot 2* are processed with the comparative rate of temperature change approach, in spite of strong temperature variations, which thereby produced spurious freezing times. Note that the time axes are longer in Figures B.14 and B.15 than in Figures 3.15(b) and 3.17(b), since the comparative rate of temperature change approach produces later freezing times of the thermistors.

B.9 Assumption of a negative ocean heat flux

Based on both the freezing front model (page 69) and the heat balance estimate (page 85) we have postulated the presence of a negative ocean heat flux in experiments *slot 10* and *slot 12*. We will quantify this postulate in this section.

B.9.1 Heat flux is due to the incorporation of frazil ice crystals

We will first convert the unbalanced heat flux into an equivalent ice volume flux, to convert the volume flux into a frazil particle flux.

Based on Figures 3.18a and b, the ocean heat flux after the formation of a snow cover is approximately $F_o = -150\,\mathrm{W\,m^{-2}}$ and $F_o = -500\,\mathrm{W\,m^{-2}}$ for *slot 10* and *slot 12*, respectively. Assuming unidirectional sea ice growth, the ocean heat flux, F_o, is

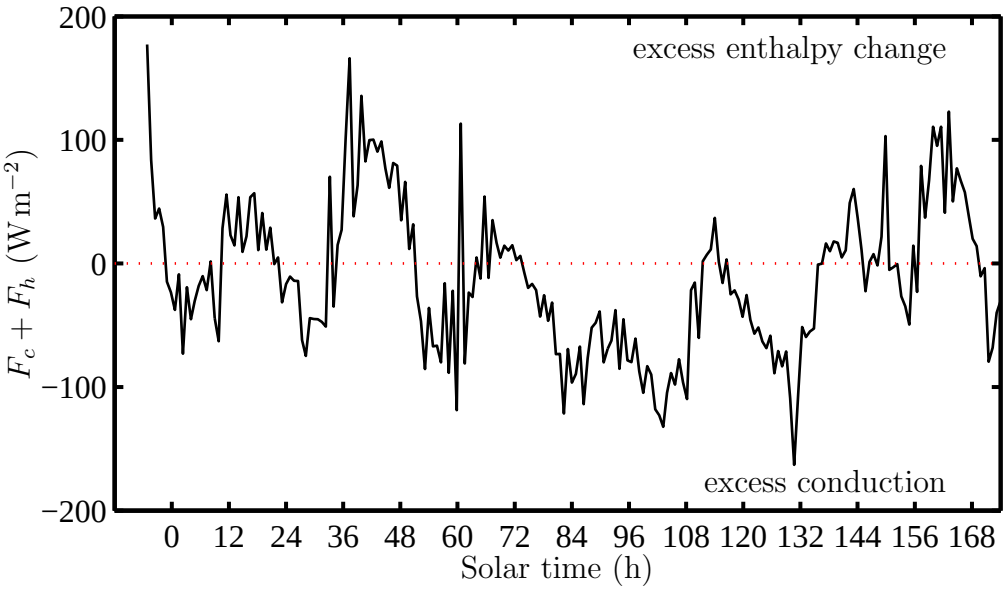

Figure B.15: Difference between conducted heat flux F_c (negative) and heat flux used in ice formation F_h (positive) in *slot 2*.

equivalent to a rate of ice accumulation, $u^\star$, of

$$u^\star = \frac{F_o}{\rho_i L}, \tag{B.22}$$

i.e. $u^\star = 5{\times}10^{-7}\,\mathrm{m\,s^{-1}}$ and $u^\star = 1.6{\times}10^{-6}\,\mathrm{m\,s^{-1}}$ during *slot 10* and *slot 12*, respectively. These growth rates are similar to the growth rates measured at the centres of the slots (Figures B.3/B.4 and B.8). This is to be expected in the presence of an insulating snow cover since freezing front movement and heat balance are based on the same set of data.

We will now convert the growth rate, $u^\star$, to an arrival rate, n (number of crystals per unit time per unit area), of frazil crystals at the ice–water interface. Assuming cylindrical frazil crystals of radius r and thickness $\alpha\, r$, the growth rate $u^\star$ is equivalent to a rate of arrival of

$$n = \frac{u^\star}{\alpha \pi r^3}. \tag{B.23}$$

The assumption of uniform crystal size is made for simplicity. In the absence of measurements, a crystal radius of $r = 1\,\mathrm{mm}$ is deemed to be realistic. The crystal aspect ratio, $\alpha = 1/20$, is taken from *Gosink and Osterkamp* (1983) (*Jenkins and Bombosch* (1995) find $\alpha \approx 1/100$ from numerical simulations, *Smedsrud and Jenkins* (2004) assume $\alpha \approx 1/50$). The necessary frazil crystal arrival rate is therefore $n = 0.3\,\mathrm{s^{-1}\,cm^{-2}}$ and $1\,\mathrm{s^{-1}\,cm^{-2}}$ for *slot 10* and *slot 12*, respectively. These numbers may be realistic.

We expect that frazil crystals incorporated into the ice could be the source of the negative ocean heat flux. However, this estimate is based on the subjective impression of frazil ice sizes and rates of arrival in September 2002, not on measurements. The frazil crystals should be visible in the thin sections since the heat flux attributed to them accounts for almost the entire ice formed (once the slots are snow covered). However,

the thin section of *slot 10* (Figure 2.16) shows elongated crystals in the centre of the crack. A thin section of *slot 12* is not available.

B.9.2 Heat flux is due to the relief of supercooling of the water

We will convert the unbalanced heat flux to a volume flux of supercooled water, to convert the volume flux into a typical convection velocity.

Suppose the ocean heat flux, F_o, has to be provided by supercooled ocean water entering the slot, where it relieves its supercooling. The flux of ocean water into the slot necessary is

$$u_{exchange} = \frac{F_o}{c_w \, \rho_w \, \Delta T_F}, \tag{B.24}$$

where ΔT_F is the supercooling of the water before it enters the slot. Assuming that the area of inflowing water is of the same size as the area of outflowing water, the magnitude of the average vertical velocity of the in- and outflowing water is

$$\bar{u} = 2\frac{F_o}{c_w \, \rho_w \, \Delta T_F}. \tag{B.25}$$

Leonard et al. (submitted) measure both supercooling 0.15 m below the ice–water interface, and the vertical temperature profile underneath growing sea ice in McMurdo Sound in the winter of 2003. They find that, starting in May, the difference between water temperature and surface freezing point is almost constant (for the purpose of this estimate) over the entire measurement range of 250 m. Hence, a large body of water is available that could arrive at the surface supercooled. The supercooling at the ice–water interface was found to be $\Delta T_F \approx 10\,\mathrm{mK}$ from June to August and $\Delta T_F = (15 \pm 4)\,\mathrm{mK}$ on 9 September, 2003.

Based on the measurement in September, the expected range for the vertical velocity is therefore $4\,\mathrm{mm\,s^{-1}} \leq \bar{u} \leq 7\,\mathrm{mm\,s^{-1}}$ and $13\,\mathrm{mm\,s^{-1}} \leq \bar{u} \leq 22\,\mathrm{mm\,s^{-1}}$ for experiments *slot 10* and *slot 12*, respectively. While the velocity range found for *slot 10* is consistent with velocities determined for brine plumes, a vertical velocity of 10 to $20\,\mathrm{mm\,s^{-1}}$ in the case of *slot 12* appears to be high.

Conclusion

Judging from the presence of elongated crystals in the thin section of *slot 10*, the determined heat flux deficit could have been balanced by a flux of supercooled water relieving supercooling in the slot. However, the large negative ocean heat flux in the case of *slot 12* suggests that a significant amount of upfloating frazil ice crystals is incorporated into the ice of the slot, possibly in addition to relieved supercooling.

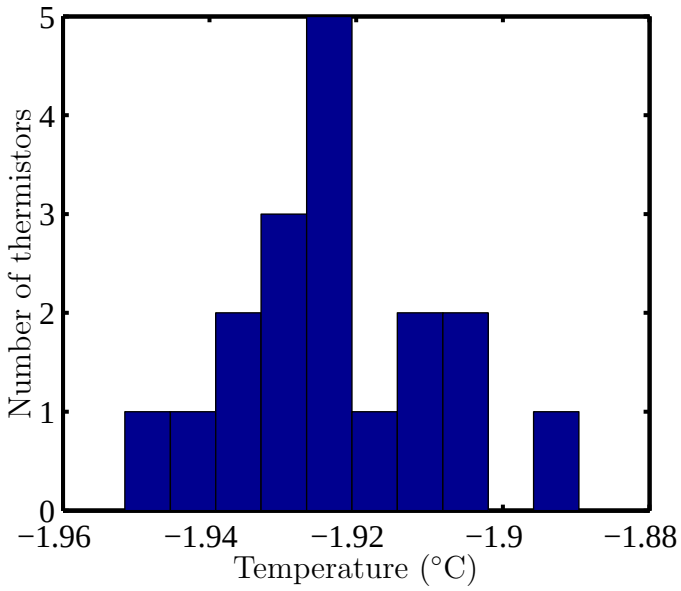

Figure B.16: Distribution of apparent initial water temperature determined from the thermistors during *slot 11*.

B.10 Water temperatures measured beneath refreezing ice, probe 2

Although absolute measurement of the water temperature was not the design target for probe 2, we can of course calculate an absolute water temperature from the calibration coefficients. Calibration experiments were performed in a saltwater bath in the cold room in the laboratory in Dunedin before the deployment of the probes. The output voltage of each thermistor was compared with measurements of a platinum resistance thermometer of resolution 0.01 °C in the temperature range $-2.00\,°\mathrm{C} \leq T \leq -1.82\,°\mathrm{C}$. The average temperature at the beginning of experiment *slot 11* determined from all but the 3 drifting thermistors[2] between hours −4.7 and 3.7 (note that the general temperature decrease did not start until some time after hour 10) is $T = -1.923\,°\mathrm{C}$. This is the freezing point of brine of $S = 35.0$ psu (*UNESCO*, 1983), which is higher by 0.3 to 0.4 psu than conductivity, temperature, and density (CTD) measurements indicate at the same site but at depth in September 2002 (*Leonard et al.*, unpublished 2002). We should also note the remark of *Lewis* (1985) that it is not possible to provide a consistent calibration of a resistance thermometer (here a thermistor with resolution better than 0.2 mK) using a device that is less precise (the platinum resistance thermometer with 10 mK resolution). The standard deviation of the average temperatures of the thermistors is 15 mK. The distribution of average thermistor temperatures is shown in Figure B.16.

Water temperature fluctuations during *slot 11* at night from hour 23 to 29 are shown in Figure B.17.

[2]The average temperature is the same with the drifting thermistors included, while the standard deviation reduces to 14 mK.

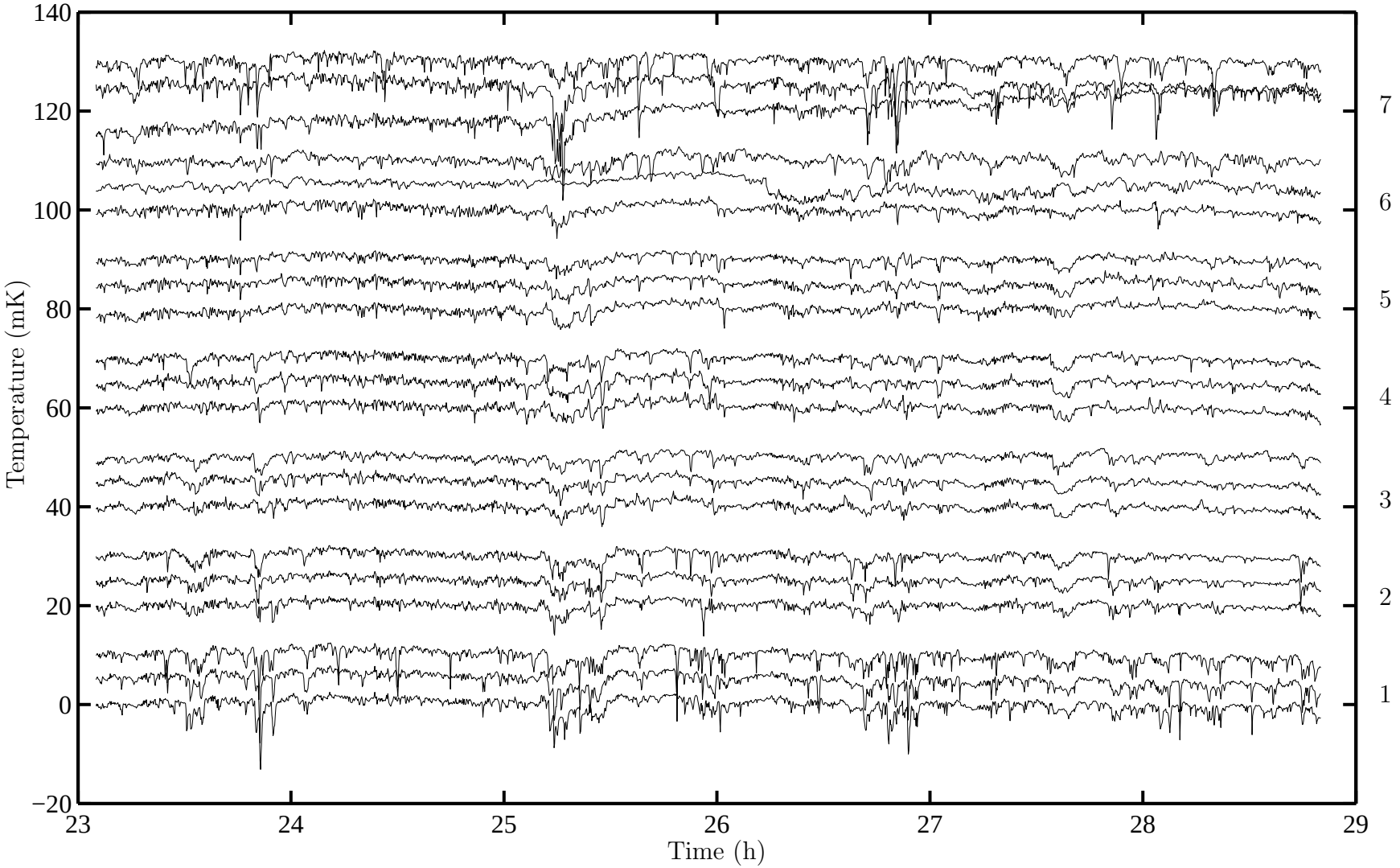

Figure B.17: Water temperature fluctuations during *slot 11* at night. Time series are offset for clarity and grouped in columns with the upper thermistor at the top. The bottom thermistor in column 7 and the centre thermistor in column 6 are drifting. Note that the temperature scale of this plot differs from the scale used in Figure 3.24 and 3.25.

The development of the standard deviation and temperature variability with time is shown in Figure B.18.

B.10.1 Radiation and activity

Figure B.19 shows the signal variation at the upper centre thermistor of *slot 11* as a function of detected illuminance during the second day of the experiment.

B.10.2 Further water temperature data

Further sections of the temperature vs. time record of *slot 11* shall be presented here. The reference thermistors used to monitor the stability of the circuit starts to drift once the signal conditioner begins to freeze into the ice. However, data may still be suitable for at least qualitative analysis. More sections during the early times of refreezing are also shown.

An overview during times of reference thermistor drift is presented in Figure B.20. Only one in twenty data points is shown for clarity. Figures B.21 to B.23 show more temperature time lines while reference thermistors are stable. Figure B.24 is a section of Figure B.23 at the scale compatible with Section 3.3.2.

Figures B.25 to B.27 show data during reference thermistor drift.

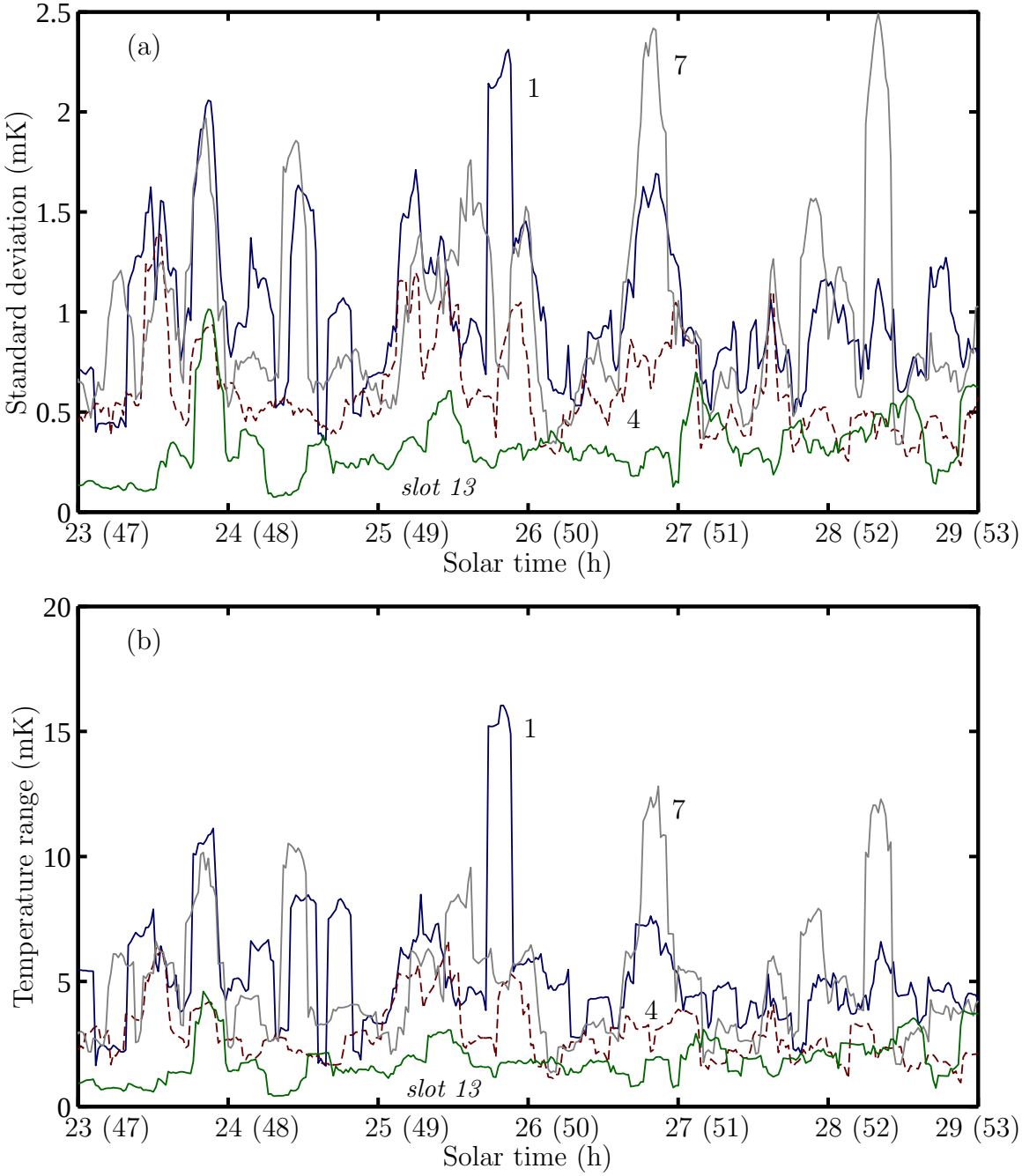

Figure B.18: (a) Standard deviation and (b) temperature variability calculated for a sliding window of 10 min for thermistors of the upper row of column 1 (dark), 4 (dashed), and 7 (light) in *slot 11*, and of *slot 13*. Times in brackets refer to *slot 13*.

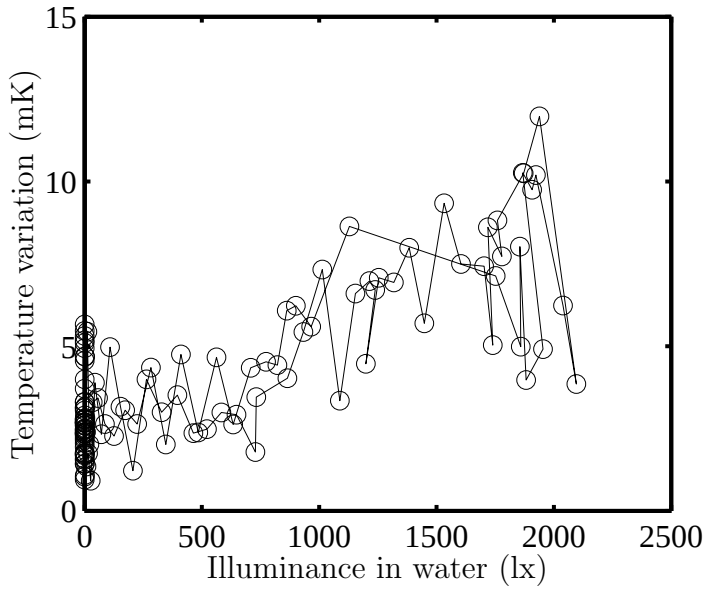

Figure B.19: Temperature variation (temperature difference per detrended 10 min window) of the upper thermistor in the centre column (column 4) in *slot 11* as a function of illuminance measured close to the thermistors in the water. Data of hour 24 to 45.

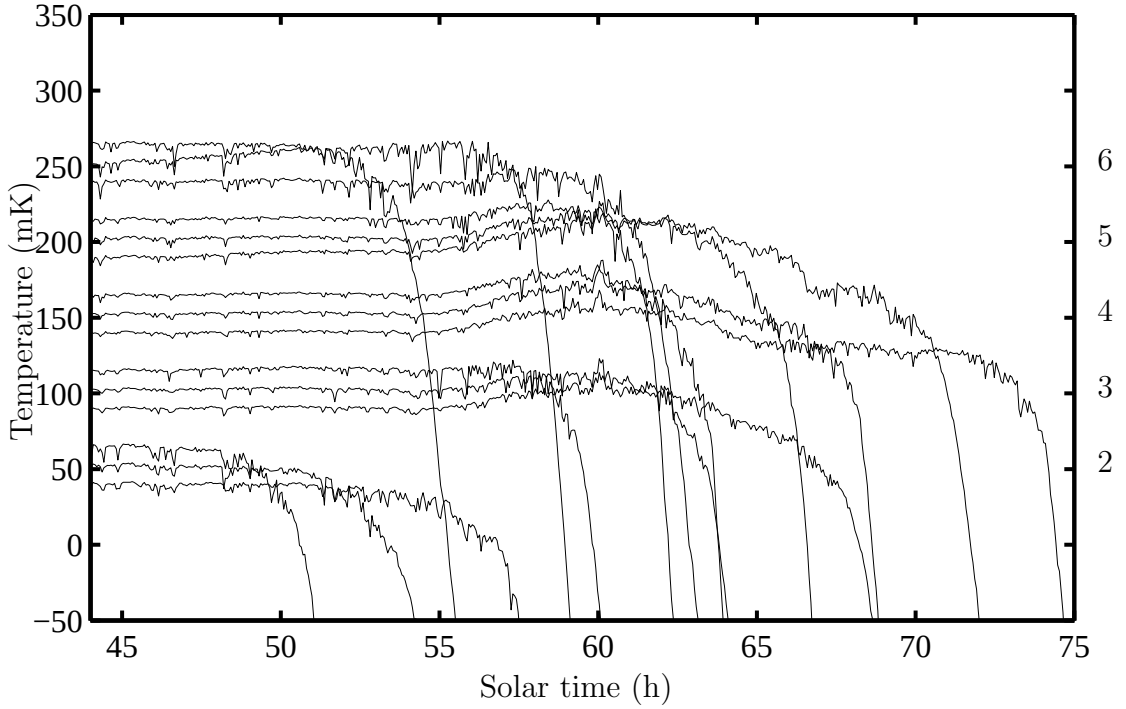

Figure B.20: Overview of water temperatures detected in *slot 11* during times of drift of the reference resistors. Temperatures are offset and only 1 in 20 data points is plotted for clarity. Vertical scale as in Figure 3.23.

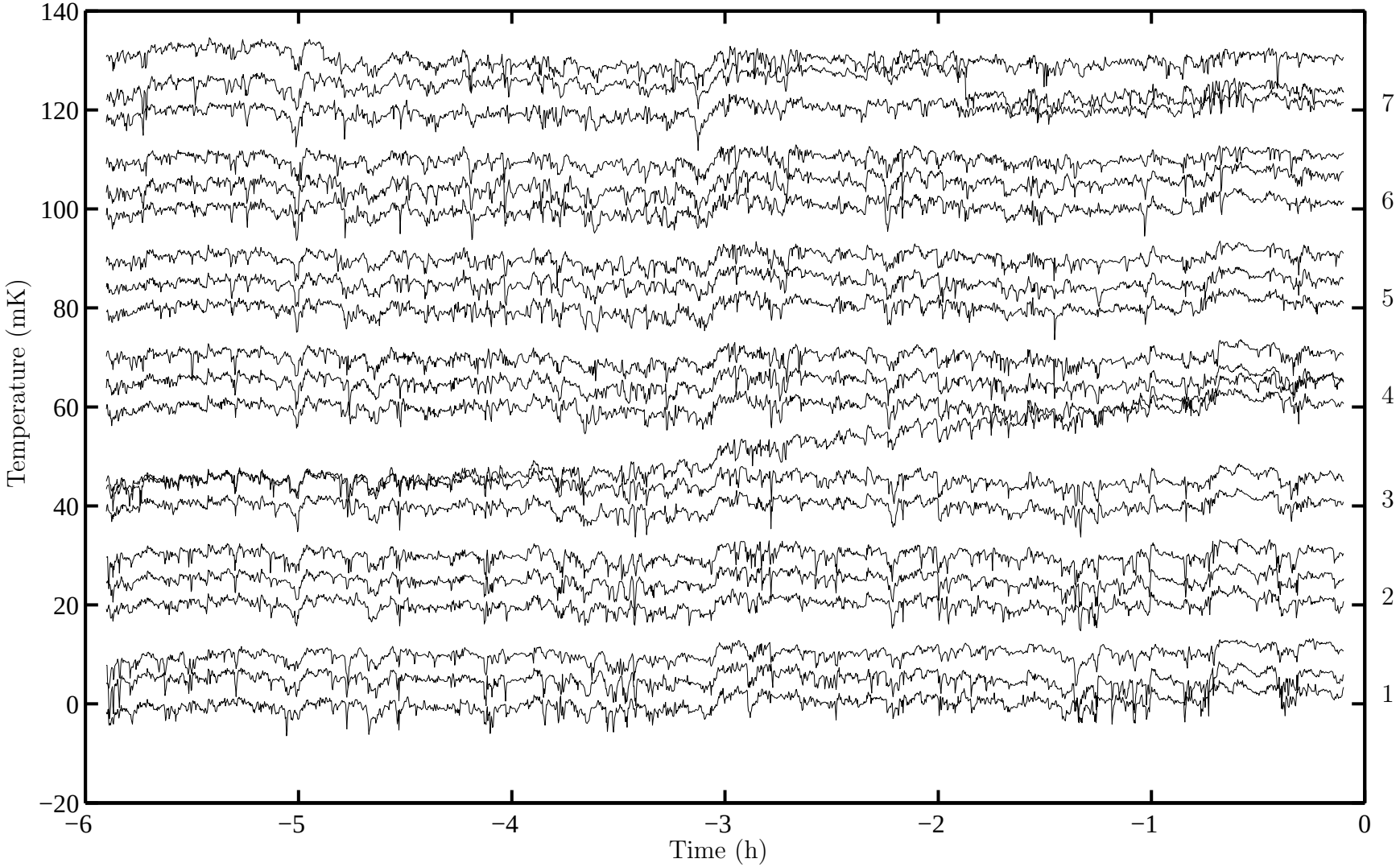

Figure B.21: Water temperature fluctuations during *slot 11*.

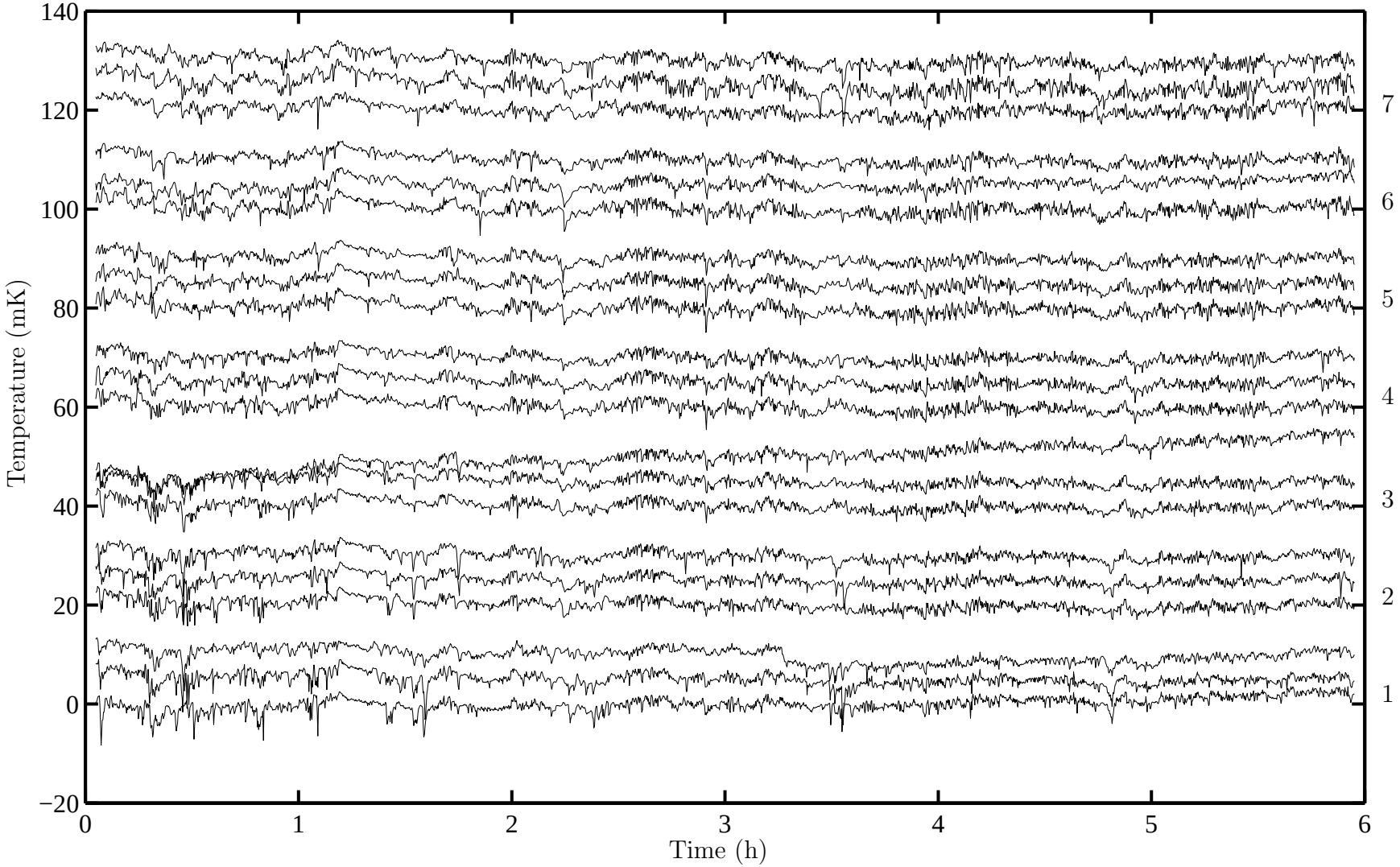

Figure B.22: Water temperature fluctuations during *slot 11*.

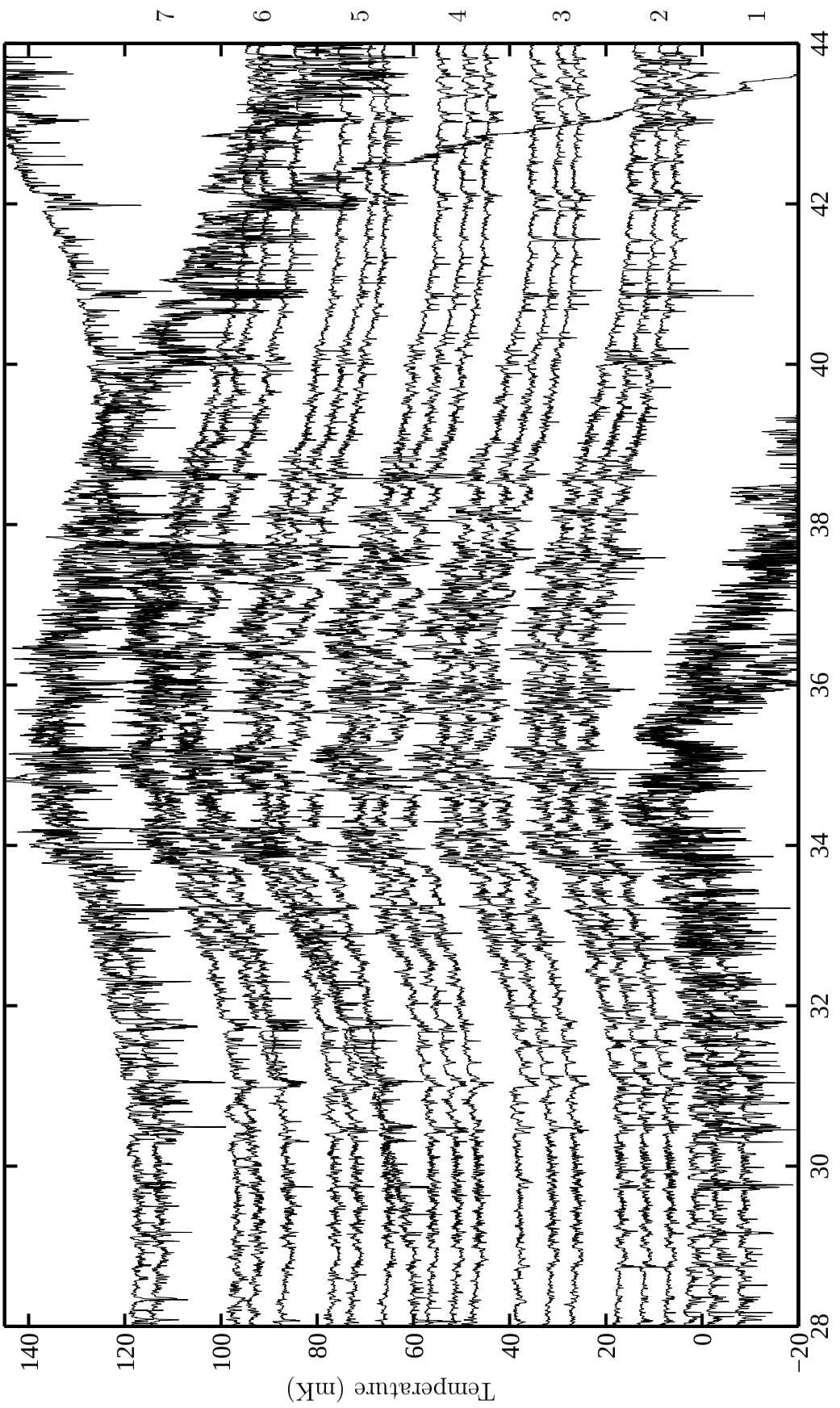

Figure B.23: Water temperature fluctuations during *slot 11.*

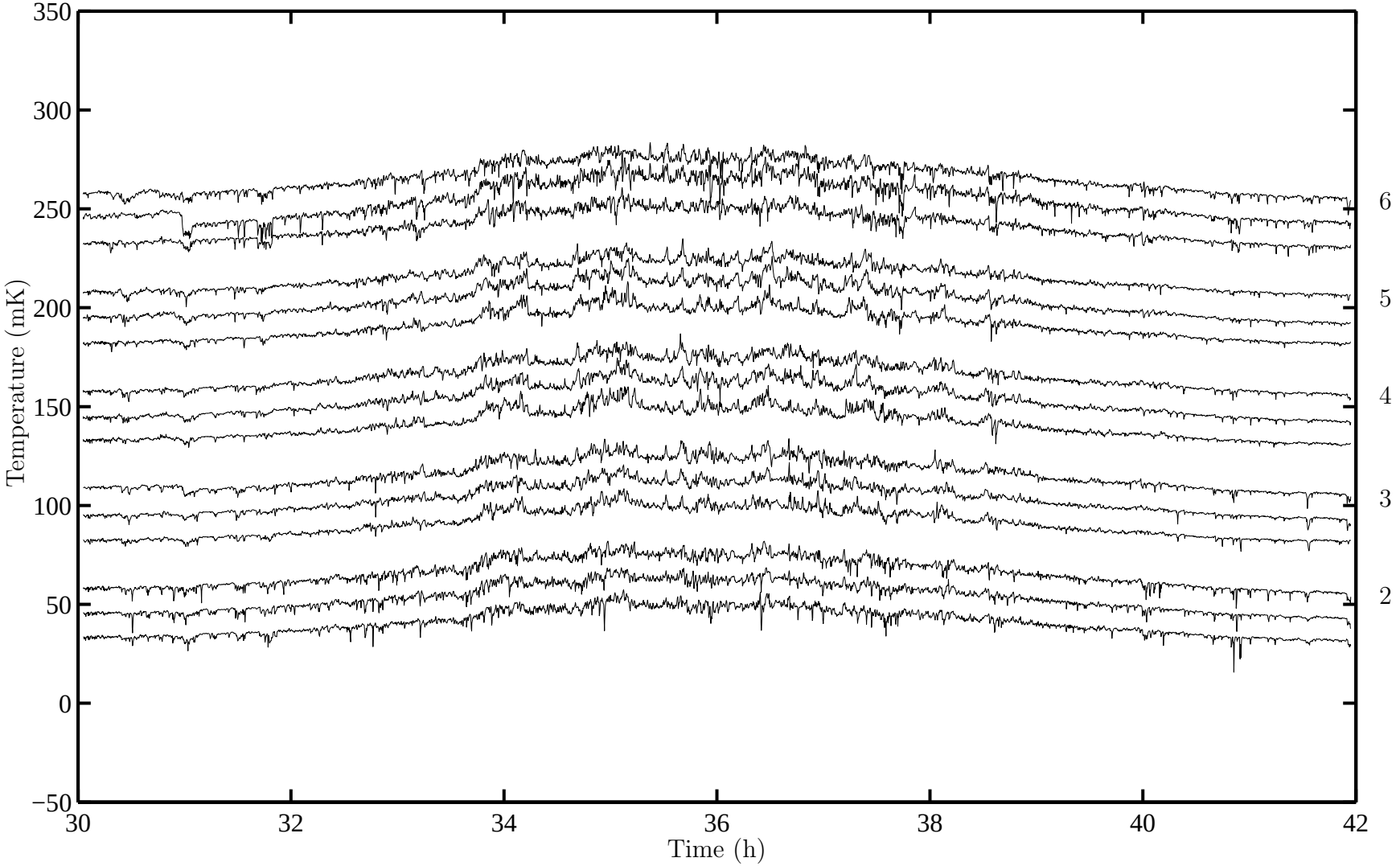

Figure B.24: Water temperature fluctuations during *slot 11*. Note that the scale is different from Figure B.23.

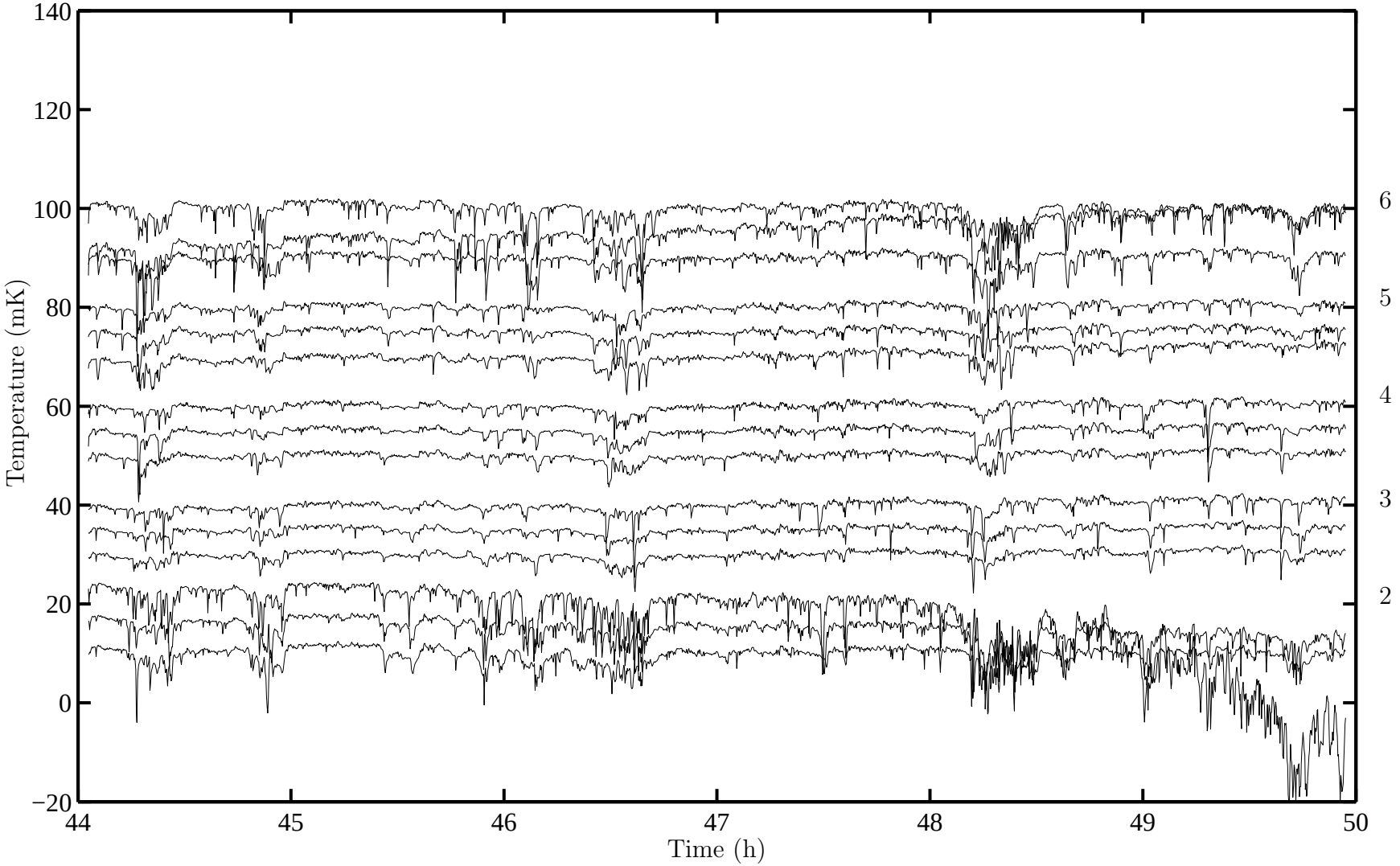

Figure B.25: Water temperature fluctuations during *slot 11*. Reference thermistors drift since the signal conditioning circuit is partially frozen into the ice.

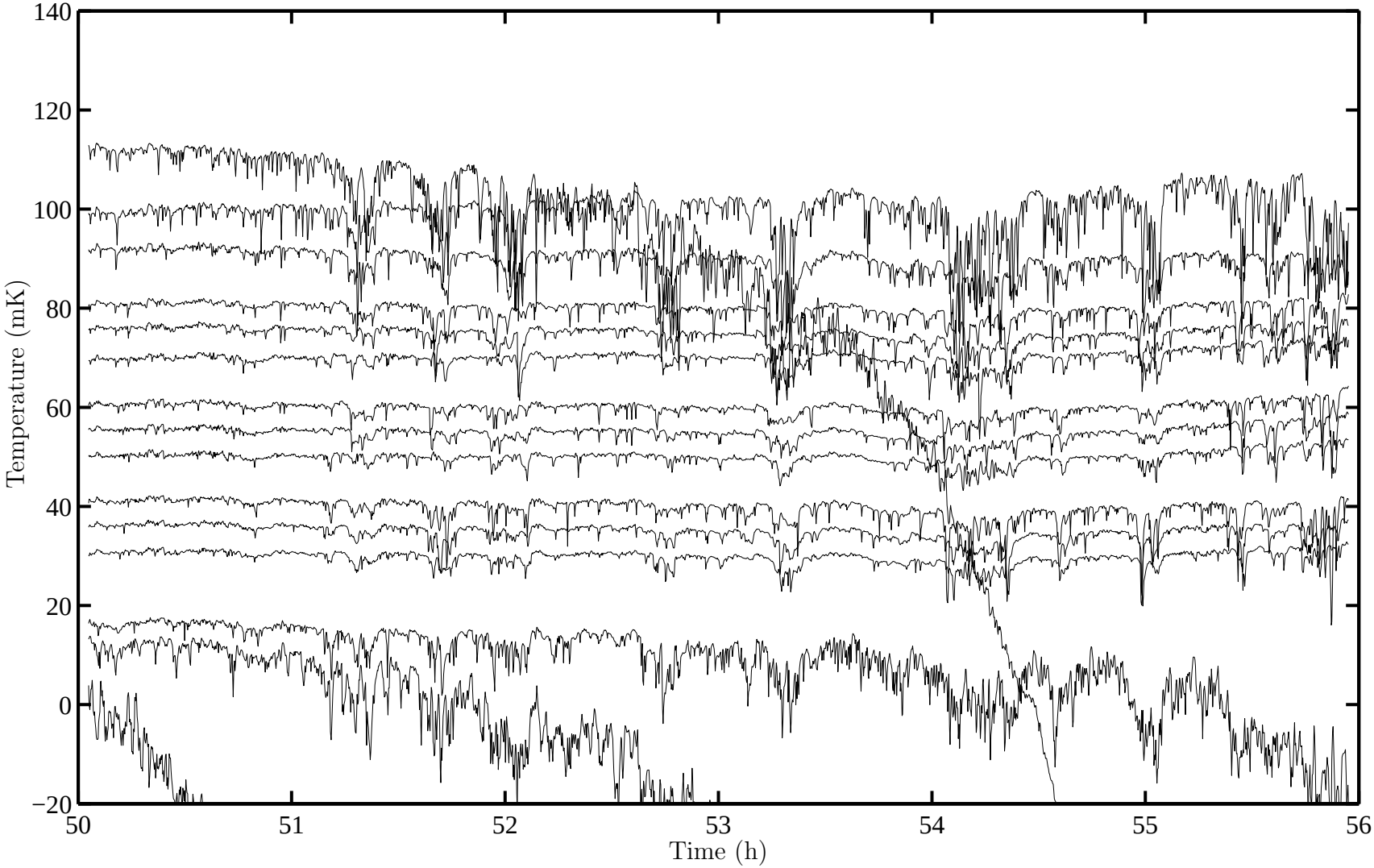

Figure B.26: Water temperature fluctuations during *slot 11*. Reference thermistors drift since the signal conditioning circuit is partially frozen into the ice.

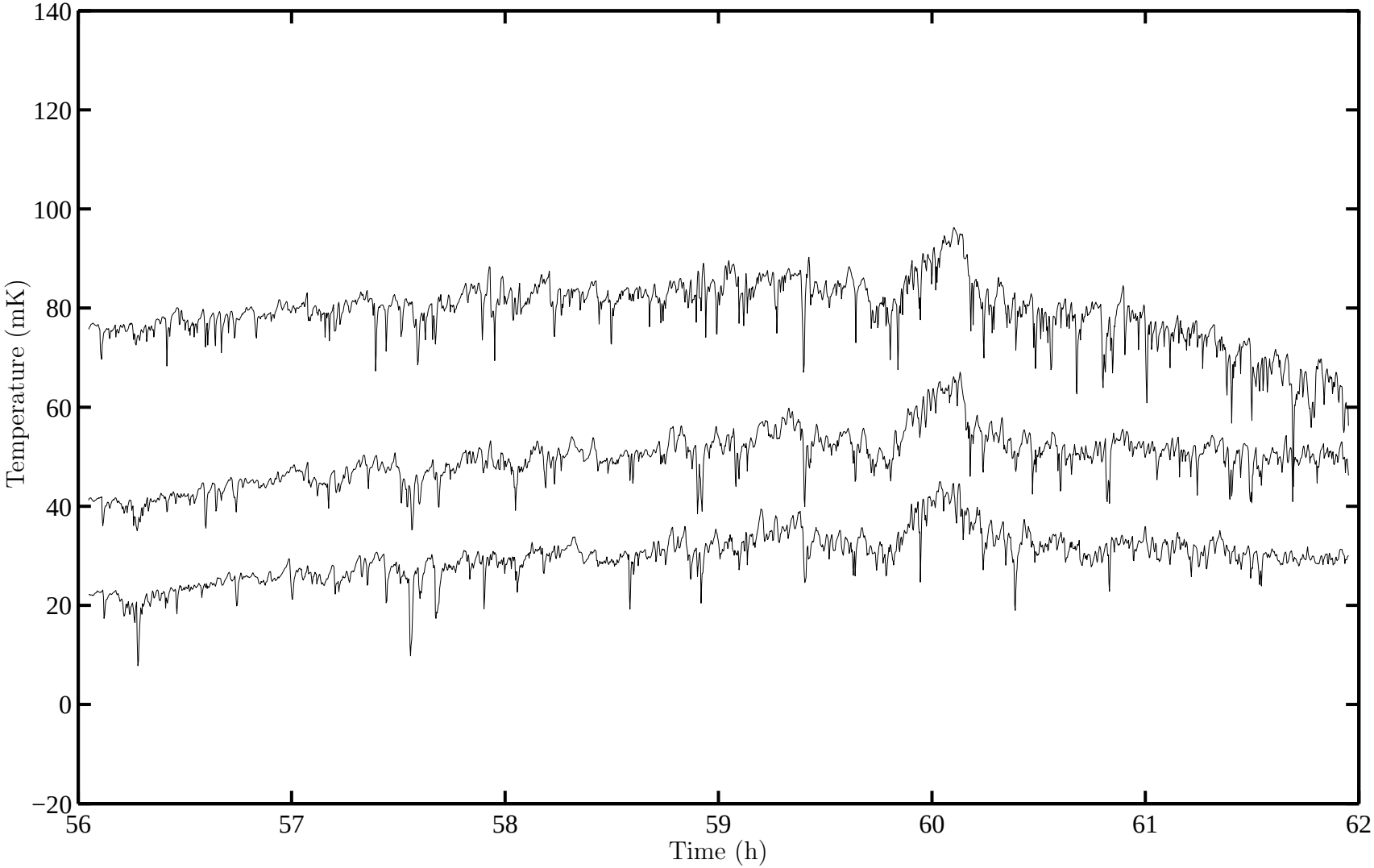

Figure B.27: Water temperature fluctuations during *slot 11*. Only the thermistors of the centre column are shown. Reference thermistors drift since the signal conditioning circuit is partially frozen into the ice.

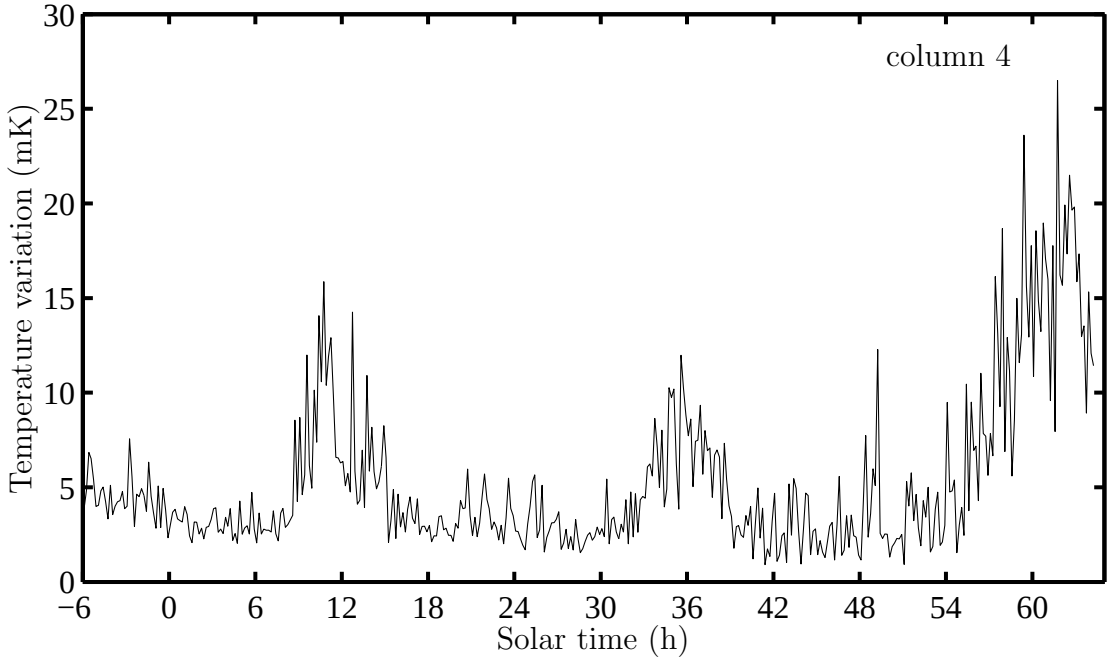

Figure B.28: Temperature variation in *slot 11* measured by the upper thermistor of the centre column (column 4).

B.10.3 Activity over the entire record

Figure B.28 shows the temperature variation (difference between highest and lowest temperature) in running windows of 10 min detected by the upper thermistor of the centre column (column 4) for the entire record of *slot 11*.

Table B.3: Transmission through snow and ice during *slot 11* and *slot 13* in the visible spectral range.

experiment	day 1	day 2	day 3	day 4
slot 11, 10:00	0.39	0.33	0.36	0.0037
slot 13, 12:00	0.025	0.0039	0.0039	–
slot 13, 6:00	0.052	0.016	0.0097	0.0081

B.11 Light transmission through snow and ice

The relationship between the illuminance registered at the sea ice surface and in the refreezing slot discussed in Section 3.4.2 shall be compared with ice and snow thicknesses here. The analysis is greatly facilitated by the fact that the LDRs used are sensitive in the visible spectral range and optical properties of snow and ice depend weakly on wavelength in that spectral range (compared to the wavelength dependence in the infrared).

Experiment *slot 11* experienced blue–sky conditions on the first day, and passing clouds on subsequent days. It was further subjected to the shadow of Ross Island, and measurements inside the slot may have been affected by shadowing from the freeboard at noon since the slot was oriented East–West. The transmission registered shortly before 10:00 is shown in Table B.3, since 10:00 is the time the experiment became exposed to direct radiation and shadowing during the first two days. The experiment was terminated before 10:00 in the fourth day, but the final value obtained is probably comparable to the values of previous days. Experiment *slot 13* was oriented North–South and experienced overcast conditions throughout. Apart from the first day transmission measurements changed throughout the day by only 10 %. The first day experienced a pronounced decrease in transmission at 13:30 that is even apparent in Figure 3.35: the illuminance registered in the water reduced by a factor of three, reducing the transmission to 0.0076. All measurements for *slot 13* are taken at 12:00 noon. Also shown are measurements during dawn at 6:00 in the morning, which would probably have reached values comparable to the readings at noon by day 6.

The transmission during *slot 13* as a function of time is shown in Figure B.29. The first value shown is a transmission of 0.58 at hour −9.25, possibly indicating an albedo of the thin frazil ice layer of $\alpha = 0.42$.

Assuming that albedo at the surface and Beer's law (Section 3.4.3) in snow and ice are sufficient to describe the observed light attenuation (but see for example *Haines et al.* (1997)) Table B.4 lists transmission through ice τ_i at different thicknesses, and Table B.5 transmission through snow τ_s of different thicknesses. Snow albedo in the visible spectral range is in the range $\alpha = 0.92$ (dry snow, *Grenfell and Maykut* (1977)) to $\alpha = 0.98$ (compacted snow, *Grenfell et al.* (1994)), while the albedo in the visible range of sea ice in refreezing slots is probably about $\alpha \approx 0.5 \pm 0.1$. The total transmission τ_t can be calculated from

$$\tau_t = (1 - \alpha)\, \tau_i\, \tau_s, \tag{B.26}$$

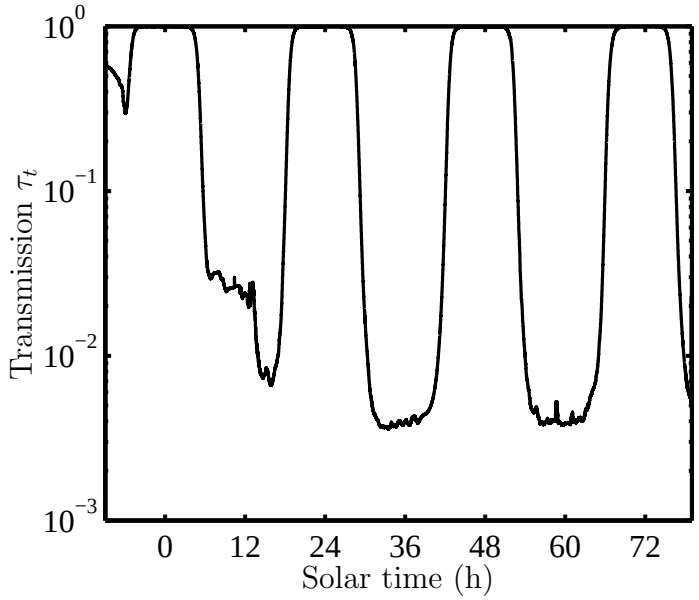

Figure B.29: Transmission registered during *slot 13*. Measurements are calibrated to 1.0 at local midnight (i.e. in the nominal absence of light).

Table B.4: Transmission of visible light through ice τ_i for absorption coefficients $1.5\,\mathrm{m}^{-1} \leq \kappa_i \leq 2.0\,\mathrm{m}^{-1}$ (*Grenfell and Maykut*, 1977).

ice thickness h (m)	$\kappa_i = 1.5\,\mathrm{m}^{-1}$	$\kappa_i = 2.0\,\mathrm{m}^{-1}$
0.01	0.99	0.98
0.05	0.93	0.90
0.1	0.86	0.81
0.2	0.74	0.67
0.4	0.55	0.45
1.0	0.22	0.14

Table B.5: Fraction of radiation transmitted through a snow cover τ_s in the visible range assuming $15\,\mathrm{m}^{-1} \geq \kappa_s \geq 8\mathrm{m}^{-1}$ (*Grenfell and Maykut*, 1977).

snow depth h (m)	$\kappa_s = 15\,\mathrm{m}^{-1}$	$\kappa_s = 8\,\mathrm{m}^{-1}$
0.01	0.86	0.92
0.05	0.47	0.67
0.1	0.22	0.45
0.2	0.050	0.20
0.5	0.00055	0.018

with transmission coefficients determined from

$$\tau = \exp(-\kappa\, h), \tag{B.27}$$

where τ is the transmission coefficient, κ the extinction coefficient, and $h > 0$ is the depth of the layer.

Assuming for example for *slot 11* a snow free ice layer with $\alpha = 0.5$, of thickness 0.1 m to 0.2 m the total transmission τ_t can be expected to be in the range 0.43 to 0.34, which is consistent with measurements during the first three days.

A snow cover of 0.2 m with an albedo between $\alpha = 0.92$ and $\alpha = 0.98$ on top of 0.05 m of ice would result in a range for τ_t between 0.0009 and 0.015, which is consistent with measurements in *slot 13*. The observed reduction in transmission during the first day by a factor of three could be due to 0.073 m ($\kappa_s = 15\,\mathrm{m}^{-1}$) to 0.14 m^{-1} ($\kappa_s = 8\,\mathrm{m}^{-1}$) snow deposited on the experiment. Using the geometric mean of aforementioned parameters, i.e. $\kappa_s = 11\,\mathrm{m}^{-1}$ and $\alpha = 0.95$ one may estimate that the snow cover on *slot 11* was 0.053 m at noon of the first day (where $\tau_t = 0.025$).

The logarithmic scale of Figure B.29 makes small changes become apparent: the increasing transmission (from $\tau_t = 0.0037$ to $\tau_t = 0.0042$ over 5.4 h) visible on the second day corresponds to a decrease of ice thickness of $3 \times 10^{-6}\,\mathrm{m\,s}^{-1}$ (assuming $\kappa_i = 2\,\mathrm{m}^{-1}$), or to a decrease of snow thickness of $5.6 \times 10^{-7}\,\mathrm{m\,s}^{-1}$ (assuming $\kappa_s = 11\,\mathrm{m}^{-1}$), or to a reduction of extinction coefficient of $3 \times 10^{-5}\,\mathrm{m}^{-1}\,\mathrm{s}^{-1}$ (assuming a snow thickness of 0.2 m). A periodicity is apparent of period 60 to 70 min.

Summary The light dependent resistors employed in probe 2 seem to be capable of documenting quantitatively ice growth and snow accumulation. Absolute thickness measurements are handicapped by the need to know extinction coefficients and albedo. However, measurements over short periods of time together with simultaneous calibration measurements may be useful to estimate for example onset and rate of snow fall on days the experiment could not be visited. Note that measurements with LDRs rely on the presence of light.

Appendix C

Estimating radiative fluxes

C.1 Estimate of clear sky solar shortwave radiation

This section summarises calculated data on solar radiation under clear sky conditions and the solar angle relevant for the experiments in McMurdo Sound in 2001 and 2002.

Brine and Iqbal (1983) present a model that allows us to approximate the spectral shortwave irradiance at the surface of the earth under clear sky conditions. Incident extraterrestrial light, solar constant $S_0 = 1367\,\mathrm{W\,m^{-2}}$, is scattered by air molecules (Rayleigh scattering) and aerosols (scattering of a set fraction, Ångström's[1] turbidity formula), and is absorbed in the absorption bands of ozone, water, and various other gases. Radiation that reaches the surface unscattered is called direct radiation. Diffuse radiation is modelled as the sum of the light scattered by air molecules and by aerosols, and light reflected between surface and atmosphere multiple times. These three diffuse contributions are of the same order of magnitude. Direct radiation and diffuse radiation are collectively referred to as global radiation. A more complete treatment of spectral irradiance modelling has been presented by *Iqbal* (1983), who summarises equations and data tables. All the information necessary to reproduce the results in this section can be found in *Iqbal* (1983) and in *Brine and Iqbal* (1983). Absorption data are taken from *Leckner* (1978) and *Vigroux* (1953). The equations used are given in Appendix C.1.1. Free parameters used are listed in Table C.1. They are not calibrated.

[1] after A. Ångström who is the grandson of A. J. "Våglängd" Ångström.

Table C.1: Free parameters used for the calculation of spectra in this section. Nomenclature as in *Iqbal* (1983) and *Brine and Iqbal* (1983).

ground albedo ρ_g	0.8
aerosol coefficient α	1.3
aerosol coefficient β	0.025 (i.e. visibility $\approx 200\,\mathrm{km}$)
diffuse aerosol scattering ω_0	1.0
ozone l	$0.255\,\mathrm{cm(NTP)}$ (i.e. 255 Dobson units)
air pressure p	$0.101325\,\mathrm{MPa}$
precipitable water w	$0.17\,\mathrm{cm}$ (e.g. $T = -20\,^\circ\mathrm{C}$, RH $= 80\,\%$)

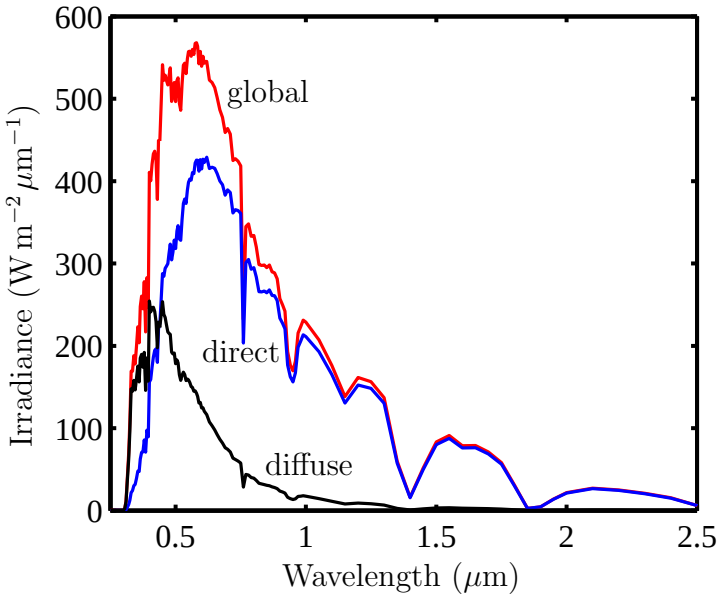

Figure C.1: Spectral irradiance on a horizontal surface at solar angle 20 ° (noon mid October). Global, direct, and diffuse radiation are shown.

The model of *Brine and Iqbal* has been used by *Zeebe et al.* (1996) to calculate radiation input in absorption modelling of the algal layer in sea ice. Using the model of *Iqbal*, we find that radiation at noon on December 12 (solar angle 35 °) in the spectral range of 400 nm to 700 nm is 285 W m^{-2}, which is consistent with the measurement of 270 W m^{-2} of *SooHoo et al.* (1987) in McMurdo Sound. The model has not been specifically designed for very low solar angles, but it is hoped that the accuracy is sufficient for order–of–magnitude estimates.

Figure C.1 shows an example spectrum for a solar angle of 20 °, i.e. noon in mid October, in a relatively clean atmosphere. Shown are global, direct, and diffuse radiation. As expected, diffuse radiation is the weaker contribution. It carries most of its energy in the blue spectral range, which is consistent with the colour of the sky. The absorption bands of water vapour and various other gases appear in the direct beam.

Figure C.2 shows the contributions of direct and diffuse radiation to the total radiation and radiation in the visible range from 400 nm to 700 nm. The predicted total direct radiation at a solar angle of 7.0 ° (noon during *slot 11*) is 66 W m^{-2} (diffuse: 30 W m^{-2}, global: 96 W m^{-2}), which is consistent with measurement of direct radiation[2] at Scott Base (data courtesy of the National Institute of Water and Atmospheric Research (NIWA), New Zealand).

Figure C.3 shows the fraction of the solar spectrum that is incident in the visible range.

Figure C.4 presents solar angle as a function of solar time of the day during the refreezing experiments of 2001 and 2002.

[2]The maximum direct radiation registered on September 9, 2002 was 50 W m^{-2}. The maximum direct radiation registered on September 7 was 65 W m^{-2} and therefore larger than 2 days later. This could be due to the variability of atmospheric conditions, or due to problems with the instrumentation.

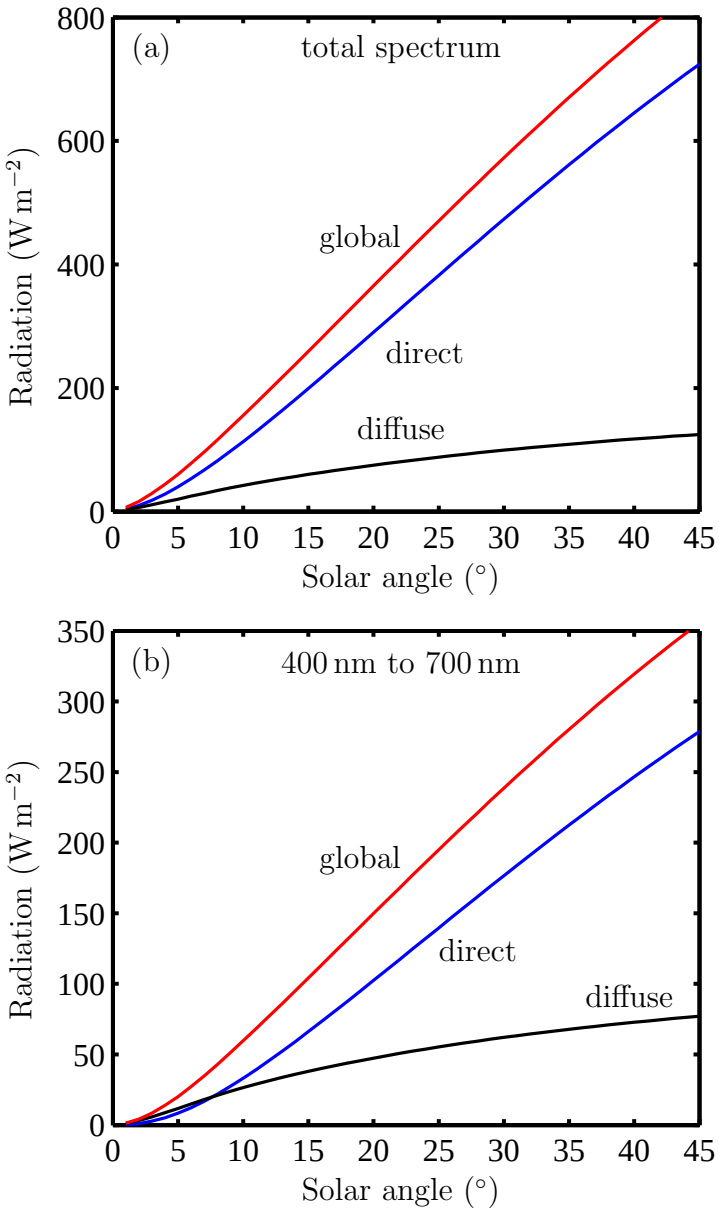

Figure C.2: Radiation incident on a horizontal surface as a function of solar angle. (a) Integration over the entire solar spectrum, (b) integration over the visible range from 400 nm to 700 nm. Global, direct, and diffuse radiation are shown.

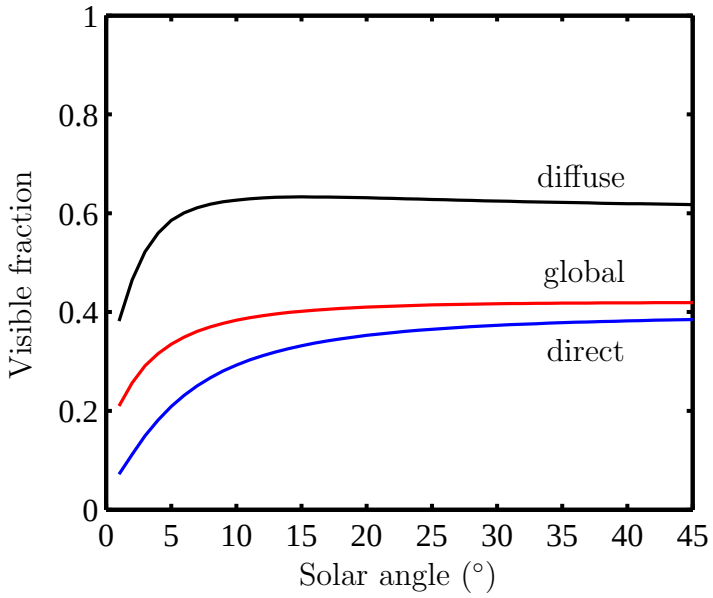

Figure C.3: Fraction of energy incident in the visible range of 400 nm to 700 nm. Shown are graphs for global, direct, and diffuse radiation. This figure shows the ratio between Figure C.2(a) and Figure C.2(b). The order of graphs is top to bottom: diffuse, global, direct.

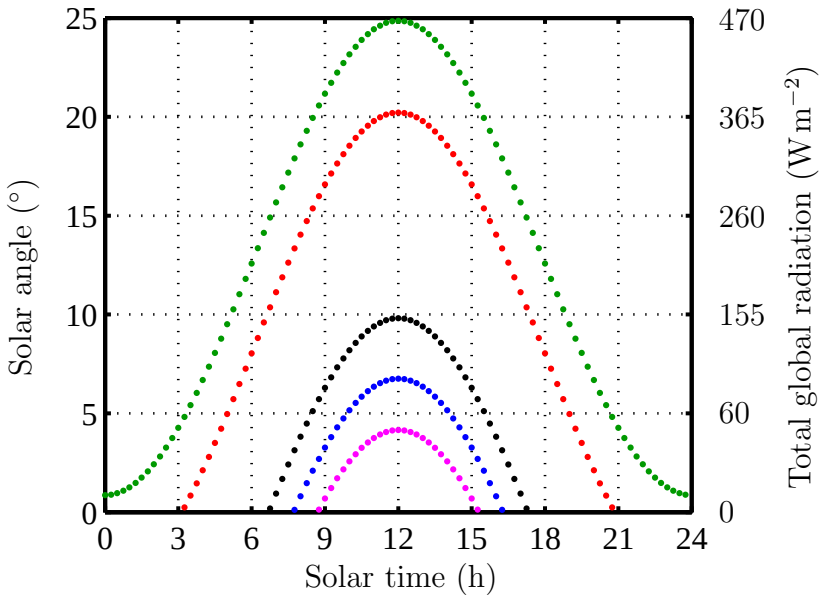

Figure C.4: Solar angle over the course of the day in McMurdo Sound calculated for September 3 (*slot 10*), September 10 (*slot 11*), September 18 (*slot 12* and *slot 13*), October 15 (*slot 1*) and October 28 (*slot 2*). Diffraction effects are not considered. A scale indicating the corresponding global radiation is also given.

Table C.2: Maximum daily radiation corresponding to Figure C.4.

	angle (°)	global ($\mathrm{W\,m^{-2}}$)	direct ($\mathrm{W\,m^{-2}}$)	diffuse ($\mathrm{W\,m^{-2}}$)
slot 10	4.2	46.1	29.7	16.4
slot 11	6.7	91.4	63.0	28.5
slot 12	9.8	152	110	41.9
slot 1	20.2	370	293	76.4
slot 2	24.9	468	379	88.6

Table C.3: Mean daily radiation corresponding to Figure C.4.

	global ($\mathrm{W\,m^{-2}}$)	direct ($\mathrm{W\,m^{-2}}$)	diffuse ($\mathrm{W\,m^{-2}}$)
slot 10	7.5	4.7	2.8
slot 11	19.2	12.8	6.4
slot 12	39.0	27.3	11.7
slot 1	149	114	34.8
slot 2	221	172	48.5

The corresponding daily maximum and mean values for radiation are shown in Tables C.2 and C.3, respectively. The minimum radiation predicted for *slot 2* is at an angle of 0.86 °, global 5.4 $\mathrm{W\,m^{-2}}$, direct 3.0 $\mathrm{W\,m^{-2}}$, diffuse 2.5 $\mathrm{W\,m^{-2}}$.

C.1.1 Governing equations

The shortwave radiative model equations adapted from *Iqbal* (1983) and from *Brine and Iqbal* (1983) shall be presented to facilitate the critical examination of the model and the choice of parameters. The implementation of the model follows the recommendations of *Iqbal* and *Brine and Iqbal*. The discussion of *Iqbal* (1983) (direct and diffuse radiation) and *Brine and Iqbal* (1983) (diffuse radiation) of the equations is not repeated here.

Position of the sun

The zenith angle, θ, can be calculated for a latitude and time of day from

$$\cos\theta = \sin\delta\,\sin\phi + \cos\delta\,\cos\phi\,\cos\omega. \tag{C.1}$$

The solar angle above the horizon is consequently $90\,^\circ - \theta$. In (C.1), ω is the hour angle, $\omega = 0\,^\circ$ at noon and $\omega = 180\,^\circ$ at midnight; ϕ is the geographic latitude with north positive, i.e. $\phi = -77.8\,^\circ$ in the present calculations. The declination, δ, is approximated by

$$\delta = 23.45\,^\circ\,\sin\left(\frac{360\,^\circ}{365}(d+284)\right), \tag{C.2}$$

where d is the day of the year ($d = 1$ on the first day of January of the Gregorian calendar).

Direct radiation

The principle of direct radiation modelling is straight–forward. An extraterrestrial spectral distribution is assumed that is scaled to yield a wavelength–integrated, shortwave radiative flux of $S_0 = 1367\,\mathrm{W\,m^{-2}}$. Then, transmission coefficients are determined for each wavelength, and the wavelength–dependent transmission coefficient for direct radiation, τ_λ, is determined from

$$\tau_\lambda = \tau_r\,\tau_a\,\tau_{wa}\,\tau_g\,\tau_o. \tag{C.3}$$

The meaning of the transmission coefficients will be explained below. The irradiance I_h incident on a horizontal plane is then calculated from the extraterrestrial irradiance I_0 following

$$I_h(\lambda) = \cos(\theta)\,\tau_\lambda\,I_0(\lambda), \tag{C.4}$$

where λ is the wavelength and θ is the zenith angle of the sun. Likewise, the direct shortwave radiative flux F_{SW}^{direct} incident on a horizontal surface is

$$F_{SW}^{direct} = \int_{\lambda_0}^{\lambda_1} I_h(\lambda)\,d\lambda. \tag{C.5}$$

The maximum range of wavelengths considered in the present model is $0.25\,\mu\mathrm{m} \leq \lambda \leq 25\,\mu\mathrm{m}$.

The amount of transmission depends on the optical path length of the solar rays in the atmosphere. This length is conveniently expressed in terms of the optical mass, m_r,

$$m_r = \left[\cos(\theta) + 0.15(93.885\,^\circ - \theta)^{-1.253}\right]^{-1}, \tag{C.6}$$

where θ is the zenith angle of the sun in degrees, i.e. $\theta = 90\,^\circ$ if the sun is at the horizon. The optical air mass, m_a, is scaled with air pressure p,

$$m_a = \frac{p}{1013.25\,\mathrm{hPa}}\,m_r. \tag{C.7}$$

Literature standards are followed in the definition of optical mass for ozone, m_o, and water vapour, m_w, i.e.

$$m_o = m_r, \tag{C.8}$$

$$m_w = m_r. \tag{C.9}$$

Transmission, after Rayleigh scattering by air molecules, is calculated from

$$\kappa_r = 0.008735\lambda^{-4.08}, \tag{C.10a}$$

$$\tau_r = \exp(-\kappa_r\,m_a), \tag{C.10b}$$

where the wavelength λ is in nm. Mie scattering of dust particles and water droplets

is parameterised by Ångström's turbidity formula for all aerosols,

$$\kappa_a = \beta\,\lambda^{-\alpha}, \tag{C.11a}$$

$$\tau_a = \exp(-\kappa_a\, m_a), \tag{C.11b}$$

where the coefficients α and β can be related to visibility $v > 5\,\mathrm{km}$ (v in km)

$$\beta = 0.55^{\alpha}\left(\frac{3.912}{v} - 0.01162\right)\left[0.02472\,(v-5) + 1.132\right]. \tag{C.12}$$

A typical value for α is $\alpha = 1.3 \pm 0.5$. Values used for α and β are given in Table C.1. Water vapour scattering is treated with a wavelength dependent tabulated coefficient κ_{wa} that is linearly interpolated as necessary and

$$\tau_{wa} = \exp\left(\frac{-0.2385\kappa_{wa}\,w\,m_w}{(1 + 20.07\kappa_{wa}\,w\,m_w)^{0.45}}\right), \tag{C.13}$$

where w is the amount of precipitable water in cm that can be calculated from relative humidity RH (in %) and air temperature T_a (in K)

$$w = \frac{1}{T_a}\,0.439\frac{\mathrm{RH}}{100}\exp\left(26.23 - \frac{5416}{T_a}\right). \tag{C.14}$$

The transmittance of uniformly mixed gases is treated similarly, i.e. with a tabulated wavelength dependent coefficient κ_g and

$$\tau_g = \exp\left(\frac{-1.41\kappa_g\,m_a}{(1 + 118.93\kappa_g\,m_a)^{0.45}}\right). \tag{C.15}$$

Finally, ozone transmittance is calculated from a wavelength dependent tabulated coefficient κ_o and

$$\tau_o = \exp\left(-\kappa_o\,l\,m_o\right), \tag{C.16}$$

with l indicating the amount of ozone in cm(NTP) (i.e. $l = 0.001$ times the amount of ozone in Dobson units).

Diffuse radiation

Diffuse shortwave radiation is only considered for the case of a horizontal surface, and the reader should refer to *Iqbal* (1983) for non–horizontal surfaces. The method of estimating diffuse radiation is not as straight–forward as in the case of direct radiation, mainly because of the presence of multiple scattering events. However, in the present model, the total diffuse, wavelength–dependent irradiance on a horizontal surface D_h is

$$D_h(\lambda) = D_r(\lambda) + D_a(\lambda) + D_m(\lambda). \tag{C.17}$$

The terms on the right hand side will be described below. In a similar way to the case of direct radiation, the wavelength–averaged diffuse flux on a horizontal surface is

calculated from

$$F_{SW}^{diffuse} = \int_{\lambda_0}^{\lambda_1} D_h(\lambda)\, d\lambda. \tag{C.18}$$

The Rayleigh–scattered, diffuse irradiance on a horizontal surface is

$$D_r(\lambda) = I_0(\lambda)\cos(\theta)\tau_o\tau_g\tau_{wa}\tau_a(1-\tau_r)F_r, \tag{C.19}$$

where $F_r = 0.5$ is the Rayleigh forward–scattering ratio. The transmission coefficients, τ, are the ones used for the calculation of direct radiation. Similarly, the aerosol scattered diffuse irradiance on a horizontal surface is

$$D_a(\lambda) = I_0(\lambda)\cos(\theta)\tau_o\tau_g\tau_{wa}\tau_r(1-\tau_a)\omega_0 F_a, \tag{C.20}$$

where $0 \leq \omega_0 \leq 1$ is the fraction of radiation that is scattered on aerosols as opposed to absorbed. F_a is a zenith–angle–dependent scattering ratio towards the earth that is tabulated for $\theta \leq 85\,^\circ$ (e.g. $F_a = 0.60$ for $\theta = 80\,^\circ$, $F_a = 0.50$ for $\theta = 85\,^\circ$, and we extrapolate $F_a = 0.50$ for $\theta > 85\,^\circ$ without further foundation). The wavelength dependence of F_a is neglected. Diffuse radiation after multiple scattering between ground and atmosphere is

$$D_m = \left[I_h(\lambda) + D_r(\lambda) + D_a(\lambda)\right]\frac{\rho_g\rho_a}{1-\rho_g\rho_a}, \tag{C.21}$$

where ρ_g and ρ_a are ground and atmospheric albedo, respectively. The ground albedo is assumed to be independent of wavelength, and the wavelength–dependent atmospheric albedo is calculated from

$$\rho_a = \tau_o'\tau_{wa}'\tau_g'\left[(1-\tau_r')\tau_a' F_r + 0.22(1-\tau_a')\omega_0\tau_r'\right]. \tag{C.22}$$

The primed transmission coefficients are calculated as above but using an air mass of $m_r = m_a = m_w = m_o = 1.9$ as that was found to give good agreement with theoretical results (*Brine and Iqbal*, 1983). The factor 0.22 is the effective back scatter ratio of aerosols evaluated at $m = 1.9$, i.e. $(1 - F_a) = 0.22$.

Global radiation

The global shortwave irradiance incident on a horizontal surface is the sum of direct irradiance and diffuse irradiance, i.e.

$$G_h(\lambda) = I_h(\lambda) + D_h(\lambda). \tag{C.23}$$

The global shortwave radiative flux is consequently

$$F_{SW} = \int_{\lambda_0}^{\lambda_1} G_h(\lambda)\, d\lambda, \tag{C.24}$$

$$F_{SW} = F_{SW}^{direct} + F_{SW}^{diffuse}. \tag{C.25}$$

C.2 Shortwave flux under overcast conditions

A simple parametrisation of the total, wavelength–integrated, all–sky, shortwave flux F_{SW}^{cloudy} in the presence of a cloud cover of fraction c shall be given here. Based on measurements at Baffin Island, Canada, *Jacobs* (1978) uses the expression

$$F_{SW}^{cloudy} = F_{SW}\,(1 - 0.33\,c) \tag{C.26}$$

that, in spite of its simplicity, performed very well, for example, in independent measurements of *Key et al.* (1996) in the Arctic region. F_{SW} is the global shortwave irradiance under cloudless skies.

Zeebe et al. (1996) use the expression previously used by *Parkinson and Washington* (1979),

$$F_{SW}^{cloudy} = F_{SW}\,(1 - 0.6\,c^3). \tag{C.27}$$

The relationship used by *Parkinson and Washington* for southern hemisphere cloud coverage is a function of latitude and month. According to that relationship cloud coverage varies between $c = 0.50$ in July and 0.65 in January at 75° South.

The cloud cover assumed by *Zeebe et al.* for McMurdo Sound, $c = 0.63$, gives a constant of proportionality of 0.81 from (C.26), and the similar value of 0.85 from (C.27).

A more sophisticated parameterisation for wavelength–averaged, shortwave radiation under cloudy skies in polar regions has been developed by *Shine* (1984). That parametrisation also accounts for cloud optical thickness.

C.3 Estimate of longwave radiative heat flux

Longwave radiation is considered only in its wavelength–averaged form in this section. For a discussion of the incident radiation spectrum in the Arctic see for example *Tobin et al.* (1999).

Longwave (infrared) radiation has an extinction coefficient that is over 7 orders of magnitude larger than visible shortwave radiation in ice (*Warren*, 1984), which makes incident and emitted longwave radiation a surface effect. Longwave radiation emitted by the surface is

$$F_{LW}\uparrow = \epsilon_s \sigma T_s^4, \tag{C.28}$$

where ϵ_s is the longwave surface emissivity, $\sigma = 5.67 \times 10^{-8}\,\mathrm{J\,K^{-4}\,m^{-2}\,s^{-1}}$ is the Stefan–Boltzmann constant, and T_s is the surface temperature in K. Although ϵ_s depends on the surface, a constant value $\epsilon_s = 0.99$ has been used, for example, by *Persson et al.* (2002), justified by the study of *Grenfell et al.* (1998) that gives a narrow range for ϵ_s of 0.98 to 0.996 (the older and thicker the ice, the larger ϵ_s). We use $\epsilon_s = 0.99$ in this section.

Incident longwave radiation is influenced by many factors (*Shupe and Intrieri*, 2004), but simple parameterisations have been used, some of which are compared against measurements in the Arctic by *Key et al.* (1996) or by *Makshtas et al.* (1998). *Key et al.* recommend the use of a combination of the parameterisation by *Efimova* (1961) for clear sky conditions with the parameterisation of *Jacobs* (1978) for all–sky

flux,

$$F_{LW}\downarrow = \epsilon_a\, \epsilon_{cl}\, \sigma T_a^4, \tag{C.29}$$

$$F_{LW}\downarrow = (0.746 + 0.0066e)\,(1 + 0.26c)\,\sigma T_a^4, \tag{C.30}$$

where T_a is the near–surface air temperature in K, e is the vapour pressure in mbar, c is the fractional cloud cover, ϵ_a is the clear sky emissivity, and ϵ_{cl} is the all–sky parameterisation. Some authors show that the appropriate parameterisation is a function of location. For example, *van den Broeke et al.* (2004) determine clear sky atmospheric emissivity, ϵ_a, between 0.63 and 0.77 at different locations in East Antarctica. *König-Langlo and Augstein* (1994) and *van den Broeke et al.* find for the von Neumayer Station values of 0.760 and 0.765, respectively, which are similar to the value used in (C.30). *Wendler and Worby* (2001) determine a value of 0.78 during a ship cruise in summer from Terre Adélie to McMurdo Sound. However, *König-Langlo and Augstein* (1994) use a different treatment of the cloud cover fraction and find that the use of

$$F_{LW}\downarrow = (0.765 + 0.22c^3)\,\sigma T_a^4 \tag{C.31}$$

amongst other expressions is suitable for use in both Arctic and Antarctica (T_a is measured 2 m above ground).

The vapour pressure e in (C.30) is estimated from relative humidity RH and air temperature T_a,

$$e = \frac{\mathrm{RH}}{100} e_s, \tag{C.32}$$

where e_s is the saturated vapour pressure calculated after[3] *Tetens* (1930) (or similarly *Buck* (1981))

$$e_s = 6.108\,\mathrm{mbar}\, \exp\left(17.27 \frac{T_a - 273.15\,\mathrm{K}}{T_a - 35.85\,\mathrm{K}}\right). \tag{C.33}$$

The interested reader may further wish to consult *Andreas et al.* (2002) for a method to estimate relative humidity RH from air temperature T_a over sea ice.

For example, consider $e = 1.0$ mbar at $T_a = 253.15$ K and RH = 80%, i.e. longwave radiative heat budget (heat gained by the ice) under clear skies with −20 °C air and surface temperature ($T = T_a = T_s = 253.15$ K), which results in

$$F_{LW} = F_{LW}\downarrow - F_{LW}\uparrow = -0.24\,\sigma T^4 \approx -58\,\mathrm{W\,m^{-2}}. \tag{C.34}$$

Further, this becomes $-30\,\mathrm{W\,m^{-2}}$ with a cloud cover of $c = 0.63$, which is the cloud cover fraction used by *Zeebe et al.* (1996) in a radiation model for McMurdo Sound (they use $c = 0.8$ for the Weddell Sea). A scheme for estimating c is provided for the Arctic and Antarctic by *Parkinson and Washington* (1979) and for the Arctic by *Makshtas et al.* (1998). However, if the surface temperature is above the air temperature, the net longwave heat flux into the atmosphere is larger than estimated above. At larger cloud cover fractions it is smaller.

[3] A comparison of (C.33) and other equations is given for example in *Lowe* (1977) and shows deviations from experiments of less than 1 % for temperatures above −25 °C, and of less than 5 % for temperatures above −50 %.

For reference, 20–day averages of one–year measurements over sea ice in the Arctic by *Intrieri et al.* (2002) show a net longwave heat flux of $-30 \pm 10\,\mathrm{W\,m^{-2}}$ apart from winter, when net fluxes as small as $-10\,\mathrm{W\,m^{-2}}$ were measured. Over ice shelf and glaciers in East Antarctica, *van den Broeke et al.* (2004) perform measurements over 3 to 4 years at 4 different automatic weather stations of longwave fluxes. Monthly averages show a distinct annual signal of $\pm 15\,\mathrm{W\,m^{-2}}$ at three of the four stations. The annual mean values of net longwave radiation flux at these stations are -22.4, -36.3, and $-44.0\,\mathrm{W\,m^{-2}}$, respectively. The fourth station, ASW9, situated in the East Antarctic plateau shows an average net radiation flux of $-29.5\,\mathrm{W\,m^{-2}}$ with an annual signal between $-15\,\mathrm{W\,m^{-2}}$ in winter and $-60\,\mathrm{W\,m^{-2}}$ in summer. Amongst other data, the annual average at von Neumayer Station is given as $-29.1\,\mathrm{W\,m^{-2}}$, varying between $-33\,\mathrm{W\,m^{-2}}$ in December and January and $-18.5\,\mathrm{W\,m^{-2}}$ in July and August. Measurements of the net longwave radiative flux by *Wendler and Worby* (2001) on a ship cruise from Terre Adélie to McMurdo Sound in summer revealed an average flux of $-40\,\mathrm{W\,m^{-2}}$, independent of the time of day.

We conclude that in the absence of measurements a reasonable guess for the net longwave radiation seems to be in the range -20 to $-40\,\mathrm{W\,m^{-2}}$.

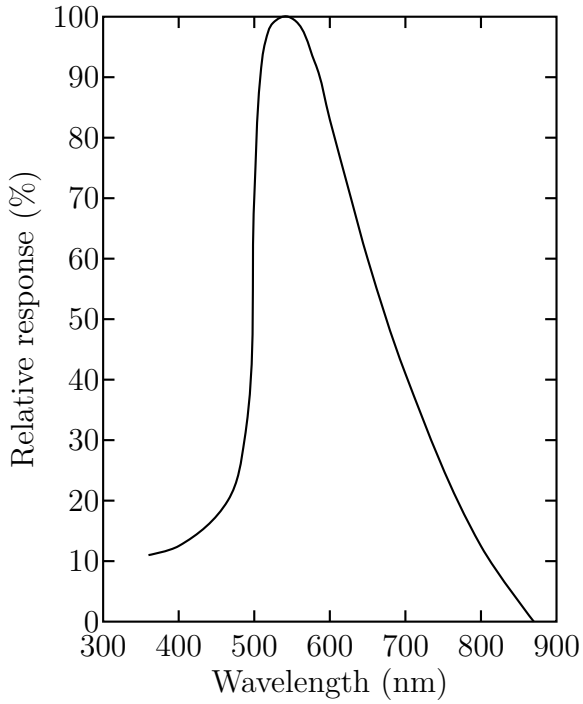

Figure C.5: Spectral response of the *NORP 12* after *RS Components* (1997).

C.4 Spectral response of the light dependent resistors

We use a light dependent resistor (LDR) of the 2002 probe to determine the correlation between water temperature and solar radiative flux in Section 3.4.2. The LDR employed, *NORP 12*, is a Cadmium Sulphide (CdS) photoconductive cell with a spectral response similar to the photobic (daylight) spectral response of the human eye (Figure C.5). For this reason a relationship exists between the resistance of the LDR and illuminance. This relationship is a power law according to the data sheet (*RS Components*, 1997). Illuminance, measured in lux (lx), is a measure for the subjective brightness of an object. For light of wavelength $\lambda = 555\,\mathrm{nm}$, a flux of $F = 1\,\mathrm{W\,m^{-2}}$ is equivalent to an illuminance of 683 lx. Generally, in order to relate illuminance to a flux F the spectral distribution of the flux and the spectral response of the human eye need to be known.

C.5 Shortwave radiation at 700 lx

C.5.1 Introduction

We will estimate the solar shortwave radiative flux arriving at probe 2 in *slot 2* at the times that increased temperature variation appears and disappears. It has been found in Section 3.3.3 that the light dependent resistor (LDR) in the water registers an illuminance of 700 lx at this time. Since the solar time is known, the angle of the

Table C.4: Shortwave radiation predicted by the model of Appendix C.1.

	angle (°)	global ($W\,m^{-2}$)	direct ($W\,m^{-2}$)	diffuse ($W\,m^{-2}$)
entire spectrum	1.5	11	6.3	4.7
400 nm − 700 nm	1.5	2.7	0.6	2.1
400 nm − 700 nm	6.7	33.2	15.9	17.3

sun above the horizon when 700 lx are detected can be calculated. This angle is very small (1.5°, 3 solar diameters), so predictions of the model in Appendix C.1 may be suspect. We will follow three methods to convert this illuminance to a flux:

1. conversion of illuminance to flux assuming a monochromatic spectral distribution of the flux under the ice,

2. calculation of the flux from the model in Appendix C.1 based on solar angle, and assuming a monochromatic spectral distribution under the ice,

3. assuming proportionality between radiative heating of the thermistor beads and flux, a monochromatic spectral distribution under the ice, and calculating the flux at noon with the model in Appendix C.1.

A fundamental assumption in all methods is that the sea ice is thick enough to absorb all but the light in the visible spectral range (*Maykut and Grenfell*, 1975). Further, since the experiment has been performed in the shade, it is assumed that only diffuse radiation will have to be considered.

C.5.2 Calculations

Conversion of illuminance

For light of wavelength 555 nm (green) the conversion between illuminance and flux is well defined. Assuming that the light arriving at the LDR is mostly in the green range, and assuming that the resistance–illuminance relationship of the data sheet of the LDRs can be used without calibration, the flux at 700 lx is

$$F = 700\,\mathrm{lx}\,\frac{1\,\mathrm{W\,m^{-2}}}{683\,\mathrm{lx}}, \tag{C.35}$$

$$F = 1.0\,\mathrm{W\,m^{-2}}. \tag{C.36}$$

Radiation model predictions

Increased temperature variation has been found to start and end at hours 8.6 (1.3 h after sunrise) and 15.3 (1.3 h before sunset), respectively, on 10 September, 2002. At this point the sun is nominally 1.5 ° degrees above the horizon. The shortwave radiation predicted by the model in Appendix C.1 for this solar angle is shown in Table C.4. Since *slot 11* has not been exposed to direct sunlight, only the diffuse contributions matter. Considering the flux under the ice, only the visible spectrum is expected to penetrate.

The spectral albedo is relatively independent of wavelength in the visible spectral range, but it depends on structure and thickness of the ice (*Perovich and Grenfell*, 1981; *Buckley and Trodahl*, 1987). For example, measurements show a value of 0.25 for young gray ice (0.4 with 20 mm snow cover) in Antarctica (*Allison et al.*, 1993); 0.4 for 200 mm thick ice the Baltic Sea (0.8 in highly scattering ice) (*Ehn et al.*, 2004); 0.4, 0.55 and 0.6 for 200 mm NaCl–ice grown at air temperatures of −10 °C, −20 °C, and −30 °C, respectively (> 0.9 if the ice is below the eutectic transition) (*Perovich and Grenfell*, 1981); 0.6 and 0.55 for bare sea ice and blue ice (surface saturated with meltwater), respectively, in the Arctic (*Grenfell and Perovich*, 1984); 0.15, 0.35, and 0.6 for 15 (grease ice), 50 and 110 mm thick bare sea ice, respectively, in Antarctica (*Schlosser*, 1988); 0.15, 0.3, and 0.65 for 20–40 mm thick, 50–100 mm thick, and young white sea ice, respectively, in Antarctica (*Zhou and Li*, 2003); 0.84 for white second year ice (*Grenfell and Maykut*, 1977); and 0.8 for Arctic multiyear ice thicker than 2 m (*Light et al.*, 1998). *Ebert and Curry* (1993) give a fit function for bare sea ice albedo, $\alpha = 0.77 + 0.14 \ln h_i$, wavelength integrated in the band 0.25 μm to 0.69 μm, as a function of ice thickness $h_i \leq 1$ m in m. According to that relationship, $h_i = 0.1$ m of sea ice exhibit an albedo of $\alpha = 0.45$.

With a surface reflectivity of the young ice in the slot of approximately 0.5 in the visible region, we may estimate that a shortwave radiative flux of as little as 1 W m^{-2} enters the ice.

With Beer's law of attenuation the flux reduces by 20 % in ice of 0.15 m thickness with an extinction coefficient of $\kappa_i = 1.5\,\mathrm{m}^{-1}$. The predicted shortwave flux at the probe, based on the diffusive flux in the visible from Table C.4, is therefore

$$F = 2.1\,\mathrm{W\,m^{-2}} \times 0.5 \times (1 - 0.2), \tag{C.37}$$

$$F = 0.84\,\mathrm{W\,m^{-2}}. \tag{C.38}$$

The shortwave fluxes are extremely sensitive to the condition of the atmosphere at low solar angles, and we should regard 2.1 W m^{-2} literally as an estimate.

Thermistor temperature scaling

We will now use the thermistor water temperature record to estimate solar radiation in the water at the time of first brine release. We see in Section 3.4 that the background temperature increase detected by the thermistor during daytime is due to direct heating from absorbed shortwave radiation. The background temperature increase detected by the thermistor is 6 mK at an illuminance of 700 lx (Figure 3.37(a)). This temperature increase is 25 % of the daytime maximum background temperature. We compare this to the maximum diffuse shortwave radiation in the visible spectral range during *slot 11*, which is predicted to be 17 W m^{-2} (Table C.4). Even at noon, the ice in the slot itself has only been exposed to diffuse radiation (see discussion on direct and diffuse radiation in *slot 11* related to Figure 3.36). Since the diffuse radiation of 17 W m^{-2} is the maximum relevant radiation, an illuminance of 700 lx corresponds to 25 % thereof, i.e. 4 W m^{-2}. Assuming again a surface reflectivity of 0.5 and 20 % absorption in the

ice we estimate that a shortwave flux of

$$F = 17.3\,\mathrm{W\,m^{-2}} \times 0.25 \times 0.5 \times (1 - 0.2), \tag{C.39}$$

$$F = 1.7\,\mathrm{W\,m^{-2}} \tag{C.40}$$

arrived at the ice–water interface when daytime brine release first started.

C.5.3 Summary

We have estimated the radiative flux at the probe using three different methods. The first method assumes that the manufacturer's data on the LDR response is accurate ($F = 1.0\,\mathrm{W\,m^{-2}}$), the second method calculates the relevant radiative flux at the required time using the radiation model in Appendix C.1 ($F = 0.8\,\mathrm{W\,m^{-2}}$), and the third method uses the radiative heating of the thermistor beads to scale the predicted daytime maximum solar flux to the time of interest ($F = 1.7\,\mathrm{W\,m^{-2}}$). The first two methods are probably the less reliable ones as neither the radiation model nor the LDRs have been calibrated under the conditions of interest. However, all estimates agree to within $1\,\mathrm{W\,m^{-2}}$, which is encouraging.

Appendix D

Volume integration

D.1 Introduction

We need to find a volume averaged form of the governing differential equations. To facilitate this, we will first introduce an average notation, and then two averaging theorems that will allow us to streamline the derivation.

We discriminate between two different volume averages, the *intrinsic* volume average of a property and the *local* volume average. An example of an intrinsic volume average in sea ice is brine salinity, while the corresponding local volume average is the salinity of the sea ice.

Let a property Ψ_l be defined in the liquid volume δV_l, and Ψ_s be defined in the solid volume δV_s. The intrinsic volume average is then

$$\langle \Psi_l \rangle^l = \frac{1}{\delta V_l} \int_{\delta V_l} \Psi_l \, \mathrm{d}V, \quad \text{and} \tag{D.1a}$$

$$\langle \Psi_s \rangle^s = \frac{1}{\delta V_s} \int_{\delta V_s} \Psi_s \, \mathrm{d}V. \tag{D.1b}$$

The values $\langle \Psi_l \rangle^l$ and $\langle \Psi_s \rangle^s$ are valid in the entire volume δV (cf. Section 4.2.2). In order to calculate the local volume average over the entire volume δV we need to extend the definition of Ψ_l into the solid phase. We follow *Gray* (1975) and set

$$\Psi_l = \begin{cases} \langle \Psi_l \rangle^l + \widetilde{\Psi}_l & \text{in } \delta V_l \\ 0; \quad \widetilde{\Psi}_l \equiv 0 & \text{in } \delta V_s, \end{cases} \tag{D.2}$$

where $\widetilde{\Psi}_l$ is the microscopic deviation from the macroscopic intrinsic volume average $\langle \Psi_l \rangle^l$. The local volume average of Ψ_l is now

$$\langle \Psi_l \rangle = \frac{1}{\delta V} \int_{\delta V} \Psi_l \, \mathrm{d}V, \tag{D.3}$$

$$= f_l \langle \Psi_l \rangle^l + f_s \langle \Psi_l \rangle^s,$$

$$= f_l \langle \Psi_l \rangle^l, \tag{D.4}$$

where

$$f_l = \frac{\delta V_l}{\delta V}, \quad \text{and} \tag{D.5a}$$

$$f_s = \frac{\delta V_s}{\delta V}, \tag{D.5b}$$

and $\delta V = \delta V_s + \delta V_l$.

The governing differential equations contain time derivatives, gradients and divergences. The following theorems allow us to average these. Their origin is laid out in Appendix D.2.

The transport theorem,

$$\langle \frac{\partial \Psi_l}{\partial t} \rangle = \frac{\partial}{\partial t} \langle \Psi_l \rangle - \frac{1}{\delta V} \int_{\delta A_{ls}(t)} \Psi_l \mathbf{u_A} \cdot \mathrm{d}\mathbf{A}_{ls}, \tag{D.6}$$

relates the average of a time derivative to the time derivative of an average. If the liquid volume δV_l is time dependent, for example during phase transition with volume expansion, then the surface integral on the right hand side of (D.6) appears. Here $\mathrm{d}\mathbf{A}_{ls}$ is a surface element between liquid and solid with the surface normal pointing from the liquid into the solid, and $\mathbf{u_A}$ the velocity of the surface.

The theorem for the volume average of a gradient is

$$\langle \nabla \Psi_l \rangle = \nabla \langle \Psi_l \rangle + \frac{1}{\delta V} \int_{\delta A_{ls}} \Psi_l \, \mathrm{d}\mathbf{A}_{ls}, \tag{D.7}$$

where the gradient is replaced by the divergence if Ψ_l is a vector. In the process of volume integration the surface integrals in (D.6) and (D.7) convey the boundary conditions at the microscopic liquid–solid interface.

D.2 Averaging Theorems

In order to simplify the derivation of the volume averaged conservation and transport equations we will introduce two theorems and one relation. The starting point of the derivation will be the microscopic form of the differential conservation equations. We will integrate them over a macroscopic volume which leaves us with an expression for the average of derivatives. However, the finite volume model is based on derivatives of average properties. The following two theorems describe the transformation from integrals of derivatives to derivatives of integrals. The relation shown subsequently will find use for the pressure term of the momentum conservation equation.

In this section we make use of the liquid volume distribution function γ that is defined as

$$\gamma = \begin{cases} 1 & \text{in } \delta V_l, \\ 0 & \text{in } \delta V_s, \end{cases} \tag{D.8}$$

D.2.1 Transport Theorem

The first theorem, the transport theorem, relates the average of the time derivative in a changing volume $\delta V_l(t)$ to the time derivative of an average property inside $\delta V_l(t)$. *Slattery* (1981, pp. 18–20) and *Bear and Bachmat* (1991, pp. 59–60) show that, for any given material volume or for any given system volume,

$$\frac{d}{dt}\int_{\delta V(t)} \Psi(\mathbf{x},t)\,\mathrm{d}V = \int_{\delta V(t)} \frac{\partial \Psi}{\partial t}\,\mathrm{d}V + \int_{\delta A(t)} \Psi \mathbf{u}_\mathbf{A}\cdot\,\mathrm{d}\mathbf{A}, \tag{D.9}$$

where the volume $\delta V(t)$ can be either the material volume or the system volume, and $\delta A(t)$ is bounding surface of $\delta V(t)$. The velocity $\mathbf{u}_\mathbf{A}$ is the velocity of the surface, and the surface element $\mathrm{d}\mathbf{A}$ points outwards from $\delta V(t)$ by convention.

Applied to the sea ice system, the liquid volume δV_l changes size with time due to volume expansion during the phase transition process. We can write Equation (D.9) for the liquid portion, $\delta V_l(t)$, of the control volume, δV, to get

$$\begin{aligned}\frac{d}{dt}\int_{\delta V_l(t)} \Psi_l(\mathbf{x},t)\,\mathrm{d}V &= \int_{\delta V_l(t)} \frac{\partial \Psi_l}{\partial t}\,\mathrm{d}V + \int_{\delta A_l(t)} \Psi_l \mathbf{u}_\mathbf{A}\cdot\,\mathrm{d}\mathbf{A}_l,\\ &= \int_{\delta V_l(t)} \frac{\partial \Psi_l}{\partial t}\,\mathrm{d}V + \int_{\delta A_{ll}(t)} \Psi_l \mathbf{u}_\mathbf{A}\cdot\,\mathrm{d}\mathbf{A}_{ll} + \int_{\delta A_{ls}(t)} \Psi_l \mathbf{u}_\mathbf{A}\cdot\,\mathrm{d}\mathbf{A}_{ls},\end{aligned} \tag{D.10}$$

where the surface normals always point outwards from liquid volume $\delta V_l(t)$. We have further split the bounding surface $\delta A_l(t)$ of $\delta V_l(t)$ into two components. The component $\delta A_{ll}(t)$ describes the surface between the liquid inside $\delta V_l(t)$ and the liquid outside $\delta V_l(t)$, while the component $\delta A_{ls}(t)$ describes the surface between the liquid in $\delta V_l(t)$ and solid.

On the other hand, we may consider Ψ_l in the entire volume δV, which does not change with time, and find from (D.9)

$$\begin{aligned}\frac{d}{dt}\int_{\delta V} \gamma\Psi_l(\mathbf{x},t)\,\mathrm{d}V &= \frac{\partial}{\partial t}\int_{\delta V} \gamma\Psi_l\,\mathrm{d}V + \int_{\delta A(t)} \gamma\Psi_l \mathbf{u}_\mathbf{A}\cdot\,\mathrm{d}\mathbf{A},\\ &= \frac{\partial}{\partial t}\int_{\delta V} \gamma\Psi_l\,\mathrm{d}V + \int_{\delta A_{ll}(t)} \gamma\Psi_l \mathbf{u}_\mathbf{A}\cdot\,\mathrm{d}\mathbf{A}_{ll} + \int_{\delta A_{ss}(t)} \gamma\Psi_l \mathbf{u}_\mathbf{A}\cdot\,\mathrm{d}\mathbf{A}_{ss}.\end{aligned}$$

Here, the bounding surface $\delta A(t)$ of $\delta V(t)$ has been decomposed into the two surface elements that connect liquid inside $\delta V(t)$ with liquid outside $\delta V(t)$, $\delta A_{ll}(t)$, and surface elements that connect solid inside $\delta V(t)$ with solid outside $\delta V(t)$, $\delta A_{ss}(t)$. We can simplify this expression with the definition of γ in (D.8) to find

$$\frac{d}{dt}\int_{\delta V_l(t)} \Psi_l(\mathbf{x},t)\,\mathrm{d}V = \frac{\partial}{\partial t}\int_{\delta V_l(t)} \Psi_l\,\mathrm{d}V + \int_{\delta A_{ll}(t)} \Psi_l \mathbf{u}_\mathbf{A}\cdot\,\mathrm{d}\mathbf{A}_{ll}. \tag{D.11}$$

Comparing Equations (D.10) and (D.11) we find

$$\frac{\partial}{\partial t}\int_{\delta V_l(t)} \Psi_l \,\mathrm{d}V = \int_{\delta V_l(t)} \frac{\partial \Psi_l}{\partial t}\,\mathrm{d}V + \int_{\delta A_{ls}(t)} \Psi_l \mathbf{u}_\mathbf{A} \cdot \mathrm{d}\mathbf{A}_{ls},$$

that we divide by the volume δV and reorder to

$$\boxed{\langle \frac{\partial \Psi_l}{\partial t} \rangle = \frac{\partial}{\partial t}\langle \Psi_l \rangle - \frac{1}{\delta V}\int_{\delta A_{ls}(t)} \Psi_l \mathbf{u}_\mathbf{A} \cdot \mathrm{d}\mathbf{A}_{ls}} \tag{D.12}$$

Equation (D.12) is the theorem for the volume average of the time derivative.

D.2.2 Theorem for the Volume Average of a Gradient

The theorem for the local volume average of a gradient describes the relationship between the volume average of a gradient and the gradient of the volume average. *Slattery* (1981, pp. 196–199) and *Bear and Bachmat* (1991, p.122) show that for an interconnected phase l

$$\frac{1}{\delta V}\int_{\delta V_l} \nabla \Psi_l \,\mathrm{d}V = \nabla\left(\frac{1}{\delta V}\int_{\delta V_l} \Psi_l \,\mathrm{d}V\right) + \frac{1}{\delta V}\int_{\delta A_{ls}} \Psi_l \,\mathrm{d}\mathbf{A}_{ls}, \tag{D.13}$$

where δA_{ls} is the liquid–solid interfacial surface in δV, and $\mathrm{d}\mathbf{A}_{ls}$ is pointing out of the liquid partial volume of δV into the solid.

Using the definition of f_l in Equation (D.5) we can write this equation as

$$\frac{f_l}{\delta V_l}\int_{\delta V_l} \nabla \Psi_l \,\mathrm{d}V = \nabla\left(\frac{f_l}{\delta V_l}\int_{\delta V_l} \Psi_l \,\mathrm{d}V\right) + \frac{1}{\delta V}\int_{\delta A_{ls}} \Psi_l \,\mathrm{d}\mathbf{A}_{ls},$$

which allows us to apply the average notation of Equation (D.1) to get

$$f_l \langle \nabla \Psi_l \rangle^l = \nabla(f_l \langle \Psi_l \rangle^l) + \frac{1}{\delta V}\int_{\delta A_{ls}} \Psi_l \,\mathrm{d}\mathbf{A}_{ls}. \tag{D.14}$$

With Equation (D.4) we find that the corresponding local average formulation is

$$\boxed{\langle \nabla \Psi_l \rangle = \nabla \langle \Psi_l \rangle + \frac{1}{\delta V}\int_{\delta A_{ls}} \Psi_l \,\mathrm{d}\mathbf{A}_{ls}} \tag{D.15}$$

If Ψ_l is a vector, the gradient simply turns into a divergence, and the area integral into a flux.

D.2.3 Gradient Relation

We will find it useful to be able to transform the gradient of the liquid volume fraction into a surface integral. We begin the with the definition of the gradient

$$\begin{aligned}\nabla f_l &= \nabla \frac{\delta V_l}{\delta V}, \\ &= \nabla \frac{1}{\delta V} \int_{\delta V_l} 1 \, dV,\end{aligned}$$

where we apply the gradient average theorem (D.13) with $\Psi_l = 1$ (*Bear and Bachmat*, 1991, p. 122),

$$\nabla f_l = \frac{1}{\delta V} \int_{\delta V_l} \nabla 1 \, \mathrm{d}V - \frac{1}{\delta V} \int_{\delta A_{ls}} 1 \, \mathrm{d}\mathbf{A}_{ls},$$

and since the gradient of a constant vanishes,

$$\boxed{\nabla f_l = -\frac{1}{\delta V} \int_{\delta A_{ls}} \mathrm{d}\mathbf{A}_{ls}} \tag{D.16}$$

D.3 Conservation equations

D.3.1 Mass conservation equation

The microscopic mass conservation equation, or continuity equation, for a fluid is (*Batchelor*, 1970; *Kundu*, 1990)

$$\frac{\partial \rho}{\partial t} + \nabla \cdot (\rho \mathbf{u}) = 0, \tag{D.17}$$

where ρ is the fluid density, t is time, and $\mathbf{u}$ is the fluid velocity. Since (D.17) is valid at every point in space, the volume integral of (D.17) over a constant representative elementary volume δV must also be valid everywhere, i.e.

$$\int_{\delta V} \frac{\partial \rho}{\partial t} \, \mathrm{d}V + \int_{\delta V} \nabla \cdot (\rho \mathbf{u}) \, \mathrm{d}V = 0. \tag{D.18}$$

Dividing (D.18) by the volume δV and using the average notation (D.3) it follows that

$$\langle \frac{\partial \rho}{\partial t} \rangle + \langle \nabla \cdot (\rho \mathbf{u}) \rangle = 0. \tag{D.19}$$

Following the definition in (D.2) we decompose the density ρ into density of the liquid, ρ_l, and solid, ρ_s, and likewise the velocity $\mathbf{u}$ into components $\mathbf{u}_l$ and $\mathbf{u}_s$, respectively. Equation (D.19) then becomes

$$\langle \frac{\partial \rho_l}{\partial t} \rangle + \langle \frac{\partial \rho_s}{\partial t} \rangle + \langle \nabla \cdot (\rho_l \mathbf{u}_l) \rangle + \langle \nabla \cdot (\rho_s \mathbf{u}_s) \rangle = 0. \tag{D.20}$$

Applying the theorem for the volume average of the time derivative (D.12) and volume average of a divergence (D.15) to the left hand side of (D.20) it follows that

$$\frac{\partial\langle\rho_l\rangle}{\partial t}+\frac{\partial\langle\rho_s\rangle}{\partial t}+\nabla\cdot\langle\rho_l\mathbf{u}_l\rangle+\nabla\cdot\langle\rho_s\mathbf{u}_s\rangle - \frac{1}{\delta V}\int_{\delta A_{ls}(t)}\rho_l\mathbf{u}_\mathbf{A}\cdot\,\mathrm{d}\mathbf{A}_{ls}-\frac{1}{\delta V}\int_{\delta A_{ls}(t)}\rho_s\mathbf{u}_\mathbf{A}\cdot\,\mathrm{d}\mathbf{A}_{sl} + \frac{1}{\delta V}\int_{\delta A_{ls}}\rho_l\mathbf{u}_l\cdot\,\mathrm{d}\mathbf{A}_{ls}+\frac{1}{\delta V}\int_{\delta A_{sl}}\rho_s\mathbf{u}_s\cdot\,\mathrm{d}\mathbf{A}_{sl}=0. \quad \text{(D.21)}$$

Combining the surface integrals it follows further

$$\frac{\partial\langle\rho_l\rangle}{\partial t}+\frac{\partial\langle\rho_s\rangle}{\partial t}+\nabla\cdot\langle\rho_l\mathbf{u}_l\rangle+\nabla\cdot\langle\rho_s\mathbf{u}_s\rangle - \frac{1}{\delta V}\int_{\delta A_{ls}(t)}\rho_l(\mathbf{u}_\mathbf{A}-\mathbf{u}_l)\cdot\,\mathrm{d}\mathbf{A}_{ls}+\frac{1}{\delta V}\int_{\delta A_{ls}(t)}\rho_s(\mathbf{u}_\mathbf{A}-\mathbf{u}_s)\cdot\,\mathrm{d}\mathbf{A}_{ls}. \quad \text{(D.22)}$$

The surface integrals in (D.22) are the mass flux at the moving solid–liquid interface in the liquid and solid, respectively. Since mass is conserved the surface integrals cancel, i.e.

$$\frac{1}{\delta V}\int_{\delta A_{ls}(t)}\rho_l(\mathbf{u}_\mathbf{A}-\mathbf{u}_l)\cdot\,\mathrm{d}\mathbf{A}_{ls}-\frac{1}{\delta V}\int_{\delta A_{ls}(t)}\rho_s(\mathbf{u}_\mathbf{A}-\mathbf{u}_s)\cdot\,\mathrm{d}\mathbf{A}_{ls}=0. \quad \text{(D.23)}$$

To expand the advection terms in (D.22) we apply the definition of (D.2) to both ρ_l and $\mathbf{u}_l$ and find

$$\nabla\cdot\langle\rho_l\mathbf{u}_l\rangle=\nabla\cdot\langle\,\langle\mathbf{u}_l\rangle^l\langle\rho_l\rangle^l+\widetilde{\mathbf{u}}_l\widetilde{\rho}_l+\langle\mathbf{u}_l\rangle^l\widetilde{\rho}_l+\widetilde{\mathbf{u}}_l\langle\rho_l\rangle^l\,\rangle, \quad \text{(D.24a)}$$

Removing the constants in δV, $\langle\rho_l\rangle^l$ and $\langle\mathbf{u}_l\rangle^l$, from the averages and applying (D.4), it follows that

$$=\nabla\cdot\Big[f_l\langle\mathbf{u}_l\rangle^l\langle\rho_l\rangle^l+\langle\widetilde{\mathbf{u}}_l\widetilde{\rho}_l\rangle+\langle\mathbf{u}_l\rangle^l\langle\widetilde{\rho}_l\rangle+\langle\widetilde{\mathbf{u}}_l\rangle\langle\rho_l\rangle^l\Big]. \quad \text{(D.24b)}$$

From the definition of the microscopic deviation in (D.2) combined with (D.1) the averages of deviations are zero, i.e. $\langle\widetilde{\mathbf{u}}_l\rangle=0$ and $\langle\widetilde{\rho}_l\rangle=0$, so that

$$=\nabla\cdot\Big[f_l\langle\mathbf{u}_l\rangle^l\langle\rho_l\rangle^l+f_l\langle\widetilde{\mathbf{u}}_l\widetilde{\rho}_l\rangle^l\Big]. \quad \text{(D.24c)}$$

We apply the Boussinesq approximation, i.e. densities ρ_l and ρ_s are homogeneous in δV and $\widetilde{\rho}_l=\widetilde{\rho}_s=0$, so that the second term on the right hand side of (D.24c) vanishes. The mass conservation equation (D.22) is therefore

$$\frac{\partial\langle\rho_l\rangle}{\partial t}+\frac{\partial\langle\rho_s\rangle}{\partial t}+\nabla\cdot\big[\langle\rho_l\rangle^l\langle\mathbf{u}_l\rangle\big]+\nabla\cdot\big[\langle\rho_s\rangle^s\langle\mathbf{u}_s\rangle\big]=0. \quad \text{(D.25)}$$

With (D.4), $\partial f_l = -\partial f_s$, and constant and homogeneous densities $\langle\rho_l\rangle^l$ and $\langle\rho_s\rangle^s$ the mass conservation equation becomes

$$\big[\langle\rho_l\rangle^l - \langle\rho_s\rangle^s\big]\frac{\partial f_l}{\partial t} + \langle\rho_l\rangle^l\nabla\cdot\langle\mathbf{u}_l\rangle + \langle\rho_s\rangle^s\nabla\cdot\langle\mathbf{u}_s\rangle = 0. \tag{D.26}$$

Since the solid is stationary, i.e. $\mathbf{u}_s = 0$, it follows simply

$$\left[1 - \frac{\langle\rho_s\rangle^s}{\langle\rho_l\rangle^l}\right]\frac{\partial f_l}{\partial t} + \nabla\cdot\langle\mathbf{u}_l\rangle = 0. \tag{D.27}$$

D.3.2 Momentum conservation equation

The microscopic momentum conservation equation is (*Ganesan and Poirier*, 1990)

$$\frac{\partial(\rho\mathbf{u})}{\partial t} + \nabla\cdot(\rho\mathbf{u}\mathbf{u}) = \nabla\cdot\sigma^{(2)} - \nabla p + \rho\mathbf{g}, \tag{D.28}$$

where ρ and $\mathbf{u}$ are density and velocity of the fluid, respectively, $\sigma^{(2)}$ is the second order stress tensor, p the pressure, and $\mathbf{g}$ the gravitational acceleration. The stress tensor for a Newtonian fluid is defined as

$$\sigma^{(2)} = \mu\big[\nabla\mathbf{u} + \{\nabla\mathbf{u}\}^T\big] - \frac{2}{3}\mu\nabla\cdot\mathbf{u}\,I^{(2)}, \tag{D.29}$$

with dynamic viscosity μ, and identity tensor of rank two, $I^{(2)}$, i.e. $I_{ij} = \delta_{ij}$, where δ_{ij} is the Kronecker delta. The superscript T denotes the transpose of a tensor. We integrate (D.28) over δV and get

$$\langle\frac{\partial(\rho\mathbf{u})}{\partial t}\rangle + \langle\nabla\cdot(\rho\mathbf{u}\mathbf{u})\rangle = \langle\nabla\cdot\sigma^{(2)}\rangle - \langle\nabla p\rangle + \langle\rho\mathbf{g}\rangle. \tag{D.30}$$

Following the definition in (D.2) we decompose the density ρ into density of the liquid, ρ_l, and solid, ρ_s. Likewise velocity $\mathbf{u}$, stress tensor $\sigma^{(2)}$, and pressure p are also decomposed. Equation (D.30) then becomes

$$\begin{aligned}\langle\frac{\partial(\rho_l\mathbf{u}_l)}{\partial t}\rangle + \langle\frac{\partial(\rho_s\mathbf{u}_s)}{\partial t}\rangle + \langle\nabla\cdot(\rho_l\mathbf{u}_l\mathbf{u}_l)\rangle + \langle\nabla\cdot(\rho_s\mathbf{u}_s\mathbf{u}_s)\rangle \\ = \langle\nabla\cdot\sigma_l^{(2)}\rangle + \langle\nabla\cdot\sigma_s^{(2)}\rangle - \langle\nabla p_l\rangle - \langle\nabla p_s\rangle + \langle\rho\mathbf{g}\rangle,\end{aligned} \tag{D.31}$$

where we leave ρ in the buoyant term to indicate that this density is not constant.

Transient and advection terms Applying the theorem for the volume average of the time derivative (D.12) and volume average of a divergence (D.15) to the left hand

side of (D.31) it follows

$$\begin{aligned}\langle\frac{\partial(\rho_l\mathbf{u}_l)}{\partial t}\rangle + \langle\frac{\partial(\rho_s\mathbf{u}_s)}{\partial t}\rangle + \langle\nabla\cdot(\rho_l\mathbf{u}_l\mathbf{u}_l)\rangle + \langle\nabla\cdot(\rho_s\mathbf{u}_s\mathbf{u}_s)\rangle \\ = \frac{\partial\langle\rho_l\mathbf{u}_l\rangle}{\partial t} + \frac{\partial\langle\rho_s\mathbf{u}_s\rangle}{\partial t} + \nabla\cdot\langle\rho_l\mathbf{u}_l\mathbf{u}_l\rangle + \nabla\cdot\langle\rho_s\mathbf{u}_s\mathbf{u}_s\rangle \\ - \frac{1}{\delta V}\int_{\delta A_{ls}(t)}\rho_l\mathbf{u}_l\mathbf{u}_\mathbf{A}\cdot\mathrm{d}\mathbf{A}_{ls} - \frac{1}{\delta V}\int_{\delta A_{ls}(t)}\rho_s\mathbf{u}_s\mathbf{u}_\mathbf{A}\cdot\mathrm{d}\mathbf{A}_{sl} \\ + \frac{1}{\delta V}\int_{\delta A_{ls}}\rho_l\mathbf{u}_l\mathbf{u}_l\cdot\mathrm{d}\mathbf{A}_{ls} + \frac{1}{\delta V}\int_{\delta A_{sl}}\rho_s\mathbf{u}_s\mathbf{u}_s\cdot\mathrm{d}\mathbf{A}_{sl}, \quad \text{(D.32)}\end{aligned}$$

and combining the surface integrals

$$\begin{aligned}\langle\frac{\partial(\rho_l\mathbf{u}_l)}{\partial t}\rangle + \langle\frac{\partial(\rho_s\mathbf{u}_s)}{\partial t}\rangle + \langle\nabla\cdot(\rho_l\mathbf{u}_l\mathbf{u}_l)\rangle + \langle\nabla\cdot(\rho_s\mathbf{u}_s\mathbf{u}_s)\rangle \\ = \frac{\partial\langle\rho_l\mathbf{u}_l\rangle}{\partial t} + \frac{\partial\langle\rho_s\mathbf{u}_s\rangle}{\partial t} + \nabla\cdot\langle\rho_l\mathbf{u}_l\mathbf{u}_l\rangle + \nabla\cdot\langle\rho_s\mathbf{u}_s\mathbf{u}_s\rangle \\ - \frac{1}{\delta V}\int_{\delta A_{ls}(t)}\rho_l\mathbf{u}_l(\mathbf{u}_\mathbf{A}-\mathbf{u}_l)\cdot\mathrm{d}\mathbf{A}_{ls} + \frac{1}{\delta V}\int_{\delta A_{ls}(t)}\rho_s\mathbf{u}_s(\mathbf{u}_\mathbf{A}-\mathbf{u}_s)\cdot\mathrm{d}\mathbf{A}_{ls}. \quad \text{(D.33)}\end{aligned}$$

The surface integrals convey momentum conservation at the moving solid–liquid interface. The surface integrals in (D.33) cancel if both the boundary velocity of liquid and solid are equal (no–slip boundary) and the momenta are equal, i.e. $\mathbf{u}_l = \mathbf{u}_s$ and $\rho_l\mathbf{u}_l = \rho_s\mathbf{u}_s$ at δA_{ls}. Considering mass conservation (D.23) at the interface as a further constraint on velocity, momentum at the moving liquid–solid interface is only conserved if both $\mathbf{u}_l = \mathbf{u}_s$ and $\rho_l = \rho_s$ at δA_{ls}. While we assume a no–slip boundary, i.e. $\mathbf{u}_l = \mathbf{u}_s$ at the interface, the densities in an ice–water system are only approximately equal $\rho_l \approx \rho_s$. However, friction effects in the porous medium are generally larger than inertia effects, so we neglect the contribution to momentum from the surface integrals (D.33). To expand the advection terms on the right hand side of (D.33) we apply the definition of (D.2) to both ρ_l and $\mathbf{u}_l$ and find

$$\nabla\cdot\langle\rho_l\mathbf{u}_l\mathbf{u}_l\rangle = \nabla\cdot\langle\,\langle\rho_l\mathbf{u}_l\rangle^l\langle\mathbf{u}_l\rangle^l + \widetilde{\rho_l\mathbf{u}_l}\widetilde{\mathbf{u}}_l + \widetilde{\rho_l\mathbf{u}_l}\langle\mathbf{u}_l\rangle^l + \langle\rho_l\mathbf{u}_l\rangle^l\widetilde{\mathbf{u}}_l\,\rangle, \quad \text{(D.34a)}$$

Removing the constants in δV, $\langle\rho_l\mathbf{u}_l\rangle^l$ and $\langle\mathbf{u}_l\rangle^l$, from the averages and applying (D.4), it follows that

$$= \nabla\cdot\left[f_l\langle\rho_l\mathbf{u}_l\rangle^l\langle\mathbf{u}_l\rangle^l + \langle\widetilde{\rho_l\mathbf{u}_l}\widetilde{\mathbf{u}}_l\rangle + \langle\widetilde{\rho_l\mathbf{u}_l}\rangle\langle\mathbf{u}_l\rangle^l + \langle\rho_l\mathbf{u}_l\rangle^l\langle\widetilde{\mathbf{u}}_l\rangle\right]. \quad \text{(D.34b)}$$

From the definition of the microscopic deviation in (D.2) combined with (D.1) the averages of deviations are zero, i.e. $\langle\widetilde{\mathbf{u}}_l\rangle = 0$ and $\langle\widetilde{\rho_l\mathbf{u}_l}\rangle = 0$, so that

$$= \nabla\cdot\left[f_l\langle\rho_l\mathbf{u}_l\rangle^l\langle\mathbf{u}_l\rangle^l + f_l\langle\widetilde{\rho_l\mathbf{u}_l}\widetilde{\mathbf{u}}_l\rangle^l\right]. \quad \text{(D.34c)}$$

The second term on the right hand side of (D.34c) is a dispersion term (*Ganesan and Poirier*, 1990). It is negligible in the porous medium where fluid flow is dominated by body friction. In the liquid, however, it may reach significant magnitudes if δV is coarse with respect to the flow pattern. However, we neglect this term with this reservation, and (D.31) may now be expressed as

$$\frac{\partial\langle\rho_l\mathbf{u}_l\rangle}{\partial t}+\frac{\partial\langle\rho_s\mathbf{u}_s\rangle}{\partial t}+\nabla\cdot\left[\langle\rho_l\mathbf{u}_l\rangle\langle\mathbf{u}_l\rangle^l\right]+\nabla\cdot\left[\langle\rho_s\mathbf{u}_s\rangle\langle\mathbf{u}_s\rangle^s\right] = \langle\nabla\cdot\sigma_l^{(2)}\rangle+\langle\nabla\cdot\sigma_s^{(2)}\rangle-\langle\nabla p_l\rangle-\langle\nabla p_s\rangle+\langle\rho\mathbf{g}\rangle. \quad \text{(D.35)}$$

Pressure and body force Considering the last three terms on the right hand side of (D.35) and applying the theorem (D.15) it follows that

$$\begin{aligned}-\langle\nabla p_l\rangle-\langle\nabla p_s\rangle+\langle\rho\mathbf{g}\rangle &= -f_l\nabla\langle p_l\rangle^l-f_s\nabla\langle p_s\rangle^s\\ &\quad-\langle p_l\rangle^l\nabla f_l-\langle p_s\rangle^s\nabla f_s-\frac{1}{\delta V}\int_{\delta A_{ls}}p_l\,\mathrm{d}\mathbf{A}_{ls}-\frac{1}{\delta V}\int_{\delta A_{sl}}p_s\,\mathrm{d}\mathbf{A}_{sl}\\ &\quad+f_l\rho_l(C,T)\mathbf{g}+f_s\rho_s(C,T)\mathbf{g}, \quad \text{(D.36)}\end{aligned}$$

or with constant solid density $\rho_s=\rho_s(C,T)$,

$$\begin{aligned}-\langle\nabla p_l\rangle-\langle\nabla p_s\rangle &= -f_l\nabla\langle p_l\rangle^l+f_l\rho_l(C,T)\mathbf{g}\\ &\quad-f_s\nabla\langle p_s\rangle^s+f_s\rho_s\mathbf{g}-\left[\langle p_l\rangle^l-\langle p_s\rangle^s\right]\nabla f_l-\frac{1}{\delta V}\int_{\delta A_{ls}}\left[p_l-p_s\right]\mathrm{d}\mathbf{A}_{ls}. \quad \text{(D.37)}\end{aligned}$$

Ganesan and Poirier (1990) express (D.37) in terms of a "form drag" $\mathbf{F}_D$ that is due to the relative motion of solid and liquid,

$$-\langle\nabla p_l\rangle-\langle\nabla p_s\rangle=-f_l\nabla\langle p_l\rangle^l+f_l\rho_l(C,T)\mathbf{g}-\frac{1}{\delta V}\mathbf{F}_D, \quad \text{(D.38)}$$

that will be treated later.

Stress tensor Considering the first and second term on the right hand side of (D.35) and applying the theorem (D.15) we may write

$$\begin{aligned}\langle\nabla\cdot\sigma_l^{(2)}\rangle+\langle\nabla\cdot\sigma_s^{(2)}\rangle &= \nabla\cdot\langle\sigma_l^{(2)}\rangle+\nabla\cdot\langle\sigma_s^{(2)}\rangle\\ &\quad+\frac{1}{\delta V}\int_{\delta A_{ls}}\sigma_l^{(2)}\cdot\,\mathrm{d}\mathbf{A}_{ls}+\frac{1}{\delta V}\int_{\delta A_{sl}}\sigma_s^{(2)}\cdot\,\mathrm{d}\mathbf{A}_{sl}. \quad \text{(D.39)}\end{aligned}$$

The surface integrals cancel for the special case of $\sigma_l^{(2)}=\sigma_s^{(2)}$ on δA_{ls} since $\mathrm{d}\mathbf{A}_{ls}=-\mathrm{d}\mathbf{A}_{sl}$. Otherwise they represent solid–liquid interaction forces (*Ganesan and Poirier*,

1990), and we deal with them later. The averages of the stress tensors in (D.39) are

$$\langle\sigma_l^{(2)}\rangle + \langle\sigma_s^{(2)}\rangle = \mu_l\langle\nabla\mathbf{u}_l\rangle + \mu_s\langle\nabla\mathbf{u}_s\rangle + \mu_l\langle\{\nabla\mathbf{u}_l\}^T\rangle + \mu_s\langle\{\nabla\mathbf{u}_s\}^T\rangle - \frac{2}{3}\mu_l\langle\nabla\cdot\mathbf{u}_l\rangle\, I^{(2)} - \frac{2}{3}\mu_s\langle\nabla\cdot\mathbf{u}_s\rangle\, I^{(2)}, \quad \text{(D.40)}$$

where we have assumed that the viscosities μ_l and μ_s are constant within δV. Applying (D.15) to the first four terms on the right hand side of (D.40) it follows that

$$\begin{aligned}\mu_l\langle\nabla\mathbf{u}_l\rangle + \mu_s\langle\nabla\mathbf{u}_s\rangle + \mu_l\langle\{\nabla\mathbf{u}_l\}^T\rangle + \mu_s\langle\{\nabla\mathbf{u}_s\}^T\rangle &= \mu_l\nabla\langle\mathbf{u}_l\rangle + \mu_s\nabla\langle\mathbf{u}_s\rangle + \mu_l\{\nabla\langle\mathbf{u}_l\rangle\}^T + \mu_s\{\nabla\langle\mathbf{u}_s\rangle\}^T \\ &+ \frac{1}{\delta V}\mu_l\int_{\delta A_{ls}}\mathbf{u}_l\,\mathrm{d}\mathbf{A}_{ls} + \frac{1}{\delta V}\mu_s\int_{\delta A_{sl}}\mathbf{u}_s\,\mathrm{d}\mathbf{A}_{sl} \\ &+ \frac{1}{\delta V}\mu_l\left\{\int_{\delta A_{ls}}\mathbf{u}_l\,\mathrm{d}\mathbf{A}_{ls}\right\}^T + \frac{1}{\delta V}\mu_s\left\{\int_{\delta A_{sl}}\mathbf{u}_s\,\mathrm{d}\mathbf{A}_{sl}\right\}^T, \quad \text{(D.41)}\end{aligned}$$

where the surface integrals cancel if $\mu_l\mathbf{u}_l = \mu_s\mathbf{u}_s$ on δA_{ls}, where $\mathbf{u}_l$ and $\mathbf{u}_s$ are subject to further constraints from the mass conservation equation (D.23) during phase transition. In our system $\mathbf{u}_l = \mathbf{u}_s = 0$ on δA_{ls} in the absence of a phase transition, and assuming that even in the presence of a phase transition the boundary velocities $\mathbf{u}_\mathbf{A}$ are very small, the surface integrals in (D.41) vanish. Applying (D.15) to the last two terms on the right hand side of (D.40) it is similarly

$$\begin{aligned}-\frac{2}{3}\mu_l\langle\nabla\cdot\mathbf{u}_l\rangle\, I^{(2)} - \frac{2}{3}\mu_s\langle\nabla\cdot\mathbf{u}_s\rangle\, I^{(2)} &= -\frac{2}{3}\mu_l\nabla\cdot\langle\mathbf{u}_l\rangle\, I^{(2)} - \frac{2}{3}\mu_s\nabla\cdot\langle\mathbf{u}_s\rangle\, I^{(2)} \\ &- \frac{2}{3}\mu_l\frac{1}{\delta V}\int_{\delta A_{ls}}\mathbf{u}_l\cdot\,\mathrm{d}\mathbf{A}_{ls}\, I^{(2)} - \frac{2}{3}\mu_s\frac{1}{\delta V}\int_{\delta A_{sl}}\mathbf{u}_s\cdot\,\mathrm{d}\mathbf{A}_{sl}\, I^{(2)}, \quad \text{(D.42)}\end{aligned}$$

where the surface integrals approximately vanish for the reasons stated above. Equation (D.39) is therefore

$$\begin{aligned}\langle\nabla\cdot\sigma_l^{(2)}\rangle + \langle\nabla\cdot\sigma_s^{(2)}\rangle &= \nabla\cdot\mu_l\nabla\langle\mathbf{u}_l\rangle + \nabla\cdot\mu_l\{\nabla\langle\mathbf{u}_l\rangle\}^T - \frac{2}{3}\nabla\cdot\left[\mu_l\nabla\cdot\langle\mathbf{u}_l\rangle\, I^{(2)}\right] \\ &+ \nabla\cdot\mu_s\nabla\langle\mathbf{u}_s\rangle + \nabla\cdot\mu_s\{\nabla\langle\mathbf{u}_s\rangle\}^T - \frac{2}{3}\nabla\cdot\left[\mu_s\nabla\cdot\langle\mathbf{u}_s\rangle\, I^{(2)}\right] \\ &+ \frac{1}{\delta V}\int_{\delta A_{ls}}\sigma_l^{(2)}\cdot\,\mathrm{d}\mathbf{A}_{ls} + \frac{1}{\delta V}\int_{\delta A_{sl}}\sigma_s^{(2)}\cdot\,\mathrm{d}\mathbf{A}_{sl}. \quad \text{(D.43)}\end{aligned}$$

We further assume that $\nabla\cdot\langle\mathbf{u}_l\rangle \approx 0$ and $\nabla\cdot\langle\mathbf{u}_s\rangle \approx 0$, and that μ_l and μ_s are globally constant, in which case (D.43) becomes

$$\langle\nabla\cdot\sigma_l^{(2)}\rangle + \langle\nabla\cdot\sigma_s^{(2)}\rangle = \mu_l\nabla^2\langle\mathbf{u}_l\rangle + \mu_s\nabla^2\langle\mathbf{u}_s\rangle + \frac{1}{\delta V}\int_{\delta A_{ls}}\left[\sigma_l^{(2)} - \sigma_s^{(2)}\right]\cdot\,\mathrm{d}\mathbf{A}_{ls}. \quad \text{(D.44)}$$

Friction Combining the last term of equations (D.38) and (D.44), *Ganesan and Poirier* (1990) combine "form drag" with "viscous drag",

$$\mathbf{f} = \frac{1}{\delta V}\Big[- \mathbf{F}_D + \int_{\delta A_{ls}} \big[\sigma_l^{(2)} - \sigma_s^{(2)}\big] \cdot \mathrm{d}\mathbf{A}_{ls}\Big]. \tag{D.45}$$

With a linear expansion in the velocity difference between liquid and stationary solid, (D.45) becomes

$$\mathbf{f} = -\mu_l R^{(2)} \langle \mathbf{u}_l \rangle^l, \tag{D.46}$$

where $R^{(2)}$ is a second rank resistance tensor. Higher order anisotropic terms are neglected in (D.46). Equation (D.46) may then be expressed in terms of permeability $\Pi^{(2)} = f_l^2 \big[R^{(2)}\big]^{-1}$,

$$\mathbf{f} = -f_l\, \mu_l \big[\Pi^{(2)}\big]^{-1} \langle \mathbf{u}_l \rangle. \tag{D.47}$$

Momentum conservation equation Collecting terms from (D.35), (D.38), (D.44) and (D.47) the momentum equation for a stationary solid with the approximations and assumptions mentioned above becomes

$$\frac{\partial \langle \rho_l \mathbf{u}_l \rangle}{\partial t} + \nabla \cdot \big[\langle \rho_l \mathbf{u}_l \rangle \langle \mathbf{u}_l \rangle^l\big] = \mu_l \nabla^2 \langle \mathbf{u}_l \rangle - f_l \nabla \langle p_l \rangle^l + f_l \rho_l(C,T)\mathbf{g} - f_l\, \mu_l \big[\Pi^{(2)}\big]^{-1} \langle \mathbf{u}_l \rangle. \tag{D.48}$$

D.3.3 Solute conservation equation

The microscopic solute conservation equation is (*Gray*, 1975)

$$\frac{\partial C}{\partial t} + \nabla \cdot (\mathbf{u} C) = -\nabla \cdot \mathbf{j}, \tag{D.49}$$

where $\mathbf{j}$ is a diffusive flux that is approximated by Fick's law in dilute systems in incompressible flow,

$$\mathbf{j} = -D \nabla C. \tag{D.50}$$

Here, C is the solute concentration in mass per unit volume, $\mathbf{u}$ the advection velocity, and D the diffusivity. If (D.49) holds at any point in space then it also holds in a constant volume δV, so that the volume integrated form of (D.49) becomes

$$\int_{\delta V} \frac{\partial C}{\partial t}\, \mathrm{d}V + \int_{\delta V} \nabla \cdot (\mathbf{u} C)\, \mathrm{d}V = -\int_{\delta V} \nabla \cdot \mathbf{j}\, \mathrm{d}V, \tag{D.51}$$

and dividing (D.51) by the volume δV and applying the average formulation (D.3) we have

$$\langle \frac{\partial C}{\partial t} \rangle + \langle \nabla \cdot (\mathbf{u} C) \rangle = -\langle \nabla \cdot \mathbf{j} \rangle. \tag{D.52}$$

Following the definition in (D.2) we decompose the concentration C into solute concentrations C_l and C_s for the liquid and solid, respectively, and likewise the velocity $\mathbf{u}$

into components $\mathbf{u}_l$ and $\mathbf{u}_s$, respectively. Equation (D.52) then becomes

$$\langle\frac{\partial C_l}{\partial t}\rangle + \langle\frac{\partial C_s}{\partial t}\rangle + \langle\nabla\cdot(\mathbf{u}_l C_l)\rangle + \langle\nabla\cdot(\mathbf{u}_s C_s)\rangle = -\langle\nabla\cdot\mathbf{j}_l\rangle - \langle\nabla\cdot\mathbf{j}_s\rangle. \tag{D.53}$$

Applying the theorem for the volume average of the time derivative (D.12) and volume average of a divergence (D.15) to the left hand side of (D.53) we have

$$\begin{aligned}\frac{\partial\langle C_l\rangle}{\partial t} + \frac{\partial\langle C_s\rangle}{\partial t} + \nabla\cdot\langle\mathbf{u}_l C_l\rangle + \nabla\cdot\langle\mathbf{u}_s C_s\rangle \\ - \frac{1}{\delta V}\int_{\delta A_{ls}(t)} C_l^b\mathbf{u}_\mathbf{A}\cdot\,\mathrm{d}\mathbf{A}_{ls} - \frac{1}{\delta V}\int_{\delta A_{ls}(t)} C_s^b\mathbf{u}_\mathbf{A}\cdot\,\mathrm{d}\mathbf{A}_{sl} \\ + \frac{1}{\delta V}\int_{\delta A_{ls}} (\mathbf{u}_l C_l)^b\cdot\,\mathrm{d}\mathbf{A}_{ls} + \frac{1}{\delta V}\int_{\delta A_{sl}} (\mathbf{u}_s C_s)^b\cdot\,\mathrm{d}\mathbf{A}_{sl} \\ = -\langle\nabla\cdot\mathbf{j}_l\rangle - \langle\nabla\cdot\mathbf{j}_s\rangle,\end{aligned} \tag{D.54}$$

where the superscript b is used to remind us that boundary values are meant. Combining the surface integrals and noting that $\mathrm{d}\mathbf{A}_{ls} = -\mathrm{d}\mathbf{A}_{sl}$ it follows that

$$\begin{aligned}\frac{\partial\langle C_l\rangle}{\partial t} + \frac{\partial\langle C_s\rangle}{\partial t} + \nabla\cdot\langle\mathbf{u}_l C_l\rangle + \nabla\cdot\langle\mathbf{u}_s C_s\rangle \\ - \frac{1}{\delta V}\int_{\delta A_{ls}(t)} C_l^b(\mathbf{u}_\mathbf{A} - \mathbf{u}_l^b)\cdot\,\mathrm{d}\mathbf{A}_{ls} + \frac{1}{\delta V}\int_{\delta A_{ls}(t)} C_s^b(\mathbf{u}_\mathbf{A} - \mathbf{u}_s^b)\cdot\,\mathrm{d}\mathbf{A}_{ls} \\ = -\langle\nabla\cdot\mathbf{j}_l\rangle - \langle\nabla\cdot\mathbf{j}_s\rangle,\end{aligned} \tag{D.55}$$

Since the mass of solute in δV is conserved at the moving interface[1] $\delta A_{ls}(t)$, we may write

$$\frac{1}{\delta V}\int_{\delta A_{ls}(t)} C_l^b(\mathbf{u}_\mathbf{A} - \mathbf{u}_l^b)\cdot\,\mathrm{d}\mathbf{A}_{ls} - \frac{1}{\delta V}\int_{\delta A_{ls}(t)} C_s^b(\mathbf{u}_\mathbf{A} - \mathbf{u}_s^b)\cdot\,\mathrm{d}\mathbf{A}_{ls} = 0. \tag{D.56}$$

Equation (D.55) therefore simplifies with mass conservation at the solid–liquid interface (D.56) to

$$\frac{\partial\langle C_l\rangle}{\partial t} + \frac{\partial\langle C_s\rangle}{\partial t} + \nabla\cdot\langle\mathbf{u}_l C_l\rangle + \nabla\cdot\langle\mathbf{u}_s C_s\rangle = -\langle\nabla\cdot\mathbf{j}_l\rangle - \langle\nabla\cdot\mathbf{j}_s\rangle. \tag{D.57}$$

[1] Note that the boundary velocities $\mathbf{u}_l^b$ and $\mathbf{u}_s^b$ in (D.56) are the velocities at which solute is transported at the boundary, which is not necessarily the same as the velocities at which the fluid moves at the boundary. For example, if the solute concentration in the solid is $C_s \equiv 0$, i.e. $C_s^b = 0$, but $C_l^b \neq 0$ then (D.56) states that the solute in the liquid during phase transition follows the interface with $\mathbf{u}_l^b = \mathbf{u}_\mathbf{A}$.

Applying the average theorem of a divergence (D.15) to the right hand side of (D.57) gives

$$\frac{\partial\langle C_l\rangle}{\partial t}+\frac{\partial\langle C_s\rangle}{\partial t}+\nabla\cdot\langle\mathbf{u}_l C_l\rangle+\nabla\cdot\langle\mathbf{u}_s C_s\rangle=\nabla\cdot\langle D_l\nabla C_l\rangle+\nabla\cdot\langle D_s\nabla C_s\rangle + \frac{1}{\delta V}\int_{\delta A_{ls}}\mathbf{j}_l^b\cdot\,\mathrm{d}\mathbf{A}_{ls}+\frac{1}{\delta V}\int_{\delta A_{sl}}\mathbf{j}_s^b\cdot\,\mathrm{d}\mathbf{A}_{sl}, \quad \text{(D.58)}$$

where we have also used (D.50). The surface integrals on the right hand side of (D.58) cancel since $\mathrm{d}\mathbf{A}_{ls}=-\mathrm{d}\mathbf{A}_{sl}$, and since it is $\mathbf{j}_l^b=\mathbf{j}_s^b$ in the absence of sources at the interface. Applying the average theorem of a gradient (D.15) to the right hand side of (D.58) now gives for constant diffusivities D_l and D_s within δV

$$\begin{aligned}&\frac{\partial\langle C_l\rangle}{\partial t}+\frac{\partial\langle C_s\rangle}{\partial t}+\nabla\cdot\langle\mathbf{u}_l C_l\rangle+\nabla\cdot\langle\mathbf{u}_s C_s\rangle\\&=\nabla\cdot D_l\left[\nabla\langle C_l\rangle+\frac{1}{\delta V}\int_{\delta A_{ls}}C_l^b\,\mathrm{d}\mathbf{A}_{ls}\right]+\nabla\cdot D_s\left[\nabla\langle C_s\rangle+\frac{1}{\delta V}\int_{\delta A_{sl}}C_s^b\,\mathrm{d}\mathbf{A}_{sl}\right].\end{aligned} \quad \text{(D.59)}$$

We now assume that the boundary values C_l^b and C_s^b are homogeneous along δA_{ls}, which allows us to take them out of the integrals,

$$\begin{aligned}&\frac{\partial\langle C_l\rangle}{\partial t}+\frac{\partial\langle C_s\rangle}{\partial t}+\nabla\cdot\langle\mathbf{u}_l C_l\rangle+\nabla\cdot\langle\mathbf{u}_s C_s\rangle\\&=\nabla\cdot D_l\left[\nabla\langle C_l\rangle+C_l^b\frac{1}{\delta V}\int_{\delta A_{ls}}\mathrm{d}\mathbf{A}_{ls}\right]+\nabla\cdot D_s\left[\nabla\langle C_s\rangle-C_s^b\frac{1}{\delta V}\int_{\delta A_{ls}}\mathrm{d}\mathbf{A}_{ls}\right].\end{aligned} \quad \text{(D.60)}$$

With the gradient relation (D.16), equation (D.60) becomes

$$\begin{aligned}&\frac{\partial\langle C_l\rangle}{\partial t}+\frac{\partial\langle C_s\rangle}{\partial t}+\nabla\cdot\langle\mathbf{u}_l C_l\rangle+\nabla\cdot\langle\mathbf{u}_s C_s\rangle\\&=\nabla\cdot D_l\left[\nabla\langle C_l\rangle-C_l^b\nabla f_l\right]+\nabla\cdot D_s\left[\nabla\langle C_s\rangle-C_s^b\nabla f_s\right].\end{aligned} \quad \text{(D.61)}$$

The solute concentration at the microscopic boundary layer, C_l^b and C_s^b, is approximated by the respective average value in the liquid and solid, $C_l^b=\langle C_l\rangle^l$ and $C_s^b=\langle C_s\rangle^s$. With (D.4) the diffusion terms simplify and the time derivatives expand to

$$\begin{aligned}&f_l\frac{\partial\langle C_l\rangle^l}{\partial t}+f_s\frac{\partial\langle C_s\rangle^s}{\partial t}+\left[\langle C_l\rangle^l-\langle C_s\rangle^s\right]\frac{\partial f_l}{\partial t}+\nabla\cdot\langle\mathbf{u}_l C_l\rangle+\nabla\cdot\langle\mathbf{u}_s C_s\rangle\\&=\nabla\cdot\left[f_l D_l\nabla\langle C_l\rangle^l\right]+\nabla\cdot\left[f_s D_s\nabla\langle C_s\rangle^s\right].\end{aligned} \quad \text{(D.62)}$$

To expand the advection terms in (D.62), the fourth and fifth terms on the left hand side, we apply the definition of (D.2) to both $\mathbf{u}_l$ and C_l and find

$$\nabla\cdot\langle\mathbf{u}_l C_l\rangle=\nabla\cdot\langle\,\langle\mathbf{u}_l\rangle^l\langle C_l\rangle^l+\widetilde{\mathbf{u}}_l\widetilde{C}_l+\langle\mathbf{u}_l\rangle^l\widetilde{C}_l+\widetilde{\mathbf{u}}_l\langle C_l\rangle^l\,\rangle, \quad \text{(D.63a)}$$

and removing the constants in δV, $\langle C_l\rangle^l$ and $\langle \mathbf{u}_l\rangle^l$, from the averages and applying (D.4),

$$= \nabla\cdot\Big[f_l\langle\mathbf{u}_l\rangle^l\langle C_l\rangle^l + \langle\widetilde{\mathbf{u}}_l\widetilde{C}_l\rangle + \langle\mathbf{u}_l\rangle^l\langle\widetilde{C}_l\rangle + \langle\widetilde{\mathbf{u}}_l\rangle\langle C_l\rangle^l\Big]. \tag{D.63b}$$

From the definition of the microscopic deviation in (D.2) combined with (D.1) the averages of deviations are zero, i.e. $\langle\widetilde{\mathbf{u}}_l\rangle = 0$ and $\langle\widetilde{C}_l\rangle = 0$, so that

$$= \nabla\cdot\Big[f_l\langle\mathbf{u}_l\rangle^l\langle C_l\rangle^l + f_l\langle\widetilde{\mathbf{u}}_l\widetilde{C}_l\rangle^l\Big]. \tag{D.63c}$$

We have already assumed that the boundary values are equal to the volume averages, $C_l^b = \langle C_l\rangle^l$ and $C_s^b = \langle C_s\rangle^s$, i.e. the microscopic deviations are $\widetilde{C}_l = 0$ and $\widetilde{C}_s = 0$, there. If we further assume that C_l and C_s are relatively homogeneous throughout the volume δV_l and δV_s, respectively, then we may neglect the second term on the right hand side in (D.63c). Equation (D.62) may therefore be written

$$f_l\frac{\partial\langle C_l\rangle^l}{\partial t} + f_s\frac{\partial\langle C_s\rangle^s}{\partial t} + \big[\langle C_l\rangle^l - \langle C_s\rangle^s\big]\frac{\partial f_l}{\partial t} + \nabla\cdot\big[\langle\mathbf{u}_l\rangle\langle C_l\rangle^l\big] + \nabla\cdot\big[\langle\mathbf{u}_s\rangle\langle C_s\rangle^s\big] = \nabla\cdot\big[f_l D_l\nabla\langle C_l\rangle^l\big] + \nabla\cdot\big[f_s D_s\nabla\langle C_s\rangle^s\big]. \tag{D.64}$$

Further, if the solute concentration in the solid, $\langle C_s\rangle^s$, is constant with time and if the solute concentration does not make a contribution to diffusion between volumes δV, i.e. $D_s = 0$, and that the solid is stationary ($\mathbf{u}_s = 0$) then (D.64) becomes

$$f_l\frac{\partial\langle C_l\rangle^l}{\partial t} + \big[\langle C_l\rangle^l - \langle C_s\rangle^s\big]\frac{\partial f_l}{\partial t} + \nabla\cdot\big[\langle\mathbf{u}_l\rangle\langle C_l\rangle^l\big] = \nabla\cdot\big[f_l D_l\nabla\langle C_l\rangle^l\big]. \tag{D.65}$$

Considering that in sea ice the solute concentration in the solid is orders of magnitude smaller than the solute concentration in the liquid, i.e. $\langle C_s\rangle^s \ll \langle C_l\rangle^l$, the solute conservation equation is simply

$$f_l\frac{\partial\langle C_l\rangle^l}{\partial t} + \langle C_l\rangle^l\frac{\partial f_l}{\partial t} + \nabla\cdot\big[\langle\mathbf{u}_l\rangle\langle C_l\rangle^l\big] = \nabla\cdot\big[f_l D_l\nabla\langle C_l\rangle^l\big]. \tag{D.66}$$

D.3.4 Energy conservation equation

During phase transition, the enthalpy, H, is constant. We define the volumetric enthalpy H of a volume δV as

$$h = \frac{H}{\delta V}, \tag{D.67}$$

which is the quantity that has to be conserved. Similar to the case of the solute conservation equation it is the microscopic energy conservation equation

$$\frac{\partial h}{\partial t} + \nabla\cdot(\mathbf{u}h) = -\nabla\cdot\mathbf{j}, \tag{D.68}$$

where $\mathbf{j}$ is a diffusive heat flux that is approximated by Fourier's law,

$$\mathbf{j} = -k\nabla T. \tag{D.69}$$

Equation (D.68) neglects heat due to friction in the liquid, which is small in water at velocities of concern to us (*Whitaker*, 1977). Here, T is the temperature, k is the thermal conductivity, and $\mathbf{u}$ is the advection velocity. Since (D.68) holds at any point in the system, its average in a volume of constant size δV will also obey that relationship. With the definition of the average in (D.3) it is in δV

$$\langle\frac{\partial h}{\partial t}\rangle + \langle\nabla\cdot(\mathbf{u}h)\rangle = -\langle\nabla\mathbf{j}\rangle. \tag{D.70}$$

Following the definition in (D.2) we decompose the enthalpy density h into enthalpy of the liquid, h_l, and solid, h_s, and likewise the velocity $\mathbf{u}$ into components $\mathbf{u}_l$ and $\mathbf{u}_s$ for liquid and solid, respectively. Equation (D.70) then becomes

$$\langle\frac{\partial h_l}{\partial t}\rangle + \langle\frac{\partial h_s}{\partial t}\rangle + \langle\nabla\cdot(\mathbf{u}_l h_l)\rangle + \langle\nabla\cdot(\mathbf{u}_s h_s)\rangle = -\langle\nabla\mathbf{j}_l\rangle - \langle\nabla\mathbf{j}_s\rangle. \tag{D.71}$$

Applying the theorem for the volume average of the time derivative (D.12) and volume average of a divergence (D.15) to the left hand side of (D.71) it is

$$\begin{aligned}\frac{\partial\langle h_l\rangle}{\partial t} + \frac{\partial\langle h_s\rangle}{\partial t} + \nabla\cdot\langle\mathbf{u}_l h_l\rangle + \nabla\cdot\langle\mathbf{u}_s h_s\rangle \\ - \frac{1}{\delta V}\int_{\delta A_{ls}(t)} h_l^b\mathbf{u}_\mathbf{A}\cdot\mathrm{d}\mathbf{A}_{ls} - \frac{1}{\delta V}\int_{\delta A_{ls}(t)} h_s^b\mathbf{u}_\mathbf{A}\cdot\mathrm{d}\mathbf{A}_{sl} \\ + \frac{1}{\delta V}\int_{\delta A_{ls}} (\mathbf{u}_l h_l)^b\cdot\mathrm{d}\mathbf{A}_{ls} + \frac{1}{\delta V}\int_{\delta A_{sl}} (\mathbf{u}_s h_s)^b\cdot\mathrm{d}\mathbf{A}_{sl} \\ = -\langle\nabla\mathbf{j}_l\rangle - \langle\nabla\mathbf{j}_s\rangle.\end{aligned} \tag{D.72}$$

where the superscript b is used to remind us that boundary values are meant. Combining the surface integrals and noting that $\mathrm{d}\mathbf{A}_{ls} = -\mathrm{d}\mathbf{A}_{sl}$ it is

$$\begin{aligned}\frac{\partial\langle h_l\rangle}{\partial t} + \frac{\partial\langle h_s\rangle}{\partial t} + \nabla\cdot\langle\mathbf{u}_l h_l\rangle + \nabla\cdot\langle\mathbf{u}_s h_s\rangle \\ - \frac{1}{\delta V}\int_{\delta A_{ls}(t)} h_l^b(\mathbf{u}_\mathbf{A} - \mathbf{u}_l^b)\cdot\mathrm{d}\mathbf{A}_{ls} + \frac{1}{\delta V}\int_{\delta A_{ls}(t)} h_s^b(\mathbf{u}_\mathbf{A} - \mathbf{u}_s^b)\cdot\mathrm{d}\mathbf{A}_{ls} \\ = -\langle\nabla\mathbf{j}_l\rangle - \langle\nabla\mathbf{j}_s\rangle.\end{aligned} \tag{D.73}$$

Since the enthalpy in δV is conserved when the solid–liquid interface $\delta A_{ls}(t)$ moves, i.e. during phase transition, it follows that

$$\frac{1}{\delta V}\int_{\delta A_{ls}(t)} h_l^b(\mathbf{u}_\mathbf{A} - \mathbf{u}_l^b)\cdot\mathrm{d}\mathbf{A}_{ls} - \frac{1}{\delta V}\int_{\delta A_{ls}(t)} h_s^b(\mathbf{u}_\mathbf{A} - \mathbf{u}_s^b)\cdot\mathrm{d}\mathbf{A}_{ls} = 0. \tag{D.74}$$

Equation (D.73) therefore simplifies with energy conservation at the solid–liquid interface (D.74) to

$$\frac{\partial\langle h_l\rangle}{\partial t}+\frac{\partial\langle h_s\rangle}{\partial t}+\nabla\cdot\langle\mathbf{u}_l h_l\rangle+\nabla\cdot\langle\mathbf{u}_s h_s\rangle=-\langle\nabla\mathbf{j}_l\rangle-\langle\nabla\mathbf{j}_s\rangle. \tag{D.75}$$

Applying the average theorem for a divergence (D.15) to the right hand side of (D.75) gives

$$\begin{aligned}\frac{\partial\langle h_l\rangle}{\partial t}+\frac{\partial\langle h_s\rangle}{\partial t}+\nabla\cdot\langle\mathbf{u}_l h_l\rangle+\nabla\cdot\langle\mathbf{u}_s h_s\rangle&=\nabla\cdot\langle k_l\nabla T_l\rangle+\nabla\cdot\langle k_s\nabla T_s\rangle\\&\quad+\frac{1}{\delta V}\int_{\delta A_{ls}}\mathbf{j}_l^b\cdot\,\mathrm{d}\mathbf{A}_{ls}+\frac{1}{\delta V}\int_{\delta A_{sl}}\mathbf{j}_s^b\cdot\,\mathrm{d}\mathbf{A}_{sl},\end{aligned} \tag{D.76}$$

where we have also used (D.69). The surface integrals on the right hand side of (D.76) cancel since $\mathrm{d}\mathbf{A}_{ls}=-\mathrm{d}\mathbf{A}_{sl}$, and since the heat flux out of the solid is equal to the heat flux into the liquid, i.e. $\mathbf{j}_l^b=\mathbf{j}_s^b$. Applying the average theorem of a gradient (D.15) to the right hand side of (D.76) now gives for constant thermal conductivites k_l and k_s within δV

$$\begin{aligned}&\frac{\partial\langle h_l\rangle}{\partial t}+\frac{\partial\langle h_s\rangle}{\partial t}+\nabla\cdot\langle\mathbf{u}_l h_l\rangle+\nabla\cdot\langle\mathbf{u}_s h_s\rangle\\&\quad=\nabla\cdot k_l\left[\nabla\langle T_l\rangle+\frac{1}{\delta V}\int_{\delta A_{ls}}T_l^b\,\mathrm{d}\mathbf{A}_{ls}\right]+\nabla\cdot k_s\left[\nabla\langle T_s\rangle+\frac{1}{\delta V}\int_{\delta A_{sl}}T_s^b\,\mathrm{d}\mathbf{A}_{sl}\right].\end{aligned} \tag{D.77}$$

We now assume that the boundary values T_l^b and T_s^b are homogeneous along δA_{ls}, which allows us to take them out of the integrals,

$$\begin{aligned}&\frac{\partial\langle h_l\rangle}{\partial t}+\frac{\partial\langle h_s\rangle}{\partial t}+\nabla\cdot\langle\mathbf{u}_l h_l\rangle+\nabla\cdot\langle\mathbf{u}_s h_s\rangle\\&\quad=\nabla\cdot k_l\left[\nabla\langle T_l\rangle+T_l^b\frac{1}{\delta V}\int_{\delta A_{ls}}\mathrm{d}\mathbf{A}_{ls}\right]+\nabla\cdot k_s\left[\nabla\langle T_s\rangle+T_s^b\frac{1}{\delta V}\int_{\delta A_{sl}}\mathrm{d}\mathbf{A}_{sl}\right].\end{aligned} \tag{D.78}$$

With the gradient relation (D.16), equation (D.78) becomes

$$\begin{aligned}\frac{\partial\langle h_l\rangle}{\partial t}+\frac{\partial\langle h_s\rangle}{\partial t}+\nabla\cdot\langle\mathbf{u}_l h_l\rangle+\nabla\cdot\langle\mathbf{u}_s h_s\rangle&\\=\nabla\cdot k_l\left[\nabla\langle T_l\rangle-T_l^b\nabla f_l\right]+\nabla\cdot k_s\left[\nabla\langle T_s\rangle-T_s^b\nabla f_s\right],&\end{aligned} \tag{D.79}$$

and with (D.4) the diffusion terms turn into

$$\begin{aligned}&\frac{\partial\langle h_l\rangle}{\partial t}+\frac{\partial\langle h_s\rangle}{\partial t}+\nabla\cdot\langle\mathbf{u}_l h_l\rangle+\nabla\cdot\langle\mathbf{u}_s h_s\rangle\\&=\nabla\cdot k_l\left[f_l\nabla\langle T_l\rangle^l+(\langle T_l\rangle^l-T_l^b)\nabla f_l\right]+\nabla\cdot k_s\left[f_s\nabla\langle T_s\rangle^s+(\langle T_s\rangle^s-T_s^b)\nabla f_s\right],\end{aligned} \tag{D.80}$$

and with $\nabla f_l = -\nabla f_s$

$$\frac{\partial\langle h_l\rangle}{\partial t} + \frac{\partial\langle h_s\rangle}{\partial t} + \nabla\cdot\langle \mathbf{u}_l h_l\rangle + \nabla\cdot\langle \mathbf{u}_s h_s\rangle = \nabla\cdot f_l k_l \nabla\langle T_l\rangle^l + \nabla\cdot f_s k_s \nabla\langle T_s\rangle^s + \nabla\cdot\big[k_l(\langle T_l\rangle^l - T_l^b) - k_s(\langle T_s\rangle^s - T_s^b)\big]\nabla f_l. \quad \text{(D.81)}$$

Since the heat flux from solid to boundary is equal to the heat flux from boundary to liquid, i.e. $k_l(\langle T_l\rangle^l - T_l^b) + k_s(\langle T_s\rangle^s - T_s^b) = 0$, the last term on the right hand side of (D.81) may be conveniently expressed as

$$\frac{\partial\langle h_l\rangle}{\partial t} + \frac{\partial\langle h_s\rangle}{\partial t} + \nabla\cdot\langle \mathbf{u}_l h_l\rangle + \nabla\cdot\langle \mathbf{u}_s h_s\rangle = \nabla\cdot f_l k_l \nabla\langle T_l\rangle^l + \nabla\cdot f_s k_s \nabla\langle T_s\rangle^s + \nabla\cdot\big[2\,k_l(\langle T_l\rangle^l - T_l^b)\big]\nabla f_l, \quad \text{(D.82)}$$

where $(\langle T_l\rangle^l - T_l^b)$ represents the degree of supercooling at the microscopic solid–liquid interface. The advection terms in (D.82) can be expressed following (D.63),

$$\frac{\partial\langle h_l\rangle}{\partial t} + \frac{\partial\langle h_s\rangle}{\partial t} + \nabla\cdot\langle \mathbf{u}_l\rangle\langle h_l\rangle^l + \nabla\cdot\langle \mathbf{u}_s\rangle\langle h_s\rangle^s + \nabla\cdot\langle \widetilde{\mathbf{u}}_l\widetilde{h}_l\rangle + \nabla\cdot\langle \widetilde{\mathbf{u}}_s\widetilde{h}_s\rangle = \nabla\cdot f_l k_l \nabla\langle T_l\rangle^l + \nabla\cdot f_s k_s \nabla\langle T_s\rangle^s + \nabla\cdot\big[2\,k_l(\langle T_l\rangle^l - T_l^b)\big]\nabla f_l. \quad \text{(D.83)}$$

Assuming that temperature and enthalpy is homogeneously distributed in solid and liquid, respectively, i.e. $T_l = T_l^b$, $T_s = T_s^b$, $\widetilde{h}_l = 0$, and $\widetilde{h}_s = 0$, the energy conservation equation is

$$\frac{\partial\langle h_l\rangle}{\partial t} + \frac{\partial\langle h_s\rangle}{\partial t} + \nabla\cdot\langle \mathbf{u}_l\rangle\langle h_l\rangle^l + \nabla\cdot\langle \mathbf{u}_s\rangle\langle h_s\rangle^s = \nabla\cdot f_l k_l \nabla\langle T_l\rangle^l + \nabla\cdot f_s k_s \nabla\langle T_s\rangle^s, \quad \text{(D.84)}$$

where

$$h_l = c_l\rho_l T_l, \qquad \text{and} \quad \text{(D.85)}$$

$$h_s = c_s\rho_s T_s - \rho_s L. \quad \text{(D.86)}$$

with heat capacities c_l and c_s, and densities ρ_l and ρ_s of liquid and solid, respectively, and latent heat of fusion L. If further solid and liquid are in thermal equilibrium in δV, i.e. they are at the same temperature $T = \langle T_l\rangle^l = \langle T_s\rangle^s$, and c_l, c_s, ρ_l, ρ_s and L are constant with time, then from (D.4)

$$(c_l\rho_l f_l + c_s\rho_s f_s)\frac{\partial T}{\partial t} + (c_l\rho_l T - c_s\rho_s T + \rho_s L)\frac{\partial f_l}{\partial t} + \nabla\cdot\langle \mathbf{u}_l\rangle(c_l\rho_l T) + \nabla\cdot\langle \mathbf{u}_s\rangle(c_s\rho_s T - \rho_s L) = \nabla\cdot(f_l k_l + f_s k_s)\nabla T, \quad \text{(D.87)}$$

where $\partial f_s = -\partial f_l$. If the solid is stationary, i.e. $\mathbf{u}_s = 0$, and c_l and ρ_l are homogeneous, then the energy conservation equation is

$$(c_l\rho_l f_l + c_s\rho_s f_s)\frac{\partial T}{\partial t} + (c_l\rho_l T - c_s\rho_s T + \rho_s L)\frac{\partial f_l}{\partial t} + c_l\rho_l \nabla\cdot\langle\mathbf{u}_l\rangle T = \nabla\cdot(f_l k_l + f_s k_s)\nabla T. \quad \text{(D.88)}$$

Appendix E

Numerical methods

E.1 Discretisation

We will now illustrate the principle of discretising the governing equations for the finite volume scheme. We will largely skip over the issue of accuracy. Although much can be said about this, it has been treated before, for example in *Ferziger and Perić* (2002). This section is to be understood as a brief "how to do", the results are shown in Appendix E.2.

In order to find equations that describe transport of volume averaged properties between computational cells we integrate the differential form of the transport equation over the cell volume. Divergences can then be expressed by Gauss' theorem as fluxes through cell boundaries. We therefore obtain an adequate description of the dynamics of a cell if we know the conditions at the boundary. Finding appropriate boundary values is the next step, and the method of choice determines the accuracy of the solution.

For the sake of demonstration we use the generic one–dimensional scalar transport equation

$$\frac{\partial \Phi}{\partial t} + \frac{\partial u\Phi}{\partial x} = \frac{\partial}{\partial x}\left[\Gamma \frac{\partial \Phi}{\partial x}\right] + s, \tag{E.1}$$

with diffusion coefficient Γ and discretise it on an equidistant one–dimensional grid.

We integrate (E.1) over the cell volume δV and obtain a conservation equation for an extensive quantity,

$$\int_{\delta V} \frac{\partial \Phi}{\partial t}\,\mathrm{d}V + \int_{\delta V} \frac{\partial u\Phi}{\partial x}\,\mathrm{d}V = \int_{\delta V} \frac{\partial}{\partial x}\left[\Gamma \frac{\partial \Phi}{\partial x}\right]\,\mathrm{d}V + \int_{\delta V} s\,\mathrm{d}V. \tag{E.2}$$

The transient term simplifies[1] since Φ is the average value in δV, and the advection and diffusion volume integrals are transformed to surface integrals with Gauss' theorem, giving

$$\delta V \frac{\partial \Phi}{\partial t} + \int_{\delta A} u\Phi\, dA = \int_{\delta A} \Gamma \frac{\partial \Phi}{\partial x}\, dA + \delta V\, s, \tag{E.3}$$

[1]For the reader who has worked through the derivation of governing equations in Appendix D: integration is now a trivial task as the integration volume δV is not time variable, and Φ is well defined throughout all of δV.

where δA is the bounding surface of δV. Each cell P in our one–dimension system has two neighbouring cells, W and E, and two corresponding boundaries w and e. If Φ, u and Γ are homogeneous along a cell boundary, and if the area of each of the cell boundaries is A then we can write

$$\delta V \frac{\partial \Phi_P}{\partial t} + A u_e \Phi_e - A u_w \Phi_w = A\Gamma_e \left(\frac{\partial \Phi}{\partial x}\right)_e - A\Gamma_w \left(\frac{\partial \Phi}{\partial x}\right)_w + \delta V \, s_P, \tag{E.4}$$

or with the linear size of the cell $\Delta x = \delta V / A$,

$$\frac{\partial \Phi_P}{\partial t} + \frac{u_e}{\Delta x}\Phi_e - \frac{u_w}{\Delta x}\Phi_w = \frac{\Gamma_e}{\Delta x}\left(\frac{\partial \Phi}{\partial x}\right)_e - \frac{\Gamma_w}{\Delta x}\left(\frac{\partial \Phi}{\partial x}\right)_w + s_P. \tag{E.5}$$

We see at once in (E.5) the advantage of using a staggered velocity grid: the velocity components u_e and u_w are actually known. What remains is to determine the boundary values Φ_e and Φ_w for the advection term, and the gradients of Φ at the boundaries for the diffusion term. We will deal with the transient term after that.

Advection term

The simplest scheme for the advection term is the first order accurate *upwind differencing scheme*. The value at the cell boundary is approximated by the average cell value according to the direction of flow. For example, Φ_e is approximated

$$\Phi_e = \begin{cases} \Phi_P & \text{if} \quad u > 0, \\ \Phi_E & \text{if} \quad u < 0. \end{cases} \tag{E.6}$$

This is the only scheme that never yields numerical oscillations, i.e. it is unconditionally *bounded*. It is numerically diffusive, however, with a numerical diffusion coefficient Γ^{num}

$$\Gamma_e^{num} = u_e \frac{\Delta x}{2}. \tag{E.7}$$

This false diffusion (*Patankar*, 1980) is even bigger in multidimensional flow if flow is not perpendicular to the cell boundaries. The boundedness of the upwind differencing scheme is its advantage. Even higher order schemes often reduce to upwind differencing with a correction source term in order to obtain boundedness (*Hayase et al.*, 1992; *Norris*, 2001).

The *central difference scheme* is another basic differencing scheme. It approximates the value at the cell boundary by linear interpolation between cell values, i.e.

$$\Phi_e = \frac{\Phi_P + \Phi_E}{2}. \tag{E.8}$$

It is second order accurate but it not bounded and leads to unphysical solutions even at moderate velocities. Since it does not contain conditionals we will use it later in this section to demonstrate how to transform the transport equation (E.5) into a matrix form.

We learn from experience that in sea ice growth simulations only first order schemes like *upwind differencing*, *hybrid*, or *power*[2] (*Patankar*, 1980; *Versteeg and Malalasekera*, 1995) seem to retain boundedness. Using a monotonic second order upwind scheme (*Norris*, 2001), unboundedness reveals itself in cells neighbouring freezing cells by producing a salinity below 35 psu in an environment that is otherwise 35 psu. This happens in the absence of melting. For the simulation of freezing sea ice the potential problems of this unboundedness are more severe than the issue of excessive diffusion of first–order upwind schemes. All the present sea ice growth simulations therefore use first–order upwind differencing, usually the *power* scheme. Some commercial CFD packages use this scheme as the default scheme (*Versteeg and Malalasekera*, 1995). For a comparison between the performance of various discretisation schemes see, for example, *Hayase et al.* (1992), *Versteeg and Malalasekera* (1995) or *Norris* (2001).

Diffusion term

While the discretisation of the advection term continues to be a target of brainpower, little attention is given to the diffusion term. Second order central differences are accurate enough in many instances, and we follow the crowd by approximating the gradient

$$\left(\frac{\partial \Phi}{\partial x}\right)_e = \frac{\Phi_E - \Phi_P}{\Delta x}. \tag{E.9}$$

Transient term

Although we performed volume integration to obtain (E.5), we did not perform integration over time. This has been done for the convenience of presentation, as experience again shows that we have to limit ourselves to a first–order discretisation scheme if we are interested in a stable solution in the presence of a phase transition.

We use a *fully implicit* time discretisation scheme. In this scheme, the value Φ_P^n at time step n is evaluated based on the calculated distribution and flow field at time step n alone. This means that (E.5) can be written as

$$\frac{\Phi_P^n - \Phi_P^{n-1}}{\Delta t} + \frac{u_e}{\Delta x}\Phi_e^n - \frac{u_w}{\Delta x}\Phi_w^n = \frac{\Gamma_e}{\Delta x}\left(\frac{\partial \Phi}{\partial x}\right)_e^n - \frac{\Gamma_w}{\Delta x}\left(\frac{\partial \Phi}{\partial x}\right)_w^n + s_P, \tag{E.10}$$

where Δt is the time step, and Φ_P^{n-1} the value of Φ at P one time step before n. Typically, the most current available values for advection velocity u, diffusion coefficient Γ, and source term s_P are used. As they may be intermediate results they are written without superscript, here.

The matrix equation

Having made decisions regarding discretisation schemes for the advection, diffusion, and transient terms, an expression can be formulated for the relationship between

[2]The *hybrid* scheme uses the central difference scheme at low advection velocities, and upwind differencing at high velocities. The *power* scheme sets diffusion to zero at high velocities, and blends upwind differencing and central differences depending on advection velocity.

a particular value Φ_P^n at time n and the condition of the rest of the computational domain. We shall find that this relationship is surprisingly simple.

Combining (E.10) with the central differencing schemes for advection (E.8) and diffusion (E.9) we obtain

$$\frac{\Phi_P^n - \Phi_P^{n-1}}{\Delta t} + \frac{u_e}{\Delta x}\frac{\Phi_P^n + \Phi_E^n}{2} - \frac{u_w}{\Delta x}\frac{\Phi_P^n + \Phi_W^n}{2} = \frac{\Gamma_e}{\Delta x}\frac{\Phi_E^n - \Phi_P^n}{\Delta x} - \frac{\Gamma_w}{\Delta x}\frac{\Phi_P^n - \Phi_W^n}{\Delta x} + s_P. \tag{E.11}$$

After rearranging terms it becomes

$$\left(\frac{1}{\Delta t} + \frac{u_e}{2\Delta x} - \frac{u_w}{2\Delta x} + \frac{\Gamma_e + \Gamma_w}{(\Delta x)^2}\right)\Phi_P^n + \left(\frac{u_e}{2\Delta x} - \frac{\Gamma_e}{(\Delta x)^2}\right)\Phi_E^n + \left(-\frac{u_w}{2\Delta x} - \frac{\Gamma_w}{(\Delta x)^2}\right)\Phi_W^n = \frac{\Phi_P^{n-1}}{\Delta t} + s_P. \tag{E.12}$$

Since all terms in brackets and on the right hand side of (E.12) are constant during the solution of (E.12)[3], we may substitute them by coefficients a and a constant f, respectively. It is then

$$a_P\,\Phi_P^n + a_E\,\Phi_E^n + a_W\,\Phi_W^n = f_P, \tag{E.13}$$

and similarly in two–dimensions

$$a_P\,\Phi_P^n + a_E\,\Phi_E^n + a_W\,\Phi_W^n + a_N\,\Phi_N^n + a_S\,\Phi_S^n = f_P, \tag{E.14}$$

or short

$$a_P\,\Phi_P^n + \sum_{i=N,S,E,W} a_i\,\Phi_i^n = f_P. \tag{E.15}$$

Equation (E.15) connects only five cells with each other. The configuration of the cells P, N, S, E, and W is referred to as a five–point computational molecule, which is the most commonly used molecule.

There are four basic rules that the coefficients a and f in (E.15) should obey in order to ensure physical solutions (*Patankar*, 1980). First, consistency at the control volume faces has to be ensured. When a face is common to two adjacent control volumes, the flux across it must be represented by the same expression in the discretisation equations for the two control volumes. This is to say that the flux from one cell P into the neighbouring cell has to be the same magnitude as the flux into the neighbouring cell coming from P. For example, since the diffusive transfer coefficients $\bar{k}$ and fD in equations (4.6) and (4.10) generally depend on position (since porosity f depends on position), they have to be computed for each cell face. Simply taking the mean value assigned to a particular cell P would generally violate the principle of heat and solute mass conservation (e.g. equation (E.83) in Appendix E.2). Second, the sign of the coefficients a_i ($i = \{N, S, E, W\}$) has to be the opposite of the sign of a_P. If this condition is fulfilled then an increase of a value in one cell will lead to an increase (not a

[3]The solution process of this equation is called an *inner iteration*. Inner and outer iterations are discussed in Section 4.3.2.

decrease) of the value in a neighbouring cell (e.g. equations (E.31) and (E.34)). Third, the linearisation of the source term has to have a negative slope. If this condition is violated then a positive feedback loop may exist (e.g. the porous medium friction source term in (4.4) (cf. (E.39)) has a negative slope in fu). Fourth, in the absence of source terms the sum of transfer coefficients a_i has to be equal to $-a_P$, i.e. $a_P = -\sum a_i$. The implication here is that if a field Φ is a solution to the differential equation then the field $\Phi + c$ (where c is an arbitrary constant) is also a solution (e.g. the pressure correction equation (E.73)).

We may write the system of equations (E.15) for all cells of the domain in form of a matrix equation

$$A\,\mathbf{\Phi}^n = \mathbf{f}, \tag{E.16}$$

with a sparse (i.e. most elements are zero) matrix A. Equations with sparse matrices can be solved efficiently by numerical methods. We use a multigrid matrix solver in this project (*Briggs et al.*, 2000). It is introduced in Appendix E.4, since the technical details are not crucial for the understanding of the model, yet they are very interesting and important. It is a fact of life that not every numerical solver is able to find a stable solution to every flow problem.

One condition that is sufficient (but not necessary) for the numerical solution of the matrix equation (E.15) with the popular Gauss–Seidel method (Appendix E.4) is the Scarborough criterion (*Patankar*, 1980). It demands that

$$\frac{\sum |a_i|}{|a_P|} \qquad \begin{cases} \leq 1 & \text{for all equations,} \\ < 1 & \text{for one equation.} \end{cases} \tag{E.17}$$

This criterion can be satisfied in the discretisation schemes employed in this work by choosing a small time step (cf. equations (E.34) and (E.36) in Appendix E.2).

Boundary conditions

We discriminate between two basic boundary conditions, named after *Dirichlet* and *von Neumann*. A *Dirichlet* boundary condition prescribes a specific constant value, while a *von Neumann* boundary condition prescribes a gradient. In order to avoid instabilities we incorporate either boundary condition by adjusting the matrix coefficients a.

Imagine a prescribed boundary value Φ_b at the West side of a cell P. In this case, there is no cell W that coefficient a_W can refer to, so although a_W represents the strength of exchange in West direction, it has actually to be set to 0. But how does this affect the other coefficients? In the framework of a one–dimensional second order scheme (and equidistant cells) we can write

$$\Phi_b = \frac{\Phi_P + \Phi_W}{2}, \tag{E.18}$$

where Φ_W is a virtual value, i.e. the value of the cell a_W would refer to if cell W existed. We can calculate the virtual value Φ_W from

$$\Phi_W = 2\Phi_b - \Phi_P, \tag{E.19}$$

and substitute it in the matrix equation

$$a_W\Phi_W + a_E\Phi_E + a_P\Phi_P = f_P, \tag{E.20}$$
$$2a_W\Phi_b - a_W\Phi_P + a_E\Phi_E + a_P\Phi_P = f_P. \tag{E.21}$$

After rearranging we find the new relation

$$a_E\Phi_E + (a_P - a_W)\Phi_P = f_P - 2a_W\Phi_b. \tag{E.22}$$

Obviously, the dependence on Φ_W has been removed, so that the transformation of the matrix coefficients at a *Dirichlet* boundary is

$$\begin{aligned} a_E &\to a_E, \\ a_P &\to a_P - a_W, \\ f_P &\to f_P - 2\Phi_b a_W, \\ a_W &\to 0. \end{aligned} \tag{E.23}$$

The same method can be applied to the *von Neumann* boundary condition, where we start with

$$\left(\frac{\partial\Phi}{\partial x}\right)_w = \frac{\Phi_P - \Phi_W}{\Delta x}, \tag{E.24}$$

to find

$$\begin{aligned} a_E &\to a_E, \\ a_P &\to a_P + a_W, \\ f_P &\to f_P + \left(\tfrac{\partial\Phi}{\partial x}\right)_w \Delta x\, a_W, \\ a_W &\to 0. \end{aligned} \tag{E.25}$$

We face an ugly situation when we mix second order discretisation in the diffusion term with first order discretisation in the advection term. In this case the treatment of the *Dirichlet* boundary condition will be inconsistent either for advection or for diffusion. We will always apply second order boundary conditions in this project, since this confines the error to locations of inflow. There, instead of advecting the prescribed boundary values Φ_b, values slightly closer to the present cell value Φ_P are advected, i.e. the actual boundary value is bounded by Φ_b. This helps to avoid oscillations, and represents physical behaviour.

E.2 Discretised equations

The discretised equation and the numerical algorithm of the fluid dynamics simulation are outlined this section.

Most explanations are omitted in this section. The reader is advised to consult for example *Versteeg and Malalasekera* (1995), particularly for illustrations on the process of pressure–velocity coupling.

Notation The compass notation is followed, where P is denotes the cell of interest and N, E, S, and W refer to the neighbouring cells in vertical (N, S) and horizontal (E,

W) direction. The location of the cell boundaries of P are similarly referred to as n, s, e, and w (Figure 4.2 on page 127). Cell averaged temperature T, solute concentration in the liquid C, pressure p, and porosity (liquid volume fraction) f are stored in P. Velocity components are staggered by half a grid size. The horizontal components fu are located at Pw, which is the west face of a cell P, while the vertical components fv are located at Ps, which is the south face of a cell P (Figure 4.2). Note that references such as Pw and We, or Pn and Ns refer to identical locations.

The equations are solved for the volume average of the velocity components fu and fv, and for the intrinsic solute concentration C (as opposed to the volume averaged value fC) and for temperature T (as opposed to the enthalpy h).

Note that f is used in two different ways: f without index is the source term at P. If f is indexed, it refers to the porosity of the cell specified (P, N, S, E, W).

The linear dimensions of the computation cell are Δx, Δy, and Δz. The cell volume is $V = \Delta x\,\Delta y\,\Delta z$. Cell surface areas are defined as $A_x = \Delta y\,\Delta z$, and $A_y = \Delta x\,\Delta z$. The time step is Δt.

The = sign is to be understood either as an assignment operator or as a boolean operator, depending on the context.

Start The following fields contain the initial conditions at time step n: velocity $(fu)^n$ and $(fv)^n$, temperature T^n, solute concentration C^n, and porosity f^n. Ideally, an estimate of the pressure field p^n exists, but this is not a requirement, and it is even unnecessary in the case of the SIMPLER algorithm. Since a transient problem is simulated, a field that stores the accumulated mass imbalance MB is needed and set to zero initially. The following fields are then copied into "current best guess" fields: fu, fv, T, C, f, and p. The outer iteration begins with the phase transition.

Phase transition The following process is repeated for all cells P. If the temperature T_P is above the freezing point $T_F(C_P)$ and $f_P == 1$, continue with the next cell.

If freezing front tracking is active: if $f_P == 1$ and the porosity at the cell interface not is low enough for ice growth in P, continue with the next cell.

Since thermodynamic equilibrium is not established in P, follow Appendix E.3 and estimate the new porosity from temperature, T_P, solute concentration, C_P, and current porosity, f_P,

$$f_P = f_P + \left[aC_P + b - T_P\right]\left[\frac{L - (c_l - c_s)T_P}{(c_l\rho_l - c_s\rho_s)f_P + c_s\rho_s}\rho_l + \frac{aC_P}{f_P}\right]^{-1}, \tag{E.26}$$

where the coefficients a and b are derived from a linear approximation of the liquidus at $C = C_P$,

$$T_F = aC + b. \tag{E.27}$$

The solution of (E.26) improves with successive outer iterations.

Transport coefficients for the momentum conservation equation fu If simulation is in the nominal absence of advection in the liquid, perform the following test for all cells: if $f_P = 1$ and ($f_S = 1$ or $f_N = 1$) and ($f_W = 1$ or $f_E = 1$) then overwrite

velocity components

$$(fu)_{Pe} = (fu)_{Pw} = (fv)_{Pn} = (fv)_{Ps} = 0. \tag{E.28}$$

The change of horizontal momentum of $(fu)_{Pw}$ is considered. Advective contributions to momentum transfer are

$$m_e = \frac{(fu)_{Pw} + (fu)_{Pe}}{2f_P}\rho_w A_x, \tag{E.29a}$$

$$m_w = \frac{(fu)_{Ww} + (fu)_{Pw}}{2f_W}\rho_w A_x, \tag{E.29b}$$

$$m_n = 2\frac{(fv)_{Pn} + (fv)_{Wn}}{f_P + f_N + f_{NW} + f_W}\rho_w A_y, \tag{E.29c}$$

$$m_s = 2\frac{(fv)_{Ps} + (fv)_{Ws}}{f_P + f_S + f_{SW} + f_W}\rho_w A_y. \tag{E.29d}$$

The diffusive (viscosity) contributions are

$$d_e = \mu\frac{A_x}{\Delta x}, \tag{E.30a}$$

$$d_w = \mu\frac{A_x}{\Delta x}, \tag{E.30b}$$

$$d_n = \mu\frac{A_y}{\Delta y}, \tag{E.30c}$$

$$d_s = \mu\frac{A_y}{\Delta y}. \tag{E.30d}$$

Next, advective and diffusive contributions are combined to give the transfer coefficients. Some first–order schemes are given here:

The most fundamental first order upwind scheme (cf. *Norris* (2001)) is:

$$a_E = -\max(-m_e, 0) - d_e, \tag{E.31a}$$

$$a_W = -\max(m_w, 0) - d_w, \tag{E.31b}$$

$$a_N = -\max(-m_n, 0) - d_n, \tag{E.31c}$$

$$a_S = -\max(m_s, 0) - d_s. \tag{E.31d}$$

The hybrid scheme is

$$a_E = -\max(0, \max(-m_e, d_e - m_e/2)), \tag{E.32a}$$

$$a_W = -\max(0, \max(m_w, d_w + m_w/2)), \tag{E.32b}$$

$$a_N = -\max(0, \max(-m_n, d_n - m_n/2)), \tag{E.32c}$$

$$a_S = -\max(0, \max(m_s, d_s + m_s/2)). \tag{E.32d}$$

The power scheme (*Versteeg and Malalasekera*, 1995) is

$$a_E = -(d_e \max(0, (1 - 0.1 \text{ abs}((m_e/d_e)^5))) + \max(-m_e, 0)), \tag{E.33a}$$
$$a_W = -(d_w \max(0, (1 - 0.1 \text{ abs}((m_w/d_w)^5))) + \max(m_w, 0)), \tag{E.33b}$$
$$a_N = -(d_n \max(0, (1 - 0.1 \text{ abs}((m_n/d_n)^5))) + \max(-m_n, 0)), \tag{E.33c}$$
$$a_S = -(d_s \max(0, (1 - 0.1 \text{ abs}((m_s/d_s)^5))) + \max(m_s, 0)). \tag{E.33d}$$

Should any of the diffusive transfer coefficients d_i be zero, the first order advection scheme for that direction following $a_i = -\max(-m_i, 0)$ is used instead of the power scheme. The function "max" returns the larger one of two values, and the function "abs" returns the absolute value of a number.

Finally, in all schemes,

$$a_P = -(a_E + a_W + a_N + a_S) + (m_e - m_w + m_n - m_s). \tag{E.34}$$

So far, the source term f is zero. At this point, transport coefficients a_i and source term f are modified at the boundary according to the boundary condition.

Now contributions to the source term are added. The buoyancy contribution is

$$f = f + \frac{f_P + f_W}{2} V g_x \left\{ \rho \left(\frac{1}{2}[T_P + T_W], \frac{1}{2}[C_P + C_W] \right) - \rho_0 \right\}, \tag{E.35}$$

where ρ is the function that describes density as depending on temperature T and solute concentration C, and ρ_0 is a random constant that, if chosen to be a typical density, facilitates convergence of the SIMPLE/SIMPLEC algorithm at the beginning of computation. The transient term affects both, a_P and source term f,

$$a_P = a_P + \frac{V \rho_w}{\Delta t}, \tag{E.36}$$
$$f = f + \frac{V \rho_w}{\Delta t} \left[(fu)_{Pw} \right]^n. \tag{E.37}$$

If drainage of low porosity cells ($f_P \leq f_c$, where f_c is the critical porosity) is to be avoided: if $f_P < f_c$ or $f_W < f_c$ then set

$$a_P = a_N = a_S = a_E = a_W = f = 0. \tag{E.38}$$

The Darcy friction term is treated implicitly (i.e. added to a_P) for numerical stability,

$$a_P = a_P + V \frac{f_P + f_W}{2} \frac{1}{2} \left[\frac{\mu}{\Pi_x(f_P)} + \frac{\mu}{\Pi_x(f_W)} \right]. \tag{E.39}$$

Note that not the average of permeability Π_x at P and at W is calculated in (E.39), but the average of the reciprocal, i.e. fluid flow resistance. This procedure is advisable if the term mediating conductivity (here: permeability) varies significantly between cells (*Patankar*, 1980).

Should the SIMPLER algorithm be used, the pseudo velocity $\widehat{fu}_{Pw}$ is calculated

$$\widehat{fu}_{Pw} = \frac{-a_E\,(fu)_{Ew} - a_W\,(fu)_{Ww} - a_N\,(fu)_{Nw} - a_S\,(fu)_{Sw} + f}{a_P}. \tag{E.40}$$

If underrelaxation of velocity (r_v) for the SIMPLE algorithm is desired, it is applied as

$$f = f + (1 - r_v)\frac{a_P}{r_v}\left[(fu)_{Pw}\right]^n, \tag{E.41}$$

$$a_P = \frac{a_P}{r_v}. \tag{E.42}$$

$$\tag{E.43}$$

Next, coefficients du are calculated for the pressure equation (SIMPLER) and pressure correction equation. These are for SIMPLE and SIMPLER

$$du_{Pw} = \frac{f_P + f_W}{2}\frac{A_x}{a_P}, \tag{E.44}$$

and for SIMPLEC

$$du_{Pw} = \frac{f_P + f_W}{2}\frac{A_x}{a_P + a_E + a_W + a_N + a_S}. \tag{E.45}$$

All matrix coefficients a_i and f are stored for future use.

Transport coefficients for the momentum conservation equation fv The same procedure is followed for the vertical velocity component $(fv)_{Ps}$. Advective contributions to momentum transfer are

$$m_e = 2\frac{(fu)_{Pe} + (fu)_{Se}}{f_P + f_E + f_{SE} + f_S}\rho_w A_x, \tag{E.46a}$$

$$m_w = 2\frac{(fu)_{Pw} + (fu)_{Sw}}{f_P + f_W + f_{SW} + f_S}\rho_w A_x, \tag{E.46b}$$

$$m_n = \frac{(fv)_{Ps} + (fv)_{Ns}}{2f_P}\rho_w A_y, \tag{E.46c}$$

$$m_s = \frac{(fv)_{Ss} + (fv)_{Ps}}{2f_S}\rho_w A_y. \tag{E.46d}$$

The diffusive (viscosity) contributions are

$$d_e = \mu \frac{A_x}{\Delta x}, \tag{E.47a}$$

$$d_w = \mu \frac{A_x}{\Delta x}, \tag{E.47b}$$

$$d_n = \mu \frac{A_y}{\Delta y}, \tag{E.47c}$$

$$d_s = \mu \frac{A_y}{\Delta y}. \tag{E.47d}$$

Next, advective and diffusive contributions are combined to give the transfer coefficients. The equations are exactly as shown above.

So far, the source term f is zero. At this point, transport coefficients a_i and source term f are modified at the boundary according to the boundary condition.

The contributions to the source term are added. The buoyancy contribution is

$$f = f + \frac{f_P + f_S}{2} V g_y \left\{ \rho \left(\frac{1}{2}[T_P + T_S], \frac{1}{2}[C_P + C_S] \right) - \rho_0 \right\}, \tag{E.48}$$

where ρ is the function that describes density as depending on temperature T and solute concentration C, and ρ_0 is a random constant that, if chosen to be a typical density, facilitates convergence of the SIMPLE/ SIMPLEC algorithm at the beginning of computation. The transient term affects both, a_P and source term f,

$$a_P = a_P + \frac{V \rho_w}{\Delta t}, \tag{E.49}$$

$$f = f + \frac{V \rho_w}{\Delta t} \left[(fv)_{Ps} \right]^n. \tag{E.50}$$

If drainage of low porosity cells ($f_P \leq f_c$, where f_c is the critical porosity) is to be avoided: if $f_P < f_c$ or $f_W < f_c$ then set

$$a_P = a_N = a_S = a_E = a_W = f = 0. \tag{E.51}$$

The Darcy friction term is treated implicitly (i.e. added to a_P) for numerical stability,

$$a_P = a_P + V \frac{f_P + f_S}{2} \frac{1}{2} \left[\frac{\mu}{\Pi_y(f_P)} + \frac{\mu}{\Pi_y(f_S)} \right]. \tag{E.52}$$

Note that, not the average of permeability Π_y at P and S is calculated in (E.52), but the average of the reciprocal, i.e. fluid flow resistance.

Should the SIMPLER algorithm be used, the pseudo velocity $\widehat{fv}_{Ps}$ is calculated

$$\widehat{fv}_{Ps} = \frac{-a_E (fv)_{Es} - a_W (fv)_{Ws} - a_N (fv)_{Ns} - a_S (fv)_{Ss} + f}{a_P}. \tag{E.53}$$

If underrelaxation of velocity (r_v) for the SIMPLE algorithm is desired, it is applied

as

$$f = f + (1 - r_v)\frac{a_P}{r_v}\left[(fv)_{Ps}\right]^n, \tag{E.54}$$

$$a_P = \frac{a_P}{r_v}. \tag{E.55}$$

$$\tag{E.56}$$

Next, the coefficients dv are calculated for the pressure equation (SIMPLER) and pressure correction equation. These are for SIMPLE and SIMPLER

$$dv_{Ps} = \frac{f_P + f_S}{2}\frac{A_y}{a_P}, \tag{E.57}$$

and for SIMPLEC

$$dv_{Ps} = \frac{f_P + f_S}{2}\frac{A_y}{a_P + a_E + a_W + a_N + a_S}. \tag{E.58}$$

All matrix coefficients a_i and f are stored for future use.

SIMPLER pressure equation If SIMPLE or SIMPLEC is used, skip this paragraph.

If an open boundary is present and mass conservation is to be mediated by the pressure gradient, then the pressure gradient boundary condition is set for all cells along the open boundary to

$$\nabla p = \frac{\alpha}{\Delta t\,(N\,A_\perp)}, \tag{E.59}$$

where $(N\,A_\perp)$ is the area of the open boundary (i.e. the number of cells times the area perpendicular to the boundary of each individual cell (A_x or A_y)), and α is the sum of the current mass imbalance of all cells in the domain combined, i.e.

$$\begin{aligned}\alpha = \sum \Big\{ &\frac{V}{\Delta t}\mathrm{MB}_P + \\ &\rho_w A_x\left[\widehat{fu}_{Pe} - \widehat{fu}_{Pw}\right] + \rho_w A_y\left[\widehat{fv}_{Pn} - \widehat{fv}_{Ps}\right] - V\rho_w\left(1 - \frac{\rho_i}{\rho_w}\right)\frac{f_P - f_P^n}{\Delta t}\Big\}.\end{aligned} \tag{E.60}$$

This procedure is, however, not used for simulations of refreezing cracks, where instead $\nabla p = 0$ at the open boundary and mass conservation is achieved later.

Set up the matrix coefficients for all cells.

$$a_E = -f_P\,du_{Ew}\,A_x\rho_w, \tag{E.61a}$$

$$a_W = -f_P\,du_{Pw}\,A_x\rho_w, \tag{E.61b}$$

$$a_N = -f_P\,dv_{Ns}\,A_y\rho_w, \tag{E.61c}$$

$$a_S = -f_P\,dv_{Ps}\,A_y\rho_w. \tag{E.61d}$$

Should a coefficient du or dv not be defined (at the boundary), use the closest coefficient

available inside the field. Further,

$$a_P = -a_E - a_W - a_N - a_S. \tag{E.62}$$

The source term comprises of accumulated mass imbalance MB (*Patankar*, 1980),

$$f = \frac{V}{\Delta t}\mathrm{MB}_P, \tag{E.63}$$

the apparent degree of violation of the mass conservation equation in $\widehat{fu}$ and $\widehat{fv}$,

$$f = f + \rho_w \left[\left(\widehat{fu}_{Pw} - \widehat{fu}_{Pe} \right) A_x + \left(\widehat{fv}_{Ps} - \widehat{fv}_{Pn} \right) A_y \right], \tag{E.64}$$

and the source term of the mass conservation equation due to volume expansion

$$f = f - V\rho_w \left(1 - \frac{\rho_i}{\rho_w} \right) \frac{f_P - f_P^n}{\Delta t}. \tag{E.65}$$

Next, boundary conditions are applied.

If an open boundary is present and mass conservation is not to be mediated by the pressure, then the source term, f, is adjusted in all cells at the open boundary condition according to

$$f = f + \frac{1}{N}\alpha, \tag{E.66}$$

where N is the number of cells at the open boundary, and α is calculated according to (E.60).

With all matrix coefficients a_i and f defined, use the current pressure field p as start value to solve the matrix equation. The result is the new pressure field p.

Solve for fu and fv Add the pressure source term to the momentum conservation equation of $(fu)_{Pw}$,

$$f = f - \frac{f_P + f_W}{2} A_x \left(p_P - p_W \right), \tag{E.67}$$

unless drainage of low porosity cells is to be avoided and $f_P \leq f_c$ or $f_W \leq f_c$.

With all matrix coefficients a_i and f defined, use the current velocity field fu as start value to solve the matrix equation. The result is the new velocity field fu.

Now add the pressure source term to the momentum conservation equation of $(fv)_{Ps}$,

$$f = f - \frac{f_P + f_S}{2} A_y \left(p_P - p_S \right), \tag{E.68}$$

unless drainage of low porosity cells is to be avoided and $f_P <= f_c$ or $f_S <= f_c$.

With all matrix coefficients a_i and f defined, use the current velocity field fv as start value to solve the matrix equation. The result is the new velocity field fv.

If simulation is in the nominal absence of advection in the liquid, perform the following test for all cells: if $f_P = 1$ and ($f_S = 1$ or $f_N = 1$) and ($f_W = 1$ or $f_E = 1$)

then overwrite velocity components

$$(fu)_{Pe} = (fu)_{Pw} = (fv)_{Pn} = (fv)_{Ps} = 0. \tag{E.69}$$

Pressure correction equation All algorithms, SIMPLE, SIMPLEC, and SIMPLER use a pressure correction equation to enforce mass conservation. The matrix coefficients are identical to the matrix coefficients of the SIMPLER pressure equation, apart from the fact that fu and fv are used in the source term in place of $\widehat{fu}$ and $\widehat{fv}$.

If an open boundary is present and mass conservation is to be mediated by the pressure gradient, then the pressure gradient boundary condition is set for all cells along the open boundary to

$$\nabla p = \frac{\alpha}{\Delta t\,(N\,A_\perp)}, \tag{E.70}$$

where $(N\,A_\perp)$ is the area of the open boundary (i.e. the number of cells times the area perpendicular to the boundary of each individual cell), and α is the sum of the current mass imbalance of all cells in the domain combined, i.e.

$$\alpha = \sum \Big\{ \frac{V}{\Delta t}\mathrm{MB}_P + \rho_w A_x \big[(fu)_{Pe} - (fu)_{Pw}\big] + \rho_w A_y \big[(fv)_{Pn} - (fv)_{Ps}\big] - V\rho_w \left(1 - \frac{\rho_i}{\rho_w}\right) \frac{f_P - f_P^n}{\Delta t} \Big\}. \tag{E.71}$$

This procedure is, however, not used for simulations of refreezing cracks, where instead $\nabla p = 0$ at the open boundary and mass conservation is achieved later.

Set up the matrix coefficients for all cells.

$$a_E = -f_P\,du_{Ew}\,A_x\rho_w, \tag{E.72a}$$
$$a_W = -f_P\,du_{Pw}\,A_x\rho_w, \tag{E.72b}$$
$$a_N = -f_P\,dv_{Ns}\,A_y\rho_w, \tag{E.72c}$$
$$a_S = -f_P\,dv_{Ps}\,A_y\rho_w. \tag{E.72d}$$

Should a coefficient du or dv not be defined (at the boundary), use the closest coefficient available inside the field. Further,

$$a_P = -a_E - a_W - a_N - a_S. \tag{E.73}$$

The source term comprises of accumulated mass imbalance MB (*Patankar*, 1980),

$$f = \frac{V}{\Delta t}\mathrm{MB}_P, \tag{E.74}$$

the apparent degree of violation of the mass conservation equation in fu and fv,

$$f = f + \rho_w \left[((fu)_{Pw} - (fu)_{Pe})\,A_x + ((fv)_{Ps} - (fv)_{Pn})\,A_y\right], \tag{E.75}$$

and the source term of the mass conservation equation due to volume expansion

$$f = f - V\rho_w \left(1 - \frac{\rho_i}{\rho_w}\right) \frac{f_P - f_P^n}{\Delta t}. \tag{E.76}$$

Next, boundary conditions are applied.

If an open boundary is present and mass conservation is not to be mediated by the pressure then the source term, f, is adjusted in all cells at the open boundary condition according to

$$f = f + \frac{1}{N}\alpha, \tag{E.77}$$

where N is the number of cells at the open boundary, and α is calculated according to (E.71).

With all matrix coefficients a_i and f defined, use a field of 0 as start value for the pressure correction equation and solve the matrix equation. The resulting field is the pressure correction field p^c.

If SIMPLE or SIMPLEC are used, update the pressure field with pressure under-relaxation factor r_p according to

$$p_P = p_P + r_p\, p_P^c. \tag{E.78}$$

In any case adjust the velocity field to be mass conserving

$$(fu)_{Pw} = (fu)_{Pw} + du_{Pw}\,\left(p_W^c - p_P^c\right), \tag{E.79}$$

$$(fv)_{Ps} = (fv)_{Ps} + dv_{Ps}\,\left(p_S^c - p_P^c\right). \tag{E.80}$$

If an open boundary is present then the velocity components normal to the open boundary are adjusted to obtain mass conservation in these cells. For each individual cell at the open boundary set

$$(fv)_s = (fv)_s - \frac{1}{\rho_0 A_y}\Big\{\frac{V}{\Delta t}\mathrm{MB}_P + \rho_w A_x\big[(fu)_{Pe} - (fu)_{Pw}\big] + \rho_w A_y\big[(fv)_{Pn} - (fv)_{Ps}\big] - V\rho_w\left(1 - \frac{\rho_i}{\rho_w}\right)\frac{f_P - f_P^n}{\Delta t}\Big\}. \tag{E.81}$$

Equation (E.81) is formulated for an open boundary at the south face of the domain. For an open boundary at the west side substitute $(fu)_w$ and A_x.

Automated stability check All cells are checked for violation of a Courant condition, i.e. whether the velocity is too large with respect to the field size. Should a violation be detected, then the time step Δt is reduced, and the velocity fields fu and fv are restored to the result of the previous iteration n. The results obtained so far are disregarded, and the solution is continued above by defining the transport coefficients for the momentum conservation equation of fu.

Transport equations Heat and solute transport equations are identical apart from the source terms and coefficients. Let Φ be either temperature T or solute concentration C. Coefficients are defined as follows:

	$\Phi = T$	$\Phi = C$	
$\mathcal{T}_l$	$c_w\rho_w$	1	storage in liquid
$\mathcal{T}_s$	$c_i\rho_i$	0	storage in solid
$\mathcal{A}_l$	$c_w\rho_w$	1	advection in liquid
$\mathcal{D}_l$	k_w	D	diffusion in liquid
$\mathcal{D}_s$	k_i	0	diffusion in solid

The advection contributions are

$$m_e = \mathcal{A}_l (fu)_{Pe} \frac{1}{\Delta x}, \tag{E.82a}$$

$$m_w = \mathcal{A}_l (fu)_{Pw} \frac{1}{\Delta x}, \tag{E.82b}$$

$$m_n = \mathcal{A}_l (fv)_{Pn} \frac{1}{\Delta y}, \tag{E.82c}$$

$$m_s = \mathcal{A}_l (fv)_{Ps} \frac{1}{\Delta y}. \tag{E.82d}$$

The diffusion contributions are

$$d_e = \frac{\mathcal{D}_l(f_E + f_P) + \mathcal{D}_s(2 - f_E - f_P)}{2(\Delta x)^2}, \tag{E.83a}$$

$$d_w = \frac{\mathcal{D}_l(f_W + f_P) + \mathcal{D}_s(2 - f_W - f_P)}{2(\Delta x)^2}, \tag{E.83b}$$

$$d_n = \frac{\mathcal{D}_l(f_N + f_P) + \mathcal{D}_s(2 - f_N - f_P)}{2(\Delta y)^2}, \tag{E.83c}$$

$$d_s = \frac{\mathcal{D}_l(f_S + f_P) + \mathcal{D}_s(2 - f_S - f_P)}{2(\Delta y)^2}. \tag{E.83d}$$

Next, advective and diffusive contributions are combined to give the transfer coefficients. The equations are exactly as shown above.

So far, the source term f is zero. At this point, transport coefficients a_i and source term f are modified at the boundary according to the boundary condition.

Now the contribution of the phase change is added to the source term. If solution is for temperature $\Phi = T$, then

$$f = f - \left[\rho_i L + T_P^n (c_w\rho_w - c_i\rho_i)\right] \frac{f_P - f_P^n}{\Delta t}. \tag{E.84}$$

If solution is for the solute concentration $\Phi = C$, then

$$f = f - C_P^n \frac{f_P - f_P^n}{\Delta t}. \tag{E.85}$$

Finally, the transient term is added,

$$a_P = a_P + \frac{\mathcal{T}_l f_P + (1 - f_P)\mathcal{T}_s}{\Delta t}, \tag{E.86}$$

$$f = f + \Phi^n \frac{\mathcal{T}_l f_P + (1 - f_P)\mathcal{T}_s}{\Delta t}. \tag{E.87}$$

With all matrix coefficients a_i and f defined, use Φ as start value for the transport equation and solve the matrix equation. The result is the new field Φ.

Convergence check If the current solution is not yet stable, continue with the phase transition.

Mass balance Update the overall mass imbalance MB,

$$\mathrm{MB}_P = \mathrm{MB}_P + \Big\{ \rho_w \big[\left((fu)_{Pw} - (fu)_{Pe}\right) A_x + \left((fv)_{Ps} - (fv)_{Pn}\right) A_y \big] - V \rho_w \left(1 - \frac{\rho_i}{\rho_w}\right) \frac{f_P - f_P^n}{\Delta t} \Big\} \frac{\Delta t}{V}. \tag{E.88}$$

Increase iteration counter $n \to n + 1$, and transfer $T \to T^n$, $C \to C^n$, $f \to f^n$, $p \to p^n$, $fu \to (fu)^n$, and $fv \to (fv)^n$. Continue with the phase transition.

E.3 Thermodynamic equilibrium

The equation determining the change of porosity to obtain thermodynamic equilibrium will be derived. Let a cell be at temperature T_0, brine concentration C_0, and porosity f_0. By what amount *df* does the porosity have to change in order to bring cell temperature T and brine concentration C into thermodynamic equilibrium? We assume that *df* is a small number.

First, we determine a linear approximation to the freezing point depression as a function of solute concentration,

$$T_F = aC + b, \tag{E.89}$$

where coefficients a and b are determined at concentration $C = C_0$. Two quantities are to be conserved, the enthalpy, H,

$$H = c_l M_l T + c_s M_s T - M_s L, \tag{E.90}$$

with heat capacities c_l and c_s of liquid and solid, respectively, masses M_l and M_s of liquid and solid, respectively, and latent heat of fusion L, and the mass of solute, M_c,

$$M_c = C_0 f_0 V, \tag{E.91}$$

where V is the total volume of the cell. Conserving the enthalpy it follows from (E.90) and mass conservation $dM_l + dM_s = 0$

$$dH = 0, \tag{E.92}$$
$$= (c_l M_l + c_s M_s)dT + (c_l T - c_s T - L)dM_l. \tag{E.93}$$

Further from (E.91) it follows

$$Cf = C_0 f_0, \tag{E.94}$$
$$C = C_0 \frac{f_0}{f}, \tag{E.95}$$
$$C = C_0 \frac{f_0}{f_0 + df}. \tag{E.96}$$

With the temperature $T = T_0 + dT$ we find the condition for thermodynamic equilibrium

$$0 = T - T_F, \tag{E.97}$$

with (E.89) and (E.96)

$$= T_0 + dT - aC_0 \frac{f_0}{f_0 + df} - b \tag{E.98}$$

and from (E.93)

$$= T_0 + \frac{-c_l T + c_s T + L}{c_l M_l + c_s M_s} dM_l - aC_0 \frac{f_0}{f_0 + df} - b. \tag{E.99}$$

With $M_l = f\rho_l V$ and $M_s = (1-f)\rho_s V$ (E.99) becomes

$$0 = T_0 + \frac{-c_l T + c_s T + L}{c_l f_0 \rho_l + c_s (1-f_0)\rho_s} \rho_l df - aC_0 \frac{f_0}{f_0 + df} - b. \tag{E.100}$$

Equation (E.100) results in quadratic expression for df. However, if $df \ll f_0$ the third term on the right hand side of (E.100) can be linearly expanded to

$$0 = T_0 + \frac{-c_l T + c_s T + L}{c_l f_0 \rho_l + c_s (1-f_0)\rho_s} \rho_l df - aC_0 \left(1 - \frac{df}{f_0}\right) - b, \tag{E.101}$$

so that df is obtained from

$$aC_0 + b - T_0 = \left[\frac{L - (c_l - c_s)T}{(c_l \rho_l - c_s \rho_s) f_0 + c_s \rho_s} \rho_l + \frac{aC_0}{f_0}\right] df. \tag{E.102}$$

E.4 Multigrid solver

During each time step, a system of linear algebraic equations of the form

$$A\mathbf{\Phi} = \mathbf{f} \tag{E.103}$$

has to be solved, where $\mathbf{\Phi}$ is the scalar field to be solved for, A is the matrix of transfer coefficients a_P, a_E, a_W, etc. (Section E.1) for all fields, and $\mathbf{f}$ are the source terms. We will apply (E.103) to the example that we will use for illustration in the multigrid section starting on page 327, which is a one–dimensional field with 4 cells. We may write in that case

$$A\mathbf{\Phi} = \begin{bmatrix} a_{1P} & a_{1E} & & \\ a_{2W} & a_{2P} & a_{2E} & \\ & a_{3W} & a_{3P} & a_{3E} \\ & & a_{4W} & a_{4P} \end{bmatrix} \begin{bmatrix} \Phi_1 \\ \Phi_2 \\ \Phi_3 \\ \Phi_4 \end{bmatrix} = \begin{bmatrix} f_1 \\ f_2 \\ f_3 \\ f_4 \end{bmatrix} = \mathbf{f}. \tag{E.104}$$

A variety of linear solvers has been developed. They split into the groups of direct methods and indirect methods. Direct methods attempt to solve the system exactly by analytical means, while indirect methods are iterative procedures that terminate once the obtained solution is deemed sufficiently accurate. Solving equation (E.103) exactly it is usually very time consuming. Considering that an error has already been introduced by the discretisation scheme, it is often not even sensible to try to solve for machine accuracy (*Ferziger and Perić*, 2002, p. 97). Iterative schemes can save a considerable amount of time if the solution is known approximately, or if it is possible to guess the solution reasonably well. In transient simulations the solution of the next time step is known approximately, as it is the solution of the current time step.

Smoother

In our case, (E.103) represents a system of linear equations that can be described at every control volume P by a five–point computational molecule of the form

$$\begin{aligned} a_P\Phi_P + a_W\Phi_W + a_E\Phi_E + a_S\Phi_S + a_N\Phi_N &= f_P, \\ a_P\Phi_P + \sum_{i=W,E,S,N} a_i\Phi_i &= f_P. \end{aligned} \tag{E.105}$$

The simplest method to solve (E.103) for a system that can be described at every control volume by (E.105) is the Jacobi method (or simultaneous displacement method). Approximate field values for the iterative step, $n+1$, are obtained from the current best guess at n by means of

$$\Phi_P^{n+1} = \frac{f_P - a_W\Phi_W^n - a_E\Phi_E^n - a_S\Phi_S^n - a_N\Phi_N^n}{a_P}. \tag{E.106}$$

This method converges slowly, and it can be shown that the computational effort to solve (E.103) increases with the square of the number of grid points (*Ferziger and Perić*, 2002). Improvement by a factor of two is gained through a modification referred to

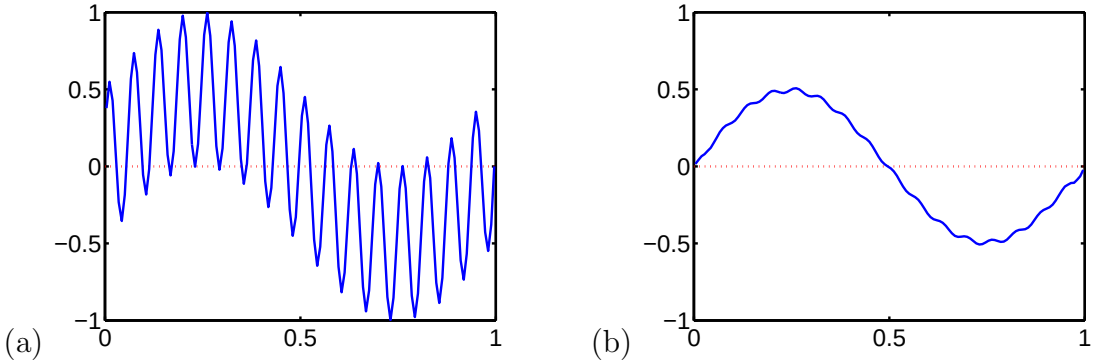

Figure E.1: Example of the high frequency smoothing feature of the Jacobi algorithm. (a) Initial guess of the solution. (b) Result after 10 iterations of the Jacobi solver.

as Gauss–Seidel method (or successive displacement method), where newly calculated values for $\Phi_P^\star$ are used immediately in the calculation of subsequent values $\Phi_P^\star$. It is further of considerable advantage to overrelax the result according to

$$\Phi_P^\star = \omega \frac{f_P - a_W \Phi_W - a_E \Phi_E - a_S \Phi_S - a_N \Phi_N}{a_P} + (1 - \omega)\, \Phi_P. \tag{E.107}$$

The factor ω is between 1 and 2 for accelerated convergence, and the optimum value depends on the peculiarities of the system. A method like this is referred to as successive over–relaxation (SOR). With optimum ω the number of iterations is proportional to the number of grid points in one direction (*Ferziger and Perić*, 2002). A feature of the Gauss–Seidel algorithm is that convergence depends on the order, in that (E.107) is applied to the control volumes P. Popular methods include Symmetric Gauss–Seidel, where control volumes are computed line by line, and the direction of this process is reversed after each sweep through the field. The author's favourite method is Red–Black Gauss–Seidel, where control volumes are tagged red or black in an alternating fashion, and the solution algorithm first solves for all red volumes before solving for all black volumes. This approach can be easily parallelised. *Briggs et al.* (2000) discuss variants and parameter choice of Gauss–Seidel solvers. Typical overrelaxation values used in calculations in this thesis are $1.2 \leq \omega \leq 1.5$, and they are optimised through trial–and–error, which is standard (*Briggs et al.*, 2000).

Jacobi and Gauss–Seidel solvers characteristically smooth out the error in wavelengths of comparable size to the grid spacing much more efficiently than the error in larger wavelengths. For example Figure E.1 shows an attempt to solve the one–dimensional steady state diffusion equation

$$\frac{\partial^2 \Phi}{\partial x^2} = 0, \tag{E.108}$$

with Dirichlet boundary conditions $\Phi(x = 0, t) = 0$ and $\Phi(x = 1, t) = 0$. For any control volume but the ones at the boundary the discretised formulation of the problem using central differences is

$$2\Phi_P - \Phi_W - \Phi_E = 0. \tag{E.109}$$

Figure E.1(a) shows the initial guess that is a superposition of two waves. The

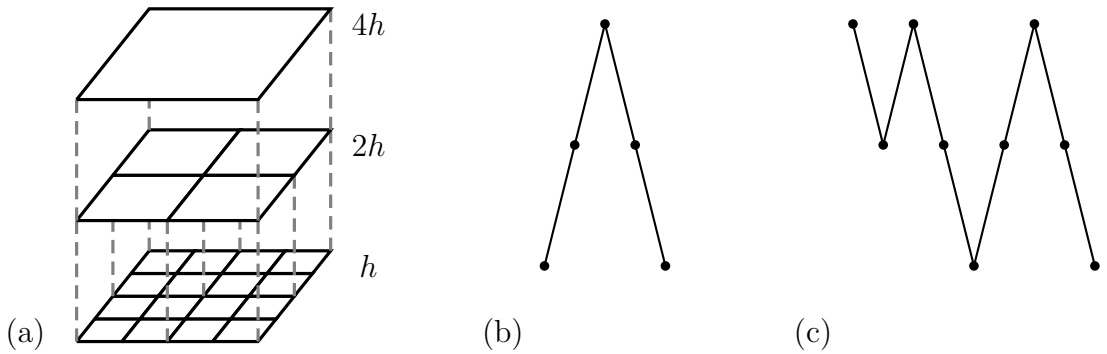

Figure E.2: Implementation of the finite volume multigrid. (a) Cell interfaces of the grids line up. (b) Multigird V–cycle. (c) Full multigrid cycle.

wavelengths are 128 and 8 grid spacings, respectively, and the amplitude is 0.5 in both cases. The domain is divided into a grid of 128 control volumes. Figure E.1(b) is the improvement after 10 Jacobi iterations. It is obvious that the short wavelength, or high frequency error has been smoothed very efficiently, while the low frequency error has hardly been reduced. We can exploit the smoothing feature of the Jacobi/ Gauss–Seidel algorithm to build a very efficient solver for all frequencies of error. Instead of smoothing only the grid we are interested in, we can apply the smoother on a coarser grid of the problem and incorporate the result appropriately in the solution of the fine grid. This method is referred to as multigrid method and it operates with any algorithm that exhibits a high frequency smoothing characteristic similar to the SOR solvers.

Multigrid Method

The multigrid method improves the convergence of solution algorithms that smooth out errors in small wavelengths better than errors in large wavelengths. The idea is surprisingly simple. Take a system of linear equations

$$A\mathbf{\Phi} = \mathbf{f} \tag{E.110}$$

that we want to solve for vector $\mathbf{\Phi}$. We suppose that the solution is unique. We apply some smoothing algorithm such as SOR introduced in the previous section to calculate an approximate solution $\mathbf{\Phi}^\star$. This process is referred to as relaxation. If we knew the error $\mathbf{e}$ in the approximation $\mathbf{\Phi}^\star$ we could calculate the exact solution from

$$\mathbf{\Phi} = \mathbf{\Phi}^\star + \mathbf{e}. \tag{E.111}$$

With this incentive we will next calculate the error. Although we do not know the error, we have ready access to the residual $\mathbf{r}$ from

$$\mathbf{r} = \mathbf{f} - A\mathbf{\Phi}^\star. \tag{E.112}$$

Substituting (E.111) we find the residual equation

$$A\mathbf{e} = \mathbf{r}, \tag{E.113}$$

where the error $\mathbf{e}$ satisfies the same set of equations as the solution $\mathbf{\Phi}$ when $\mathbf{f}$ is replaced by the residual $\mathbf{r}$.

The idea of the multigrid is to calculate an approximation on the finest grid (h), and solve for the error on a coarser grid ($2h$). This idea can be implemented recursively, which then means solving for the error of the error on an even coarser grid ($4h$) and so on. The cream of the crop is that an exact solution has to be obtained only on the coarsest grid, which is computationally relatively inexpensive (or in the extreme case of a 1×1 grid even trivial). However, with the multigrid method we are not able to create information from nothing. Each time we apply the error correction (E.111) with the error obtained on the coarser grid $(2n)h$ we introduce an error on the finer grid nh. But since that error is at small wavelengths we can easily smooth it out with an SOR sweep. The algorithm discussed in this paragraph is commonly referred to as multigrid V–cycle. It is illustrated in Figures E.2(a) and (b). We should recall that the partial solution of the problem on coarser grids serves two purposes. First, we are able to tackle errors in large wavelengths and second, we reduce computational effort. We will next need to detail the transformation operators between the grids.

Introductions to multigrid algorithms seem to focus on the application to the finite difference method. The location of boundaries with respect to the cells is, however, different in finite volume problems. Although the matrix solver should be able to solve problems independent of the physical problem considered, we will use an implementation that follows the intuitive spirit of the finite volume method. The two issues to be discussed are first how to transfer the residual to the next coarser grid (restrict the residual) and the error back to the next finer grid (prolong the error), and second how to obtain the matrix coefficients for the coarse grids.

Consider an alignment between coarse grid and fine grid such that the location of boundaries coincide (Figure E.2(a)). Any rate of change of an extensive property (momentum, energy, mass) on grid $2h$ corresponds to the sum of the rates of change of that extensive properties in the underlying fields in h. The rate of change of the extensive property is expressed by the source term $\mathbf{f}$ in (E.110). Remembering that the residual $\mathbf{r}$ in h relates to the source term $\mathbf{f}$ in $2h$ we define

$$f_P^{2h} = r_{NW}^h + r_{NE}^h + r_{SW}^h + r_{SE}^h, \tag{E.114}$$

$$\mathbf{f}^{2h} = I_h^{2h}\mathbf{r}^h. \tag{E.115}$$

The tensor I_h^{2h} is the restriction operator. For the one–dimensional case it is for a system with 4 fields in h

$$\mathbf{f}^{2h} = \begin{bmatrix} f_1^{2h} \\ f_2^{2h} \end{bmatrix} = \begin{bmatrix} 1 & 1 & & \\ & & 1 & 1 \end{bmatrix} \begin{bmatrix} r_1^h \\ r_2^h \\ r_3^h \\ r_4^h \end{bmatrix} = I_h^{2h}\,\mathbf{r}^h. \tag{E.116}$$

Similarly, in the prolongation step the error correction in a field in h is the corresponding field value calculated in $2h$. As field values are state variables like velocity, temperature, and concentration, they are not additive when transferred between grids. The state variable is expressed by $\mathbf{\Phi}$ in (E.110). We define

$$e^h_{NE} = e^h_{NW} = e^h_{SE} = e^h_{SW} = \Phi^{\star 2h}_P, \tag{E.117}$$

$$\mathbf{e}^h = I^h_{2h} \mathbf{\Phi}^{\star 2h}. \tag{E.118}$$

The tensor I^h_{2h} is the prolongation operator. For the one–dimensional case of a system with 4 fields in h, it is

$$\mathbf{e}^h = \begin{bmatrix} e^h_1 \\ e^h_2 \\ e^h_3 \\ e^h_4 \end{bmatrix} = \begin{bmatrix} 1 & & \\ 1 & & \\ & & 1 \\ & & 1 \end{bmatrix} \begin{bmatrix} \Phi^{\star 2h}_1 \\ \Phi^{\star 2h}_2 \end{bmatrix} = I^h_{2h}\, \mathbf{\Phi}^{\star 2h}. \tag{E.119}$$

The matrix coefficients of A represent fluxes through the interface of a cell, and transient contributions. The interface fluxes on a coarse grid $2h$ are the sum of the corresponding fluxes on the fine grid h, i.e.

$$\left.\begin{array}{rcl} a^{2h}_E &=& a^h_{(NE)E} + a^h_{(SE)E}, \\ a^{2h}_N &=& a^h_{(NW)N} + a^h_{(NE)N}, \\ a^{2h}_W &=& a^h_{(NW)W} + a^h_{(SW)W}, \\ a^{2h}_S &=& a^h_{(SW)S} + a^h_{(SE)S}, \end{array}\right\} \tag{E.120}$$

and accounting for the fluxes between cells in h that are contained in a single cell in $2h$ we find

$$a^{2h}_P = \sum_{\substack{j=\{P,N,S,E,W\} \\ i=\{NW,NE,SW,SE\}}} a^h_{(i)j} - \sum_{k=\{N,S,E,W\}} a^{2h}_k. \tag{E.121}$$

For the one–dimensional case with 4 fields in h, the matrix A^h is defined in (E.104), and the corresponding matrix A^{2h} is

$$A^{2h} = \begin{bmatrix} a^{2h}_{1P} & a^{2h}_{1E} \\ a^{2h}_{2W} & a^{2h}_{2P} \end{bmatrix} = \begin{bmatrix} a^h_{1P} + a^h_{1E} + a^h_{2W} + a^h_{2P} & a^h_{2E} \\ a^h_{3W} & a^h_{3P} + a^h_{3E} + a^h_{4W} + a^h_{4P} \end{bmatrix}. \tag{E.122}$$

Alternatively, combining (E.110), (E.113), (E.115), and (E.118) we find the Galerkin condition (*Briggs et al.*, 2000, p.75)

$$A^{2h}\, \mathbf{\Phi}^{2h} = I^{2h}_h\, A^h\, I^h_{2h}\, \mathbf{\Phi}^{2h}, \tag{E.123}$$

a general definition for the coarse grid operator A^{2h}. Applied to our one–dimensional

example we notice that it is, indeed,

$$
\begin{aligned}
I_h^{2h} A^h I_{2h}^h &= \begin{bmatrix} 1 & 1 & & \\ & & 1 & 1 \end{bmatrix} \begin{bmatrix} a_{1P}^h & a_{1E}^h & & \\ a_{2W}^h & a_{2P}^h & a_{2E}^h & \\ & a_{3W}^h & a_{3P}^h & a_{3E}^h \\ & & a_{4W}^h & a_{4P}^h \end{bmatrix} \begin{bmatrix} 1 & \\ 1 & \\ & 1 \\ & 1 \end{bmatrix} \\
&= \begin{bmatrix} a_{1P}^h + a_{1E}^h + a_{2W}^h + a_{2P}^h & a_{2E}^h \\ a_{3W}^h & a_{3P}^h + a_{3E}^h + a_{4W}^h + a_{4P}^h \end{bmatrix} \\
&= A^{2h}. \qquad \text{(E.124)}
\end{aligned}
$$

We will use an optimised version of the multigrid V-cycle described on page 328. In the V–cycle shown in Figure E.2(b) we start at the finest grid, relax the initial guess and restrict the residual to the next coarser grid. We repeat this procedure on subsequently coarser grids initially guessing that the error will be zero. We finally reach the coarse grid where we solve the residual equation. We then successively prolong the error and relax the solution back to the finest grid. This V–cycle supposes that we are in possession of an initial guess on the finest grid. In the absence of a suitable guess we may obtain a starting point for the V–cycle from multigrid cycles on coarser grids as follows. Assuming initially the solution on the finest grid (and on all coarser grids) be zero we can restrict $\mathbf{f}^h$ straight to the coarsest grid, and solve the residual equation there. We then prolong the error to the next finer grid, and start a V–cycle from there, prolong the result to the next finer grid, and so on, until we reach the finest grid. Thus, we have obtained an initial guess for the finest grid and continue with a V–cycle from there. This cycle is referred to as full multigrid V–cycle (illustrated in Figure E.2(c)). The extra cycles necessary to obtain the initial guess generally pay for themselves.

We will use full multigrid V-cycles with typically one or two relaxations before restriction, and three relaxations after prolongation on each grid.

E.5 Surface boundary condition

The boundary conditions of the modified Stefan model in Section 3.2.4 are applied to the CFD model. Their implementation for the surface boundary (north) is described here. The boundary condition is

$$
\begin{aligned}
(T_a - T_i)\mathfrak{h} &= \frac{\partial T}{\partial y} k_n, \qquad \text{(E.125)} \\
&= \frac{T_i - T_P}{\frac{\Delta y}{2}} k_n, \qquad \text{(E.126)}
\end{aligned}
$$

with $k_n = d_n(\Delta y)^2$ the heat conductivity at the boundary derived from the diffusion coefficient d_n of the discretised equation (E.83), $\mathfrak{h} = k/h_0$ the heat transfer coefficient, T_i the temperature at the interface, T_a the air temperature, T_P the temperature in cell P, and Δy the linear dimension of the cell. The interface temperature is therefore

$$
T_i = T_P \frac{1}{1+\gamma} + T_a \frac{\gamma}{1+\gamma}, \qquad \text{(E.127)}
$$

where

$$\gamma = \frac{\mathfrak{h}\Delta y}{2k_n}. \tag{E.128}$$

We impose a von Neumann boundary condition, i.e.

$$\frac{T_N - T_P}{\Delta y} k_n = \frac{\partial T}{\partial y} k_n, \tag{E.129}$$

$$= \frac{T_i - T_P}{\frac{\Delta y}{2}} k_n, \tag{E.130}$$

from which we find that the temperature in N is

$$T_N = 2T_i - T_P, \tag{E.131}$$

i.e. the temperature at the interface T_i is the linear average of the temperatures in cell P and in the imaginary cell N.

After substitution of (E.127) into (E.131) and (E.131) into

$$a_N T_N + a_P T_P + a_S T_S = f \tag{E.132}$$

it becomes

$$a_N \left[2\left(T_P \frac{1}{1+\gamma} + T_a \frac{\gamma}{1+\gamma} \right) - T_P \right] + a_P T_P + a_S T_S = f, \tag{E.133}$$

$$\left[a_P - a_N \frac{1-\gamma}{1+\gamma} \right] T_P + a_S T_S = f - 2a_N T_a \frac{\gamma}{1+\gamma}. \tag{E.134}$$

The transfer coefficients are therefore adjusted according to

$$f \to f - 2a_N T_a \frac{\mathfrak{h}\Delta y}{2k_n + \mathfrak{h}\Delta y}, \tag{E.135a}$$

$$a_P \to a_P - a_N \frac{2k_n - \mathfrak{h}\Delta y}{2k_n + \mathfrak{h}\Delta y}, \tag{E.135b}$$

$$a_N \to 0. \tag{E.135c}$$

E.6 Finite permeability

The permeability cannot be set to zero, or even arbitrarily small, in simulations that account for volume expansion upon freezing. When brine pockets in sea ice cool, some liquid freezes and expands in volume. This results in a pressure build–up and leads to brine expulsion, possibly after micro–cracking. While in natural sea ice this pressure relief can take place towards the top, the bottom, or into air inclusions, the fluid dynamics model allows relief in only one direction: towards the bottom of the domain. This is the location of the open boundary that is designed to enforce global volume conservation at the expense of mass conservation. Therefore, from every location in

the domain that experiences phase transition there has to exist a possible path of fluid motion towards the open boundary.

The flow resistance along this pressure relief path cannot be arbitrarily large. Since the mass conservation equation is enforced through the pressure term, large flow resistances cause large pressure gradients to develop: in a numerical model local mass conservation is never achieved exactly (even a relative error of 10^{-10} is not exact). In order to avoid the development of numerical mass sources and sinks in transient calculations the accumulated mass deficit or mass surplus of each computational cell has to be recorded, and it has to be added as additional source term to the pressure correction (mass conservation) equation (*Patankar*, 1980). This is equivalent to making the incompressible fluid compressible: if complete mass conservation cannot be achieved in one time step, then the pressure builds up (or reduces), and mass conservation is enforced again during the following time step with increased forcing. The numerical model is therefore perfectly capable of producing stable solutions in the absence of local mass conservation. A situation prone to low frequency pressure oscillations can occur if islands of high permeability develop that are completely enclosed by a ring of low permeability. Should the range of permeabilities be large enough and the thermodynamic condition be suitable (the exact relationship is unknown to me) then pressure will slowly build up in the island, reach a threshold, slowly be relieved, an underpressure will develop, reach a threshold, and slowly be relieved, and so on. Periods of this numerical oscillation (in simulated time) are in the low minute region and independent of time step. They therefore appear to be real phenomena, while in fact they are more likely to be a manifestation of a situation in which the code operates at the numerical resolution limit.

There are two things that can be done about this situation: either manual intervention can be used to melt a bit of ice in the low permeability ring, leading to instantaneous pressure relief, or the permeability can be artificially kept above a numerically critical value such that these low frequency oscillations do not appear in the first place. In practice, a permeability of $10^{-20}\,\mathrm{m}^2$ is often big enough to avoid oscillations, although occasionally they appeared even at permeabilities as high as $10^{-14}\,\mathrm{m}^2$. For consistency, the lower limit of permeability has been fixed to $10^{-13}\,\mathrm{m}^2$ in the simulations discussed in this project.

Appendix F

Development of the permeability–porosity relationship

F.1 Distribution coefficient – *Cox and Weeks* (1975)

Cox and Weeks (1975) give extensive salinity profile data in their appendices that allow us to estimate the stable distribution coefficient k_{eff}^{stable} of their experiments. Naturally, their data are scattered (typically less than ± 1 psu), even once salinity has stabilised. However, this is not of concern to us since the purpose of this exercise is only to get an approximate measure of the magnitude of their experimental k_{eff}^{stable}. *Cox and Weeks* give several salinity profiles of two experimental runs taken at various times throughout the experiment. No data are given for the skeletal layer that *Cox and Weeks* assume to be of constant thickness.

1st method For each of the first few profiles taken at time t for each run, we take the bottommost salinity S_i at depth d, estimate the growth velocity v from

$$v = \Delta d / \Delta t \tag{F.1}$$

between two consecutive profiles, and calculate the distribution coefficient from

$$k_{eff}^{stable} = \frac{S_f}{S_w}, \tag{F.2}$$

where S_f is the salinity at depth d at the end of the freezing experiment, and S_w is the time–dependent salinity of the water. We estimate S_w based on the average salinity of the ice sheet, $\bar{S}$, thickness of the ice ,d, and the height, H, of the growth chamber. We substitute

$$S_w = S_0 + (S_0 - \bar{S}) \frac{d}{H - d} \frac{\rho_i}{\rho_w}, \tag{F.3}$$

where $H = 690\,\mathrm{mm}$ is the height of the growth chamber, $\rho_i = 920\,\mathrm{kg\,m^{-3}}$ and $\rho_w = 1000\,\mathrm{kg\,m^{-3}}$ are densities of ice and water, respectively, $\bar{S}$ is the average salinity of the already grown ice sheet, and $S_0 = 34.7\,\mathrm{psu}$ is the salinity of the water at the beginning of the run. The temperature at the cooling interface was $-20\,^{\circ}\mathrm{C}$ in run 2 and $-10\,^{\circ}\mathrm{C}$

Table F.1: Data taken from appendix C and appendix D of *Cox and Weeks* (1975) to estimate the stable distribution coefficient of the laboratory experiments of *Cox and Weeks*. Water salinity was $S = 34.7$ psu at the beginning of the experiment. Terminal salinities S_f are taken from profiles R2–14 (582 h) and R3–17 (950 h), respectively.

profile	t (h)	d (cm)	S_i (psu)	S_f (psu)	$\bar{S}$ (psu)
R2–3	9	9	28.5	12.3	21.9
R2–4	13	13	30.7	10.9	19.2
R2–5	48	21	35.5	9.6	15.6
R2–6	76	26	58.5	11.1	14.5
R2–7	101	29	39.0	8.3	14.7
R2–8	124	32	–	–	–
R3–3	15	7	29.1	7.5	16.5
R3–4	22	9	32.3	6.5	14.3
R3–5	54	14	36.0	6.2	11.8
R3–6	77	17	42.9	6.1	11.4
R3–7	104	19	–	–	–

Table F.2: Calculated stable distribution coefficients k_{eff}^{stable} as a function of growth velocity v from laboratory data of *Cox and Weeks*.

	v ($\mathrm{m\,s^{-1}}$)	k_{eff}^{stable}	2nd method k_{eff}^{stable}
Run 2	1.23E-06	0.34	0.35
	7.41E-07	0.29	0.29
	4.96E-07	0.23	0.22
	3.33E-07	0.24	0.16
	3.62E-07	0.17	0.18
Run 3	7.94E-07	0.21	0.22
	4.34E-07	0.17	0.17
	3.62E-07	0.16	0.14
	2.06E-07	0.15	0.12

in run 3. Data used to calculate k_{eff}^{stable} is listed in Table F.1, and the corresponding calculated distribution coefficients are shown in Table F.2.

However, Table F.1 also shows the initial salinity of the sea ice, S_i, just above the skeletal layer. Run R2–6 has a large final salinity, S_f, which is apparently related to the large initial salinity S_i. However, using (F.3), S_i is not considered in the estimate of stable distribution coefficient. We will therefore validate the results with a second approach, estimating the water salinity close to the interface, S_w, from the initial salinity.

2nd method Assuming a constant initial distribution coefficient, k_{eff}, we can estimate the salinity at the freezing interface, S_w, from the initial salinity salinity of the ice, S_i,

$$S_w = \frac{S_i}{k_{eff}}. \tag{F.4}$$

With data from the first profile of each run, R2–3 and R3–3, it is $k_{eff} = S_i/34.7 = 0.83$. Using the definition of (F.4) with $k_{eff} = 0.83$ for all salinity profiles, we obtain the stable distribution coefficients listed in Table F.2 from (F.2). The resulting values for k_{eff}^{stable} are consistent with the ones obtained previously. The expected exception is run R2–6, which now fits the trend.

Another uncertainty is in the estimate of v. One might argue that instead of using forward differences one could use backward differences, or more sophisticated schemes. In either case velocities would be systematically lower than listed. Alternatively, this is equivalent to saying their k_{eff}^{stable} is in fact higher than listed in Table F.2.

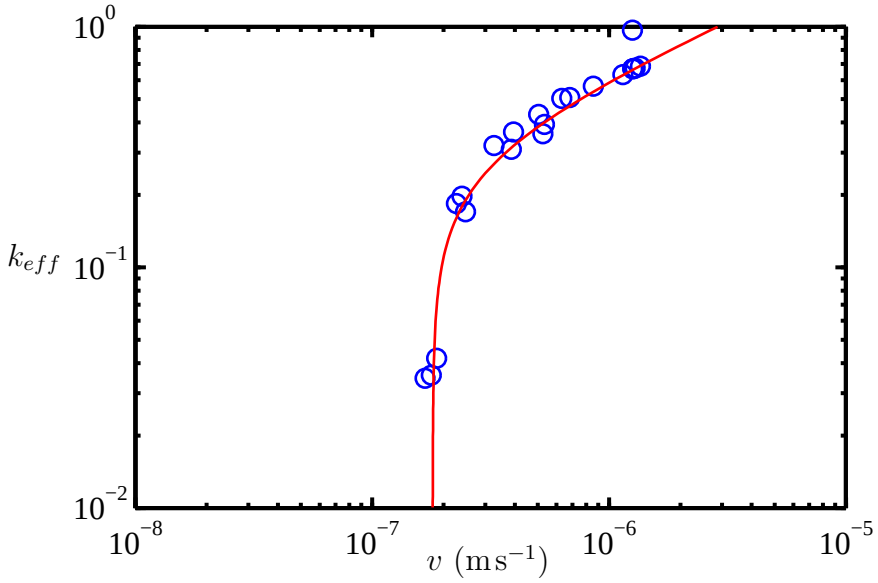

Figure F.1: Data of *Wakatsuchi and Ono* (1983) scaled as distribution coefficient k_{eff} as a function of growth velocity v. Note that the distribution coefficient may be in between stable distribution and initial distribution.

F.2 Distribution coefficient – *Wakatsuchi and Ono* (1983)

Wakatsuchi and Ono (1983) measure the amount of brine expelled during ice growth by catching brine plumes with a funnel. The laboratory tank is $0.5 \times 0.44\,\mathrm{m}^2$ at the top, and 0.75 m deep, the experiments in the Arctic are performed in pools inside ice sheets with top cross section $2 \times 2\,\mathrm{m}^2$ and pool depths of 0.85 m and 0.90 m, respectively. The measurements are averages of the growth of an ice sheet of 40 to 90 mm thickness or of sections of ice sheets, each 40 to 55 mm high.

We will derive from their data the distribution coefficient, k_{eff}, and the ratio of brine plume salinity to seawater salinity, S_b/S_0.

F.2.1 Distribution coefficient

One way they present their data is as mass density of salt ($\mathrm{kg\,m^{-3}}$) rejected from the ice versus average growth velocity v. Since they also give the salinity, S_w, of the water, we may calculate an effective distribution coefficient, k_{eff}, from their data. We assume for simplicity that $1\,\mathrm{kg\,m^{-3}} = 1$ psu for the range of 0 to 35 psu. The error in this is less than 4 %. Figure F.1 shows their scaled data together with a line drawn by eye. The line follows the form

$$k_{eff} = 0.119 \left(\frac{v - 1.8 \times 10^{-7}\,\mathrm{ms^{-1}}}{1.35 \times 10^{-7}\,\mathrm{ms^{-1}}} \right)^{0.451} . \tag{F.5}$$

The distribution coefficient cannot necessarily be viewed as an initial distribution coefficient as *Wakatsuchi and Ono* observe brine channels, at least in experiments at low

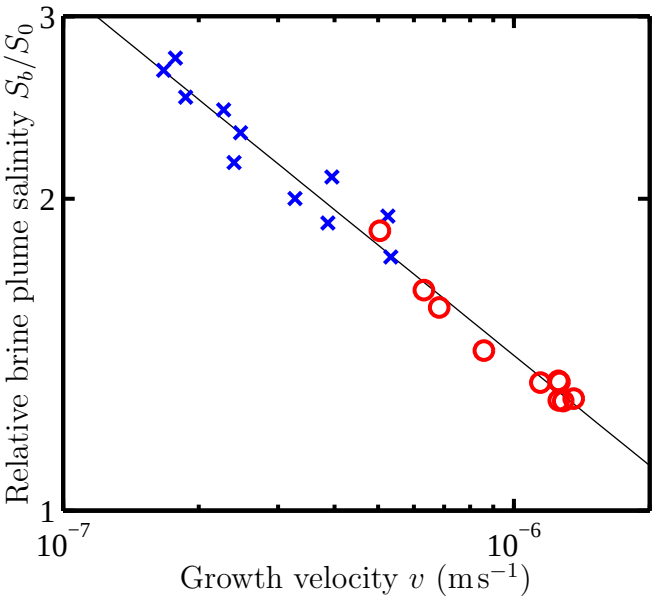

Figure F.2: Brine plume salinity derived from data of *Wakatsuchi and Ono* (1983) as a function of growth velocity v. Crosses refer to laboratory experiments, circles are from experiments in the Arctic.

growth velocity v. The scale in Figure F.1 is similar to Figure 5.3, but the vertical axis stretches over two orders of magnitude. The group of three points of very low k_{eff} arises from a single experiment at constant growth rate. The significance of the observation of almost complete brine drainage at an velocity as high as $2 \times 10^{-7}\,\mathrm{m\,s^{-1}}$ is not quite clear. Results for high growth rates, however, fit reasonably well into Figure 5.3.

F.2.2 Brine plume salinity

Wakatsuchi and Ono (1983) give ice sheet thickness and time of growth for all of their experiments, which allows the average growth velocity, v, to be calculated. They further give the salinity of the water at the beginning and at the end of the experiment, and they give the calculated salinity of the brine plumes, S_b. We use the linear average of initial and final water salinity as reference salinity S_0. The enrichment of brine plumes with respect to the salinity of the water is shown in Figure F.2 as a function of growth velocity. The best fit power law shown in Figure F.2 follows

$$\frac{S_b}{S_0} = 0.0107\, v^{-0.353}, \tag{F.6}$$

with growth velocity v in $\mathrm{m\,s^{-1}}$. According to the relationship (F.6), the salinity of brine plumes emerging from ice growing at $v = 10^{-7}\,\mathrm{m\,s^{-1}}$ and $v = 10^{-6}\,\mathrm{m\,s^{-1}}$ is $S_b = 100\,\mathrm{psu}$ and $S_b = 50\,\mathrm{psu}$, respectively ($S_0 = 34\,\mathrm{psu}$).

Table F.3: INTERICE I velocity and salinity data. The initial water salinity is $S_0 = 32\,\mathrm{psu}$, the under–ice current is $0.16\,\mathrm{m\,s^{-1}}$.

Depth (m)	interpolated velocity v ($10^{-7}\,\mathrm{m\,s^{-1}}$)	mean salinity S_{ice} (psu)	$k_{eff} = S_{ice}/S_0$	
0.01	4.25	7.45	0.233	
0.03	3.92	5.8	0.181	(plotted)
0.05	3.55	5.55	0.173	(plotted)
0.07	3.16	5.425	0.170	
0.09	2.77	5.9	0.184	
0.11	2.39	11.05	0.345	

Table F.4: Summary of dependencies of some sea ice properties on under–ice current, u, and growth velocity, v.

	if u increases...	if v increases...
platelet separation a_0	decreases	decreases
sea ice salinity S_{ice}	decreases	increases
total porosity f_t	decreases	increases

F.3 Distribution coefficient – INTERICE I

Ice growth during the INTERICE I tank experiments took place at the Hamburgische Schiffbauversuchsanstalt in a basin of size $30 \times 6 \times 1.2\,\mathrm{m^3}$ that was filled with artificial seawater of salinity $S_0 = 32\,\mathrm{psu}$ prepared by dissolving Aquarium Systems "Instant Ocean" seasalt in tapwater (*Eicken*, 1998; *Eicken et al.*, 2000). Data shown in Section 5.2.2 aries from a freezing experiment run at air temperature $-17.5\,^\circ\mathrm{C}$ with imposed under–ice water current of $0.16\,\mathrm{m\,s^{-1}}$. Measurements of the position of the freezing interface were fitted to an exponential function to derive the velocity versus time relationship. Four cores were taken at the end of the experiment to measure the ice sheet salinity. The cores were sectioned into samples of 0.02 m height, and salinity measurements were averaged for each height. The cores are dated 9 December, 1996. Both velocity and salinity data have been used in *Eicken* (2003). Data provided by *Hajo Eicken* (personal communication) are shown in Table F.3. Also marked are the two data points plotted in Section 5.2.2 that are deemed to reflect stable salinity.

F.4 The effect of under–ice currents and growth velocity

The purpose of this section is to summarise the influence of under–ice currents and growth velocity on sea ice salinity, porosity, and platelet separation (as has been done in Table F.4). The incentive is to find an explanation for the differences of the sea ice salinities observed in different experiments (Section 5.2.2), with attention to the platelet structure that we used to describe the relationship between effective and total porosity in Section 5.4.2.

F.4.1 Platelet structure

Current velocity As far as the platelet structure of sea ice is concerned it has been suggested (*Lofgren and Weeks*, 1969) and observed (*Haas*, 1999; *Eicken et al.*, 2000) that the platelet separation a_0 decreases with increasing under–ice current velocity u. In fact, sea ice grown in the presence of large currents loses the orderly arrangement of brine layers and sub–layers (*Haas*, 1999; *Eicken et al.*, 2000). *Lofgren and Weeks* (1969) suggest that the principal reason for the decreases of a_0 with increasing u is the reduction of salinity at the freezing interface to values closer to the salinity of the liquid reservoir. Experiments of *Rohatgi and Adams* (1967) indicate that platelet separation a_0 increases with increasing salinity of the water.

Growth velocity According to *Bolling and Tiller* (1960), the platelet separation a_0 decreases with increasing sea ice growth velocity v following

$$a_0\, v = \mathcal{R} \tag{F.7}$$

at small v and in the absence of under–ice currents u. According to measurements of *Lofgren and Weeks* (1969) small growth velocities in this sense are $v \leq 10^{-6}\,\mathrm{m\,s^{-1}}$. The constant of proportionality, $\mathcal{R}$, is $\mathcal{R} = 1 \times 10^{-10}\,\mathrm{m^2\,s^{-1}}$ and $\mathcal{R} = 5 \times 10^{-10}\,\mathrm{m^2\,s^{-1}}$ in field experiments of *Nakawo and Sinha* (1984) and laboratory experiments of *Lofgren and Weeks* (1969), respectively. A thin section of INTERICE I and INTERICE II tank experiments (*Eicken et al.*, 1998; *Haas et al.*, 1999) shown by *Haas* (1999) suggests that $\mathcal{R}$ is probably in the same range as the two results mentioned above. The constant of proportionality predicted by the model of *Bolling and Tiller* (1960) is $\mathcal{R} = 1 \times 10^{-10}\,\mathrm{m^2\,s^{-1}}$ for a solute diffusion coefficient $D = 7 \times 10^{-10}\,\mathrm{m^2\,s^{-1}}$ (*Eicken*, 1998). To explain the differences in $\mathcal{R}$ we should probably consider the differences in the experimental conditions. The cooling surface in the experiments is a constant temperature plate (*Lofgren and Weeks*, 1969), air at approximately constant temperature (*Haas*, 1999), and a surface exposed to natural changes in ambient conditions (e.g. air temperature, solar radiation, snow cover) (*Nakawo and Sinha*, 1984), respectively. Further, ice was grown in a small ($0.01\,\mathrm{m^3}$) apparatus (*Lofgren and Weeks*, 1969), a large ($180\,\mathrm{m^3}$) tank (*Haas*, 1999), and in the Eclipse Sound (water depth $150 - 660\,\mathrm{m}$) (*Nakawo and Sinha*, 1984), respectively. The ice of *Nakawo and Sinha* (1984) is aligned, indicating the presence of some current. *Nakawo and Sinha* (1984) also observe that a correlation exists between c–axis orientation and platelet spacing. The size of the tank should also affect the convection pattern. While the reason for the difference in $\mathcal{R}$ cannot be nailed down at this point, it is clear that the measurements of platelet spacing versus growth velocity referred to in this paragraph were conducted under different circumstances, i.e. they may simply not be comparable without a theory accounting for the different growth conditions (thermal, current).

F.4.2 Salinity and porosity

Growth velocity As far as the amount of solute retained in sea ice is concerned, there seems to be little doubt that the amount of solute retained in the sea ice generally

increases with increasing sea ice growth velocity v (*Weeks and Lofgren*, 1967; *Cox and Weeks*, 1975; *Nakawo and Sinha*, 1981). Simply speaking, rejected solute is removed from the freezing front at a certain rate, and as the ice growth velocity increases more solute is trapped in the ice matrix. Since entrapped brine is in thermodynamic equilibrium with the surrounding ice an increase in salinity is equivalent to an increase in porosity at a given temperature. However, the actual amount of solute retained seems to vary by at least a factor of 2 for a given velocity v between experiments. Measurements on the small side are the laboratory experiments of *Cox and Weeks* (1975), while measurements on the large side are experiments in Eclipse Sound of *Nakawo and Sinha* (1981). Experiments of *Wakatsuchi* (1983) and *Wakatsuchi and Ono* (1983) are consistent with *Nakawo and Sinha*.

Current velocity The tank experiments of *Eicken et al.* (1998) that are performed at high under–ice currents u are consistent with the results of *Cox and Weeks* (1975). Since the experiments of *Cox and Weeks* (1975) were performed in a small apparatus, we may conclude that similar under–ice currents were present during freezing as those assumed to be present by *Lofgren and Weeks* (1969) in their own experiments. In a direct comparison of two ice samples grown in the absence of under–ice currents and in the presence of under–ice currents, respectively, *Eicken et al.* (2000) find the lower porosity in the ice grown in the presence of under–ice currents. Supposing thermodynamic equilibrium, this means that the sea ice salinity decreases with increasing under–ice current u. This conclusion is consistent with the boundary layer thickness argument used by *Verbeke et al.* (2002) to correlate under–ice currents with sea ice salinity. The different stable distribution coefficient of *Cox and Weeks* (1975) and *Nakawo and Sinha* (1981) seen in Figure 5.4 may therefore be due to the presence of currents of significant magnitude in the experiments of *Cox and Weeks* (1975).

F.4.3 Summary

There appears to be no one–to–one relationship between platelet structure and sea ice salinity. Both structure and salinity decrease with increasing current u as a consequence of a reduction in salinity at the freezing interface. An increased growth velocity v results in a decreased brine layer spacing and increased salinity essentially because solute is not removed fast enough from the interface to avoid getting trapped. An effect of platelet spacing on sea ice salinity should therefore only come about indirectly through modifications of fluid flow through sea ice.

Appendix G

Monte Carlo model

G.1 Algorithm

This section outlines the algorithm of the Monte Carlo model. A large number of pockets (of the order of 10^6), their interconnections and their overlaps have to be managed. Present day processors operate at speeds that are much higher than memory can be accessed in random order. For example, the desktop computer used for the present simulations needs 88 and 273 clock cycles for the execution of a random (non–cached) read and write access, respectively, which is slow considering that the processor is able to perform three independent floating point operations in a single clock cycle (numbers are based on own measurements). The maxim of the algorithm is therefore to keep random memory access to a minimum. The strategy followed is to replace search loops by lists wherever possible, and to update lists and to update (not to recalculate) all parameters required for later analysis every time a new pocket is added. This refers specifically to volume fractions f_t and f_e, volume fractions of individual clusters, membership of pockets to clusters, and to flags indicating if a certain cluster connects to a specific domain boundary.

Regions Since a test of overlap (hit test) has to be performed every time a pocket is added, the domain is divided into regions, and a list is kept for each region indicating which pockets fall (partially or completely) into a particular region. Upon the addition of a new pocket, the region(s), intersected by that pocket, are determined and a hit test is performed only with pockets whose indices are entered in the particular lists.

Hit test The hit test is performed recursively. If an intersection of the new pocket with an existing pocket is detected, the volume of the newly added pocket is split into as many as 8 rectangular sub–volumes of which one volume is identical to the overlap. At the same time, the volume size of the new pocket is reduced by the size of the overlapping volume. The hit test is continued with all sub–volumes that did not overlap. Once a hit test has been performed with all relevant pockets, clusters are joined if the pocket was found to connect to more than one cluster. Clusters are joined by changing the cluster assignment of all pockets of one of the clusters, appending the pocket member list of one cluster to the pocket member list of another cluster,

updating cluster volume and boundary intersection flags, and entering a pointer to the now obsolete cluster data structure of one of the clusters to the obsolete–cluster list for future quick reference (i.e. an empty data structure will be found without loop). Finally, an index to the new pocket is added to the cluster, the pocket index is added to the relevant region lists, and the cluster assignment of that pocket is set. The cluster volume is increased by the non–overlapping volume of the new pocket, and the boundary intersection flags of the cluster are updated depending on the location of the new pocket.

For the sandwich model: if the new pocket does not connect to any cluster, and if it falls entirely into a "platelet", then the pocket is rejected.

Periodic boundaries Periodic boundaries are simulated by modifying the entry point of the hit test. First, it is checked whether the new pocket intersects a periodic boundary. Should that be the case then the pocket is split into two sub–pockets, one sub–pocket on either side of the boundary. The sub–pocket outside the domain is then repositioned to the opposite side of the domain, and the periodic boundary entry point is called again, once with each of the two generated sub–pockets. (This recursive call is used since a pocket may have to be split multiple times in three dimensions.) Finally, the clusters of the two sub–pockets are joined (unless both have been assigned to the same cluster), and the pocket counter of that cluster is adjusted to ensure that pockets intersecting periodic boundaries are not counted twice.

For the sandwich model: should one of the sub–pockets have been added successfully, while the other sub–pocket has been rejected since it fell into a "platelet" then the rejected pocket will be added, anyway.

G.2 Critical porosity

Table G.1 shows critical porosities determined for the systems of concern to us from Monte Carlo experiments by various groups (*Baker et al.*, 2002). Also shown are results for average critical porosities determined from the present model for different domain sizes. Some experimental observations for three dimensional percolating systems are further summarised by *Janzen* (1975). Since the critical porosity is expected to scatter if the domain is finite (*Berkowitz and Ewing*, 1998), the mean $\bar{f}_c$ and standard deviation σ of the distribution are given in Table G.1. The 95 % confidence interval is calculated as $1.96 \times \sigma/\sqrt{N}$. Alternative methods to find the percolation threshold of the present model could involve curve fitting or extrapolation (*Baker et al.*, 2002; *Thomsen*, 2002; *Yi and Sastry*, 2004). (For example, one may use the convergence of the critical porosity $\bar{f}_{c,L}$ as a function of domain size L (*Stauffer and Aharony*, 1992),

$$\bar{f}_{c,L} - f_c \propto L^{-1/\nu}, \tag{G.1}$$

where L is the size of the finite domain (domains of $L \times L$ ($2d$) or $L \times L \times L$ ($3d$)), f_c is the percolation threshold for an infinite domain, and the coefficients ν are $\nu = 4/3$ and $\nu \approx 0.88$ in $2d$ and $3d$, respectively. Data in Table G.1 scatter a bit, but reasonably straight lines can be obtained for $f_c = 0.6670$ and $f_c = 0.2771$ in two and three

Table G.1: Percolation threshold f_c for squares and cubes. Determination is by Monte Carlo simulation unless otherwise stated. For results of average percolation thresholds $\bar{f}_c$ from this work standard deviation σ, domain size and number of samples N are given. The 95% confidence interval for the mean is ± 1 of the least significant digit of the mean, apart from where the last digit is given in brackets.

system	critical porosity	f_e/f_c (%)	comment
squares	$f_c = 0.65 \pm 0.02$		cited in *Baker et al.* (2002)
squares	$f_c = 0.6666 \pm 0.0004$		*Baker et al.* (2002)
squares	$f_c = 0.668 \pm 0.003$		cited in *Baker et al.* (2002)
squares	$f_c = 0.6753 \pm 0.0008$		cited in *Baker et al.* (2002)
squares, experiment	$f_c = 0.613 \pm 0.013$		cited in *Baker et al.* (2002)
squares	$\bar{f}_c = 0.663, \sigma = 0.097$	91	5×5, $N = 182113$
squares	$\bar{f}_c = 0.648, \sigma = 0.065$	79	10×10, $N = 134569$
squares	$\bar{f}_c = 0.651, \sigma = 0.042$	70	20×20, $N = 80688$
squares	$\bar{f}_c = 0.658, \sigma = 0.022$	61	50×50, $N = 40697$
squares	$\bar{f}_c = 0.661, \sigma = 0.013$	56	100×100, $N = 11607$
squares	$\bar{f}_c = 0.6635, \sigma = 0.0080$	51	200×200, $N = 50447$
squares	$\bar{f}_c = 0.665, \sigma = 0.0041$	46	500×500, $N = 1162$
squares	$\bar{f}_c = 0.665(9 \pm 2), \sigma = 0.0024$	44	1000×1000, $N = 722$
squares	$\bar{f}_c = 0.666(3 \pm 2), \sigma = 0.0015$	41	2000×2000, $N = 121$
squares	$\bar{f}_c = 0.666(5 \pm 3), \sigma = 0.0012$	40	3000×3000, $N = 79$
cubes	$f_c = 0.280 \pm 0.005$		cited in *Baker et al.* (2002)
cubes	$f_c = 0.2773 \pm 0.0002$		*Baker et al.* (2002)
cubes	$\bar{f}_c = 0.306, \sigma = 0.057$	74	$5 \times 5 \times 5$, $N = 130570$
cubes	$\bar{f}_c = 0.279, \sigma = 0.029$	47	$10 \times 10 \times 10$, $N = 6230$
cubes	$\bar{f}_c = 0.274, \sigma = 0.015$	30	$20 \times 20 \times 20$, $N = 3556$
cubes	$\bar{f}_c = 0.275, \sigma = 0.0055$	17	$50 \times 50 \times 50$, $N = 744$
cubes	$\bar{f}_c = 0.276, \sigma = 0.0025$	12	$100 \times 100 \times 100$, $N = 159$
cubes	$\bar{f}_c = 0.2768, \sigma = 0.0012$	8.7	$200 \times 200 \times 200$, $N = 538$
cubes	$\bar{f}_c = 0.276(9 \pm 2), \sigma = 0.00075$	6.8	$300 \times 300 \times 300$, $N = 278$

dimensions, respectively.) Table G.1 further shows the *average* ratio of effective porosity f_e and critical porosity f_c at the point where the critical porosity f_c is reached. The ratio f_e/f_c has a wider distribution than f_c (Figure G.1(b)). Figure G.1(a) shows the distributions of f_c for a domain 200×200, and Figure G.1(b) shows the corresponding dependence of f_e/f_c on f_c at f_c.

All domains are either cubical or square. If a domain is widened (leaving the size in the non–periodic direction constant), the distribution of f_c shifts towards lower porosities and distorts. This could be calculated by folding the distribution. Likewise, the distribution shifts towards larger porosities if the domain is made narrow.

The limiting factor of these Monte Carlo simulations is memory size. For example, our implementation uses approximately 1 GByte of memory for 10^7 pockets in a domain of size 3000×3000. In that domain, 1×10^7 pockets are needed to obtain percolation. Percolation in a domain $300 \times 300 \times 300$ requires approximately 9×10^6 pockets. Computation is rather quick, e.g. a single run from $f_t = 0$ to $f_t = f_c$ in a 200×200 domain takes less than one second on a desktop computer.

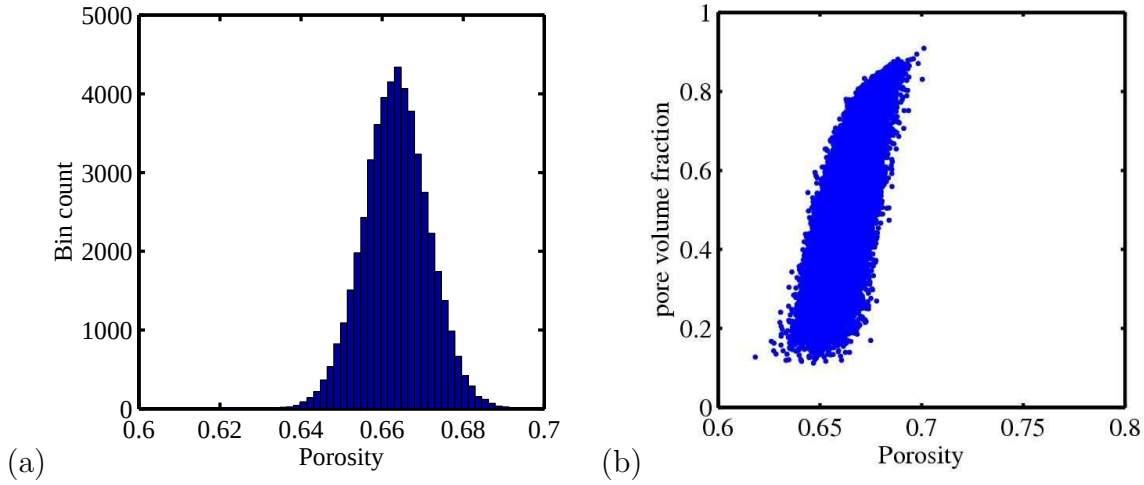

Figure G.1: (a) Histogram of the distribution of f_c from multiple runs in a domain 200×200. $N = 50447$. (b) Effective pore volume fraction f_e/f_c as a function of critical porosity f_c at the critical porosity of the same data set.

G.3 Cluster size distribution

We shall investigate the cluster size distribution produced by the Monte Carlo model of Chapter 5. We define the size of a cluster as the total *volume* occupied by the pockets it contains. *Perovich and Gow* (1996) analyse the size distribution of the horizontal cross sectional area of brine and air inclusions in sea ice. They fit their data to a lognormal distribution, which they have chosen based on quality of fit, small number of parameters, and physical meaningfulness. This observation is consistent with the suggestion of a lognormal distribution by *Eicken* (1991) which is likewise based on horizontal inclusion size distribution. In a later work, *Freitag* (1999) shows that his measurements of horizontal brine pocket area distribution can also be fitted to a lognormal distribution. *Eicken et al.* (2000) determine brine inclusion size distribution from vertical and horizontal thin sections, and from magnetic resonance imagery of sea ice. They do not fit data with any particular function. An analysis by eye of their published data suggests that, depending on the sample, either a lognormal distribution function or a power law may possibly be used to fit their data. *Light et al.* (2003) measure the vertical and horizontal brine pocket size distribution of sea ice of the same ice as *Perovich and Gow* (1996), but at lower temperature. They show that their data is best fitted to a power law distribution. The horizontal inclusion size distributions shown by *Cole et al.* (2004) suggest a power law distribution at small sizes that gets steeper towards larger inclusion sizes, possibly resembling a lognormal distribution as shown in the quantitatively very similar comparison of data of *Light et al.* (2003). Such a distribution appears to be similar to the observation by *Carmona and Ravier* (2003) in carbon black.

Based on these observations we expect to see model cluster size distributions of lognormal or power law type. On a loglog plot, a power law function produces a straight line, while a lognormal plot produces a curve that looks parabolic. As such, we may regard the power law function as a special case of the lognormal distribution function, in particular in regions far away from the maximum where (loglog) curvature is small. The lognormal probability density function (PDF) is

$$\mathrm{PDF}(v) = \frac{1}{\sqrt{2\pi}\,\sigma}\frac{1}{v}\exp\left(-\frac{1}{2}\left[\frac{\ln v - \mu}{\sigma}\right]^2\right), \tag{G.2}$$

where v is the dimensionless cluster volume, μ is the mean of $\ln v$, and σ is the standard deviation, or width of the distribution. The PDF is normalised, i.e. the infinite integral is 1. Although it would be worth considering, we will not perform fits to other functions, in particular piecewise defined functions.

In order to categorise the cluster size distribution produced by the model we bin clusters logarithmically, normalise the count, calculate the probability density for each bin by dividing the normalised cluster count by the bin width, and fit the logarithm of the resulting distribution to the logarithm of

$$\mathrm{PDF}(v) = \frac{1}{A}\,\frac{1}{\sqrt{2\pi}\,\sigma}\frac{1}{v}\exp\left(-\frac{1}{2}\left[\frac{\ln v - \mu}{\sigma}\right]^2\right). \tag{G.3}$$

The cluster size v is expressed in multiples of pocket size. A scaling parameter A has been introduced in the fit function as a quality indicator. If we fit a normalised lognormal distributed set of data to (G.3), then the best fit value for A will be $A = 1$. If A is substantially different from 1 we can interpret this as sign for the inappropriateness of a lognormal fit[1]. In fact, we choose this approach from experience: the computer generated size distribution is sometimes close to or even obviously lognormal, while it is sometimes obviously power law. In order to avoid plotting every one of the hundreds of distribution functions individually to argue for or against power law, we will only plot the best–fit parameters A, μ, and σ and recognise the empirical (and not surprising) relationship between types of distribution and best–fit parameters. A power law distribution with a negative exponent (i.e. negative slope on a loglog plot) fitted with (G.3) will return μ close to negative infinity and A close to zero. This is the function–indicator used in the presentation of this chapter. Every single set of data and corresponding best–fit has been inspected by eye, and it has been found that the above approach is fully consistent with subjective human perception[2].

In the following discussion it is assumed that the pocket volume is always 1×1 in two dimensions, and $1 \times 1 \times 1$ in three dimensions. Domain sizes are given as multiples of the pocket size. We impose periodic boundaries in all but one dimension. The bins are sized such that they divide every change of one order of magnitude in cluster sizes into 15 bins[3].

Modelled cluster size distributions suffer from finite size effects close to the pocket size. Figure G.2 shows an example distribution with small bin sizes (100 bins per order of magnitude) that clearly reflects that it is much less likely for two or more pockets to form a cluster of volume $v = 1.1$ than it is for them to form a cluster of $v = 1.9$. This is a purely geometric constraint.

G.3.1 Infinite domain in two dimensions

As a qualitative introduction to the cluster size distributions we are concerned with, Figure G.3 shows four characteristic examples. Distributions at low porosities generally follow a lognormal relationship shown in Figure G.3(a). An increase in porosity changes the distribution such that the small clusters follow a power law distribution, while larger clusters still exhibit the curvature characteristic for lognormal relationships (Figure G.3(b)). The distribution turns into a power law around the percolation threshold as shown in Figure G.3(c) and as expected (*Stauffer*, 1986; *Stauffer and Aharony*, 1992). A non–normalised lognormal distribution shown in Figure G.3(d) develops upon further increase in porosity.

As pockets are continuously added to the domain the cluster size distribution changes with porosity. One apparent feature of this process is that the absolute number of clusters is highest at a porosity of about $f_t = 0.36$ in two–dimensional systems ($f_t = 0.17$ in three dimensions). At higher porosities, adding a pocket is more likely

[1] We also note that in the absence of free normalisation parameter A, best fit lines can be obtained (particularly at high porosities) that lie systematically below the observed probability density.

[2] Exceptions are small sets of scattered data, in which case best fit parameters are meaningless.

[3] As expected, fits obtained from linearly equally sized bins return almost the same fit coefficients as long as the range of volumes considered extends over not much more than one order of magnitude.

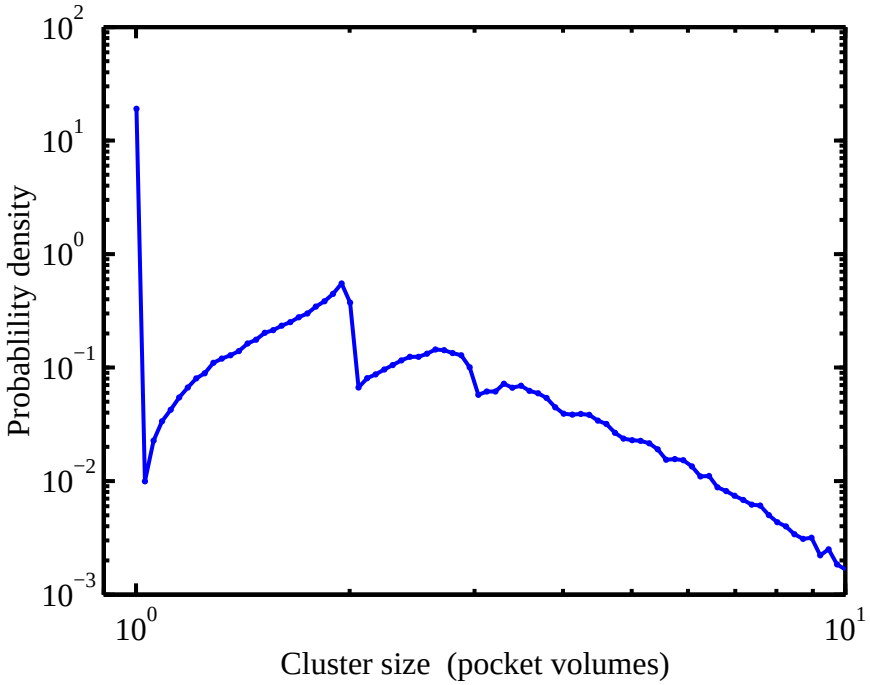

Figure G.2: Finite size effects of the cluster size distribution close to the pocket size at $f_t = 0.20$, domain size 1200×1200.

to join two clusters that had been previously independent than it is to produce a new, one–pocket cluster. Analogous observations have been made by *Perovich and Gow* (1996) and *Eicken et al.* (2000).

Figure G.4(a) shows the development of the cluster size distribution with porosity in a domain of size 2000×2000. Only clusters that do not connect to the non–periodic side are considered. We can clearly discern three regions. Below the percolation threshold μ and σ increase monotonically, around the critical threshold A reduces by several orders of magnitude, while the apparent mean cluster size $v = \exp \mu$ shifts to very small values, and σ increases. Here, it would be appropriate to fit a power law, instead of a lognormal distribution. Above the percolation threshold normalisation parameter A is still more than half an order of magnitude smaller than 1, although the distribution shows some curvature that fits well to the lognormal functional dependence. *Lubensky and McKane* (1981) give expressions for cluster size distributions well below and above the critical porosity, respectively.

Figure G.4(b) shows the region of monotonic increase of μ and σ. We see that, from about $f_t = 0.15$ to $f_t = 0.40$ σ increases by a factor 1.6, while $\exp \mu$ increases by a factor 1.8. These are essentially the same ratios as those shown in the inset of figure 12 in *Perovich and Gow* (1996) for the same range of porosities. The similarity in increase in cluster size, $\exp \mu$, might be expected if the brine inclusion area fraction in horizontal thin sections (measured by *Perovich and Gow*) is proportional to the brine inclusion volume fraction (i.e. cluster size) (Delesse theorem). *Eicken* (1991) and *Cole et al.* (2004) claim that the Delesse theorem applies for sea ice (*Yi et al.* (2004) suggest a method to verify the random distribution of inclusions).

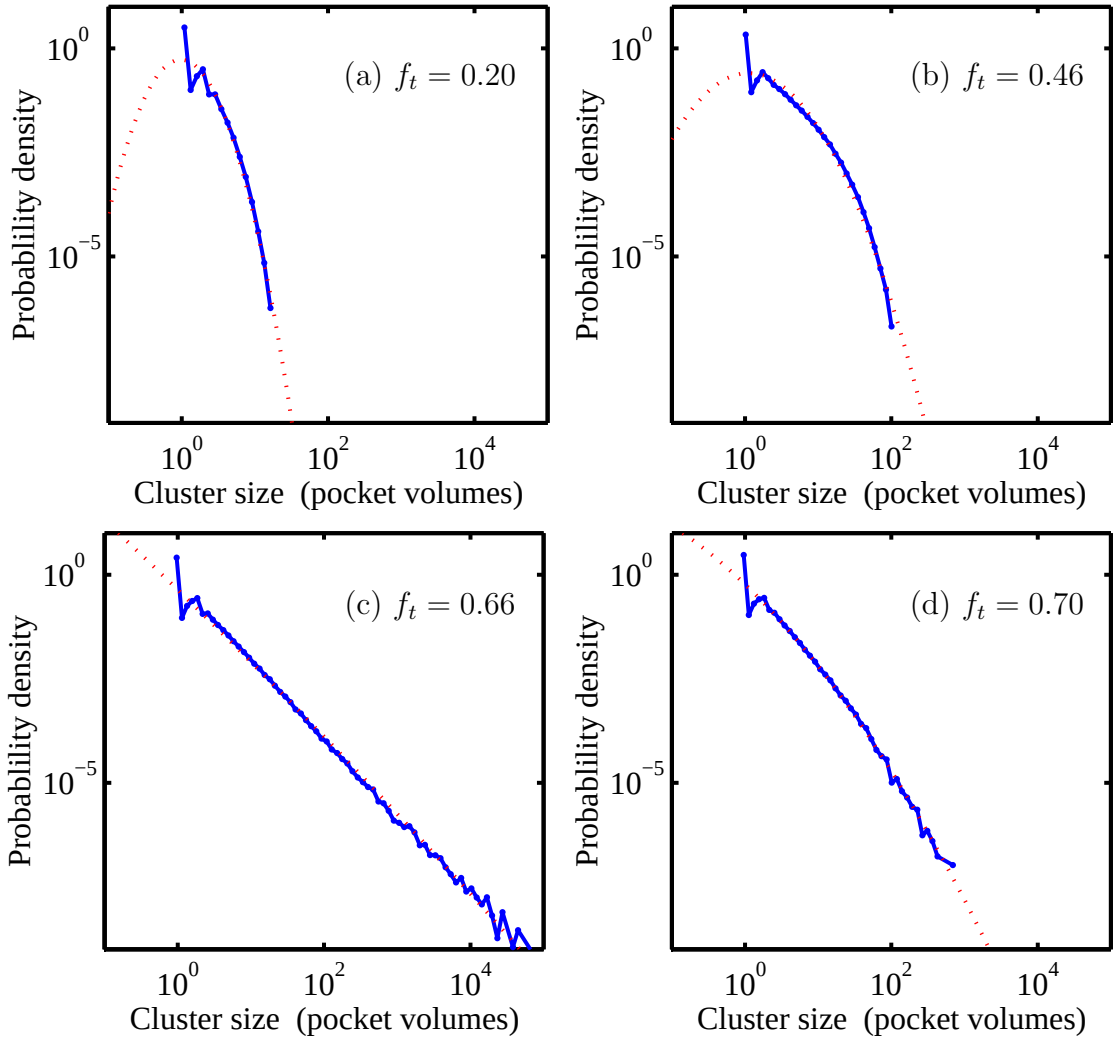

Figure G.3: Cluster size distributions of clusters that do not interact with any side of the domain (a) at $f_t = 0.20$, fit to the lognormal curve shown by the dotted curve; (b) at $f_t = 0.46$, systematic deviations from the lognormal curve in the form of straight lines on the loglog plot; (c) at $f_t = 0.66$, power law; (d) at $f_t = 0.70$, non–normalised lognormal.

G.3.2 Distribution in three dimensions

The cluster size distribution in three dimensions (Figure G.5(a) and (b), domain size $200 \times 200 \times 200$) follows a similar pattern to the distribution in two dimensions. A lognormal distribution is assumed at low porosities, that slowly widens (σ increases) and shifts towards larger mean cluster sizes (μ increases), until power law distribution is assumed at the critical porosity of about 0.28. From then on the distribution follows a non–normalised lognormal distribution, until at even higher porosities above 0.50 the distribution become ambiguous but seems closer to power law than to lognormal.

Figures G.6(a) and (b) show the cluster size distributions of a domain $200 \times 200 \times 200$ at $f_t = 0.10$ ($N = 530000$ clusters) and at $f_t = 0.20$ ($N = 570000$ clusters), respectively, and Figures G.7(a) and (b) show the cluster size distributions of a domain

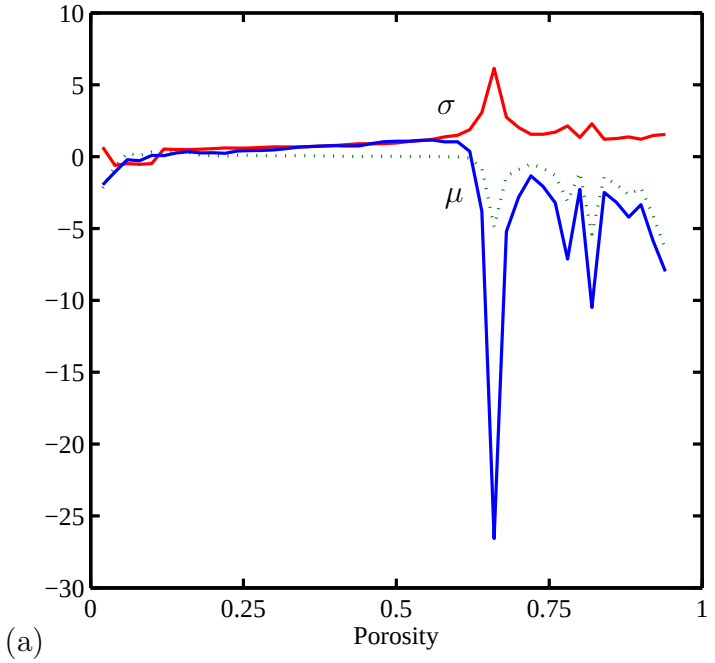

(a)

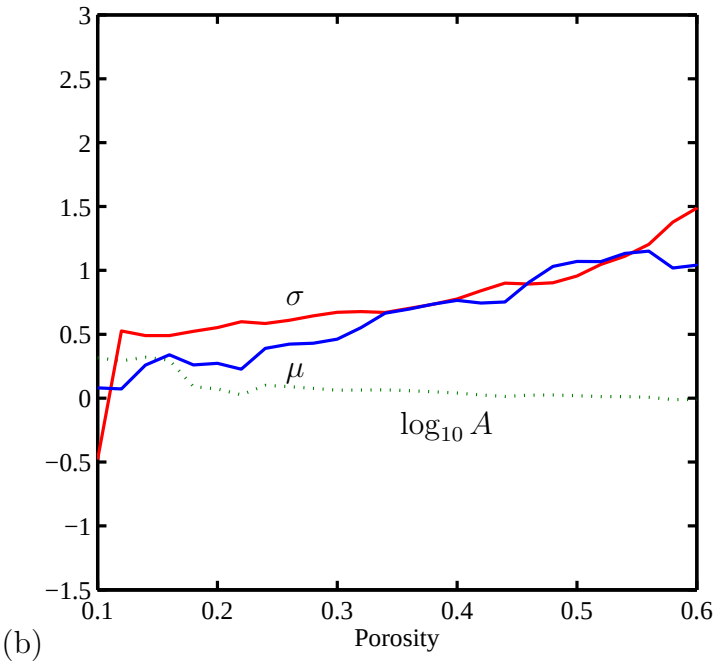

(b)

Figure G.4: Fit parameter development as a function of porosity f_t for domain 2000×2000. (a) Overview, (b) enlargement. The top line is σ, the bottom line is μ, and the dotted line is $\log_{10} A$. The large peaks appear at the percolation threshold of $f_c = 0.67$, which is the region where A begins to deviate significantly from $A = 1$.

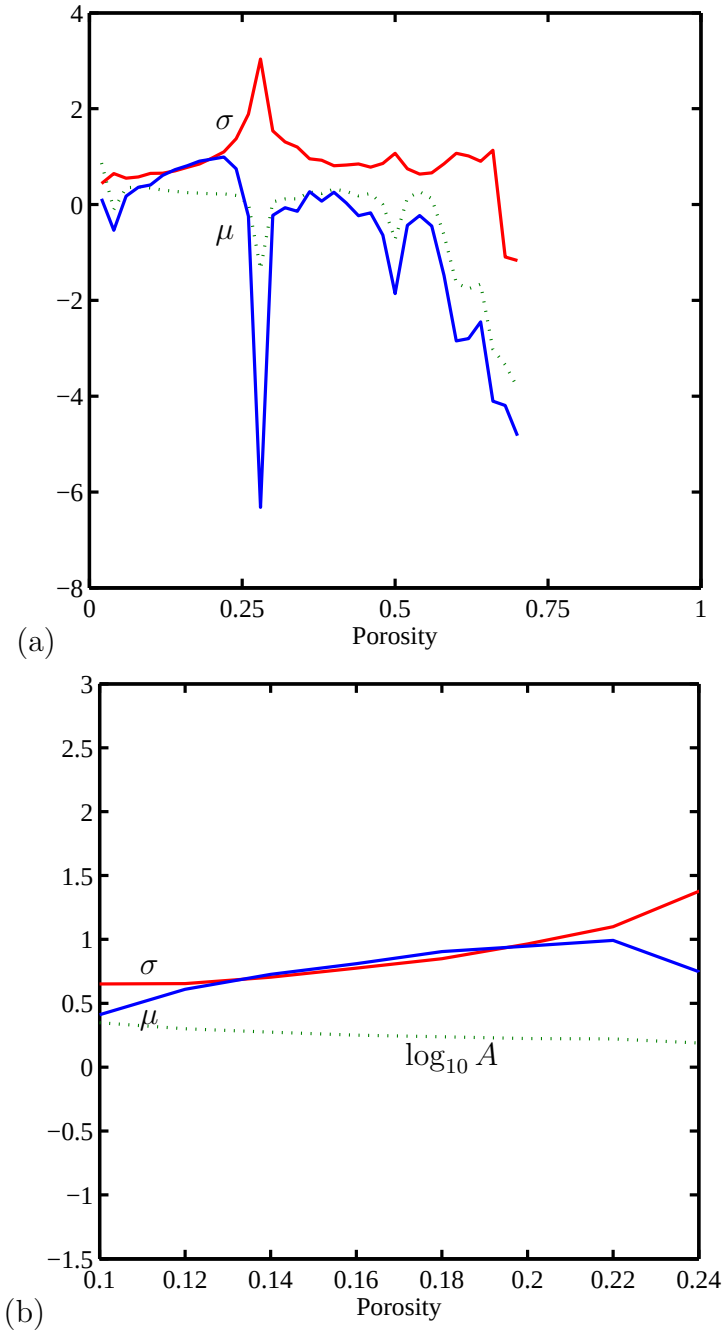

Figure G.5: Fit parameter development as a function of porosity f_t for domain $200 \times 200 \times 200$. (a) Overview, (b) enlargement. The top line is σ, the bottom line is μ, and the dotted line is $\log_{10} A$. The large peaks appear at the percolation threshold of $f_c = 0.28$, which is the region where A begins to deviate significantly from $A = 1$.

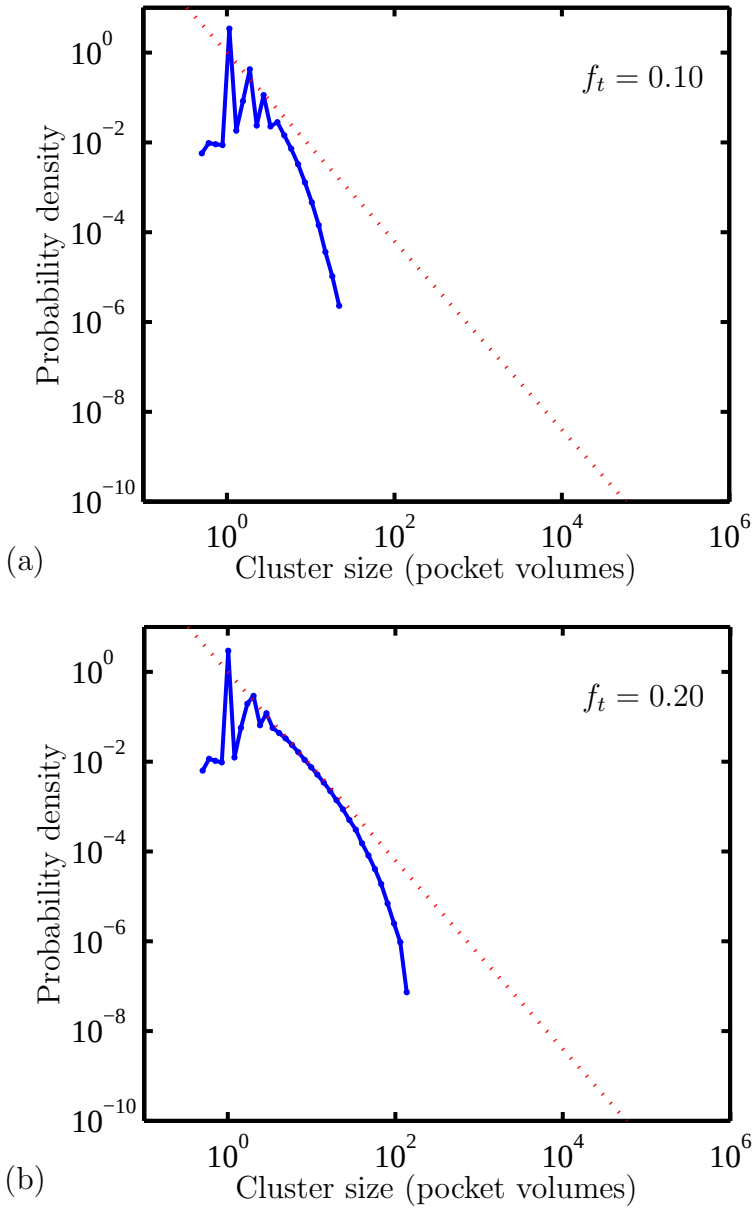

Figure G.6: Cluster size distribution of a domain $200 \times 200 \times 200$ at (a) $f_t = 0.100$, (b) $f_t = 0.200$.

$200 \times 200 \times 200$ at the percolation threshold $f_t = f_c = 0.276$ (370000 clusters) and at $f_t = 0.40$ ($N = 100000$ clusters), respectively. The dotted lines follow the function

$$\mathrm{PDF}(v) = v^{-2.1}, \tag{G.4}$$

where v is the cluster volume in multiples of pocket volumes. An exponent of -2.1 has been found by *Klug et al.* (2002) for example to describe the pore structure of volcanic products (*Gaonac'h et al.*, 2003). A power law size distribution can be expected in the presence of coalescence (*Gaonac'h et al.*, 1996; *Namiki et al.*, 2003).

The number density distribution (inclusions per volume), $N(V)$, of brine inclusions in sea ice with respect to inclusion volume, V, used by *Light et al.* (2004) at $-15\,^{\circ}\mathrm{C}$

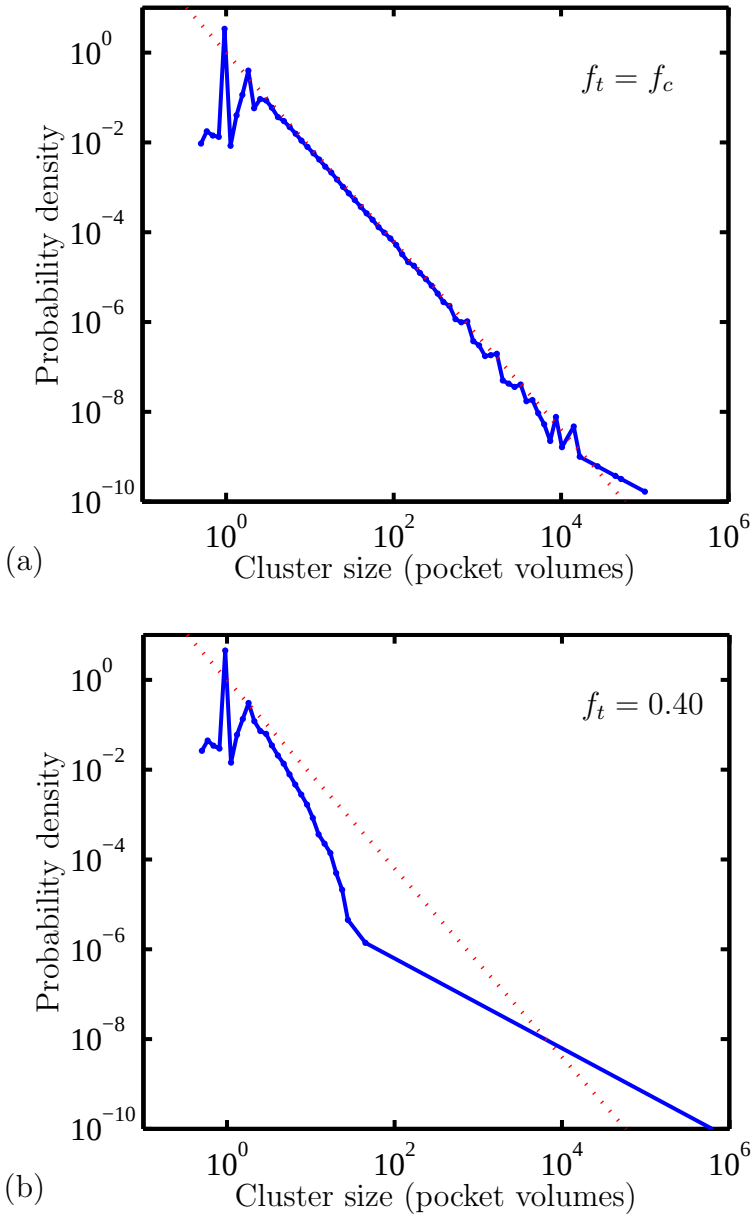

Figure G.7: Cluster size distribution of a domain $200 \times 200 \times 200$ at (a) $f_t = f_c = 0.276$, (b) $f_t = 0.400$.

follows a power law with exponent -1.1 that changes to -1.4 upon warming to $-1\,^{\circ}\mathrm{C}$, considering merging of inclusions.

G.3.3 Distribution in the sandwich model

Corresponding to the sandwich model in Section 5.4.3, Figure G.8 shows the cluster size distribution of a domain $192 \times 200 \times 200$ with brine layer width $b = 36$ at the percolation threshold ($N = 64750$ clusters). The dotted line again follows (G.4). The distribution is indistinguishable from the distribution in Figure G.7(a).

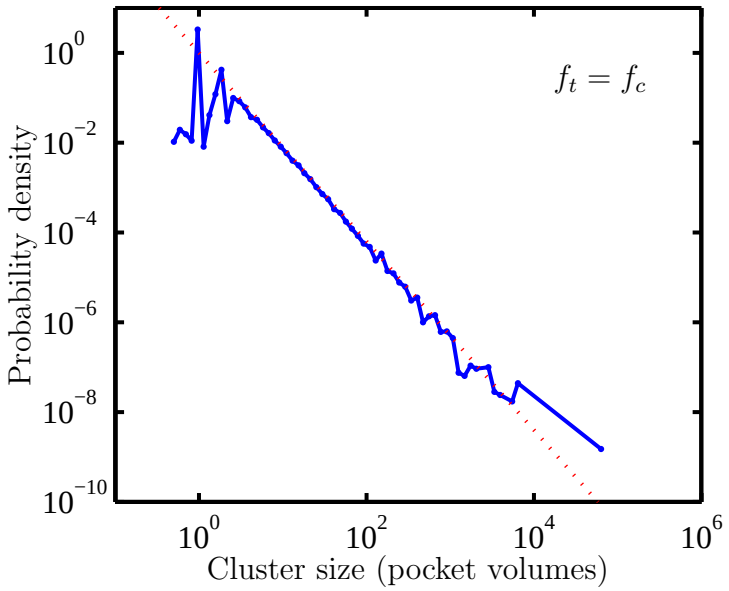

Figure G.8: Cluster size distribution at the critical porosity of a domain $192 \times 200 \times 200$ with brine layer width $b = 36$, $f_t = f_c = 0.0526$.

Table G.2: Coefficients for aligned anisotropic pockets. N is the number of realisations considered, $f_t - f_c$ is the interval used for fitting α and β.

a	domain size	N	f_c	$f_t - f_c$ (10^{-3})	α	β
17.3	$1200 \times 1200 \times 1200$	5	0.0542	$[3, 10]$	0.36	0.48
5	$100 \times 100 \times 100$	120	0.156	$[5, 20]$	0.81	0.50
5	$200 \times 200 \times 200$	109	0.156	$[5, 20]$	0.73	0.47
5	$500 \times 500 \times 500$	17	0.156	$[5, 20]$	0.64	0.43
2	$200 \times 200 \times 200$	41	0.249	$[20, 60]$	0.84	0.41

G.4 Anisotropic pockets

We will use a different pocket size distribution of the Monte Carlo model to estimate again a relationship between total porosity and effective porosity. It has been noted that anisotropic, ellipsoid pockets, randomly oriented and distributed throughout a domain, exhibit a critical porosity that decreases with increasing aspect ratio of the pockets (*Garboczi et al.*, 1995; *Yi and Sastry*, 2004). It has further been shown for the two dimensional case of ellipses that this effect is also observed if pockets are not oriented randomly but aligned with the rectangular domain boundaries, resulting in the same reduction of critical porosity as if orientation was continuous (*Xia and Thorpe*, 1988). However, it was shown in a precision study comparing aligned and randomly oriented squares and cubes that the critical porosity of randomly oriented pockets is lower by 6 %, and 22 %, respectively (*Baker et al.*, 2002).

We expect to be able to reduce the critical porosity with anisotropic, box shaped pockets aligned with the domain boundaries in a way similar to randomly oriented ellipsoids. However, a systematic investigation is beyond the scope of this thesis. We distribute anisotropic pockets of dimensions $a \times 1 \times 1$, $1 \times a \times 1$, and $1 \times 1 \times a$ randomly throughout a domain. The resulting effective porosity–total porosity relationships are shown in Table G.2. Coefficients α and β refer to the relationship between effective porosity, f_e, and total porosity, f_t, near the critical porosity, f_c,

$$f_e = \alpha \, (f_t - f_c)^\beta \quad \text{for} \quad f_t \gtrsim f_c. \tag{G.5}$$

For reference, with pocket aspect ratio $a = 17.3$ and a domain of $1200 \times 1200 \times 1200$, 5.5×10^6 pockets are present at the critical porosity of $f_c \approx 0.0542$.

The calculations are probably affected by finite size effects. This view is supported by the difference of the exponents from the expected value $\beta = 0.41$ in three dimensions, and by the notion that β approaches 0.41 as the linear domain size increases with respect to the pocket length a (shown for $a = 5$). One way of reducing finite size effects would be to make the y–direction periodic, and to test for wrapping of clusters in y–direction to determine percolation.

Appendix H

Latent heat of fusion

H.1 Latent heat of fusion of sea ice

Sea ice is a binary system that does not undergo a phase transition at one temperature but throughout the entire temperature range of its existence. A temperature change of sea ice is therefore always accompanied by a phase transition, which acts to increase the apparent heat capacity of sea ice (*Ono*, 1966). Using an expression for the apparent heat capacity of sea ice, temperature changes of sea ice can be calculated conveniently. However, this approach may complicate calculations if interest is not in temperature changes (mediated by the heat capacity) but in changes of the amount of sea ice (mediated by the latent heat of fusion). In the latter case the heat capacity is often ignored (cf. the Stefan problem) since it is rather small compared to the latent heat of fusion of ice. Under such circumstances it may be more convenient to fold the heat capacity of ice and brine into an apparent latent heat of fusion. A sea ice latent heat of fusion has been defined that accounts for both, phase transition and redistribution of heat between liquid and solid (*Yen*, 1981). We will derive an expression for effective latent heat of fusion of sea ice suitable for use with the fluid dynamics program. Section H.1.1 briefly presents the foundation of the expression for sea ice latent heat of fusion that finds common use in the literature. Section H.1.2 is concerned with the derivation of an effective latent heat relevant for the freezing process.

H.1.1 Sea ice latent heat

The sea ice heat capacity is the amount of energy needed to change the temperature of a mass of sea ice by a certain amount while the sea ice salinity remains constant. *Malmgren* (1927) introduces an expression for sea ice heat capacity as a function of heat capacities of ice, brine, water, and latent heat released since thermodynamic equilibrium between brine and ice demands that a change in sea ice temperature is accompanied by a phase transition. *Ono* (1966) simplifies the expression for the sea ice heat capacity of *Malmgren* by assuming a linear relationship between brine salinity and freezing temperature for $T > -8.2\,^{\circ}\mathrm{C}$ (the eutectic transition of $Na_2SO_4 \cdot 10H_2O$).

Without neglecting any terms, he obtains

$$c^\star = c_i - mL\frac{S_{ice}}{T^2} + (c_w - c_i - \beta)\frac{S_{ice}}{1000} - m\beta\frac{S_{ice}}{T}, \tag{H.1}$$

where c_i and c_w are the specific heat capacities of ice and water, respectively, $\beta \geq 0$ is the difference between specific heat capacity of water and brine, S_{ice} is the sea ice salinity in psu, T the temperature in °C, and $m < 0$ the slope of the liquidus. *Ono* continues to use a constant β, although he remarks that β is a function of temperature and salinity. The result of *Ono* (1966) as cited by *Yen* (1981) includes somewhat different terms. This could be due to a more sophisticated treatment of β by *Yen*, however, the reason is not discussed. *Yen* (1981) integrates the expression for sea ice heat capacity over temperature (from temperature T to complete melting) and calls the result the latent heat of fusion of sea ice. His expression is again a function of sea ice temperature T and sea ice salinity S_{ice}. The sea ice latent heat of *Yen* is therefore the heat that has to be added to a quantity of sea ice in order to raise the temperature of the sea ice to the melting point of brine of salinity S_{ice} plus the heat necessary to melt the ice. In particular, it is not the heat that has to be removed in order to form a quantity of ice *at* a given temperature T.

We will next derive an expression for the latent heat of sea ice similar to the one found by *Yen*. We will, however, assume that the dissolved solute has no influence on the capability of the brine to store heat. We further assume that although the solute depresses the freezing point, it does not contribute to the mass of the sea ice sheet. These two assumptions are consistent with the fluid dynamics model. Following *Yen* (1981), it is first assumed that the sea ice salinity remains constant upon temperature change. However, since sea ice *growth* is generally accompanied by a change of sea ice salinity due to brine rejection, we will further derive an expression for the latent heat of sea ice that accounts for the difference between the salinity of the ocean and the salinity of the sea ice.

H.1.2 Sea ice latent heat calculated

Starting with water of mass M that may contain solute (but the solute mass is not part of M) at the freezing temperature T_F, the enthalpy is simply

$$H_F = c_w T_F M. \tag{H.2}$$

We then form ice and cool the ice and the solute to temperature T. Using f_m to describe the mass fraction of the water, i.e. $(f_m\, M)$ is the mass of the water and $(1 - f_m)M$ is the mass of the ice, the enthalpy of the sea ice is

$$H_T = -L(1 - f_m)M + c_i T(1 - f_m)M + c_w T f_m\, M. \tag{H.3}$$

The heat that had to be removed can therefore be expressed as

$$-L^\star M = H_T - H_F, \tag{H.4}$$

where $L^\star$ is the effective sea ice latent heat of fusion during sea ice formation. Substituting (H.2) and (H.3) into (H.4) we find

$$L^\star = L(1 - f_m) - c_i T(1 - f_m) - c_w T f_m + c_w T_F, \tag{H.5}$$
$$= L - L f_m - c_i T - (c_w - c_i) T f_m + c_w T_F. \tag{H.6}$$

In the absence of desalination

Assuming thermodynamic equilibrium, we have

$$f_m = m \frac{S_{ice}}{T}, \quad \text{and} \tag{H.7}$$
$$T_F = m\, S_{ice}, \tag{H.8}$$

where S_{ice} is the salinity of the sea ice equal to the salinity of the surrounding water, and $m < 0$ is the slope of the liquidus. Equation (H.6) can then be written as

$$L^\star = L - c_i T + c_i\, m\, S_{ice} - L\, m \frac{S_{ice}}{T}. \tag{H.9}$$

Plugging in $L = 334 \times 10^3\,\mathrm{J\,kg^{-1}}$, $c_i = 2100\,\mathrm{J\,kg^{-1}\,K^{-1}}$, and $m = -0.054\,^\circ\mathrm{C\,psu^{-1}}$ it is with T in °C, S_{ice} in psu, and $L^\star$ in $\mathrm{J\,kg^{-1}}$

$$L^\star = 334 \times 10^3 - 2100\, T - 113\, S_{ice} + 18000 \frac{S_{ice}}{T}. \tag{H.10}$$

Equation (H.10) is essentially the equation suggested by *Yen* (1981) for practical purposes. An exact comparison is impossible since *Yen* does not elaborate on the origin of the terms and coefficients in his equation. The dominant term in (H.10) is usually the fourth term on the right hand side, which reduces the effective latent heat due to finite sea ice porosity (S_{ice}/T is proportional to f_m). The second term on the right hand side is the heat necessary to cool the solid, while the third term is an adjustment to this accounting for the fact that part of the sea ice is liquid. Note that (H.9) does not contain a reference to the heat capacity of the liquid, i.e. the heat stored in the liquid of mass M at T_F and the heat stored in the liquid of mass $(f_m\, M)$ at T are the same.

In the presence of desalination

Assuming thermodynamic equilibrium, we have

$$f_m = m \frac{S_{ice}}{T}, \quad \text{and} \tag{H.11}$$
$$T_F = m\, S_0, \tag{H.12}$$

where S_{ice} is the salinity of the sea ice and S_0 is the original salinity of the seawater. Equation (H.6) can now be written as

$$L^\star = L - L\,m\frac{S_{ice}}{T} - c_i T + c_i\,m\,S_{ice} + c_w\,m\,(S_0 - S_{ice}). \tag{H.13}$$

Since S_0 is generally known, we write

$$L^\star = L + c_w\,m\,S_0 - L\,m\frac{S_{ice}}{T} - c_i T - (c_w - c_i)\,m\,S_{ice}. \tag{H.14}$$

Plugging in $L = 334 \times 10^3\,\mathrm{J\,kg^{-1}}$, $c_i = 2100\,\mathrm{J\,kg^{-1}\,K^{-1}}$, $c_w = 4200\,\mathrm{J\,kg^{-1}\,K^{-1}}$, $S_0 = 34\,\mathrm{psu}$ and $m = -0.054\,^\circ\mathrm{C\,psu^{-1}}$ it is with T in °C, S_{ice} in psu, and $L^\star$ in $\mathrm{J\,kg^{-1}}$

$$L^\star = 326 \times 10^3 - 2100\,T + 113\,S_{ice} + 18000\frac{S_{ice}}{T}. \tag{H.15}$$

The latent heat of fusion of sea ice calculated from (H.15) is about 2 % smaller than the latent heat of fusion of sea ice calculated from (H.10) for common values of S_{ice} and T. Latent heat calculated from (H.10) is therefore too large during freezing, since ice formation starts at the freezing temperature of the ocean T_F irrespective of the final sea ice salinity S_{ice}.

The desalination process is accompanied by a heat transfer process, with hot seawater entering the sea ice and cold brine being rejected. However, we will not incorporate this advective process into an expression for the latent heat.